VORTEX-INDUCED VIBRATION OF A 5:1 RECTANGULAR CYLINDER

New Computational and Mathematical Modelling Approaches

Dinh Tung Nguyen, BEng (Hons)

Supervisors: Dr David M. Hargreaves and Dr John S. Owen

Department of Civil Engineering, Faculty of Engineering,

University of Nottingham

Thesis submitted to the University of Nottingham

for the degree of Doctor of Philosophy

May 9, 2017

Abstract

As a the limit-cycle oscillation, vortex-induced vibration (VIV) does not cause catastrophic failure but it can lead to fatigue in long and slender structures and structural elements, especially for long span bridges. Assessing this behaviour during the design stage is therefore very important to ensure the safety and serviceability of a structure. Currently, this task requires very time-consuming wind tunnel or computational simulation since a reliable mathematical model is not available. Moreover, knowledge of the underlying physical mechanism of the VIV and, particularly, of the turbulence-induced effect on the VIV is insufficient. Turbulence is normally considered to produce suppressing effects on the VIV; however, this influence appears to depend on cross sections and a comprehensive explanation is yet to be found. This issue can be resulted from some limitation that most wind tunnel or computational studies have used sectional models. The flow field is therefore dominated by 2D flow features.

In this research study, the 5:1 rectangular cylinder is selected as the case study since it is considered as the generic bride deck geometry. Using the wind tunnel at the University of Nottingham, a series of wind tunnel tests using a static and elastically supported sectional model is conducted in smooth flow. This wind tunnel study is complemented by a computational study of a static and dynamic sectional model; the computational simulations are carried out using the Computational Fluid Dynamics software OpenFOAM and the High Performance Computer system at the University of Nottingham. A Fluid-structure-interaction (FSI) solver is built to model the heaving VIV. By comparing the surface pressure measurement between these two studies, it uncovers the two separate flow mechanisms and associated flow features, which are both responsible for the VIV.

The series of wind tunnel static and dynamic tests is also repeated in different turbulent flow regimes. By analysing the forces, moment, surface pressure and structural response, it reveals the mechanism of the turbulence-induced effect on the aerodynamic characteristics as well as on VIV.

By improving the proposed FSI solver, a novel computational approach is introduced to simulate the VIV of a flexible 5:1 rectangular cylinder excited at the first bending mode shape. Employing the Proper

Orthogonal Decomposition (POD) technique and comparing against results of the sectional model, some emerging span-wise flow features are revealed together with their influences on the mechanism of the bending VIV.

The Hartlen and Currie mathematical model for the VIV is generalised so that it is able to simulate the VIV response of a 3D flexible structure. Such modifications and improvements are originated from and assessed by results of the computational simulation of the flexible model. A case study of the Great Belt East bridge is then carried out to verify this modified model.

Acknowledgements

Without the following individuals, it would be impossible for the complete this research study and the thesis.

My very sincere thanks go to my main supervisor **Dr David M. Hargreaves**. I would like to thank David for being the greatest supervisor ever, for giving guidance and inspiration on the computational study, for patiently providing endless support when I am in difficult situations, for always motivating and inspiring me when I feel depressed and for being a really good friend who always listen and give me advice on my importance decisions.

I am very grateful to my co-supervisor **Dr John S. Owen** for his inspiration throughout this research study, for his endless support and knowledge sharing, for his ability to make me think outside a box and look at a bigger picture and for the time and effort he has put into my wind tunnel tests.

I would like to thank the following people for their valuable supports

- James Meakin and Steve Lawton, for their understanding and wonderful help during the preparation stages of wind tunnel tests,
- James Derbyshire, for his contribution to the design and manufacturing the load cells,
- Prof. Dragos Axinte and his research group, in particularly, Alessio Spampinato, for their generous support and help me with the final tests of the wind tunnel study,
- Anh Ba Thai, for taking his time to be my laboratory assistant and to willingly help me during the challenging period of wind tunnel tests,
- Dr Joseph Genora and Dr Stephen Ambrose, my former CFD research peers, for the inspiring discussions about CFD and every other aspects of life.

I would like to express my gratitude to the University of Nottingham for awarding me the Dean of Engineering Research Scholarship for International Excellence so that I can pursuit this research study.

My special thanks go to my best friends in the UK and in Vietnam for being supportive and understanding to ease off pressure and stress throughout my study.

Last but not least, I want to thank my parents and my sister for their supports, trusts, encouragement and love, for always saying the truth to motivate me!

Table of Contents

Abstract i

Acknowledgements iii

Table of Contents v

List of Figures xi

List of Tables xix

1 Introduction 1

1.1 Background 1

1.2 Overview of Bridge Aeroelasticity 3

1.3 Aims and Objectives of Research 4

1.3.1 Aims of Research 4

1.3.2 Objectives and Methodology of Research 5

1.4 Organisation of the Thesis 6

2 Overview of Bridge Aeroelasticity 8

2.1 Overview of Turbulence 8

2.1.1 Nature of Turbulence 9

2.1.2 Descriptions of Turbulence 11

2.2 Aerodynamics of Flow Separation and Reattachment 14

2.3 Vortex Shedding from a Static Body 19

2.3.1 Circular Cylinder 19

2.3.2 Rectangular Cylinder 28

2.4 Vortex-induced Vibration (VIV) 36

2.4.1 Lock-in 36

2.4.2 Mass-damping Parameters 38

2.4.3 VIV of a Circular Cylinder 39

2.4.4 VIV of a Rectangular Cylinder . . . 44
2.5 Mathematical Modelling of Vortex-Induced Oscillation . . . 48
2.5.1 Single-degree-of-freedom Models for VIV . . . 49
2.5.2 Second-degree-of-freedom Models for VIV . . . 53
2.5.3 Summary of the Mathematical Models of VIV . . . 57
2.6 Flutter . . . 58
2.6.1 Mechanism of Classical Flutter . . . 58
2.6.2 Flutter Model . . . 59
2.6.3 Free-vibration Method of Finding Aerodynamic Derivatives . . . 61
2.6.4 Forced-vibration Method of Finding Aerodynamic Derivatives . . . 63
2.7 Buffeting . . . 65
2.7.1 Buffeting Model . . . 65
2.8 Turbulence Effects . . . 69
2.8.1 Effects of Turbulence on Bridge Aerodynamics . . . 69
2.8.2 Breakdown of Strip Assumption . . . 73
2.8.3 Turbulence-induced Stabilisation and Span-wise Coherence of Aerodynamic Forces and Moment . . . 75
2.9 Conclusion of the Chapter . . . 77

3 Computational Fluid Dynamics **79**
3.1 Navier-Stokes Equations . . . 79
3.2 Main Components of Computational Fluid Dynamics . . . 80
3.3 Discretisation Scheme . . . 81
3.3.1 Spatial Discretisation . . . 81
3.3.2 Equation Discretisation . . . 84
3.3.3 Temporal Discretisation . . . 85
3.4 Pressure-velocity Coupling Scheme . . . 86
3.5 Turbulence Modelling . . . 87
3.6 RANS Models . . . 88
3.6.1 RANS Equations . . . 88
3.6.2 k-ε Turbulence Model . . . 89
3.6.3 k-ω Turbulence Model . . . 90
3.6.4 Shear Stress Transport (SST) k-ω Turbulence Model . . . 91
3.6.5 Near-wall Modelling . . . 91
3.7 LES Models . . . 95
3.7.1 LES Equations . . . 95

3.7.2 Smagorinsky SGS Turbulence Model . . . 96
3.7.3 Dynamic Smagorinsky SGS Turbulence Model . . . 97
3.8 Fluid Structure Interaction . . . 99
3.8.1 Arbitrary Lagrangian-Eulerian Methods . . . 99
3.8.2 Dynamic Mesh Algorithm . . . 105
3.8.3 Coupling Schemes . . . 107
3.8.4 Discretisation . . . 113
3.9 Application of CFD in Bridge Aerodynamics and Aeroelasticity . . . 114
3.10 Conclusion of the Chapter . . . 118

4 Methodology: CFD Simulation 120
4.1 Introduction to OpenFOAM . . . 120
4.2 Mesh Generation . . . 122
4.2.1 Domain Geometry . . . 124
4.2.2 Computational Grid . . . 125
4.3 Static Simulation . . . 129
4.3.1 `constant` Directory . . . 129
4.3.2 `0` Directory . . . 130
4.3.3 `system` Directory . . . 131
4.4 Mesh Sensitivity Study . . . 135
4.4.1 Method . . . 136
4.4.2 Results . . . 136
4.5 Dynamic Simulation . . . 140
4.5.1 Fluid Solver . . . 140
4.5.2 Structural Solver . . . 142
4.5.3 Dynamic Mesh Algorithm . . . 148
4.5.4 Coupling Scheme . . . 150
4.5.5 `constant` Directory . . . 150
4.5.6 `0` Directory . . . 152
4.5.7 `system` Directory . . . 152
4.6 Proper Orthogonal Decomposition . . . 154
4.6.1 Overview of POD . . . 155
4.6.2 Mathematical Background . . . 156
4.6.3 OpenFOAM and MATLAB Implementation . . . 158
4.7 Conclusion of the Chapter . . . 161

5 Methodology: Wind Tunnel Experiments **163**

5.1 Overall Methodology 163

5.1.1 Static Test Procedure 167

5.1.2 Dynamic Test Procedure 169

5.2 Overview of Data Acquisition System 170

5.3 Velocity Measurement 173

5.3.1 Hot-wire Probes 173

5.3.2 Anemometer 176

5.3.3 X-wire Calibration 177

5.3.4 Measurement with the X-wire 181

5.4 Force and Moment Measurement - Strain-Gauge Approach 183

5.4.1 Design of Strain-gauge-based Load Cell 183

5.4.2 Calibration of Strain-gauge-based Load Cell 184

5.4.3 Measurement with Strain-gauge-based Load Cell 186

5.5 Force and Moment Measurement - Piezoelectric Approach 187

5.5.1 Design of Piezoelectric-based Load Cell 187

5.5.2 Calibration of Piezoelectric-based Load Cell 191

5.5.3 Measurement with Piezoelectric-based Load Cell 197

5.6 Pressure Measurement 199

5.7 Displacement Measurement 201

5.8 Investigation of Grid-generated Turbulence 203

5.8.1 Method 203

5.8.2 Results and Discussion 204

5.8.3 Mathematical Decay Profile 213

5.9 Conclusion of the Chapter 218

6 Results and Discussion **219**

6.1 Aerodynamics of Flow Field around a Static 5:1 Rectangular Cylinder 219

6.1.1 Force Coefficients and Strouhal Number 219

6.1.2 Investigation of Distribution and Correlation of Surface Pressure 227

6.2 Turbulence-induced Effects on Flow Field around a Static 5:1 Rectangular Cylinder . . . 233

6.3 VIV Mechanism of the 5:1 Rectangular Cylinder 239

6.3.1 Heaving VIV of the 5:1 Rectangular Cylinder 239

6.3.2 Pitching VIV of the 5:1 Rectangular Cylinder 248

6.4 Turbulence-induced Effects on VIV of the 5:1 Rectangular Cylinder 251

6.5 Further Analysis on Emerging Span-wise Flow Features and VIV Mechanism of the Bending 5:1 Rectangular Cylinder . . . 256
6.5.1 Emerging Span-wise Flow Features . . . 262
6.5.2 VIV Mechanism of the Bending 5:1 Rectangular Cylinder . . . 272
6.6 Conclusion of the Chapter . . . 274

7 Theoretical Modelling of VIV **278**
7.1 Introduction . . . 278
7.2 3D Complete Hartlen and Currie Model . . . 279
7.2.1 Structural Equation . . . 279
7.2.2 Fluid Equation . . . 281
7.2.3 Application of 3D Complete Hartlen and Currie Model . . . 282
7.3 3D Fully-correlated Hartlen and Currie Model . . . 290
7.3.1 Mathematical Development . . . 290
7.3.2 Application and Validation . . . 292
7.4 3D Partly-correlated Hartlen and Currie Model . . . 294
7.5 Investigation of Analytical Solutions of the Hartlen and Currie Model . . . 295
7.6 Parameter Optimisation Process . . . 298
7.6.1 Parametric Study . . . 298
7.6.2 Iterative Parameter Estimating Process . . . 300
7.6.3 Surface-searching-based Parameter Optimisation Process . . . 304
7.7 Application of Parameter Optimisation Process . . . 305
7.7.1 Application of Iterative Parameter Estimating Process . . . 306
7.7.2 Application of Surface-searching-based Parameter Optimisation Process . . . 310
7.8 Comparison of Hartlen and Currie Model Parameters . . . 319
7.9 Application of 3D Hartlen and Currie Models . . . 321
7.10 Case Study of the Great Belt East Bridge to Verify the Proposed Improvement on the Hartlen and Currie Model . . . 322
7.10.1 Great East Belt Bridge . . . 322
7.10.2 Full-scale Measurement of the Great Belt East Bridge . . . 323
7.10.3 Wind Tunnel Sectional Model Test of the Great Belt East Bridge . . . 326
7.10.4 Identification of Model Parameters of the Hartlen and Currie Model . . . 328
7.10.5 Prediction of Full-scale VIV Responses of the Great Belt East Bridge . . . 331
7.10.6 Summary of the Case Study of the Great Belt East Bridge . . . 333
7.11 Conclusion of the Chapter . . . 334

8 Conclusion 336

8.1 Summary . . . 336

8.2 Findings and Observation . . . 338

8.3 Conclusions . . . 341

8.4 Potential Areas for Future Research . . . 341

References 343

Appendix A OpenFOAM Source Files and MATLAB Scripts 360

A.1 OpenFOAM Source Files . . . 360

A.1.1 `dynamicHeavingFreeUDFFvMesh.C` . . . 360

A.1.2 `dynamicBendingFreeUDFFvMesh.C` . . . 368

A.2 MATLAB Scripts . . . 378

A.2.1 POD Pre-processing - Data Sorting . . . 378

A.2.2 POD Pre-processing - Data Assembling . . . 382

A.2.3 POD Processing . . . 384

Appendix B Wind Tunnel Standard Operating Procedure 387

Appendix C Force Measuring Systems 391

C.1 Detailed Design of Strain-gauge based Load Cells . . . 391

C.2 Calibration Graphs of Strain-gauge based Load Cells . . . 392

C.3 Detailed Design of Piezoelectric based Load Cells . . . 396

C.4 Calibration Results of Piezoelectric based Load Cells . . . 406

C.4.1 Angle of Attack $\alpha = 2°$ . . . 406

C.4.2 Angle of Attack $\alpha = 4°$ . . . 407

C.4.3 Angle of Attack $\alpha = 6°$ . . . 408

C.4.4 Angle of Attack $\alpha = 8°$ . . . 409

Appendix D Supplementary Results 410

D.1 Surface Pressure Distribution around a Static 5:1 Rectangular Cylinder in the Smooth Flow 411

D.2 Surface Pressure Distribution around a Static 5:1 Rectangular Cylinder in the Turbulent Flow . . . 415

List of Figures

1.1 The Tacoma Narrows Bridge (Engineering.com-Library, 2006). 2

1.2 Collapse of the Tacoma Bridge (Hodgkinson and Cooper, 2008). 2

2.1 Kolmorogov's ranges of length scale; the length scale increases from left to right. 11

2.2 Power spectral density functions for the alongwind component (Dyrbye and Hansen, 1999). 15

2.3 Overall flow field around a airfoil at a low angle of attack (Houghton and Carpenter, 2008). 16

2.4 Velocity profiles at different chordwise positions along the airfoil (Houghton and Carpenter, 2008). 16

2.5 Development of the boundary layer around a thin flat plate (Houghton and Carpenter, 2008). 17

2.6 Velocity profiles of laminar and turbulent boundary layers (Houghton and Carpenter, 2008). 17

2.7 Flow separation over a streamlined body (Houghton and Carpenter, 2008). 18

2.8 Wake formation behind a circular cylinder (Simiu and Scanlan, 1996). 20

2.9 The Strouhal number of a circular cylinder (Lienhard, 1966). 21

2.10 The Strouhal number of a circular cylinder (low Reynolds numbers) (Williamson, 1992). . 22

2.11 A transition in the vortex shedding mode as the Reynolds number increases (Williamson, 1989). 25

2.12 Visualisation of different vortex shedding modes (Williamson, 1989). 26

2.13 Evolution of the vortex loop in the mode A vortex shedding (Williamson, 1988b). 27

2.14 Flow field of the mode B vortex shedding (Williamson, 1988b). 28

2.15 Symmetry of the mode A and mode B vortex shedding (Williamson, 1997). 28

2.16 Vortex shedding of a $B/D = 8$ rectangular prism (Ohya et al., 1992). 29

2.17 Streamlines around a $B/D = 4$ rectangular prism (Ohya et al., 1992). 30

2.18 The Strouhal number of a $B/D = 2$ rectangular prism (Okjima, 1982). 31

2.19 Variation of Strouhal number against aspect ratios. 32

2.20 Variation of Strouhal number against aspect ratios (Nakamura et al., 1991). 33

2.21 Time series of the lift coefficient C_L for the $B/D = 8$ rectangular cylinder (Ozono et al., 1992) 33

2.22 Flow field around a $B/D = 8$ rectangular cylinder (Ozono et al., 1992) 34

2.23 The Strouhal number of the rectangular cylinder having $B/D = 6$ to 10 (Mills et al., 2003). 35

2.24 Description of the VIV lock-in. 37

2.25 The VIV of a freely vibrating circular cylinder (Govardhan and Williamson, 2000). 41

2.26 Vorticity in the wake region of a vibrating circular cylinder (Govardhan and Williamson, 2000). 42

2.27 Vorticity in the wake region at every quarter-cycle (Govardhan and Williamson, 2000). . . 43

2.28 Comparison of the vorticity in the wake region (Govardhan and Williamson, 2000). 43

2.29 Motion-induced vortex in the heaving and pitching VIV response (Matsumoto et al., 2008). 47

2.30 Variation of the Ehsan and Scanlan model parameters (Ehsan and Scanlan, 1990). 51

2.31 Variation of the Ehsan and Scanlan model parameters (Ehsan and Scanlan, 1990). 52

2.32 Comparison of the Griffin plots (Marra et al., 2015). 53

2.33 Variation of the Ehsan and Scanlan model parameters (Marra et al., 2015). 53

2.34 Flutter mechanism, adopted from Houghton and Carruthers (1976). 59

2.35 Bridge deck in the wind field. 60

2.36 Effects of torsional amplitude on flutter derivatives (Noda et al., 2003). 64

2.37 Frequency-domain analysis of Davenport (1962b). 66

2.38 Pressure amplitude and phase distribution in smooth and turbulent flow (Haan and Kareem, 2009). 71

2.39 Pressure phase diagram in a relation to the formation of the motion-induced shear layer; adopted from (Haan and Kareem, 2009). 72

2.40 $C_p^* \sin(\psi)$ plotted versus stream-wise position (Haan and Kareem, 2009). 72

2.41 Root coherence spectrum of the buffeting lift force on a rectangular prism (Kimura et al., 1997). 75

2.42 Cross correlation coefficient of the self-excited lift force (Haan and Kareem, 2007). 76

2.43 Cross correlation coefficient of the buffeting lift force (Haan and Kareem, 2007). 76

3.1 An example of a 2D computational domain. 81

3.2 An example of a control volume. 82

3.3 An example of a 2D block-structured grid (Sun et al., 2008). 83

3.4 Close-up of the grid shown in Figure **??** (Sun et al., 2008). 83

3.5 A triangular unstructured grid for a simulation of a airfoil (Versteeg and Malalasekera, 2007). 84

3.6 General boundary layer structure next to the wall. 92

3.7 Interaction of three domains in the ALE description, adopted from Donea et al. (2004). . 103

3.8 Examples of the Lagrangian, Eulerian and ALE description, adopted from Donea et al. (2004). 104

3.9 Conventional serial staggered algorithm. 108

3.10 Conventional serial staggered algorithm with subcycling. 109

3.11 Sub-iteration procedure. 110

3.12 Improved serial staggered algorithm. 111

3.13 Conventional parallel staggered algorithm. 112

3.14 Improved parallel staggered algorithm. 112

3.15 Three bridge deck sections used in the 3D CFD simulation by Bai et al. (2013). 116

3.16 Flutter derivatives of section G1 (Bai et al., 2013). 117

4.1 Typical file structure of a OpenFOAM case. 122

4.2 Domain geometry and boundary conditions of selected patches. 124

4.3 Dimensions of the computational domain geometry. 126

4.4 The computational grid in the x-z plane. 127

4.5 Schematic diagram of the 3D flexible model. 128

4.6 The computational grid used in the 3D heaving simulation. 128

4.7 Variability of the Strouhal number against the filtering width. 137

4.8 Variability of the surface pressure in a comparison against BARC data 139

4.9 Variation of the analytical solutions at different damping ratios. 145

4.10 Variation of the numerical solutions at different damping ratios (backward Euler method). 146

4.11 Variation of the numerical normalised amplitude at different damping ratios (other methods). 146

4.12 Flow chart of the member function in the source codes `dynamicBendingFreeUDFFvMesh.C`. 147

4.13 Illustration of 9 different blocks in the computational domain. 149

4.14 File structure of the directory `PODPressure`. 160

5.1 Selected aspects of the wind tunnel's hardware. 164

5.2 Details of the turbulence generating grids. 165

5.3 Selected components of the wind tunnel sectional model. 166

5.4 Arrangement of pressure taps on the wind tunnel model. 167

5.5 The clamping blocks are attached on the frame and inside the model. 168

5.6 The model is supported on an aluminium frame rigidly clamped inside the wind tunnel. . 168

5.7 Schematic of the set-up of the dynamic test. 170

5.8 Accelerometers are mounted on the perspex plates via nylon spacers. 170

5.9 Overall data acquisition system. 171

5.10 General structure of a VI file. 172

5.11 Typical HWA system (Jorgensen, 2002). 173
5.12 Detailed dimension of the TSI X-wire 1241-T1.5 (TSI-Incorporated, 2003). 175
5.13 Relationship between the orientation angle and the angles between sensors and the flow. . 175
5.14 Wheatstone bridge circuit of the IFA-300 CTA, adopted from TSI-Incorporated (2010a). . 177
5.15 Built-in signal conditioning circuit (TSI-Incorporated, 2010a) 178
5.16 Set-up diagram of the IFA-300 CTA system. 178
5.17 Main components of the TSI 1127 calibrator unit, adopted from TSI-Incorporated (2010b). 179
5.18 Iterative process to calculate the King's Law and yaw coefficients. 180
5.19 Results of the velocity calibration. 181
5.20 Results of the directional calibration. 182
5.21 Fitting errors of the velocity calibration. 182
5.22 Fitting errors of the directional calibration. 183
5.23 The coordinate system of and the layout of the strain gauges on the load cell. 184
5.24 Set-up of the static calibration of the load cell. 186
5.25 Schematic diagram of the set-up of the load cells and the wind tunnel model. 187
5.26 The arrangement of three force sensors in one load cell and the cantilever mechanism. . . 189
5.27 Results of the optimisation study of the piezoelectric load cells. 190
5.28 Selected aspects involving the arrangement and set up of the piezoelectric load cells. . . . 192
5.29 Schematics of the data acquisition system used for the piezoelectric load cells. 193
5.30 Corrections of a force output from the piezoelectric load cells. 195
5.31 Results of the calibration of the piezoelectric load cells; the angle of attack 0°. 196
5.32 The HCLA02X5DB pressure transducer contains two pressure ports. 200
5.33 The reference pressure box with taps to provide the reference pressure to all transducers. 201
5.34 Schematic arrangement of accelerometers. 201
5.35 Position of the velocity measurement. 204
5.36 Variation of turbulence intensities with distance from Grid A at $2\,\mathrm{m\,s^{-1}}$. 205
5.37 Variation of turbulence intensities with distance from Grid A at $4\,\mathrm{m\,s^{-1}}$. 206
5.38 Variation of turbulence intensities with distance from Grid A at $6\,\mathrm{m\,s^{-1}}$. 206
5.39 Variation of turbulence length scale with distance from Grid A at $2\,\mathrm{m\,s^{-1}}$. 207
5.40 Variation of turbulence length scale with distance from Grid A at $4\,\mathrm{m\,s^{-1}}$. 207
5.41 Variation of turbulence length scale with distance from Grid A at $6\,\mathrm{m\,s^{-1}}$. 208
5.42 Variation of turbulence intensities with distance from Grid B at $2\,\mathrm{m\,s^{-1}}$. 210
5.43 Variation of turbulence intensities with distance from Grid B at $4\,\mathrm{m\,s^{-1}}$. 210
5.44 Variation of turbulence intensities with distance from Grid B at $6\,\mathrm{m\,s^{-1}}$. 211
5.45 Variation of turbulence length scale with distance from Grid B at $2\,\mathrm{m\,s^{-1}}$. 211

5.46 Variation of turbulence length scale with distance from Grid B at $4\,\mathrm{m\,s^{-1}}$. 212
5.47 Variation of turbulence length scale with distance from Grid B at $6\,\mathrm{m\,s^{-1}}$. 212
5.48 Fitting of the mathematical model on the turbulence intensity developed by Grid A. . . . 215
5.49 Fitting of the mathematical model on the turbulence length scale developed by Grid A. . 216
5.50 Fitting of the mathematical model on the turbulence intensity developed by Grid B. . . . 216
5.51 Fitting of the mathematical model on the turbulence length scale developed by Grid A. . 217

6.1 The forces and moment coefficients and the Strouhal number against the Reynolds number. 221
6.2 The forces and moment coefficients against the angle of attack. 222
6.3 Comparison of the Strouhal number identified from two different methods. 222
6.4 The power spectral density of the lift force. 225
6.5 Isosurfaces of the Q-criterion around the model and in the wake region. 226
6.6 Variability of the surface pressure with respect to the Reynolds number; the angle of attack $0°$. 228
6.7 Span-wise correlation of the surface pressure at the Reynolds number of 31200. 229
6.8 Span-wise correlation of the surface pressure predicted by the static simulation. 230
6.9 Span-wise coherence of the surface pressure predicted by the static simulation. 230
6.10 Variation of the surface pressure distribution with respect to the angle of attack; Re = 52000. 232
6.11 Surface pressure distribution in different flow conditions; Re = 52000. 234
6.12 Effect of turbulence levels on the span-wise pressure correlation. 235
6.13 Surface pressure distribution in the turbulent flow; Re = 52000. 236
6.14 Variability of the span-wise pressure correlation on the bottom surface in the turbulent flow. 237
6.15 Variability of the span-wise pressure correlation on the bottom surface in the turbulent flow. 238
6.16 Results of the wind tunnel dynamic test of the sectional model restrained to the heaving mode. 240
6.17 Results of the 3D heaving simulation of the sectional model. 241
6.18 Phase angles of vortices rolling on the surface of the cylinder in the heaving VIV lock-in. . 242
6.19 Contour plots of the Q-criterion along the mid-span plane from the 3D heaving simulation. 243
6.20 Wind tunnel results of the span-wise pressure correlation. 245
6.21 Computational results of the span-wise pressure correlation. 246
6.22 Pressure field on the top surface of the cylinder in 3D heaving simulation. 247
6.23 The development of the motion-induced leading-edge vortex during the heaving VIV lock-in. 248
6.24 Results of the wind tunnel dynamic test of the sectional model restrained to the pitching mode. 249
6.25 Phase angles of vortices rolling on the surface of the cylinder in the pitching VIV lock-in. 250

6.26 Wind tunnel results of the span-wise pressure correlation. 251
6.27 The development of the motion-induced leading-edge vortex during the pitching VIV lock-in. 251
6.28 The heaving and pitching response of the cylinder at different turbulence levels. 252
6.29 Examples of time-histories of the heaving acceleration. 253
6.30 Wind tunnel results of the span-wise pressure correlation in turbulent flow (heaving). . . . 254
6.31 Wind tunnel results of the span-wise pressure correlation in turbulent flow (pitching). . . 255
6.32 Results of the 3D bending simulation of the flexible model. 257
6.33 Contour plots of the time-averaged pressure coefficient. 258
6.34 Contour plots of the standard deviation of the time-varying pressure coefficient. 258
6.35 Surface pressure distribution at different span-wise positions. 258
6.36 Power spectral densities of the lift forces at different span-wise positions. 259
6.37 Power spectral densities of the velocity measured in the wake at different span-wise positions. 260
6.38 Span-wise distribution of the dominant fluctuating flow features. 261
6.39 Variability of the power spectral densities of the POD coefficients. 263
6.39 Variability of the power spectral densities of the POD coefficients (continued). 264
6.40 The oblique vortex shedding mode observed on the flexible cylinder. 267
6.41 Q-criterion of the flow field around the flexible cylinder. 268
6.42 Variation of the span-wise pressure gradient on the top surface of the flexible cylinder. . . 269
6.43 Two phase-averaged profiles of the flow field along the span-wise line. 270
6.44 The arrangement of two pairs of the stream-wise vortices. 271
6.45 Span-wise variability of C'_L and ϕ_{F_L-z} in case of the flexible cylinder. 273

7.1 Comparison of the structural response of a 3D flexible circular cylinder having a unit mode shape. 284
7.2 Results of the 3D complete Hartlen and Currie model; the first bending mode shape. . . . 287
7.3 Results of the 3D complete Hartlen and Currie model; the second bending mode shape. . 288
7.4 Results of the 3D complete Hartlen and Currie model; the third bending mode shape. . . 289
7.5 Comparison of the 3D fully-correlated and 3D complete Hartlen and Currie models. . . . 293
7.6 Comparison of the time-integrated and analytical solutions. 297
7.7 Dependence between the model parameters and the VIV response of the cylinder. 299
7.8 Flow chart describing the iterative estimating process of the parameter b. 301
7.9 Flow chart describing the iterative estimating process of the parameters α and γ. 303
7.10 Flow chart describing the surface-searching-based optimisation process of the parameters α and γ. 304
7.11 Comparison of results of the heaving simulation against analytical and time-integrated solutions. 308

7.12 Plots of the surface A of the peak response during the lock-in. 312
7.13 Relationship between the error quantity $E_{\alpha,\gamma}$ with respect to the parameters α and γ. . . 313
7.14 Comparison of results of the heaving simulation against analytical and time-integrated solutions. 314
7.15 Plots of the surface A of the peak response during the lock-in. 316
7.16 Relationship between the error quantity $E_{\alpha,\gamma}$ with respect to the parameters α and γ . . 317
7.17 Comparison of results of the WT test against analytical and time-integrated solutions. . . 318
7.18 Comparison of the Griffin plots derived from the computational and wind tunnel studies. 320
7.19 Comparison of the Griffin plots predicted by the modified Hartlen and Currie models. . . 322
7.20 Key dimensions of the Great East Belt Bridge (Weight, 2009). 323
7.21 Primary mode shapes of the Great Belt East bridge (Frandsen, 2001). 324
7.22 The wind tunnel sectional model test of the Great Belt East bridge. 327
7.23 Results of the wind tunnel sectional model test of the Great Belt East bridge. 327
7.24 Comparison between results of the wind tunnel test and the analytical solution. 329
7.25 Surface of the maximum structural response during the lock-in. 329
7.26 Variability of the error between the wind tunnel test and the Hartlen and Currie model. . 330
7.27 Comparison of the response at the mid-span predicted by the modified Hartlen and Currie models. 332
7.28 Comparison of the Giffin plots of the VIV response at the mid-span. 333

C.1 Detailed drawing of the load cell. 391
C.2 Detailed layout of the strain gauges. 392
C.3 Calibration graph of Case 1 of the load cell 1. 392
C.4 Calibration graph of Case 2 of the load cell 1. 393
C.5 Calibration graph of Case 3 of the load cell 1. 393
C.6 Calibration graph of Case 4 of the load cell 1. 394
C.7 Calibration graph of Case 1 of the load cell 2. 394
C.8 Calibration graph of Case 2 of the load cell 2. 395
C.9 Calibration graph of Case 3 of the load cell 2. 395
C.10 Calibration graph of Case 4 of the load cell 2. 396
C.11 Results of the calibration of the piezoelectric load cells; the angle of attack 2°. 406
C.12 Results of the calibration of the piezoelectric load cells; the angle of attack 4°. 407
C.13 Results of the calibration of the piezoelectric load cells; the angle of attack 6°. 408
C.14 Results of the calibration of the piezoelectric load cells; the angle of attack 8°. 409

D.1 Variability of the surface pressure with respect to the Reynolds number; the angle of attack 2°. 411
D.2 Variability of the surface pressure with respect to the Reynolds number; the angle of attack 4°. 412
D.3 Variability of the surface pressure with respect to the Reynolds number; the angle of attack 6°. 413
D.4 Variability of the surface pressure with respect to the Reynolds number; the angle of attack 8°. 414
D.5 Surface pressure distribution in different flow conditions; Re = 41600. 415
D.6 Surface pressure distribution in different flow conditions; Re = 31200. 416
D.7 Surface pressure distribution in different flow conditions; Re = 20800. 417
D.8 Surface pressure distribution in the turbulent flow; Re = 52000. 418
D.9 Surface pressure distribution in the turbulent flow; Re = 52000. 419

List of Tables

3.1 Meaning of terms in Equation ??. 85

4.1 Summary of the face sizing and edge sizing of the computational grid. 126

4.2 Summary of span-wise discretisation $\Delta y/B$, number of cells and boundary conditions of y patches in three different simulations. 128

4.3 Computational grids in the mesh sensitivity study. 136

5.1 Distance between the array of pressure taps and the centre line of the model. 167

5.2 Variation of the Reynolds stresses with the wind speed at four distances away from Grid A. 209

5.3 Variation of the Reynolds stresses with the wind speed at four distances away from Grid B. 213

5.4 Summary of selected characteristics of turbulence generated from Grid A. 214

5.5 Summary of selected characteristics of turbulence generated from Grid B. 214

5.6 Summary of selected turbulent flow regimes for wind tunnel tests. 218

6.1 Variability of C_L' against the angle of attack and the Reynolds number. 225

6.2 Comparison of force coefficients and Strouhal number. 226

7.1 Summary of the results of the parametric study as the model parameter increased (symbol $-$ means no effects). 299

7.2 Variability of the final results of the model parameter b and the converging error E_b with respect to the initial guess b_1. 309

7.3 Variability of the final results of the model parameters α and γ, the converging error $E_{\alpha,\gamma}$ and the percentage difference $E_{location}$ with respect to the initial guesses α_1 and γ_1. . . . 309

7.4 Summary of the Hartlen and Currie model parameters estimated using results obtained from the wind tunnel test and the computational simulation 319

7.5 Natural frequencies, maximum root-mean-spared (r.m.s) vertical displacements recorded at the main span during the lock-in and damping ratios associated with each primary mode which was observed during the full-scale measurement; data was extracted from Frandsen (2001). 324

Chapter 1

Introduction

1.1 BACKGROUND

Long-span bridges are certainly a marvel of civil engineering; the structures featuring tall towers and slender large spans supported by cables attract a lot of admiration. These very characteristics, however, highlight the downside of long-span bridges, which is a reduction in stiffness and high susceptibility to wind loading. Wind-induced oscillation has therefore become a major issue; this well-known phenomenon was responsible for the collapse of several bridges throughout the world in the last 200 years.

Levy and Salvadori (2002) reported, in 1836, a moderate wind speed caused a serve damage to the Chain Pier at Brighton, making headlines as one of the first wind-related incidents recorded in the UK. About 40 years later, the collapse of Tay Rail Bridge in 1879 raised an alarm and exposed the major weakness of British civil engineering which, based on Martin and Macleod (1995), was the lack of awareness of wind load in bridge design. American engineers, who spent more efforts on wind load on bridge decks, were still having trouble ensuring the safety and serviceability of bridges. After completion in 1937, the Golden Gate Bridge was soon stiffened by trusses after it exhibited some large oscillations induced by the wind. The collapse of the Tacoma Narrows Bridge (Figure 1.1) in 1940, finally, drew attention to the need of in-depth study and more appropriate design codes for the wind-induced response of bridges.

The collapse of the Tacoma Bridge (Figure 1.2) has produced a lasting impact on civil engineers in terms of technical, economic and ethical implication in bridge designs. Collings (2008) reported, following this disaster, the additional stiffening trusses were approved to install to a number of bridges constructed prior to 1940. Blockley (1980) emphasised the importance of the wind tunnel in the design phase to ensure the dynamic characteristics of suspension bridges avoiding similar failures in the future. On top of that, the Tacoma Bridge also inspired researchers to find and understand the failure mechanism, which laid the foundation for the development of research into bridge aeroelasticity.

Figure 1.1: The Tacoma Narrows Bridge (Engineering.com-Library, 2006).

Figure 1.2: Collapse of the Tacoma Bridge (Hodgkinson and Cooper, 2008).

1.2 OVERVIEW OF BRIDGE AEROELASTICITY

Bridge aeroelasticity is defined as an interaction between the inertia of a bridge deck and the elastic and aerodynamic forces acting on it. Mathematically, this relationship can be expressed as

$$M\ddot{\mathbf{x}} + c\dot{\mathbf{x}} + k\mathbf{x} = \mathbf{F}_a(U, \dot{\mathbf{x}}(t), \mathbf{x}(t)) + \mathbf{F}_e(t), \tag{1.1}$$

where M, c and k are the mass, damping and stiffness of bridge deck; they represent the dynamic characteristics of the system. $\mathbf{F}_a$ is the aerodynamic forces applied on the bridge deck; these loads depend on the averaged wind speed, U, and the motion of the system, which is expressed via the displacement, $\mathbf{x}(t)$, and the velocity of motion, $\dot{\mathbf{x}}(t)$. The final term is the external force, $\mathbf{F}_e(t)$, which is independent of the motion of structure; in turbulent flow, this force can arise due to a gust in the oncoming wind.

The aerodynamic forces, $\mathbf{F}_a$, are very complicated to understand and quantify due to the nature of the bridge deck. Unlike a streamlined body, which is characterised by smooth and attached flow conditions, the bridge deck is classified as a bluff body with sharp edges leading to separation of the flow and continuous variation of pressure on its surface. This unsteady condition around the bridge deck is completely described by the highly non-linear Navier-Stokes equations. In addition, bridge aeroelasticity is characterised by the turbulence in the oncoming wind, which appears in Equation 1.1 via $\mathbf{F}_e(t)$. Scanlan (1997) and Haan and Kareem (2007) have found the turbulence in the wind produces significant effects on the flow condition around the bridge deck and, thus, on the aerodynamic behaviour of the structure.

The wind tunnel is the most well-known and frequently-used approach and has been used frequently to investigate bridge aeroelasticity. This approach involves the construction of a scaled physical model, which can be a 3D full aeroelastic model or a 3D sectional model. The former is a small-scale representation of a real structure with some minor and unimportant details being neglected; on the other hand, the latter just captures a short section of the structure. They are compared in detail by Walshe (1977). The model is then subjected to the flow generated in the wind tunnel; pressure tappings and pressure transducers are commonly used to extract pressure distribution for further analysis. The main disadvantage of this method is the high cost due to building models and running wind tunnels, particularly for the full aeroelastic models; the sectional models are thus normally tested. The results from the wind tunnel tests using sectional models have been showed to be sufficient predicting most behaviours of full-scale bridges. However, Haan and Kareem (2009) showed that the sectional model was not capable of fully predicting the response of bridge decks in turbulent wind, due to the finite span-wise length and the dominance of 2D flow features; the use of longer sectional models or even full-aeroelastic models is required to further investigate this situation.

Thanks to the advances in computational technology, Computational Fluid Dynamics (CFD) has been extensively used for modelling bridge aeroelasticity. This method is considerably cheaper than the use of wind tunnels; however it is very computationally demanding to simulate full aeroelastic bridge models. Even with the current computational power, the use of CFD has only been developed for 2D models or short 3D sectional models. In addition, results are very dependent on numerical schemes; it can yield results which are very different from the wind-tunnel tests. Therefore, simulating the flow around bridge decks remains as a challenge in terms of computational resources and validation of results. For this reason, bridge aeroelasticity is still mainly investigated experimentally, using wind tunnels. The experimental measurements and observations are then used as a benchmark to validate or calibrate the numerical approach.

1.3 AIMS AND OBJECTIVES OF RESEARCH

The research in bridge aeroelasticity has achieved remarkable findings, which clarified and aided the understanding of interaction between bridge decks and wind. Due to certain obstacles, the understanding is still very limited in the case of the responses of bridges in turbulent wind. This complex phenomenon, characterised by the coherent structure of the fluctuating wind components and the aerodynamic forces, has recently attracted a lot of attention (Cao, 2015). Published results have shown the effect of turbulence on the stability of bridge decks and span-wise correlation of forces; none of them, however, have been able to back up the hypothesis proposed by Scanlan (1997). Based on the wind tunnel tests, he found that the bridge models appeared to be more stable in turbulent flow, due to the reduction of span-wise correlation of forces and surface pressure. A similar argument has also been used to explain for the turbulence-induced stabilising effect on the vortex-induced vibration (VIV) of bridge decks. However, many researches have showed that turbulence can also produce the destabilising effect on the VIV. Based on Kareem and Wu (2013), the knowledge of the underlying physical mechanism of this wind-induced response in both of the smooth and turbulent wind is still very insufficient.

1.3.1 Aims of Research

The hypothesis proposed by Scanlan (1997) has remained a challenge to researchers in bridge aeroelasticity. The current research study aims to test this hypothesis regarding to the VIV of bridge decks by conducting wind tunnel studies and computational simulations using the convention 3D sectional model of a 5:1 rectangular cylinder. These studies help gain an in-depth understanding of the VIV mechanism and turbulence-induced effects. Moreover, knowing the limitation of the current research that wind tunnel and computational models are still 2D in nature, this research study introduces a novel computational approach to simulate the VIV of a flexible 5:1 rectangular cylinder, which is an analogue of a full-aeroelastic wind tunnel model or a flexible bridge deck. Selective results are extracted to bring more insights into the VIV mechanism and the span-wise flow feature as well as to support the improvement of mathematical models for VIV.

1.3.2 Objectives and Methodology of Research

To achieve the aims of this research, four objectives have been set:

- The 5:1 rectangular cylinder is chosen for this research study since it is considered as a generic bridge deck cross section and has been studied in a lot of research. A physical 3D sectional model will be built and tested in the wind tunnel at the University of Nottingham. A series of static and dynamic wind tunnel test will be conducted in smooth and turbulent flow having different turbulence intensities and length scales. The surface pressure distribution as well as the structural response will be interpreted to investigate the mechanism of VIV and the influence of turbulence.

- The open-source CFD software named OpenFOAM and the High Performance Computer (HPC) system at the University of Nottingham are used to perform computational simulation of a 3D static and dynamic sectional model restrained to the heaving mode only in smooth flow. A Fluid Structure Interaction (FSI) solver will be proposed to model the response of the cylinder. This computational study will complement wind tunnel results, revealing the mechanism of the VIV.

- A flexible 5:1 rectangular cylinder will be introduced and this proposed FSI solver will be developed to simulate the bending VIV. The span-wise variation of the surface pressure distribution will be analysed to reveal the appearance of the span-wise flow features and their effect on the surface pressure and VIV.

- As one of the most well-known VIV mathematical models, the Hartlen and Currie model will be selected and studied in detail. A parameter optimisation process is developed to efficiently extract the model parameters from some key results obtained from wind tunnel and computational studies. Further improvement will be introduced to generalise this model so that it can model the VIV response of a 3D flexible structure; such modification will be verified using the computational results of the 3D flexible 5:1 rectangular cylinder as well as the full-scale measurement of the Great Belt East bridge.

1.4 ORGANISATION OF THE THESIS

The current chapter, **Chapter 1**, introduces some well-known wind-induced incidents of bridges in the last few decades and the development of research in bridge aeroelasticity which mainly forms the inspiration of this research. The objectives and methodology applied in the research are also mentioned in this chapter.

In **Chapter 2**, the author presents an overview of bridge aerodynamics and aeroelasticity. The main responses will be pointed out and discussed in detail regarding their physical characteristics and relevant mathematical models. In addition, this chapter will look closely at the influence of the turbulence, particularly the stabilising effect on the VIV. A number of controversial findings and observations will be reviewed, showing the limitation of the current research regarding the understanding of the VIV mechanism as well as the turbulence-induced effect. This provides motivation for the present research.

Chapter 3 introduces the background knowledge of CFD and the finite volume method. The relevant turbulence models will be selected and reviewed together with the potential and future of CFD in Wind Engineering, in general, and in bridge aerodynamics and aeroelasticity, in particular.

The methodologies to conduct the computational study and the wind tunnel study are presented in **Chapters 4** and **5** respectively. All relevant aspects to conduct a simulation using the open-source CFD software OpenFOAM will be introduced in **Chapter 4**. It is focused on a novel computational approach to simulate the VIV of a flexible 5:1 rectangular cylinder, which includes the development and integration of the structural solver and the dynamic mesh algorithm into the OpenFOAM fluid solver. A mesh sensitivity study is also performed to point out limitations of this approach, subjecting to the scope and aims of the research. **Chapter 5** is devoted to discussing the method to conduct the static and dynamic wind tunnel tests together with essential techniques to measure velocity, surface pressure, aerodynamic forces and moment and structural acceleration. Different grids are used to create the turbulence in the wind tunnel; this grid-generated turbulence will be studied regarding the homogeneous and isotropic characteristics and the stream-wise decaying process.

In **Chapter 6**, results from the wind tunnel tests and computational simulations are discussed and compared to uncover the mechanism of the VIV for the 5:1 rectangular cylinder. By comparing the distribution and span-wise correlation of the surface pressure measured in the smooth and turbulent flow, it shows the effect of the turbulence on this mechanism, which will eventually influence the VIV. Moreover, final sections in this chapter will be devoted to analysis results of the CFD simulation using the flexible cylinder, concentrating on the span-wise variation of the pressure fluctuation.

Chapter 7 presents an in-depth study of the Hartlen and Currie model; an optimisation process is developed to extract model parameters, allowing model outputs to be compared against both of wind tunnel and computational studies. Also, it is discussed further improvements to generalise this model so that the response of a 3D flexible structure could be estimated.

In **Chapter 8**, this research study is summarised with key findings and conclusions, particularly relating to the hypothesis mentioned in Section 1.3. Limitations as well as potential areas of further research are discussed and recommended.

Chapter 2

Overview of Bridge Aeroelasticity

When a bluff body as opposed to a streamline structure is immersed in a wind field, induced pressure gradients cause the wind to detach from surfaces of the body, resulting in a surface of velocity discontinuity and pressure differential which can trigger large structural responses. The wind-induced responses of a bluff body can be classified into different phenomena as follows:

- Buffeting
- Flutter
- Vortex-induced vibration
- Galloping
- Divergence instabilities

The response of a bluff body is also dependent on the turbulence inherent in the wind. Experimental and computational literature have shown that the turbulent winds can produce either stabilising or destabilising effects to the vortex-induced vibration of a bluff body, which are the main behaviours to be studied in this research.

Prior to classifying and reviewing the aeroelastic phenomena of a bluff body, it is of importance to present some key concepts of turbulent flow and the aerodynamic aspects of flow separation and re-attachment.

2.1 OVERVIEW OF TURBULENCE

A fluid parcel in the flow experiences the inertial, viscous and pressure forces, which are responsible for transportation of energy, momentum and materials throughout the flow. The ratio of the first two forces are defined as the Reynolds number, Re, which is also a measure of laminar or turbulence characteristic of the flow,

$$\mathrm{Re} = \frac{UL}{\nu}, \tag{2.1}$$

where ν is the kinematic viscosity of the fluid, U is the mean speed and L is the characteristic length of the flow. When the Reynolds number is below a certain critical value, the viscosity dominates, which can effectively damp out any possible randomness in the flow. Such a flow regime is called laminar (Pope, 2000). At higher Reynolds numbers, the viscous effect decreases; a disturbance in the flow can then develop, leading to continuous variation of flow properties with time over substantial flow regions. The behaviour of flow is random and chaotic, which is referred as turbulent flow.

In this section, the physical nature and mechanism of turbulence is discussed via the concept of energy cascade and Kolmogorov's hypothesis. In addition, the randomness of turbulence is quantified and expressed using statistical approaches.

2.1.1 Nature of Turbulence

Turbulence in natural wind is originated from velocity discontinuities which are induced by many sources. As for the atmospheric boundary layer, the heating or cooling of the Earth's surface during a day (buoyancy mechanism) or the presence of structures such as high-rise buildings or bridge decks (mechanical mechanism) can yields instabilities in the atmosphere which can then interact and develop into turbulence in the wind. Its characteristics are dependent on the length- and time-scale of the generating mechanism.

Flow visualisation reveals turbulent flow can be considered to be composed of many structures of swirling fluid or turbulence eddies of different sizes. Each eddy is characterised by a length scale l, a velocity scale $u(l)$, a time scale $\tau(l) = l/u$ and a eddy Reynolds number

$$\mathrm{Re}_{eddy} = \frac{ul}{\nu}. \tag{2.2}$$

Kolmogorov theory offers detailed explanation and description of behaviour of eddies of different length scales at significantly high Reynolds numbers. This is summarised in Figure 2.1 where L is the characteristic length of the flow while l_o, as defined in Section 2.1.2, is the turbulence length scale of the flow which is considered to be the size of eddies that are dominant and contains the most of energy of the flow. Therefore, any eddies possessing length scales which are comparable to l_o or, strictly speaking, greater than $l_{EI} = l_o/6$ are belong to the energy containing range. These eddies are generated directly from the external mechanism; their behaviour and characteristics are thus largely dependent on boundary conditions of the flow. In this regime, the inertial force is dominant while the effect of the viscous force is negligible. The former transfers the energy from large-scale eddies to small-scale eddies via an inviscid process called the vortex stretching. With the effect of viscosity being ignored, the angular momentum of a large-scale eddy is conserved. It is then conceived that the eddy rotates more quickly, stretching itself into a unstable, long and thin cylindrical eddy which ultimately breaks up into smaller and more stable eddies. This inertia-driven process allows the energy to be transferred from the largest-scale eddies to smaller and smaller eddies until the eddy Reynolds number equals to 1 where the energy is effectively dissipated by the molecular viscosity; Richardson (1922) described this process as the energy cascade.

Together with the vortex stretching process, the directional information of the large-scale eddies is lost due the pressure force. The pressure fluctuation at a point in the flow is mostly contributed by the velocity fluctuation. The positive pressure fluctuation can be thought as a pool storing energy which afterwards is released without any preferable directions. The pressure force, therefore, spreads the energy uniformly to all directions making the flow become isotropic. The eddies having the length scale smaller than l_{EI} are isotropic and their statistics are in a sense of universal. This regime is called the universal equilibrium range characterised by a comparable effect of inertial and viscous forces. For the very high Reynolds-number flow, this regime is separated into the inertial subrange and the dissipation range. In the former, the isotropic universal eddies mostly experience the inertial force while the viscous effect is predominant in the latter including eddies having the length scale smaller than $l_{DI} = 60\eta$ which is determined by the Kolmogorov scale that

$$\eta = \left(\frac{\nu^3}{\varepsilon}\right)^{1/4}, \tag{2.3}$$

where ε and ν are the energy dissipation rate and the kinematic viscosity of the flow respectively. The Kolmogorov scale η also represents the smallest-scale eddies in the flow; accordingly, the velocity scale u_η and the time scale τ_η of the smallest-scale eddies are

$$u_\eta = (\varepsilon\nu)^{1/4}, \tag{2.4}$$

$$\tau_\eta = \left(\frac{\nu}{\varepsilon}\right)^{1/2}. \tag{2.5}$$

Pope (2000) indicated that the rate of energy transfer in the energy cascade is complicated and dependent on several factors. In the energy containing regime, the transfer rate is non-universal and significantly influenced by boundary conditions of the flow and the details of energy contents. However, it is fully established in the inertial subrange where the rate of energy transfer equals to the rate of energy insertion. The energy dissipation rate ε in the dissipation range is also universal and defined by the velocity scale u_o and the length scale l_o of the most-energy-containing eddies as

$$\varepsilon \propto \frac{u_o^3}{l_o}. \tag{2.6}$$

However, the conventional Kolmogorov theories (Kolmogorov, 1941) and deduced results are limited to very high Reynolds numbers. Many experimental studies including George and Hussein (1991) showed that, even at the Reynolds number of 10000, the anisotropic behaviour maintains during the inertial subrange and dissipation range. The other oversimplification applied in the Kolmogorov theory is that the energy is transferred from large-scale eddies to small-scale eddies only. The opposite process which is named as backscatter has been showed to be responsible to transfer a portion of energy to larger-scale eddies (Pope, 2000).

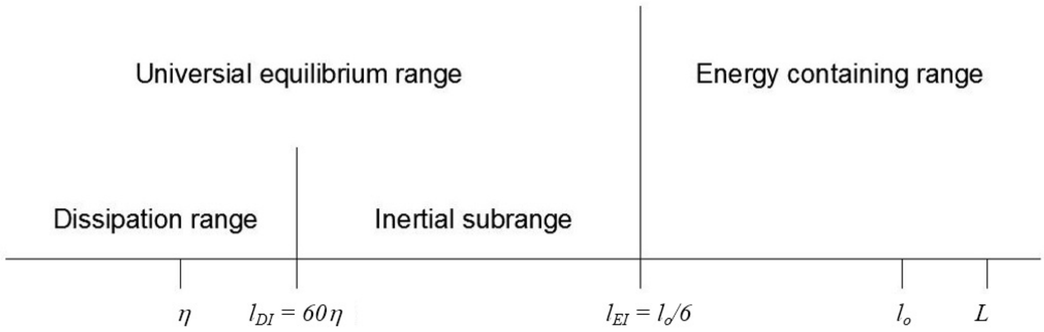

Figure 2.1: Kolmorogov's ranges of length scale; the length scale increases from left to right.

2.1.2 Descriptions of Turbulence

Using Reynolds decomposition, the velocity measurement at a point in the turbulent flow is considered to be a combination of the mean wind speed and the fluctuating components

$$U_t(x, y, z, t) = U(x, y, z) + u(x, y, z, t) + v(x, y, z, t) + w(x, y, z, t), \tag{2.7}$$

where U_t is the wind speed in the x direction. The mean wind speed U is defined as the average of U_t over a selected time interval t_p

$$U(x, y, z) = \frac{1}{t_p} \int_0^{t_p} U_t(x, y, z, t)\, \mathrm{d}t. \tag{2.8}$$

The main characteristics of the fluctuating velocity components $u(t)$, $v(t)$ and $w(t)$ are described using the statistical approach.

Turbulence Intensity

The turbulence intensity is the measure of the level of velocity fluctuation in each direction, which provides a good indication on the strength of turbulence in the wind. The turbulence intensity in one direction is defined as the ratio of the standard deviation of the fluctuating velocity component in this direction and the mean wind speed

$$I_u = \frac{\sigma_u}{U}, \tag{2.9}$$

$$I_v = \frac{\sigma_v}{U}, \tag{2.10}$$

$$I_w = \frac{\sigma_w}{U}, \tag{2.11}$$

where I_u, I_v and I_w are the turbulence intensity and σ_u, σ_v and σ_w are the standard deviation of the fluctuating component in the stream-wise, horizontal and vertical cross-wind direction respectively. Taking the stream-wise direction as an example

$$\sigma_u = \sqrt{\frac{1}{t_p}\int_0^{t_p} u^2(t)\,\mathrm{d}t}. \tag{2.12}$$

Turbulence Length Scale

The velocity fluctuation in the wind can be considered as a superposition of conceptual eddies transported by the mean wind speed (Simiu and Scanlan, 1996). An eddy can be considered as a parcel of air rotating at a frequency f. Applying the travelling wave theory, the wavelength of the eddy, λ, can be defined as $\lambda = U/f$; this wavelength parameter is the size measurement of one eddy. The size of eddies in the wind is very critical; if the size of a structure immersed in the turbulent wind is similar to the size of eddies in the wind, a dramatic structural response can occur. However, it is impossible to measure the size of all eddies in the wind; the turbulence length scale, therefore, is used as a measure of average size of turbulent eddies in the wind that contain most of energy. The size of one eddy is defined in x, y and z directions; therefore, each fluctuating component is accompanied by three different length scales. In total, there are 9 turbulent length scales for 3 fluctuating components along three directions,

$$\begin{array}{ccc} L_u^x & L_u^y & L_u^z, \\ L_v^x & L_v^y & L_v^z, \\ L_w^x & L_w^y & L_w^z, \end{array} \tag{2.13}$$

where L_u^i, L_v^i and L_w^i are the turbulent length scale of the component u, v and w respectively along the direction i where $i = x, y, z$.

Mathematically, L_u^x is defined over a distance Δ_x

$$L_u^x = \frac{1}{\sigma_u^2} \int\limits_0^{\infty} \rho_{uu}(\Delta_x)\, \mathrm{d}\Delta_x, \tag{2.14}$$

where

$$\rho_{uu}(\Delta_x) = \lim_{T \to \infty} \frac{1}{T} \int\limits_{-\frac{T}{2}}^{\frac{T}{2}} u(x, y, z, t) u[x + \Delta_x, y, z, t]\, \mathrm{d}t. \tag{2.15}$$

Here, the autocorrelation function $\rho_{u_1 u_2}(\Delta_x)$ is essentially a measure of similarity between u measured simultaneously at two points separated by a distance Δ_x. In addition, the turbulence length scale can be determined using Taylor's hypothesis that the turbulence in the wind is assumed to be 'frozen', travelling at the mean wind speed. Using the idea of frozen turbulence, the turbulence length scale is defined using the fluctuating velocity component u at a same point at times t and $t + \tau$. The temporal autocorrelation is defined as

$$\rho_{uu}(\tau) = \lim_{T \to \infty} \frac{1}{T} \int\limits_{-\frac{T}{2}}^{\frac{T}{2}} u(t) u(t + \tau) \mathrm{d}t. \tag{2.16}$$

The turbulent length scale is then given by

$$L_u^x = \frac{U}{\sigma_u^2} \int\limits_0^{\infty} \rho_u(\tau) \mathrm{d}\tau. \tag{2.17}$$

Similar definitions apply to the other turbulent length scales.

Wind Spectrum

In turbulent wind, the velocity fluctuation in each direction can be thought as a summation of several sinusoidal components. The alongwind fluctuating component $u(t)$ can be expressed as

$$u(t) = \int\limits_0^{\infty} A_n \sin\left(2\pi f t\right)\, \mathrm{d}f, \tag{2.18}$$

where A_n and f are the amplitude and frequency of each sinusoidal component. The frequency distribution of the turbulent velocity component u is described by the power spectral density, $S_u(f, z)$, whose integration results in the variance of this component

$$\sigma_u^2 = \int_0^\infty S_u(f,z)\mathrm{d}f. \tag{2.19}$$

The wind spectrum is the plot of the non-dimensional power spectral density, $R_u(f,z)$ defined as

$$R_u(f,z) = \frac{fS_u(f,z)}{\sigma_u^2(z)}, \tag{2.20}$$

against the non-dimensional frequency f_L

$$f_L = \frac{fL_u^x(z)}{U(z)}. \tag{2.21}$$

There are some specified wind spectra commonly used in engineering bridge aerodynamic analysis; one of them is the non-dimensional von Kármán spectrum which is

$$R_u(f,z) = \frac{4f_L}{(1+70.8f_L^2)^{5/6}}. \tag{2.22}$$

As for the design of bridge structure, the Eurocode spectrum is usually applied; this spectrum is given by

$$R_u(f,z) = \frac{6.8f_L}{(1+10.2f_L^2)^{5/3}}. \tag{2.23}$$

In addition, Davenport (1962a) suggested one of the first wind spectra as

$$R_u(f,z) = \frac{2}{3}\frac{f_L^2}{(1+f_L^2)^{4/3}}. \tag{2.24}$$

For the Davenport's spectrum, f_L is defined in a slightly different way,

$$f_L = \frac{fL}{U(z)}, \tag{2.25}$$

where $L = 1200$(m). As can been seen in Equations 2.22 to 2.24, the wind spectrum is expressed as a function of the non-dimensional frequency; these functions share some common characteristics. Figure 2.2 illustrates the shape of these three selected spectra; the von Kármán and Eurocode spectra are quite similar while the Davenport spectrum gives the largest energy value at a slightly higher frequency.

2.2 AERODYNAMICS OF FLOW SEPARATION AND REATTACHMENT

Together with the inherent turbulence in the oncoming flow, the flow separation and reattachment are other sources of excitation which can cause significant fluctuation of the surface pressure around a bluff body and then may lead to aeroelastic instabilities.

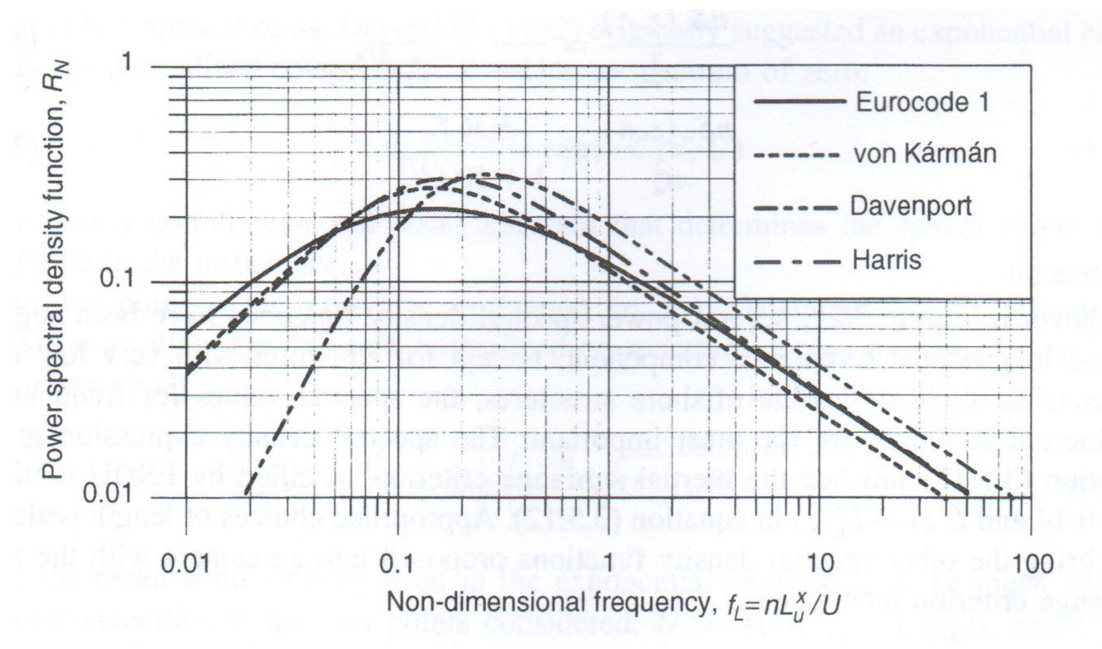

Figure 2.2: Non-dimensional power spectral density functions for the alongwind turbulence component (Dyrbye and Hansen, 1999).

The mechanism of the flow separation is governed by the behaviour of the boundary layer. Considering a reasonably slender body such as a airfoil at a low angle of attack and a relative high Reynolds number as shown in Figure 2.3, the viscous effect is negligibly small except for the thin layer of fluid immediately adjacent to the airfoil. This is known as the boundary layer where a considerable velocity gradient in the direction normal to the solid boundary may exist.

For most of the streamlined bodies such as the airfoil in this example, the boundary layer is usually very thin providing that the angle of attack is small and the Reynolds number is sufficiently high. Acknowledging the assumption of a non-slip boundary, i.e. a zero relative velocity between the fluid and the solid boundary and a large mainstream velocity, it is evident that significant shearing velocity gradients exist in this layer. Also, under the same condition, the boundary layer as illustrated in Figures 2.3 and 2.4 is classified as a laminar layer. The fluid remains attached to the surface of the airfoil and the separation occurs very close to the trailing edge (denoted by the point S in Figure 2.4) leading a narrow wake region.

The other type of the boundary layer is a turbulent layer; these two types of the boundary layer can co-exist in some engineering applications such as flow in the pipe or flow around a very thin and flat plate as shown in Figure 2.5. A thin laminar boundary layer is formed from the leading edge and extends up to about half of the chord length. Inside this region, the layers of fluid slide smoothly over one another and

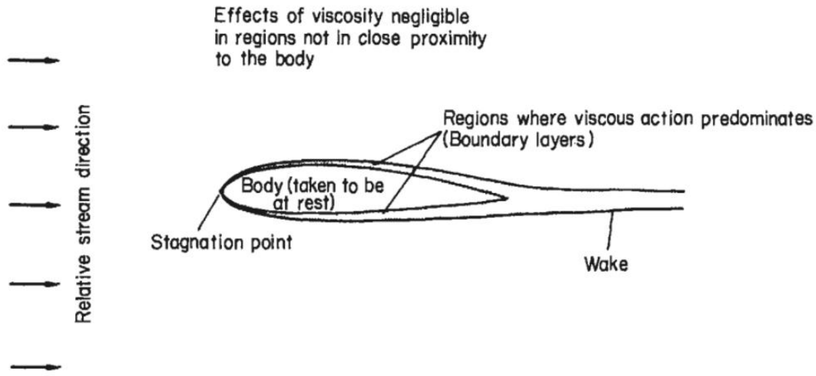

Figure 2.3: Overall flow field around a airfoil at a low angle of attack (Houghton and Carpenter, 2008).

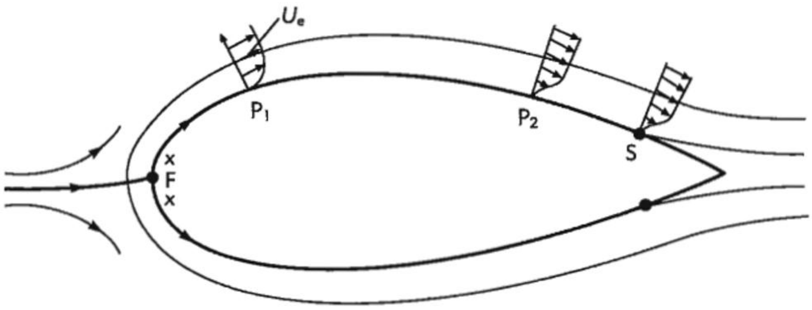

Figure 2.4: Velocity profiles at different chordwise positions along the airfoil (Houghton and Carpenter, 2008).

there is no fluid mass being interchanged between each layers. Thus, the energy from the mainstream is transferred throughout the boundary layer purely by the mean of viscosity. Further downstream, the skin friction slows down the layer of fluid immediately next to the solid boundary (points P1 and P2 in Figure 2.4). It then increases the thickness of the boundary layer and enhances the dominance of the viscous effects. A transition occurs and the boundary layer becomes turbulent. The key difference is the presence of the Reynolds stresses which promote the fluid mass interchange and lead to more energy being transferred through the boundary layer. This effect divides the boundary layer into two sub regions: the viscous sub-layer and the buffer layer. The former is adjacent to the solid boundary where the viscosity again dominates and the fluid speed increases linearly as shown in Figure 2.6. The other conclusions could be drawn that the turbulent boundary layer contains more energy than the laminar one and the velocity gradient close to the solid boundary in the turbulent boundary layer is also larger than that of the laminar one.

For the streamlined bodies, the boundary layer separation, for instance the point S in Figure 2.4, is initiated by the adverse pressure gradient that the pressure increases with the distance downstream. Figure 2.7 illustrates the evolution of the velocity profile normal to the solid boundary prior to and beyond

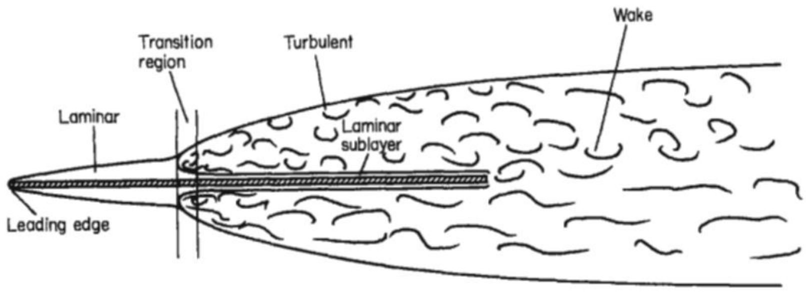

Figure 2.5: Development of the boundary layer around a thin flat plate (Houghton and Carpenter, 2008).

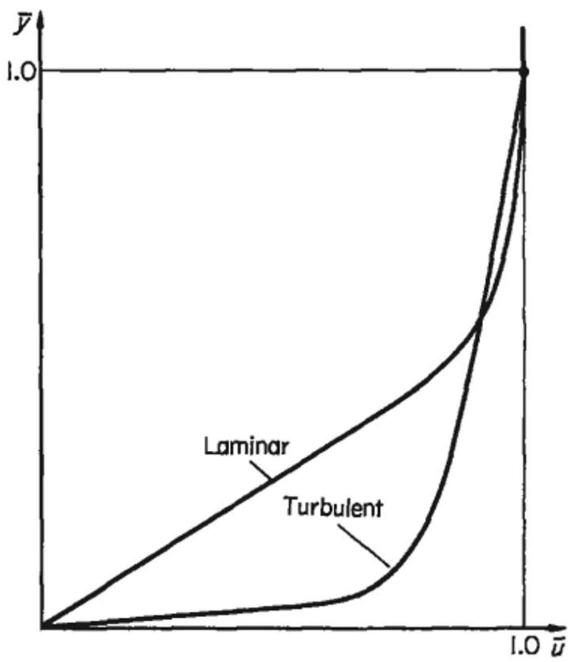

Figure 2.6: Non-dimensional velocity profiles normal to the solid boundary of laminar and turbulent boundary layers (Houghton and Carpenter, 2008).

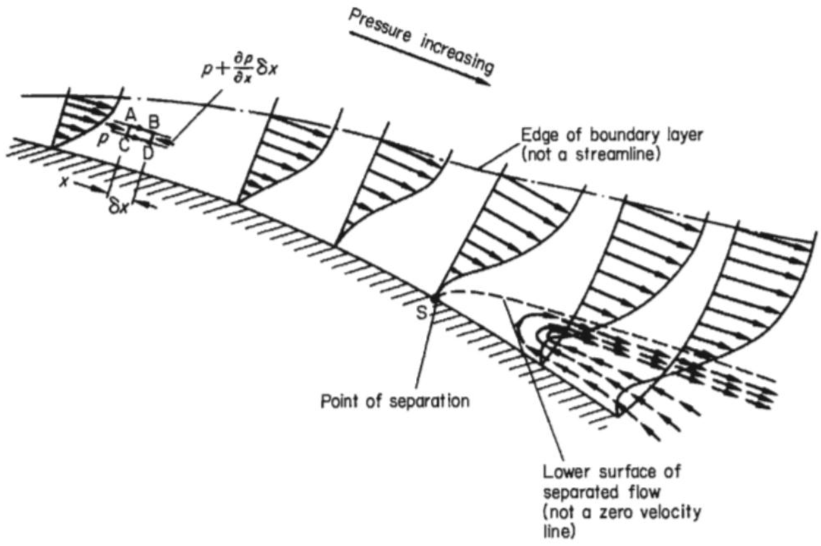

Figure 2.7: Flow separation over a streamlined body (Houghton and Carpenter, 2008).

the separation point S. The slowing-down effect due to the positive pressure gradient and the viscosity is more pronounced near the solid boundary since the accelerating effect of the mainstream is minimum there. Eventually, at the point S, the velocity gradient in the direction normal to the solid boundary is zero; the positive pressure gradient will then initiate the adverse flow next to the surface in the upstream direction and cause a sudden increase in the boundary layer thickness.

Recalling the noted difference between the laminar and turbulent boundary layers, due to the lower energy level and the greater extent of low-energy fluid next to the solid boundary, flow separation occurs earlier for the laminar boundary layer than for the turbulent boundary layer.

After the flow separation, two post-separation behaviours are known to exist (Williams, 1977). In some cases, especially for the streamlined bodies or bluff bodies with short after-body length in smooth flow, the original boundary-layer fluid never reattaches to the surface of the body but passes downstream and creates a wake region of recirculating fluid. The characteristic length scale of the recirculating region is of the same order as the dimensions of the body. In other cases, such as the bluff bodies with long after-body length in the smooth flow, the flow always separates at the leading edge. The boundary layer passes over a region of recirculating fluid and reattaches to the body at some point further downstream. A bubble of recirculating fluid is trapped underneath the boundary layer; it is convected towards the trailing edge where another flow separation occurs. This very interaction leads to a very complicated flow field around a rectangular cylinder with a long after-body length, particularly with the aspect ratio greater than 5. In addition, a variation in the Reynolds number, the level of turbulence of the incoming flow and the angle of attack could alter the post-separation behaviour or the position of the reattachment point. These aspects including the effect of the Reynolds number and the turbulence will be discussed further in the next section.

2.3 VORTEX SHEDDING FROM A STATIC BODY

The shear layers separating from the upstream body, which is either a streamlined or bluff body, interact together to form a recirculating flow pattern which is well known as the von Kármán vortex street. It is characterised by equally-spaced vortices in the wake alternately shed from the separation points on the body. This regularity of vortex shedding is described by the non-dimensional Strouhal number, St, which is defined by

$$\mathrm{St} = f_s \frac{B}{U}, \tag{2.26}$$

where f_s is the frequency of the vortex shedding and U is the upstream wind speed. Here B is the characteristic dimension of the body which, as for the circular cylinder, is the diameter. For the rectangular cylinder, either the depth D or the width B is used. In this research study, the width B is selected for consistency purposes and to highlight the effect of the after-body length which will be discussed further in this section.

Similar to the behaviour of the boundary layer as discussed in Section 2.2, the characteristics of the vortex shedding phenomenon depend on the Reynolds number, the geometry of the body (streamlined or bluff bodies; aspect ratio) and the turbulence of the incoming flow.

2.3.1 Circular Cylinder

The behaviour of the boundary layer around the circular cylinder is very similar to that around a streamlined body, such as the airfoil, except that the boundary layer is inevitably separated at high Reynolds number due to excessive adverse pressure gradients induced by the curvature of the surface. A general behaviour of the wake region behind the circular cylinder is summarised in Figure 2.8; the Reynolds-number limits quoted here are only an approximation. At very low Reynolds numbers, the boundary layer around the circular cylinder is laminar and the flow remains completely attached to the surface. As the Reynolds number increases, the laminar boundary layers on the upper and lower surfaces separate at two points very close to each other and a narrow turbulent wake is formed behind the body. The wake keeps broadening up to the point that the laminar boundary-layer separation points are well separated and a pair of symmetrical vortices appear in the wake very close to the cylinder. For the Reynolds number between 30 and 150, these two vortices stretch downstream and form a laminar von Kármán

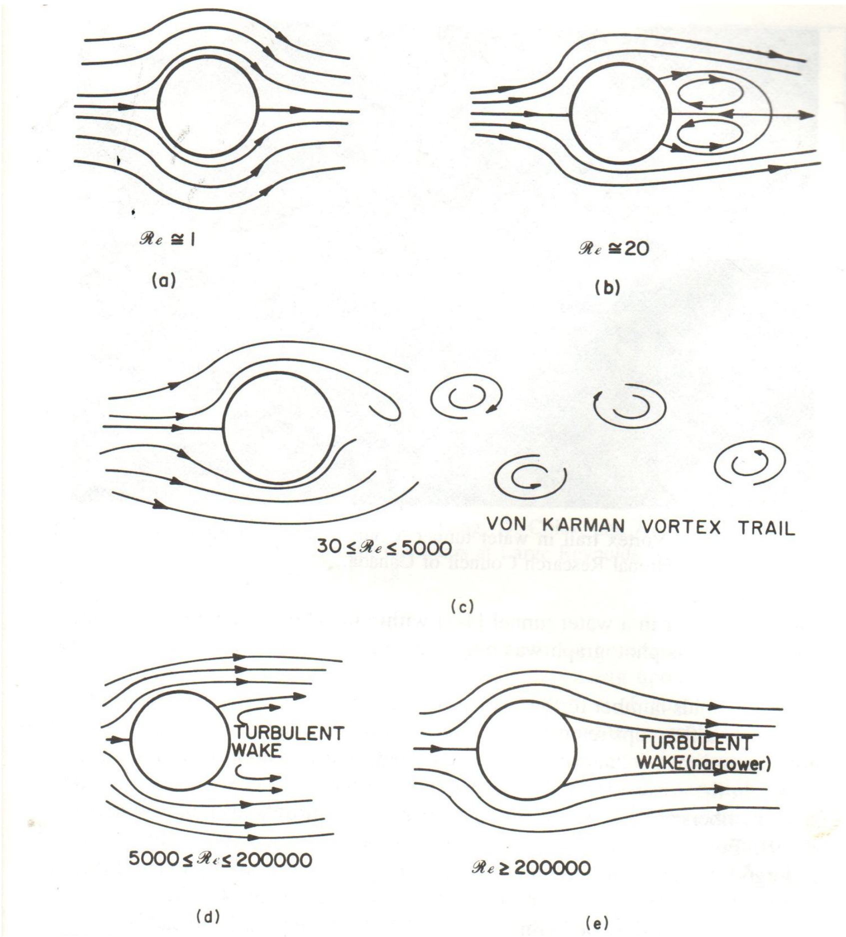

Figure 2.8: Wake and vortex formation behind a circular cylinder at different Reynolds numbers (Simiu and Scanlan, 1996).

vortex street. If the Reynolds number keeps increasing, a transition where the vortex structure in the wake becomes turbulent occurs and eventually, the vortex street becomes fully turbulent at the Reynolds number between 3×10^2 and 2×10^5. At higher Reynold numbers, the laminar boundary layer undergoes a turbulent transition; the wake is narrower and clear vortical structure is apparent. At very high Reynolds number (Re $\geq 3.5 \times 10^6$), the boundary layer is completely turbulent and the wake region is thin.

A summary of different flow regimes is shown in Figure 2.9 together with the Reynolds-number-dependence characteristics of the Strouhal number of the circular cylinder. This relationship was estimated from a number of different experiments; the results are presented in the $\pm 5\%$ envelops except for the range of Reynolds number from 2×10^5 to 3×10^6. In this range, a generic dependence of the Strouhal-Reynolds number relationship on the surface roughness of the cylinder is shown; the upper curve is for a smooth cylinder while the lower one is for a rough cylinder. This behaviour is directly related to the narrowing of the wake region induced by the transition from the laminar boundary layer to the turbulent boundary layer as the Reynolds number increases. As discussed further in Section 2.2, this

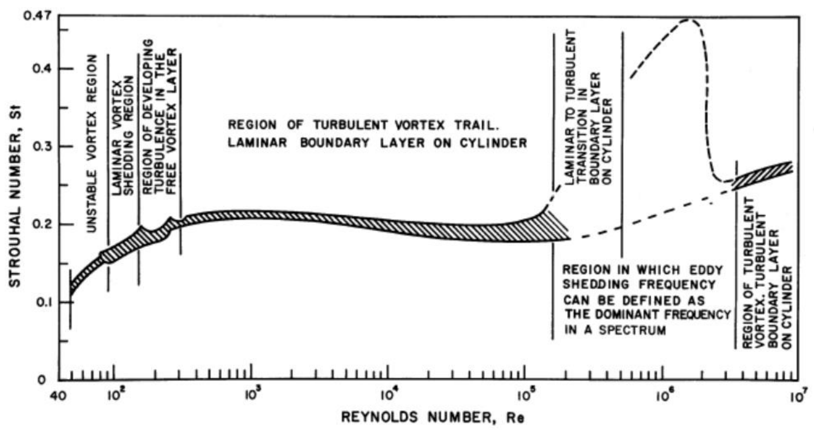

Figure 2.9: Relationship between the Strouhal number and Reynolds number of a circular cylinder (Lienhard, 1966).

transition occurs more abruptly in the case of a smooth cylinder, leading a significant step change in the Strouhal number. This step change becomes less by imposing more roughness to the surface of the cylinder (Achenbach and Heinecke, 1981).

In the Reynolds number range between 3×10^2 and 2×10^5, the Strouhal number shows very small dependence on the Reynolds number; the value of the Strouhal number there is about 0.2. It is corresponding to the flow regime where the boundary layer around the circular cylinder is laminar and the vortex street is fully turbulent. For the lower range of Reynolds number, from 50 to 3×10^2, a power-law relationship between the Strouhal and Reynolds number can be observed. However, a number of works from Williamson (Williamson, 1988a, 1996, 1997) shows, in this range, there is a transition from the laminar to three-dimensional regime of the cylinder wake and the von Kármán vortex street can be a too simplified model to represent the vortex structure in the cylinder wake. A relationship between the Strouhal and Reynolds number in the range of low Reynolds number is shown in Figure 2.10.

Apart from the two discontinuities marked in Figure 2.10, there is another discontinuity occurring at Re = 65. A number of works have been devoted to find the answer for this issue and to confirm the existence of a universal Strounal and Reynolds number relationship at low Reynolds numbers. Tritton (1959) was one of the first researchers reporting this discontinuity; during his experiment, he found two Strouhal number curves separated near Re = 100. He suggested the mechanism of this effect was due to a transition between an instability originated in the wake and one originated in the immediate vicinity of the cylinder. Similar behaviour at Re = 100 was also observed by Gerrard (1978). By analysing the vortex strength just behind the cylinder and the base pressure coefficients, he confirmed that this discontinuity in the Strouhal-Reynolds number relationship was related to a shift in the vortex formation induced by

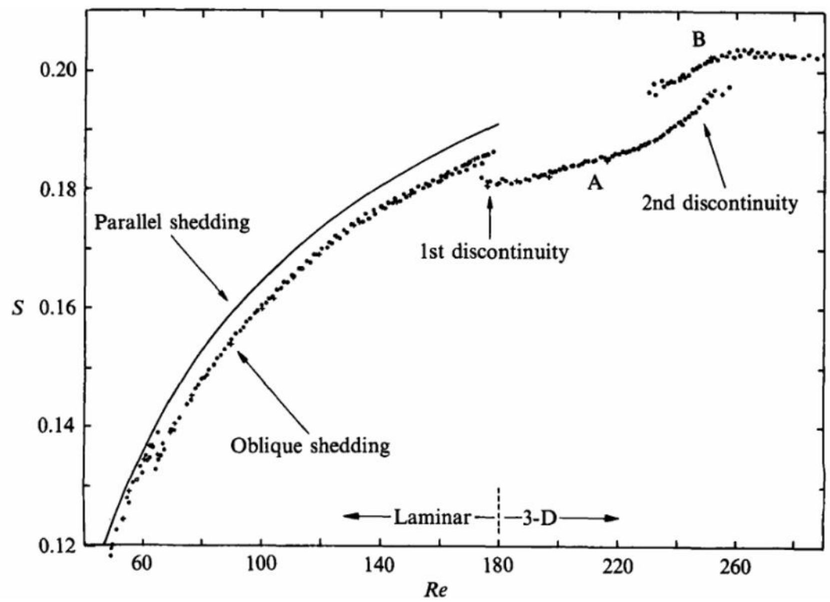

Figure 2.10: Relationship between the Strouhal number and Reynolds number of a circular cylinder at low Reynolds number (Williamson, 1992).

the variation of the vorticity diffusion at different Reynolds numbers. At Reynolds numbers lower than 100, the diffusion of the vorticity is dominant allowing a pair of symmetry eddies to form behind and close to the cylinder. At Reynolds numbers higher than 100, however, the effect of the vorticity diffusion decreased and the convection effect preceded breaking the stable structure of these symmetry eddies, which then increases the base pressure and reduces the vortex strength in this region. Later, experiments conducted by Van Atta and Gharib (1987) also observed similar discontinuity. The spectral analysis of the oscillation of the cylinder and the velocity fluctuation in the wake showed convincingly that this discontinuity was due to the vibration of the cylinder. It was also the reason that they observed other small discontinuities at higher Reynolds numbers which corresponded to other harmonics of the cylinder oscillation. They also suggested that if the circular cylinder was perfectly rigid, no early discontinuities in Reynolds number between 40 and 160 could be seen.

Further investigations have been carried out with an attempt to uncover the mechanism of this laminar shedding regime. Eventually, Williamson (1988a) confirmed the existence of the discontinuity of the Strouhal-Reynolds-number relationship and eliminated the association of the vibration of the cylinder and the turbulence in the upstream flow to this discontinuity. In fact, this laminar vortex shedding region is directly related to the phenomenon of oblique shedding and the discontinuity here is due to a transition from one oblique shedding mode to the other oblique shedding mode. Figure 2.11 represents a generic transition from one oblique vortex shedding mode to the other oblique vortex shedding mode as the Reynolds number increases. As can be seen in Figure 2.11a, for the Reynolds number above 64, the visualised vortex structure appears in a 'chevron'-shaped pattern across most of the span-wise length of the cylinder; a single dominant frequency f_L is found in this region. There are two small regions near either end of the cylinder where the vortex shedding occurs at a lower frequency f_e. As the Reynolds number decreases to below 64, a more complicated vortex configuration is observed in the wake as schematically sketched in Figure 2.11b. The central portion of the span of the cylinder is occupied by the vortex shedding at the frequency value f_u. This region is sandwiched by two regions where the vortices are shed at a lower frequency f_L. Similarly, two small regions of the vortex shedding frequency f_e near the ends of the cylinder exists but they are very difficult to identify from the flow visualisation as shown in Figure 2.12. At the boundary between two neighbouring regions, some interference between two vortices being shed at different frequencies is observed to occur. If the two vortices on the two sides of the boundary happen to be in phase, the vortices in the low-frequency region tend to get induced downstream by those in the high-frequency region, which makes the vortices oblique at an angle to the cylinder. The other process when two vortices on either sides are out of phase is known as the vortex dislocation. During this process, a vortex tube breaks at the boundary; the vortex in the low-frequency region will then connect to some vortex in the high-frequency region which has the same sign and phase. The vortex dislocation is formed and progressively shifted in the span-wise direction as it moves downstream. This phenomenon also possesses the periodic characteristics; it repeats itself after a number of vortex shedding cycles.

The presence of the oblique vortex shedding is due to the effect of the end plate. Williamson (1989) showed that, initially, the vortices in the wake are shed parallel to the cylinder; the effect from the end plate gradually builds up and imposes a certain oblique angle on the flow which leads to the oblique vortex shedding mode. By manipulating the end plates, which was to incline their leading edge inwards, certain control on the flow over the entire span of the cylinder was achieved and the parallel shedding mode was the final state. Without any imposing mechanism, the parallel shedding mode is found unstable and is considered as 2D simplified representative of the cylinder wake. A relationship between the Strouhal number and Reynolds number of the "universal" parallel and oblique vortex shedding was also proposed by Williamson (1989) as

$$\mathrm{St}_o = \frac{\mathrm{St}_\theta}{\cos\theta}, \tag{2.27}$$

where St_θ is the Strouhal number of the oblique vortex shedding at an oblique angle θ and St_o is the Strouhal number of the "universal" parallel shedding. By using this equation, a continuous Strouhal-Reynolds-number relationship has been confirmed for the laminar shedding regime.

The end plate is also the physical cause leading to the transition from one oblique vortex shedding mode to the other oblique vortex shedding mode. The wake region behind the cylinder is interfered by the flow over the central span of the cylinder and the flow induced by the end boundary conditions. At

Reynolds numbers larger than 64, a good synchronisation between these two flow features is achieved and a stable oblique vortex shedding mode is established. As the Reynolds number decreases, the oblique vortex shedding frequency reduces upto a point when the frequency over the central span of the cylinder falls out synchronisation with the one induced by the end plate. Therefore, a transition between two different oblique vortex shedding modes occurs.

The results plotted in Figure 2.10 also show other two discontinuities in the transition to three-dimensionality of the wake region. The first occurs at the Reynolds number of 180 marking a reduction in the Strouhal number while the second is associated with a restoration of the Strouhal number at a higher Reynolds number of 240 approximately. This unsteadiness in the near wake region involves the formation of the vortex loop and stream-wise vorticity and has been observed and reported in a number of studies. Eventually, Williamson (1988b) ruled out the possibility of the secondary Kelvin-Helmholtz vortices in the shear layer, which only begin to form at Reynolds numbers of around 1000, and concluded that the cause of this unsteady behaviour is the deformation of the primary vortices themselves, which lead to the formation of the three-dimensional loops and stream-wise vortices. The existence of the two discontinuities is related to the two different scales of the 3D vortical structure in the wake region.

The visualisation of the so-called mode A and mode B vortex shedding is showed in Figures 2.13 and 2.14. They consist of the primary von Kármán vortices superimposed by the small scale stream-wise vortices. The von Kármán vortices in the mode A appears in the wavy fashion and strings of vortex loops are formed at the same span-wise positions. The span-wise length scale of this vortex shedding mode is about 3 to 4 cylinder diameters. Regarding the direction of the stream-wise vortices, mode A vortex shedding is classified to be non-symmetry (Williamson, 1997). Each vortex loop contains a pair of counter-rotating stream-wise vortices (Figure 2.15a). On the other hand, as for the mode B vortex shedding, the primary von Kármán vortices are very uniform in the span-wise direction and the stream-wise vortices appear in a much finer scale and are in phase between a half cycle (Figure 2.15b).

The differences in the characteristic flow features between mode A and mode B vortex shedding indicate two distinct associated underlying physical mechanisms. Observing the formation of the mode A vortex shedding as the flow started to pass the cylinder, Williamson (1996) found this vortex shedding mode is initiated by the span-wise waviness of the von Kármán vortices, which is transferred from one vortex to the other after half cycle. Therefore, this vortex shedding mode is suggested to be due to an instability on the von Kármán vortex core. It agrees with the observation that the length scale of the stream-wise vortices is approximately equal to the von Kármán vortex core. The fine scaled stream-wise vortices observed in the mode B vortex shedding, on the other hand, suggests that this mode is associated with a small-scale flow feature that is the instability of the braid shear layer, which is the thin layer of vorticity connecting two von Kármán vortices every half cycle. This could explain the symmetry and in-line arrangement of the stream-wise vortices as described above (Williamson (1997); Leweke and Williamson (1998)).

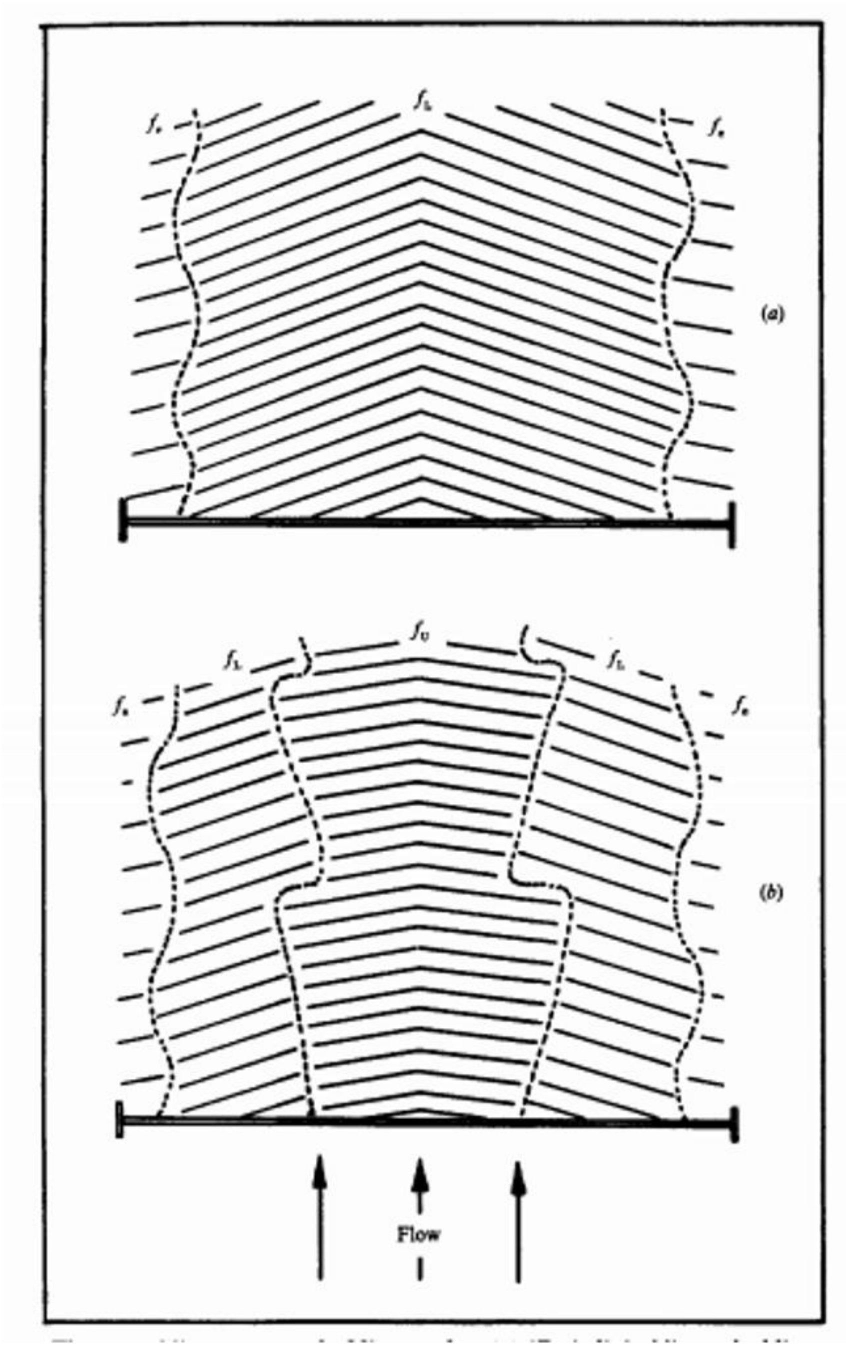

Figure 2.11: Schematic of a transition in the vortex shedding mode in the wake as the Reynolds number decreases from (a) Re = 64 to 178 to (b) Re < 64; the flow in the upward direction (Williamson, 1989).

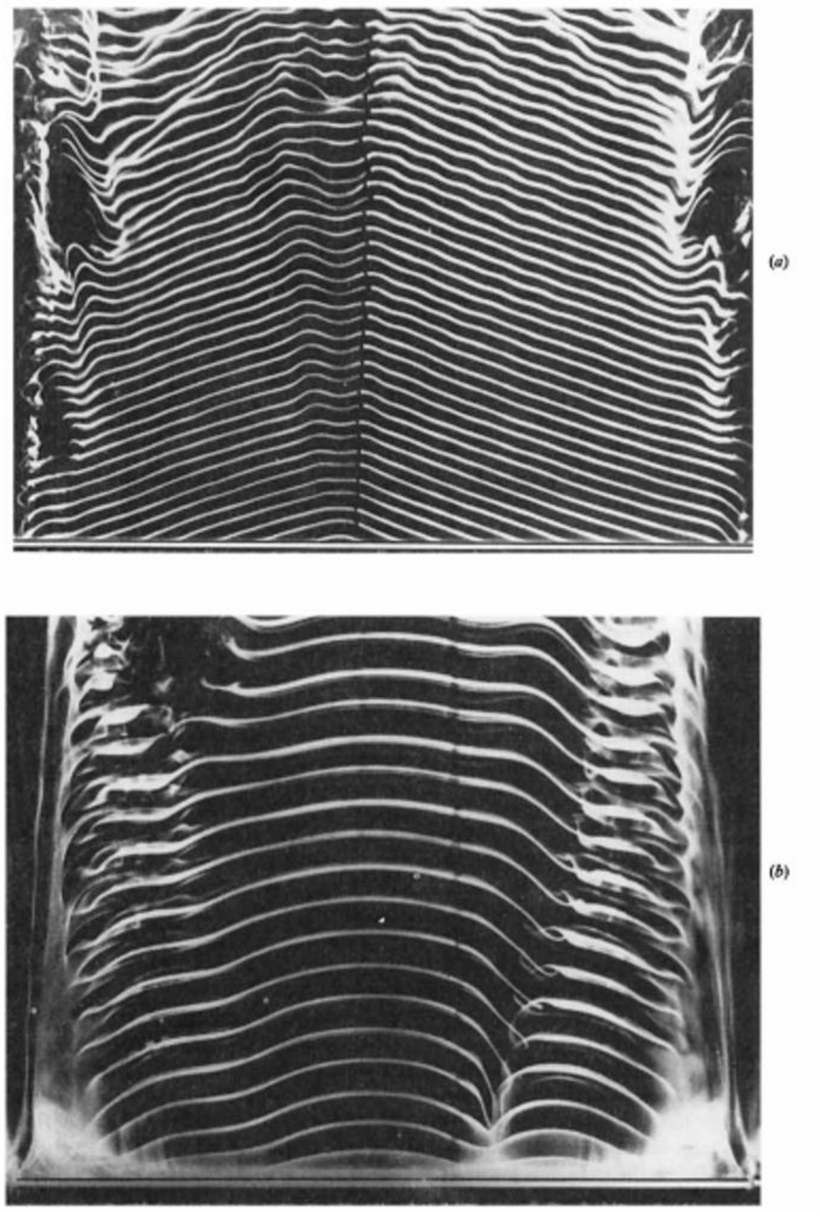

Figure 2.12: Visualisation of different vortex shedding modes for the Reynolds numbers (a) Re = 85 and (b) Re = 60; the flow in the upward direction (Williamson, 1989).

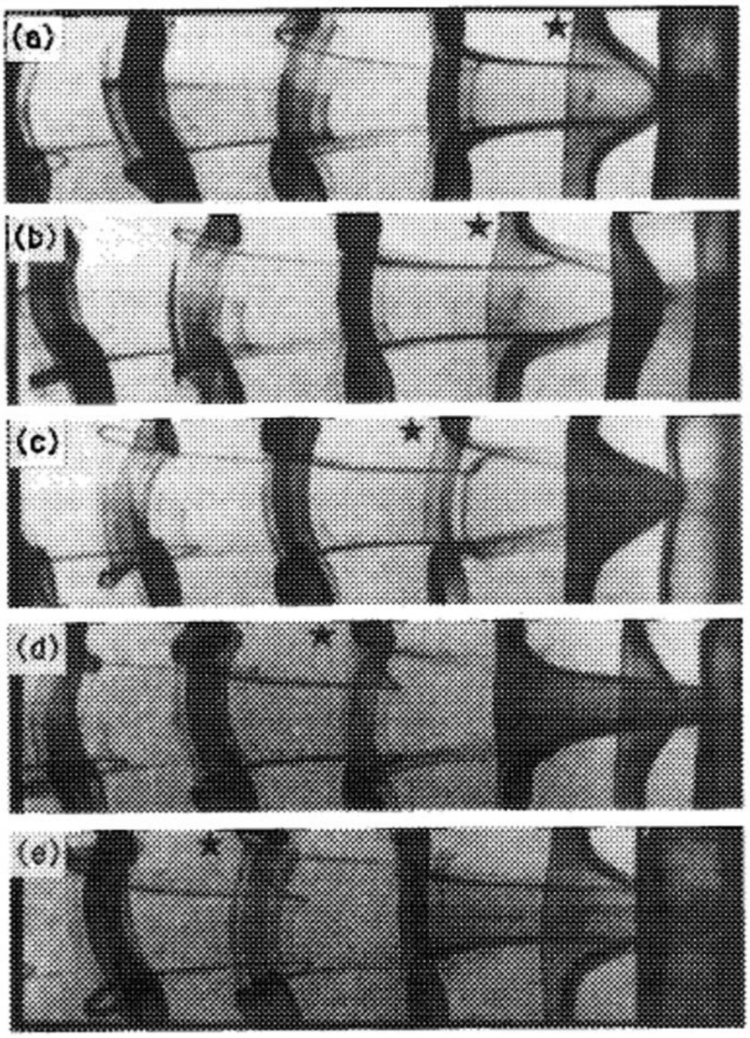

Figure 2.13: Evolution of the vortex loop marked with a star in the mode A vortex shedding at the Reynolds number of around 180 (Williamson, 1988b).

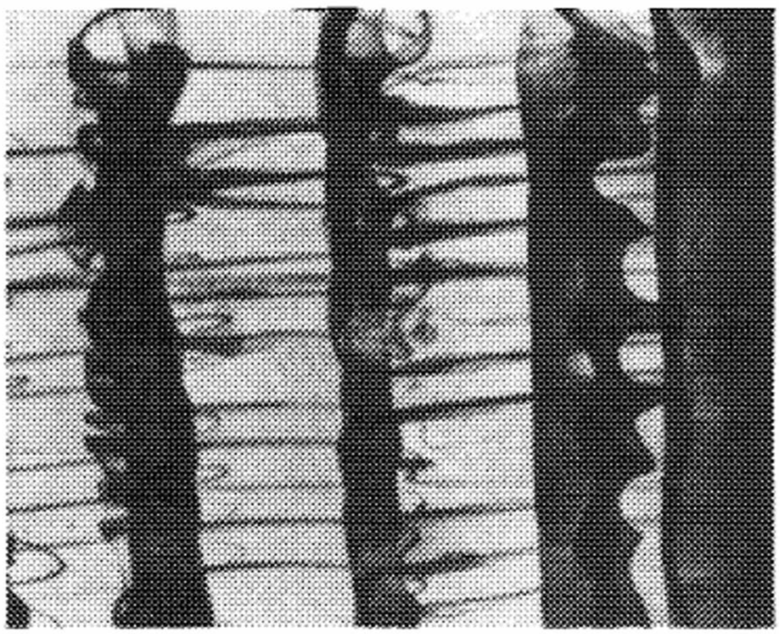

Figure 2.14: Flow field of the mode B vortex shedding at the Reynolds number of 285 (Williamson, 1988b).

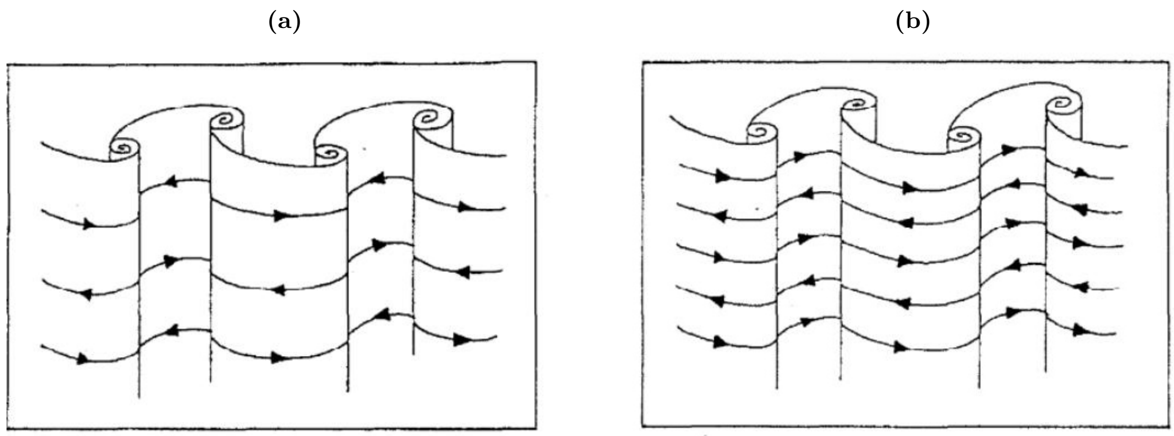

Figure 2.15: Symmetry of the mode A and mode B vortex shedding (Williamson, 1997).

2.3.2 Rectangular Cylinder

On the contrary to the circular cylinder, the rectangular cylinder with sharp edges is characterised by the presence of fixed separation points which can be either the leading edge or the trailing edge. Based on the wind tunnel results, Shiraishi and Matsumoto (1983) reported there are three types of vortex shedding which is dependent on the geometrical shape factors of the section. This observation was later confirmed by Nakamura et al. (1991) and Naudascher and Wang (1993). The vortex shedding associated to the rectangular cylinder is classified into: the leading-edge, impinging leading-edge and trailing edge vortex shedding. The classification was found mainly to depend on the cross section of the bluff body, the width-to-depth (B/D) ratio and the geometrical shape of the leading edge.

The leading-edge vortex shedding occurs with the rectangular cylinder having the B/D ratio of 2 to 3. With the permanent separation points located at the leading edge, two shear layers are created on the top and bottom surfaces of the bluff body. A short after-body length will not allow the shear layers to reattach; instead, they interact quickly downstream forming the regular vortex street, which is the well-known von Kármán vortices.

The trailing-edge vortex shedding occurs on thinner rectangular cylinders with the B/D ratio of 6 to 9. Due to the long after-body length, the shear layers generated from the leading edge have enough time to diffuse and the flow reattachment can happen as showed in Figure 2.16. The flow separation occurs again at the trailing edge and vortices are shed into the wake region in the manner of the von Kármán vortex street.

Figure 2.16: Vortex shedding of a $B/D = 8$ rectangular prism (Ohya et al., 1992).

The impinging leading-edge vortex shedding is normally observed on the rectangular cylinder having medium B/D ratios (about 4 to 6). This phenomenon involves the impingement of unstable shear layers caused by the flow separation at the leading edge. When the flow passes the bluff bodies, two cavities are formed on the top and bottom surfaces; inside these cavities, vortices shed from the leading edge impinge onto the position close to the trailing edge as illustrated in Figure 2.17. It causes a sudden increase in pressure and velocity around the impingement point; this perturbation then strongly affects the flow around the leading edge increasing the level of instability of the cavities. Eventually, vortices are released into the wake behind the body. This vortex shedding phenomenon is very prone for a cross section containing square trailing edges such as H-shaped sections as investigated by Nakamura and Nakashima (1986). The presence of the trailing causes a strong impinging shear layer instability on the top and bottom surfaces of the prism; the interaction of these unstable layers downstream generates the von Kármán vortex street.

As can be seen, the classification of the vortex shedding phenomenon of the rectangular cylinder is

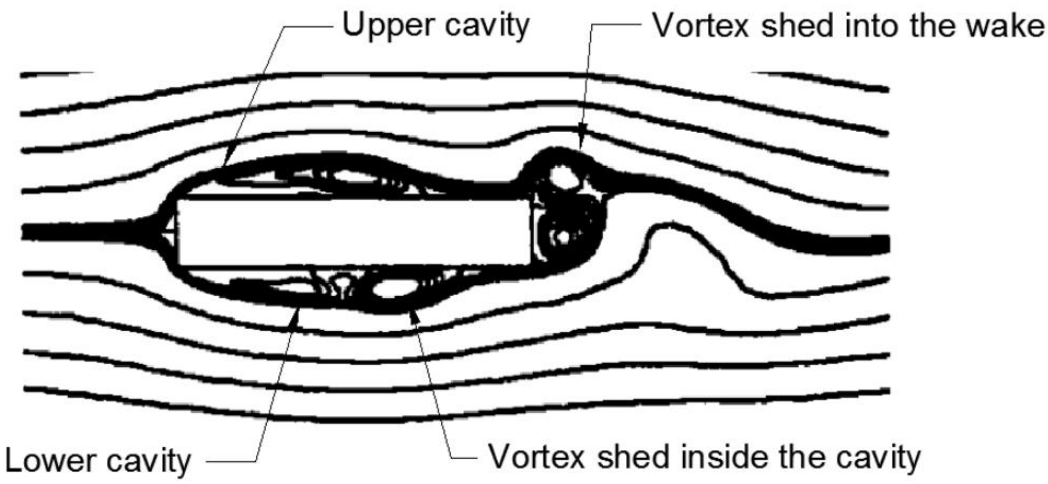

Figure 2.17: Streamlines around a $B/D = 4$ rectangular prism adapted from Ohya et al. (1992).

mainly dependent on the behaviour of the separation bubble on the top and bottom surfaces or the separated shear layer, which can be affected by a variation in the Reynolds number. Therefore, it is inevitable that the relationship between the Strouhal and Reynolds number is not universal; instead, it is affected by the aspect ratio B/D of the cross section.

For the bluff body having a very small aspect ratio or a square cross section, two shear layers never reattach to the surfaces of the body; they quickly interact downstream generating the von Kármán vortex street. Therefore, a variation in the Reynolds number poses a minimum effect on the vortical structure in the wake; the Strouhal number is quite constant for a large range of Reynolds number (Okjima, 1982).

If the bluff body has a large aspect ratio, the reattachment of the separation bubbles can occur and a more complicated relationship between the Strouhal number and Reynolds number is observed. Okjima (1982) found a very strong dependence of the Strouhal number on the Reynolds number for the $B/D = 2$ rectangular cylinder as shown in Figure 2.18. The result shows a transition region where there is a sudden discontinuity in the Strouhal-Reynolds-number relationship curve at the Reynolds number of about 450. At the lower Reynolds numbers, the Strouhal number increases with the Reynolds number while, beyond this region, the Strouhal number is seen not to vary significantly with the Reynolds number. The sudden reduction of the Strouhal number was explained by the variation of the separated flow on the top and bottom surfaces of the cylinder. At low Reynolds number, the separated flow from the leading edge always reattaches to the surface; the flow then separates again at the trailing edge. During the transition, the separated flow from the leading edge cannot detach completely from the surfaces of the body; instead, it reattaches to either the top or bottom surfaces during each cycle of the vortex shedding. Therefore, the reattachment point becomes intermittent. When the Reynolds number keeps increasing,

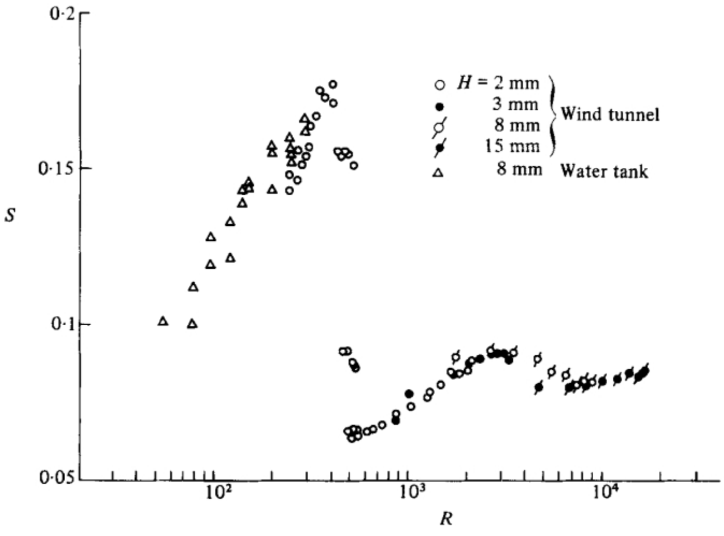

Figure 2.18: Variation of Strouhal number, S, against Reynolds number, R, for a $B/D = 2$ rectangular prism; both are defined using the dimension D (Okjima, 1982).

the separated flow is found to detach completely from the surfaces, leading to a broader wake accompanied by a decrease of the vortex shedding frequency and the Strouhal number. Similar variation in the flow features and the Strouhal number against the Reynolds number was also observed for the rectangular cylinder having the aspect ratio of $B/D = 3$; the transition, however, does not occur until the Reynolds number of 10^3 instead of around 500 as in the case of $B/D = 2$ rectangular cylinder (Okjima, 1982). A longer after-body length, thus, tends to prevent the separated flow from detachment and to keep them attached on the side surfaces. The results obtained by Okjima (1982) also suggest the dependence of the Strouhal number on the aspect ratio which was later observed by Yu and Kareem (1998) and Shimada and Ishihara (2002). Their results are summarised in Figure 2.19. This figure collected data from a lot of studies using a variation of approaches to measure the Strouhal number. The Strouhal number of the $B/D = 2$ and 3 rectangular cylinder is found to be multiple values due to the transition in the flow feature as discussed above.

It is noticed that the Strouhal numbers presented in Figures 2.18 and 2.19 are defined by the depth D which is the shorter dimension of the cross section. Nakamura et al. (1991) calculated the Strouhal number using the width B of the cross section and presented the dependence of this Strouhal number on the aspect ratio as shown in Figure 2.20. At the Reynolds number of 10^3, a so-called stepwise increase in the Strouhal number is observed at the aspect ratios of 5 to 6, 8 to 9 and 11 to 12. According to Nakamura et al. (1991), the Strouhal number of the rectangular cylinder exists in different branches, each of which has a nearly constant value. As the aspect ratio of the rectangular cylinder gets larger, the Strouhal number increases in a stepwise manner to a value which is approximately equal to an integer multiple of 0.6. In addition, the points where these branches start are on a straight line passing through the origin.

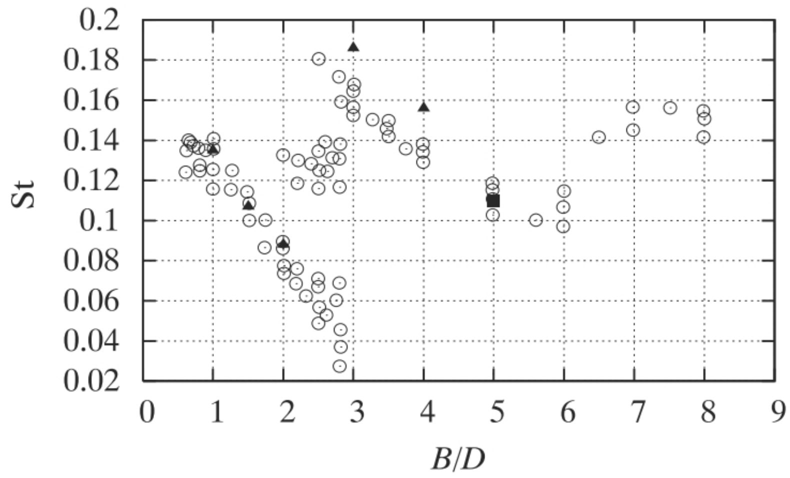

Figure 2.19: Variation of Strouhal number against aspect ratios; ⊙: Shimada and Ishihara (2002); ▲: Yu and Kareem (1998); ■: (Bruno et al., 2010); the Strouhal number is defined using the dimension D.

Another numerical study conducted by Ozono et al. (1992) also showed similar stepwise behaviour of the Strouhal number despite the fact that the limitation of the computational power at that time caused an offset in the Strouhal number of rectangular cylinders of large aspect ratios ($B/D > 5$).

For the rectangular cylinders having a unique Strouhal number, spectra of the velocity fluctuations measured in the wake showed only one sharp dominant frequency component which was correspondent to the vortex shedding frequency (Nakamura et al., 1991). An analysis of the phase relationship of the surface pressure fluctuation at the dominant frequency relative to that measured at the leading edge revealed a simple relationship between the wavelength of the surface pressure fluctuation and the width of the cylinder. In fact, the wavelength of the surface pressure fluctuation was found to equal to an integer multiple of the cylinder's width. And this integer multiplication was identical to what was associated with each branch of the Strouhal number as shown in Figure 2.20. The flow visualisation latter confirmed that this integer multiplication essentially represented the number of vortices appearing on the side surface during one cycle of the vortex shedding. Therefore, the stepwise increase in the Strouhal number of the rectangular cylinder with long after-body length is associated with different modes of the vortex shedding involving a sudden change in the flow structure or, in particular, the number of vortices propagating on the side surface. The Strouhal number of the rectangular cylinder having a long after-body length is defined as

$$\mathrm{St} = 0.6n, \tag{2.28}$$

where n is the number of vortices propagating on the side of the cylinder. Regarding the stepwise increase

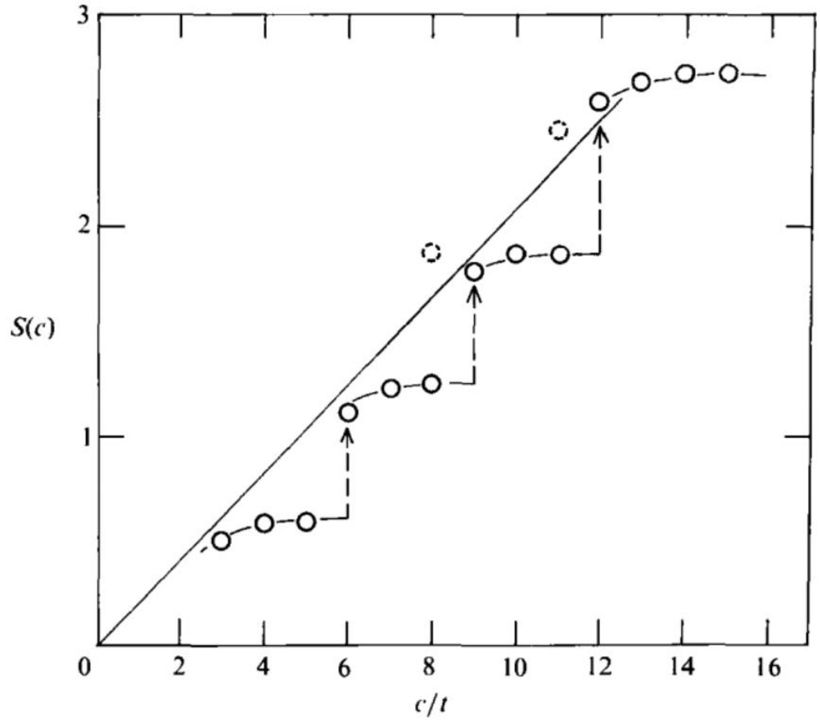

Figure 2.20: Variation of Strouhal number, $S(c)$ based on the width c against aspect ratios c/t at the Reynolds number of 10^3 (Nakamura et al., 1991)

.

in the Strouhal number, the $B/D = 8$ rectangular cylinder is taken as an example. The spectrum of the velocity fluctuation in the wake showed two sharp peaks at distinct frequencies; the higher component appeared to be sightly less dominant compared to the lower one (Ozono et al., 1992). The analysis of the phase relationship of the pressure fluctuation at these two dominant frequencies revealed two different associated vortex structures or two different modes of the vortex shedding. Ozono et al. (1992) further showed that these two modes of the vortex shedding did not exist together. Instead, after a short transition period with irregular fluctuations, it appeared that these two modes occurred spontaneously and the transition between them was intermittent. As showed in Figure 2.21, the first part of the time history of the lift coefficient (up to 1150 s) is associated with the second mode of the vortex shedding represented by two vortices on the upper surface of the cylinder (Figure 2.22a). After that the vortex shedding mode suddenly changes to the third mode with three vortices appearing on the upper surface of the cylinder (Figure 2.22b).

The physical mechanism of the dependence between the wavelength of the pressure fluctuation on the side surface and the width of the cylinder was first explained by Nakamura et al. (1991) as a result of the impinging shear-layer instabilities. As for the rectangular cylinder with long after-body length, the shear layer separated from the leading edge interacts directly with the trailing edge. This emits a pressure pulse propagating upstream and controlling the formation of the leading-edge shear layer in the next

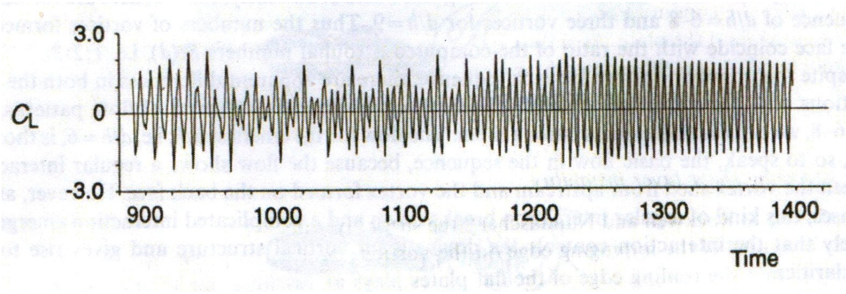

Figure 2.21: Time series of the lift coefficient C_L for the $B/D = 8$ rectangular cylinder (Ozono et al., 1992)

.

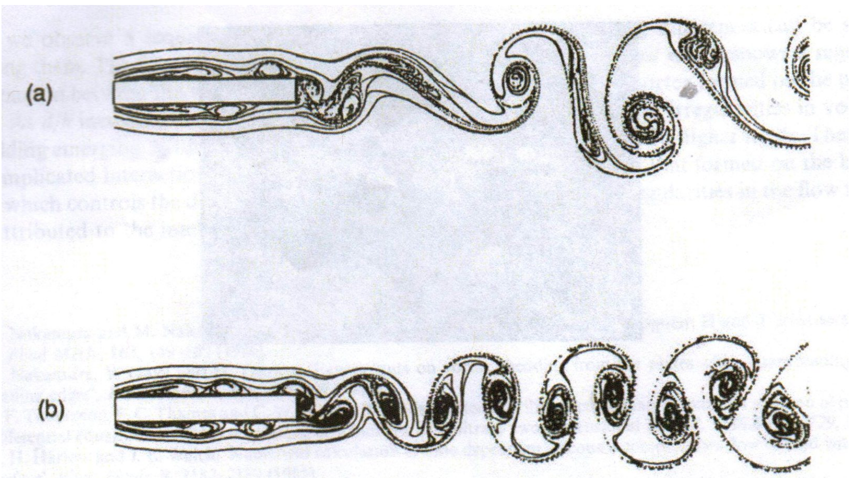

Figure 2.22: Streamlines of the flow field around a $B/D = 8$ rectangular cylinder: (a) second mode of the vortex shedding, (b) third mode of the vortex shedding (Ozono et al., 1992)

.

cycle of the vortex shedding. After a transition period, a control feedback loop is established generating a synchronisation between the impingment of the leading-edge shear layer close to the trailing edge and the formation of the other leading-edge shear layer in the next cycle.

However, Naudascher and Rockwell (1994) and Mills et al. (1995) pointed out that for the rectangular cylinder with larger aspect ratios ($B/D > 6$), the aforementioned explanation could not be appropriate because the shear layer did not directly interact with the trailing edge. Instead, it was found that the leading-edge shear layer rolls up forming a vortex which then propagates downstream. When the leading-edge vortex approaches the trailing edge, it interacts with another vortex being shed from here. This interaction creates a pressure pulse travelling upstream to the receptive shear layer generated from the leading edge on the same side of the cylinder in the next cycle and a feedback loop is achieved as discussed above (Tan et al. (1998); Mills et al. (2003)). If this synchronisation is strong, a unique mode of the vortex shedding and the Strouhal number is observed. On the contrary, some rectangular cylinder with sufficient after-body length experiences a relatively weak feedback loop; a transition to the next mode of the vortex shedding then occurs intermittently, increasing the number of vortices simultaneously appearing on the side surface every cycle.

In addition, Mills et al. (2003) suggested that the pressure pulse generating from the trailing edge is hydrodynamic in nature; therefore, it can be interrupted or weakened by the turbulence in the flow or an increase in the Reynolds number. In fact, Mills et al. (2003) found that at a higher Reynolds number, the stepwise increase in the Strouhal number could be observed at a rectangular cylinder having a smaller aspect ratio, which was similar to the suggestion made by Okjima (1982). An increase in the Reynolds number promoted a transition from a laminar boundary layer to a turbulent boundary layer. This transition could shorten the separation bubble and the width of the vortex, weakening the aforementioned synchronisation and allowing the higher mode of the vortex shedding to occur.

As for the main object in this research study which is the 5:1 rectangular cylinder, the aerodynamic characteristics of the flow around the cylinder are classified as the impinging shear layer vortex shedding. However, it was found that the reattachment point of the separation bubble is very close to the trailing edge and the separated flow from the leading edge of the cylinder does not fully attach to the side surface of the cylinder. Figure 2.20 indicates that the first stepwise increase in the Strouhal number occurs at the aspect ratio of $B/D = 5$. In fact, Stokes and Welsh (1986) found the vortex shedding of the 5:1 rectangular cylinder spontaneously switched between the first and second modes. These findings have shown the highly unsteady flow field around the cylinder, attracting further investigation from researchers and make it become the main subject of the study “A Benchmark on the Aerodynamics of a Rectangular

5:1 Cylinder" (BARC) (Bruno et al., 2010).

Thereafter, understanding the importance of the cylinder's width, the Strouhal number predicted in the experimental wind tunnel or computational studies will be defined based on the width B of the cylinder.

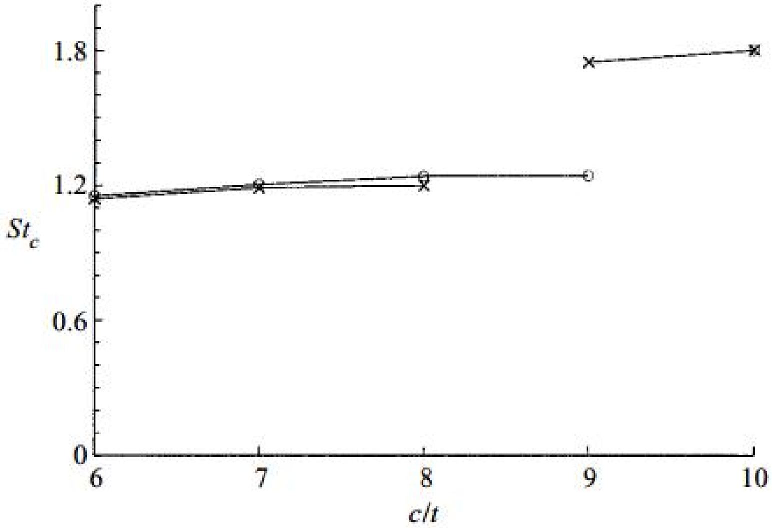

Figure 2.23: Comparison of the Strouhal number, St_c, for the rectangular cylinder having the aspect ratio c/t between 6 and 10; ∘: Re = 490 (Mills et al., 2003) and ×: Re = 1000 (Nakamura et al., 1991); adopted from Mills et al. (2003); Strouhal number is defined based on the width c.

2.4 VORTEX-INDUCED VIBRATION (VIV)

As discussed in Section 2.3, the presence of a flow around a body can cause flow separation and lead to the formation of vortices either in the wake region or along the side surfaces, in case of a bluff body having a long after-body length. This process of vortex shedding alternately varies the pressure on either side surface of the body, which leads to a force acting on the body in the transverse direction to the flow forcing the body into an oscillatory state. The resonance effect as well-known in a pure structural system can be observed if the vortex shedding frequency matches one of its modal natural frequencies. This oscillation of the body is called the Vortex-induced Vibration (VIV).

The VIV is an Instability-Induced Excitation, where the excitation acting on the structure is caused by the flow instability due to the presence of the structure. VIV is observed to occur on both the circular cylinder and the rectangular cylinder; the physical mechanism is however slightly different between geometries, which will be explained later in this section. Regardless of the geometry, VIV is accompanied by the lock-in phenomenon.

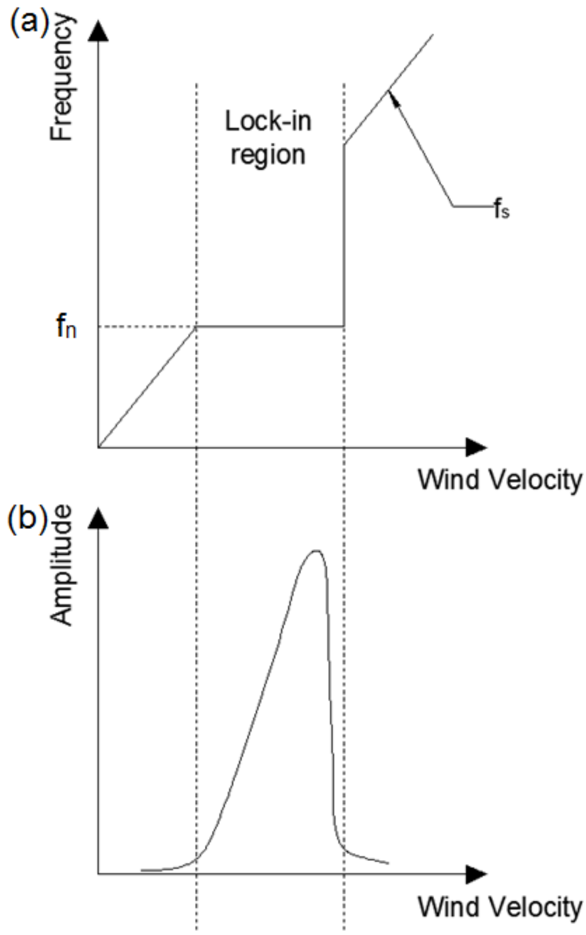

Figure 2.24: Lock-in accompanied by (a) a constant vortex shedding frequency and (b) a rapid increase in the amplitude of oscillation.

2.4.1 Lock-in

The lock-in of the system undergoing VIV is associated with a large increase in the amplitude of structural oscillation and a constant vortex shedding frequency close to the natural frequency of the body (Figure 2.24). Outside the lock-in region, the vortex shedding frequency f_s varies linearly with the wind speed U; the proportionality constant is the Strouhal number as expressed in Equation 2.26.

As can be seen from Figure 2.24a, when f_s coincides with one of the modal natural frequencies of the bluff body f_n, f_s is locked on f_n regardless of the wind speed. The lock-in corresponds to an interval when the bluff body oscillates at f_n, irrespective of wind speed, and the amplitude steadily increases. The amplitude as shown in Figure 2.24b reaches the peak at the upper end of the lock-in before sharply decreasing towards the end of the lock-in. When the system reaches the lock-out, the body keeps oscillating at the natural frequency f_n while the vortices are shed at the frequency f_s defined by the Strouhal number.

The lock-in phenomenon only occurs over a short range of the wind speed where the vortex shedding frequency and one of the modal natural frequencies of the body are similar. The maximum displacement during the lock-in depends on the mass, damping and the aerodynamic shape of the structure. The principle to reduce the amplitude of oscillation of the structure undergoing VIV is to interrupt the formation of vortices by either to increase the surface roughness of the body or to create a more streamlined body particularly for the rectangular cylinder. The installation of the splitting plate in the wake region was also found to effectively suppress VIV; however, as being discussed later in this section, this methodology is not appropriate for most rectangular cylinders with long after-body length.

The VIV response illustrated in Figure 2.24 is only a brief visualisation of this phenomenon. The variation of the damping ratio, particularly in the case of the circular cylinder, can yield completely different behaviour regarding the structural response and the flow feature in the wake region.

2.4.2 Mass-damping Parameters

Before discussing the characteristics of the VIV of the circular and rectangular cylinders, it is essential to look at one of the most fundamental questions which has been debated over the last 30 years; this question concerns which mass-damping parameters should be used in order to predict the peak-amplitude response (Williamson and Govardhan, 2004). The use of the mass-damping parameter was first suggested by Vickery and Watkins (1964) who plotted the peak amplitude during the lock-in of flexible circular cantilevers against the proposed stability parameter $K_s = \pi^2 m^* \zeta$ where $m^* = (4m)/(\rho\pi D^2)$ is the mass ratio, m is the mass of the structure per unit length, ρ is the density of the fluid, D is the characteristic dimension of the structure (the diameter of the cylinder) and ζ is the structural damping ratio. Later, Scruton (1963) introduced a new parameter, proportional to K_s, for his wind tunnel tests of elastically-mounted cylinders; this parameter was then named as Scruton number $\mathrm{Scr} = 2K_s/\pi = \pi m^* \zeta/2$. Using results from different experiments, Skop et al. (1973b) conducted a separate analytical study and proposed a different combined response parameter which was later termed as Skop-Griffin parameter $\mathrm{S_G} = 2\pi^3 \mathrm{St}^2 (m^* \zeta)$.

The common feature between the three parameters listed above is the presence of the so-called mass-damping term $m^* \zeta$. The use of this combined term in estimating the VIV peak amplitude of the circular cylinder has been the primary debating point in literature. According to Sarpkaya (1978) and Sarpkaya (1979), the dynamic response of the structure in the lock-in is dependent on the mass ratio m^* and the damping ratio ζ terms individually, as well as on the combined term $m^* \zeta$. The use of the Skop-Griffin parameter or the combined term $m^* \zeta$ should be limited to the structure having $\mathrm{S_G} > 1$ (Sarpkaya, 1978).

However, Griffin and Ramberg (1982) has showed this proposed limitation is controversial. By conducting two sets of experiments using circular cylinders having similar Skop-Grifffin parameters $S_G = 0.5$

to 0.6 and different mass ratios $m^* = 4.8$ and 43, the dependence of the extend of the lock-in on the mass ratio was found; the lower mass ratio led to a larger lock-in interval. More importantly, the peak responses in two cases were found to be indistinguishable even though the value of $\mathrm{S_G}$ violated the limitation proposed by Sarpkaya (1978).

Later, Williamson and Govardhan (2004) reported significant scatter in the plot of the peak amplitude during the lock-in against the Skop-Griffin parameter for different VIV systems. However, considering only the elastically mounted circular cylinder, a good agreement between different sets of experiment could be seen. This also shows that the applicability in using the mass-damping parameter can be extend down to $\mathrm{S_G} = 0.01$ rather than the limit proposed by Sarpkaya (1978).

It is obvious that the relationship between combined mass-damping parameter $m^*\zeta$ and the peak amplitude during the lock-in has not been fully uncovered. According to the extensive review conducted by Williamson and Govardhan (2008), Zdravkovich (1982) and Zdravkovich (1990), the mass-damping parameter $m^*\zeta$ or the Scruton number Scr will be used in the discussion of the VIV of the circular and rectangular cylinder in the following section, particularly for the application in wind engineering. However, since the development of the Scruton number was based the circular cylinder, certain modification to the definition of the Scruton number must be applied in the case of the rectangular cylinder to preserve its meaning (Marra et al., 2011). Instead of using only the dimension D as the characteristic length scale, it is more sensible to apply both of the width B and the depth D to normalise the mass ratio $m^* = m/(\rho BD)$ and to calculate the Scruton number $\mathrm{Scr} = (\pi m\zeta)/(\rho BD)$.

2.4.3 VIV of a Circular Cylinder

Regarding a freely vibrating circular cylinder, there exist two distinct VIV responses depending on whether the system has a low or high combined mass-damping parameter $m^*\zeta$. Nevertheless, the onset reduced wind velocity $U_{R,\mathrm{onset}}$ of the VIV lock-in is identical, which is dependent on the Strouhal number St as

$$U_{R,\mathrm{onset}} = \frac{1}{\mathrm{St}}. \tag{2.29}$$

As shown in Figure 2.25, the VIV amplitude response of a system having a high combined mass-damping parameter includes two branches, which are the initial excitation branch determining the maximum response reached and the lower branch. A number of experimental works showed the transition between these two branches possesses hysteristic characteristics and occurs over a long time period of a few hundred oscillation cycles. In an attempt to compare against the experimental results produced by

Feng (1968), Govardhan and Williamson (2000) confirmed the presence of these two response branches; they also found different modes of vortex structure in the wake associated to each branch. For the initial branch, analysing the vorticity measured in the wake during one cycle of the structural oscillation showed the formation of only one vortex during the first half of the period and another one in the final half of the period but in the opposite rotation (Figures 2.26a and b). This mode of the vortex structure is called the 2S mode corresponding to two single counter-rotating vortices being formed in every cycle of the oscillation. When the circular cylinder undergoes the lower branch, distinct vortex structure is observed; as can be seen in Figure 2.26c, during a half of the period, a pair of counter-rotating vortices is shed into the wake, for which it is named the 2P mode. This mode of vortex structure is originated by the deformation and splitting of the vortex, for example the *red* vortex on the lower surface as shown Figure 2.27a by the counter-rotating *blue* vortex formed from the upper surface. This results in a pair of a secondary small *red* vortex next to a primary strong *blue* vortex being transported downstream (Figure 2.27b). The same process repeats for the vortex on the upper surface (Figures 2.27c and d). The secondary vortex is quickly weakened by the primary one, which is probably due to the excessive strain of the stronger vortex; thus, the 2P mode eventually becomes the 2S mode, creating certain difficulties in identifying its characteristics in experiments. Moreover, comparing the vorticity plots in Figures 2.26a and c as the circular cylinder reaches its minimum displacement, it is obvious that there exists a change in timing of vortex shedding, which is thought to be responsible to the switch from the 2S mode to the 2P mode and the transition from the initial to lower branch. In addition, the vortex shedding frequency in the high combined-mass-damping system stays close the natural frequency of the structure during the entire lock-in.

On the other hand, a circular cylinder having a low combined-mass-damping parameter can undergo three different branches as the wind speed increases, which is the initial branch, the upper branch where the maximum response during the lock-in occurs and the lower branch. Experimental studies including Khalak and Williamson (1999) show the transition between the initial and upper branch is hysteresis while the upper branch switches to the lower branch in an intermittent manner. Each of the three branches is associated to distinct modes of vortex structure (Govardhan and Williamson, 2000). If the mode 2S is observed in the initial branch, the mode 2P is present in the other two branches. More importantly, the transition between the mode 2S and the mode 2P involves a switch in timing of vortex shedding. Comparison of the vorticity measured in the wake between the initial and upper branches (Figure 2.28a) clearly shows a 180° phase shift in the timing of vortex shedding, indicating a change in the mode of vortex structure. On the other hand, the timing of the vortex shedding as well as the mode of vortex structure in the upper and lower branches is similar, which is shown by similarity in the near-wake vorticity dynamics (Figures 2.28a and b). The frequency response of the low combined-mass-damping structure

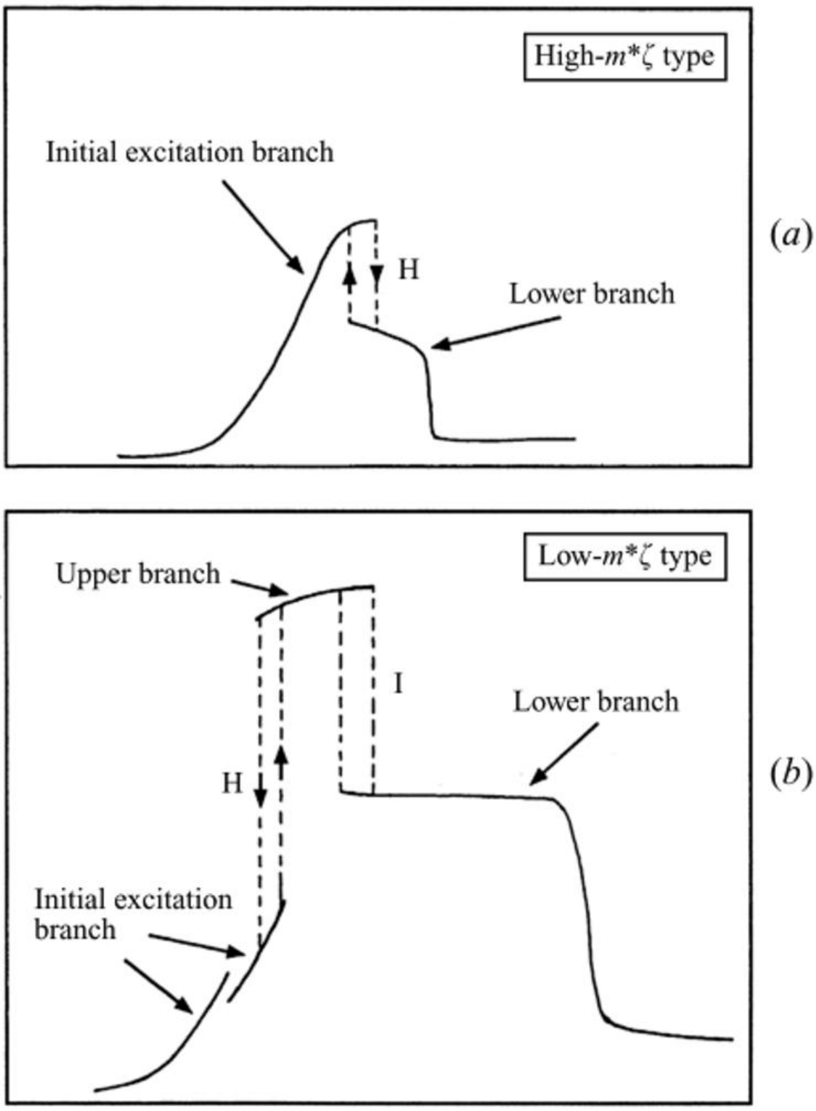

Figure 2.25: Schematic showing two different types of VIV responses of a freely vibrating circular cylinder (Govardhan and Williamson, 2000).

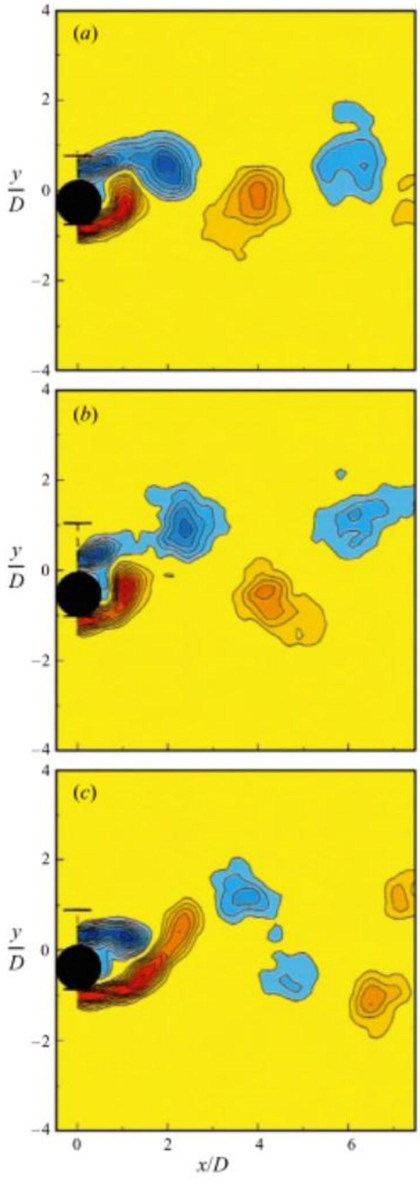

Figure 2.26: Vorticity plots of the wake region showing different modes of the vortex structure: Mode 2S in the initial branch (a,b) and Mode 2P in the lower branch (c) (Govardhan and Williamson, 2000).

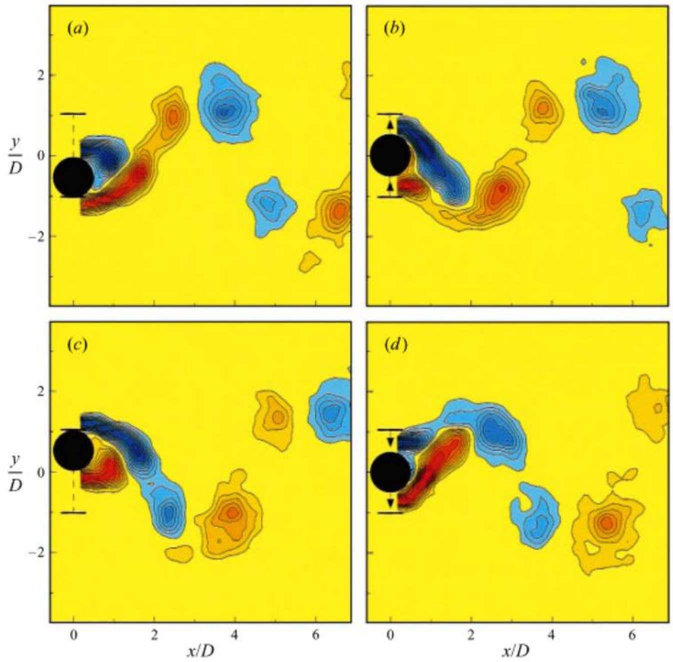

Figure 2.27: Vorticity plots at every quarter-cycle during one cycle of the oscillation illustrating the formation of the 2P mode of vortex structure (Govardhan and Williamson, 2000).

was also found to be different from the high combined-mass-damping one. In fact, the vortex shedding frequency can be significantly higher than the natural frequency of the structure. For a structure having a very low mass ratio ($m^* \approx 1$), the vortex shedding frequency was found to linearly increase during the upper branch before locked into a value which was nearly double the natural frequency of the cylinder (Govardhan and Williamson, 2000).

An investigation of a simple elastically-mounted cylinder with a uniform circular cross section has showed different modes of vortex shedding depending on the amplitude response branches and the combined mass-damping parameters. For a more complex structure having non-uniform circular cross section or experiencing varied amplitude of response in the span-wise direction, the modes 2S and 2P discussed above were found to co-exist along the span-wise length of the structure. It is called the hybrid 2S-2P mode after Techet et al. (1998) observed this effect in their study of a tapered circular cylinder. Also, by studying a very low mass ratio pivoted circular cylinder freely to move in both the stream-wise and cross-wind direction, Flemming and Williamson (2003) discovered a new mode of vortex structure named as the mode 2C which comprises two co-rotating vortices forming in each half of the oscillation cycle. Further discussion on the behaviour of the circular cylinder was summarised and reviewed in Govardhan and Williamson (2000), Williamson and Govardhan (2004) and Williamson and Govardhan (2008).

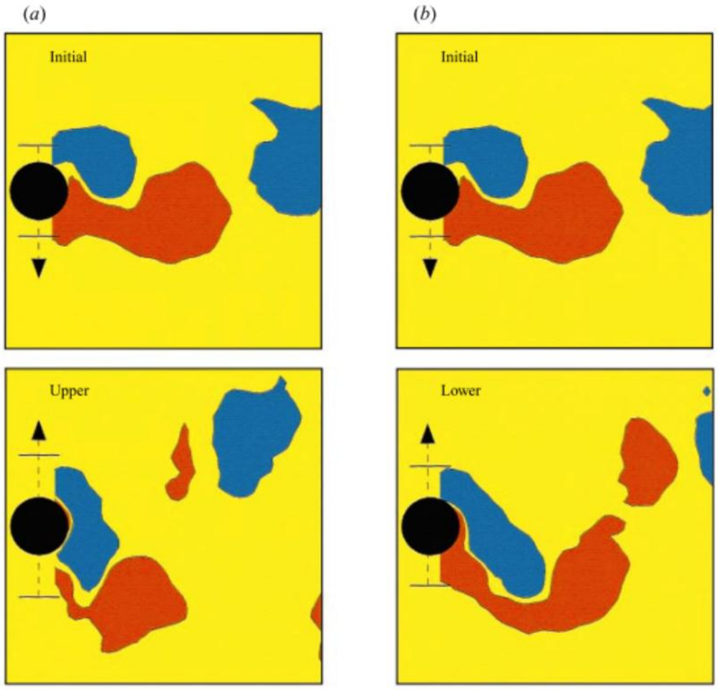

Figure 2.28: Comparison of the vorticity in the wake: (a) between the intial and the upper branches and (b) between the initial and lower braches; the black arrows indicate the direction of the motion of the circular cylinder (Govardhan and Williamson, 2000).

2.4.4 VIV of a Rectangular Cylinder

The rectangular cylinder is considered as a generic geometry for bridge decks or tall buildings; these structures are characterised by high values of the mass ratio and damping ratio. Therefore, the VIV response of the rectangular cylinder is normally classified as a high combined-mass-damping type response. The structural and frequency responses of the VIV of a rectangular cylinder particularly possess all features described in Figure 2.24. During the lock-in, a single response branch is observed where the amplitude of the response gradually increases and then rapidly falls down after the peak response is reached and the vortex shedding frequency is closely equal to the naturally frequency of the structure. Similar to the circular cylinder, the peak response reached during the VIV lock-in depends on the combined mass-damping parameter while the range of the lock-in is governed by the mass ratio given that combined mass-damping parameter is constant.

The rectangular cylinder can undergo the VIV response in two different modes which are the heaving mode, i.e. crosswind oscillation and the pitching mode, i.e. torsional oscillation; these two modes can be coupled also. However, the onset velocity of VIV responses for each mode could be different depending the aspect ratio.

As discussed in Section 2.3.2, the shear layers created from the permanent separation points at the leading edge of the cylinder can interact together directly in the wake or with the after-body length. This formation can be enhanced by the heaving or pitching motion of the cylinder and has a phase relationship with the oscillation of the cylinder, at which point it is normally referred as the motion-induced shear layer.

For the rectangular cylinder having small aspect ratio ($B/D \leq 1$) in either stationary or oscillatory state, these shear layers interact directly together forming the von Kármán vortex street. This flow feature is responsible for triggering the VIV response of a dynamic cylinder if the frequency of the von Kármán vortex street reaches the natural frequency of either the heaving or pitching mode. Therefore, the onset reduced velocity of the VIV heaving and pitching response for the rectangular cylinder having $B/D \leq 1$ is related to the Strouhal number as

$$U_{R,\text{onset,heaving}} = U_{R,\text{onset,pitching}} = \frac{1}{\text{St}}. \tag{2.30}$$

It is noticed that the Strouhal number for this type of rectangular cylinder is unique over a certain range of Reynolds number; therefore, only a single VIV heaving or pitching response can be observed at the reduced velocity defined in Equation 2.30.

On the contrary, the oscillating rectangular cylinder with a larger aspect ratio, $B/D > 1$, possesses a more complex flow structure around the cylinder and harmonics of VIV heaving and pitching responses can be observed at different reduced velocities. An interaction between the motion-induced shear layer and the after-body length leads to an instability in the shear layer. It is normally called the impinging-shear-layer instability, which is the single layer instability in contrast to the von Kármán vortex street which is the double layer instability. This forms the motion-induced vortex which travels down the surface of the body towards the trailing edge at the velocity measured to be about 60% of approaching flow (Shiraishi and Matsumoto, 1983). Apart from this main flow feature, it is found that the secondary vortex can also be shed from the separation point at the trailing edge; this secondary vortex is generally in phase with the motion-induced vortex created from the leading edge on the same side surface if the cylinder undergoes the heaving motion and on the opposite side surface if it is in the pitching motion. This very feature leads to different response characteristics between the heaving and pitching VIV. During the lock-in, Shiraishi and Matsumoto (1983) found that the motion-induced leading edge vortex arrived at the trailing edge and coalesced with the secondary vortex there after the elapse of $n\,T_{\circ,\text{heaving}}(n \geq 1)$ where $T_{\circ,\text{heaving}}$ is the natural period of the heaving mode of the structure in the heaving motion and the elapse of $(n + 1/2)\,T_{\circ,\text{heaving}}(n \geq 0)$ where $T_{\circ,\text{pitching}}$ is the natural period of the pitching mode of the structure in the pitching motion. This coagulation can be illustrated in Figure 2.29. The onset velocity for the heaving and pitching VIV could therefore be defined as

$$\text{VIV Heaving:} \qquad U_{R,\text{onset,heaving}} = \frac{1}{n}\frac{1}{0.6}, \tag{2.31}$$

$$\text{VIV Pitching:} \qquad U_{R,\text{onset,pitching}} = \frac{2}{2n-1}\frac{1}{0.6}, \tag{2.32}$$

where $n \geq 1$ is the harmonic of the VIV response which is corresponding to the number of vortices appearing on one side of the rectangular cylinder during one cycle. From Equation 2.31, the expression for the Strouhal number of the rectangular cylinder can be deduced to be $\mathrm{St} = 0.6n$ as being showed in Equation 2.28. Later, Nakamura and Nakashima (1986) studied the VIV responses of the rectangular cylinder having different aspect ratios between 2 and 6 and demonstrated that the impinging-shear-layer instability as the mechanism of the VIV of the rectangular cylinder. They also observed the first and second harmonics of the heaving and pitching VIV responses occurring at the onset reduced velocities given by Equations 2.31 and 2.32. However, for the pitching motion, similar to Shiraishi and Matsumoto (1983), they did not find the first harmonic for the rectangular cylinder having aspect ratios larger than 4. Also, the VIV response in the pitching mode is affected by varying the centre of the rotation, which includes a change in the onset reduced velocity and a presence of the other harmonics. Equation 2.32 is effectively only valid in the case that the centre of the rotation is located at the mid-chord of the cylinder.

Studying the flow pattern around an oscillating rectangular cylinder, Deniz and Staubli (1997) observed the coagulation of the motion-induced vortex shed from the leading edge and the secondary vortex created from the trailing edge. More importantly, when the fluid and structure system reaches the lock-out, they found an abrupt increase in the phase shift of the lift force at the excitation frequency and the motion of the cylinder. This sudden change in the phase corresponds to a variation in the timing of the secondary vortex formation in the trailing edge, breaking down the synchronisation with the motion-induced leading-edge vortex. The fact that the phase increases to 180° also indicates the energy flow is switched; during the lock-in, the energy transfers from the fluid to structure, causing the amplitude of the response to raise; when the system reaches lock-out, the energy flow is from structure to fluid and the amplitude of the VIV response rapidly decreased. In addition, during the lock-in, the phase shift possesses some relationship with the amplitude of the response. Instead of remaining to be constant as seen in other wind-induced behaviours such as flutter, the phase shift gets larger with an increase in the amplitude of the response, which indicates that less energy is transferred from the fluid to the structure. Therefore, the VIV tends to have a finite maximum response during the lock-in, for which this wind-induced response is classified to be the limit cycle oscillation.

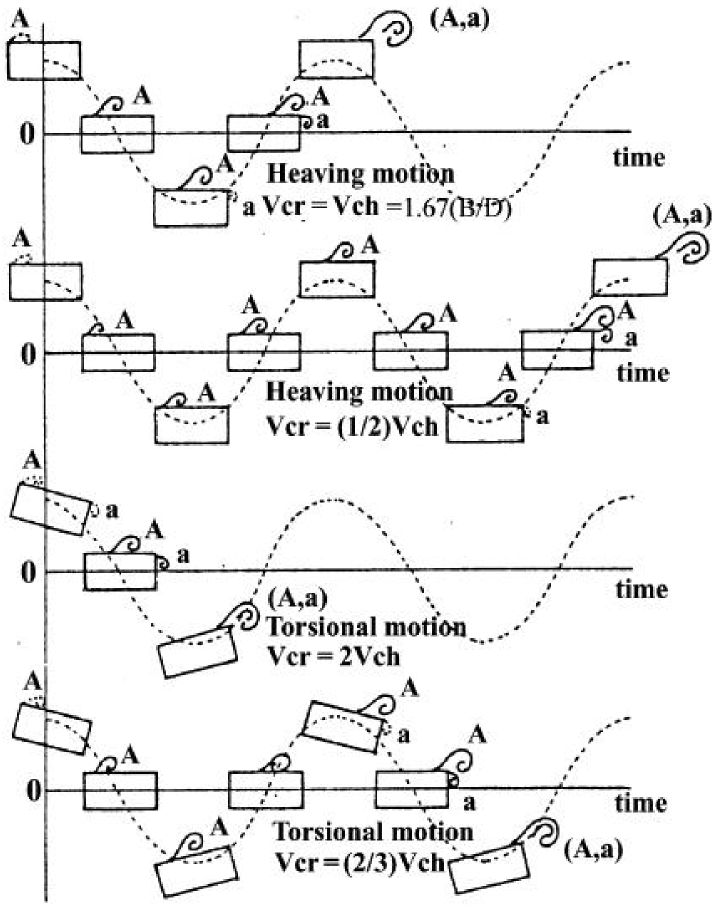

Figure 2.29: Motion-induced vortex shed from the leading edge (A) and secondary vortex shed from the trailing edge (b) in the heaving and pitching VIV response (Matsumoto et al., 2008).

Since the impinging-shear-layer instability or the motion-induced vortex is the primary mechanism of the VIV, placing a splitter plate in the wake region behind the cylinder can not reduce the amplitude of the response. In fact, it was found that, in this case, the VIV response can be increased. Kotmasu and Kobayashi (1980) and Matsumoto et al. (2008) confirmed there is an interaction between the aforementioned primary motion-induced vortex and the secondary vortex. By studying the VIV response of the $B/D = 4$ rectangular cylinder restrained to the heaving and pitching mode, Matsumoto et al. (2008) found the secondary vortex produces a mitigating effect on the motion-induced vortex, reducing the strength of the motion-induced vortex but not to pose any impact on its travel along the side surface of the cylinder. Therefore, breaking down the formation of the secondary vortex by, for example, placing a splitter plate in the wake, can effectively increase the VIV response caused by the motion-induced vortex. In order to reduce the VIV response caused by the impinging shear layer instability, installation of triangular fairings at the leading edge is an effective method to prevent the formation of the motion-induced leading-edge vortex, which significantly reduces the amplitude of the VIV response during the lock-in. Also, by increasing the damping of the structure, the amplitude of the response can be suppressed.

2.5 MATHEMATICAL MODELLING OF VORTEX-INDUCED OSCILLATION

As discussed in Section 2.4, the VIV is classified as the limit cycle oscillation having a certain displacement during the lock-in which cannot produce catastrophic failures. However, the VIV can result in the fatigue damage and reduction of the structural health and level of comfort for users. The importance of understanding this wind-induced phenomenon is apparent and a detailed study during the design stage to carefully predict the VIV response of the structure is essential to ensure safety and serviceability after the completion of construction.

The prediction of the VIV of astructure can be done by using either wind tunnel or computational fluid dynamics approach. However, taking into account the need of varying the aerodynamic shape of the structure and the damping of the structure, the major disadvantage of both methods is time-consuming. Therefore, a reliable and practical semi-empirical model for the VIV is necessary during the early designing phase before further investigation using the wind tunnel of computational fluid dynamics can be invested.

The difficulties in modelling the VIV arises from the intrinsic complexity of this behaviour. As identified by Bishop and Hassan (1964), the interaction between the fluid and the oscillating cylinder is highly non-linear, especially during the lock-in. Particularly, this non-linearity is also highlighted by the variation of the phase shift between the lift force and the displacement during the lock-in and by the abrupt jump to 180° when the system reaches lock-out.

Since 1970s, a number of different semi-empirical models for the VIV of circular and rectangular cylinders have been proposed; they can be classified into two main groups which are the single- and two-degree-of-freedom modes. The first group can be further divided into: negative-damping models (Vickery and Basu (1983); Larsen (1995); Scanlan (1998)) and force-coefficient data models (Sarpkaya (1978); Iwan and Botelho (1985)). As suggested by its name, the underlying physical mechanism of the former is the negative-damping type instability created by the decrease in the total damping of the structure, leading to an energy transfer from the fluid to structure and an increase in the response. Force-coefficient data models utilise the forced vibration technique measuring the force coefficients, from which the maximum response during the lock-in can be predicted; however, this technique is complicated and rarely available in most of wind tunnel facilities. The two-degree-of-freedom model which is also called as the wake-oscillator or lift-oscillator model can be grouped into two subclasses: those based on the Bishop-Hassan concept (Bishop and Hassan, 1964) where the wake is considered to be a non-linear oscillator (Hartlen and Currie (1970); Skop and Griffin (1973a); Dowell (1981); Diana et al. (2006)) and those based on the Birkoff (Birkhoff, 1953) concept where the wake is considered to be a plate oscillating from side to side (Tamura and Matsui, 1979). Despite the difference in the physical mechanism of the wake, both models include two variables: a structure response variable and an arbitrary fluid dynamic variable that is associated with the lift coefficient.

2.5.1 Single-degree-of-freedom Models for VIV

Among the single-degree-of-freedom models, the Ehsan and Scanlan model (Ehsan and Scanlan, 1990) has gained popularity thanks to its ability to model and predict the amplitude of the VIV of the rectangular cylinder or bridge decks in general, and its simple methodology to estimate the model parameters. The Ehsan and Scanlan model is given by

$$m\left(\ddot{y} + 2\zeta\omega_o\dot{y} + \omega_o^2 y\right) = F\left(y, \dot{y}, U, t\right), \tag{2.33}$$

where m is the mass of the structure per unit length, ζ is the damping ratio, ω_o is the circular natural frequency of the model in the heaving mode, y, $\dot{y}$ and $\ddot{y}$ is the displacement, velocity and acceleration of the structure in the heaving mode, U is the mean wind speed and F is the force acting on the structure in the cross-wind direction. The non-linearity of the VIV is inherent in the expression of the force defined as

$$F\left(y, \dot{y}, U, t\right) = \frac{1}{2}\rho U^2(2D)\left[Y_1(K)\left(1 - \epsilon\frac{y^2}{D^2}\right)\frac{\dot{y}}{U} + Y_2(K)\frac{y}{D} + \frac{1}{2}C_L(K)\sin(\omega t + \theta)\right]. \tag{2.34}$$

Here, $K = (\omega D/U)$ is the reduced frequency during the VIV with ω being the corresponding circular frequency of vibration under the wind and D being the diameter of the circular cylinder or the depth of the rectangular cylinder. C_L is the lift coefficient of the vortex-shedding component of the force and θ is the phase shift of this component against the motion of the cylinder. In this force term, $Y_1(K)$, ϵ, $Y_2(K)$ and $C_L(K)$ are the model parameters that need to be identified.

As can be seen in Equation 2.34, the total lift force acting on the structure is expressed as an uncorrelated summation of: (1) the motion-induced lift force as a summation of the aerodynamic damping component that is in phase with the velocity and the aerodynamic stiffness component that is in phase with the displacement, and (2) the vortex shedding force; the components are listed in the order as they appear in Equation 2.34. The first term of the force expression involves the parameter $Y_1(K)$ and ϵ which are correspondent to the linear and non-linear components of the aerodynamic damping respectively. This is essentially adopted from the van der Pol-type equation, which is also used in many different studies regarding modelling VIV. Given that $\epsilon > 0$, the limit-cycle-oscillation characteristic of VIV can be achieved. According to Ehsan and Scanlan (1990), during lock-in, when large VIV amplitude occurs, the vortex shedding part of the force becomes negligible compared to the motion-induced component; therefore the final term in Equation 2.34 can be ignored as

$$F\left(y, \dot{y}, U, t\right) = \frac{1}{2}\rho U^2 (2D) \left[Y_1(K) \left(1 - \epsilon \frac{y^2}{D^2} \right) \frac{\dot{y}}{U} + Y_2(K) \frac{y}{D} \right]. \tag{2.35}$$

In addition, the VIV response of the rectangular cylinder or bridge deck structures is classified as high combine-mass-damping type. There is not appreciable variation between the natural frequency of the structure in oscillatory state and the one measured in still air; therefore the aerodynamic stiffness term can also be neglected

$$F\left(y, \dot{y}, U, t\right) = \frac{1}{2}\rho U^2 (2D) \left[Y_1(K) \left(1 - \epsilon \frac{y^2}{D^2} \right) \frac{\dot{y}}{U} \right]. \tag{2.36}$$

Due to the high non-linearity inherent in the force term, an analytical solution to the Ehsan and Scanlan model is difficult to achieve. However, by applying the method of slowly varying parameters proposed by van der Pol (1920), an approximate solution of the non-dimensional limit-cycle-oscillation amplitude β can be found as

$$\beta = \frac{y_o}{D} = \frac{2}{\sqrt{\epsilon}} \sqrt{1 - \frac{B}{D} \frac{\mathrm{ScrSt}}{Y_1}}. \tag{2.37}$$

Here, y_o is the maximum amplitude of the limit cycle oscillation and Scr and St are the Scruton and Strouhal numbers as defined in Section 2.4.2 and 2.3.2 respectively. It is noticed that Equation 2.37 suggests the maximum amplitude of the VIV response is dependent on the Scruton number rather than the mass ratio and dampling ratio separately. With this solution, Ehsan and Scanlan (1990) also proposed a method to extract the model parameters Y_1 and ϵ by conducting a single free decay-to-resonance test at the wind speed corresponding to the maximum response during the lock-in starting from an amplitude larger than the limit-cycle-oscillation amplitude; this method has later been validated by Marra et al. (2011). More importantly, Ehsan and Scanlan (1990) emphasised on the requirement of wind tunnel tests to identify these parameters since the interaction between the fluid and the structure in the VIV is highly effected by the properties of the system such as the mass ratio and the damping ratio. This is confirmed by results showed in Figure 2.30, which illustrate the variability of the model parameters with respect to the damping ratio or the Scruton number. Also, it seems that the relationship between the model parameters and the damping ratio or the Scruton number is also distinct between cross section geometries. This point brings up the main disadvantage of the Ehsan and Scanlan model; the model parameters are highly dependent on the Scruton number; the model parameters identified from a system of fluid and structure are not able to predict correct VIV responses of the other systems having either a different aerodynamic cross section or different damping ratio. This disadvantage is also present in most of VIV models, limiting their reliability and practicability (Marra et al., 2011) . In addition, another disadvantage of the Ehsan and Scanlan model is the variability of the model parameters at different wind velocities, especially the parameter ϵ as shown in Figure 2.31. This limits the capability of the Ehsan and Scanlan model to predict VIV response at wind velocities that differ from those corresponding to the maximum response during the lock-in.

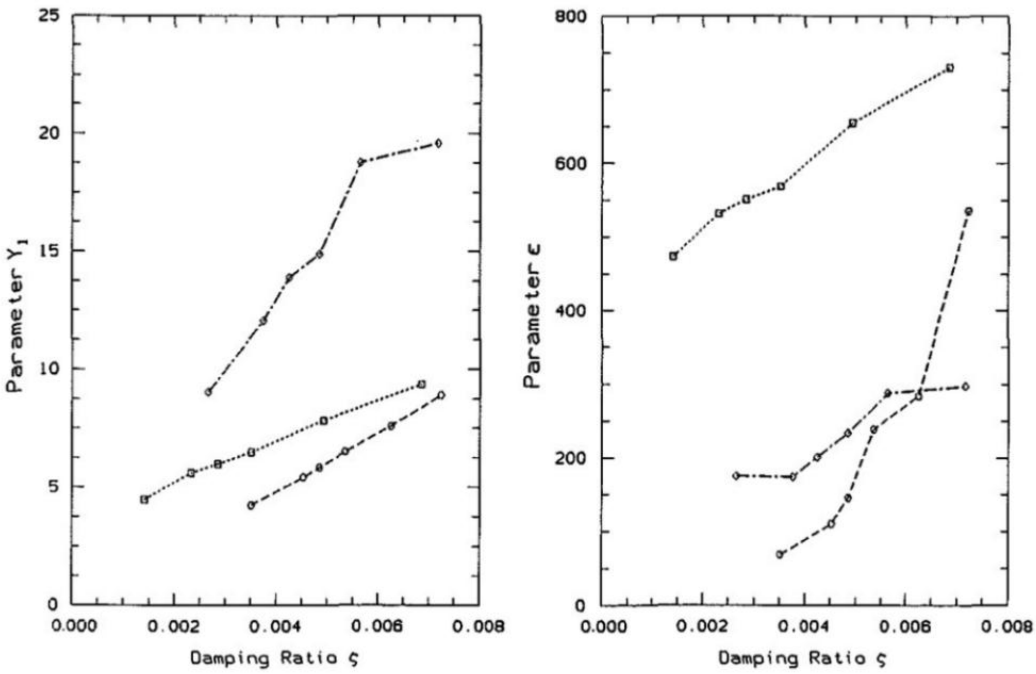

Figure 2.30: Variation of the Ehsan and Scanlan model parameter Y_1 and ϵ against the damping ratio ζ for: Deer Isle Bridge section ($\circ$); Tacoma Narrows Bridge section ($\Diamond$) and rectangular cylinder with the 4 : 1 aspect ratio ($\Box$) (Ehsan and Scanlan, 1990).

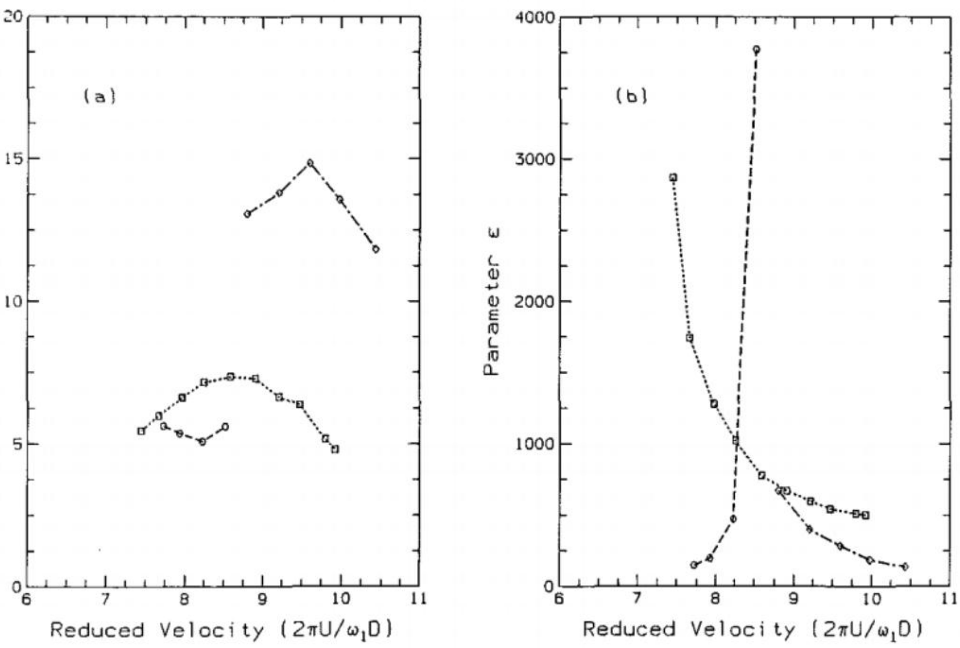

Figure 2.31: Variation of the Ehsan and Scanlan model parameter Y_1 and ϵ with against the reduced wind speed $(2\pi U)/(\omega_o D)$ for: Deer Isle Bridge section (○); Tacoma Narrows Bridge section (◇) and rectangular cylinder with the 4 : 1 aspect ratio (□) (Ehsan and Scanlan, 1990).

In an attempt to improve the Ehsan and Scanlan model, an intensive wind tunnel study has been conducted by Marra et al. (2015) where the VIV of the 4 : 1 rectangular cylinder were measured at nine different values of the Scruton number. This allowed the Griffin plot to be achieved; the Griffin plot is the plot of the maximum amplitude of the structural response during the VIV lock-in with respect to the Scruton number. The model-parameter identification method proposed by Ehsan and Scanlan (1990) were used to extract Y_1 and ϵ. The dependence of the model parameters on the Scruton number were confirmed; the Griffin plot predicted using the model parameters identified at one value of the Scruton number did not agree with the experimental Griffin plot (Figure 2.32). However, for this particular geometry, a relationship between the model parameters and the Scruton number could be drawn as shown in Figure 2.33; the parameter Y_1 varies linearly while the parameter ϵ increases quadratically with respect to the Scruton number, which is given by

$$Y_1(\text{Scr}) = a_1\text{Scr} + a_o \tag{2.38}$$

$$\epsilon(\text{Scr}) = c_2\text{Scr}^2 + c_1\text{Scr} + c_o, \tag{2.39}$$

where the coefficients a_o, a_1, c_o, c_1 and c_2 are estimated from the best fit curves in Figure 2.33. By substituting Equations 2.38 and 2.39 into the expression of β in Equation 2.37, the five coefficients in

Equations 2.38 and 2.39 can be identified by performing three decay-to-resonance tests at three different values of the Scruton number (Marra et al., 2015). These proposed relationship improved the accuracy and reliability of the Ehsan and Scanlan model when predicting the maximum response in the VIV lock-in at any values of the Scruton number or damping ratio especially during the design stage. However, whether the relationship between the model parameter Y_1 and ϵ and the Scruton number is independent of the aerodynamic shape of the cross section and the wind speed is still a question requiring further investigation.

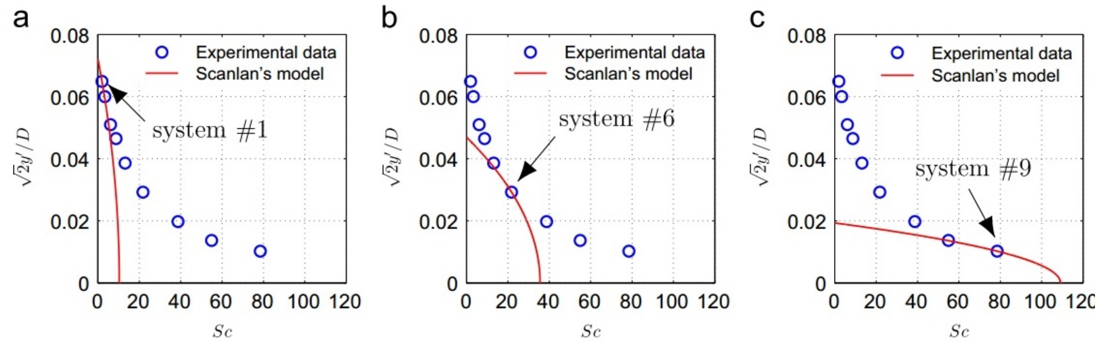

Figure 2.32: Comparison between the Griffin plots obtained from the wind tunnel test and predicted using the model parameters identified for: (a) Scr = 1.9; (b) Scr = 21.7; (c) Scr = 78.1 (Marra et al., 2015).

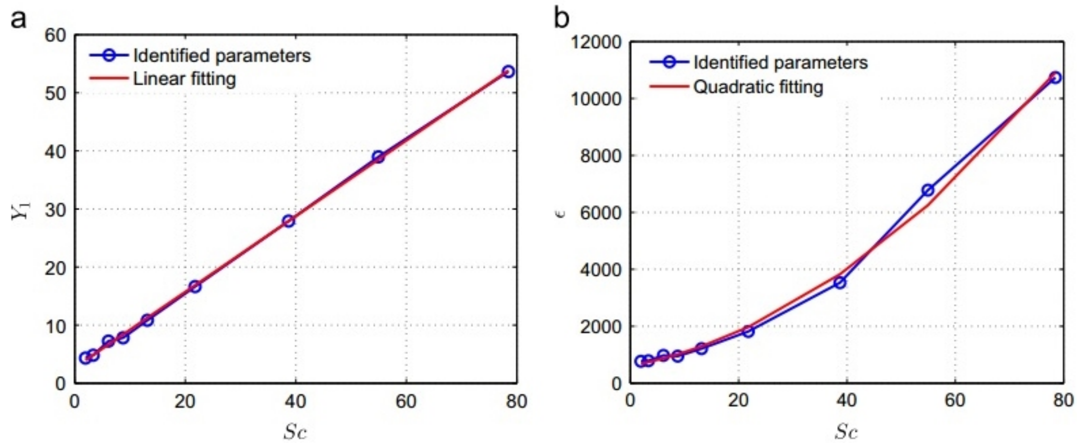

Figure 2.33: Variation of the model parameters (a) Y_1 and (b) ϵ against the Scruton number Sc and their corresponding best fit curves (Marra et al., 2015).

2.5.2 Second-degree-of-freedom Models for VIV

As for the second-degree-of-freedom model, the wake-oscillator or lift-oscillator model is considered to be the most appropriate semi-empirical model of the VIV of the rectangular cylinder or bridge deck cross section and also the circular cylinder. This model can simulate all characteristics of the VIV including the limit cycle oscillation, the lock-in, the hysteresis and the response branches (Xu et al., 2015).

The most noteworthy among the wake oscillator models is the one proposed by Hartlen and Currie (1970), which was first used to model the VIV of the circular cylinder. This model contains a pair of equations which are the linear structural equation and non-linear fluid equation as

$$\text{Structure}: \qquad \ddot{x_r} + 2\zeta\dot{x_r} + x_r = a\Omega_o^2 c_L, \tag{2.40}$$

$$\text{Fluid}: \qquad \ddot{c_L} - \alpha\Omega_o\dot{c_L} + \frac{\gamma}{\Omega_o}\dot{c_L}^3 + \Omega_o^2 c_L = b\dot{x_r}. \tag{2.41}$$

Here, $\ddot{x_r}$, $\dot{x_r}$ and x_r are the non-dimensional acceleration, velocity and displacement normalised against the depth of the rectangular cylinder or the diameter of the circular cylinder D. The derivative is with respect to the non-dimensional time $\tau = 2\pi f_n t$ with f_n is the natural frequency of the structure. $\Omega_o = f_o/f_n = \mathrm{St}[U/(f_n B)]$ is the non-dimensional velocity; f_o is the vortex shedding frequency. c_L is the lift coefficient. $a = (\rho B^2 L)/(8\pi^2 \mathrm{St} M)$ (M and L is the mass and span-wise length of the cylinder) and b are the two interaction parameters representing the coupling between the two equations. Similar to the Ehsan and Scanlan model, the Rayleigh equation, which is the van der Pol-type equation, is applied into the fluid equation, modelling a non-linear fluid oscillation and allowing the self-sustain and self-limited characteristics of the VIV to be simulated. α and γ are the van der Pol coefficient; together with b, they are the three model parameters of the Hartlen and Currie model that are required to be identified. By assuming a sinusoidal solution of the structural response x_r and the lift coefficient c_L with a phase shift ϕ at the non-dimensional frequency $\Omega = f_s/f_n$ with f_s being the frequency of the structural response, the analytical solutions of the system of Equations 2.40 and 2.41 can be derived as

$$X_r^2 = \frac{4a^2\Omega_o^5}{3\gamma\Omega^3}\frac{(1-\Omega^2)(\Omega_o^2-\Omega^2) + 2\alpha\zeta\Omega_o\Omega^2}{8\zeta^3\Omega^3 + 2\zeta\Omega(1-\Omega^2)^2}, \tag{2.42}$$

$$\Omega_o^2 = \Omega^2\frac{(1-\Omega^2)^2 + 4\zeta^2\Omega^2}{(1-\Omega^2)^2 + 4\zeta^2\Omega^2 - 2ab\zeta\Omega^2}, \tag{2.43}$$

$$\tan\phi = \frac{2\zeta\Omega}{1-\Omega^2}, \tag{2.44}$$

$$C_{Lo} = \frac{1}{\sin\phi}\frac{2\zeta\Omega X_r}{a\Omega_o^2}. \tag{2.45}$$

Here, X_r and C_{Lo} are the maximum non-dimensional structural response and lift coefficient respectively. Also, the van der Pol coefficients α and γ are found to relate to the maximum lift coefficient of a static cylinder $C_{Lo,\text{static}}$ as

$$C_{Lo,\text{static}} = \frac{4\alpha}{3\gamma}. \tag{2.46}$$

However, these above analytical solutions are only an approximation; a number of assumptions, including the removal of higher-order sinusoidal terms relating to the lift coefficient, are made during the derivation. This can lead to a large difference between the analytical solution of the maximum lift coefficient and the one that is directly achieved by integrating Equations 2.40 and 2.41.

It should be noticed that the force term on the right-hand side of Equation 2.41 is taken to be proportional to the velocity of the cylinder, $\dot{x_r}$. In fact, it is obvious that this force term must be related to the motion of the cylinder; in the original paper, Hartlen and Currie (1970) proposed an arbitrary linear relationship based on the velocity of the cylinder, which is called as the velocity coupling. This coupling scheme has been accepted and used in many researches including Skop et al. (1973b), Landl (1975), and more recently, Plaschko (2000) and Xu et al. (2015). According to Krenk and Nielsen (1999), the selection of the velocity coupling scheme based on Hartlen and Currie (1970) did not satisfied the flow of energy between the fluid and structure equation. They then proposed the displacement coupling, bx_r, to enforce the transfer of energy generated by the damping term in the fluid equation to the structure equation where this energy is dissipated by the structural damping term. The displacement coupling scheme was also applied by Williams and Suaris (2006) and Williams et al. (2010) to model the response of an isolated circular cylinder as well as the the wake interference between two circular cylinders. Even though Williams et al. (2010) showed that this approach is more mathematically suitable for modelling the VIV response of an isolated circular cylinder, a good agreement between the numerical-integrated solutions of the response and experiment data could not be drawn. The analytical solutions produced by Krenk and Nielsen (1999) showed the presence of two response branches but the hysteresis and the frequency response were not accurately simulated. Also, the lift coefficient showed no peak values during the lock-in. Later, Facchinetti (2004) proposed the acceleration coupling scheme, $b\ddot{x_r}$, based on the hypothesis of the linear inertial effect of the structure. The analytical solutions however showed behaviours which are more related to the circular cylinder having a low combined-mass-damping parameter, especially when investigating the relationship between the range of the lock-in and the mass ratio. The displacement response contained the upper branch; the phase shift of the lift force against the displacement involved two dramatic increases just after the onset of the lock-in and just before the system reached lock-out. However, the presence of hysteresis when the lock-in started and terminated requires further clarification and explanation. A comparison between three aforementioned coupling schemes was conducted by Facchinetti (2004); taking into account the high mass-damping characteristics of rectangular cylinders or bridge deck structures, the velocity coupling scheme did qualitatively and, in some respect, quantitatively simulate all features of the VIV.

Another issue about the Hartlen and Currie model that has been addressed by Sarpkaya (1979) is the lack of fluid-mechanical argument during the derivation, especially the damping term in the fluid equation. Instead of the Rayleigh equation originally used by Hartlen and Currie (1970), Skop et al. (1973b) implemented a slight modification to this term together with an addition empirical parameter in the stiffness term of the fluid equation. A trial-and-error with some guidelines allowed all parameters to be identified based on the maximum amplitude of the response during the lock-in and the velocity of this occurrence; a qualitatively good agreement comparing against selected wind tunnel results of the circular cylinder could be drawn. However, no significant improvement to the original Hartlen and Currie model was found. Nevertheless, a logarithmic relationship between the model parameters and the structural parameters such as damping ratio, mass and geometry dimension have been reported and the Griffin plot was in good agreement with the wind tunnel data. Another attempt to improve the Hartlen and Currie model was conducted by Landl (1975). By introducing an additional fifth-order non-linear term into the damping term of the fluid equation and still using the velocity coupling, the upper branch of the VIV response of the circular cylinder having a low combined mass-damping parameter was simulated and in a good qualitative agreement with the wind tunnel data extracted from Parkinson et al. (1968). Some features of the high combined-mass-damping type of VIV responses of the circular cylinder was also modelled but no wind tunnel data was present to make a comparison. Later, Krenk and Nielsen (1999) combined both the Rayleigh equation and the van der Pol equation to model the negative damping in the fluid equation. However, Facchinetti (2004) pointed out that using either the Rayleigh and/or van der Pol equation does not affect the capability of modelling the limit cycle oscillation.

Using the modified model previously originated by Skop et al. (1973b), Skop and Balasubramanian (1997) proposed a new twist, that the lift force in the structure equation comprised of two components. The first component was modelled by the van der Pol-type equation driven by the velocity of the cylinder; while the second term was called a stall term $(2\beta\dot{x_r})/\Omega_o$ with β being the stall coefficient. This implementation allowed the asymptotic and self-limiting structural response to be accurately predicted at zero structural damping. However, the model parameters were related to the physical and structural parameters, restraining the practicability of this model. Scanlan (1998) later formulated a new lift force expression for the equation of motion of bridge decks during the VIV and similarly, he also included a stall term together with the lift force coefficient. The stall term in this case was proposed to be dependent on the flutter derivative H_1^*, given that during the lock-in, the heaving motion of the structure was dominant. The flutter derivative H_1^* was also assumed to be constant during the lock-in Scanlan (1998). This flutter-derivative-depending stall term was later implemented by Xu et al. (2015) in an attempt to generalise the Hartlen and Currie model to simulate the VIV response of the bridge deck structure. The lift coefficient was represented using the van der Pol-type equation and driven by the velocity of the structure as being used by Skop and Balasubramanian (1997). In fact, the Hartlen and

Currie model was first used to model the VIV response of the rectangular cylinder by Callander (1989). He was able to model the VIV response of the rectangular cylinder standing at an non-zero angle of attack and restrained to oscillate along the longitudinal direction. A good agreement with experimental data was achieved although he used all model parameters listed in the original paper by Hartlen and Currie (1970) and made some assumption about the lift coefficient based the value of the circular cylinder.

2.5.3 Summary of the Mathematical Models of VIV

The need of a reliable semi-empirical model to simulate the VIV of bridge deck structures is apparent nowadays. A number of incidents related to VIV, including the recent large oscillation of the Volgograd bridge in Russia with the peak-to-peak amplitude to be measured about 800 mm (Weber et al., 2013), have highlighted the importance of better understanding of VIV of bridge decks and a more proper VIV model which can be used in the design stage.

There have been a large numbers of attempts to derive semi-empirical models of the VIV where model parameters can be identified via wind tunnel tests or computational studies as discussed in Sections 2.5.1 and 2.5.2. Some models have gained their notice and significant improvement has been proposed. However, up to now, a reliable and practical model of the VIV is not yet to be found. The main disadvantage of most current VIV models is that the model parameters are not universal; they are all dependent on physical and structural parameters such as mass and damping ratio and also on the aerodynamic shape of the cross section. This limits their usability in the initial phase of the design state where wind tunnel tests or computational simulations need to be conducted to fully understand the relationship between the maximum VIV response and the Scruton numbers for a given structure. This process is very time-consuming and, if the Scruton number during this process is different from the prototype for some reason, no useful information can be extracted. Therefore, a reliable mathematical model for the VIV with all model parameters to be universal is a more practical mean to handle this task. The other downside of some models is the lack of physical explanation during the derivation and of the model parameters themselves. They have been accepted and received further improvement mostly due to their ability to produce results that include all features of the VIV and qualitatively agree with those obtained from wind tunnel experiments rather than due to their capacity to help further understand this phenomenon via relationships between model parameters and other physical and structural parameters.

2.6 FLUTTER

Flutter is an aeroelastic instability featuring a combination of bending and torsional modes having relatively similar natural frequencies. Each mode can be very stable; however, their combination may produce very large structural responses because, during flutter, the self-excited forces can cause further movement of the structure.

According to Simiu and Scanlan (1996), flutter can be classified into four different types of responses which are: classical flutter, single-degree-of-freedom flutter, stall flutter and panel flutter. The last two types are less relevant to bridge deck structures and rectangular cylinders. The classical flutter is also known as the two-degree-of-freedom flutter which was originally found as an instability phenomenon of thin air foils restrained to both of the vertical translation and rotation. Matsumoto (2004) also observed this type of flutter in the case of bridge deck structures or rectangular cylinders with the aspect ratio B/D larger than 12. For the rectangular cylinders having shorter after-body length, i.e. $4 < B/D < 11$, they only experience the classical flutter at very high reduced wind speeds, where the aerodynamics of the flow field around cylinders shares some similar characteristics as the one around the cylinder with the aspect ratio $B/D > 12$ undergoing similar type of flutter responses. Based on Matsumoto (2004), the primary flutter behaviour which is found to occur with bridge decks of rectangular cylinder having the aspect ratio B/D from 4 to 11 is the single-degree-of-freedom flutter. This is normally referred to be the torsional flutter and it is found to be associated to structures exhibiting strongly separated flow.

2.6.1 Mechanism of Classical Flutter

The mechanism of flutter is very complicated due to the interaction between the bending and torsional modes; Figure 2.34 can help to explain why the combination of two these modes of oscillation can produce divergent response. Series of images (a) in Figure 2.34 illustrates a structure undergoing a full cycle of the torsional oscillation. With the assumption that the aerodynamic centre is closer to the trailing edge than the shear center, which is normally observed for bridge decks or rectangular cylinders having long after-body length, the aerodynamic force generates a restoring moment; its magnitude gets larger with an increase in the angular deflection of the structure and its direction possesses a tendency to reduce this angular deflection throughout every cycle. On the other hand, series (b) represents a full oscillation cycle when a structure undergoes the bending mode. Due to the vertical motion of the structure, the relative wind direction changes continuously throughout the cycle. The more the relative angle of attack, the larger the aerodynamic force acting on the structure. Also, this force is always in the opposite direction to the motion of the structure; therefore, it acts as the restoring force. Both modes of oscillation are separately stable; however, if these two modes are allowed to occur together and it assumes that the torsional mode is 90° ahead of the bending one as shown in series (c), the response of the structure becomes divergent. In this case, the aerodynamic force acts on the model in the direction of the bending motion; therefore, it becomes a destabilising factor, significantly reducing the damping of the bending mode. However, the moment induced by this aerodynamic force assists the rotation of the structure in only half of the cycle. Therefore, with respect to both modes, the aerodynamic damping is changed significantly.

In terms of energy, the flutter can be explained that, due to its movement, the structure can extract energy from the wind flow; the oscillation energy on the other hand is then dissipated through the mechanical damping system. The divergent response will occur if the extracted energy is larger than the dissipated energy or the overall damping of the system is reduced due to additional negative aerodynamic damping caused by excessive flow separation; this dividing line is characterised by the critical flutter velocity (Simiu and Scanlan, 1996).

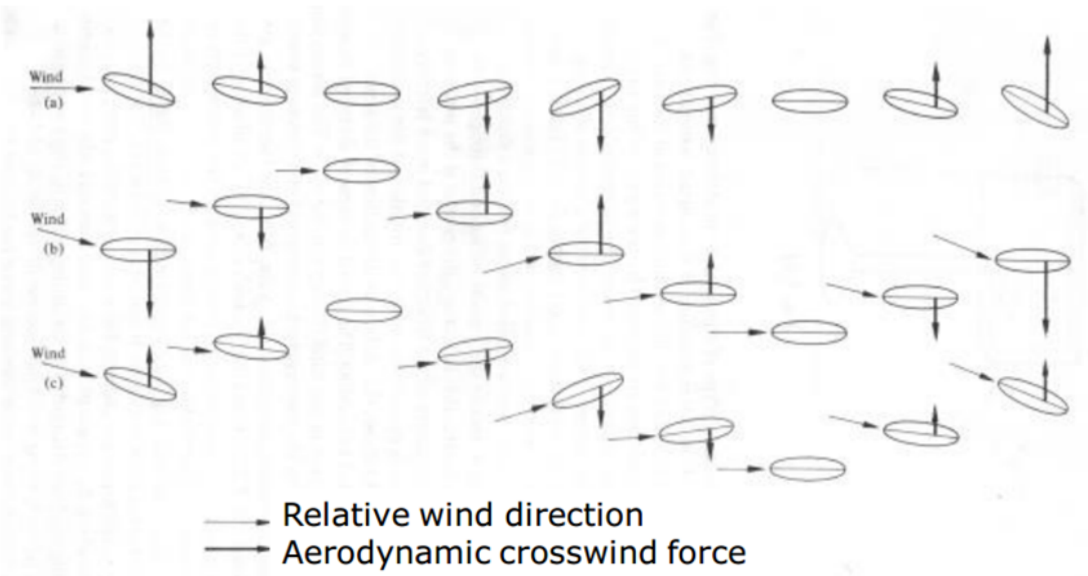

Figure 2.34: Flutter mechanism, adopted from Houghton and Carruthers (1976).

2.6.2 Flutter Model

The flutter model of bridge decks was first introduced by Selberg (1961). By borrowing the classical airfoil flutter theory in aeronautical engineering established by Theoderson (1935), he was able to approximately determine the flutter onset velocity, with the limitation to streamlined bridge deck sections only. Later, following the same method, Scanlan's flutter model (Scanlan and Tomko, 1971) was developed, featuring a system of equations of motion of bridge decks in the wind and 18 flutter derivatives, which related the aerodynamic forces to structural responses. The flutter or aerodynamic derivatives can be experimentally or numerically determined.

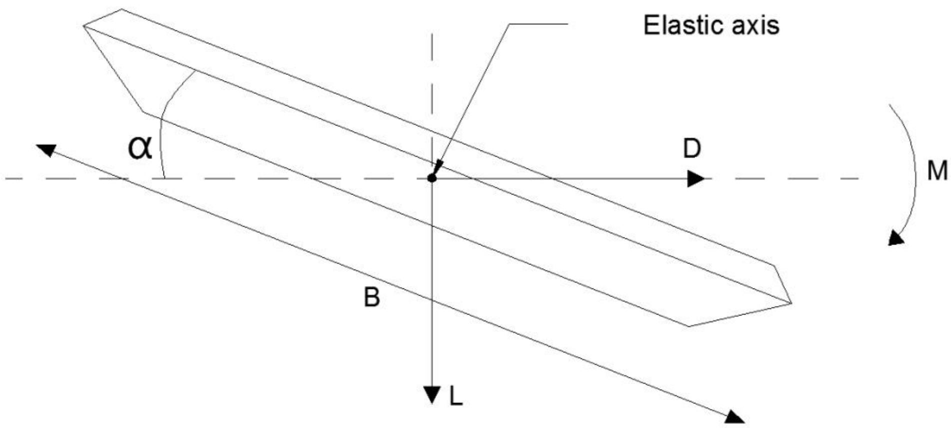

Figure 2.35: Bridge deck in the wind field.

Similar to the airfoil theory, the bridge deck has two degrees of freedom which are bending and torsional modes (Figure 2.35); the equations of motion of the bridge deck in flutter are described as

$$m(\ddot{h} + 2\zeta_h\omega_h\dot{h} + \omega_h^2) = L_{se}, \tag{2.47}$$

$$I(\ddot{\alpha} + 2\zeta_\alpha\omega_\alpha\dot{\alpha} + \omega_\alpha^2) = M_{se}, \tag{2.48}$$

where m and I are the mass and moment of inertia of the bridge deck, h, $\dot{h}$ and $\ddot{h}$ are the bending displacement, velocity and acceleration, α, $\dot{\alpha}$ and $\ddot{\alpha}$ are the angular or torsional displacement, velocity and acceleration, ζ_h and ζ_α are the heaving and angular damping ratio, ω_h and ω_α are the bending and torsional natural circular frequency. In flutter, wind-induced forces and moment, L_{se} and M_{se} respectively, are self-excited because they are generated by the movement of bridge deck in the wind.

Scanlan and Tomko (1971) proposed mathematical formulae to relate the aerodynamic force and moments to the heaving and torsional motion of the bridge deck as

$$L_{se} = \frac{1}{2}\rho U^2 B\left(KH_1^*\frac{\dot{h}}{U} + KH_2^*\frac{B\dot{\alpha}}{U} + K^2H_3^*\alpha + K^2H_4^*\frac{h}{B}\right), \tag{2.49}$$

$$M_{se} = \frac{1}{2}\rho U^2 B^2\left(KA_1^*\frac{\dot{h}}{U} + KA_2^*\frac{B\dot{\alpha}}{U} + K^2A_3^*\alpha + K^2A_4^*\frac{h}{B}\right). \tag{2.50}$$

Scanlan's model assumes the linear relationship between the aerodynamic forces and moment with the heaving and angular displacement h and α and their first derivatives. The coefficients of linearity are the flutter derivatives, H_i^* and A_i^*, which relate the self-excited forces and moments to the bridge responses. These flutter derivatives are a function of reduced frequency given by

$$K = \frac{B\omega}{U}, \tag{2.51}$$

where ω is the heaving or torsional angular oscillatory frequency of bridge deck. This very dependence causes a lot of difficulties to solve the flutter equations of motion. A number of mathematical expressions were proposed to relate the flutter derivatives of the bridge deck to solutions of an airfoil based on either Theodorsen's circulation function in the frequency domain (Theoderson, 1935) or indicial functions in the time domain (Garrick (1938); Jones (1940)) which were used in a number of studies of the bridge aeroelasticity (Zhang et al. (2003); Caracoglia and Jones (2003b)). Scanlan (2002) and Caracoglia and Jones (2003a) pointed out that the flutter derivatives of the bridge deck can be estimated from wind tunnel tests; providing that the linearity holds true, it was shown that the bridge flutter derivatives estimated by the use of Theodorsen's circulation function, indicial functions or wind tunnel experiments are interchangeable. However, the circulation function as well as the indicial functions were developed based on the airfoil aerodynamics or the finite wing theory; with the assumption of irrotational potential flow, these functions effectively defines a two-dimensional system and ignores the third dimension of the flow field. Therefore, the use of the flutter derivatives calculated from these two methods is limited for the case of bridge aeroelasticity. On the other hand, if a 3D model is used in the wind tunnel test, the experimentally measured flutter derivatives inherently include the three dimensional characteristics of the flow field and yield more accurate identification of the aeroelastic parameters. There are two methods to measure the flutter derivatives in the wind tunnel: the free-vibration method and the force-vibration method.

2.6.3 Free-vibration Method of Finding Aerodynamic Derivatives

The main idea of the free-vibration method is that the bridge deck model is immersed in a wind field and it is allowed to oscillate without any interference except the damping and stiffness of the system; the forces and moment are calculated based on the pressure distribution. The four pieces of information extracted from each mode of oscillation (heaving and torsional modes) such as modal frequency, modal damping, amplitude and phase lag are then used to determine the flutter derivatives. This method was first applied by Scanlan and Tomko (1971); however, the main limitation of their method is the requirement that the heaving and torsional modes in coupled oscillations of bridge decks must have the same frequency at each wind speed. Later on, researchers have focused on developing the free-vibration method, applying further analysis techniques to eliminate the frequency requirement of coupled oscillations and to simplify the experimental procedure; the coupled free-vibration method is widely used to obtain the flutter derivatives directly.

Considering the aerodynamic self-excited lift force and moment, Iwamoto and Fujino (1995) reported one major issue with the coupled free-vibration method. Because the oscillation involves two modes, i.e. two distinct modal frequencies, Equations 2.49 and 2.50 become

$$\begin{aligned} L_{se} =& \frac{1}{2}\rho U^2 B \left(K_1 H_{11}^* \frac{\dot{h}_1}{U} + K_1 H_{12}^* \frac{B\dot{\alpha}_1}{U} + K_1^2 H_{13}^* \alpha_1 + K_1^2 H_{14}^* \frac{h_1}{B} \right) \\ &+ \frac{1}{2}\rho U^2 B \left(K_2 H_{21}^* \frac{\dot{h}_2}{U} + K_2 H_{22}^* \frac{B\dot{\alpha}_2}{U} + K_2^2 H_{23}^* \alpha_2 + K_2^2 H_{24}^* \frac{h_2}{B} \right), \end{aligned} \tag{2.52}$$

$$\begin{aligned} M_{se} =& \frac{1}{2}\rho U^2 B^2 \left(K_1 A_{11}^* \frac{\dot{h}_1}{U} + K_1 A_{12}^* \frac{B\dot{\alpha}_1}{U} + K_1 A_{13}^* \alpha_1 + K_1^2 A_{14}^* \frac{h_1}{B} \right) \\ &+ \frac{1}{2}\rho U^2 B^2 \left(K_2 A_{21}^* \frac{\dot{h}_2}{U} + K_2 A_{22}^* \frac{B\dot{\alpha}_2}{U} + K_2 A_{23}^* \alpha_2 + K_2^2 A_{24}^* \frac{h_2}{B} \right). \end{aligned} \tag{2.53}$$

Here, there are 16 flutter derivatives; eight of them, H_{1i}^* and A_{1i}^* $(i = 1, ..., 4)$, correspond to the heaving mode while the other eight, H_{2i}^* and A_{2i}^* $(i = 1, ..., 4)$, correspond to the torsional mode. The first eight flutter derivatives are the function of the non-dimensional heaving reduced frequency

$$K_1 = \frac{B\omega_1}{U}, \tag{2.54}$$

where ω_1 is the oscillatory frequency of the heaving mode. Similarly, the other eight are the function of the non-dimensional torsional reduced frequency

$$K_2 = \frac{B\omega_2}{U}, \tag{2.55}$$

where ω_2 is the oscillatory frequency of the torsional mode. (h_1, h_2) and (α_1, α_2) are components of the heaving and torsional modes respectively. With only eight pieces of information available, it is impossible to completely obtain all sixteen flutter derivatives. Iwamoto and Fujino (1995), therefore, proposed a solution to reduce the unknown flutter derivatives. Based on observation during the wind tunnel test, it was found that the coupling effect was very weak at intermediate wind speed (8 $\mathrm{m\,s^{-1}}$); thus, is was reasonable to drop all terms involving h_2, α_1 and their derivatives. Equations 2.52 and 2.53 were simplified, containing only eight flutter derivatives, which allowed these authors to extract them successfully. The results showed a good agreement with other analysis techniques; their method, however, was questionable about the guidance on how to efficiently reduce the number of flutter derivatives or, in other words, which flutter derivatives are critical.

Extracting the flutter derivatives using the free-vibration method, the aerodynamic drag forces and the lateral movement of bridge decks are normally neglected, which helps reduce the number of unknowns. This simplification was thought to affect the accuracy of results. However, Chen and Kareem (2008) pointed out that the bridge deck flutter is not largely influenced by this. The bridge deck is normally considered to exhibit the hard flutter in which the self-excited lift force and moment are caused by the heaving and torsional motion of bridge decks respectively. The hard flutter is characterised by a rapid variation of modal damping with an small increase in wind speed. For this type of flutter, the additional damping caused by the self-excited drag force has very little effect on the critical flutter velocity.

2.6.4 Forced-vibration Method of Finding Aerodynamic Derivatives

In the forced-vibration method, the bridge deck model is made to undergo a prescribed harmonic motion of constant amplitude; the forces and moment are measured and controlled by either force sensors or by pressure integration. This method is preferable since it can be applied to analyse the effect of turbulence and the amplitude of oscillation as well as the mean wind attack angle can be easily controlled. The mean wind speed is normally kept constant; by varying the frequency of the prescribed harmonic motion, it is possible to obtain the flutter derivatives for different reduced wind velocity defined by

$$U_R = \frac{U}{\omega B}. \tag{2.56}$$

The common question for this method is the dependence of solutions on the prescribed oscillation amplitude. Noda et al. (2003) conducted an investigation of the effects of oscillation amplitude on the flutter derivatives of the thin rectangular cylinder with $B/D = 13$ or 150; these cross sections are very well-known for their flutter stability at small oscillation amplitude. The results showed the minor effects of heaving amplitude on flutter derivatives. However, the torsional amplitude produced significant influences; a large torsional amplitude could produce positive A_2^* at a considerably lower wind speed (Figure 2.36) causing the flutter instability. These findings indicate that some cross sections with stable aerodynamic derivatives at a very small amplitude may become unstable followed by a small increase in initial oscillatory amplitude. To apply this technique to extract the flutter derivatives of bridge decks, a study of the effect of oscillatory amplitude on the flutter derivatives have to be carried out so that a proper value of prescribed amplitudes can be selected.

The forced-vibration method involves more complex devices than the free-vibration method, which is the main reason for its limited application at the moment. Nevertheless, together with other appropriate analysis techniques, the forced-vibration method is preferable dealing with non-linearity, high wind speed and non-stationary wind.

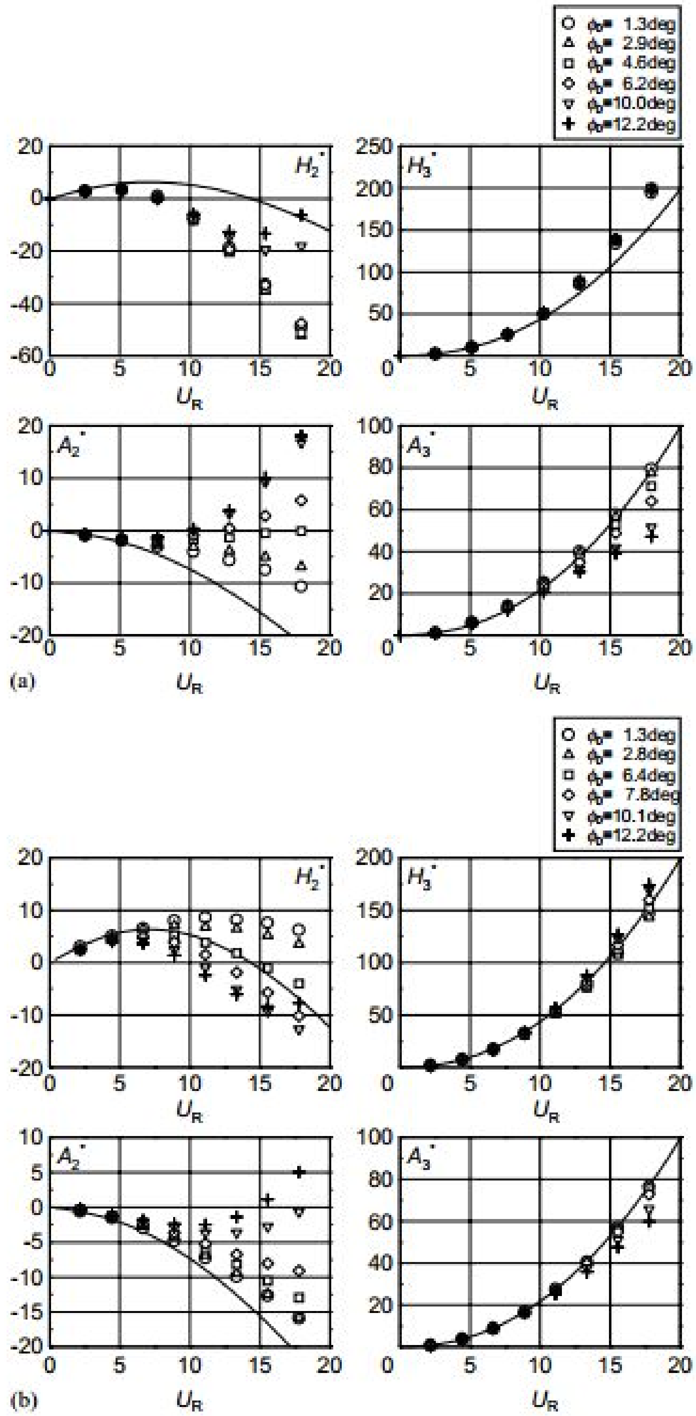

Figure 2.36: Effects of torsional amplitude on flutter derivatives of (a) $B/D = 13$ and (b) $B/D = 150$; the solid lines represented the theoretical values (Noda et al., 2003).

2.7 BUFFETING

Buffeting is the unsteady loading of structures caused by high intensity and high frequency velocity fluctuations (turbulence) in the oncoming wind. A bridge deck immersed in the turbulent wind experiences the self-excited forces and moment due to flutter and the buffeting ones due to turbulence; in this case, the aerodynamic forces and moment acting on the bridge deck has to be written as

$$L_{ae} = L_{se} + L_b, \tag{2.57}$$

$$D_{ae} = D_{se} + D_b, \tag{2.58}$$

$$M_{ae} = M_{se} + M_b, \tag{2.59}$$

where L, D and M represent the lift force, drag force and moment. The subscript se stands for self-excited; b means buffeting and ae is aerodynamic. Equations 2.57 to 2.59 indeed suggest a conventional aerodynamic analysis technique that the aerodynamic forces and moment acting on an oscillatory model can be decomposed into self-excited and buffeting components for separated investigation. Haan and Kareem (2009) compared the buffeting force acting on static cylinder and oscillating cylinders. A maximum of 10% difference was observed; however the effect of this difference on responses of bridge deck was insignificant. Therefore, this conventional technique is shown to be adequate to perform analysis in the bridge aeroelasticity.

2.7.1 Buffeting Model

Using the quasi-steady theory, Simiu and Scanlan (1996) proposed a buffeting model involving the velocity fluctuation components u and w defined as

$$\frac{L_b}{\frac{1}{2}\rho U^2 B} = 2C_L \frac{u}{U} + \left(C_L^{'} + C_D\right)\frac{w}{U}, \tag{2.60}$$

$$\frac{D_b}{\frac{1}{2}\rho U^2 B} = 2C_D \frac{u}{U} + C_D^{'} \frac{w}{U}, \tag{2.61}$$

$$\frac{M_b}{\frac{1}{2}\rho U^2 B^2} = 2C_M \frac{u}{U} + C_D^{'} \frac{w}{U}, \tag{2.62}$$

where C_L, C_D and C_M are the lift, drag and moment coefficients respectively measured on a static cylinder at the angle of attack 0°. C_L', C_D' and C_M' are the first derivatives of lift, drag and moment coefficients at the angle of attack 0°. This quasi-steady buffeting force theory has proved to be sufficient in some cases, but, in other cases, corrections were found of importance. The buffeting force coefficients

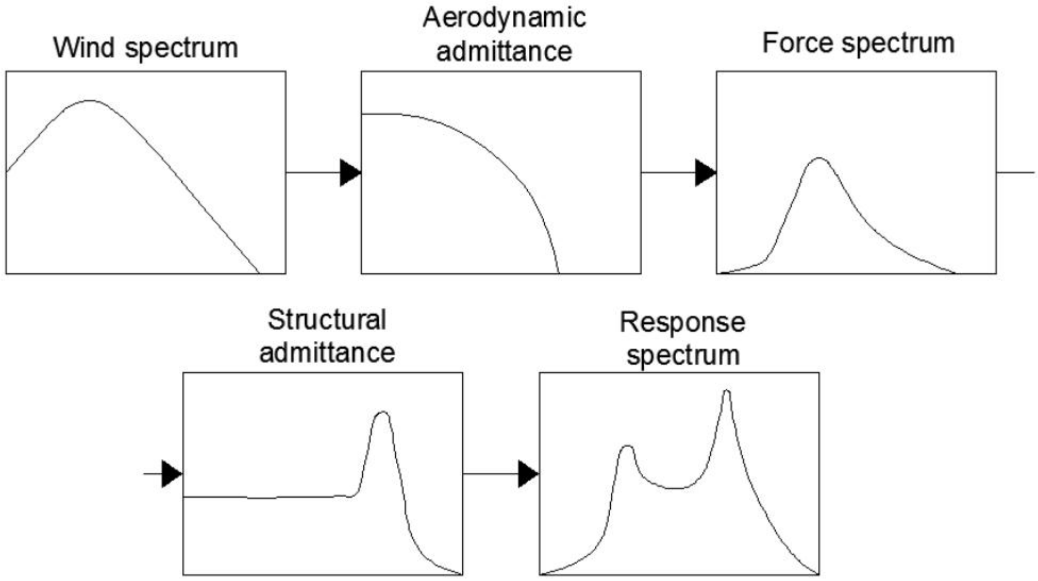

Figure 2.37: Frequency-domain analysis of Davenport (1962b); the x axis is $\ln(f)$.

in Equations 2.60 to 2.62 are specified as fixed or steady-state values which fail to hold if the oncoming wind includes a large mean wind speed and relatively rapidly time-varying gust velocities.

Davenport (1962b) proposed a method to improve this quasi-steady model and to predict the spectrum of structural response based on the wind spectrum and other transfer functions. The process is summarised in Figure 2.37 and is known as the Davenport wind loading chain.

Based on the buffeting model presented in Equations 2.60, 2.61 and 2.62, the spectrum of the buffeting lift, $S_L(f)$, drag, $S_D(f)$, and moment, $S_M(f)$ is calculated as

$$\frac{S_L(f)}{\left[\frac{1}{2}\rho U^2 B\right]^2} = 4C_L^2\frac{S_u(f)}{U^2} + \left(C_L' + C_D\right)^2\frac{S_w(f)}{U^2}, \tag{2.63}$$

$$\frac{S_D(f)}{\left[\frac{1}{2}\rho U^2 B\right]^2} = 4C_D^2\frac{S_u(f)}{U^2} + C_D'\frac{S_w(f)}{U^2}, \tag{2.64}$$

$$\frac{S_M(f)}{\left[\frac{1}{2}\rho U^2 B^2\right]^2} = 4C_M^2\frac{S_u(f)}{U^2} + \left(C_L' + C_D\right)^2\frac{S_w(f)}{U^2}, \tag{2.65}$$

where $S_u(f)$ and $S_w(f)$ is the spectrum of the velocity fluctuating component u and w respectively. These force and moment spectra are then multiplied by the aerodynamic admittance function $\mid X_a(f)\mid^2$, a frequency-dependent transfer function, which is included to account for the unsteady feature of the aerodynamic forces due to turbulence in the wind. In addition, the correlation of the aerodynamic forces and the turbulent components is inherent in this function. The value of this function is close to 1 at low frequencies (Figure 2.37); it represents that large eddies rotating slowly with the wind have more chance to engulf structures, producing significant aerodynamic responses. At higher frequencies, this function sharply decreases to 0, indicating that quickly rotating smaller eddies contribute less effects on structural responses because they are highly uncorrelated to each other.

The structural admittance function, $\mid X_s(f) \mid^2$, is also included; it is the characteristic of structures. This function represents the response of structures over a range of frequencies. The peak response in Figure 2.37 occurs at the natural frequency of the structure; away from this frequency, the response becomes less significant.

There is another transfer function that is usually applied to this method is the joint acceptance function $\mid X_j(f) \mid^2$. This function is used to make a transition from a point-like structure to a line-like structure. Their main difference is that the line-like structure can be excited at a combination of different structural mode shapes $\phi_i(y)$.

Eventually, the spectrum of the structural response of a line-like structure in the span-wise direction y is evaluated as

$$S_z(y,f) = \sum_{i=1}^{n} \phi_i^2(y) \ \mid X_{s,i}(f) \mid^2 \mid X_{j,i}(f) \mid^2 \ S_L(f) \ \mid X_a(f) \mid^2, \tag{2.66}$$

and is illustrated in Figure 2.37. The spectrum may contain a number of spectral peaks which correspond to the excitation due to background turbulence in the wind or due to resonance of the structure. The design application is to move the latter, the peak resonance, further away from the former, the peak gust.

The accuracy of the structural buffeting response estimated from the aforementioned Davenport-based approach is highly dependent on two following components: the wind spectra and the aerodynamic admittance function. For the latter component, there are a number of mathematical expressions which successfully describe this transfer function such as the Sears function. However, the applicability of these functions is limited to circular cylinders where the potential flow theory is hold; using these expressions can overestimate the buffeting response of the bridge deck structure. More importantly, the first component has received excessive attention recently and it has been pointed the need of better definitions of the wind spectra or model to represent the wind as observed at full scale and, especially, the interaction between the wind and the aerodynamic admittance function.

As pointed out by Davenport (1983), the first component, i.e. the wind spectrum, is generally considered to be the most important; it derives information of the wind speed which will be used to evaluate either wind loads or wind energy. Up to now, it is still a challenge for wind engineers to produce an acceptable mathematical model to physically represent the wind field measured at full scale. Gomes and Vickery (1978) were potentially the first researchers to suggest the importance of separating extreme wind events from the conventional turbulent wind observed in a neutrally stable atmospheric boundary layer. The latter is referred as the synoptic wind characterised by its stationary and Gaussianity; it has been applied in many codes of practice to calculate the wind load on structures. As suggested by its name, the former is locally strong wind events generated from thunderstorms, tornadoes, downbursts and gust fronts, which is classified as the non-synoptic wind. A number of later studies determined some fundamental characteristics (non-stationary and non-Gaussian) as well as the dominance and importance of the non-synoptic wind so that it has been prompted to include these wind events into wind maps for further calculation (Twisdale and Vickery (1992); Letchford et al. (2002); Holmes et al. (2008)). It was found that the lowest layer of the wind field in these extreme wind events is very complicated and associated with the highest wind speeds and fast spatial and temporal variation in wind speeds and direction (Kosiba and Wurman (2013); Lambardo et al. (2014)). As pointed out by Kareem and Wu (2013), these non-synoptic wind events are usually associated to rapid and substantial changes in the local flow around structures and are likely to be correlated over a large area, which potentially results in stronger aerodynamic loads. Together with the departure in statistical attributes of the wind field, this very property further complicates the wind-load assessment and questions the validity of the conventional analysis framework in calculating wind loads induced by these phenomena.

Moreover, these fundamental differences in physics have raised the need of better quantitative definition of these events and establishment of analysis and modelling tools to capture these features. The Gust-front factor (GFF) proposed by Kwon and Kareem (2009) was probably one of well-known approach and was developed based on the conventional wind loading chain and the gust factor first introduced by Davenport (1967). The GFF approach is associated with a number of modifying factors to systematically account for the transient non-synoptic wind and the non-linear wind-structure interaction. Adapting from the earthquake engineering dealing with transient events, Solari (2014) and Solari et al. (2015) introduced a method named the Thunderstorm Response Spectrum approach. This approach uses several time histories of non-synoptic wind velocities and, by conducting the velocity decomposition, yields the spatial-varying and temporal-varying components. These results help to evaluate the spatial and temporal correlation of the wind field and, thus, to estimate the wind loading on structures.

However, Letchford and Lombardo (2015) pointed out a number of disadvantages of current approaches to model transient wind loadings; one of them is the dependence on the full-scale measurement of non-synoptic winds, which is still very limited up to now. In recent years, an increase in observational capacities have facilitated further studies, revealing more insights into the characteristics of the synoptic wind (Lambardo et al. (2014); Gunter and Schroeder (2015)) and promoting the developments of theoretical and computational analysis frameworks where these extreme wind events and their associated wind loads on structure can be modelled (Wang et al. (2016); Nasir and Bitsuamlak (2016); Kareem et al. (2016); Solari and Rainisio (2016); Le and Caracoglia (2016); Jesson and Sterling (2016)). In addition, to integrate the non-synoptic wind into the analysis framework to estimate wind loadings on structures, Holmes (2015) and Letchford and Lombardo (2015) suggested some alterations to the conventional Davenport's wind loading chain. The wind spectrum needs to be assessed to determine whether it is a synoptic or non-synoptic driven phenomenon, which will govern the other components (the aerodynamic admittance function and the structural admittance function) as well as the design criteria. Also, cross-links or feedback loops should be introduced between the wind spectrum and later components to effectively model the non-linearity and non-stationary in the wind-structure interaction.

In the next section, Section 2.8, the effect of turbulence in the oncoming wind on the wind-induced responses, especially flutter and VIV, will be considered.

2.8 TURBULENCE EFFECTS

A bridge deck immersed in turbulent wind simultaneously experiences self-excited forces due to flutter and vortex shedding and buffeting forces due to turbulence components. In addition, the presence of turbulence is seen to affect aerodynamic parameters and forces.

Vickery (1966) investigated the influence of turbulence on fluctuating lift and drag forces acting on a long square cylinder. The large-scale turbulence in the wind was found to have significant impacts on both the steady and fluctuating forces; this influence was more considerable at small angles of attack. Also, a turbulence-induced reduction in suction at the downstream face and in the fluctuating lift were recorded. These sets of results have helped to form an initial hypothesis that the turbulence produces stabilising effect; this finding was later confirmed by Scanlan (1997).

2.8.1 Effects of Turbulence on Bridge Aerodynamics

As an attempt to understand the turbulence-induced effect on the flutter as well as to uncover its underlying mechanism, Haan and Kareem (2007) and Haan and Kareem (2009) conducted a very in-depth wind tunnel study using the forced-vibration method. A sectional model having the aspect ratio of $B/D = 6.7$ was built and tested in four different wind conditions having 6% and 12% turbulence intensity I_u and approximately $1.8D$ and $4.9D$ turbulence length scale L_u^x. The pressure taps were located on the surfaces of model to obtain the surface distribution of pressure amplitude and phase. The analysis of results confirmed the turbulence-induced stabilising effect on flutter and suggest an explanation for this mechanism.

The results of the surface pressure amplitude C_p^* and phase ψ distribution can be seen in Figure 2.38. The basic shallow-peak shape is evident for the pressure amplitude distribution; with an increase in turbulence intensity, these peaks are shifted to the leading edge. The increase in turbulence length scale suppresses the peaks; this influence is more pronounced with larger reduced wind speeds. As for the pressure phase distribution, the turbulence intensity produces more significant effect compared to the turbulence length scale; the region of rapidly increasing phase shown in Figure 2.39 is brought closer to the leading edge with an increase in turbulence intensity as illustrated in Figures 2.38c and d. This upstream shift indicated turbulence increased the curvature of separated shear layer and caused the reattachment point to move closer to the leading edge reducing the size of separation bubble.

The upstream shift was also found to affect the flutter derivatives, especially A_2^* which is known to be responsible for the flutter instability if it becomes positive. In terms of pressure amplitude and phase, Haan and Kareem (2009) defined A_2^* as

$$A_2^* = \frac{1}{4K^2} \int_{-1}^{1} 2x^* C_p^* \sin(\psi) \, \mathrm{d}x^*, \tag{2.67}$$

where the pressure amplitude C_p^* and the pressure phase ψ were functions of the dimensionless stream-wise position x^*

$$x^* = \frac{x}{B/2}. \tag{2.68}$$

The effect of turbulence on the integrand of A_2^*, which was $C_p^* \sin(\psi)$, is plotted in Figure 2.40 where the shaded regions corresponds to unstable or positive values of A_2^*. The increase in turbulence intensity was found to shift the basic shape of $C_p^* \sin(\psi)$ upstream, moving it out of the shaded regions and significantly decreasing the value of A_2^*. This pattern was also observed for H_2^*; the turbulence, therefore, was shown to have the stabilising effect on the flutter. Despite supporting the hypothesis of Vickery (1966) and Scanlan (1997), this aforementioned study contains a number of limitations including the selection of the forced-vibration method and, particularly, the aerodynamic shape of the cross section. They are probably the main reason that this study can not explain the flutter behaviour of the Messina Bridge which was found to be enhanced or destabilised by the turbulence (Diana et al., 2003).

Concentrating on the VIV, Wu and Kareem (2012), Kareem and Wu (2013) and Cao (2015) have pointed out the insufficiency in both of the quantitative and qualitative understanding of the turbulence-induced effect on the VIV of the bluff body with a generic aerodynamic cross section and a bridge deck

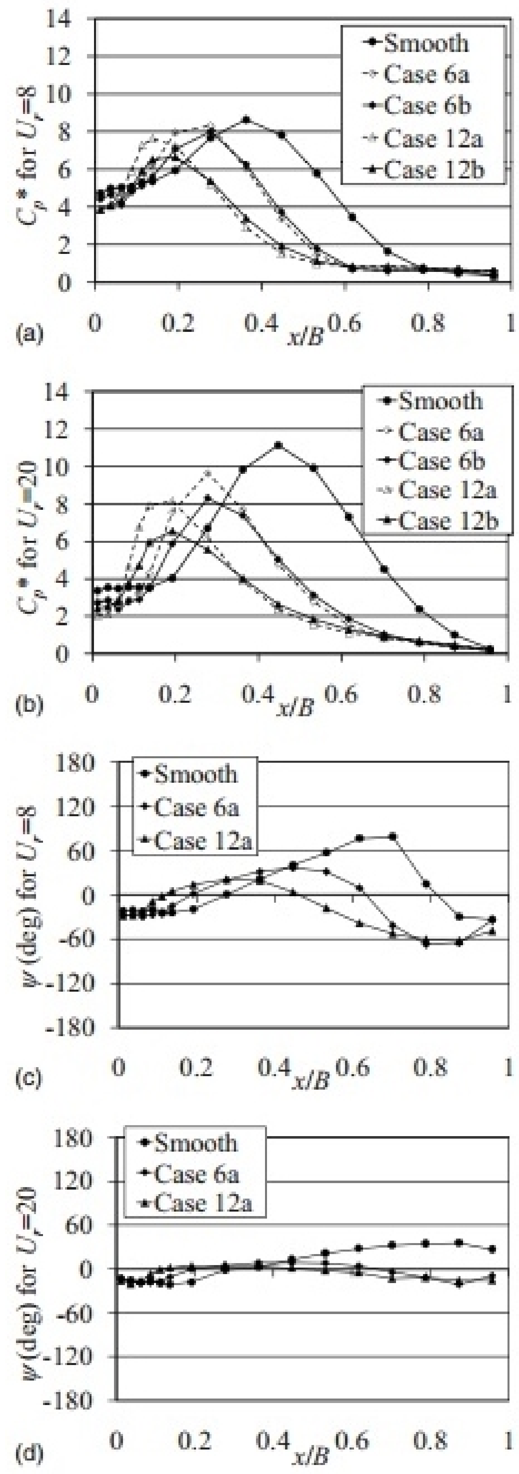

Figure 2.38: Plots of pressure amplitude distribution for (a) $U_R = 8$ and (b) $U_R = 20$ and plots of pressure phase distribution in smooth flow and small-scale turbulence for (c) $U_R = 8$ and (d) $U_R = 20$ (Haan and Kareem, 2009).

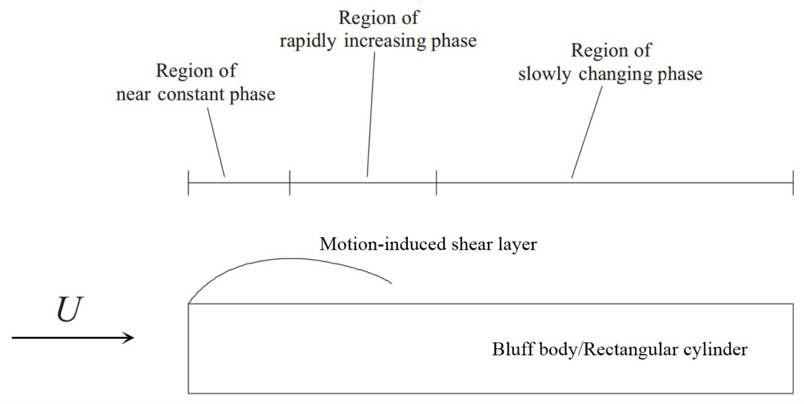

Figure 2.39: Pressure phase diagram in a relation to the formation of the motion-induced shear layer; adopted from (Haan and Kareem, 2009).

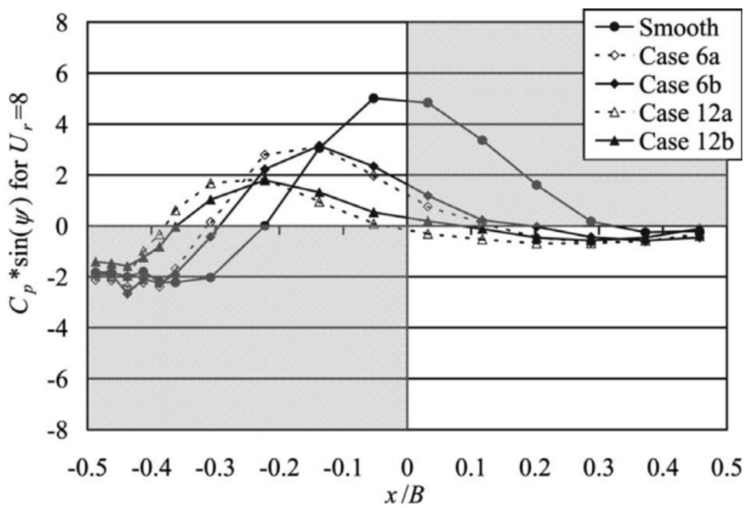

Figure 2.40: $C_p^* \sin(\psi)$ plotted versus stream-wise position for all wind conditions at $U_R = 8$ (Haan and Kareem, 2009).

cross section. Studies on the latter was found comparatively less than those on the former. Similar to the aforementioned hypothesis of the turbulence effect, a number of collective studies on the circular cylinder reviewed by Cao (2015) have led to the conclusion that the turbulence produces a very strong effect on the VIV, especially during the lock-in, reducing the structural response and, in some cases, the turbulence is able to completely suppress the VIV phenomenon. However, the wind tunnel study conducted by Goswami et al. (1993) showed that, the variation of the VIV structural response of a freely-vibrating circular cylinder in turbulent flow was minimal compared to that measured in smooth flow. As for the bridge deck cross section including the rectangular cylinder, Kobayashi et al. (1990), Kobayashi et al. (1992), Kawatani et al. (1993) and Kawatani et al. (1999) conducted a series of wind tunnel tests investigating the effects of turbulence properties such as turbulence length scale, turbulent intensity and high and low fluctuating components on the VIV behaviour of two-dimensional rectangular and hexagonal cylinders having different aspect ratios. It was found that the turbulence suppression effect was not observed for all cross sections. Later, Wu and Kareem (2012) and Kareem and Wu (2013) also pointed out this issue and suggested this is due to the difference in the mechanism of the VIV – whether it is motioned-induced-vortex or von-Kármán-vortex driven VIV. Nevertheless, more studies are required to clarify these inconsistencies and provide a more comprehensive explanation on the mechanism of the turbulence-induced effect on the bridge aerodynamics in general and on the VIV and the motion-induced vortex in particular.

2.8.2 Breakdown of Strip Assumption

The turbulence and buffeting analysis began in the 1960s with the application of the strip assumption proposed by Davenport (1962a). This assumption concerns the size of the structure in comparison with the size of gusts that, if the structures are sufficiently slender for the secondary span-wise flow and re-distribution of pressures to be neglected, the pressures on any section of the span are only due to the wind incident on that section. Davenport stated that the use of the strip assumption can help to describe the wind loading on structures which, when combined with a given mode shape, leads to the calculation of the modal structural response. However, he also stressed this method seems reasonable for slender structures such as thin cables or open lattice trusses but seems to be invalid for structures having large area normal to the flow such as bridge decks.

In the strip theory, Davenport implied the spatial distribution of the dynamic loading due to gusts on structures is similar to the spatial distribution of the oncoming gusts; many researchers have focused on validating this assumption in cases of bridge decks.

After Davenport, many researchers have believed that the turbulence in the oncoming wind, turbulence-induced pressures and forces are coherent fields that the value at one point is affected by not only this point itself but also other surrounding points. This spatial influence is normally expressed as correlation functions or coherence functions. For bridge decks immersed in turbulent wind, this is the key point in the theory of gust response prediction; the turbulence-induced forces are affected by turbulence at this point and surrounding it as well. Therefore, it has been strongly believed the spatial coherence of forces is higher than that of turbulence.

Later, Kimura et al. (1997) used the concept of root coherence to obtain the coherence structure of buffeting forces and turbulence in the wind. The root coherence spectrum CO_{XY} between two time series $X(t)$ and $Y(t)$ is given by

$$CO_{XY}(f) = \frac{\mid S_{XY}(f) \mid}{\sqrt{S_X(f)S_Y(f)}}, \tag{2.69}$$

where the cross-spectrum S_{XY} is defined as

$$S_{XY}(f) = 2\int_{-\infty}^{\infty} \rho_{XY}(\tau)\cos(2\pi f\tau)\,\mathrm{d}\tau. \tag{2.70}$$

Here, $\rho_{XY}(\tau)$ is the cross-covariance of $X(t)$ and $Y(t)$,

$$\rho_{XY}(\tau) = \lim_{T\to\infty}\frac{1}{T}\int_{-\frac{T}{2}}^{\frac{T}{2}} X(t)Y(t+\tau)\,\mathrm{d}\tau. \tag{2.71}$$

$S_X(f)$ and $S_Y(f)$ in Equation 2.69 are the power spectrum of $X(t)$ and $Y(t)$ respectively. They have the same definition; for instance, the power spectrum of $X(t)$ is

$$S_X(f) = 2\int_{-\infty}^{\infty} \rho_X(\tau)\cos(2\pi f\tau)\,\mathrm{d}\tau, \tag{2.72}$$

where $\rho_X(\tau)$ is the autocovariance of $X(t)$,

$$\rho_X(\tau) = \lim_{T\to\infty}\frac{1}{T}\int_{-\frac{T}{2}}^{\frac{T}{2}} X(t)X(t+\tau)\,\mathrm{d}\tau. \tag{2.73}$$

The physical meaning of root coherence is the measure of correlation of two signals in the frequency domain. By conducting the wind tunnel tests on fixed sectional hexagonal and rectangular cylinders and using this analysis technique, Kimura et al. (1997) produced plots of root coherence spectrum of buffeting lift force with different span-wise separation, Δy, and different wind speeds; one set of results for the rectangular prism is shown in Figure 2.41. The coherence of buffeting lift forces reduces with an increase in span-wise separation; the main observation is that the buffeting lift force are better correlated compared to the transverse fluctuating velocity component w. Jakobsen (1997) and Larose and Mann (1998), conducting the wind tunnel tests on motionless sectional bridge deck models, also reported the similar results. Later, Larose (2003) concluded the limits of the strip assumption which are the higher span-wise correlation of the aerodynamic forces and moment compared to the oncoming wind fluctuation and neglect of 3D characteristic of gust loading. The energy from a wind gust tends to spread in the span-wise direction rather than concentrates at the point of impact; the span-wise correlation coefficient of buffeting forces and moment is therefore higher than the turbulence in the oncoming wind.

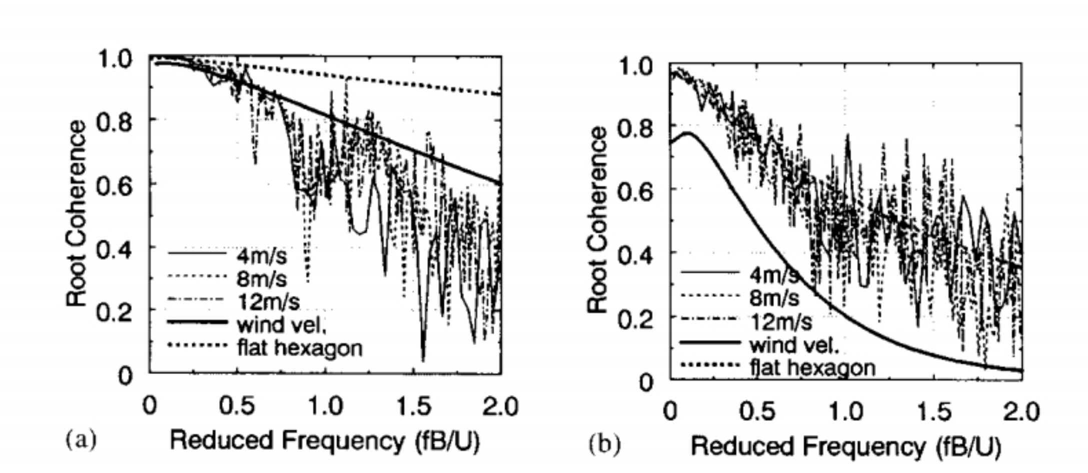

Figure 2.41: Root coherence spectrum of the buffeting lift force on the rectangular prism at (a) $\Delta y = 10\,\text{mm}$ and (b) $\Delta y = 50\,\text{mm}$ (Kimura et al., 1997).

2.8.3 Turbulence-induced Stabilisation and Span-wise Coherence of Aerodynamic Forces and Moment

The relationship between turbulence-induced stabilisation and span-wise coherence of aerodynamic forces and moment were first addressed by Scanlan (1997). By conducting a wind tunnel study on Golden Gate Bridge, he was able to confirm the stabilising effect of turbulence and observed the significant impact of less-than-perfect coherence of the self-excited force on aerodynamic damping. Further experimental results and field observation suggested the self-excited forces do not maintain perfect coherence in the span-wise direction in the turbulent flow; this coherence loss enhances the flutter stability and increases the critical flutter velocity.

Recent researchers, however, did not fully agree with the above findings. From Haan and Kareem (2007), it could be seen that the self-excited forces were found to have near unity coherence over the entire span-wise separation range; for large turbulent length scale, a slight decrease in span-wise coherence was noticed (Figure 2.42). The buffeting force was found to be less correlated in the span-wise direction compared to the self-excited forces (Figure 2.43).

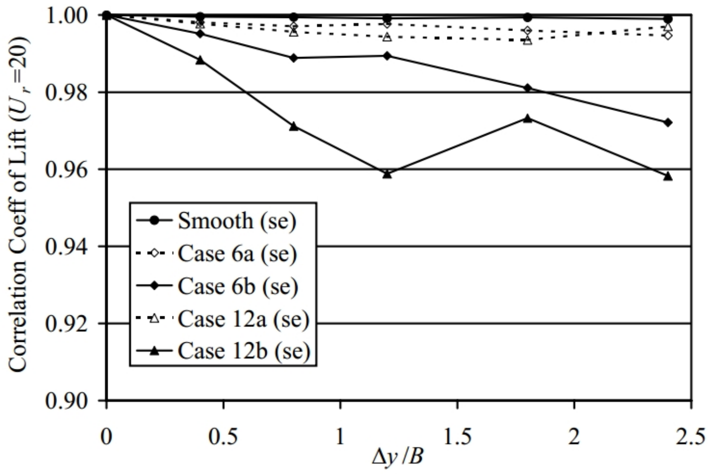

Figure 2.42: Cross correlation coefficient of the self-excited (se) lift force at $U_R = 20$ (Haan and Kareem, 2007).

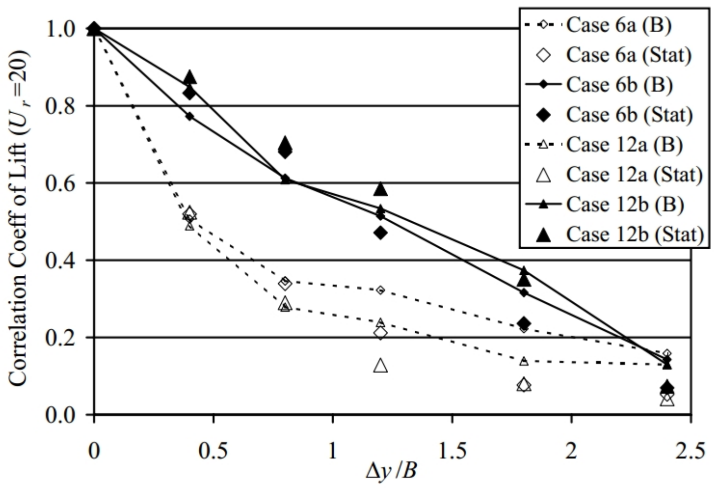

Figure 2.43: Cross correlation coefficient of the buffeting lift force acting on the oscillating model (B) and on the fixed model (Stat) at $U_R = 20$ (Haan and Kareem, 2007).

Therefore, the results of Haan and Kareem (2007) confirm the turbulence-induced flutter stabilisation but do not support the hypothesis of Scanlan (1997) that a decrease in the span-wise correlation of self-excited forces causes the turbulence-induced increase in the critical flutter velocity. The reduction in the span-wise correlation of the aerodynamic forces and moment as well as the surface pressure is also the common argument to explain the decrease of the VIV structural response in turbulence flow. However, as mentioned in Section 2.8.1, further study is required to bring more insight into the underlying physical mechanism of this behaviour, which is still rather limited at the moment. The other reason that can lead to this discrepancy is a limitation inherently included in most of the current studies. Due to a number of different obstacles, the models used in either wind tunnel or numerical studies of bridge aerodynamics and aeroelasticity are considered to be rigid. The influence of the combination of structural mode shapes on the aerodynamic characteristics of the flow field is therefore not fully captured.

2.9 CONCLUSION OF THE CHAPTER

65 years after the collapse of the Tacoma Narrows Bridge, a lot of lessons in bridge design and construction have been learned and researchers in the bridge aerodynamics and aeroelasticity have achieved many milestones. Motivated by the need of better understanding of structural responses under wind loads, these achievements have helped not only to uncover the underlying physical mechanism of these complicated wind-induced effects but also to provide supports for the development of a number of theoretical models, which allows researchers and engineers to predict the wind-induced responses in terms of structural responses and on-set velocities. Moreover, some of these models have been integrated into codes of practice forming analysis frameworks to access wind loads and safety of bridge structures.

However, there still have a number of areas in the bridge aerodynamics and aeroelasticity whose related knowledge is still insufficient. In term of the theoretical modelling, even though its underlying theory was adopted from the aerospace engineering, the bridge flutter model, which uses the flutter derivatives to represent the linear dependence between forces and structural responses, has enjoyed numerous successes and is widely accepted to assess the flutter of bridge structures. The theoretical models of VIV and buffeting, on the other hand, still contain significant disadvantages, which requires further studies to improve their applicability and usability. For the latter, its limitation is due the assumption that the wind is stationary and Gaussian; in fact, most wind events, especially the extreme ones, are non-synoptic, i.e. transient and non-Gaussian. However, the lack of full-scale measurement has caused obstacles to model these wind events as well as to integrate them into an effective analysis framework. Also, non-linear structures are insufficiently modelled and addressed. For the former, the VIV, there exist a number of theoretical models; most of them are capable to capture all characteristics of a VIV lock-in including its non-linearity; however, the usability and practicability regarding to the need of bridge designers and engineers are still very limited. Most models require extensive wind tunnel or computational studies to comprehensively define model parameters before it can be applied to fully assess the safety of a real structure.

The effect of the turbulence on bridge aerodynamics and aeroelasticity has been found to be surprisingly inadequate. As suggested by the hypothesis developed by Scanlan (1997), it is common to accept that the turbulence produces stabilisation and therefore, the turbulence is not considered to be a conclusive parameter in bridge design, especially for the VIV. However, a number of wind tunnel and numerical studies together with full-scale measurements have showed the opposite effect where the turbulence produces destabilisation. In addition, the argument that the turbulence reduces the span-wise correlation of aerodynamic forces and surface pressure has not been supported by recent researchers. This discrepancy can be due to the fact that most studies up to now have utilised rigid sectional models; thus the aerodynamics of the flow field is dominated by 2D features while the 3D flow feature including some span-wise fluctuation is overlooked.

As stated in Chapter 1, the aim and objectives of this research project is to conduct wind tunnel tests and computational simulations using a sectional model in smooth and turbulence flow to uncover the mechanism of the VIV, particularly for the 5:1 rectangular cylinder. Also, it provides some insight into the turbulence-induced effect on the VIV as well as its related underlying mechanism. More importantly, this research study introduces a new approach in the 3D computational modelling using the state-of-the-art flexible rectangular cylinder to model the bending motion, which is an analogue of a real suspension bridge deck. Selected results are then extracted and used to improve the Hartlen and Currie model so that it can be used to predict the VIV of a flexible structure.

Chapter 3

Computational Fluid Dynamics

In this chapter, key concepts and theories of CFD are introduced; they include the governing equations and background knowledge of a CFD code as well as different turbulence models that can be applied to simulate the flow field around structures. In addition, the application of CFD in Wind Engineering, in general, and in bridge aerodynamics and aeroelasticity, in particularly, will be presented, showing the potential and future of CFD as not only a designing tool during a feasibility study but also an important analysis tool for research purposes, in complement with wind tunnel tests, to help bring more insights into a physical phenomenon.

3.1 NAVIER-STOKES EQUATIONS

Navier-Stokes equations are a very famous set of mathematical equations derived by the French engineer Claude Navier and the Irish mathematician George Stokes; these equations describe a broad range of fluid motions. The fundamental ideas behind these equations are the continuity of flow and the conservation of momentum. The vector form of the Navier-Stokes equations is

Continuity equation

$$\frac{\partial \rho}{\partial t} + \rho \nabla \cdot \mathbf{U} = 0, \tag{3.1}$$

Momentum equation

$$\rho \left(\frac{\partial \mathbf{U}}{\partial t} + \mathbf{U} \cdot \nabla \mathbf{U} \right) + \nabla p - \mu \nabla^2 \mathbf{U} - \mathbf{F} = 0, \tag{3.2}$$

Here, vector quantities are indicated by the bold font. $\mathbf{U}$ is the velocity field of the flow, p is the pressure and $\mathbf{F}$ are the external forces acting on the flow. In case that there are no external forces, i.e. $\mathbf{F} = 0$ and the fluid is considered to be incompressible, i.e.

$$\frac{\partial \rho}{\partial t} = 0, \tag{3.3}$$

Equations 3.1 and 3.2 can be rewritten in the differential form as

$$\frac{\partial u_i}{\partial t} = 0, \tag{3.4}$$

$$\frac{\partial \rho u_i}{\partial t} + \frac{\partial \rho u_i u_j}{\partial x_j} = -\frac{\partial p}{\partial x_i} + \frac{\partial}{\partial x_j}\left(\mu \frac{\partial u_i}{\partial x_j}\right), \tag{3.5}$$

where i and j are the tensor notation denoting the components of displacement x and velocity u along the x, y and z directions. From the left to right, the terms in Equation 3.5 are the transient, inertial, pressure and viscous terms respectively. The Navier-Stokes equations are highly non-linear; the use of CFD can produce numerical solutions for these complex equations to an acceptable degree of accuracy in many situation.

3.2 MAIN COMPONENTS OF COMPUTATIONAL FLUID DYNAMICS

There are different commercial CFD codes that can be used to numerically solve the Navier-Stokes equations. All of them contain three main components: pre-processor, solver and post-processor.

Pre-processor is where users can define the fluid problem in a form which is suitable for use by the solver. The flow is enclosed in a region of interest called the computational (or flow) domain which is built from a lot of smaller and non-overlapping sub-domains called grids (or mesh) of cells (Figure 3.1). The bluff body or the submerged structure is actually subtracted from the mesh. The structure of the computational domain depends on the objectives of the user. In addition, users are required to identify the essential properties of the flow and the body and the boundary conditions of the computational domain as well as to select the physical models which are required to be modelled.

The solver is basically a programme written to obtain the numerical solutions of the Navier-Stokes equations. It uses appropriate discretisation and iteration schemes to compute the parameters of the flow. Because the governing equations are solved iteratively, residuals which are the difference between solutions obtained from two successive iterations appear. Solutions are achieved if residuals are smaller than tolerance values set by users, i.e. the solutions converge.

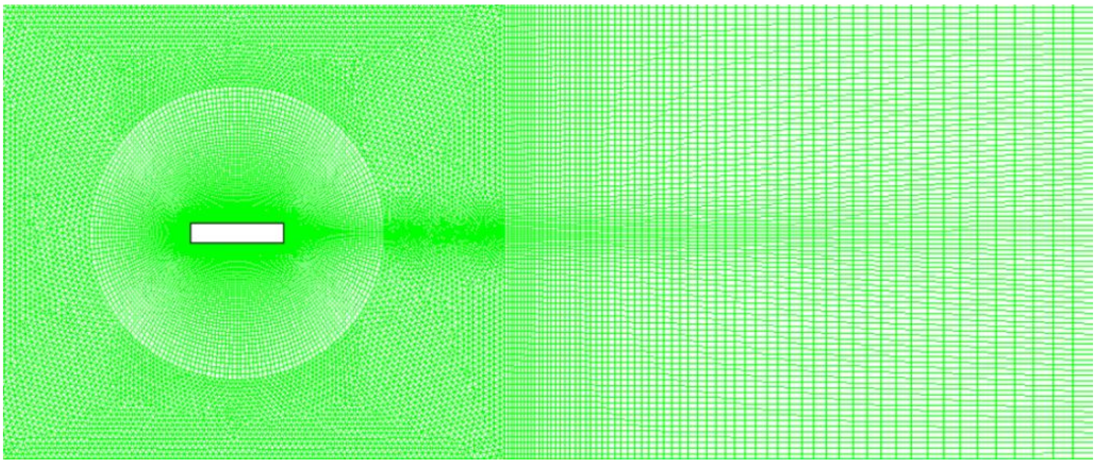

Figure 3.1: An example of a 2D computational domain constructed from triangle-, quadrilateral- and rectangular-shape cells.

In post-processing, users can make the full use of versatile visualisation tools to transform the results obtained from the solver into graphical presentation. Important properties of flow such as pressure, velocity and vorticity magnitude can be demonstrated by the use of vectors, contours or streamlines.

The principle idea of CFD codes is to discretise the governing equations and to solve them iteratively; in the next sections, the discretisation and iterative schemes will be discussed in detail.

3.3 DISCRETISATION SCHEME

The discretisation scheme is a process to transform the partial differential Navier-Stokes equations into algebraic equations so that a computer can produce numerical solutions at discrete points in the domain at a specified time. There are three major parts in descretising a fluid problem, which are spatial, equation and temporal discretisation.

3.3.1 Spatial Discretisation

Spatial discretisation deals with the structure of the computational domain; this process divides the domain into a number of finite control volumes or cells (Figure 3.2). All CFD computational domains contain many cells where the governing Navier-Stokes equations are solved numerically. The solutions obtained at one cell are quickly transferred to neighbouring cells via appropriate numerical techniques.

The geometry and structure of the computational domain control the number, size and shape of control volumes. The mesh is normally classified into three different types: structured, unstructured and multi-block structured. A structured grid is built based on a coordinate system which is normally the Cartesian system; therefore it is also named as the Cartesian grid. It is constructed from a number of

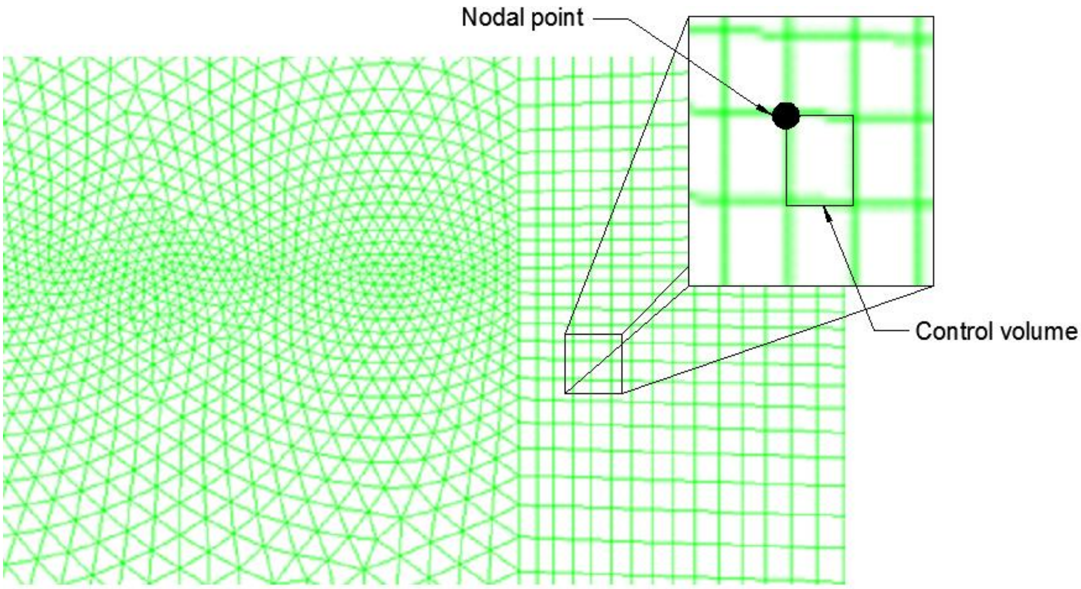

Figure 3.2: An example of a control volume.

quadrilaterals (in 2D problems) or hexahedra (in 3D problems) in a regular pattern. In addition, all grid points or nodal points in a structured grid are placed at the intersection of coordinate lines and have a fixed number of neighbouring points. The structured grid is advantageous in coding and in accuracy when the flow is predominantly aligned with the grid lines. With more complicated geometries, the structured curvilinear or body-fitted grid is preferred. This type of structured grids is based on mapping of the flow domain onto the computational domain. As for the body-fitted grid, all of the domain boundaries are coincident with the coordinate lines; thus, the flow along curve boundaries can be resolved correctly. However, the mesh generation can be very difficult.

To overcome difficulties when modelling complicated geometries, the block-structured grid can be applied; it is also known as the multi-block grid. Applying this grid generation method, the domain is divided into different regions or blocks, each of which has a structured mesh. The mesh structure in each block can be different and defined based on different coordinate systems. These characteristics result in higher flexibility compared to the ordinary structured grids. n simple example of block-structured grids is shown in Figures 3.3 and 3.4 where the computational domain consists of 8 separate blocks; the mesh structure of each block is defined using the Cartesian coordinate system. However, the detailed mesh structure can be distinguished between them. The block-structured grid combines the advantages of the traditional structured grid and the body-fitted grid; it is easy to generate and accommodate curve boundaries (Versteeg and Malalasekera, 2007).

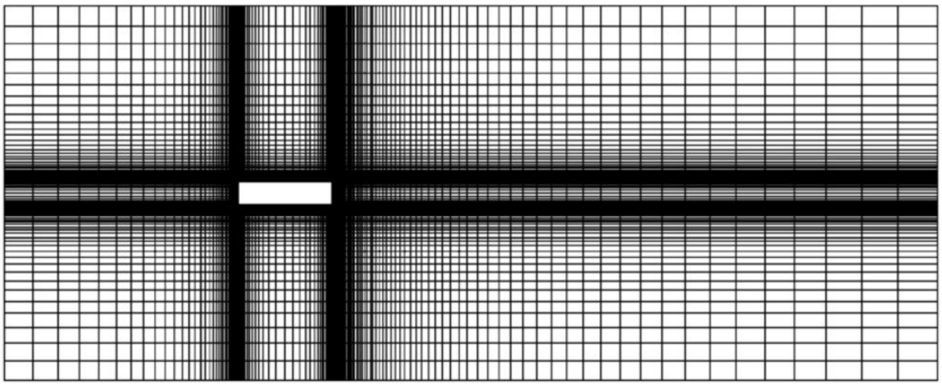

Figure 3.3: An example of a 2D block-structured grid (Sun et al., 2008).

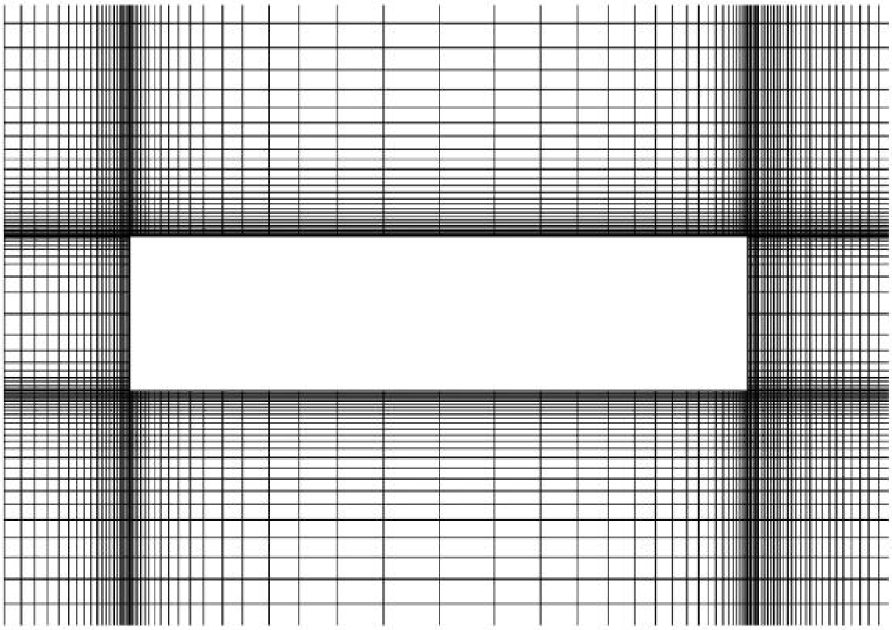

Figure 3.4: Close-up of the grid shown in Figure 3.3 (Sun et al., 2008).

The other type of computation domains is the unstructured grid which is built from triangles and quadrilaterals in 2D and triangular prisms and hexaderals in 3D; each cell is considered as a block of the unstructured grid (Figure 3.5). Therefore, with a large amount of blocks, the unstructured grid is very capable of modelling complicated geometries. This type of grids does not involve any implicit coordinate lines; therefore all cells are arranged in an irregular order, making it very difficult to access adjacent cells or nodes. The irregular pattern allows the grid refinement to be concentrated at the regions of interest; however, for a simple geometry, the unstructured grid contains more nodes, leading to higher cost in terms of computational resources and time. In addition, the shape of the control volume varies greatly throughout the unstructured grid, which requires advanced numerical schemes.

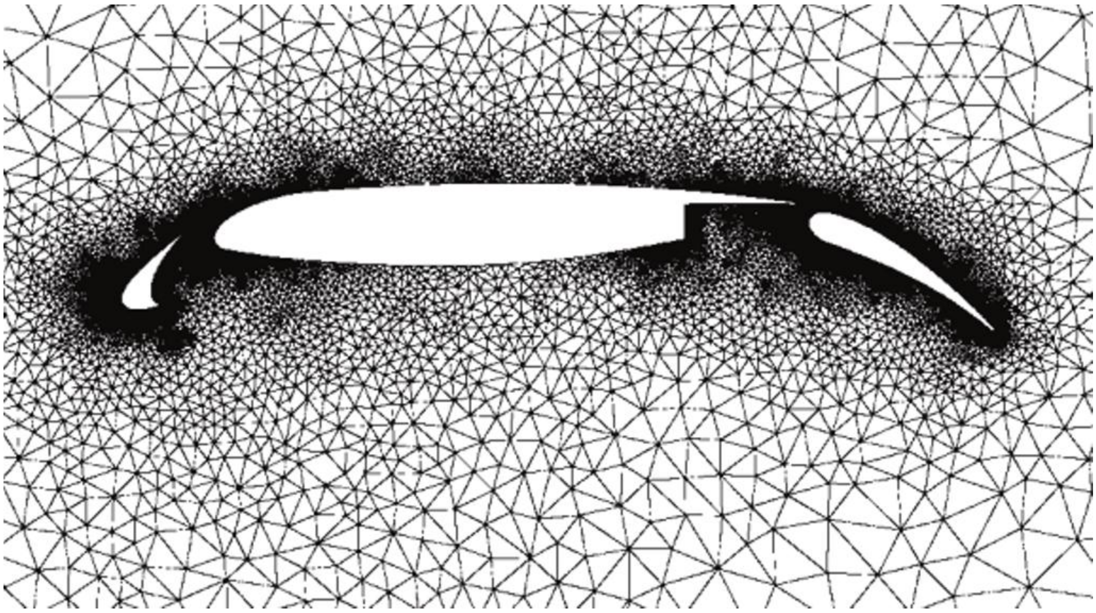

Figure 3.5: A triangular unstructured grid for a simulation of a airfoil (Versteeg and Malalasekera, 2007).

3.3.2 Equation Discretisation

Equation discretisation is the process of transforming the partial differential governing equations into a numerical analogue so that it can be solved by computers. In the fluid problem, the Navier-Stokes equations can be discretised using the finite difference method, the finite element method or the finite volume method. As shown in Section 3.3.1, the whole computational domain is separated into a number of control volumes; hence, the finite volume method is preferable in CFD.

The approach of the finite volume method is that, after the computational domain is divided into separate control volumes, the governing equations are integrated over a control volume, using the conservation of mass and momentum for each control volume; the general integration result of the Navier-Stokes equations for a flow variable ϕ is

$$\int_V \frac{\partial \rho\phi}{\partial t}\mathrm{d}V + \int_A \mathbf{n}\cdot(\rho\phi\mathbf{U})\,\mathrm{d}A = \int_A \mathbf{n}\cdot(\Gamma_\phi\nabla\phi)\,\mathrm{d}A + \int_V S_\phi \mathrm{d}V, \tag{3.6}$$

where V and A are the volume and surface area of the control volume respectively, $\mathbf{n}$ is the normal area vector, Γ_ϕ is the diffusion coefficient of ϕ and S_ϕ is the source of ϕ in a control volume. The meaning of each term in Equation 3.6 is listed in Table 3.1. CFD codes contain different discretisation schemes to appropriately treat the integrated transient, diffusion, convection and source terms. The result is a set of algebraic equations that can be solved simultaneously to obtain the flow parameters inside the control volume. The solutions of a control volume are transferred to the adjacent ones, which allows the flow

Table 3.1: Meaning of terms in Equation 3.6.

Term	Meaning
$\int_V \frac{\partial \rho\phi}{\partial t} \mathrm{d}V$	Rate of change of ϕ in the control volume with respect to time (transient term)
$\int_A \mathbf{n} \cdot (\rho\phi\mathbf{U})\mathrm{d}A$	Rate of decrease of *phi* due to convection into the control volume (convection term)
$\int_A \mathbf{n}\cdot(\Gamma_\phi \nabla\phi)\mathrm{d}A$	Rate of increase of ϕ due to diffusion into the control volume (diffusion term)
$\int_V S_\phi \mathrm{d}V$	Rate of creation of ϕ inside the control volume (source term)

to be simulated throughout the computational domain. This process is repeated based on an iteration approach until convergence is achieved. The flow is then fully modelled throughout the domain.

3.3.3 Temporal Discretisation

Temporal discretisation is applied in a transient simulation which involves a time-dependent or transient term. This process discretises the time into discrete time steps, which results in a system of equations in time where unknown variables at the current time step are computed based on the knowledge of previous time steps or neighbouring nodes. The explicit and implicit methods are the two popular techniques.

In the explicit method, the unknown variable ϕ at the time step $t_n + \Delta t$ is calculated using its value at the previous time step t_n. This method is easy to implement and requires less computational memory but the size of the time step Δt is very crucial. It needs to be small enough to maintain the stability and convergence of the solving process; however, a too small time-step size can lead to very long computational time. As for the implicit method, the unknown variable ϕ of one node at the time step t_n is computed based on the values of this node at previous time step and of adjacent nodes at the same time step. This approach implies a very large set of discretised equations which can be solved simultaneously to model the flow throughout the domain.

To maintain the accuracy, stability and convergence of this numerical solving process, the computational domain and the time must be discretised properly; the relationship between the process of the spatial and temporal discretisation is expressed via the Courant number, Co, which is defined as

$$\mathrm{Co} = \frac{U \Delta t}{\Delta x}, \tag{3.7}$$

where U is the mean speed of flow and Δx is the characteristic cell size which is effectively the average cell size across the entire computational domain. Δx, thus, is given by

$$\text{2D domain: } \Delta x = \left[\frac{1}{N} \sum_{i=1}^{N} \Delta A_i \right]^{\frac{1}{2}}, \tag{3.8}$$

$$\text{3D domain: } \Delta x = \left[\frac{1}{N} \sum_{i=1}^{N} \Delta V_i \right]^{\frac{1}{3}}. \tag{3.9}$$

Here, N is the number of cells in the domain, ΔA_i and ΔV_i are the face area and volume of cell i respectively. The characteristic cell size is computed using the area-average-based approach for 2D domains while, for 3D domains, the volume-average-based approach is applied. If using the characteristic cell size, the Courant number is considered as an average value of the domain. However, rigorously, each cell in the domain has its own dimension and flow speed; therefore the Courant number varies from cells to cells. It is found that $\mathrm{Co} \leq 1$ at every cell to ensure the stability in solving partial differential equations. Hence, the small cells concentrating in the regions having the large gradient of flow parameters become important due to the inversely proportional relationship between Co and Δx. Knowing the cell size, the time-step size Δt is chosen accordingly to fulfil the requirement that $\mathrm{Co} \leq 1$, or, in other words, the distance the fluid travels in one time step has to be smaller than the cell size so that it can be modelled accurately.

3.4 PRESSURE-VELOCITY COUPLING SCHEME

After the discretisation schemes are selected and applied, the pressure and velocity fields across the entire domain are solved iteratively using the pressure-velocity solver. There are segregated and coupled pressure-velocity solvers; they differ by the fact that the discretised governing equations are solved sequentially in the segregated solver while the coupled solver simultaneously solves the system of momentum and continuity equations. This method requires more computational resources and time. In this research study, the segregated solver is used; the SIMPLE and PISO schemes are two segregated solvers commonly used in CFD.

The SIMPLE scheme stands for Semi-Implicit Method for Pressure-Linked Equations. This method solves the governing equations sequentially that the momentum equation is solved first to obtain the velocity field based on an assumed pressure field or pressure gradient. The result of the velocity field is substituted into the continuity equation to correct the pressure field, which can be put back in the momentum equation. This process is repeated until the residuals are smaller than specified tolerances. In addition, some essential parameters at some monitoring points have to be assessed to ensure their behaviour is consistent; for example, in a steady-state simulation, the values at these points should tend towards a fixed value.

The PISO scheme or the Pressure Implicit with Splitting Operators is originally developed for non-iterative computation of unsteady (transient) flows. However, it can be adapted for the iterative solution of steady problems (Versteeg and Malalasekera, 2007). The steady PISO scheme is very similar to the SIMPLE scheme; each iteration, however, includes a second correction of the pressure field to enhance the accuracy and convergence.

These two schemes can be developed for the computation of transient problems. The transient SIMPLE scheme basically conducts the SIMPLE loop discussed above at each time step until the convergence is reached. As for the transient PISO scheme, it is originally the non-iterative transient solver that, at each time step, only one PISO loop is carried out and the twice-corrected pressure and velocity fields are considered as the correct fields. Due to this non-iterative approach, the accuracy of the transient PISO scheme largely depends on the temporal discretisation scheme. Versteeg and Malalasekera (2007) has reported that, with sufficiently small time steps, the non-iterative transient PISO scheme is capable to yield accurate results. Also because, at one time step, the iteration approach is not required, the PISO scheme occupies less computational resources and time. Therefore, the PISO scheme is preferable to the transient SIMPLE scheme to simulate transient problems.

3.5 TURBULENCE MODELLING

Modelling turbulent flow has been seen as the major challenge for all CFD codes; it is due to the nature of turbulence that contains eddies having a wide range of scales. Turbulent energy is transferred from large-scale eddies to small-scale eddies where it is dissipated due to viscosity (Section 2.1). To model the turbulent flow accurately, all of the turbulent eddies must be successfully resolved; therefore, grids must be fine enough so that the smallest eddies can be simulated. These simulations are known as Direct Numerical Simulation (DNS).

DNS is capable of resolving directly turbulence in the flow without any turbulence models, using the unmodified Navier-Stokes equations together with a very fine grid and very small time steps. The results obtained from DNS are very accurate; Versteeg and Malalasekera (2007) showed that, to successfully resolve turbulence using DNS, the grid cell requirement is $N_{cell} \cong \mathrm{Re}^{9/4}$ and the computational time is CPU time $\cong \mathrm{Re}^3$. These requirements make DNS limited to low Reynolds number flow only. Dealing with high Reynolds number flow, a turbulence model is necessary; Reynolds Averaged Navier-Stokes (RANS) and Large Eddy Simulation (LES) models are the common and appropriate approaches in this research study.

3.6 RANS MODELS

RANS models are widely used to simulate turbulent flows in fluid-structure interaction problems, producing reasonable numerical results with acceptable compromise between accuracy and computational cost (Brusiani et al., 2013). Using the RANS approach, the turbulence in the flow is not resolved directly; instead, the overall turbulent effects are fully reproduced by the adoption of appropriate turbulence models, depending on the aims and objectives of simulations (Versteeg and Malalasekera, 2007). Regarding this computational study, two-equation RANS models are of interest; the k-ε, k-ω and SST models are discussed in detail in this section.

3.6.1 RANS Equations

RANS models apply the time-averaging operation on the governing equations. Similar to Equation 2.7, the wind speed in the i direction, u_i, is decomposed into the mean component $\bar{u}_i$ and the fluctuating component u_i' as

$$u_i = \bar{u}_i + u_i', \tag{3.10}$$

where the mean of u_i' is 0. The notations used in this section are slightly different from Section 2.1 in order to maintain the consistency with the Navier-Stokes equations defined in Equations 3.4 and 3.5. The time-averaging operation is performed on the original governing equations; the time-averaged terms of the momentum equation, as an example, are

$$\text{Transient term: } \overline{\frac{\partial \rho u_i}{\partial t}} = \frac{\partial \rho \bar{u}_i}{\partial t}, \tag{3.11}$$

$$\text{Pressure term: } \overline{\frac{\partial p}{\partial x_i}} = \frac{\partial \bar{p}}{\partial x_i}, \tag{3.12}$$

$$\text{Viscous term: } \overline{\frac{\partial}{\partial x_j}\left(\mu \frac{\partial u_i}{\partial x_j}\right)} = \frac{\partial}{\partial x_j}\left(\mu \frac{\partial \bar{u}_i}{\partial x_j}\right), \tag{3.13}$$

$$\text{Inertial term: } \overline{\frac{\partial \rho u_i u_j}{\partial x_j}} = \overline{\frac{\partial}{\partial x_j}[\rho(\bar{u}_i + u_i')(\bar{u}_j + u_j')]} = \frac{\partial}{\partial x_j}(\rho \bar{u}_i \bar{u}_j) + \frac{\partial}{\partial x_j}(\rho \overline{u_i' u_j'}). \tag{3.14}$$

The same procedure can be applied to the original continuity equation; the RANS equations of an incompressible flow, thus, are defined as

$$\frac{\partial \bar{u}_i}{\partial x_i} = 0, \tag{3.15}$$

$$\frac{\partial \rho \bar{u}_i}{\partial t} + \frac{\partial}{\partial x_j}(\rho \bar{u}_i \bar{u}_j) = -\frac{\partial \bar{p}}{\partial x_i} + \frac{\partial}{\partial x_j}\left(\mu \frac{\partial \bar{u}_i}{\partial x_j}\right) - \frac{\partial}{\partial x_j}(\rho \overline{u_i' u_j'}). \tag{3.16}$$

Using the RANS approach, the modified Navier-Stokes momentum equation includes an additional term which is the last term in Equation 3.16. It is called the Reynolds stress term representing the interaction of fluctuating velocity components in the flow. The Reynolds stresses include three normal stresses which are

$$\tau_{ii} = -\rho \overline{u_i'^2}, \tag{3.17}$$

$$\tau_{jj} = -\rho \overline{u_j'^2}, \tag{3.18}$$

$$\tau_{kk} = -\rho \overline{u_k'^2}, \tag{3.19}$$

and three shear stresses which are

$$\tau_{ij} = \tau_{ji} = -\rho \overline{u_i' u_j'}, \tag{3.20}$$

$$\tau_{ik} = \tau_{ki} = -\rho \overline{u_i' u_k'}, \tag{3.21}$$

$$\tau_{jk} = \tau_{kj} = -\rho \overline{u_j' u_k'}. \tag{3.22}$$

The existence of these Reynolds stresses means there are more unknowns than the number of equations. Therefore, extra turbulence models and equations need introducing to solve the Reynolds stresses, which is known as the closure problem.

3.6.2 k-ε Turbulence Model

The k-ε turbulence model introduces two additional transportation equations to reproduce the turbulence characteristic of the flow; one expresses the turbulent kinetic energy, k, and the other is for the rate of dissipation of turbulent kinetic energy, ε, which are given by

$$k = \frac{1}{2}\left(\overline{u_1'^2} + \overline{u_2'^2} + \overline{u_3'^2}\right), \tag{3.23}$$

$$\varepsilon = \frac{\partial k}{\partial t}, \tag{3.24}$$

where u_1', u_2' and u_3' are the velocity fluctuating components in the x_1, x_2 and x_3 (or x, y and z) directions respectively. The turbulence of the flow is described by the k and ε transportation equations, which are derived from the time-averaged Navier-Stokes equations (Versteeg and Malalasekera, 2007)

$$k \text{ equation: } \frac{\partial \rho k}{\partial t} + \frac{\partial \rho u_j k}{\partial x_j} = \frac{\partial}{\partial x_j}\left(\frac{\mu_t}{\sigma_k}\frac{\partial k}{\partial x_j}\right) + G_k - \rho\varepsilon, \tag{3.25}$$

$$\varepsilon \text{ equation: } \frac{\partial \rho \varepsilon}{\partial t} + \frac{\partial \rho u_j \varepsilon}{\partial x_j} = \frac{\partial}{\partial x_j}\left(\frac{\mu_t}{\sigma_\varepsilon}\frac{\partial \varepsilon}{\partial x_j}\right) + C_{1\varepsilon}\frac{\varepsilon}{k}G_k - C_{2\varepsilon}\rho\frac{\varepsilon^2}{k}, \tag{3.26}$$

where $C_{1\varepsilon} = 1.44$, $C_{2\varepsilon} = 1.92$, $\sigma_k = 1.00$ and $\sigma_\varepsilon = 1.30$ are model constants. The variable μ_t in Equations 3.25 and 3.26 is the eddy, or turbulent, viscosity, representing the diffusion of momentum and energy of the flow caused by turbulent eddies. It has the same units and the physical meaning as the molecular (dynamic) viscosity which is also known as the dynamic viscosity of the flow. The eddy viscosity of the k-ε model is defined as

$$\mu_t = \rho C_\mu \frac{k^2}{\varepsilon}, \tag{3.27}$$

where the constant C_μ is 0.09. The term G_k is the production rate of the turbulent kinetic energy k; it is given by

$$G_k = 2\mu_t S_{ij} S_{ij}. \tag{3.28}$$

Here, S_{ij} is the mean rate of strain tensor, which is given by

$$S_{ij} = \frac{1}{2}\left(\frac{\partial u_i}{\partial x_j} + \frac{\partial u_j}{\partial x_i}\right). \tag{3.29}$$

The k-ε turbulence model is widely used in a lot of industrial applications, showing its reliability, robustness and affordability. However, this model has some certain downsides, such as it over-predicts the turbulence near stagnation points and fails to resolve flows containing large strain (for example, flows around the boundary layers).

3.6.3 k-ω Turbulence Model

The k-ω turbulence model is capable to accurately resolve flows around the boundary layers by replacing the dissipation rate of the turbulent kinetic energy ε with the dissipation rate per unit kinetic energy ω

$$\omega = \frac{1}{C_\mu}\frac{\varepsilon}{k}, \tag{3.30}$$

where the constant C_μ is the same as in Equation 3.27. The two transportation equations of this turbulence model are

$$k \text{ equation: } \frac{\partial \rho k}{\partial t} + \frac{\partial \rho u_j k}{\partial x_j} = \frac{\partial}{\partial x_j}\left(\frac{\mu_t}{\sigma_k}\frac{\partial k}{\partial x_j}\right) + G_k - \rho\beta' k\omega, \tag{3.31}$$

$$\omega \text{ equation: } \frac{\partial \rho \omega}{\partial t} + \frac{\partial \rho u_j \omega}{\partial x_j} = \frac{\partial}{\partial x_j}\left(\frac{\mu_t}{\sigma_\omega}\frac{\partial \omega}{\partial x_j}\right) + \rho\alpha\frac{\omega}{k}G_k - \rho\beta\omega^2. \tag{3.32}$$

where $\alpha = 5/9$, $\beta = 0.075$, $\beta' = 0.09$, $\sigma_k = 2.00$, and $\sigma_\omega = 2.00$ are the model constants. The eddy viscosity μ_t of the k-ω turbulence model is

$$\mu_t = \rho\alpha\frac{k}{\omega}. \tag{3.33}$$

By using the variable ω, it is found to be easier to integrate the ω transportation equation through the boundary layer next to the wall; this feature, therefore, allows the k-ω turbulence model to resolve the flow near wall better than the k-ε model. These improvements are discussed in detail in Section 3.6.5. However, the k-ω cannot accurately model the flow in the free-stream zone away from the wall due to the overprediction of the eddy viscosity value.

3.6.4 Shear Stress Transport (SST) k-ω Turbulence Model

The SST turbulence model is considered as the combination of the k-ε and k-ω models. The main idea of this model is to utilise the advantages of each model to overcome the near-wall issue of the k-ε model and the issue with the free-stream zone in the k-ω model.

A blending function F_1, is applied to the governing equations of the two models,

$$F_1[k\text{-}\omega] + (1 - F_1)[k\text{-}\varepsilon], \tag{3.34}$$

where F_1 returns to 1 in the near-wall region and has a value of 0 in the free-strain zone. The use of this blending function allows a smooth transition between the k-ω model assigned around the boundary layer and the k-ε assigned to the free-stream region.

3.6.5 Near-wall Modelling

The near-wall modelling is challenging to any CFD codes and turbulence models due to its complicated nature as discussed in Section 2.2. The presence of a structure in the flow produces certain disturbance to the velocity profile. Theoretically, the molecules next to the wall are stationary relative to the wall; the wall-parallel velocity rapidly increases in the wall-normal direction, leading to large velocity gradients and thus production of turbulence (Equations 3.28 and 3.29). The boundary layer next to the wall is divided into two different regions: the outer and inner regions (Figure 3.6). The outer region is relatively far away

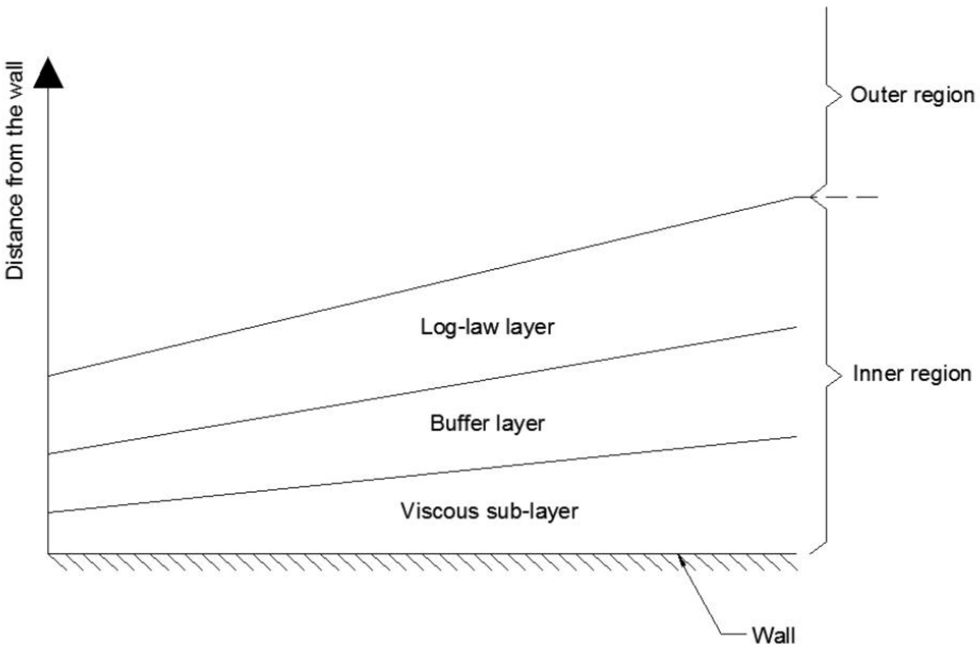

Figure 3.6: General boundary layer structure next to the wall.

from the wall, where the size of eddies is constant and proportional to the distance from the wall. The region just next to the wall is called the inner region; it is more interesting and requires more effort to model.

The structure of the boundary layer is classified and defined based on two non-dimensional parameters which are z^+ and u^+. z^+ is the dimensionless distance from the wall; it is given by

$$z^+ = \frac{\sqrt{\rho\tau_w}}{\mu} z, \tag{3.35}$$

where z is the normal distance from the wall and τ_w is the wall shear stress. In this research study, the z^+ quantity is used instead of the ordinary y^+ to keep the consistency with computational simulations. The dimensionless quantity u^+ is

$$u^+ = \frac{u}{u_\tau}. \tag{3.36}$$

Here, u is the flow velocity at a distance z from the wall while u_τ is the friction velocity defined based on the wall shear stress τ_w as

$$u_\tau = \sqrt{\frac{\tau_w}{\rho}}. \tag{3.37}$$

In Figure 3.6, the very first layer next to the wall is the viscous sub-layer which is very thin (the depth is about 0.01 mm) and has the maximum z^+ value of 5. There are no turbulent fluctuations in this region and the flow characteristic is dominated by the viscosity of the flow. The shear stress in this layer, τ_{flow}, is constant and equal to the wall shear stress, τ_w, as

$$\tau_{flow} = \mu \frac{\partial u}{\partial z} = \tau_w. \tag{3.38}$$

Equation 3.38 can be integrated resulting in the velocity profile of the flow in this region, which is

$$u = \frac{\tau_w}{\mu} z, \tag{3.39}$$

$$\text{or: } u^+ = z^+. \tag{3.40}$$

The buffer layer is a transition from the viscous sub-layer and the log-law layer. This layer is characterised by the damping of turbulent eddies and a balance between turbulence and viscous effects. The furthest layer in the inner region is the log-law region, ranging from the z^+ of 30 up to 500. The flow in this layer is dominated by turbulence effects. The shear stress, τ_{flow}, is varied with distance from the wall; hence the velocity profile in this layer is expressed as

$$u = \frac{u_\tau}{\kappa} \ln E \frac{\sqrt{\rho \tau_w}}{\mu} z, \tag{3.41}$$

$$\text{or: } u^+ = \frac{1}{\kappa} \ln E z^+, \tag{3.42}$$

where the von Karman's constant, κ, is equal to 0.4, E is an empirical constant that depends on the roughness of the wall. Equations 3.39 to 3.42 can be used to accurately describe the behaviour of the near-wall flow. In terms of the CFD approach, the use of these equations must be accompanied by such a fine computational domain that there are enough cells inside the viscous sub-layer to resolve the flow. This requirement can result in a large number of cells, especially for 3D simulations at high Reynolds numbers. To avoid the need of very thin cells around the wall, the wall-function approach is an alternative solution.

The wall-function approach differs slightly between each turbulence model. This approach was first produced and applied together with the k-ε model; it is named the standard wall-function approach. For the k-ε turbulence model, the wall-function strategy replaces very thin cells in the wall-normal direction by coarser ones; the target z^+ value is between 30 to 300, which can ensure the the first cell centroid is placed far enough from the wall to be in the log-law region. The wall-function approach assumes the wall shear stress of the near-wall cells is calculated based on the velocity at the near-wall node. The governing Navier-Stokes equations are not solved directly in the near-wall cells; instead, the wall-function approach estimates the mean production and dissipation rates of the turbulent kinetic energy k, which are then used to solve the discretised transportation equation for k. The standard wall function of the k-ε model uses the log-law approach to model the near-wall flow; the wall function can be expressed as

$$u^+ = \frac{1}{\kappa}\ln(Ez^+), \tag{3.43}$$

$$k = \frac{u_\tau^2}{\sqrt{C_\mu}}, \tag{3.44}$$

$$\varepsilon = \frac{u_\tau^3}{\kappa z}. \tag{3.45}$$

The main drawback of this standard wall-function approach is the assumption of uniform flow in the boundary layer and the estimation of the production and dissipation rate of k. In addition, the standard wall function is only limited to high-Reynolds-number flows; when modelling the low-Reynolds-number flows, the log-law approach is invalid. Therefore further modifications are required for either the wall function or the turbulence model, which leads to the development of the low-Reynolds-number turbulence models such as the k-ω, SST k-ω and low Re k-ε models. These models use the low-Reynolds-number method to take into account the viscous effect near the wall, which is ignored in the standard wall function. This modified approach allows the near-wall flow to be fully resolved by directly solving the flow parameters without any mathematical representation of the velocity profile.

Using the time-averaging method, RANS can be considered as a steady-state model to predict the time-averaged flow and turbulence properties. RANS can indeed be used as a transient model which is suitable to model flow where the small scale turbulence is not very significant to the aerodynamic behaviour of structures. This approach normally refers to unsteady RANS (URANS) simulation. To verify the suitability of using the RANS model in the bridge aeroelasticity, Sun et al. (2009) conducted computational simulations using the RANS k-ω turbulence model. The numerical results confirmed the applicability of the RANS turbulence model to investigate the fluid-structure interaction of bridge decks, especially the VIV and flutter. The simulations also revealed the higher computational efficiency of RANS compared to LES and its better flow visualisation comparing with the discrete vortex method. On the other hand, the authors pointed out one of the main disadvantages of the RANS models that the RANS models limit the turbulence profile to be prescribed via the turbulent intensity and length scale. This very prescription assumes an isotropic turbulence structure which causes the loss of span-wise vortices in 3D problems.

3.7 LES MODELS

3.7.1 LES Equations

LES models apply a spatial-decomposition operation on the Navier-Stokes equations. This decomposition method involves a spatial filtering function and a characteristic filtering width Δ; eddies of size larger than Δ are called as large-scale eddies while the others are called small-scale eddies. In LES models, the large-scale eddies are of interest; in the flow, they transport mass, energy and momentum, which can significantly affect the behaviour of the flow and immersed structures. Also, they are problem-dependent, easily influenced by boundary conditions of the flow. LES models, therefore, directly resolve the large-scale eddies while the small-scale ones are modelled and assumed to be isotropic.

The filtering function can spatially decompose any flow parameters. Taking the velocity component U_i in the i direction as an example, it can discretised as

$$U_i = \bar{u}_i + u_i', \tag{3.46}$$

where $\bar{u}_i$ is the resolved part and u_i' is the unresolved part. The resolved velocity at a point x at a time t is calculated using the filtering function $G(x, x', \Delta)$ as

$$\overline{u(x,t)} = \int_{\text{domain}} U(x', t) G(x, x', \Delta) \mathrm{d}x'. \tag{3.47}$$

The selection of Δ in the filtering function $G(x, x')$ determines the size of large and small eddies in the flow. Using the finite volume method, Versteeg and Malalasekera (2007) suggested to use the averaged grid size as the filtering width as

$$\Delta = (\Delta x \Delta y \Delta z)^{\frac{1}{3}} = \Delta V^{\frac{1}{3}}, \tag{3.48}$$

where Δx, Δy and Δz are the dimension of a cell in the x, y and z direction respectively while ΔV is the volume of a cell. Using the cell size as the cut-off width, any eddies which are smaller than the cell size are not resolved. Instead, they are mathematically modelled and represented by values at the centroid of the control volume. Applying this spatial discretisation, the filtered governing equations are

$$\frac{\partial \bar{u}_i}{\partial x_i} = 0, \tag{3.49}$$

$$\frac{\partial \rho \bar{u}_i}{\partial t} + \frac{\partial}{\partial t}(\rho \bar{u}_i \bar{u}_j) = -\frac{\partial \bar{p}}{\partial x_i} + \frac{\partial}{\partial x_j}\left(\mu \frac{\partial \bar{u}_i}{\partial x_j}\right) - \frac{\partial \tau_{ij}}{\partial x_j}. \tag{3.50}$$

where $\tau_{ij} = \rho(\overline{u_i u_j} - \bar{u}_i \bar{u}_j)$, which is called as the sub-grid scale (SGS) stress involving the interaction between the resolved and unresolved eddies. The SGS stress τ_{ij} can be decomposed as

$$\begin{aligned}\tau_{ij} &= \rho(\overline{u_i u_j} - \bar{u}_i \bar{u}_j) \\ &= \rho(\overline{\bar{u}_i \bar{u}_j} - \bar{u}_i \bar{u}_j) + \rho(\overline{\bar{u}_i u'_j} + \overline{u'_i \bar{u}_j}) + \rho\overline{u'_i u'_j}.\end{aligned} \tag{3.51}$$

The decomposed SGS stress includes three distinctive terms which are the Leonard stress, L_{ij}, the cross stress, C_{ij} and the LES Reynolds stress, R_{ij}, corresponding to the order in Equation 3.51. The Leonard stress purely contains the information of resolved eddies only, representing effects at the resolved scale. The cross stress involves both the resolved and unresolved components, showing the interaction of the modelled eddies with the resolved flow. The final term which is the LES Reynolds stress is caused by the diffusion of momentum between the SGS eddies. Similar to the Reynolds stress in the RANS models, this term has to be modelled by SGS turbulence models.

3.7.2 Smagorinsky SGS Turbulence Model

The Smagorinsky SGS turbulence model is commonly used to model the SGS stress; this model defines R_{ij} as

$$R_{ij} = -2\mu_{\text{SGS}}\bar{S}_{ij} + \frac{1}{3}R_{ii}\delta_{ij}. \tag{3.52}$$

Here, $\bar{S}_{ij}$ is the strain rate tensor of the resolved flow, which is given by

$$\bar{S}_{ij} = \frac{1}{2}\left(\frac{\partial \bar{u}_i}{\partial x_j} + \frac{\partial \bar{u}_j}{\partial x_i}\right). \tag{3.53}$$

The final term in Equation 3.52 involved the normal LES Reynolds stress R_{ii} and the function δ_{ij} which is equal to 1 if $i = j$ and returns to 0 if $i \neq j$. This term is included to ensure the balance between the modelled SGS stress and the kinetic energy of the SGS eddies (Versteeg and Malalasekera, 2007) and is ignored when considering the incompressible fluid. μ_{SGS} is the SGS viscosity which, similarly the eddy viscosity in RANS models, is required to be modelled. The Smagorinsky model defines μ_{SGS} based on the an assumption of the balance between the energy production and dissipation of the small-scale eddies, which leads to the expression as

$$\mu_{\text{SGS}} = \rho L_s^2 \mid \bar{S} \mid, \tag{3.54}$$

where $\mid \bar{S} \mid = \sqrt{2\overline{S_{ij}S_{ij}}}$ and $L_s = C_s\Delta$. $C_s = 0.1$ is the Smagorinsky constant. Defining C_s as a constant is the main limitation of the standard Smagorinsky SGS model. Versteeg and Malalasekera (2007) showed that different values of C_s are obtained when using LES models to solve variety flow problems; these values range from 0.1 up to 0.25. In addition, for a single LES simulation, the value of C_s is not likely to remain constant. In some flow problems, due to the interaction of the flow with immersed structures or confining walls, the flow includes sub-regions having different flow conditions compared to the others. This effect can lead to problems for choosing a constant C_s. The other disadvantage is that the Smagorinsky is a overly diffusive model, where the energy is transferred from the large-scale eddies to the small-scale eddies only. The backscatter process involving the transportation of energy in the opposite direction (Section 2.1.1) is not accurately modelled. These limitations of the standard Smagorinsky SGS model lead to the development of more general SGS models.

3.7.3 Dynamic Smagorinsky SGS Turbulence Model

The dynamic SGS model may be considered as a modified Smagorinsky SGS model involving further mathematical expressions to overcome the limitation of the standard SGS model. One of the well-known dynamic SGS model is proposed by Germano et al. (1991), which applies an additional filtering function to locally model the SGS stress τ_{ij} and the Smagorinsky coefficient C_s in space and in time. Using two filtering functions with different values of the filtering width, the SGS stress is given by

$$\tau_{ij} = \rho \left(\overline{\overline{u_i u_j}} - \bar{\bar{u}}_i \bar{\bar{u}}_j \right). \tag{3.55}$$

Compared to Equation 3.51, each filtered term in Equation 3.55 has two bars on top, indicating a double filtering process. The Smagorinky coefficient C_s is now defined as

$$C_s = -\frac{1}{2} \frac{\mathcal{L}_{ij} M_{ij}}{M_{ij}^2}. \tag{3.56}$$

Here, $\mathcal{L}_{ij}$ is the resolved turbulence stress (Germano et al., 1991) which is defined as

$$\mathcal{L}_{ij} = -\left(\overline{\bar{u}_i \bar{u}_j} - \bar{\bar{u}}_i \bar{\bar{u}}_j \right), \tag{3.57}$$

and, M_{ij} is

$$M_{ij} = \Delta_2^2 \mid \bar{\bar{S}} \mid \bar{\bar{S}}_{ij} - \Delta_1^2 \overline{\mid \bar{S} \mid \bar{S}_{ij}}. \tag{3.58}$$

The LES models have been successfully applied to solve the fluid-structure interaction in the turbulent flow due to its capability to capture the turbulence structure in the flow (Sun et al., 2008). The LES simulation is more computationally demanding compared to the time-averaging RANS models. It is due to fact that the LES models requires higher grid resolution, particularly at the near-wall region. In addition, LES simulations typically require smaller time steps to accurately resolve the small-scale eddies.

Moreover, unlike RANS simulations, to model the turbulence with LES, it requires to provide temporal and spatial varying inflow conditions. Commercial CFD codes usually contain built-in utilities which can produce turbulence at inlets for LES simulations; however, the generated turbulence field is reported to lose certain statistical properties of the wind. In order to generate the turbulence at the inlet of LES simulations, two different techniques are normally applied, which are the precursor simulation method and the synthesis turbulence method. The core concept of this latter method is to represent the fluctuating component of the turbulence by the white noise; however, due to the lack of the temporal and spatial coherence characteristics, further mathematical operations are required to generate these desired statistical properties as well as to match specified Reynolds-stress tensors (Tabor and Baba-Ahmadi, 2010). This method has been developed and studied in detail by Lund et al. (1998), Klein et al. (2003), di Mare et al. (2006) and Xie and Castro (2008). Falling in the same category is the Proper Orthogonal Decomposition (POD) method, which, based on the property of the POD technique, allows the turbulence to be generated using spatially limited experimental wind speed data (Perret et al., 2008); the POD technique will be discussed in Section 4.6. A more recent approach to generate the inlet turbulence is the vortex method or synthetic eddy method (Benhamadouche et al., 2006), where vortices are introduced at the inlet and transported into the computational domain. The length scale of vortices as well as their distribution on the inlet are determined based on the statistical properties of the synthesis turbulence (Kornev and Hassel, 2007). This particular method is focused and favourable at the moment since it requires a shorter length of the computational domain downstream of the inlet is required to fully develop the turbulence (Tabor and Baba-Ahmadi, 2010). As suggested by the name, the precursor simulation method involves an explicit and separate calculation of an equilibrium turbulent flow, which is then stored into a library and re-introduced at the inlet of the main LES simulation. The library can be generated by performing a simulation using a short precursor cyclic domain where the flow at the output is input the inlet; the velocity field on a plane normal to the stream-wise direction is extracted and stored. The library can be created before or in parallel with the main simulation as proposed by Lund et al. (1998) with a notice that the velocity data should be extracted in a region in which the turbulent flow is in an equilibrium and well-known condition. This issue together with the fact that a separate simulation is required are the main disadvantage of this method when generating the turbulence with specific properties. On the other hand, the synthetic turbulence method offers better computational efficiency, more flexibility to generate the inlet turbulence with prescribed parameters and an ease to integrate into a LES simulation. A comprehensive review and comparison between these methods are presented in a paper by Tabor and Baba-Ahmadi (2010).

These requirements somehow overshadow the positive aspects of the LES models in a comparison with the RANS models. Over the past three decades, the RANS models have been a favourable choice of industry in a variation of applications, such as design and optimisation processes, because they are simple, economic and computational affordable. However, with the current development in computer technology, in the near future, Hanjalic (2005) believed the LES models will be preferable in most of the industrial application while the RANS models with some innovations will be used for some kinds of appraisal simulations.

3.8 FLUID STRUCTURE INTERACTION

The fluid-structure-interaction phenomena arises in many aerospace engineering applications including airfoil oscillations, flutter predictions and a large class of other aeroelastic instability problems. In the bridge aeroelasticity, the numerical simulation of the fluid-structure interaction (FSI) has been developed to investigate the vortex-induced vibration and flutter in particular. A FSI problem is characterised by the coupling of three different fields including the fluid, structure and mesh or dynamic mesh. The first component, the fluid, is described the well-known Navier-Stokes equations. The dynamic properties of the second component, the structure, is governed by

$$\boldsymbol{M}\ddot{\boldsymbol{u}}_{\boldsymbol{s}} + \boldsymbol{C}\dot{\boldsymbol{u}}_{\boldsymbol{s}} + \boldsymbol{K}\boldsymbol{u}_{\boldsymbol{s}} = \boldsymbol{F}(t), \tag{3.59}$$

where $\boldsymbol{M}$, $\boldsymbol{C}$ and $\boldsymbol{K}$ are the mass, damping and stiffness matrices. $\boldsymbol{u}_{\boldsymbol{s}}$ is the displacement of the structure while $\boldsymbol{F}(t)$ is the force acting on the structure due to pressure and viscosity obtained by solving the Navier-Stokes equations. The last element is the mesh which can be viewed as a pseudo-structural system with its own dynamics. A dynamic mesh algorithm has to be implemented to deform or move the mesh to accommodate the deflection of the structure. An appropriate kinematic description of the continuum which is either the fluid or structure is then required to accurately determine the relationship between the mesh and the deforming continuum and to provide an accurate resolution of material interfaces and mobile boundaries (Donea et al., 2004).

3.8.1 Arbitrary Lagrangian-Eulerian Methods

There are two classical descriptions of motions that are generally used to form the algorithm of continuum mechanics: the Lagrangian description and Eulerian description (Malvern, 1969).

Lagragian Description

Two domains that are commonly used in the continuum mechanics are the material domain $R_{\boldsymbol{X}}$ and the spatial domain $R_{\boldsymbol{x}}$ with their corresponding coordinate systems $\boldsymbol{X}$ and $\boldsymbol{x}$ respectively.

Applying the Lagragian description in numerical solvers, the grid nodes are permanently attached to the material nodes. Therefore, individual nodes of the computation domain follows the associated material particles during their motion. The motion of the material particle relates the material coordinate to the spatial coordinate, which can be mathematically represented by the one-to-one mapping operation φ defined as

$$(\boldsymbol{x}, t) = \varphi(\boldsymbol{X}, t). \tag{3.60}$$

The gradient matrix of φ is

$$\frac{\partial \varphi}{\partial(\boldsymbol{X}, t)}(\boldsymbol{X}, t) = \begin{pmatrix} \frac{\partial \boldsymbol{x}}{\partial \boldsymbol{X}} & \boldsymbol{v} \\ \\ \mathbf{0} & 1 \end{pmatrix}, \tag{3.61}$$

where $\mathbf{0}$ is a zero vector and the material velocity $\boldsymbol{v}$ is defined as

$$\boldsymbol{v}(\boldsymbol{X}, t) = \frac{\partial \boldsymbol{x}}{\partial t}\bigg|_{\boldsymbol{X}}, \tag{3.62}$$

which can be interpreted as the time variation of the coordinate $\mathbf{x}$ holding the material particle $\mathbf{X}$ fixed.

Each finite element of a Lagrangian mesh always contains the same material particle. This helps eliminate the convection effect and facilitates an ability of tracking free surfaces and interfaces between different materials. Also, the Lagrangian description is preferable to model the problems involving materials with history-dependent behaviour which is very typical in the structural mechanics. However, the Lagrangian mesh is unfavourable to simulations involving very sudden and large distortions of the continuum. A frequent remeshing operation can preserve the quality of the mesh against the excessive distortion but it is limited by very high computational demand.

Eulerian Description

The disadvantages of the Lagrangian mesh are overcome by using the Eulerian algorithm. In the Eulerian description, the spatial domain is used as the referential domain instead of the material domain. In this case, all material quantities at a given mesh node at a coordinate $\boldsymbol{x}$ are correspondent to the quantities of the material point coincident with the considered node at the considered time t. Therefore, the Eulerian algorithm only involves variables and functions having an instantaneous significance in a fixed region of space (Donea et al., 2004).

The basic idea of the Eulerian formulation is that the grid nodes are disassociated from the material nodes. The mesh is fixed and the continuum moves and deforms with respect to the computational grid; therefore, the numerical solver must take the convection effect into account. The Eulerian mesh is very popular in fluid mechanics including examining a physical quantity at a fixed region of space as time evolves. However, in addition to numerical difficulties to model convection, the application of the Eulerian algorithm is very limited to moving boundaries and deforming material interfaces.

Arbitrary Lagrangian-Eulerian Description

The brief review of the classical Lagrangian and Eulerian descriptions has emphasised the positives and negatives of each method. It also highlighted the main differences between them which are the selection of the referential domain, how the mesh is treated and their application. The Lagrangian mesh is the most suitable to solve problems of structure dynamics while simulations in fluid dynamics are mostly performed by applying the Eulerian algorithm.

The arbitrary Lagrangian-Eulerian (ALE) description is considered as a generalised algorithm which combines at best the interesting aspects of the classical mesh descriptions while minimising their downsides as far as possible. It was originated by Noh (1964) and later improved by Farhat et al. (1995). The ALE methods have been implemented in a number of research including Farhat et al. (1998a), Farhat and Lesoinne (2000), Degand and Farhat (2002), Farhat et al. (2006),Wood et al. (2010) and Habchi et al. (2013).

In the ALE algorithm, neither the material domain $R_{\boldsymbol{X}}$ nor the spatial domain $R_{\boldsymbol{x}}$ is taken as the referential domain. In stead, a new domain is introduced – the referential domain $R_{\boldsymbol{\chi}}$ together with the referential coordinate $\boldsymbol{\chi}$. This new configuration holds the position of the grid nodes of the computational domain. Figure 3.7 shows three domains involving in the ALE algorithm as well as three one-to-one mapping operations relating the domains together.

The referential domain $R_{\boldsymbol{\chi}}$ is mapped into the spatial domain $R_{\boldsymbol{x}}$ by the transformation Φ. This mapping operation represents the motion of the grid nodes in the spatial domain and can be mathematical defined as

$$(\boldsymbol{x}, t) = \Phi(\boldsymbol{\chi}, t). \tag{3.63}$$

The gradient matrix of Φ is

$$\frac{\partial \Phi}{\partial(\boldsymbol{\chi}, t)}(\boldsymbol{\chi}, t) = \begin{pmatrix} \frac{\partial \boldsymbol{x}}{\partial \boldsymbol{\chi}} & \hat{\boldsymbol{v}} \\ & \\ \mathbf{0} & 1 \end{pmatrix}, \tag{3.64}$$

where the grid velocity $\hat{\boldsymbol{v}}$ is given by

$$\hat{\boldsymbol{v}}(\boldsymbol{\chi}, t) = \left.\frac{\partial \boldsymbol{x}}{\partial t}\right|_{\boldsymbol{\chi}}, \tag{3.65}$$

which can be interpreted as the time variation of the spatial coordinate $\boldsymbol{x}$ of the grid node $\boldsymbol{\chi}$ fixed.

Finally, the transformation Ψ maps the referential domain $R_{\boldsymbol{\chi}}$ to the material domain $R_{\boldsymbol{X}}$ and it describes the motion of the material particle in the referential domain. The inverse of this operation is defined as

$$(\boldsymbol{\chi}, t) = \Psi^{-1}(\boldsymbol{X}, t), \tag{3.66}$$

whose matrix gradient is

$$\frac{\partial \psi^{-1}}{\partial(\boldsymbol{X}, t)}(\boldsymbol{X}, t) = \begin{pmatrix} \frac{\partial \boldsymbol{\chi}}{\partial \boldsymbol{X}} & \boldsymbol{w} \\ & \\ \mathbf{0} & 1 \end{pmatrix}. \tag{3.67}$$

The velocity $\boldsymbol{w}$ is given by

$$\boldsymbol{w}(\boldsymbol{X}, t) = \left.\frac{\partial \boldsymbol{\chi}}{\partial t}\right|_{\boldsymbol{X}}, \tag{3.68}$$

thus representing the time variation of the referential coordinate $\boldsymbol{\chi}$ of the material particle $\boldsymbol{X}$ fixed; therefore, it can be defined as the particle velocity as being seen from the referential domain.

Figure 3.7 also suggests the interdependence of these three mapping operations as $\varphi = \Phi \circ \Psi^{-1}$ whose the derivative yields the relationship between three different velocities as

$$\boldsymbol{v} = \hat{\boldsymbol{v}} + \frac{\partial \boldsymbol{x}}{\partial \boldsymbol{\chi}} \boldsymbol{w}. \tag{3.69}$$

Equation 3.69 can be rewritten as

$$\boldsymbol{c} = \boldsymbol{v} - \hat{\boldsymbol{v}} = \frac{\partial \boldsymbol{x}}{\partial \boldsymbol{\chi}} \boldsymbol{w}, \tag{3.70}$$

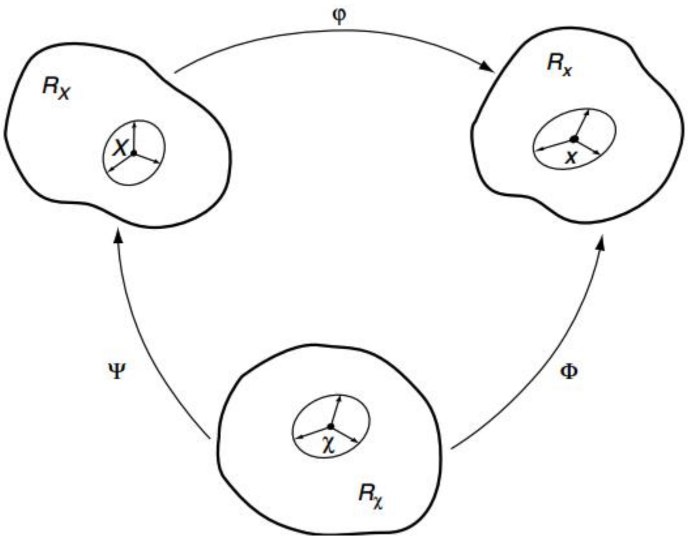

Figure 3.7: Interaction of three domains in the ALE description, adopted from Donea et al. (2004).

which is the convection velocity or the relative velocity between the material and the mesh. These fundamental formulations of the ALE description can then be used to derive the Lagrangian and Eulerian algorithm. In the Lagrangian description, the material domain attaches to the referential domain, i.e. $\boldsymbol{X} \equiv \boldsymbol{\chi}$ which implies that the material and the grid velocities are identical based on Equations 3.62 and 3.65. Therefore, the convection velocity $\boldsymbol{c}$ is null. On the other hand, the Eulerian mesh is fixed in space; thus $\boldsymbol{x} \equiv \boldsymbol{\chi}$. Equation 3.65 then implies a null grid velocity and the convection velocity $\boldsymbol{c}$ is simply coincident with the material velocity.

By introducing the referential domain to hold the position of the grid nodes, the ALE algorithm allows the mesh to move freely with respect to the material and the spatial domain. Figure 3.8 clearly illustrates the difference between the original descriptions and the ALE algorithm. The ability of the ALE algorithm to freely move the mesh is very attractive. It helps eliminate the drawbacks of using either the Lagrangian or Eulerian description alone. Also, the ALE algorithm is capable to modelling problems involving excessive distortions of continuum without compromising the mesh quality or demanding some remeshing procedures. However, the ALE formulation treats the mesh as a dynamic structural system on its own, which then requires a so-called mesh-update procedure to handle the deformation of the mesh.

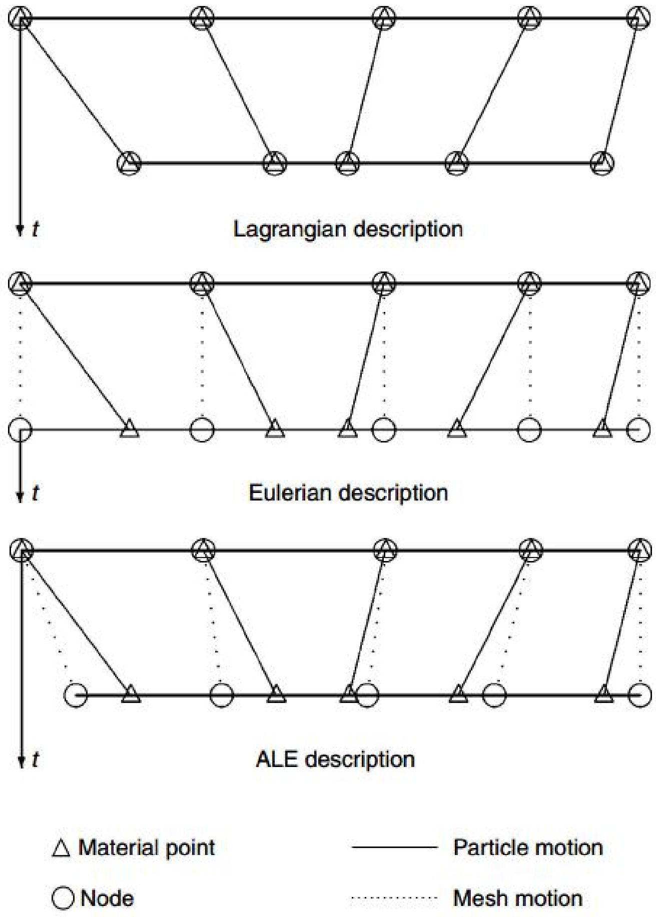

Figure 3.8: Illustration of one-dimensional example of the Lagrangian, Eulerian and ALE description, adopted from Donea et al. (2004).

With the use the ALE algorithm, the convection effect must be taken into account; therefore, the conservation of mass and momentum has to be altered as

$$\left.\frac{\partial \rho}{\partial t}\right|_{\boldsymbol{X}} = \left.\frac{\partial \rho}{\partial t}\right|_{\boldsymbol{\chi}} + \boldsymbol{c} \cdot \nabla \rho = -\rho \nabla \cdot \boldsymbol{v}, \tag{3.71}$$

$$\rho \left.\frac{\partial \boldsymbol{v}}{\partial t}\right|_{\boldsymbol{X}} = \rho \left[\left.\frac{\partial \boldsymbol{v}}{\partial t}\right|_{\boldsymbol{\chi}} + (\boldsymbol{c} \cdot \nabla) \boldsymbol{v} \right] = \nabla \cdot \boldsymbol{\sigma} + \rho \boldsymbol{g}, \tag{3.72}$$

where ρ is the density, $\boldsymbol{\sigma}$ is the Cauchy stress tensor and $\boldsymbol{g}$ denotes the body force vector. By comparing Equations 3.71 and 3.72 against the original conservation mass and momentum in the Eulerian form, certain differences can be noticed, which includes the appearance of the grid velocity $\hat{\boldsymbol{v}}$ representing via the relative velocity between the material and the grid $\boldsymbol{c}$. In addition, all of the time derivatives in both equations are performed in the referential domain or the computational grid domain rather than in the spatial domain.

When the ALE algorithm is used to numerically model the fluid-structure interaction, a number of continuity boundary conditions must be enforced at the fluid-structure interface, such that no fluid particles can cross the interface, i.e. $\boldsymbol{n} \cdot \boldsymbol{w} = 0$ or $\boldsymbol{n} \cdot \boldsymbol{v} = \boldsymbol{n} \cdot \hat{\boldsymbol{v}}$. In here, $\boldsymbol{n}$ is the normal vector of the interface. In addition, at the interface, the fluid and the structure do not detach or overlap during the motion, which means

$$\boldsymbol{v_f} = \boldsymbol{v_s}. \tag{3.73}$$

Here, $\boldsymbol{v_f}$ is the fluid velocity. If the fluid is inviscid, the conditions in Equation 3.73 only applies to the direction normal to the interface. In the problems involving the coupling between the motion of the structure and the fluid flow, the dynamic condition requires to be fulfilled by setting the stress in the fluid equal to the stress in the structure at the interface, which is

$$-p\boldsymbol{n} + 2\nu \left(\boldsymbol{n} \cdot \nabla^S\right) \boldsymbol{v} = \boldsymbol{n} \cdot \sigma_s, \tag{3.74}$$

where p is the fluid pressure, S is the surface of the interface and ν is the kinematic viscosity of the fluid. If the fluid is inviscid, the second term on the left hand side is ignored.

The use of the ALE algorithm allows the movement of the fluid grid is independent of the fluid motion. At the interface, the fluid grid is restrained to remain contiguous to the structural grid. This configuration leads a permanent alignment of nodes at the interface, which facilitates the coupling between the fluid and structure. The condition is achieved by prescribing the grid velocity of the fluid nodes at the interface to equal to the material velocity of the adjacent structural nodes. Mathematically, it is expressed as

$$\text{Displacement: } \boldsymbol{u} = \boldsymbol{u_s}, \tag{3.75}$$

$$\text{Velocity: } \boldsymbol{v} = \boldsymbol{v_s}. \tag{3.76}$$

3.8.2 Dynamic Mesh Algorithm

The other component of the fluid-structure-interaction problems is the dynamic mesh which is modelled to accommodate the moving fluid-structure interfaces. The first method is to re-generate the fluid mesh at each time step or at least when the structure is advanced. Later, this method is improved into the so-called mesh adaptation method which have shown advantages in simulating the fluid-structure-interaction problems in the time domain. This technique not only facilitates displacement of the moving boundaries but also optimises the computational mesh by relocating grid nodes towards zones of strong solution gradients predicted by the fluid solver without varying the number of nodes (Donea et al., 2004).

However, this technique is very computational expensive and cumbersome, especially for 3D problems. For the second method, the existing mesh is allowed to deform to follow the moving fluid-structure interface. The mesh is therefore viewed as a pseudo-structural system with its own dynamic properties which can be expressed by an equation sharing some analogies with Equation 3.59 as

$$\tilde{\boldsymbol{M}}\ddot{\boldsymbol{u}} + \tilde{\boldsymbol{C}}\dot{\boldsymbol{u}} + \tilde{\boldsymbol{K}}\boldsymbol{u} = K_c\boldsymbol{u_s}, \tag{3.77}$$

where $\tilde{\boldsymbol{M}}$, $\tilde{\boldsymbol{C}}$ and $\tilde{\boldsymbol{K}}$ are fictitious mass, damping and stiffness matrices associated with the moving grid. K_c is the transformation matrix that converts the displacement $\boldsymbol{u_s}$ of the structure at the interface into the action on the moving mesh. In many problems, the quasi-steady form of Equation 3.77 is required

$$\tilde{\boldsymbol{K}}\boldsymbol{u} = K_c\boldsymbol{u_s}. \tag{3.78}$$

In addition, an algorithm is implemented to deform the mesh or at least a portion of the mesh whilst maintaining the connectivity of the original mesh and the required mesh quality. Shankar and Ide (1988) have proposed one of the first dynamic mesh update algorithms where the speeds of the interior grid nodes are calculated by interpolating the speed of the structure and the zero value at the outer boundaries along a constant coordinate line. Later, the spring analogy algorithm proposed by Batina (1990) has been widely used to model the interaction between the fluid and structure, particularly for unstructured grids. This approach is an iterative strategy where the edges of the mesh are modelled to behave like linear springs connecting the mesh vertices; the stiffness of the springs is inversely proportional to the length of the edges. In addition, the grid nodes on the outer boundaries of the mesh are held fixed whereas the grid nodes on the structure are fixed relatively to the moving interface. This dynamic mesh approach is called the lineal spring-analogy algorithm which has been shown to be successful subjected to a relatively small amplitude of the moving interface and coarse meshes with simple geometry.

The limitation of the lineal spring-analogy algorithm is due to the fact that the stiffness of linear springs does not contain information of areas nor angles of the mesh faces. Therefore, it cannot prevent the mesh vertices from colliding with each other and with the opposite edges, leading to collapse of the mesh faces. Farhat et al. (1998a) proposed a solution by introducing additional torsional springs on the mesh vertices. The stiffness of these torsional springs is directly related to the area of the mesh faces avoiding the vertex colliding and the crossover of the mesh vertices. Later, Degand and Farhat (2002) fully developed this technique to solve 3D problems. Some preliminary tests showed the superiority of the torsional spring-analogy algorithm in maintaining the high quality of the mesh. Therefore, it helps improve the computational performance and the capability of the use of large time-step. However, the calculation of the torsional stiffness matrix is very demanding due to the complicated mathematics. Thus, although the torsional spring-analogy algorithm is very versatile, the lineal one should be selected if the mesh is geometrically simple and characterised by relatively small deformation.

3.8.3 Coupling Schemes

In Section 3.8.1, the fluid-structure interaction has been defined as a three-field problem involving the fluid, the structure and the dynamic fluid mesh. These field elements are governed by the Navier-Stokes equation, Equations 3.59 and 3.77 respectively. The three equations are highly coupled together, which is represented by Equations 3.73 to 3.76. A monolithic or partitioned procedure is frequently used to numerically solve the fluid-structure interaction problems.

Monolithic Scheme

The monolithic scheme is a fully coupled approach; the complete system of the fluid, structural and dynamic mesh governing equations are treated by the same manner and solved simultaneously. This scheme is favourable due to its robustness, stability, quick convergence and capability of using a large time-step (Wood et al., 2010).

However, Farhat et al. (1995) stated that the use of the monolithic scheme to solve the fluid-structure interaction problem is numerically inefficient and unmanageable regarding software issues. It is mainly due to the different nature of the three governing equations. While the structural and dynamic mesh equations can be linear or non-linear, the fluid is governed by the highly non-linear Navier-Stokes equations. Different numerical schemes are normally used to discretise and solve these equations. By treating all equations simultaneously, the monolithic approach requires a single numerical scheme to be able to solve all of them in a single block. This requirement makes the monolithic approach become less modular and the coding process is very challenging, especially taking into account the fact that the nature of the fluid-structure interaction problems is implicit rather explicit (Habchi et al., 2013).

Partitioned Scheme

On the contrary, using the partitioned scheme, each governing equation is separately treated, discretised and numerically solved. The fluid and structure equations can be solved in a staggered or non-staggered manner; however, the solving processes always occur in four distinct steps. The traditional partitioned scheme called as Conventional Serial Non-staggered Algorithm is described in Figure 3.9; there are 4 different steps involving which are

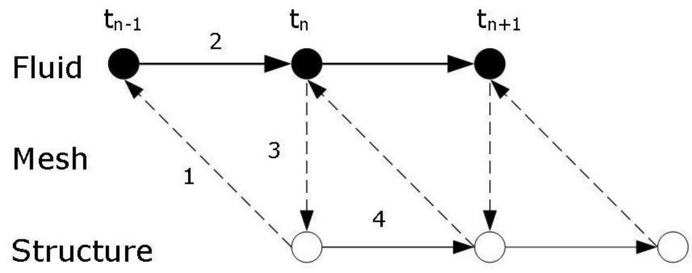

Figure 3.9: Conventional serial staggered algorithm.

1. Update the fluid mesh based on the new structural boundary,
2. Solve the Navier-Stokes equations and advance the fluid domain with the new boundary conditions,
3. Use the new fluid solutions to calculate the new pressure loads acting on the structure,
4. Solve the structural equation with the new pressure loads and advance the structural domain.

This algorithm earns its popularity for aeroelastic computations in the time domain thanks to its simplicity and capability to easily implement into any commercial CFD software. Well-establish numerical and discretisation schemes can be integrated to this algorithm without the need to develop a separate set of schemes. The 4-step block described in Figure 3.9 ensures the solution in each sub-system being transferred between each other at certain synchronised points in time. However, the good coupling only occurs around the fluid-structure interface while, further away from the interface, the fluid-structure coupling is quite loose. Also, this method is only 1st order accuracy even though higher order numerical schemes are applied to solve the governing equations (Piperno et al. (1995); Farhat et al. (1995)). In addition, this algorithm facilitates a similar time-step to discretise the fluid and structural equations; due to the high nonlinearity, the former requires a smaller time-step than the latter does (Farhat and Lesoinne, 2000).

To improve the efficiency of this algorithm, the sub-cycling idea has been implemented to the fluid solver as shown in Figure 3.10. By performing a number of fluid syb-cycles in each block, a bigger time step size can be applied to solve the structural domain without impairing the stability of the fluid solver. This technique helps reduce the computational cost since the structure is advanced fewer times and there is less exchange of information between the fluid and structure subsystems (Farhat and Lesoinne, 2000). The structure equation is solved using the pressure loads calculated at the last fluid sub-cycle or the average pressure loads calculated throughout the entire block. Piperno et al. (1995) however pointed out that the latter is advantageous in preserving the numerically stability of the algorithm. In addition, the stability limit of the algorithm is dictated by the number of fluid cycles in each block; increasing this number can improve the efficiency but significantly reduce the overall stability of the algorithm.

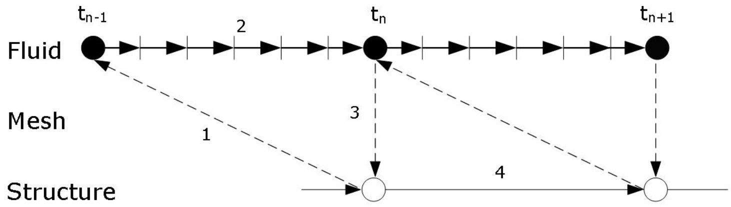

Figure 3.10: Conventional serial staggered algorithm with subcycling.

To improve the order of accuracy of the algorithm, the sub-cycling idea is developed into a full sub-iteration procedure where at each time step the fluid and structure domain is solved iteratively until the convergence is reached. This procedure involves a prediction step and a corrector step as illustrated in Figure 3.11. In the prediction step,

1. The predicted displacement of the structure $\boldsymbol{u}_{\boldsymbol{s},\mathbf{0}}^{\boldsymbol{predicted}}$ at the iteration $i = 0$ is obtained based on the structure solutions at the final iteration in the previous time step. The fluid mesh is then updated using this displacement,

2. The fluid equation is solved and the fluid parameters at the iteration i is calculated,

3. The pressure loads at the iteration i is calculated and transferred to the structural equation to calculate the new structural displacement $\boldsymbol{u}_{\boldsymbol{s},\mathbf{0}}$ which is then compared against $\boldsymbol{u}_{\boldsymbol{s},\mathbf{0}}^{\boldsymbol{predicted}}$.

If the difference is smaller than the pre-defined tolerance, the corrector step is ignored and $\boldsymbol{u}_{\boldsymbol{s},\mathbf{0}}^{\boldsymbol{predicted}}$ is taken as the final displacement for the structure after the time step n. Otherwise, the the displacement residual between $\boldsymbol{u}_{\boldsymbol{s},\mathbf{0}}^{\boldsymbol{predicted}}$ and $\boldsymbol{u}_{\boldsymbol{s},\mathbf{0}}$ is calculated and the corrector step is performed as

4. The displacement residual is used to obtain the predicted displacement $\boldsymbol{u}_{\boldsymbol{s},\mathbf{1}}^{\boldsymbol{predicted}}$ at the iteration $i + 1$,

5. The predicted displacement is then applied to update the fluid mesh,

6. With the new structure boundary condition and grid velocity, the fluid solver is solved again and the fluid parameter at the iteration $i + 1$ is obtained,

7. The pressure loads are then calculated and transferred to the structural solver to calculate the new displacement $\boldsymbol{u}_{\boldsymbol{s},\mathbf{1}}$ at the iteration $i + 2$. The calculation of the displacement residual is performed and if it is unsatisfied, another corrector step is carried out. Otherwise, $\boldsymbol{u}_{\boldsymbol{s},\mathbf{1}}^{\boldsymbol{predicted}}$ is the final solution of the structural displacement.

This sub-iteration procedure is presented in detail in papers by Wood et al. (2010) and Habchi et al. (2013). Here, the convergence of the algorithm is checked using the structural solutions; it can also be achievable using the flow variables. The sub-iteration procedure allows a bigger time-step size to discretise both the fluid and structural equations without violating the stability limit of the algorithm which is

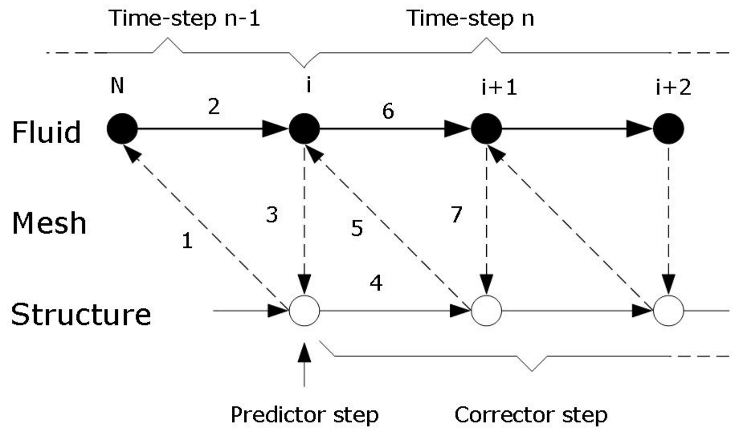

Figure 3.11: Sub-iteration procedure.

beneficial in saving of the computational cost and an increase in the order of accuracy and the coupling between the fluid and structure domain even in the region far away from the interface. Therefore it is also referred as a strong-coupled algorithm. However, the computational resources associated with the iteration process can overshadow the advantage of the large time-step.

Farhat et al. (2006) pointed out that the lack of accuracy and numerical stability in the conventional serial staggered algorithms is not entirely due to the loose aspect of their coupling. More importantly, these deficiencies are caused by the ability of the fluid time-integrator to preserve its order of accuracy on moving meshes and the lack of an appropriate structure predictor. The former is priority; if the fluid time-integrator on moving meshes cannot preserve the order of accuracy established on fixed meshes, the coupling scheme suffers a reduction in the accuracy eventually, even for a strongly coupled monolithic scheme. To overcome these disadvantages, the author introduced a second-order accurate predictor to predict the structural displacement at the time step t^{n+1} using the structural solutions at the previous time steps. Also, an appropriate fluid time-integrator which is capable to extend to moving meshes without impairing its accuracy was adopted; this time-integrator is presented in detail in a paper by Geuzaine et al. (2003). The result is a loosely-coupled second-order accurate staggered algorithm which is known as the Generalised Serial Staggered algorithm. This procedure shows its advantages in keeping the stability of the conventional serial staggered algorithm over the monolithic schemes without complicating the computational implementation and increasing the computational cost.

Another modification of the Conventional Serial Staggered Algorithm is proposed by Farhat and Lesoinne (2000); this improvement is named as the Improved Serial Staggered Algorithm and is illustrated in Figure 3.12. Similar to the conventional algorithm, the improved procedure is a sub-iteration-free method; the key difference is that the structural and fluid computations are offset by a half of the coupling time step. This algorithm is originally developed by Farhat and Lesoinne (2000) with the aim of

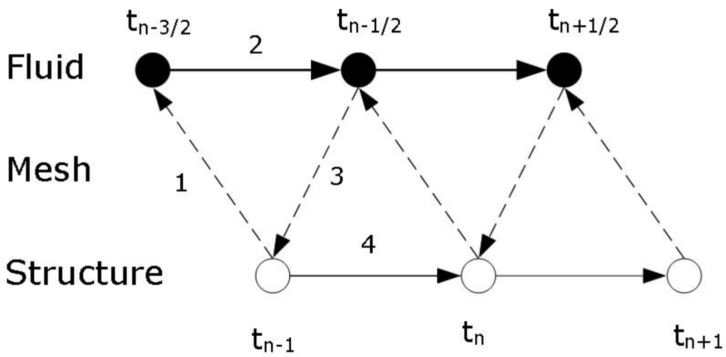

Figure 3.12: Improved serial staggered algorithm.

better modelling the energy exchange between the fluid and structure at the interface. Through some preliminary validation tests, the author pointed out that the numerical stability of the improved algorithm is less restrictive than the conventional one. A larger coupling time-step which are comparable to the monolithic schemes can be used. Thus, the sub-cycle or sub-iteration procedures are unnecessary even though they can be implemented with ease.

The Conventional Serial Staggered Algorithm is also well known to inhibit the inter-field parallelism; the structure domain cannot be advanced until the fluid subsystem is updated and solved. Advancing the fluid and structural subsystems simultaneously in a loosely coupling manner is favourable to reduce the total computational cost. Weeratunga and Pramono (1994) proposed a partitioned algorithm to simulate aeroelastic problems with the inter-field parallelism implemented as shown in Figure 3.13. This algorithm is called the Conventional Parallel Staggered algorithm and includes two steps which are

1. The fluid domain is updated using the structural displacement. At the same time, the pressure solution from the fluid solver is transferred to the structural domain to calculate the new pressure loads exerting on the structure,

2. The fluid and structural equations are solved and both subsystems are updated simultaneously.

Later, Piperno et al. (1995) emphasised that this parallel algorithm achieved the inter-field parallelism at the expense of amplified numerical errors in the fluid and structural solvers. It is due to the lack of feedback loops between the fluid and structural domain within one time step. Therefore this algorithm is shown to be very prone to the numerical instability; a very small coupling time-step size must be used to obtain reasonable results. Farhat and Lesoinne (2000) proposed an improvement to this procedure by introducing an exchange of information between the subsystems at half of the time step. This procedure is the Improved Parallel Staggered algorithm and is shown in Figure 3.14. In the first half of the time step, this algorithm is very similar to the conventional parallel algorithm, except that the fluid and the structural domains are only updated to $t_{n+1/2}$. In the second half of the time step,

3. The structural displacement is used to update the fluid mesh while the pressure information is transferred to the structural sub-system,

4. The fluid domain is advanced from $t_{n+1/2}$ to t_n; the structural equation is solved using the pressure loads calculated at $t_{n+1/2}$ and the structure is updated from t_n to t_{n+1}.

This method can be interpreted as: the structural solver uses the so-called time-averaged pressure loads to advance the structure through the whole time-step while the structural solutions obtained at half of the time step is used to correct the fluid mesh and the fluid solutions. This proposal allows better feedback between the fluid and structure; thus, a large time-step can be employed without impairing the numerical stability and accuracy of the algorithm. This is shown to outweigh some disadvantages including the introduction of one more communication loop between the sub-systems and one more fluid solution in each time step.

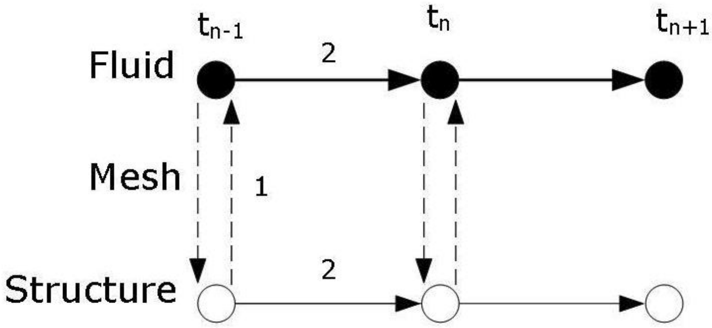

Figure 3.13: Conventional parallel staggered algorithm.

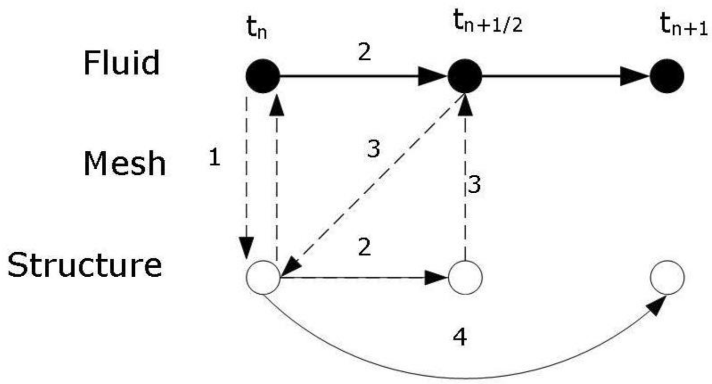

Figure 3.14: Improved parallel staggered algorithm.

3.8.4 Discretisation

In terms of the equation discretisation, the finite volume method is applied to the fluid solver while the finite element method is implemented to solve the structural equation. This configuration has been shown to be effective especially when the partitioned coupling schemes are used. However, as for the monolithic schemes, they require the consistency between the fluid and structure equation; the finite element method is therefore applied for both equations.

The spatial discretisation of the fluid and structural domains raises a significant concern at the fluid-structure interface. In general, the fluid and structural meshes can have two independent configurations of discretisation at the interface. If these configurations are identical, i.e. every grid node on the fluid mesh is also a structural node, the exchange information between the fluid and structural domain including the pressure loads and structural displacement is a trivial process (Farhat et al., 1995). However, in most realistic problems, the fluid and structural meshes are incompatible mostly because the fluid and structural problems require different mesh resolutions. For example, for an aeroelastic problem, the fluid mesh is typically finer than the structural one. This incompatibility is also due to the fact that the fluid and structure meshes are separately designed and validated, which offers researchers an ability to refine each mesh independently. In such cases, an extrapolation or interpolation algorithm is needed to allow information to be transferred across the interface between two non-conforming meshes.

Farhat et al. (1995) programmed the Matcher utility which is a one-step process to match the different discretisation of the fluid and structural meshes rather than the fluid and structural solutions. This algorithm is capable to handling the case where two discrete interfaces are not coincident. The pressure information is exchanged by linking the structural grid nodes to associated fluid cells. Their pressure is then used to calculate the pressure loads exerting on the structure. If the structural mesh is coarser than the fluid one, a number of additional points are introduced on the structural mesh element and the pressure loads are evaluated using the Gauss quadrature rule. On the other hand, a fluid grid node at the interface is associated to a corresponding point on the structural element and its displacement is interpolated from the structural solution. This algorithm is classified as the consistent interpolation based method and has been shown to perform well in aeroelastic problems (Farhat et al. (1995); Piperno et al. (1995)). However Farhat et al. (1998b) pointed out the lack of conservativity of this algorithm which is due the non-matching discrete interface, resulting to the non-similarity between the calculated forces exerting on the structure and the forces computed on the fluid interface. In addition, the consistent method is not mathematically optimum. The interpolation of the fluid displacement at the interface causes an increase in the discretisation error which degrades the solution of the fluid-structure-interaction problems.

Farhat et al. (1998b) also stated that the solution for a non-conservative algorithm is to compute the force on both sides of the interface using the discretisation method and the mesh of the same field, either the fluid or structure. The authors then proposed the virtual-work based method to calculate the finite element force exerting on the structural interface using exclusively the discretisation configuration applied to solve the fluid equation. This technique also enforce the zero momentum and energy of the interface loads at all time-steps. In addition, the velocity condition in Equation 3.76 was enforced by introducing a weighting residual multiplier, which is referred as the mortar based method (Farhat et al., 1998b). The implementation of this modification allows the discretisation error at the interface to be reduced. Meanwhile, the computational cost associated with solving the discretised Equation 3.76 including the multiplier becomes prohibitive for a 3D problem and a sufficiently fine fluid mesh. Also, with a very fine fluid mesh compared to a structural mesh, the consistent interpolation method and the conservative method are equally accurate in term of the interface error. Performing by the authors, the validation test simulating the transient response of the ARW-2 wing using the fluid mesh that was four-time finer than the structural one highlighted this drawback. The relative errors of some selected monitoring variables were very small and could be improved by introducing more Gaussian points in the consistent method. This result however cannot outweigh the accuracy, reliability and robustness of their proposed conservative method.

3.9 APPLICATION OF CFD IN BRIDGE AERODYNAMICS AND AEROELASTICITY

CFD has been used widely in many domains ranging from the engine engineering to the aerospace engineering, simulating single-phase problems to multi-phase problems involving chemical reactions. The use of CFD in the wind engineering has led to the evolving field of research which is named Computational Wind Engineering (CWE). CWE employs a CFD piece of software to model a wind engineering phenomenon in complement with wind tunnel tests. By utilising the advantages of each method, it can become a very effective hybrid tool to design and analyse flow fields and structural responses. Cochran and Derickson (2011) pointed out some cases where CFD can be used as a stand-alone tool such as modelling atmospheric problems and studying pedestrian level wind. However, current CFD codes still create troublesome performing structural analysis under wind loading particularly when studying bluff bodies such as tall buildings or generic bridge deck cross sections (Holmes, 2015). This issue is caused by the complexity of the flow field; not only fine mesh resolution but also improvement in turbulence models should be implemented to better capture these features (Cochran and Derickson, 2011). Nevertheless, the potential and future of CFD in the Wind Engineering has been showed; together with the development in computational resources and turbulence modelling, current limitations can be fully addressed, increasing the confidence level in the CFD methodology.

Together with the wind tunnel tests, the development of CFD allows researchers to computationally model the vortex shedding from a rectangular cylinder and its associated structural behaviour. Ohya et al. (1992) conducted a numerical study applying the finite difference method to solve the two-dimensional Navier-Stoke equations and analysed the flow field around a rectangular cylinder having square leading and trailing edges. A similar study was later conducted by Tan et al. (1998) except the fact that the finite element method was applied. Even though relatively coarse grids were used, results of these two computational studies are in a good agreement with experimental results such as Nakamura et al. (1991) and Ozono et al. (1992). The step-wise increase of the Strouhal number with the aspect ratio was captured and, thanks to the availability of the flow field visualisation and the numerous surface pressure sampling points, it showed that this Strouhal number variation is related to the synchronisation between the shear layer created at the leading edge and the vortex shed at the trailing edge and there are more than one vortices rolling on the surface, depending on the aspect ratio. Later, using the discrete vortex method, Larsen and Walther (1998) performed a two-dimensional computational simulation studying the aerodynamics of five generic bridge deck sections. The results produced by the computer code DVM-FLOW were in good agreement with previous wind tunnel tests suggesting this might be an efficient tool in bridge design. Using different computational software named Fluent, Owen et al. (2006) carried out an computational study of VIV of the Kessock Bridge using the RANS SST k-ω turbulence model. The prediction of the VIV lock-in including the on-set wind velocity as well as the maximum structural response was comparable with the full-scale measurement. Also, the computational results revealed a significant variation in the surface pressure fluctuating component during the lock-in, which could then affect the structural response. Similar phenomena were found in wind tunnel tests performed at Nanyang Technology University in Singapore (Choi et al., 2004).

Another useful application of CFD is its ability to extract aerodynamic parameters such as force and moment coefficients as well as flutter derivatives. Taking the second Nanjing Bridge in China as an example, Xiang and Ge (2002) performed a flutter analysis on different designs of cross sections using the wind tunnel and CFD approaches; the authors showed the flutter on-set velocities predicted by the wind tunnel were agreed well by the ones obtained from CFD. Later, Sun et al. (2009) conducted a detailed study where the RANS k-ω turbulence model was applied to simulate the wind-induced responses of a $B/D = 4$ cross section; using the forced-vibration method, all of 18 flutter derivatives were identified. The results showed the selected CFD method is potentially suitable for simulating VIV and flutter of bridge decks; all 18 flutter derivatives and aerostatic parameters are reasonably accurate compared to the wind tunnel results. Also, this showed the appropriateness of this CFD approach in balancing between the computational efficiency and accuracy. A later study of Waterson and Baker (2010) also demonstrated the accuracy and potential of the CFD approach. Their results illustrated an excellent application of commercial CFD software to simulate the 2D flutter responses of 5 different bridge deck cross sections, including the original Tacoma Narrows Bridge. For each bridge deck, the critical flutter velocity predicted by CFD showed a good agreement with other studies, which suggested CFD is a reliable method that can be widely applied in the bridge design.

2D CFD modelling has proved its potential and accuracy in analysis and modelling of bridge deck aerodynamic and aeroelasticity; however, Bai et al. (2013) showed that the 3D CFD modelling will be the future of this field of research. They conducted CFD simulations using the hybrid RANS-LES approach to compute the aerodynamic force coefficients and the flutter derivatives of three different bridge deck sections as shown in Figure 3.15. Section G1 is a streamlined structure while the others are treated as bluff bodies with sharp edges; particularly, section G3 is famous for its aerodynamic instability as observed in the Tacoma Narrows incident. The 2D and 3D CFD simulations of each cross section were conducted and the numerical results were compared against wind tunnel tests. For the lift and moment coefficients of fixed models, the 3D results showed better agreement in a comparison with experiments. The forced-vibration method was applied to calculate the flutter derivatives of bridge deck sections. One set of results for section G1 was shown in Figure 3.16, which, in overall, represented a better agreement between the 3D CFD and experimental results, particularly, for A_2^* which is a well-known critical parameter of flutter. Their comparisons illustrate the 3D CFD method is a more accurate simulation tool to investigate the aerodynamic stability of bluff bodies.

Inspired by the applicability of the 3D CFD modelling, Zhu and Chen (2013) carried out a numerical study on the aerodynamic behaviour of a fixed section replicating the Third Nanjing Yangtze River Bridge in a turbulence-free inflow condition using the LES turbulence model. The results agreed well with the wind tunnel experiments conducted on the same scaled model. Also, they showed that LES is efficient in capturing the unsteadiness in the wind and evaluating the aerodynamic behaviour of bridge decks, particularly when performing 3D simulations. The use of RANS in a 3D simulation implies the assumption of isotropic turbulence, which will effect the accuracy in modelling the oncoming turbulence wind and vortices around the model and in the wake region. For this reason, at the current state of the computational development, LES is becoming a more favourable tool to perform 3D simulations in a purpose to investigate the flow field and understand the underlying physical mechanism such as the BARC study promoted by Bruno et al. (2010). On the other hand, RANS has been used mostly in industrial applications and in the feasibility study stage to select the aerodynamic shape of the bridge deck cross section. Ding et al. (2016) proposed a integrated CFD-based aerodynamic shape optimisation strategy. Driven by RANS simulation, this algorithm was shown to be affordable thanks its computational efficiency and optimisation performance in mitigating the aerodynamic response of bluff bodies.

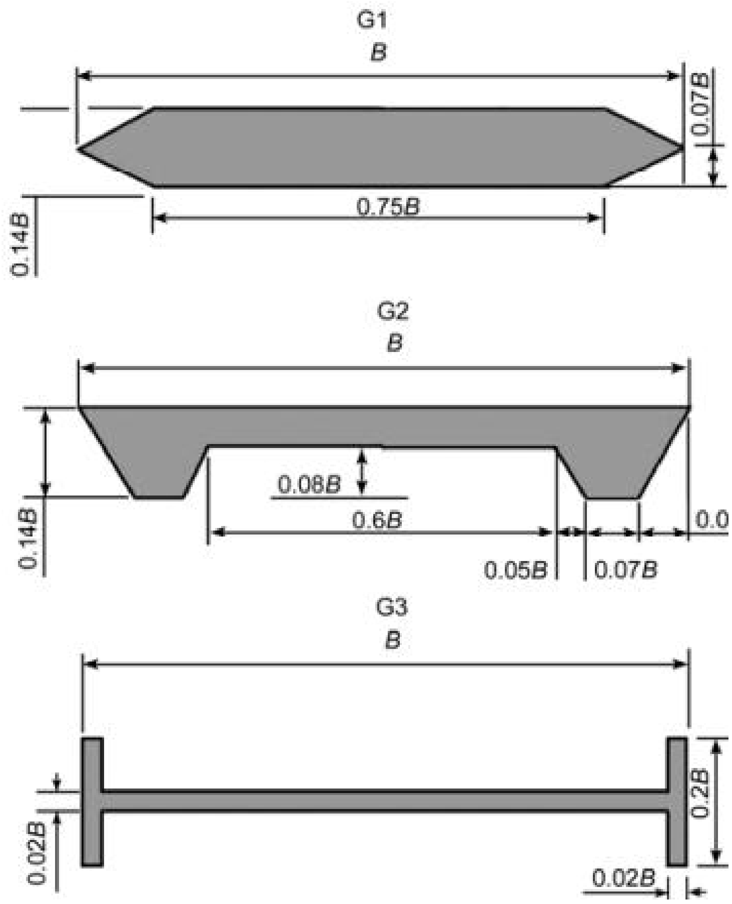

Figure 3.15: Three bridge deck sections used in the 3D CFD simulation by Bai et al. (2013).

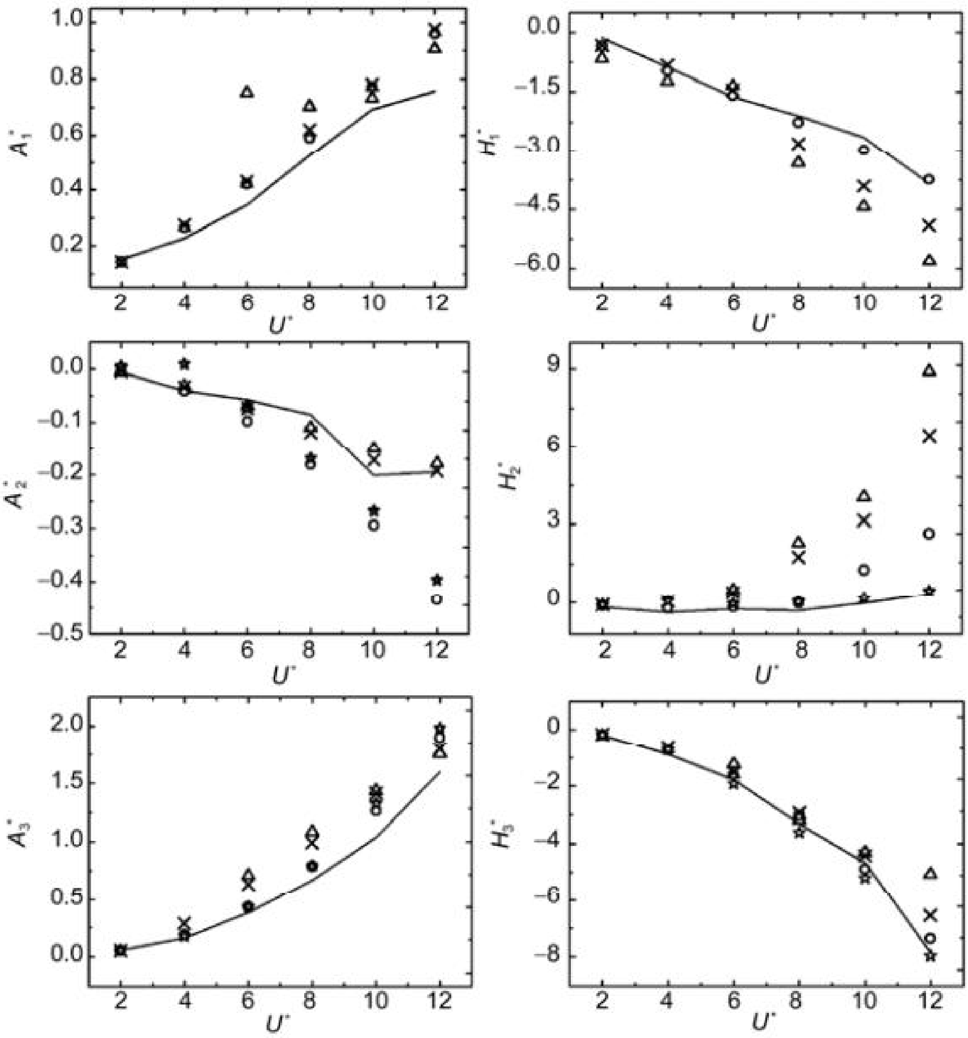

Figure 3.16: Flutter derivatives of section G1 obtained from two-dimensional (∘ symbols), three-dimensional (× symbols) CFD simulation and wind tunnel experiments (△ symbols) compared to results obtained via Discrete Vortex Method (lines) (Bai et al., 2013).

3.10 CONCLUSION OF THE CHAPTER

The first part of this chapter was devoted to introduce fundamental knowledge of CFD, the underlying mathematical background of relevant turbulence models as well as the theory relating to modelling a FSI problem. It also highlighted the basic difference between RANS and LES models together with assumptions or further requirements when applying these models.

The application of CFD in Wind Engineering, in general, and in bridge aerodynamics and aeroelasticity, in particular, has received many successes and, in complement with wind tunnel tests, contributed significantly to the knowledge in this domain. In addition, CFD has been recognised as an economical tool in the decision making during the designing phase when the aerodynamic behaviour of a proposed structure can be tested and observed without the need for physical models and wind tunnel tests. The CFD approach still contains a number of disadvantages including the inaccuracy in estimating the wind loading on a bluff body, which is mostly due to the complexity of the flow field to be modelled. Nevertheless, the development of computational resources and turbulence models will address and resolve these issues and the potential and future of CFD will be guaranteed.

LES and RANS have been shown to serve different purposes as performing 3D CFD simulations. If RANS is mostly used in the feasibility study stage as a part of the aerodynamic shape optimisation process, LES is a more favourable selection from the research point of view. LES has been shown to be more advantageous than RANS thanks to the characteristics of LES which is to physically resolve large eddies in the flow; therefore, it is capable to capture the unsteadiness and vortical structure around the bluff body and in the wake region. For this typical reason together with considering the aim and objectives of this research study, LES will be selected and the methodology to perform the computational study will be presented in Chapter 4.

Chapter 4

Methodology: CFD Simulation

In this chapter, all aspects relating to setting up CFD simulations are described. Following a short description of the CFD software package OpenFOAM, the computational domain used in both of static and dynamic simulations is presented accompanied by all information required by OpenFOAM. A mesh sensitivity study is then demonstrated focusing on the effect of the span-wise discretisation on the Strouhal number.

The following sections are devoted to introduce a dynamic mesh algorithm together with a structural solver, which will be shown to be successfully integrated in OpenFOAM. With appropriate settings, they are capable to modelling the structural response of either a rigid or a flexible 5:1 rectangular cylinder in the smooth wind.

In this computational study, three different types of simulation were conducted, which were 3D static simulation, 3D heaving simulation and 3D bending simulation. The first two used the rigid 5:1 rectangular cylinder which can be considered as the conventional sectional model tested in the wind tunnel. As for the final one, the flexible 5:1 rectangular cylinder was introduced, which can be excited at some bending or torsional mode shapes. These two models will be discussed further in later sections. Also, there exist some differences between the computational domain used in the static simulation and those used in the dynamic simulation, which includes the heaving and bending simulation; a clear explanation for this variation will be offered in Section 4.2.

4.1 INTRODUCTION TO OPENFOAM

The computational study of this project is conducted using OpenFOAM v2.2.2, which is a piece of open source and freely distributed CFD simulation software. OpenFOAM is designed as a C++ library which is essentially used to create executables, also known as applications. OpenFOAM is delivered with a substantial number of pre-compiled applications; they are categorised into solvers, which are designed to model a specific problem in continuum mechanics, and utilities, which are mainly used to perform simple pre- and post-processing activities such as mesh generation, data manipulation and algebraic calculations. Using C++ as its core technology and programming language, OpenFOAM offers users a great flexibility and potential to modify existing applications or even create their own ones to meet their objectives, with some pre-requisite knowledge of the underlying physics and programme techniques.

Instead of a normal user interface, OpenFOAM interacts with users via a text-file-based platform where all settings are stored in text files as dictionary entries under some general syntax rules which help maintain their consistency and accessibility. A typical OpenFOAM case contains directories and files as shown in Figure 4.1. The `constant` directory contains a full description of the computational domain in the subdirectory `polyMesh`; also, users are able to define relevant physical properties of the simulated continuum problem as well as to specify the numerical model in other text files such as `transportProperties`. In the `system` directory, setting parameters for the numerical solver are defined; the discretisation schemes used in the governing equations of the continuum problem are selected in the `fvSchemes` file, while solvers for each governing equations, tolerances and other control parameters are listed in the `fvSolution` file. Including in the `system` directory is also the `controlDict` file containing run control parameters including start time, end time, time-step size and relevant settings used by OpenFOAM utilities to sample data during processing, which will be stored in the `postProcessing` directory. Any dictionary entries in the `controlDict` file can be defined by static values or, using benefit offering by the `#codeStream` directive, C++ code can be included, which is compiled and executed at the start of the processing to deliver the dictionary entry. The time directories are a series of directories, each of which contains a number of files storing solutions of the computational problem at this specific time instance. The `0` time directory is special and is always required since it defines initial conditions for the problem and boundary conditions of the computational domain.

Similar to other commercial CFD software packages, OpenFOAM offers the possibility of performing parallel computations using the method of domain decomposition. In this method, the entire computational domain and all associated fields are divided into a number of partitions; each of which is allocated to a separate processor to be solved. The domain decomposition is performed using the OpenFOAM utility `decomposePar` together with relevant control parameters defined in the `decomposeParDict`, which is also found in the `system` directory. The output of this utility is the appearance of a series of `processor[...]` directories; in each of them contains the definition of the allocated computational domain in the subdirectory `polyMesh` and solutions of the associated field in the time directories. After a case is run in parallel, it can be reconstructed for further post-processing analysis using the OpenFOAM utility `reconstructPar`,

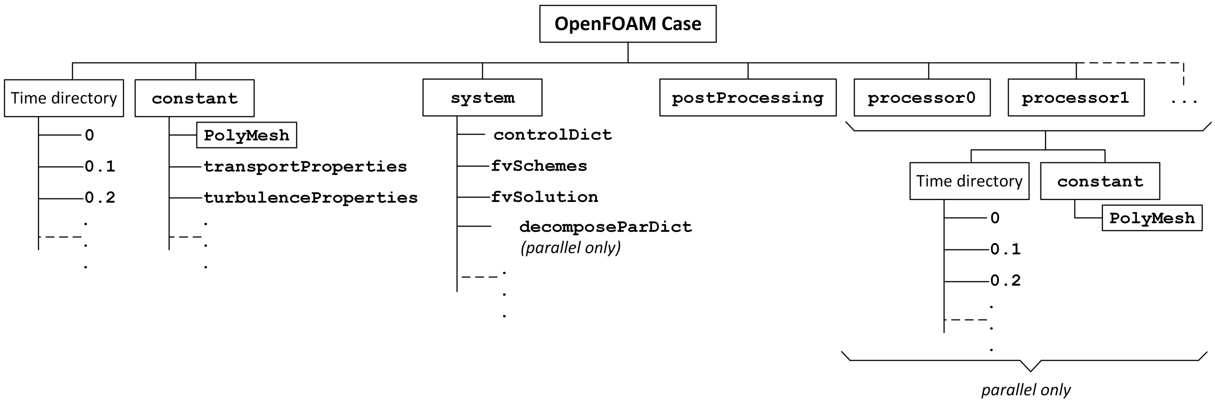

Figure 4.1: Typical file structure of a OpenFOAM case.

which effectively merges the sets of time directories from all `processor[...]` directories into a single set of time directories.

Understanding the file structure of a OpenFOAM case, the set-up of the static and dynamic simulations in later sections will be described and discussed based on this unique feature the aforementioned terminology. First and foremost, the generation of the computational domain used in the computational study will be presented in the following section, which reveal a disadvantage of OpenFOAM's utilities in mesh generation.

4.2 MESH GENERATION

A computational grid or a mesh used in OpenFOAM simulations is called the `polyMesh`, which is defined as a mesh of arbitrary polyhedral cells in 3D, bounded by arbitrary polygonal faces. By convention, each cell can have an unlimited number of faces and each face can contain an unlimited number of edges; there is no restriction on edges' alignment either. OpenFOAM is delivered with a number of very strict mesh specification and validity constraints to ensure good mesh quality; however, they can pose certain difficulties when using meshes generated by conventional tools. Information about the `polyMesh` is stored in a number of separate files in the subdirectory `polyMesh` under the `constant` directory, which typically are `points`, `faces`, `cells` and `boundary` files. As suggested by the name, the `boundary` file contains dictionary entries defining a set of boundary surfaces of the mesh, known as patches and their associated boundary conditions. A `patch` can be a group of boundary surfaces which are not physically connected together.

Unlike other pieces of commercial CFD software, the mesh in OpenFOAM is 3D by default. Simulations of 1D, 2D and axi-symmetric continuum problems, therefore, are made possible by using one-cell-thick meshes or by applying appropriate boundary conditions such as `empty` or `wedge`.

A `polyMesh` in OpenFOAM can be created using either of these two OpenFOAM utilities: `blockMesh` or `snappyHexMesh`. The `blockMesh` utility reads the `blockMeshDict` located in the `constant/polyMesh` directory; this utility effectively decomposes the domain geometry into a set of 3D hexahedral blocks and the mesh is defined by the number of cells on edges of the block, which can be straight lines, arcs or splines. The outcome of this process is a 3D structured grid whose mesh data is stored in `points`, `faces`, `cells` and `boundary` files in the same directory. By varying the number of cells and cell expansion ratios on edges, users are able to control the refinement of the mesh around region interested.

The `snappyHexMesh` mesh generator works in the principle which is more like a mesh morpher. Based on a background hexahedral mesh and a base level mesh density, this utility conforms the mesh to a surface of interest by refining the starting mesh and morphing the resulted split-hexahedral mesh to the surface using dictionary entries stated in the `snappyHexMeshDict` located in the `system` directory. The outcome of this process is a 3D unstructured grid containing hexahedral and split-hexahedral cells.

The mesh generated by these two utilities satisfies all requirements by OpenFOAM; the mesh quality can be verified using the `checkMesh` utility, from which users are presented a summary of the mesh and a number of different quality-control parameters such as mesh skewness and orthogonality. Based on these results, users can make further decision on where the quality of the mesh is adequate to model the continuum problem. Regarding this computational study, it involves external aerodynamics simulations, in which the flow field around and the structural response of a 5:1 rectangular cylinder in the smooth flow is modelled. Since the fluid is computationally modelled using the Large Eddy Simulation (LES), the computational grid needs to be checked in terms of the skewness and orthogonality to ensure eddies in the flow, particularly around the cylinder and in the wake region, to be resolved properly and not to be substantially damped by additional diffusion resulting from a highly skewed non-orthogonal mesh. Also, the mesh needs to offer easy accessibility to points and cells so that a dynamic mesh algorithm and a structural solver can be proposed and implemented to the fluid solver to simulate the structural response. The mesh generated by the `snappyHexMesh` is not a viable solution since the accessibility to grid points as well as the control over the refinement and the consistency in cell sizes is restricted. On the other hand, the `polyMesh` generated by the `blockMesh` utility contains several issues related to the computational efficiency and accuracy. As a structured grid, the `polyMesh` can have high cell-density in regions where it is unnecessary, which effectively reduces the overall efficiency, particularly for a 3D simulation. Also, for this study, it becomes apparent that it is impossible to maintain a relatively similar skewness across the entire computational grid; there exists some regions of significant variation in skewness, which largely impair the accuracy in solving the fluid. Therefore, a different method to generate the computational grid was proposed such as

- A 2D Fluent `.msh` mesh was created using Workbench which is a mesh editor offered by Ansys; this software gives users more freedom to control over the mesh quality as well as the consistency across the entire computational grid,
- The OpenFOAM utility `fluentMeshToFoam` was used to import the `.msh` mesh file and converted it into a 3D one-cell thick `polyMesh`-format mesh.
- A complete 3D mesh was created using the other OpenFOAM utility `extrudeMesh`. This utility effectively stacks a number of the one-cell thick meshes together in a predefined direction. These pieces of information together with the width of each one-cell thick mesh is defined in the `extrudeMeshDict` file located in the `system` directory.

4.2.1 Domain Geometry

The domain geometry used in this computational study is illustrated in Figure 4.2; dimensions of the domain geometry are expressed relative to the width B of the 5:1 rectangular cylinder. For the purposes of this study, the width of the cylinder was selected to be $B = 0.5\,\mathrm{m}$ and the depth was $D = 0.1\,\mathrm{m}$. The span-wise length of the cylinder as well as the length L of the domain varied between the static simulation and the dynamic simulation, which will be discussed further in Section 4.2.2.

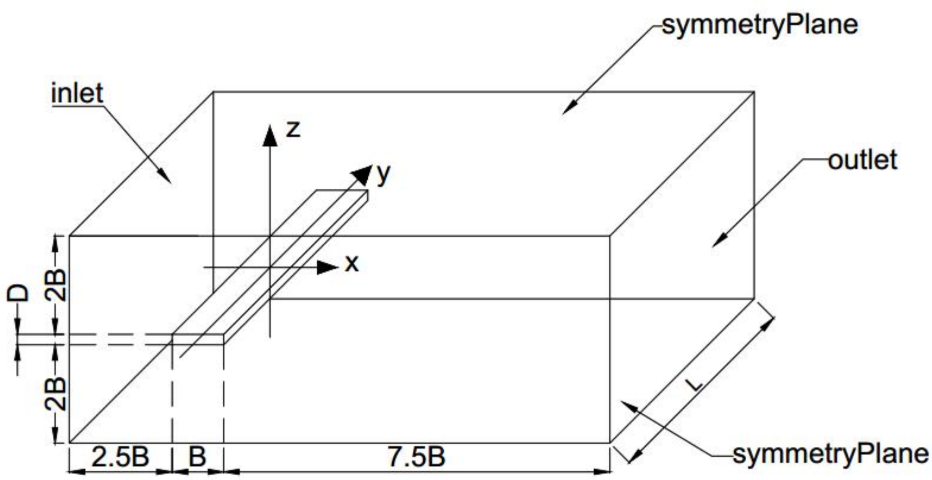

Figure 4.2: Domain geometry and boundary conditions of selected patches.

In addition, some key boundary conditions are summarised in Figure 4.2. A zero gradient condition for velocity and a constant value of zero gauge pressure were imposed on the outlet. As for the inlet, a non-zero x-component wind speed and a zero gradient condition for pressure were specified to simulate smooth flow. The `movingWallVelocity` was applied on the surface of the model to accurately capture a zero normal-to-wall velocity component, particularly in the dynamic simulation. The `symmetryPlane` boundary condition was used for the two z patches. As for the two y patches, the `cyclic` boundary condition was selected in the 3D static and heaving simulations. However, in the 3D bending simulation where half of the first bending mode shape was modelled, the displacement of one of the y patches limited the use of the `cyclic` boundary condition. Instead, the `symmetryPlane` boundary condition was employed and the computational domain needed to be corrected to reduce the effect induced by this boundary condition on the flow field around the region of interest. Further details of the boundary condition on other patches are explained in later sections.

4.2.2 Computational Grid

As briefly mentioned before, the meshing operation to the domain geometry was conducted using ANSYS-Meshing within Workbench. This piece of software gives users more control over the refinement as well as the consistency throughout the entire domain in terms of cell size, cell density and other quality-control parameters such as skewness. It is noticed that, in this case, the outcome of the Workbench software was a 3D one-cell thick Fluent `.msh` mesh, which will be imported and converted to a 3D mesh using OpenFOAM utilities.

In Workbench, the domain geometry was constructed from 11 different blocks (Figure 4.3a). By assigning different face sizing values to each block and altering their dimensions, good consistency across the mesh could be achieved and bad cells with high skewness and aspect ratio could be prevented. Values of the face sizing for each block are summarised in Table 4.1, which effectively controlled the overall cell size in all blocks. In addition, the cell size in the layer next to four surfaces of the model, i.e. Edges 1 to 4 (Figure 4.3b), was defined using the edge sizing as listed in Table 4.1. A 6-cell thick inflation layer was imposed around these four edges, with the thickness of cells next to the wall of 1×10^{-3} m and the growth rate of 1.2. Also, along Edges 5 and 6, there was implemented another 5-cell thick inflation layer, where the thickness of the first cell layer was 4×10^{-3} m and the growth rate was 1.2.

The results of this meshing process was the domain geometry was discretised as a 3D one-cell thick hybrid hexahedral grid as shown in Figure 4.4a. The grid contains a 6-cell thick structured grid imposed around the model (Figure 4.4b), where the thickness of cells next to the model is $\Delta z/B = 2 \times 10^{-3}$ and grows by the ratio of 1.2. The constant discretisation in the along-wind direction is $\Delta x/B = 2\Delta z/B$. The unstructured grid is used for the remaining part of the x-z plane. Upstream of the model, there exists a region of highly constant cell density and cell size, which allows eddies in the flow to be properly resolved and maintained, particularly in case of the turbulence wind. In addition, the computational grid was significantly finer around the model and in the wake so that any unsteadiness in these regions such as shear layers and vortex shedding can be captured and modelled.

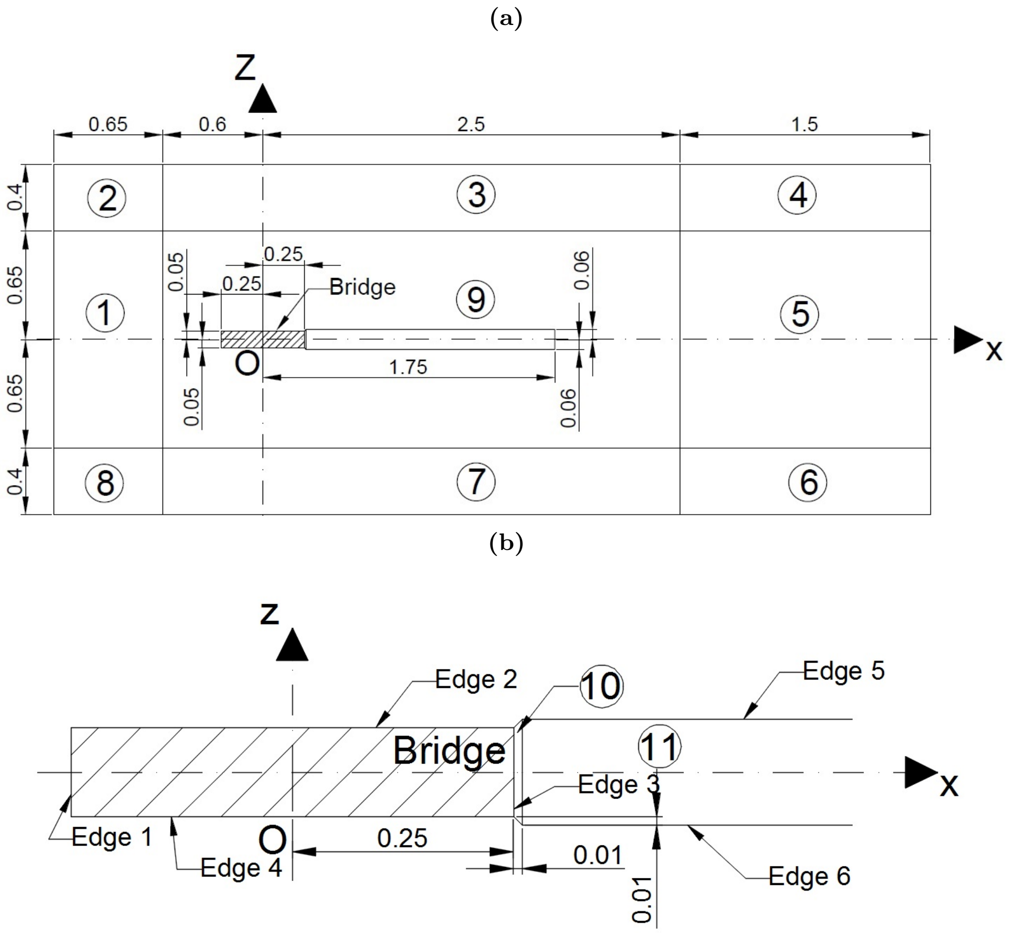

Figure 4.3: Dimensions of (a) the overall computational domain geometry and (b) the details of the geometry behind the model; unit is metre.

Table 4.1: Summary of the face sizing and edge sizing of the computational grid.

Face/Edge sizing	Object	Dimension
Face sizing	Block 1	2×10^{-2} m
	Blocks 2 to 8	5×10^{-2} m
	Block 9	4×10^{-2} m
	Blocks 10 and 11	4×10^{-3} m
Edge sizing	Edges 1 to 4	2×10^{-3} m
	Edges 5 to 6	4×10^{-3} m

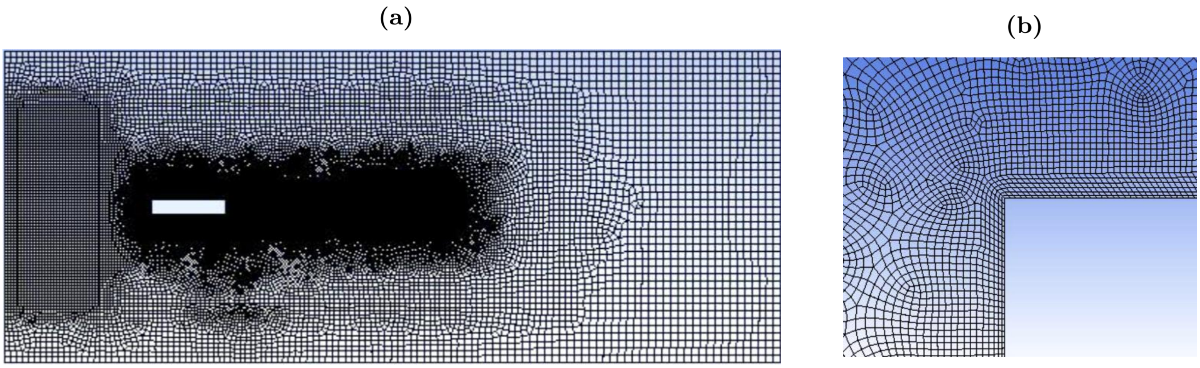

Figure 4.4: The computational grid in the x-z plane (a) for the entire domain and (b) zoomed-in around the leading edge.

By using the utility `fluentMeshToFoam`, this 3D one-cell thick hybrid hexahedral grid was then imported to OpenFOAM. The 3D computational grid was constructed by effectively projecting this one-cell thick grid along the y direction in a structured manner. This process could be achieved by using the OpenFOAM utility `extrudeMesh` and the associated dictionary file `extrudeMeshDict`, where information relating to the number of one-cell thick grids, `nLayers`, and the length of the domain, `thickness` are defined. The rigid 5:1 rectangular cylinder or the 3D sectional model has the span-wise length of $3B$; this model will be used in both of the 3D static and heaving simulations. On the other hand, the flexible 5:1 rectangular cylinder or the 3D flexible model was designed as a cantilever having the span-wise length of $5B$, which represented a half of the main span and was capable to simulate half of the first bending mode shape; this model will be used in the 3D bending simulation. The use of the `symmetryPlane` boundary condition on the two y patches can produce some suppression effect on the flow field on the mid-span region; therefore, the span-wise length of the 3D flexible model was extended to $7B$ including a B long abutment section which is an analogue of a static section and a B long extension at the mid span, as shown in Figure 4.5. Due to the current limitation in the computational resources and the need to perform dynamic simulations at a number of wind speeds, the computational grid used in static simulations has finer span-wise discretisation as compared to the ones used in dynamic simulations. Table 4.2 summaries all differences between computational grids used in the three simulations; the effect of variation in the span-wise discretisation on the fluid solution will be addressed and discussed in Section 4.4. As an example, Figure 4.6 shows the computational grid used in the 3D heaving simulation.

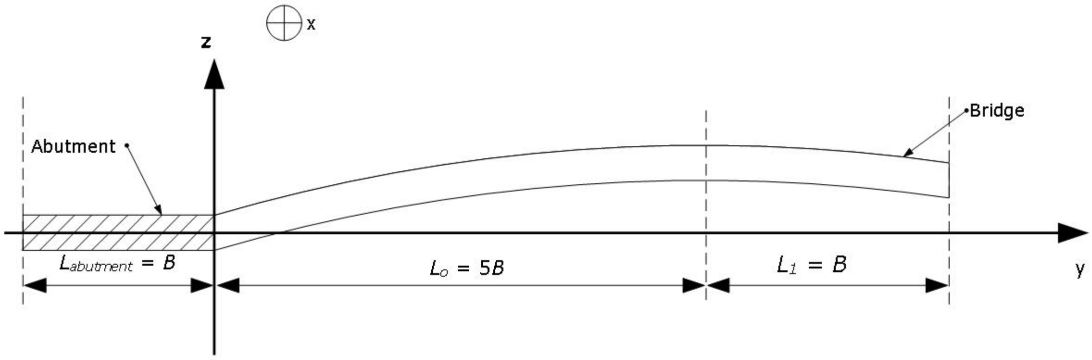

Figure 4.5: Schematic diagram of the 3D flexible model; $L_o = 5B$ is the half of the main span.

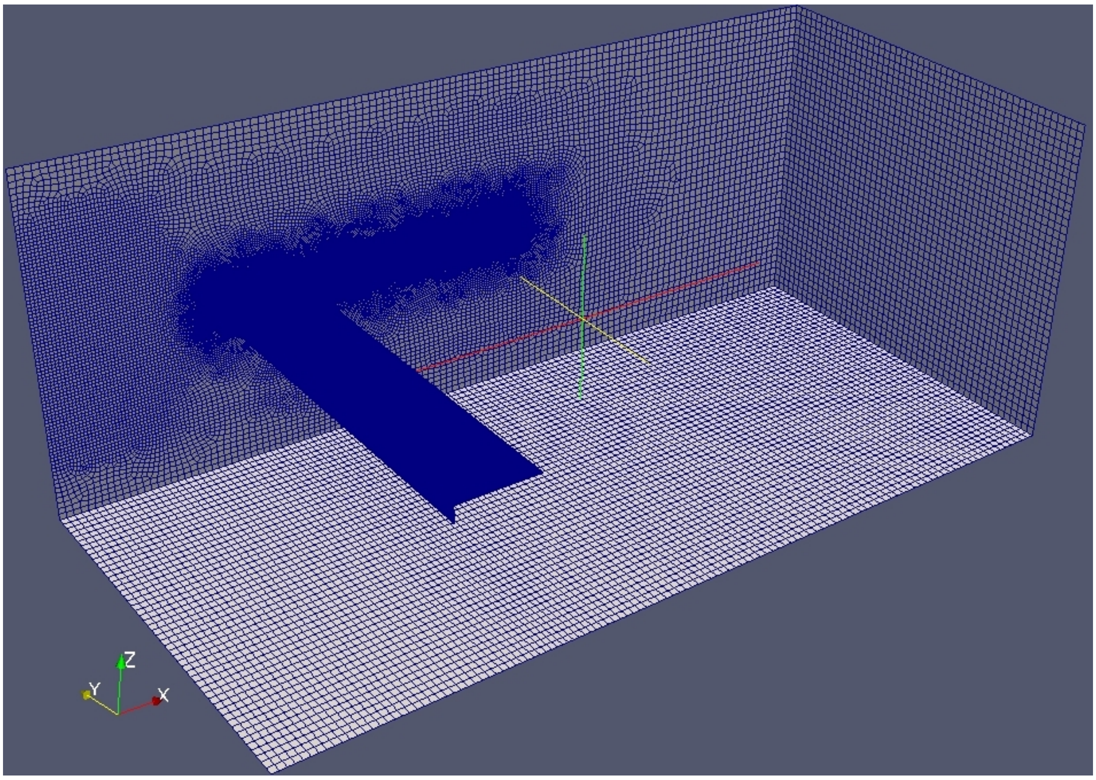

Figure 4.6: The computational grid used in the 3D heaving simulation.

Table 4.2: Summary of span-wise discretisation $\Delta y/B$, number of cells and boundary conditions of y patches in three different simulations.

Simulations	L/B	$\Delta y/B$	Number of layers	Number of cells	Boundary conditions of y patches
3D static simulations	3	0.02	150	10.5 million	`cyclic`
3D heaving simulations	3	0.1	30	2.1 million	`cyclic`
3D bending simulations	7	0.1	70	4.9 million	`symmetryPlane`

4.3 STATIC SIMULATION

The unsteady flow around the 5:1 rectangular cylinder is governed by the Navier-Stokes equations which are modelled using a LES approach where the fluid governing equations are spatially filtered by the cell size in an implicit manner. The sub-grid scale (SGS) viscosity is modelled by the use of the conventional Smagorinsky SGS model. However, to avoid the overestimation of the Smagorinsky constant and to account for the effects of convection, diffusion, production and destruction on the SGS velocity scale, an additional transportation equation is embedded to determine the distribution of the kinetic energy of the SGS eddies k_{SGS}

$$\frac{\partial}{\partial t}\rho k_{SGS} + \frac{\partial}{\partial x_j}\rho k_{SGS}\bar{u}_j = \frac{\partial}{\partial x_j}\left(\mu_{SGS}\frac{\partial k_{SGS}}{\partial x_j}\right) + 2\mu_{SGS}\bar{S}_{ij}\bar{S}_{ij} - C_\varepsilon\frac{k_{SGS}^{3/2}}{\Delta}, \tag{4.1}$$

where $\mu_{SGS} = \rho C_{SGS}\Delta k_{SGS}^{1/2}$, the constant are set equal to $C_\varepsilon = 1.048$ and $C_{SGS} = 0.094$ and Δ is the characteristic length scale of the filter which is related to the mesh size and defined as the cubic root of the cell volume. In addition, to remove the over-dissipation of the kinetic energy in the near-wall region, a filtered width δ according to the van Driest approach is introduced as

$$\delta = \min\left\{\Delta, \frac{k}{C_\Delta}y\left(1 - \exp^{-\frac{y^+}{A^+}}\right)\right\}, \tag{4.2}$$

where $k = 0.4187$ is the von Karman constant, $C_\Delta = 0.158$ and $A^+ = 26$ are the van Driest constants and y and y^+ are the normal distance and non-dimensional normal distance to the wall respectively. In other words, in the near-wall region, the length scale of the filter is not essentially related to the mesh cell size; the minimum value between Δ and the one obtained from the damping function in Equation 4.2 is locally adopted.

In a OpenFOAM case, this definition of the fluid problem is implemented via a number of dictionary files in the `constant` directory.

4.3.1 `constant` Directory

The LES simulation was enabled by the dictionary file `turbulenceProperties`, where the keyword `simulationType` was defined as `LESModel`. Properties and constants relating to the LES simulation were given by the `LESProperties` dictionary file; a short summary of this file is:

```
LESModel                    Smagorinsky;
delta                       vanDriest;
vanDriestCoeffs
{
```

```
        delta                cubeRootVol;
        cubeRootVolCoeffs
        {
             deltaCoeff      1;
        }
        Aplus                 26;
        Cdelta               0.158;
    }
```

As being indicated by the entry `LESModel`, the Smagorinsky SGS model was selected to model the SGS viscosity; it is noticed that in OpenFOAM, this SGS model is improved by the implementation of the transportation equation as shown in Equation 4.1. Details of this implementation can be found in the following source files: `Smagorinsky.H`, `Smagorinsky.C`, `GenEddyVisc.H` and `GenEddyVisc.C` located in the directory `$FOAM_SRC\turbulenceModels\incompressible\LES\`. The length scale of the implicit filtering function was calculated using the van Driest approach as indicated by selecting `vanDriest` for the keyword `delta`. All required coefficients were then defined in the subdictionary `vanDriestCoeffs`; detailed explanation for this function can be found in `$FOAM_SRC\turbulenceModels\incompressible\LES\vanDriestDelta\`. The fluid was classified as Newtonian and the kinematic viscosity was given by $\nu = 1.5 \times 10^{-5}\,\mathrm{m}^2\,\mathrm{s}^{-1}$, as defined in the dictionary file `transportProperties`.

4.3.2 `0` Directory

In the `0` directory, three dictionary files defined the boundary conditions including `p`, `U` and `nuSgs`, which corresponds to pressure, velocity and SGS viscosity. In addition to the boundary conditions of pressure and velocity stated in Section 4.2.1, a (0,0,0) velocity and a zero gradient condition for pressure was imposed on the surface of the model. As for the SGS viscosity `nuSgs`, the boundary condition type `calculated` was used on the inlet and on the surface of the model while a zero gradient of SGS viscosity, `zeroGradient`, was imposed on the outlet of the computational domain.

The non-zero x-component wind speed `u` of the static simulation was defined in the dictionary file `U` as

```
internalField                uniform (u 0 0);
boundaryField
{
    inlet
    {
```

```
        type            fixedValue;
        value           unform (u 0 0);
    }
}
```

where the wind speed of the simulation was given by the value of `u`. The static simulation was repeated at three different wind speeds: 1, 2 and $4\,\mathrm{m\,s^{-1}}$.

4.3.3 `system` Directory

All subdictionaries and keywords in the `fvSchemes` dictionary file are summarised as:

```
ddtSchemes
{
    default                         backward;
}
gradSchemes
{
    default                         cellLimited Gauss linear 1;
}
divSchemes
{
    default                         none;
    div(phi,U)                      Gauss limitedLinearV 1;
    div(nuEff*dev(T(grad(U))))      Gauss linear;
}
laplacianSchemes
{
    default                         none;
    laplacian(nuEff,U)              Gauss linear corrected;
    laplacian((1|A(U)),p)           Gauss linear corrected;
    laplacian(DkEff,k)              Gauss linear corrected;
    laplacian(DBEff,B)              Gauss linear corrected;
    laplacian(DnuTildaEff,nuTila)   Gauss linear corrected;
}
interpolationSchemes
{
    default                         linear;
```

```
}
snGradSchemes
{
    default                         corrected;
}
```

The numerical schemes used to discrete the governing equations were defined in the subdictionaries `gradSchemes`, `divSchemes` and `laplancianSchemes`, which are corresponding to the gradient, divergence and laplacian terms respectively. Based on these entries, it was decided to spatially discretise the governing equations using the second-order schemes; the limited linear scheme was applied to the divergence term while the second-order central differencing scheme was used to the laplacian term. As for the temporal discretisation, the backward difference scheme was selected; based on OpenFOAM's development, this scheme is classified as a implicit and second-order accurate scheme. However, due to the fact that the pressure field and the velocity field are solved in a staggered manner, this time scheme is essentially semi-implicit only. For this very reason, the solution of the pressure and velocity fields were selected to be under-relaxed, which was defined in the `relaxationFactors` subdictionary in the `fvSolution` dictionary file. The relaxation factor of the pressure field was 0.3 while the one applied to the velocity field was equal 0.7. This factor effectively reduces the amount which a solution varies from one iteration to the next one, which effectively improves the stability of the numerical computation. Also, to increase the stability of the solution without compromising the efficiency of transient simulations, the pressure-velocity coupling was achieved by means of the PIMPLE algorithm, which is merged PISO-SIMPLE solver, which is known as the `pimpleFoam` solver in OpenFOAM. It performs two PISO loops, in each of which, the pressure undergoes another correction; this leads to better coupling between pressure and velocity and allows bigger time-steps and Courant numbers. These settings were defined in the keywords `nCorrectors` (controlling numbers of pressure corrections in each PISO loop) and `nOuterCorrectors` (controlling numbers of PISO loops) under the subdirectory `PIMPLE`. Also, due to the use of unstructured grid which was mostly non orthogonal around the model and in the wake region, the keyword `nNonOrthogonalCorrector` was set to equal `1`. Other control parameters of solvers applied to the governing equations are listed in the `fvSolution` dictionary file as

```
p
{
    solver                  GAMG;
    tolerance               1e-6;
    relTol                  0.1;
    smoother                GaussSeidel;
```

```
        nPreSweeps               0;
        nPostSweeps              2;
        cacheAgglomeration       on;
        agglomerator             faceAreaPair;
        nCellsInCoarestLevel     10;
        mergeLevels              1;
    }
    pFinal
    {
        solver                   GAMG;
        tolerance                1e-6;
        relTol                   0.1;
        smoother                 GaussSeidel;
        nPreSweeps               0;
        nPostSweeps              2;
        cacheAgglomeration       on;
        agglomerator             faceAreaPair;
        nCellsInCoarestLevel     10;
        mergeLevels              1;
    }
    U
    {
        solver                   PBiCG;
        preconditioner           DILU;
        tolerance                1e-6;
        relTol                   0.01;
    }
    UFinal
    {
        solver                   PBiCG;
        preconditioner           DILU;
        tolerance                1e-6;
        relTol                   0;
    }
    k
```

```
{
    solver              PBiCG;
    preconditioner      DILU;
    tolerance           1e-6;
    relTol              0;
}
omega
{
    solver              PBiCG;
    preconditioner      DILU;
    tolerance           1e-6;
    relTol              0;
}
R
{
    solver              PBiCG;
    preconditioner      DILU;
    tolerance           1e-6;
    relTol              0;
}
```

where the method of geometric-algebraic multi-grid (`GAMG`) was selected to solve for the pressure field; with this solver, the pressure field, which used to be the bottleneck in these simulations, could be achieved in a timely-fashion manner without compromising its accuracy comparing with standard solvers. The preconditioned bi-conjugate gradient method (`PBiCG`) was used to obtain the velocity solution. Further information on these two solvers can be found in the OpenFOAM-2.2.2 manual (OpenFOAM, 2013).

The non-dimensional time-step $\Delta t^{\star} = \Delta t U/B$ (Δt is the time-step and U is the upstream wind speed) was set equal to 2×10^{-3}; the time-step was defined in the keyword `deltaT` in the dictionary file `controlDict`. The simulating time for simulations was controlled by the keywords `startTime` and `endTime` under the same dictionary file. The entries for these keywords were varied depending on the wind speed such that each simulation was extended over 80 non-dimensional time to obtain converged statistics and data in further 120 non-dimensional time was used to perform analysis.

In the `controlDict` dictionary file, the OpenFOAM function `forceCoeffs` was enabled in order to calculate coefficients of the force and moment acting on the model. Also, `probes` functions were used to sample the pressure on the surface of the model and the velocity in wake region at a distance B behind the model and a distance $D/2$ above the top surface. This latter point was chosen in a region that would allow us to sense the presence of vortices being shed from the model. All the on-the-fly sampling processes in the static simulation mentioned here were conducted at every time-step.

All static simulations were conducted in parallel on the High Performance Computer (HPC) at the University of Nottingham. Using the `simple` decomposition method and the OpenFOAM utility `decomposePar`, the computational domains in the static simulation was divided into 32 sub-domains having relatively similar numbers of cells; the number of sub-domains is defined in the keyword `numberOfSubdomains` in the dictionary file `decomposeParDict`. Each sub-domain was assigned to a processor on the HPC; to minimise the number of faces sharing between two processors, i.e. to maximise the computational speed, the domain was separated into 8 blocks along the x direction, 2 blocks along the y direction and 2 blocks along the z direction. Based on the requirement of the physical time, each static simulation took from 1 to 1.5 months to produce adequately reliable data for further analysis.

4.4 MESH SENSITIVITY STUDY

Before discussing methodologies to perform the dynamic simulation, the reader is reminded that there exists a difference in the computational domain used in the static simulation and in the dynamic simulation. The former utilises the grid having the span-wise discretisation level of $\Delta y/B = 0.02$ while, in both of the heaving and bending simulation, the span-wise discretisation of the computational domain is 5 times as coarse, $\Delta y/B = 0.1$. As mentioned in Section 4.2.2, this selection was due to the limitation in the computational resources and the need to perform the dynamic simulations across a large range of wind speeds.

It is of importance to study the effect of the span-wise discretisation of the computational domain on the flow field being modelled by LES; the method and results of this so-called mesh sensitivity study are presented in this section. It should be noticed that a similar study is normally required to investigate the discretisation on the x-z plane or at least around the model. However, in this computational study, the sensitivity study focused on the discretisation level along the span-wise direction, i.e. the y direction, only. It was because an adequate span-wise discretisation is required to accurately capture the emerging span-wise flow feature which is expected to observe in the bending simulation. In addition, the cell density in the x-z plane, particularly cell sizes around the model and in the wake region, is strongly restricted by the computational resources and the objectives of the computational study.

4.4.1 Method

The domain geometry used in the static simulation including the length of the domain $L = 3B$ and the boundary condition of the y patches was applied in this mesh sensitivity study. Using the OpenFOAM utility `extrudeMesh` and the dictionary file `extrudeMeshDict`, four computational grid with different span-wise discretisation levels were created as shown in Table 4.3; the discretisation level used in Grids G2 and G4 was applied in the static simulation and the dynamic simulation respectively.

Table 4.3: Computational grids in the mesh sensitivity study.

Grid	$\Delta y/B$	Number of layers
G1	0.01	300
G2	0.02	150
G3	0.04	75
G4	0.1	30

The mesh sensitivity study was conducted on a static rectangular cylinder at the wind speed of $1\,\mathrm{m\,s^{-1}}$. The discretisation schemes, the solvers' settings and the initial conditions were defined similar to those applied in the static simulation as described in Section 4.3. The Strouhal number, St, was the fluid parameter selected to assess the mesh sensitivity. This parameter was determined based on the spectral analysis of the lift force coefficient acting on the model identified by the OpenFOAM utility `forceCoeffs`

4.4.2 Results

Figure 4.7 shows the variation of the Strouhal number on the normalised cell size in the y direction. The overall trend is that, using a computational domain having coarse span-wise discretisation, the numerical solution predicted a smaller value of the Strouhal number. Comparing with results from literature such as St = 0.555 measured in wind tunnel tests conducted by Schewe (2013), all of these values are acceptable, particularly for the grid G2, G3 and G4 where the percentage differences are less than 10%.

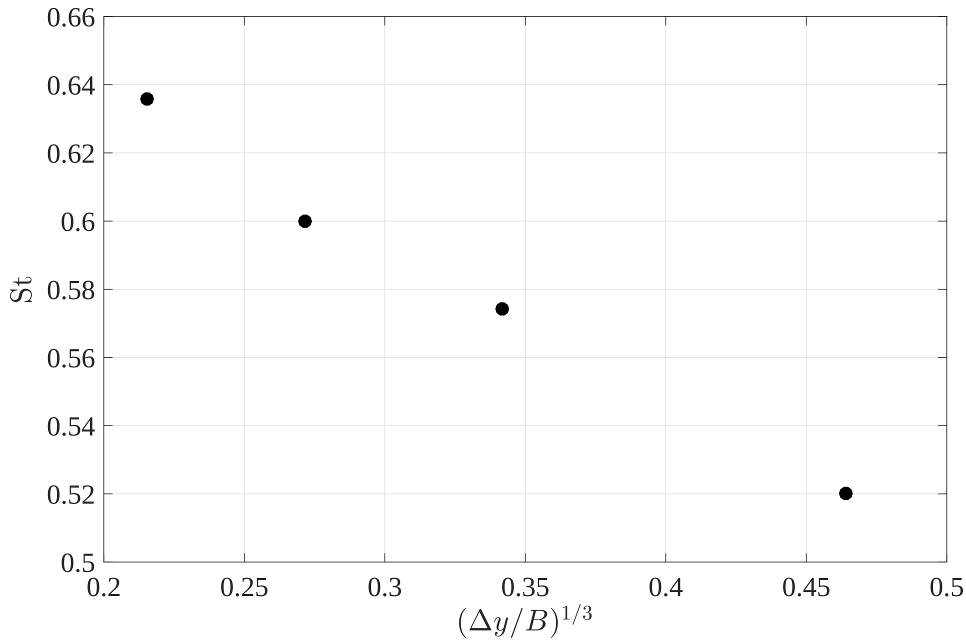

Figure 4.7: Variability of the Strouhal number, St, against the quantity, $(\Delta y/B)^{1/3}$, which is proportional to the filtering width.

Based on Roache (1997), a CFD such as static and dynamic simulations presented here is accompanied by a number of uncertainties; one of them is directly related to the spatial discretisation of the computational domain. A standard method to estimate uncertainties due to discretisation has been reported in Celik et al. (2008), where the so-called discretisation error is calculated based on completely solved solutions obtained from either coarser or finer grids and is expressed via the Grid Convergence Index (GCI). This method is called the Grid Convergence Method and a detailed description of the underlying mathematical background is introduced in Roache (1997). In the computational study presented here, the numerical uncertainties associated with the span-wise discretisation of the computational domains in the static and dynamic simulations were estimated by using the values of the Strouhal number obtained from Grids G2, G3 and G4 while the quantities $(\Delta y)^{1/3}$ was proportional to the filtering width. As a result, the static simulation was found to have a numerical uncertainty of $\mathrm{GCI}^{23}_{\mathrm{fine}} = 11\%$ while that in the dynamic simulation was estimated to be $\mathrm{GCI}^{34}_{\mathrm{coarse}} = 28\%$.

The Grid Convergence Method shows that the use of coarse span-wise discretisation level in the dynamic simulation yielded more than double numerical uncertainties than the static simulation. This result, together with the prediction of the Strouhal number, highlights some fundamental difference in the aerodynamic characteristics of the flow field around the cylinder being modelled in the static and dynamic simulation, which will need to be considered when analysing computational results. Nevertheless, compared to an extensive review in BARC (Bruno et al., 2014), the Strouhal number predicted by Grid

G4 having the same discretisation level as the dynamic simulation in the span-wise direction is within an acceptable range of both wind tunnel results and numerical results.

Figure 4.8a presents four profiles of the surface pressure distribution predicted from these simulations in a comparison against the benchmark data obtained from BARC (Bruno et al., 2014). The benchmark data is calculated from a number of selected computational studies is plotted as boxes in each of which the lower and upper ends represent the 25^{th} and 75^{th} percentiles, the red line is the median and two whiskers are the envelops of all data. All profiles including the benchmark data are plotted against the coordinate, s, measured from the stagnation point on the front face and normalised using the depth D. As for the time-averaged pressure coefficient C_p (Figure 4.8a), all four profiles lie within the BARC envelops. There is a slight variation in the length of the separation bubble as well as the reattachment point, which can also be inferred from Figure 4.8b showing the standard deviation of the time-varying pressure coefficient C_p'. The pressure fluctuation inside the separation bubble modelled in four simulations is in a good agreement with each other and with the BARC data; however, the reattachment or the pressure recovery region shows more scatter between four grids. The overall trend is that a coarse grid predicted higher pressure fluctuation; results obtained from Grids G3 and G4 were about 5% to 30% larger than the upper envelope of the BARC data.

(a)

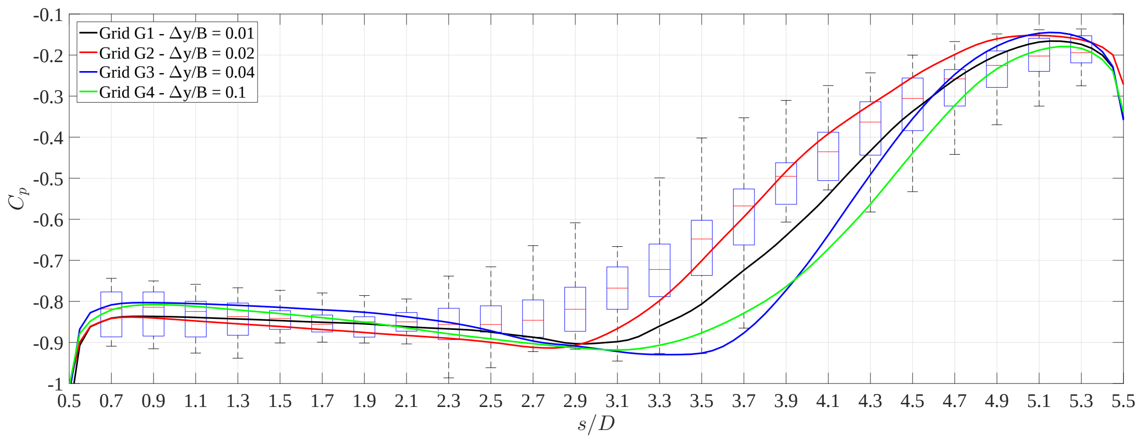

(b)

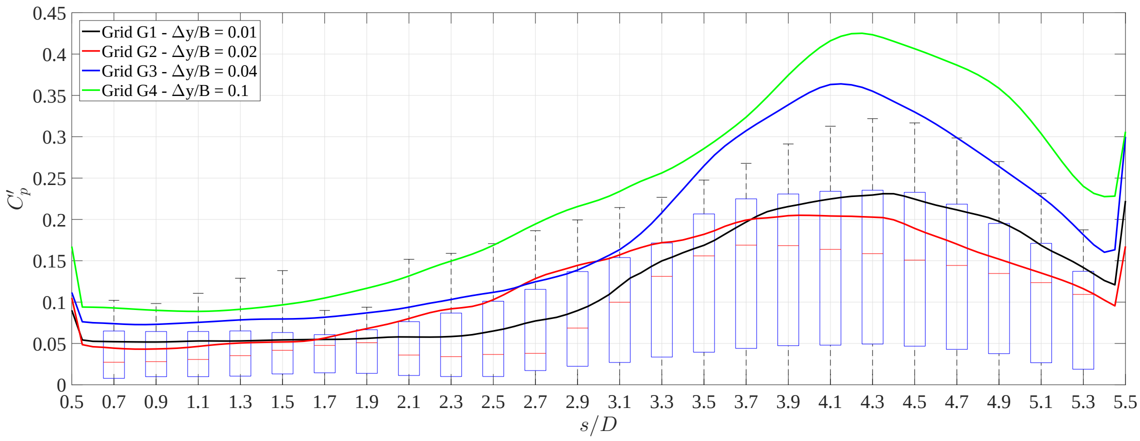

Figure 4.8: The surface distribution of (a) the time-averaged pressure coefficient C_p and (b) the standard deviation of the time-varying pressure coefficient C_p' in a comparison against BARC data.

Results of the Mesh Convergence Study as well as the analysis of the surface pressure distribution against the BARC data showed that the use of a coarse grid having the span-wise discretisation level similar Grid G4 in dynamic simulations led to some alteration in the aerodynamics of the flow field around the rectangular cylinder and over-prediction of the surface pressure fluctuation in the reattachment region. Based on the performance of Grid G1, it was suggested that a grid with high cell density not only in the span-wise direction but also in the x-z plane should be proposed. This issue has been noticed during the initial stage of the computational study. Recalling the aim and objectives where the VIV of a flexible rectangular cylinder excited at the first bending model is modelled and considering the available computational power, using a finer grid will create a substantial bottleneck in this study. The approach regarding the computation grid as mentioned in Section 4.2.2 will be applied and all issues discussed in this section will be considered as limitation of the computational study and will be fully addressed in later discussion.

4.5 DYNAMIC SIMULATION

In the dynamic simulation, the fluid-structure interaction (FSI) problem was modelled by the use of the Arbitrary Lagrangian-Eulerian (ALE) algorithm which helps eliminate the disadvantages of the conventional Lagrangian and Eulerian methods in modelling problems involving excessive distortion of continuum (either the fluid or structure) (Donea et al., 2004). The ALE algorithm however introduces the convection effect due to the motion of the grid nodes which must be embedded into the LES model as

$$\frac{\partial}{\partial t}\left(\bar{u}_i - \hat{u}\right) = 0, \tag{4.3}$$

$$\frac{\partial}{\partial t}\rho\bar{u}_i + \frac{\partial}{\partial x_j}\rho\bar{u}_j\left(\bar{u}_i - \hat{u}\right) = -\frac{\partial\bar{p}}{\partial x_i} + \frac{\partial}{\partial x_j}\left[\left(\mu + \mu_{SGS}\right)\left(\frac{\partial\bar{u}_i}{\partial x_j} + \frac{\partial\bar{u}_j}{\partial x_u}\right)\right], \tag{4.4}$$

where $\hat{u}$ is the velocity of the grid nodes. The implementation of the ALE algorithm in a dynamic CFD simulation involves a coupling between three different solvers: the fluid solver that handles the Navier-Stokes equations, the structural solver which is responsible for determining the structural deformation or displacement based on the fluid forces and the dynamic mesh solver or algorithm which deals with moving the grid nodes to accommodate the displacement or deformation of the structure without impairing the accuracy of the fluid solver.

4.5.1 Fluid Solver

The unsteady flow field around the dynamic model was solved by the use of the OpenFOAM's existing solver `pimpleDyMFoam`. Similar to the solver `pimpleFoam` used in the static simulation, by OpenFOAM, this solver is classified as the transient solver for incompressible and Newtonian fluids in a moving mesh. The convection effect induced by the relative motion between the fluid and the continuum as described in Equations 4.3 and 4.4 is calculated by the use of the functions `fvc::makeAbsolute(phi,U)` and `fvc::makeRelative(phi,U)` as well as the inclusion of the `correctPhi.H` header file to correct for pressure and velocity across the boundaries. Further details about this solver could be found in the source file `pimpleDyMFoam.C`. Control parameters regarding the fluid solver were defined in the dictionary file `fvSolution` similar to the one used in the static simulation except some differences as summarised here

```
pcorr
{
    solver          GAMG;
    tolerance       1e-6;
    relTol          0.1;
    smoother        GaussSeidel;
    nPreSweeps      0;
```

```
        nPostSweeps                 2;
        cacheAgglomeration          on;
        agglomerator                faceAreaPair;
        nCellsInCoarestLevel        10;
        mergeLevels                 1;
    }
    p
    {
        $pcorr
        tolerance                   1e-7;
        relTol                      0.1;
    }
    pFinal
    {
        $p
        tolerance                   1e-7;
        relTol                      0;
    }
```

and the solver `pimpleDyMFoam` were defined as

```
    PIMPLE
    {
        correctPhi                      yes;
        nOuterCorrectors                2;
        nCorrectors                     2;
        nNonOrthogonalCorrectors        1;
    }
```

All numerical spatial and temporal discretisation schemes used on the fluid governing equations as stated in the dictionary file `fvSchemes` were selected to be similar to the static simulation and maintained their second-order accuracy. In order to accurately model the zero velocity on the surface of the model, the `movingWallVelovity` boundary condition was applied with a constant vector as `(0 0 0)`.

The structural solver and the dynamic mesh algorithm is also inherently included in the `pimpleDyMFoam` solver. The use of the header file `dynamicFvMesh.H` provides necessary environment for the the dynamic mesh solver to be implemented; the process of calculating new positions of the grid nodes and updating the whole mesh is performed by the member function `mesh.update()`. OpenFOAM provides a number of different dynamic mesh solvers, some of which are capable to simulate a six-degree-of-freedom motion of a rigid model. The flexibility in modify these source codes is limited; therefore, it is required a separate set of a structural solver and a dynamic mesh algorithm to simulate both of the heaving motion of a rigid model and the bending motion of a flexible model.

Based on the dynamic mesh class `Foam::dynamicInkFvMesh`, two new OpenFOAM dynamic mesh classes were developed: `Foam::dynamicHeavingFreeUDFFvMesh` and `Foam::dynamicBendingFreeUDFFvMesh`, which were used to simulate the response of a rigid model and a flexible model respectively. Each dynamic mesh class contains a `.H` header file and a `.C` source file which contains C++ programmes to solve for the structural response and to move the grid nodes. Similar to a normal C++ source codes, as can be seen in Sections A.1.1 and A.1.2, the two source files contain similar ***constructors*** where key information required by the dynamic simulation is read. They include the key dimension of the computational domain (explained in Section 4.5.3) as well as the structural parameters such as mass, damping ratio and natural frequency and the initial structural response (explained in Section 4.5.2), these pieces of information are stored in the dictionary file `dynamicMeshDict` located under the `constant` dictionary. In Sections 4.5.2 and subsec:CFDSimulation:DynamicSimulation:DynamicMeshAlgorithm following, the development of the structural solver and the dynamic mesh algorithm are presented. Their integration into the OpenFOAM existing fluid solver `pimpleDyMFoam` is discussed using the dynamic mesh class `Foam:dynamicBendingFreeUDFFvMesh` as an example. Some alteration regarding the other dynamic mesh class `Foam:dynamicHeavingFreeUDFFvMesh` will be then noticed.

4.5.2 Structural Solver

One of the objectives of the dynamic simulation is to model structural responses of a flexible 5:1 rectangular cylinder undergoing the VIV. Some assumptions were introduced to simplify the structural solver. The dynamic properties of the bridge such as mass, damping ratio and natural frequencies of the bending modes were prescribed and only the first bending mode was modelled. Due to the limitation of the computational resources, only a portion was simulated as illustrated in Figure 4.5; L is the length of the flexible model simulated while L_o is half of the main span. In this section, the theory and the numerical scheme implemented to solve the structural equations are discussed. Some preliminary tests were carried out in order to validate the structural solver.

Theory and Numerical Scheme

The single-degree-of-freedom equation of motion of the model is expressed in the spatial and temporal domain with respect to the coordinate system shown in Figure 4.5 as

$$m\ddot{z}(y,t) + c\dot{z}(y,t) + kz(y,t) = f(y,t), \tag{4.5}$$

where m, c and k is the mass, damping coefficient and stiffness of the model, $f(y,t)$ is the force acting on the model, $z(y,t)$, $\dot{z}(y,t)$ and $\ddot{z}(y,t)$ are the displacement, velocity and acceleration in the z direction of a material point locating the y position at the time t respectively. The displacement $z(y,t)$ can then be rewritten as a summation of multiplication of the spatial modal function $\Phi_i(y)$ and the time-varying displacement amplitude $\tilde{z}_i(t)$ of the i mode

$$z(y,t) = \sum_{i=1}^{N} \Phi_i(y)\tilde{z}_i(t). \tag{4.6}$$

Here, only the first mode shape is taken into account which is $\Phi(y) = \Phi_o \sin\left[(\pi y)/(2L_o)\right]$; applying this method, Equation 4.5 is transformed into the generalised equation of motion in the generalised coordinate system as

$$M\ddot{\tilde{z}}(t) + C\dot{\tilde{z}}(t) + K\tilde{z}(t) = F(t), \tag{4.7}$$

with

$$M = \bar{m}\int_0^L \left[\Phi(y)\right]^2 \mathrm{d}y, \tag{4.8}$$

$$C = 2\omega_n \zeta M, \tag{4.9}$$

$$K = EI\int_0^L \left[\Phi''(y)\right]^2 \mathrm{d}y, \tag{4.10}$$

$$F = f\int_0^L \left[\Phi(y)\right] \mathrm{d}y, \tag{4.11}$$

where M is the generalised mass, C is the generalised damping, K is the generalised flexural stiffness and F is the generalised force acting on the model, $\bar{m}$ and f are the mass and force per unit length respectively, EI is the multiplication of Young's modulus and second moment of area. The modal coefficient Φ_o can be selected such that $M = 1$ which yields a simplified generalised equation of motion as

$$\ddot{\tilde{z}}(t) + 2\omega_n\zeta\dot{\tilde{z}}(t) + \omega_n^2\tilde{z}(t) = F(t). \tag{4.12}$$

with ζ is the damping ratio. Equation 4.12 can then be discretised and solved numerically using the first-order backward Euler method

$$\ddot{\tilde{z}}(t_{n+1}) = F(t_n) - 2\omega_n\zeta\dot{\tilde{z}}(t_n) + \omega_n^2\tilde{z}(t_n), \tag{4.13}$$

$$\dot{\tilde{z}}(t_{n+1}) = \dot{\tilde{z}}(t_n) + \Delta t\ddot{\tilde{z}}(t_{n+1}), \tag{4.14}$$

$$\tilde{z}(t_{n+1}) = \tilde{z}(t_n) + \Delta t\dot{\tilde{z}}(t_{n+1}), \tag{4.15}$$

Here, $\tilde{z}(t_{n+1})$, $\dot{\tilde{z}}(t_{n+1})$ and $\ddot{\tilde{z}}(t_{n+1})$ are the generalised displacement, velocity and acceleration at the time step t_{n+1}, $z(t_n)$, $\dot{z}(t_n)$ and $\ddot{z}(t_n)$ are the generalised displacement, velocity and acceleration at the time step t_n, $F(t_n)$ is the generalised force acting on the bridge at the time step t_n and Δt is the time-step size.

Validation of Structural Solver

In this section, a test case is set up in order to validate the numerical scheme proposed above. A dynamic study of an object having the mass $m = 6\,\text{kg}$ is performed; this object is suspended by a linear spring such that the natural frequency of the system is $f_n = 1.2\,\text{Hz}$. A sinusoidal force with the maximum amplitude $F_o = 0.2\,\text{N}$ and a variable frequency is applied on the object at different damping conditions. The aim of this study is to predict the dynamic responses including the amplitude and phase of the oscillation at different frequencies of the applying force ω_F and different damping ratios ζ. The dynamic response of the object is predicted by using the first-order backward Euler method as shown in Equations 4.13 to 4.15. In addition, other numerical schemes such as the improved Euler and the fourth-order Adam-Bashforth schemes are also implemented; the results obtained from three schemes are compared together and against the analytical solution.

The analytical response of this system is expressed as

$$z_{\text{analytical}} = \exp^{\beta t}\left[A\sin\phi\cos(\omega_1 t) + A\frac{\sin\phi - \omega_F\cos\phi}{\omega_F}\sin(\omega_1 t)\right] + A\sin(\omega_F t - \phi), \tag{4.16}$$

$$\text{with } A = \frac{F_o}{m}\frac{1}{\sqrt{\left(\omega_n^2 - \omega_F^2\right)^2 + 4\beta^2\omega_F^2}}, \tag{4.17}$$

$$\beta = \zeta\omega_n, \tag{4.18}$$

$$\omega_1 = \sqrt{\omega_n^2 - \beta^2}, \tag{4.19}$$

$$\phi = \tan^{-1}\left[(2\beta\omega_F)\,/\left(\omega_n^2 - \omega_F^2\right)\right]. \tag{4.20}$$

Here, ω_n is the natural circular frequency of the system and ϕ is the phase lag between the applying force and the displacement. The analytical solutions regarding the variation of the normalised amplitude and phase of the oscillation with respect to the frequency of the applying force and the damping ratio are illustrated in Figure 4.9.

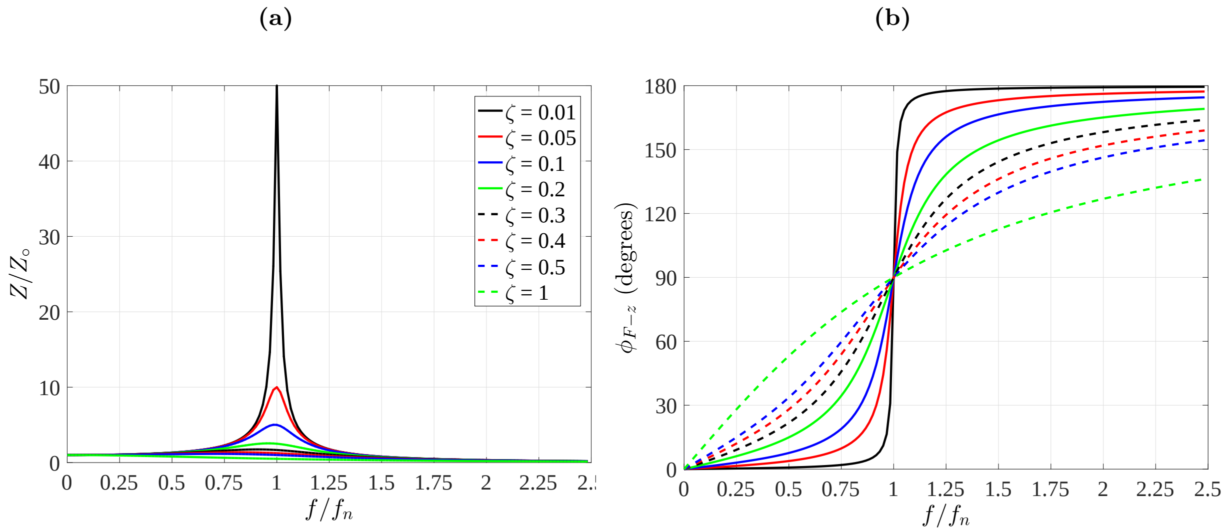

Figure 4.9: Variation of the analytical solutions including (a) the normalised amplitude and (b) phase of the oscillation with respect to the normalised frequency of the applying force f/f_n at different values of the damping ratio ζ.

The numerical results predicted by the use of the backward Euler method are shown in Figure 4.10. They showed a good agreement with the analytical solutions. Also, the numerical responses predicted by the use of the improved Euler method or the fourth-order Adam Bashforth method are shown in Figure 4.11. The overall trend of the variation of the response with respect to the frequency of the applying force and the damping ratio was observed. However, these two schemes overpredicted the response of the oscillation at the frequencies close to the natural frequency of the system. These two schemes are classified as the explicit or semi-explicit scheme; therefore, they cannot accurately model the motion of a spring-mass-damper system which is essentially an implicit problem.

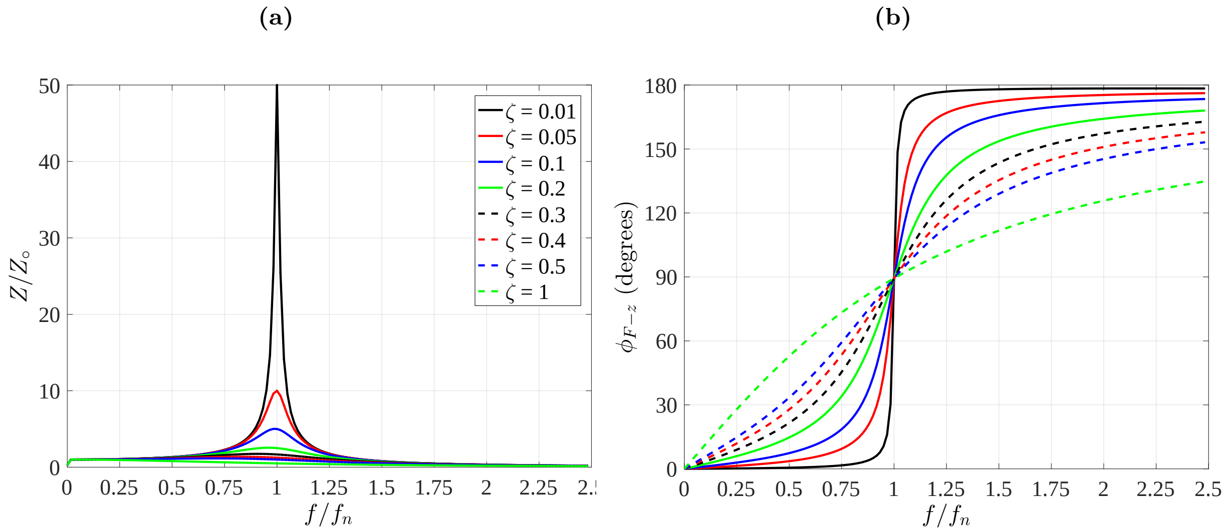

Figure 4.10: Variation of (a) the numerical normalised amplitude and (b) phase of the oscillation solved by the backward Euler method with respect to the normalised frequency of the applying force f/f_n at different values of the damping ratio ζ.

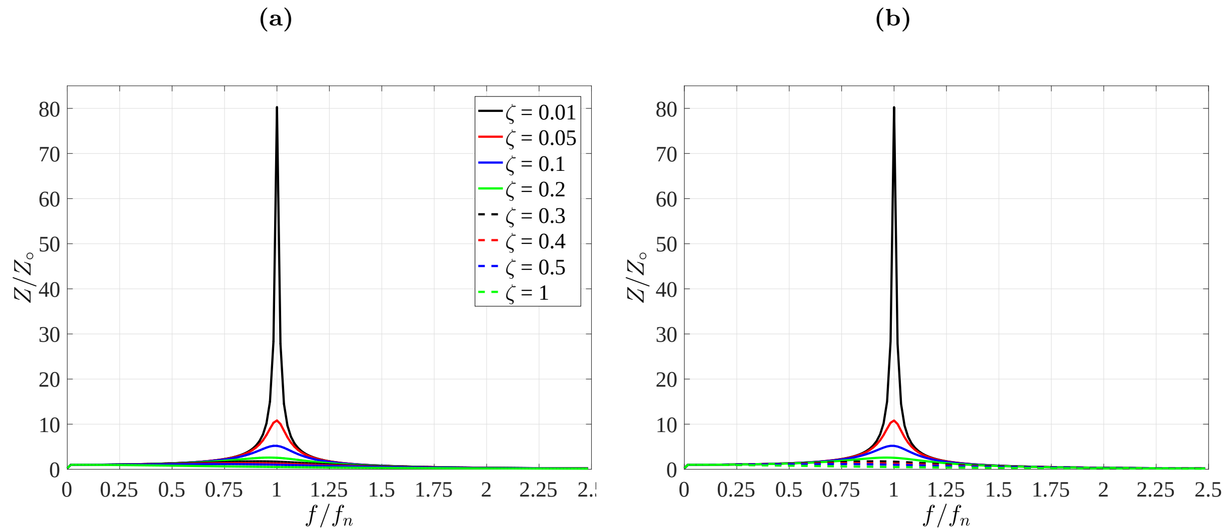

Figure 4.11: Variation of the numerical normalised amplitude solved by (a) the Adam-Bashforth method and (b) the improved Euler method with respect to the normalised frequency of the applying force f/f_n at different values of the damping ratio ζ.

In conclusion, the proposed numerical structural solver with the use of the backward Euler method has been validated by a study of the dynamic response of a simple mass-spring-damper system. This scheme was observed to be capable to model the amplitude and phase of the response due to its ability to simulate the inherent implicit characteristics of the structural system.

OpenFOAM Implementation

As was briefly mentioned above, the key structural parameters such as the natural frequency, the damping ratio, the modal coefficient, the density of the fluid and the viscosity are defined in the dictionary file `dynamicMeshDict` located in the `constant` directory. Also, this file contains the structural response including the displacement, velocity and acceleration measured at the final time instance from the previous dynamic simulation. The ***constructors*** which is from the code line 46 to 103 of the source code `dynamicBendingFreeUDFFvMesh.c` as attached in Section A.1.2 read these parameters and store them in the variable `fnb`, `quib`, `phi0`, `rho_`, `nu_`, `z_n`, `zdot_n`, `zddot_n` and `tn` respectively.

The member function `Foam::dynamicBendingFreeUDFFvMesh::update()` contains three separate pieces of codes which are structurally linked together as shown in Figure 4.12. In the first part, the lift force `FL_n`, drag force `FD_n` and moment around the centre of gravity `M_n` at the time step `tn` are calculated; these results are then printed into the log files. This part corresponds to the code line 113 to 211 and was adopted from the source file `forceCoeffs.C` of the OpenFOAM utility `forceCoeffs`, by which the six components of forces and moments acting on all mesh faces of the model were calculated. However, as for the flexible model, forces and moments acting on the abutment section, i.e. the static section, needed to be removed. This was achieved by the introduction of the scalar field `function`, which took the value of 1 for all faces belong to the main span of the model and the value of 0 for all faces belong to the static section. This process can be seen from the code line 136 to 153.

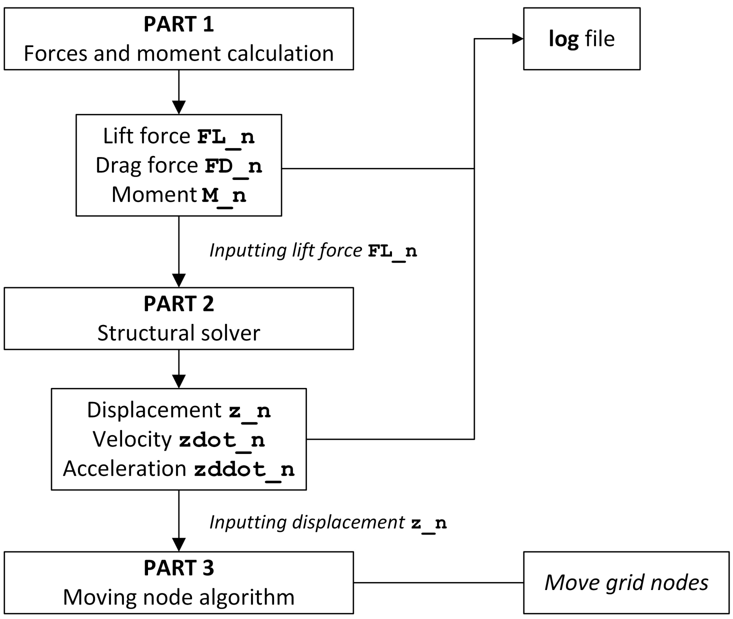

Figure 4.12: Flow chart of the member function in the source codes `dynamicBendingFreeUDFFvMesh.C`.

After that, the lift force `FL_n` was input into the second part, i.e. the structural solver, where the spatial-dependent lift force was transformed into the generalised lift force `F` and used to evaluate the generalised acceleration `zddot_n1`, velocity `zdot_n1` and displacement `zdot_n1` of the model at this current time step `t_n`. These operations were implemented as shown from the code line 212 to 240. Also, these results were outputted to the log file and then stored so that they could be recalled in the next time step as observed from the code line 304 to 310 . The generalised displacement `z_n1` was applied in the third part, i.e. the moving node algorithm, to displace the grid nodes according to the structural response.

As for the rigid model, a similar routine with some alteration was applied. Instead of using the modal coefficient, the mass of the model was directly prescribed. Also, the scalar field `function` was ignored since fluid forces calculating on all mesh faces of the model were accountable to the forces and moment acting on the model.

4.5.3 Dynamic Mesh Algorithm

In the dynamic simulation, the displacement of the rigid model or the flexible model undergoing the VIV lock-in is about 10% of the depth of the cross section; therefore, the mesh experiences relatively small deformation. Also, since the geometry of the mesh is simple, the lineal spring-analogy algorithm first proposed by Batina (1990) was adopted to model the motion of the grid nodes to accommodate the displacement of the model but still maintain good cell quality.

In the proposed dynamic mesh algorithm, the computational domain is divided into 9 separate blocks as shown in Figure 4.13. Blocks 8 and 9 are rigid where all grid nodes are effectively fixed relative to the model. The other blocks are grouped into a buffer zone where cells are allowed to deform to facilitate the displacement of the model. As for the algorithm to displace the grid nodes in the buffer zone, the edges of the mesh are modelled to behave like linear springs connecting mesh vertices; the stiffness of springs is inversely proportional to the length of the edges. In addition, the grid nodes on the outer boundaries of the mesh such as the two x patches and two y patches are held fixed whereas the ones on the model are fixed relatively to the moving boundary.

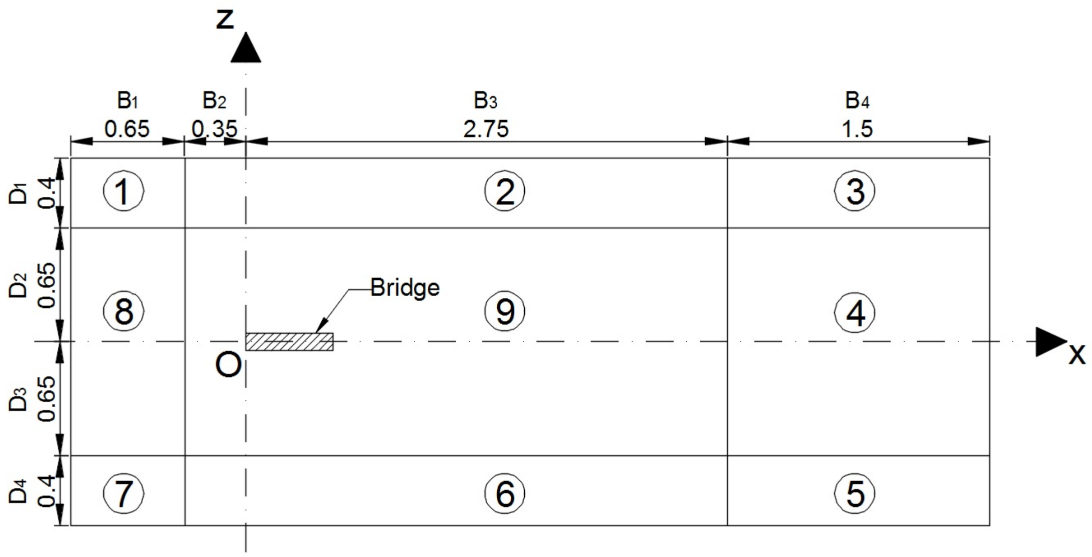

Figure 4.13: Illustration of 9 different blocks in the computational domain; dimensions are in metres.

Using the coordinate system and key dimensions of each block as indicated in Figure 4.13, assuming the displacement of the model at the position y is Z, the grid node at the position (x_p, y_p, z_p) needs to be displaced by a distance Δz as

$$\text{Blocks 8 and 9 (Rigid zone):} \quad \Delta z = Z, \tag{4.21}$$

$$\text{Blocks 1 and 2 (Buffer zone):} \quad \Delta z = Z\frac{D_1 + D_2 - z_p}{D_1}, \tag{4.22}$$

$$\text{Block 3 (Buffer zone):} \quad \Delta z = Z\left(1 - \frac{x_p - B_3}{B_4}\right)\frac{D_1 + D_2 - z_p}{D_1}, \tag{4.23}$$

$$\text{Block 3 (Buffer zone):} \quad \Delta z = Z\left(1 - \frac{x_p - B_3}{B_4}\right), \tag{4.24}$$

$$\text{Block 3 (Buffer zone):} \quad \Delta z = Z\left(1 - \frac{x_p - B_3}{B_4}\right)\frac{D_3 + D_4 + z_p}{D_4}, \tag{4.25}$$

$$\text{Blocks 1 and 2 (Buffer zone):} \quad \Delta z = Z\frac{D_3 + D_4 + z_p}{D_4}. \tag{4.26}$$

The code line 241 to 303 as shown in Section A.1.2 illustrate the implementation of Equations 4.21 to 4.26 into the member function `Foam::dynamicBendingFreeUDFFvMesh::update()`. The key dimensions as illustrated in Figure 4.13 are pre-defined in the `dynamicMeshDict` located at the `constant` directory as `B1`, `B2`, `B3`, `B4`, `D1`, `D2`, `D3` and `D4`. They are loaded at the start of a dynamic simulation together with the position of all grid nodes at the time `0`, which is stored into the variable `zeroPoints_` and remained unchanged throughout the simulation. After all of these calculation, the new position of all grid nodes are stored in the new variable `zeroPoints` and the `fvMesh` class's member function `fvMesh::movePoints(zeroPoints)` will be applied to relocate the grid nodes (the code line 318).

Similar implementation can be found in the source code `dynamicHeavingFreeUDFFvMesh.C` attached in Section A.1.1. It should be noticed that, as for the rigid model, there was no need to apply the first bending mode shape to determine the structural response at different span-wise positions.

4.5.4 Coupling Scheme

The use of the `pimpleDyMFoam` solver together with the two proposed dynamic mesh classes implies that the conventional serial staggered algorithm was applied to model the coupling between the fluid, structure and the dynamic mesh. This method was discussed in Section 3.8.3 and is illustrated in Figure 3.9.

A number of reviews have pointed out the loose coupling of this algorithm which is responsible for its instability and the need of a small time-step. Some improvements have been proposed but they can be overshadowed by an increase in the computational power. However, based on Farhat et al. (2006), the use of the second-order numerical schemes in solving the fluid governing equations can preserve the stability of this scheme without complicating the computational implementation and increasing the computational cost.

4.5.5 `constant` Directory

In the dynamic simulation, the `constant` directory had a similar file structure and keyword's entries as those applied in the static simulation except the appearance of the addition dictionary file `dynamicMeshDict`. This file contains pieces of information and parameters required by the two new developed dynamic mesh classes introduced in Sections 4.5.2 and 4.5.3. An example of the `dynamicMeshDict` used in the bending simulation is

```
FoamFile
{
    version     2.0;
    format      ascii;
    class       dictionary;
    object      dynamicMeshDict;
}
// * * * * * * * * * * * * * * * * * * * * * * * * * * * * * * * * * * * * //
dynamicFvMeshLibs  ("libdynamicBendingFreeUDFFvMesh.so");
dynamicFvMesh      dynamicBendingFreeUDFFvMesh;
motionSolverLibs   ("libfvMotionSolvers.so");
dynamicBendingFreeUDFFvMeshCoeffs
{
```

```
    // Dimensions are in SI units
    // Key dimensions of the computational domain
    B1    0.65;
    B2    0.35;
    B3    2.75;
    B4    1.5;
    D1    0.4;
    D2    0.65;
    D3    0.65;
    D4    0.4;
    // Structural parameters of the flexible model
    L     3;          //Full length of the model
    L0    2.5;        //Half of the main span of the model
    fnb   1.2;        //Natural frequency of the bending mode
    quib  0.01;       //Damping ratio
    phi0  0.363;      //Modal coefficient
    rho   1.225;      //Fluid density
    nu    0.0000146; //Kinematic viscosity of the fluid
    // Parameters for the forces and moment calculation
    patches    (bridge);
    patch      bridge;
    pName      p;
    UName      U;
    liftDir    (0 0 1);
    dragDir    (1 0 0);
    pitchAxis  (0 1 0);
    CofR       (0.25 1.5 0);
    // Structural response from the previous time-step
    z_0      -0.00671367517;
    zdot_0   -0.0365478739;
    zddot_0  0.3622957463;
    t_0      148.7;
}
```

The flexible model was prescribed such that the natural frequency `fnb` was 1.2 Hz and the damping ratio `quib` was 0.01. The model coefficient `phi0` was selected to be 0.363 so that the generalised mass was calculated to be unit. As discussed in Section 4.2.1, the full length of the flexible model `L` except the static section was 3 m or $6B$ while half of the main span where the flow field was of interest was 2.5 m or $5B$.

The final part effectively contains the solutions of the displacement, velocity and acceleration at the final time instance before a dynamic simulation is terminated. These pieces of information allow a dynamic simulation to be restarted. If a dynamic simulation is run for the first time, i.e. `t_0` equals to `0`, `z_0`, `zdot_0` and `zddot_0` are set to `0` also.

As for the heaving simulation, similar keywords and entries were used except that, instead of the the modal coefficient, the mass of the rigid model `mass` was defined as `6.56`. Also, `L0` was ignored and the full length of the model `L` was set to be `1.5`.

4.5.6 `0` Directory

The boundary conditions as well as the initial conditions for the dynamic simulation were defined using the same method as described in Section 4.3.2 in the static simulation. However, as was mentioned in Section 4.2.1, the `symmetryPlane` boundary condition was applied to the two y patches. Also, the `movingWallVelocity` with a constant and uniform zero velocity was implemented on the surface of the rigid model and the flexible model to accurately capture the zero normal-to-wall velocity component.

For both of the heaving and bending simulation, the wind speed was increased from 0.1 to 2.5 m s^{-1}. Due to the lack of the computational resources, it was decided to start each dynamic simulation when the rigid or flexible model was at its equilibrium positions. This set up could lead to a limitation that the hysteresis of the fluid and structure system was not properly captured.

4.5.7 `system` Directory

The discretisation schemes together with the control parameters of the fluid solver were discussed in Section 4.5.1. The physical time of each dynamic simulation was selected to be similar to that applied in the static simulation; this was found to be sufficient for the transient period to settle down and for the fluid and structure solutions to reach the stable oscillatory state.

Since the implemented structural solver is able to produce the forces and moment acting on the model, the OpenFOAM function `forceCoeffs` was disabled. The OpenFOAM function `probes` was still used to sample the surface pressure around the model as well as the wind velocity in the wake region during the simulation at every time-step. Due to the oscillation of the model, the probes sampling the surface pressure must be fixed relatively to the model or locked to the cell next to the model. This was achieved by following these steps

- Switching the default entry of the keyword `fixedLocation` to `false`,
- Defining the keyword `probePoints` holding the position of original probes when the model is at its equilibrium positions,
- Calculating entries for the keyword `probeLocations` using the `#codeStream` as following, taking the bending simulation as an example,

```
#include "motionProperties";
zBridge  $z_0;
phi0     $phi0;
L0       $L0;
probeLocations  #codeStream
{
    codeInclude
    #{
         #include "pointField.H"
    #};
    code
    #{
        pointField probePoints;
        scalar     zBridge;
        scalar     phi0;
        scalar     L0;
        dict.lookup("probePoint") >> probePoints;
        dict.lookup("zBridge") >> zBridge;
        dict.lookup("phi0") >> phi0;
        dict.lookup("L") >> L;
        dict.lookup("L0") >> L0;
        forAll(probePoints, pointI)
        {
             scalar probePointY = probePoints[pointI].component(1);
             scalar scaledFactor = phi0*::sin(constant::mathematical::pi/(2*L0)
              *probePointY);
             scalar probePointDz = zBridge*scaledFactor;
             probePoints[pointI].component(2) += probePointDz;
```

```
29              }
30              os << probePoints;
31          #};
32      };
```

At first, as indicated in the code line 2 to 4, the dictionary file `motionProperites` located in the `system` directory is merged, where the generalised displacement of the model at the final time instance of the previous bending simulation `zBridge`, the modal coefficient `phi0` and half of the main span `L0` are loaded; the last two variables were mentioned in Section 4.5.5. These variables are then transferred into the `#codeStream`, where the z coordinates of original probes are corrected by the displacement of the model at the corresponding y position. This was implemented as shown by the code lines 24 to 27. Results are then printed out as entries to the keyword `probeLocations` using the OpenFOAM function `os << probePoints`. It should be noticed that this approach was only applicable for sampling the surface pressure around the model only; also, similar routine could be applied for the heaving simulation with the structural mode shape being neglected.

Similar to the static simulation, all dynamic simulations were conducted in parallel using the HPC at the University of Nottingham. Due to different numbers of cells, one heaving simulation was computed on 32 processors while 64 processors were utilised to perform one bending simulation. The computational domain used in the heaving simulation was decomposed using the same method as the static simulation. Using the `simple` decomposition method, on the other hand, the computational domain in the dynamic simulation was separated into 64 blocks, 8 blocks in the x direction, 4 blocks in the y direction and 2 blocks in the z direction. In order to satisfy the requirement of the physical time, each heaving simulation took 1 to 1.5 months to finish, whereas as for each bending simulation, the simulation time was approximately 2 to 2.5 months.

4.6 PROPER ORTHOGONAL DECOMPOSITION

The flow field around and the wake region behind the flexible rectangular cylinder undergoing the bending VIV is expected to be characterised by the high unsteadiness and the inclusion of some emerging span-wise flow features. The use of the spectral analysis and related technique is very limited in this case. Therefore, the method of Proper Orthogonal Decomposition (POD) is applied to offer a quantitative analysis of the surface pressure field around the flexible cylinder as the bending VIV lock-in occurs; this technique will help to effectively reveal span-wise flow features and their potential contribution to the VIV mechanism.

In this section, the POD technique is introduced regarding its principles and theoretical background together with its application in wind engineering. Based on the underlying mathematics, a MATLAB routine is written to carry out the POD using the pressure field across the entire surface of the cylinder or around the circumference at one span-wise location as an input.

4.6.1 Overview of POD

The POD is the well-known and most frequently used procedure for modal decomposition and random multi-variate analysis (Solari et al., 2007); this statistical method has been applied in a number of different fields of research including fluid dynamics, structural analysis and bluff-body aeroelasticity. Taking a random process in both spatial and temporal domains as the input, the POD represents this process as a linear combination of the orthogonal eigenfunctions of the covariance of the process itself. These eigenfunctions, which refer as the spatial POD mode shape, is modulated by temporal random variable or the POD coefficients, which are uncorrelated with each other. No assumption about the linearity is needed even though the input data for the POD is obtained from a non-linear system. In addition to this advantage, the POD method gains its popularity thanks to its ability to represent the dominant components of the process by the first few most-energetic POD modes and the existence of a link between the so-called dominant POD modes and the underlying physical mechanisms. Based on these characteristics, the application of POD can be divided into two purposes. The first one focuses on decomposing the flow field observed in either experiments, numerical modelling or full scale to gain better insights into the flow mechanism. As for the second one, it relates to the Reduced Order Modelling which is directly involved in Computational Fluid Dynamics and Computational Structural Dynamics; the aim is to develop a reduced model which is simplified and representative and can be applied in practical applications. The computational study presented here is of the first type.

Solari et al. (2007) presented a literature review showing the development of the POD method and its implementation and usability in different disciplines such as meteorology, turbulent flows and structural analysis. As for the bluff-body aerodynamics, the POD technique owes its popularity to the ability to compress the pressure field data obtained from wind tunnel tests, computation simulations or full-scale measurements, to produce reduced aerodynamic model and to interpret the dominant mechanism of the wind loading on structures. The application of POD in this discipline originated from a paper where Armitt (1968) raised a question about the validity of the orthogonality condition inherent in POD when associating each POD mode to a unique physical cause. In an attempt to answer this question, a number of studies were conducted using a square or low-rise building as the test case. By studying the surface pressure around a square building model, Kareem and Cermak (1984) found that the first POD mode contributed predominantly to the fluctuating pressure energy and corresponded to the vortex shedding.

MacDonald et al. (1990) also observed some links between POD modes and the longitudinal and lateral fluctuating velocity components of the oncoming turbulent flow. Nevertheless, researches at this time were limited by the number of simultaneous pressure measurements. Bienkiewicz et al. (1995) made a leap forwards where they measured the pressure simultaneously at 494 taps distributed on the surface of a low-rise building model in the wind tunnel. This study was later further analysed by Tamura et al. (1997) focusing on the correlation between the POD decomposed pressure and the oncoming wind and linking the first and second POD modes to the longitudinal and lateral fluctuating velocity components. Analysing the wind forces acting on a tall building, Kikuchi et al. (1997) noticed that the along-wind and cross-wind forces could be represented by very few POD modes while the torque required more POD modes. Holmes et al. (1997) then returned to the question raised by Armitt (1968) and further addressed the constraints related to the orthogonality, which could mislead the physical interpretation of POD modes in some cases. Later Baker (2000) concluded that the fluctuating mechanisms are likely reflected by the most energetic POD modes; he agreed with Armitt (1968) that no POD modes can be associated with only one flow mechanism and vice versa.

The use of POD in aeroelasticity was recent and motivated by aerospace engineers to improve and simplify reduced order models of unsteady aerodynamic flow around airfoils and aircraft wings (Hall, 1994). Understanding its potential and capability, Dowell and Hall (2001) later suggested a wider domain of applications including the wind-induced responses of bridges and tall buildings. Even though results are rather limited, the application of POD on analysing aeroelastic phenomena in wind engineering is getting prominent and yielding encouraging findings. Selected studies conducted by Hemon and Santi (2002) and Ricciardelli et al. (2002) measured the surface pressure around a vibrating circular and a bridge deck section respectively and showed that there are systematic variations of the POD mode shapes and the harmonic content of the POD coefficients as the wind speed increases as well as the appearance of different patterns associated with different vibration regimes such as VIV, galloping, buffeting and flutter.

4.6.2 Mathematical Background

The underlying mathematical background of the POD method presented in this section can be applied to both of a vector field data or a scalar field data. In this computational study, the surface pressure field, i.e. a scalar field data, is of interest.

Taking the 2D unsteady pressure field $p(x, y, t)$ measured on the surface of the model as an input, the POD method decomposes this data as

$$p(x, y, t) = \bar{p}(x, y) + p'(x, y, t) = \bar{p}(x, y) + \sum_{n=1}^{N} a_n(t)\phi_n(x, y), \tag{4.27}$$

where $\bar{p}(x,y)$ is the time-averaged surface pressure field calculated from N time instances as

$$\bar{p}(x,y) = \frac{1}{N}\sum_{i=1}^{N} p(x,y,t_i). \tag{4.28}$$

The fluctuating component of the surface pressure field $p'(x,y,t)$ is calculated as

$$p'(x,y,t) = p(x,y,t) - \bar{p}(x,y); \tag{4.29}$$

This component is decomposed into a linear combination of N spatial-dependent POD mode shape $\phi_n(x,y)$ and N temporal-dependent POD coefficients $a_n(t)$. The main aim of the POD method is to extract the most energetic modes which represent most of the fluctuating energy of the unsteady flow; these modes could then be implemented into the process of Reduced Order Modelling. It should be noticed that the number of POD modes to be extracted depends on the number of time instances.

The POD method is based on the temporal auto-correlation matrix C of the fluctuating component of the pressure field; an element at the i^{th} row and j^{th} column is evaluated in the continuous form as

$$C(i,j) = \int_Y\int_X p'(x,y,t_i)p'(x,y,t_j)\,\mathrm{d}x\mathrm{d}y. \tag{4.30}$$

To apply Equation 4.30 into the discrete form, a numerical integration scheme can be used; as an example, the first-order trapezoidal scheme is implemented as

$$C(i,j) = \sum_{y_k=1}^{N_y-1}\left[C^y_{t_i,t_j,y_k} + C^y_{t_i,t_j,y_k+1}\right]\frac{\Delta y}{2}, \tag{4.31}$$

$$\text{with: } C^y_{i,j,y_k} = \sum_{x_k=0}^{N_x-1}\left[C^{x,y}(t_i,t_j,y_k,x_k) + C^{x,y}(t_i,t_j,y_k,x_k+1)\right]\frac{\Delta x}{2}, \tag{4.32}$$

$$C^{x,y}(t_i,t_j,y_k,x_k) = p'(x_k,y_k,t_i)\,p'(x_k,y_k,t_j). \tag{4.33}$$

In order to calculate the POD mode shapes and coefficients, the POD precess requires solutions of the eigenvalue problem

$$CA = \lambda A, \tag{4.34}$$

where $A = \left[A^1A^2\ldots A^N\right]$ is the matrix of eigenvectors A^n ($n = 1\ldots N$) and λ is the diagonal matrix whose diagonal elements are their corresponding eigenvalues. The spatial POD mode shape $\phi_n(x,y)$ is then constructed from

$$\phi_n(x,y) = \sum_{i=1}^{N} p'(x,y,t_i)A_i^n. \tag{4.35}$$

Here, A_i^n is the i^{th} element of the eigenvector A^n. The POD mode shape calculated in Equation 4.35 is normalised using the Euclidean length $\|\phi_n\|$. In addition, the temporal POD coefficient is calculated as

$$a_n(t) = \int_Y \int_X p'(x,y,t)\,\phi_n(x,y)\,\mathrm{d}x\,\mathrm{d}y. \tag{4.36}$$

If the pressure field data at N time instances is used as the input for the POD process, there will be N eigenvalues and hence, there will be N sets of spatial POD mode shapes and temporal coefficients. All of them can be used to fully reconstruct the 2D unsteady surface pressure field by following Equation 4.27. In order to extract most energetic POD modes to offer more insight in the dominant flow field or to develop reduced order models, the quantity $\lambda_{nn}/\sum_{nn=1}^{N}\lambda_{nn}$ can be inspected; this quantity effectively represents the relative contribution of each mode to the total fluctuating energy. By defining a threshold such as 5%, the dominant POD modes can be identified for further analysis.

4.6.3 OpenFOAM and MATLAB Implementation

In this section, the underlying mathematics of the POD process described in Section 4.6.2 is implemented using OpenFOAM utilities and MATLAB. There is a potential bottleneck in the aforementioned POD process which involves the calculation of the temporal auto-correlation matrix C. The use of Equations 4.31, 4.32 and 4.33 can create heavy computational burden particularly when dealing large 2D or 3D field data such as the computational study presented here where 2D unsteady surface pressure field sampled over 17500 discrete faces will be studied. This computational limitation can be overcome using the snapshot method first proposed by Sirovich (1987). As being suggested by the name, the snapshot method requires the fluctuating component of the surface pressure to be written as a matrix $P' = \left[P'^{,1} P'^{,2} \ldots P'^{,N}\right]$ with $P'^{,n}$ being a vector containing the fluctuating pressure component measured at all faces on the surface of the model at the time instance n.

OpenFOAM Sampling Utility

The surface pressure around the flexible cylinder was sampled using the OpenFOAM on-the-fly sampling utility defined in a dictionary file named `PODPressure` located inside the `system` directory and also included in the `controlDict` dictionary using `#include "PODPressure"`. The `PODPressure` dictionary file contains the following sub-dictionaries

```
PODPressure
{
    type              surfaces;
    functionObjectLibs  ("libsampling.so");
    enabled          true;
    outputControl    timeStep;
    outputInterval   20;
    surfaceFormat    foamFile;
    interpolationScheme cellPoint;
    fields
    (
         p
    );
    surfaces
    (
        bridgeSurface
        {
            type  patchInternalField;
            patches  (bridge);
            interpolate true;
            offsetMode  normal;
            distance  0.0005;
        }
    )
}
```

The pressure was sampled at a distance of 0.0005 m from the surface of the model in the vertical direction to avoid potential numerical instabilities when interpolating the pressure on the wall. The surface pressure used in the POD process was outputted at a POD time-step which is 20 times bigger than the one applied for the numerical computation. This avoided creating significantly large amount data which could lead to large burden in storage yet maintained a good temporal resolution to capture dominant flow features. A 50 s long surface pressure field will be interpreted using the POD method.

Using the `surfaceFormat` as `foamFile`, the output of the surface pressure was saved in the `postProcessing` directory under the sub-directory `PODPressure`; the structure of this sub-directory is sketched in Figure 4.14. The surface pressure is stored in the file `p` which is basically a vector whose each element holds the pressure data sampled at a point on the surface of the model at one time instance. The coordinate of the points is defined in the `points` file.

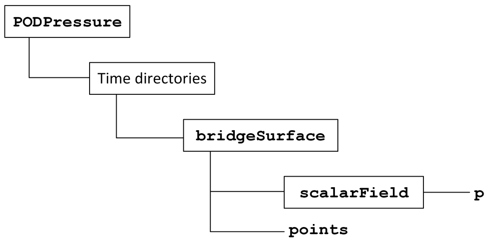

Figure 4.14: File structure of the directory `PODPressure`.

MATLAB Script

The use of the aforementioned OpenFOAM sampling utility led to some disadvantages where two additional MATLAB scripts were created to pre-process the sampled pressure data.

The first one was related to the order of the sampling points. Due to the bending motion of the flexible model, OpenFOAM is not consistent in the order of sampling, which could result in significant difference in the pressure vector data sampled at two consecutive POD time-steps. Also, after one run of a simulation is finished, a series of time directories is created inside the directory `PODPressure`, which need to be joined to create a snapshot matrix P'. The MATLAB script `PODAnalysis_DataSorting.m` as attached in Section A.2.1 is used to resolve these two issues. This piece of code uses the coordinates of the sampling point at the first POD time instance as the standard coordinate and sorts the pressure data at other time instances according to this benchmark. After that, vectors of the surface pressure data at all time instances are stacked together to form the snapshot matrix. These two processes are achieved by the code from the lines 136 to 159. The other parts of this code involves file and folder handling and to correct the z coordinate of the sampling point to where the model is in the equilibrium position for the ease of further analysis later. The output of this first part of the pre-processing is a list of following files for each run of a simulation: the `rawPressureData` file which is a snapshot matrix, `xCoor`, `yCoor` and `zCoor` holding the coordinates of the standard sampling points and `timeID` file containing the POD time stamps.

The second disadvantage is due to the fact that each bending simulation at one wind speed requires a number of runs to produce enough data for the POD analysis. Data from each run needs to be assembled together before input in the POD method. The MATLAB script `PODAnalysis_DataAssembling.m` as attached in Section A.2.2 is created for this purpose. Again, the consistency of the sampling points is checked between different runs; this is performed by the code from the line 55 to 72. Then the code searches for the time instance when a simulation was restarted and joins two snapshot matrices together. The code from the line 73 to 93 is for these two tasks. The output of this MATLAB script is a complete snapshot matrix of the fluctuating component of the surface pressure stored in the file `pressureData`, the coordinate of all sampling points in the files `xCoor`, `yCoor` and `zCoor` and the complete POD time stamps `timeID`.

At this stage, the snapshot matrix P' holding the pressure data across the entire surface of the model during a 50 s POD sampling duration is completely constructed and is ready for the POD analysis. Based on the theory described in Section 4.6.2, a piece of the MATLAB programme was coded as shown in Section A.2.2. The input of this process is the snapshot matrix `pressureData`, which is then subtracted by the temporal-averaged surface pressure `meanPressure` resulting in the snapshot matrix holding the fluctuating component of the surface pressure only `primePressureData`. The outputs of this POD process are the matrices `PODPhi`, $PODPhi = \left[PODPhi^1 \;\; PODPhi^2 \ldots PODPhi^N\right]$, and `PODCoef`, $PODCoef = \left[PODCoef^1 \;\; PODCoef^2 \ldots PODCoef^N\right]$, whose corresponding columns $PODPhi^n$ and $PODCoef^n$ are the spatial-dependent mode shape and the temporal-dependent coefficient of the POD mode n. The POD modes are sorted in the descending order of their fluctuating energy, i.e. their associated eigenvalues, which are saved in the vector `nor_cEValue` as the cumulative eigenvalues normalised against the summation of all eigenvalues. All of these outputs will be saved for further reconstruction and analysis. It should be noticed that the pressure data storing in the matrix `pressureData` and inputting into the POD process can be the pressure on the entire top or bottom surfaces of the model or just at one span-wise location. The selection is dependent on the purposes of analysis.

4.7 CONCLUSION OF THE CHAPTER

In this Chapter, the methodologies to conduct the static simulation and the dynamic simulation including the heaving and bending simulations using the piece of the open-source CFD software OpenFOAM have been presented. This involved proper definitions of all dictionary files in the `0`, `constant` and `system` directories to control all aspects of an OpenFOAM CFD simulation such as the fluid definition, the boundary and initial conditions, the solver settings and the discretisation schemes as well as the on-the-fly sampling processes.

As for the dynamic simulation, a structural solver and a dynamic mesh algorithm have been built and successfully implemented into the OpenFOAM fluid solver using a serial staggered coupling scheme. This integration was capable of modelling the heaving motion of a rigid sectional model or, as being the main aim of this computational study, the bending motion of a flexible model, which is analogue to the bending motion of bridge deck. This approach can be expanded to model the torsional motion of the flexible model also. The flow field around the flexible model is interpreted using the POD process and written MATLAB scripts in order to extract potential span-wise flow features as well as the mechanism of the bending VIV lock-in.

A number of limitations of this computational approach were mentioned, which are mostly due to the limited computational power available. The first one is that the span-wise length of the flexible model only allowed half of the first bending mode to be simulated; this can cause some restriction or suppression on the flow field particularly around the mid span. The second one is related to the spatial resolution of the domain in the span-wise direction. As was pointed out by results of the mesh convergence study, the use of the span-wise discretisation in the dynamic simulation could lead to under-prediction of the Strouhal number and some alteration in modelling the flow field, particularly around the reattachment region. These points are noticed and will be fully addressed in later analysis. The use of a finer grid not only in the span-wise direction but also in the x-z plane is better; however, such grid would cause substantial obstacles to achieve the aim and objectives of this computational study.

Chapter 5

Methodology: Wind Tunnel Experiments

5.1 OVERALL METHODOLOGY

The wind tunnel aspect of this project was conducted at the Atmospheric Boundary Layer (ABL) wind tunnel at the University of Nottingham. This wind tunnel facility is classified as a low-speed open-circuit wind tunnel and is designed to simulate the ABL and to study a number of related wind engineering problems such as modelling aerodynamics and aeroelasticity of tall buildings and measuring urban-environment wind behaviour.

The wind tunnel features a 14.5 m long working section (Figure 5.1a) and a constant width of 2.4 m. The main test section and a 2 m-diameter turntable are located at the end of a 11 m fetch. To ensure zero pressure gradient at the turntable, the height of the working section slightly increases from 1.79 m measured right after the contraction to 1.91 m after the turntable. The wind tunnel facility includes two turning parts at the inlet to direct the flow into the working section and one more turning part at the outlet to direct the flow out of the working section. At the inlet, before getting into the working section, the flow is passed through a series of honeycombs and fibremesh screens to remove the turning effect in the flow and to help straighten the flow. Therefore, close to the inlet of the working section, good homogeneity and uniformity in the flow is achieved together with a very low turbulence intensity of less then 0.2%. To simulate an ABL, a set of boards of roughness elements, spikes and a fence is set up along the working section; they are designed based on the guidelines adopted from Irwin (1981) and Simiu and Scanlan (1996) and has been confirmed to capable of generating an ABL above a suburban terrain at a scale of 1:400. Due to effects of shear layers created long the top surface of the wind tunnel, the boundary layer height of the modelled ABL is limited to 1 m.

(a)

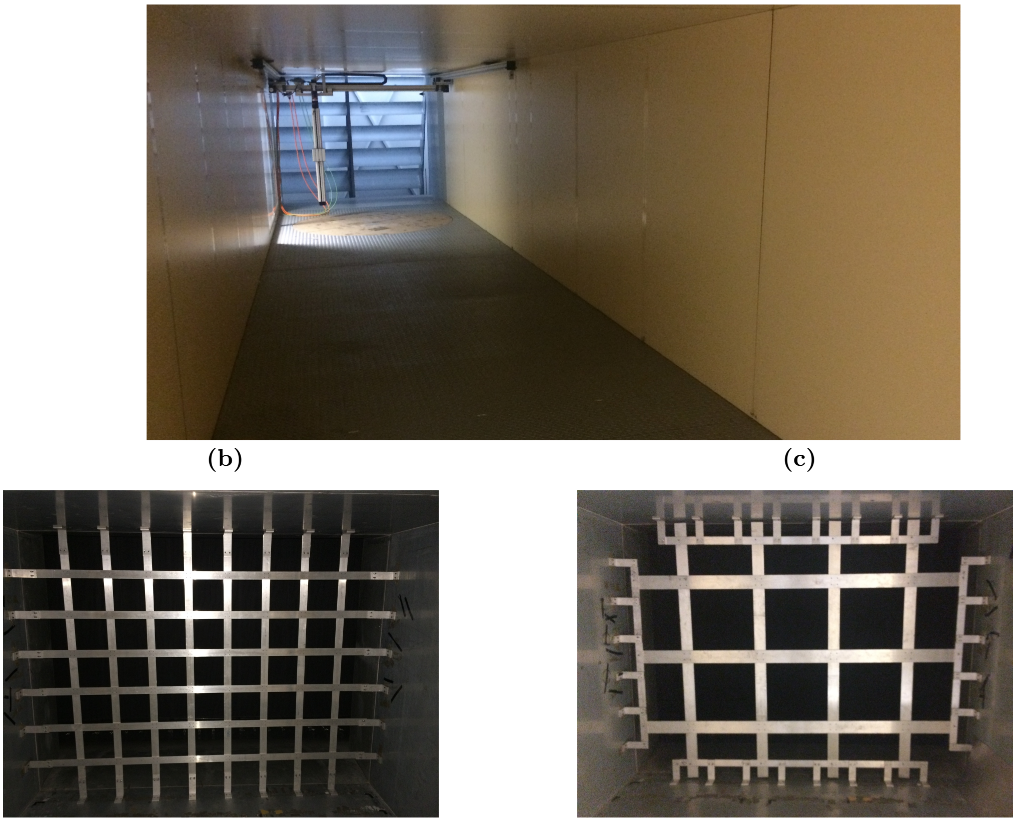

(b) **(c)**

Figure 5.1: Selected aspects of the wind tunnel's hardware: (a) working section, (b) small turbulence-generating grid and (c) large turbulence-generating grid.

All the wind tunnel tests in this project are considered to be aerodynamic tests and they all were conducted in the low turbulence section immediately downwind of the contraction. For these tests, two grids constructed from wide flat bars bolted to T-section struts of the same width in a form of square mesh grid were used to generate the turbulent flow (Figures 5.1b and 5.1c). One grid was assembled from 50.8 mm wide members and had a mesh size of 250 mm while 76.2 mm wide members were used to construct the second one resulting in a mesh size of 500 mm. Detailed dimensions of these two grids are shown in Figure 5.2; hereafter, the small grid is denoted by Grid A while the large grid is denoted by Grid B. Further discussion and analysis of the grid-generated turbulence in the wind tunnel will be presented in Section 5.8. By adjusting the position of the model relative to the grid and by using different grids, a range of turbulent regimes could be achieved.

The model used in the wind tunnel tests was the 5:1 rectangular sectional model; it was made from aluminium to reduce the overall mass. The model was 1.6 m long with a 380 mm by 76 mm cross section; inside the model, there were a number of vertical aluminium plates to stiffen the model, thus avoiding any distortions related to twisting, buckling or bending due to the wind load or its self-weight. The lid

(a) Small turbulence-generating grid – Grid A

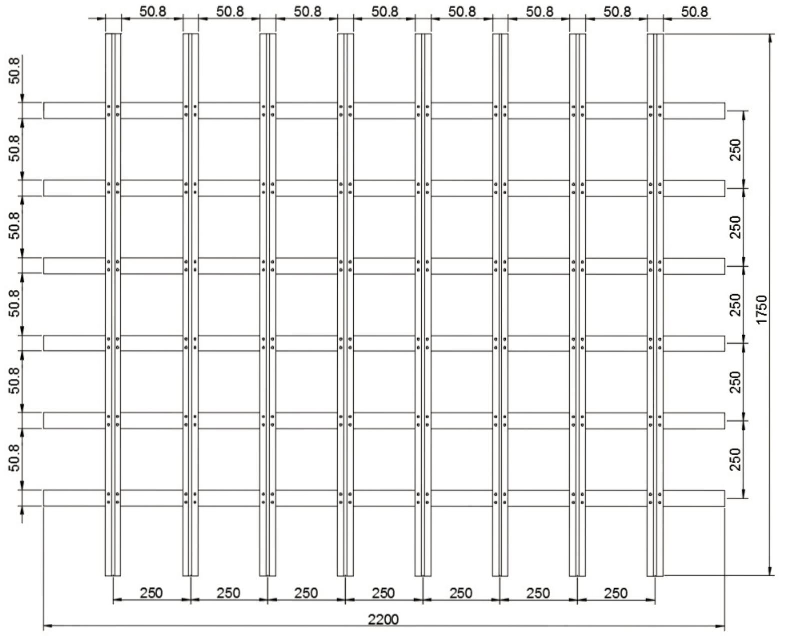

(b) Large turbulence-generating grid – Grid B

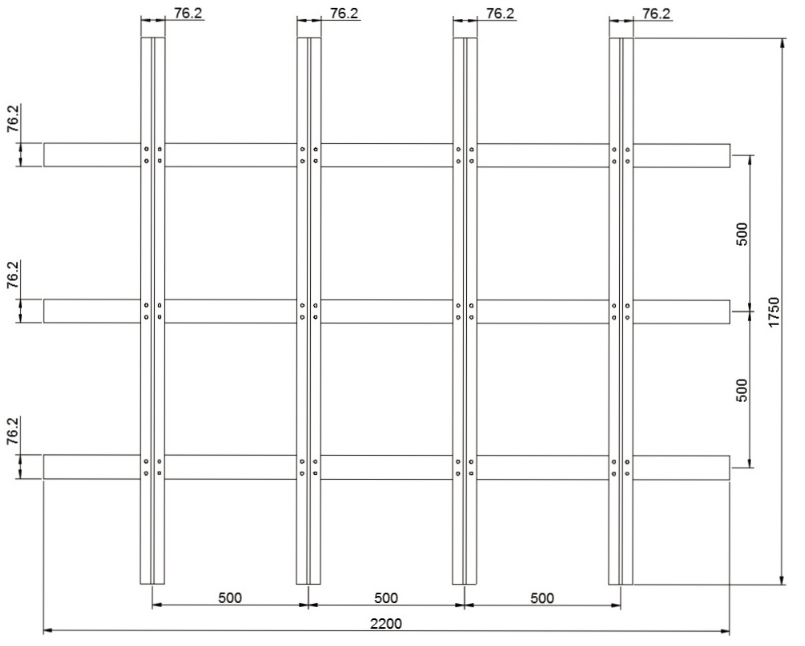

Figure 5.2: Details of (a) the small turbulence generating grid – Grid A and (b) the large turbulence generating grid – Grid B from a downwind viewpoint (dimensions are in mm).

of the model was bolted into the side walls; it could be easily removed to access sensors located inside the void of the model (Figure 5.3a). Two 35 mm diameter holes were incorporated on either side of the model to provide access for cables of the sensors. In addition, there were two 500 mm diameter acrylic end-plates attached to the two sides of the model; they helped eliminate the wrapping of flow around the two ends, which could lead to an increase in the base pressure around the lateral zones of the model (Figure 5.3b).

(a)

(b)

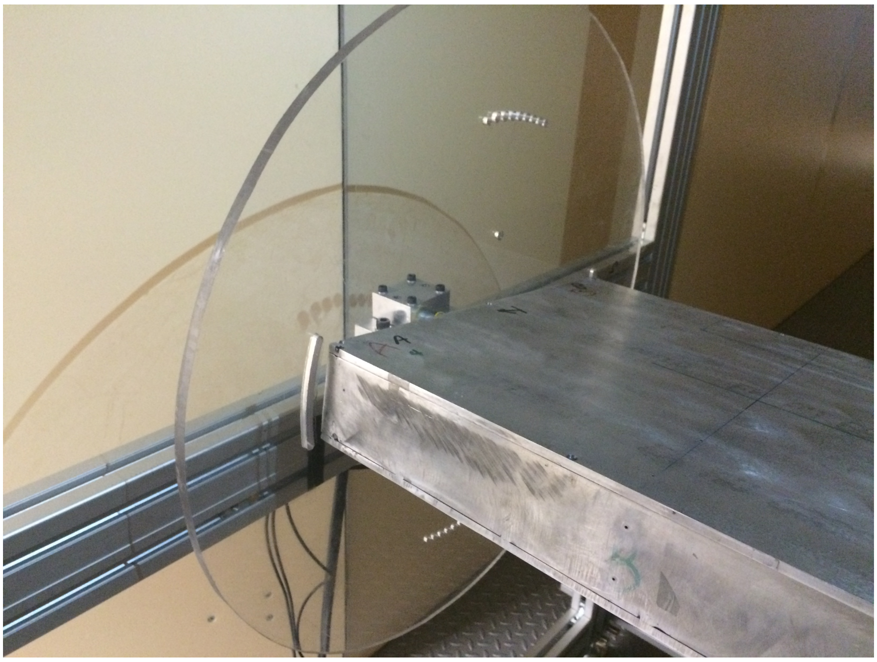

Figure 5.3: (a) The void of the model houses the strengthening plates and instrumentation; (b) The acrylic end-plates are attached at each end of the model.

The model was instrumented with 112 pressure taps; each tap included a 10 mm long titanium tube facilitating direct connection to pressure sensors. There were 7 arrays of pressure taps; their arrangement is shown in Figure 5.4a. The distance between the array and the centre line of the model is listed in Table 5.1. There are 16 pressure taps distributed around the cross section at each array as shown in Figure 5.4b. This arrangement of the pressure taps allows measurement of the pressure distribution around the cross section at one certain span-wise position as well as to investigate the pressure correlation in the span-wise direction at a stream-wise position.

Table 5.1: Distance between the array of pressure taps and the centre line of the model.

Array	1	2	3	4	5	6	7
Distance (mm)	-560	-360	-110	-60	40	340	440

(a)

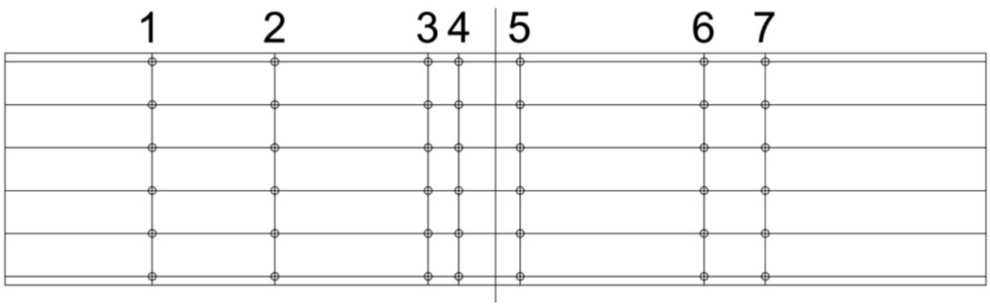

(b)

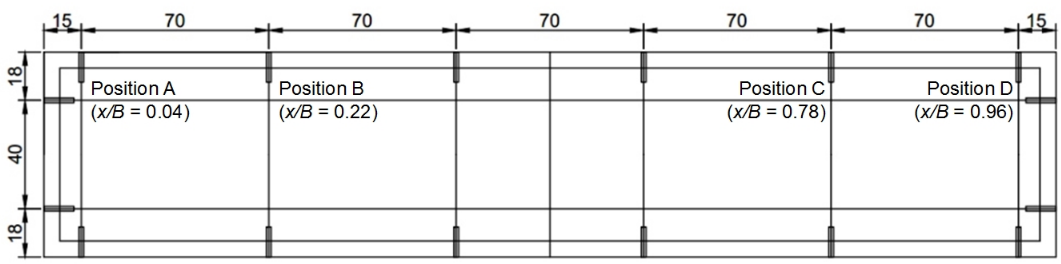

Figure 5.4: (a) Arrangement of pressure taps on the bottom surface and (b) a cross section of the model showing the distribution of pressure taps at each array (dimensions are in mm).

5.1.1 Static Test Procedure

For the static tests, the sectional model was rigidly supported on load cells in a frame using the clamping mechanism attached on the frame and inside the model (Figure 5.5). The model was situated within the aerodynamic section of the wind tunnel as shown in Figure 5.6. The model was tested at 4 different wind speeds: 4, 6, 8 and $10\,\mathrm{m\,s^{-1}}$ and at angles of attack from -8° to 8° in 2° increments measured using the digital inclinometer LD-2M. At each wind speed, the pressure distributions were measured and time-averaged and the standard deviation of the time varying force and moment coefficients were calculated from the load cell data. In addition, a X-wire probe was placed at a distance, B, behind the trailing edge and a distance, D, above the top surface to investigate the flow structure in the wake. Tests were repeated in smooth flow and in several levels of incident turbulence by adjusting the distance between the model and the grids. Further information on the turbulence level will be discussed later in Section 5.8.

(a) **(b)**

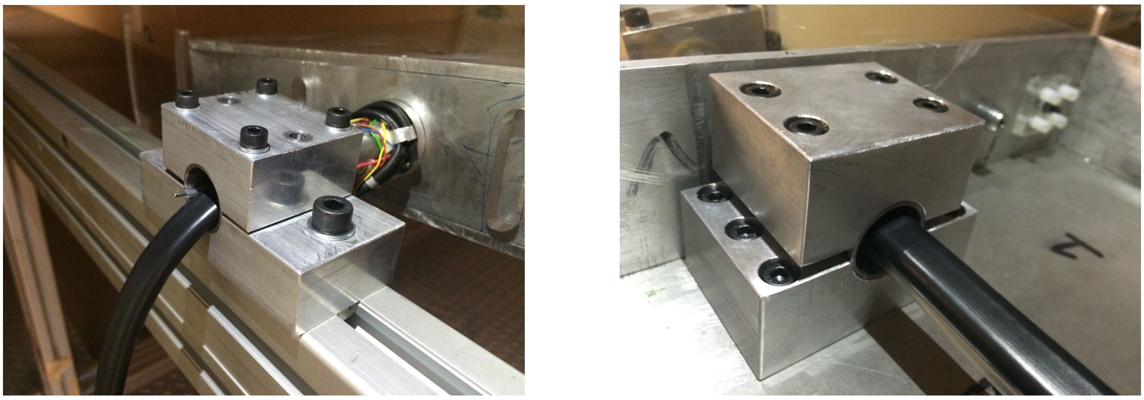

Figure 5.5: The clamping blocks are attached on the frame (a) and inside the model (b).

Figure 5.6: The model is supported on an aluminium frame rigidly clamped inside the wind tunnel.

5.1.2 Dynamic Test Procedure

For the dynamic tests, the section was mounted on a set of 8 springs and restrained by light wires so that it could respond in one of three different modes: heaving only, pitching only and heaving and pitching. A set of 8 springs E0750-115-5000-S supplied by Associated Spring Raymond was selected. These springs are manufactured from a 2.95 mm diameter stainless-steel wire and have the stiffness of 441 $\mathrm{kN\,m^{-1}}$, the outer diameter of 19.05 mm, the free length of 127 mm and the initial tension of 23.22 kN. Together with the use of cables and turnbuckles as shown in Figure 5.7, this set up provided enough extension in the springs to accommodate the VIV and torsional flutter of the cylinder. The natural frequency and damping ratio of the heaving were measured to be $f_{n,h} = 4.68\,\mathrm{Hz}$ and $\zeta_h = 0.19\%$ respectively; for the pitching mode, the natural frequency and damping ratio were $f_{n,p} = 5.70\,\mathrm{Hz}$ and $\zeta_p = 0.13\%$ respectively. The wind speed was increased in steps from 1 to $10\,\mathrm{m\,s^{-1}}$. A coarse step size was used outside the lock in region; whereas during the lock-in, small increments were used to accurately track changes in dynamic behaviour. At each wind speed, the response was recorded using accelerometers mounted on four corners of the model (Figure 5.8) and the pressure distribution was measured. A X-wire probe was located at a similar position as was used in the static tests to capture the the u and w components of the wind velocity in the wake. Tests were again repeated in the smooth flow and in three levels of incident turbulence using the turbulence-generating grids. Further information on the turbulence level will be discussed later in Section 5.8.

All wind tunnel tests mentioned here were carried out following the standard operating procedure attached in Appendix B, where information relating to wind speed adjustment and health and safety issues were included. In the following sections, theories and techniques relating to the measurement of the wind velocity, pressure, acceleration and forces will be introduced.

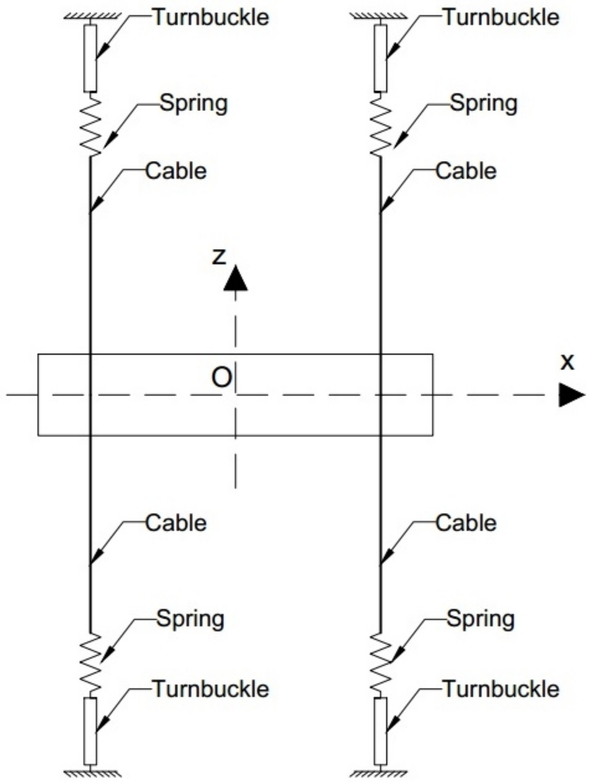

Figure 5.7: Schematic of the set-up of the dynamic test.

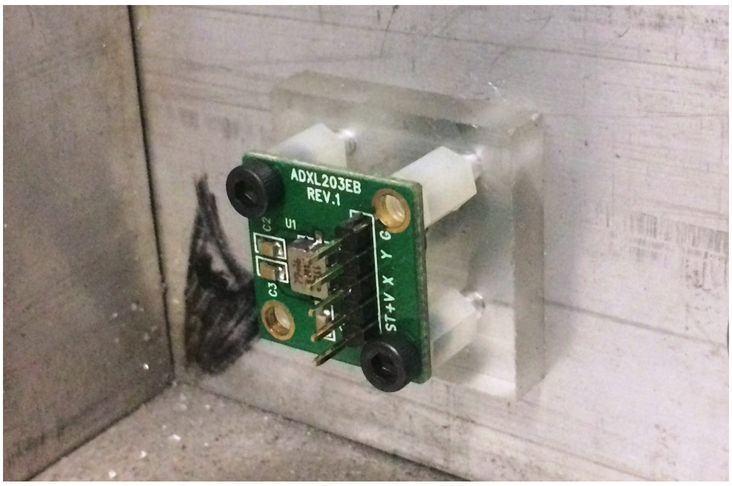

Figure 5.8: Accelerometers are mounted on the perspex plates via nylon spacers.

5.2 OVERVIEW OF DATA ACQUISITION SYSTEM

As described in the overall method in Section 5.1, a number of fluid and structural parameters needed to be monitored during wind tunnel tests, which were pressure, wind velocities, temperature, acceleration, forces and moment. Different types of sensors were used and mounted at appropriate positions to monitor and measure these parameters and the real-time data generated by sensors was captured and stored in

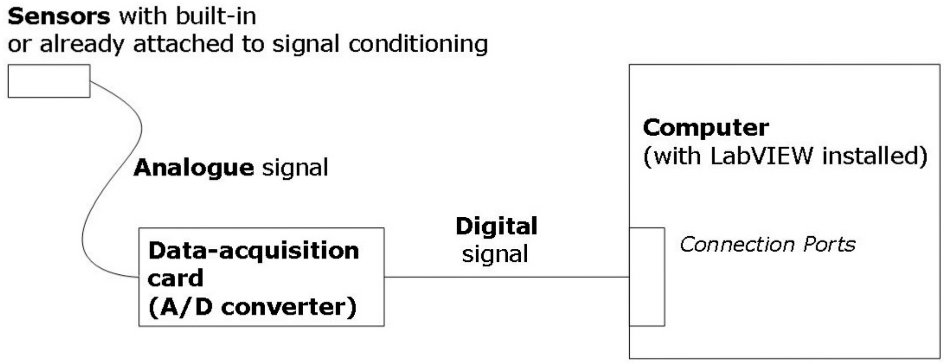

Figure 5.9: Overall data acquisition system.

a computer with the LabVIEW software installed. The purpose of this section is to briefly introduce the LabVIEW software and give an overview of the data acquisition system in the context of this wind tunnel study.

LabVIEW is an integrated development environment created by National Instruments (NI) as a part of NI's platform based approach to help engineers and scientists with application of measurement and control. With a graphical programming language, LabVIEW communicates with users in a unique way, allowing them to visualise, create and code engineering systems in a timely-fashion. LabVIEW is designed to communicate and interact with software and hardware produced either by NI or by other supported manufacturers thanks to its open-source platform. Programming with LabVIEW starts from the **back panel**; using its graphical programming language, developers can create a system which allows them to do different tasks including pure data acquisition, on-the-fly data processing and controlling and monitoring applications. Users then interact with the system via the **front panel** of the LabVIEW software where they are given the control of hardware and are able to visualise the real-time data being captured as well as results of the data analysis and processing. The powerful feature of the LabVIEW is that it has been designed as an open-source piece of software so that users can develop a system which will be optimised with respect to their requirements.

For the purposes of these wind tunnel studies, the data acquisition system was set up as illustrated in Figure 5.9. All sensors used in the wind tunnel tests had built-in or attached signal conditioning; output from these sensors was an analogue signal. A data-acquisition card was required to act as an analogue-to-digital converter (A/D converter); the digital signal was then read by a computer with the LabVIEW software installed so that it could be stored for further analysis.

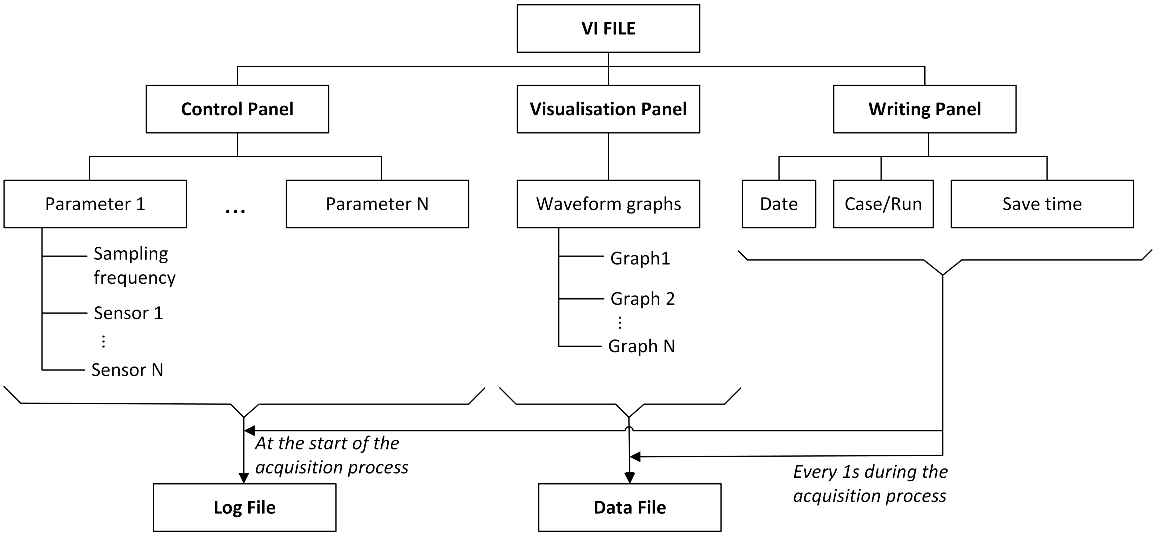

Figure 5.10: General structure of a VI file.

In these wind tunnel studies, the LabVIEW software was used to interact with the A/D converter for (i) controlling the A/D converter in terms of the idle/operation mode or the sampling frequency, (ii) acquiring the output from the A/D converter and (iii) saving them in `.csv` files for further post-processing using MATLAB. No data-analysis tools offered by the LabVIEW software were applied so that the data-acquisition process could be performed as quickly as possible to ensure that the real-time data was captured and no issues relating to internal memory or buffer size of the A/D converter could occur; all processes of analysing data were conducted after the data-acquisition process finished.

Different LabVIEW system files which are normally called as the Virtual Instrument (VI) files were created and set up to facilitate a number of data-acquisition tasks depending on the types of parameters to be acquired, number of channels used simultaneously and types of A/D converters. In fact, for the aforementioned purposes, all VI files contained **control**, **visualising** and **writing panels**; the overall structure of a VI file is described in Figure 5.10. In the **control panel**, all information relating to sampling frequencies for each acquired parameter and settings of relevant sensors (if applicable) were input. The **visualisation panel** contained a number of waveform graphs to show time histories of acquired data from all sensors for monitoring purposes. Depending on the purpose of the data-acquisition task, one graph could show signals from either a single sensor or a group of sensors. The **writing panel** was dedicated to writing data to files. At the start of the data-acquisition process, the writing panel stored all information input in the control panel to a **log file** and after every 1 second during the data-acquisition process, the writing panel saved output from sensors to equivalent **data files**. These files together with the log file will be read during the data analysis.

5.3 VELOCITY MEASUREMENT

Velocity measurement is a crucial technique in this project, providing wind speed data and information of the turbulence. Hot-wire Anemometry (HWA) and Laser Doppler Anemometry (LDA) are the principal research tools for turbulent flow studies (Bruun, 1995). Compared to the simple system including a pitot static tube and a pressure manometer, both are characterised by their high accuracy, high frequency response and wide velocity range. The HWA system is more advantageous due to its low cost, small size, low signal-to-noise ratio, simple operation and data analysis. The LDA system is however preferable in hostile environment such as combustion, solid-particle-inclusive flow where damage to HWA systems is unavoidable.

HWA is based on convective heat transfer from a heated sensor to the surrounding fluid, which is primarily related to the fluid velocity. A typical HWA system is illustrated in Figure 5.11; it includes a probe connected to a anemometer via a probe support and a cable. The analogue output from the anemometer is converted into the digital signal by an A/D converter before it is input into a computer.

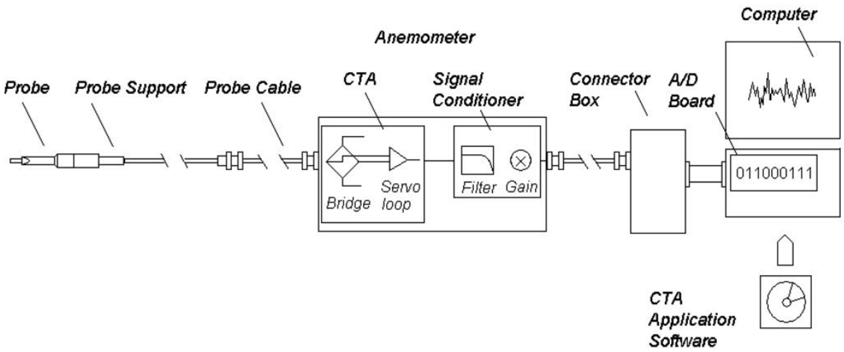

Figure 5.11: Typical HWA system (Jorgensen, 2002).

5.3.1 Hot-wire Probes

The probe contains the heated sensing element whose configuration can be a cylindrical hot-wire or a hot-film deposited on cylindrical fibres. The hot-film probe is robust, sturdy and commonly used in applications where the mean velocity component is the primary requirement. The hot-wire probe, on the other hand, is more fragile and susceptible to contamination in the flow; however, it can accurately measure fluctuating velocity components, yielding more acceptable averaged properties of the turbulent wind. The temperature of the sensor is pre-defined and kept higher than the ambient temperature (typical at 250 °C). The flow passing by the sensor induces a cooling effect reducing the sensor's temperature and resistance. Therefore, a voltage E has to be supplied to restore its original temperature; this voltage is related to the effective velocity cooling down the sensor V_{eff} via King's Law as

$$E^2 = A + BV_{\text{eff}}^n, \tag{5.1}$$

where A, B and n are constants. The physical background is discussed in detail in Bruun (1995).

The selection of hot-wire probes mainly depends on the number of velocity components to be measured. A TSI X-wire 1241-T1.5 was used in this project to facilitate simultaneous measurement of two velocity components. The overall dimensions of the selected X-wire are illustrated in Figure 5.12. The heating sensing elements are two tungsten wires of 1.25 mm in length and 5μm in diameter. They are spaced at about 1 mm apart and inclined at 45° against the probe-stem. These dimensions help minimise the thermal-wake interference where the convection heat from one sensor affects the output of the other sensor. In addition, most turbulence length scales in the flow can be effectively captured due to their small size. The length of the sensors, however, is larger than the Kolmogorov length scale; therefore, the spectral analysis using the output from this X-wire will contain a significant error at the highest frequencies.

As for the X-wire, the effective velocity V_{eff} is normally expressed by Jorgensen's equation with respect to the sensor geometry as

$$V_{\text{eff}}^2 = V^2 \left(\sin^2\alpha + k^2\cos^2\alpha\right) = U_N^2 + k^2 U_T^2, \tag{5.2}$$

where V is the flow velocity, α is the yaw angle between the sensor and the flow, U_N and U_T are the velocity component normal and tangential to the sensor respectively, k is the yaw coefficient. The King's Law for one sensor of the X-wire is then written as

$$E^2 = A + B\left[V^2\left(\sin^2\alpha + k^2\cos^2\alpha\right)\right]^{n/2}. \tag{5.3}$$

The angles between each sensor and the flow, α_1 and α_2, are related to the orientation angle β are illustrated in Figure 5.13; their relationship is mathematically expressed as

$$\text{Sensor 1: } \alpha_1 = 45^\circ + \beta, \tag{5.4}$$

$$\text{Sensor 2: } \alpha_2 = 45^\circ - \beta. \tag{5.5}$$

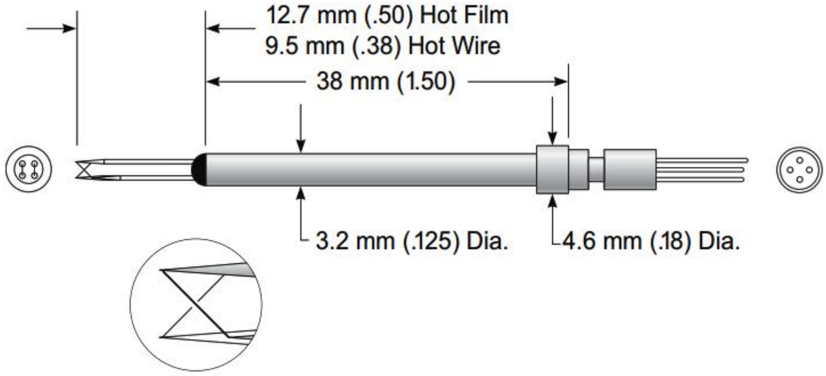

Figure 5.12: Detailed dimension of the TSI X-wire 1241-T1.5 (Dimensions in brackets are in inches) (TSI-Incorporated, 2003).

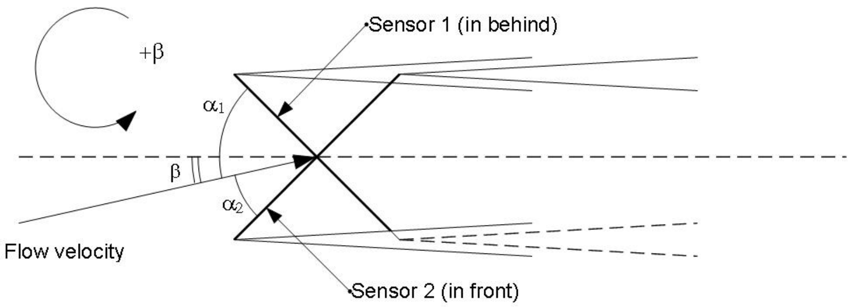

Figure 5.13: Relationship between the orientation angle β and the angle between sensors and the flow α_1 and α_2. The positive direction of the angle β is included.

5.3.2 Anemometer

Each sensor in the X-wire is connected to a Wheatstone bridge circuit which is a key component of the anemometer. The sensor can be operated in Constant-current (CC) or Constant-temperature (CT) mode. In the former configuration, by adjusting relevant resistors in the circuit, the current through the sensor is kept constant at each velocity. However, due to the thermal-inertia, the sensor cannot respond instantaneously to variation in the air flow. An additional circuit, thus, needs to be included to compensate for this thermal lag. This technique has been superseded by the CT mode where the temperature of the sensor is maintained at a constant value by incorporating a fast-response feedback differential amplifier into the main circuit. It allows the thermal inertia of the sensor to be automatically adjusted when the flow conditions vary (Bruun, 1995). To accomodate the TSI X-wire, the TSI IFA-300 multi-channel Constant-Temperature Anemometer (CTA) was used.

The IFA-300 CTA is configured for one to eight channels of anemometry, with a built-in signal conditioning circuit and a thermal circuit for measuring fluid temperature. The main electronic component of the IFA-300 CTA, the Wheatstone bridge circuit (Figure 5.14), is connected to an amplifier supported by the SMARTTUNE technology which can quickly restore the bridge balance and maintain the sensors' operating temperature $T_{\text{op}} = 250\,^{\circ}\text{C}$ by feeding an output current back to the top of the bridge. The voltage E_b at the top of the bridge circuit is related to the flow velocity by Equation 5.1. A T-type thermocouple can also be attached to the thermocouple circuit to measure the fluid temperature T_f which allows the bridge voltage E_b to be corrected as

$$E = E_b \sqrt{\frac{T_{\text{op}} - T_c}{T_{\text{op}} - T_f}}, \tag{5.6}$$

where $T_c = 20°\text{C}$ is the calibration temperature. Effectively, Equation 5.6 adjusts bridge voltages to values as if the sensor functions in the 20°C-fluid condition, which helps minimise the effect of the temperature variation.

Another component is the built-in signal conditioning circuit whose schematic is shown in Figure 5.15. The IFA-300 CTA offers versatile settings of high- and low-pass filters and gain and offset values to manipulate the bridge voltage E_b, depending on requirements of the application and other electronic devices. In this project, a low-pass filter of 300 Hz was selected and a gain of 20 and an offset of 1 V were applied to utilise the entire ±10 V input range of the NI 9125 A/D converter. The bridge voltage is then calculated from the output voltage E_{output}

$$E_b = \frac{E_{\text{output}}}{\text{Gain}} + \text{Offset}. \tag{5.7}$$

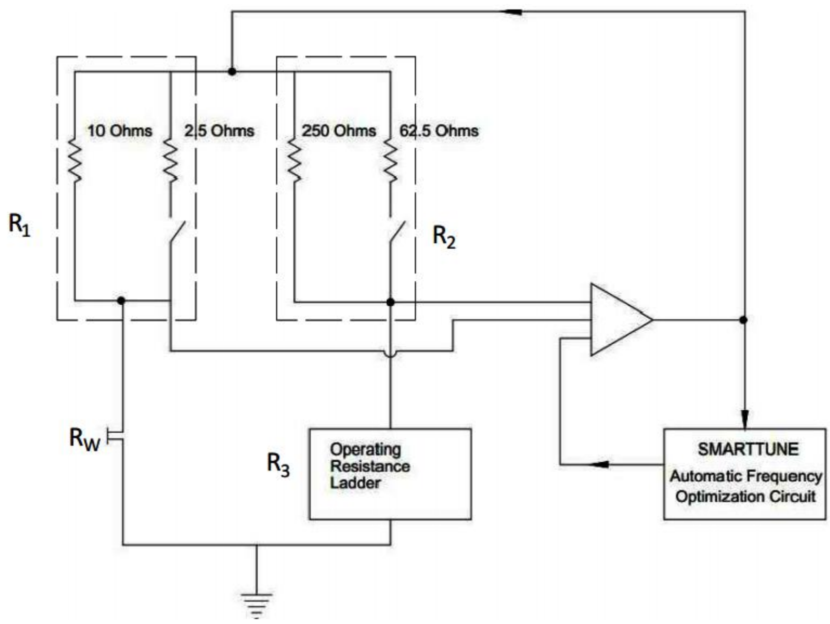

Figure 5.14: Wheatstone bridge circuit of the IFA-300 CTA, adopted from TSI-Incorporated (2010a); R_w includes the resistance of the sensor and the cable.

The IFA-300 CTA system can be set up based on the description in the manual TSI-Incorporated (2010a); however, some modifications were applied as shown in Figure 5.16, including the use of the NI 9125 A/D converter instead of the provided devices. This solution avoided the complex installation and hardware updates for the computer. In addition, this A/D converter offered better control of the number of samples and sampling frequencies and simultaneous measurement of the output voltages from two sensors. The digital output was connected to a USB port of the computer with IFA-300 ThermalPro software installed. This software allows users to control the IFA-300 cabinet and set up or measure important parameters such as the fluid temperature and resistance of sensors, probe supports and cables.

5.3.3 X-wire Calibration

The aim of the calibration process was to determine the King's Law coefficients A, B, n and the yaw coefficient k of both sensors as listed in Equation 5.3. To perform the X-wire calibration, the IFA-CTA 300 was set up as described in Section 5.3.2 and the X-wire probe was attached to the probe manipulator of the TSI 1127 calibrator unit (Figure 5.17). The calibration process consisted of two steps which were the velocity calibration and directional calibration.

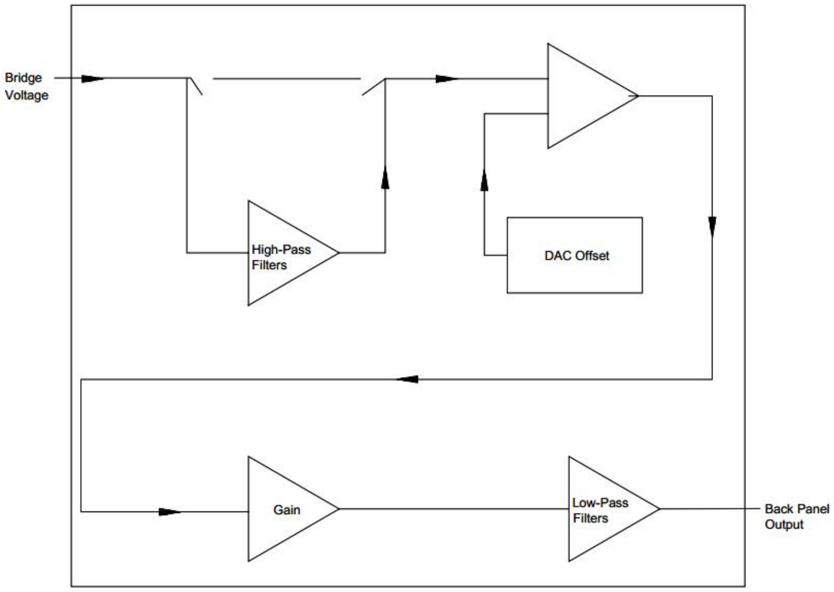

Figure 5.15: Built-in signal conditioning circuit (TSI-Incorporated, 2010a)

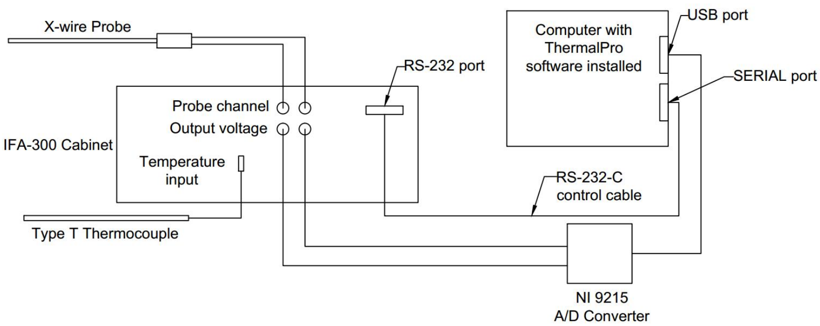

Figure 5.16: Set-up diagram of the IFA-300 CTA system.

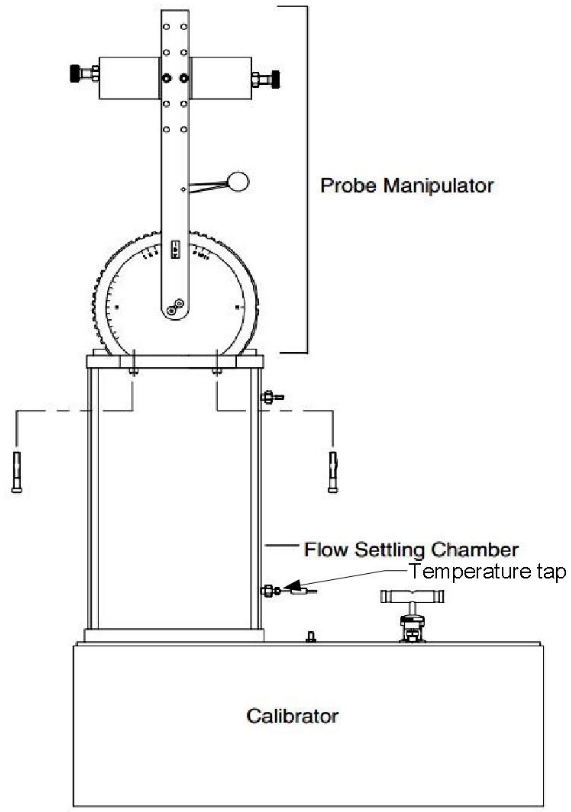

Figure 5.17: Main components of the TSI 1127 calibrator unit, adopted from TSI-Incorporated (2010b).

In the velocity calibration, the X-wire was held in the upright position above the nozzle of the calibrator unit; the gap between the sensors and the nozzle was equal to one nozzle diameter. The sensors' plane was parallel to the cantilever arm. At each nozzle speed, the differential pressure across the settling chamber measured by the FC150 micromanometer together with a 20 s record of the output voltage E_{output} were recorded at the sampling frequency of 1000 Hz. Also, the temperature of the fluid inside the chamber was measured by a thermocouple inserted in the temperature tap. E_{output} was then corrected using Equations 5.6 and 5.7.

In the directional calibration, the differential pressure across the settling chamber was kept constant. The yaw angles of two sensors were varied by rotating the cantilever arm. Again, 20 s records of E_{output} and the fluid temperature were recorded. The same correction of the output voltage was applied. It should be noticed that, in the two calibrations, the differential pressure measured by the micromanometer was converted to the flow speed at the nozzle using the method described in TSI-Incorporated (2010b).

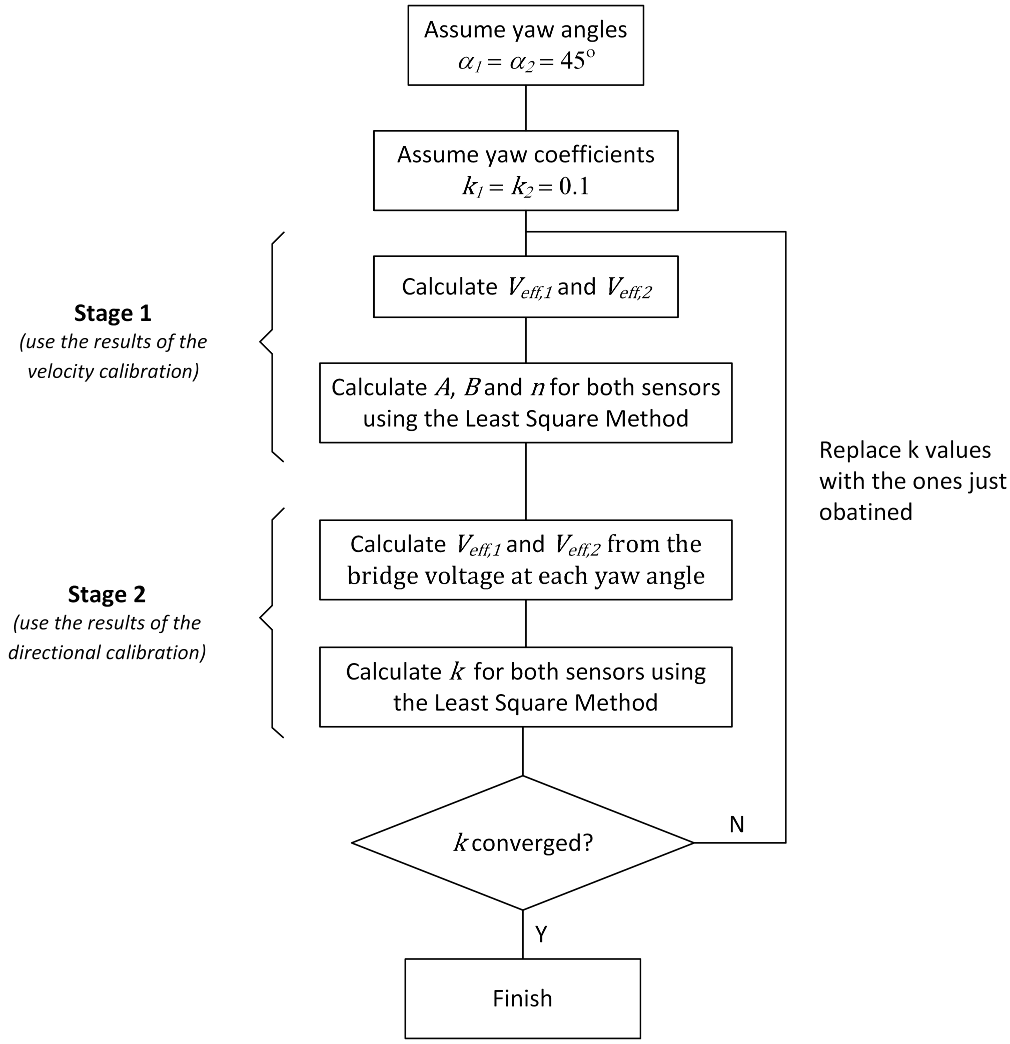

Figure 5.18: Iterative process to calculate the King's Law and yaw coefficients.

An iterative process was proposed to obtain all required coefficients as shown in Figure 5.18. Typical calibration results are illustrated in Figures 5.19a to 5.20c; the errors between the experimental measurement and the King's Law model are shown in Figures 5.21a to 5.22b. As for the velocity calibration, the errors, which are the percentage differences between the calibration and the model, were very small; the largest error was 0.6% occurring at the lowest differential pressure. It is mainly due to the fact that the calibrator unit and the micromanometer were inaccurate at very low differential pressure values. As for the directional calibration, the errors were larger, especially at the angle α from 15° to 25° between the flow and sensor. These errors emphasised the theoretical limitation of the calibration procedure that the King's Law coefficients and the yaw coefficients are assumed to be independent of the orientation angles. Therefore, the calibration results were acceptable in the range of orientation angles β between $-20°$ and 20°, which was of interest in this project.

5.3.4 Measurement with the X-wire

In order to perform the velocity measurement using the X-wire, the probe was securely situated in the wind tunnel such that the probe stem was parallel to the wind flow whereas the orientation of the probe's plane depended on the velocity components to be measured. Similar settings including the IFA-300 CTA setup, low-pass filter and sampling frequency were used. The output voltage and the fluid temperature were recorded.

The King's law and yaw coefficients obtained from the calibration were used to convert the output voltages into velocity using the methodology clearly described in TSI-Incorporated (2010b).

(a) Sensor 1 **(b)** Sensor 2

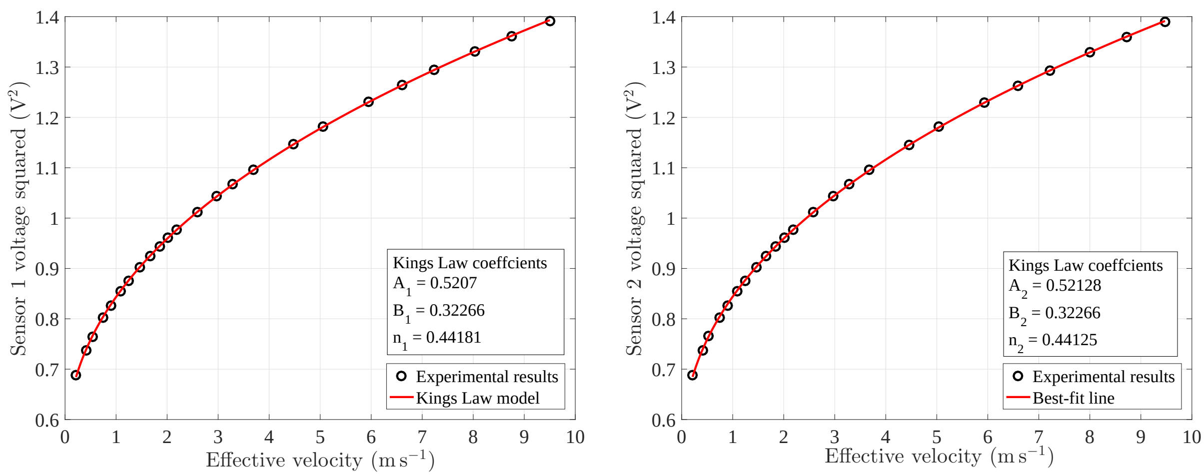

Figure 5.19: Results of the velocity calibration.

(a)

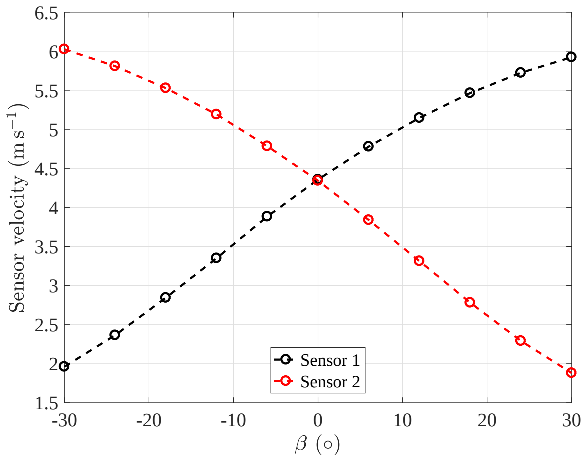

(b) Sensor 1

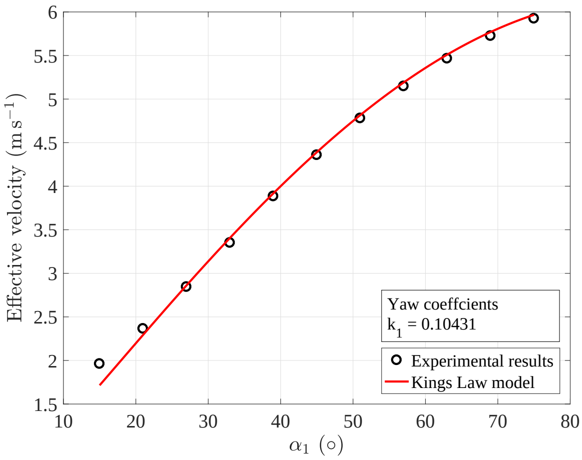

(c) Sensor 2

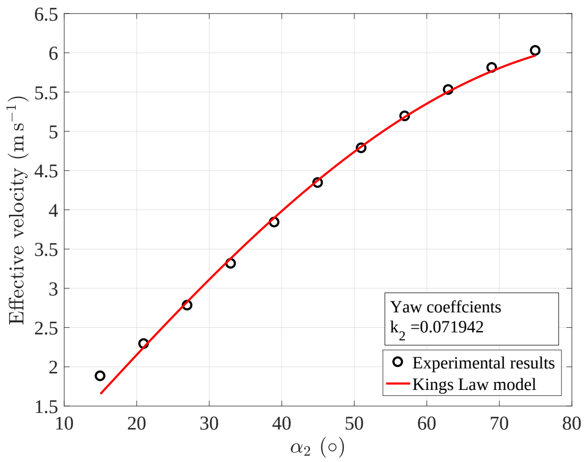

Figure 5.20: Variation of effective velocities against (a) orientation angles β, (b) angles α_1 and (c) angles α_2 between flow and sensors 1 and 2 respectively.

(a) Sensor 1

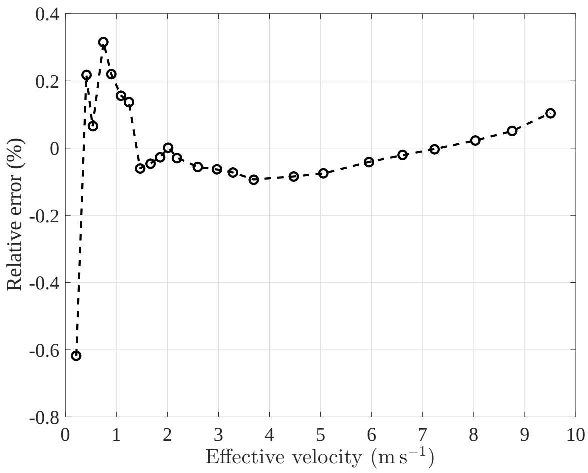

(b) Sensor 2

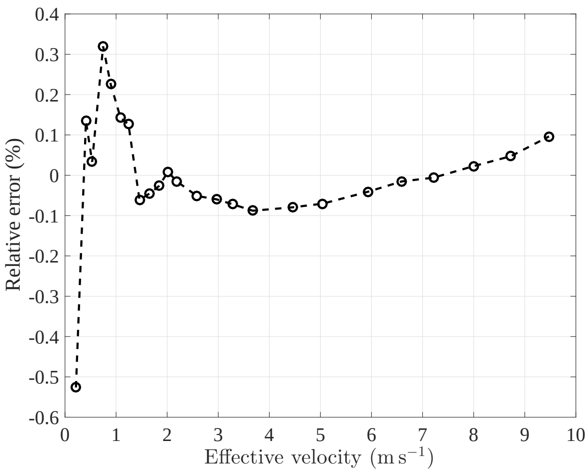

Figure 5.21: Fitting errors of the velocity calibration.

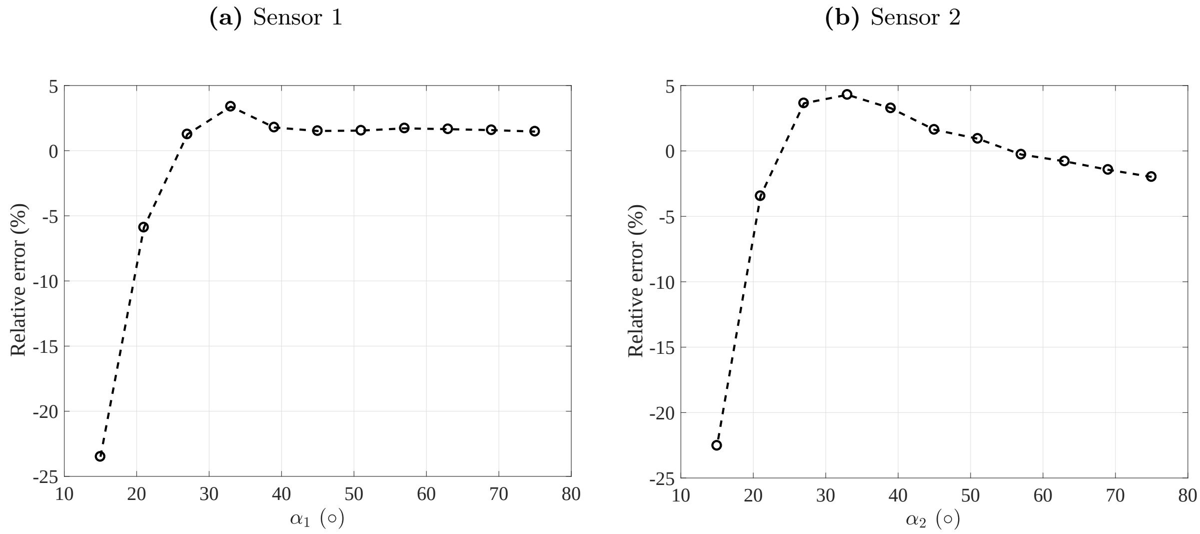

Figure 5.22: Fitting errors of the directional calibration; angles α_1 and α_2 are between flow and sensors 1 and 2 respectively.

5.4 FORCE AND MOMENT MEASUREMENT - STRAIN-GAUGE APPROACH

Currently, there are two common approaches to measure force and moment in the wind tunnel tests which are piezoelectric load cells and strain-gauge load cells. Due to its high rigidity and inherent stiffness, the former is superior in the frequency response and in the measurement of small unsteady forces. However, it suffers from zero-point drifting due to the decay of charge and the fault current, which is the limitation if the steady force and moment coefficients are of interest.

On the other hand, the strain-gauge-based load cells are very efficient at monitoring steady forces and moments. In this approach, strain gauges are bonded on a sensing element or a measuring object which is attached rigidly to the model. Any forces or moments acting on the model effectively induce strain on the gauges which then vary their resistance. This method therefore is normally referred as a passive approach. Strain gauges are normally connected to a Wheatstone bridge in quarter, half or full bridge configurations, depending on the application and requirements (Hufnagel and Schewe, 2007). An excitation voltage is applied to the bridge circuit; a variation in the resistance of the strain gauges will affect the output of the bridge voltage.

In this section, the design of the strain-gauged-based load cell will be discussed following by a description and the results of a calibration and a preliminary test for validation.

5.4.1 Design of Strain-gauge-based Load Cell

The design of the load cell was subject to a number of requirements that

- The strength of the load cell must be adequate to support the model and to avoid fatigue failure,
- The stiffness of the load cell must be high to avoid the interference or resonant effects caused by the measuring system,
- The load cell must be sufficiently sensitive to be able to measure the small forces at the $0\,^\circ$ angle of attack.

Through an optimisation study, a solution was proposed in Section C.1 in Appendix C. As can be seen in Figure C.1, the load cell was manufactured from a 175 mm long mild-steel tube with the cross section of 25.4 mm in diameter and 1.7 mm in wall thickness. The 75 mm long middle part of the tube acted as the sensing element; its wall thickness was reduced to 1 mm to increase the load cell sensitivity. The use of mild steel helped reduce the overall dimension of the load cell, minimising its disturbance to the flow and measurement without compromising the natural frequency and the sensitivity of the measuring system.

On each load cell, there were eight FLA-3-350-11 strain gauges and two FCT-2-350-11 torsional strain gauges; their detailed location is shown in Figure C.2 in Appendix C. Two load cells were assigned a similar coordinate system and orientation as illustrated in Figure 5.23; this setting must be kept consistent during the calibration and measurement. Bridge 1 including the strain gauges 1, 2, 3 and 4 was connected in a full Wheatstone bridge configuration in order to increase the load cell sensitivity, to compensate for the variation in temperature and to eliminate the dependence on loading points. This bridge primarily measures the force acting on the x (stream-wise) direction (the drag force). Similar configuration was applied for Bridge 2 including the strain gauges 5, 6, 7 and 8 and Bridge 3 formed by the rest of the strain gauges. Bridge 2 measures the force in the z direction (the lift force) while Bridge 3 measures the moment around the y axis.

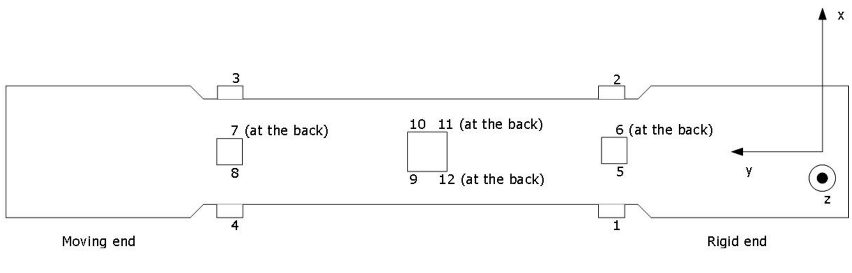

Figure 5.23: The coordinate system of and the layout of the strain gauges on the load cell.

5.4.2 Calibration of Strain-gauge-based Load Cell

The principal operation of the load cell is expressed via

$$\left\{\begin{array}{c} F_x \\ \\ F_z \\ \\ M_y \end{array}\right\} = [M] \left\{\begin{array}{c} E_1 \\ \\ E_2 \\ \\ E_3 \end{array}\right\}, \tag{5.8}$$

where F_x and F_z are forces acting on the load cell on the x and z direction respectively, M_y is the moment around the y axis, E_1, E_2 and E_3 are the output voltage of Bridges 1,2 and 3 respectively. $[M]$ is the 3×3 transformation matrix, which was identified via the static calibration of the load cell.

The static calibration of the load cell was set up as shown in Figure 5.24. The load cell was rigidly clamped on a flat surface; a small spirit level was used to verify the orientation of the load cell against the coordinate system as shown in Figure 5.23. The load was applied to the load cell by hanging weights on the moving end; the hanger could be shifted by 100 mm along the plate to apply moments to the load cell. The load cell was also rotated by 90 ° to completely calibrate all bridges. The load was increased from 0 to 4.9 N using 0.49 N increments and from 4.9 N to 9.81 N using 0.98 N increments. For each load value, 20 s records of the bridge voltages were sampled at the sampling frequency of 500 Hz. The excitation voltage of 10 V was supplied by the 8 channel bridge input module NI-PXIe 4330. The load cell was subjected to four different loading scenario which were $(0, -F_z, 0)$, $(0, -F_z, M_y)$, $(-F_x, 0, 0)$ and $(-F_x, 0, M_y)$. All calibration graphs of the two load cells are included in Appendix C. The results of two transformation matrices are

$$M_1 = \begin{bmatrix} 1.847 \times 10^6\,\mathrm{N\,V^{-1}} & -1.192 \times 10^5\,\mathrm{N\,V^{-1}} & -5.265 \times 10^4\,\mathrm{N\,V^{-1}} \\ 1.391 \times 10^5\,\mathrm{N\,V^{-1}} & -1.964 \times 10^6\,\mathrm{N\,V^{-1}} & -1.749 \times 10^4\,\mathrm{N\,V^{-1}} \\ 4.224 \times 10^2\,\mathrm{N\,m\,V^{-1}} & -1.307 \times 10^3\,\mathrm{N\,m\,V^{-1}} & -8.148 \times 10^4\,\mathrm{N\,m\,V^{-1}} \end{bmatrix}, \tag{5.9}$$

$$M_2 = \begin{bmatrix} -1.794 \times 10^6\,\mathrm{N\,V^{-1}} & 2.069 \times 10^5\,\mathrm{N\,V^{-1}} & -5.876 \times 10^3\,\mathrm{N\,V^{-1}} \\ -5.475 \times 10^4\,\mathrm{N\,V^{-1}} & 1.761 \times 10^6\,\mathrm{N\,V^{-1}} & 9.651 \times 10^3\,\mathrm{N\,V^{-1}} \\ -3.219 \times 10^2\,\mathrm{N\,m\,V^{-1}} & 5.548 \times 10^3\,\mathrm{N\,m\,V^{-1}} & 8.483 \times 10^4\,\mathrm{N\,m\,V^{-1}} \end{bmatrix} \tag{5.10}$$

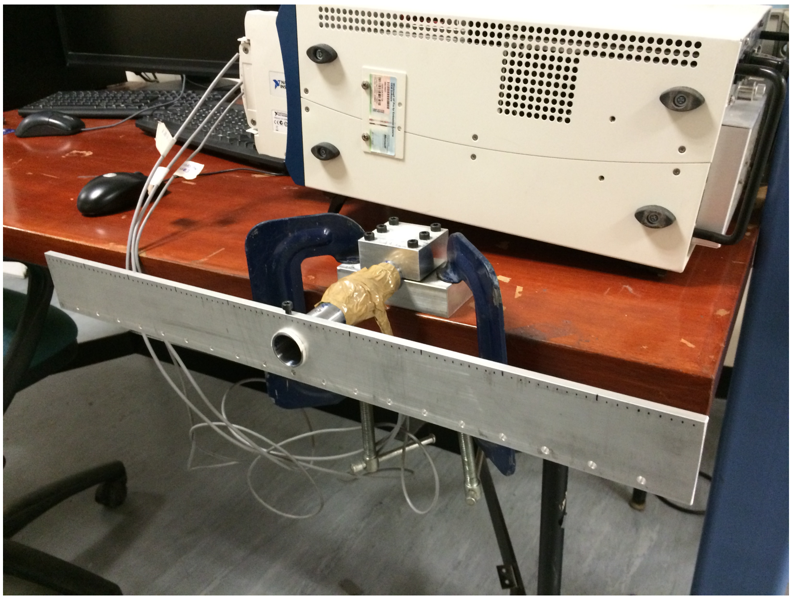

Figure 5.24: Set-up of the static calibration of the load cell.

The matrices M_1 and M_2 together with the calibration graph indicate the similar behaviour of two load cells regarding the linear relationship between the loads and moment and the bridge voltages. The cross-talk between Bridges 1 and 2 was about 10% which was mainly due to the clamping mechanism supporting the load cells.

5.4.3 Measurement with Strain-gauge-based Load Cell

During the static wind tunnel tests, the load cells were rigidly attached to the bridge (Figure 5.5); their orientation angles were fixed relatively to the bridge. In addition, the load cells only measure forces and moments with respect to their own coordinate systems (Figure 5.23); therefore, a correction must be implemented in case of non-zero angles of attack. With the position of the load cell relative to the general coordinate system of the wind tunnel as shown in Figure 5.25, the forces and moment acting on the model at the angle of attack α are given by

$$F_D = (-F_{x1} + F_{x2}) \cos\alpha + (F_{z1} + F_{z2}) \sin\alpha, \tag{5.11}$$

$$F_L = -(-F_{x1} + F_{x2}) \sin\alpha + (F_{z1} + F_{z2}) \cos\alpha, \tag{5.12}$$

$$M = -M_{y1} + M_{y2}. \tag{5.13}$$

A similar set-up as the calibration including the hardware configuration and the sampling frequency of 500 Hz was applied. It should be noticed that reference bridge voltages at zero wind speed were recorded to eliminate the self-weight of the model and any additional strains induced by the clamping mechanism.

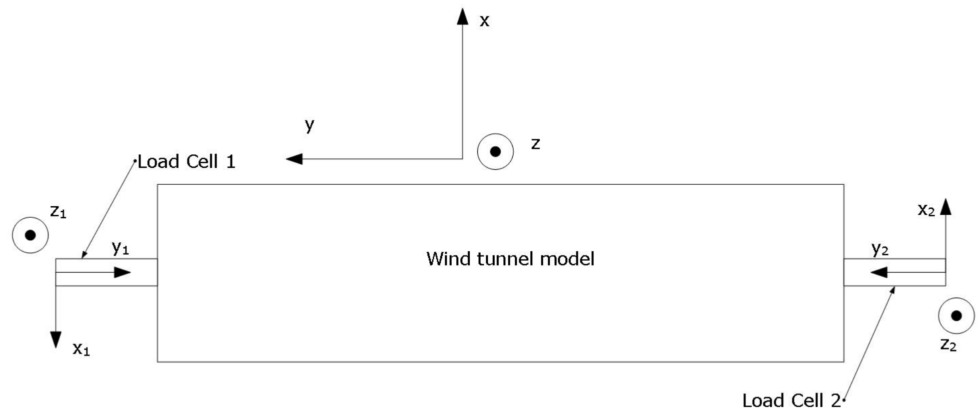

Figure 5.25: Schematic diagram of the set-up of the load cells and the wind tunnel model.

Preliminary wind tunnel static tests using these strain-gauge based load cells revealed two critical issues relating to their design and usability. The first one was found to relate to the air temperature inside the wind tunnel. Continuous operation of the wind tunnel would lead to an increase in the air temperature and, together with wind-induced cooling effects, it could change the resistance of strain gauges, resulting in a drift in output voltages. The drift rate was found to vary depending on the ambient temperature and wind speeds; a method to compensate or correct the temperature-induced drift was impossible to propose. Also, the strain-gauge based force measuring system was so flexible that there existed interference with output voltages at the wind speed of 6 to $8\,\mathrm{m\,s^{-1}}$. These two issues therefore limited the practicability of this approach.

5.5 FORCE AND MOMENT MEASUREMENT - PIEZOELECTRIC APPROACH

The strain-gauge based load cells were found to possess strong dependence on temperature, largely limiting their usability. This effect was vital since, during operation, the temperature inside the wind tunnel could vary significantly depending on the ambient temperature. Knowing this limitation, a new load cell design was proposed utilising piezoelectric sensors.

5.5.1 Design of Piezoelectric-based Load Cell

Similar to the strain-gauge based load cells, the piezoelectric-based load cells had to satisfy the three criteria listed in Section 5.4.1. Piezoelectric sensors are advantageous thanks to their rigidity; therefore, load cells utilising piezoelectric sensors possess high stiffness limiting the resonant effects caused by the force measuring system. However, appropriate solutions were required to overcome difficulties relating to small forces and the drift behaviour.

Piezoelectric sensors are produced by many manufacturers and range from single-component sensors to six-component sensors. Two six-component sensors could be an ideal solution; however, their practicability for further application in this wind tunnel facility was very limited. Instead, six single-component compression sensors 9313AA1 offered by KISTLER were selected to construct two three-component piezoelectric-based load cells supporting either side of the wind tunnel model. Even though these sensors are classified as compression sensors, with pre-loads, they are capable of measuring both tension or compressive forces acting normal to the surface of sensors. Moreover, these sensors can be severely damaged if they are subject to shear forces acting tangential to their surfaces; this becomes another requirement for the design of the load cells. Since the selected sensors only measure normal forces, on one load cell, three of them were arranged as shown schematically in Figure 5.26a. Sensor 3 was located at the back and oriented in the horizontal direction, and was responsible for measuring any compressive force induced by the horizontal force, i.e. the drag force. Sensors 1 and 2, on the other hand, were oriented in the vertical direction so that they could measure any compressive forces induced by the vertical force, i.e. the lift force. Also, by being separated by a distance δ, these two sensors were also capable of measuring the vertical forces induced by the moment around the centre of gravity; the closer the better, in terms of measuring resolution but the more difficult, in terms of manufacturing and assembling the load cells. More importantly, this design led to another issue which was the cross-talk between three sensors. In detail, any vertical forces measured by Sensors 1 and 2 simultaneously acted as shear forces on Sensor 3; this cross-talk effect could damage Sensor 3 and led to inaccurate measurement of the vertical forces. Similar influence could be found when measuring the horizontal forces. Using pin-pin-supported shear links between the loading block and each sensor was proposed to eliminate any shear forces being transferred to sensors. Pin supports for shear links were facilitated by the use of 638/4ZZ-SFK deep groove ball bearings, which helped to reduce losses in force measurement due to friction.

Among the three forces and moments to be measured, which were the lift force, drag force and moment around the centre of gravity, the first component posed most challenges. At the angle of attack $0°$, the mean lift coefficient was expected to equal 0 and, based on literature, the root-mean-squared (rms) value of the lift coefficient was found to be approximately 0.08 (Schewe, 2013). At the wind speed of $4\,\mathrm{m\,s^{-1}}$, the rms value of the lift force acting on the wind tunnel model was calculated to be $0.47\,\mathrm{N}$; therefore, each of the four vertical sensors only measured $0.12\,\mathrm{N}$. This value fell in the lower measurement range of most sensors and it implied a poor resolution when measuring vertical forces. To overcome this issue, a mechanical amplifier was proposed as shown in Figure 5.26b where the tube acted as a cantilever. One side of the tube was fixed to a GE35TXE2LS-SFK maintenance-free spherical radial plain bearing acting as a pivot for the tube and facilitating three degree-of-freedom rotation with minimum loss due to

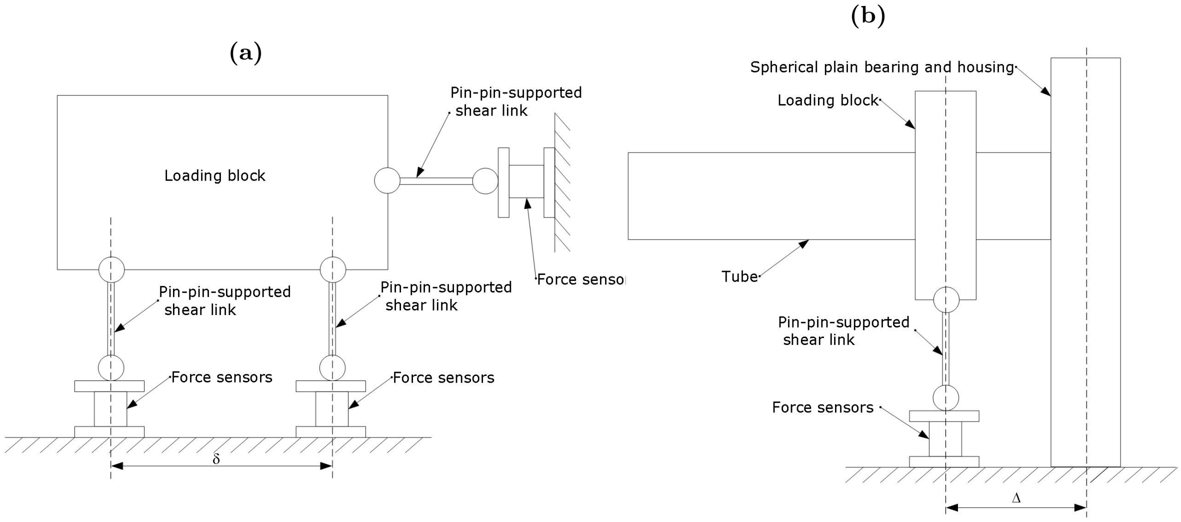

Figure 5.26: Schematics describing (a) the arrangement of three force sensors in one load cell and (b) the cantilever mechanism.

friction. The other side of the tube was attached to the model using the similar clamping mechanism as the one was used with the strain-gauge based load cells. By varying the overall length of the tube and the distance Δ between the pivot point, i.e. the centre of the spherical plain bearing, and the loading block which was rigidly clamped to the tube, different amplifying factors could be achieved. However, an increase in the length of the tube would lead to a reduction in the stiffness and rigidity of the overall force measurement system. Therefore, a parametric study needed to be conducted to determine the balance between the amplifying factor, the overall rigidity and the ease of assembly.

Structurally, the force measuring system could be simplified as a cantilever beam of the length L; at one end, it was simply supported at two points separated by a distance Δ while half of the weight of the model acted on the other end. The natural frequency f_n for the first mode of this structure was calculated to be

$$f_n = \frac{1}{2\pi}\sqrt{\frac{3\pi}{M}\left[R^4 - (R-t)^4\right] E \, \frac{\Delta}{L(L-\Delta)(L^2 - 2L\Delta - 2\Delta^2)}}. \tag{5.14}$$

Here, $M = 38.5\,\mathrm{kg}$ is the total mass of the model including sensors located inside the void; $R = 17.5\,\mathrm{mm}$ and $t = 3\,\mathrm{mm}$ are the outer diameter and the wall thickness of the tube. To improve the rigidity of the design, a steel tube was selected; thus the Young's modulus E is 200 GPa. Figure 5.27 shows the dependence of the natural frequency f_n on the dimensions Δ and L. As expected, an increase in L significantly reduced the stiffness of the measuring system; as for Δ, during the range from 20 mm to 40 mm, an increase in Δ helped to stiffen the system. Taking into account the requirement of the natural frequency of the system so that the influence on the force measurement would be minimum and of the space constraint, the length $L = 120\,\mathrm{mm}$ and the separation $\Delta = 30\,\mathrm{mm}$ were selected; it yielded the

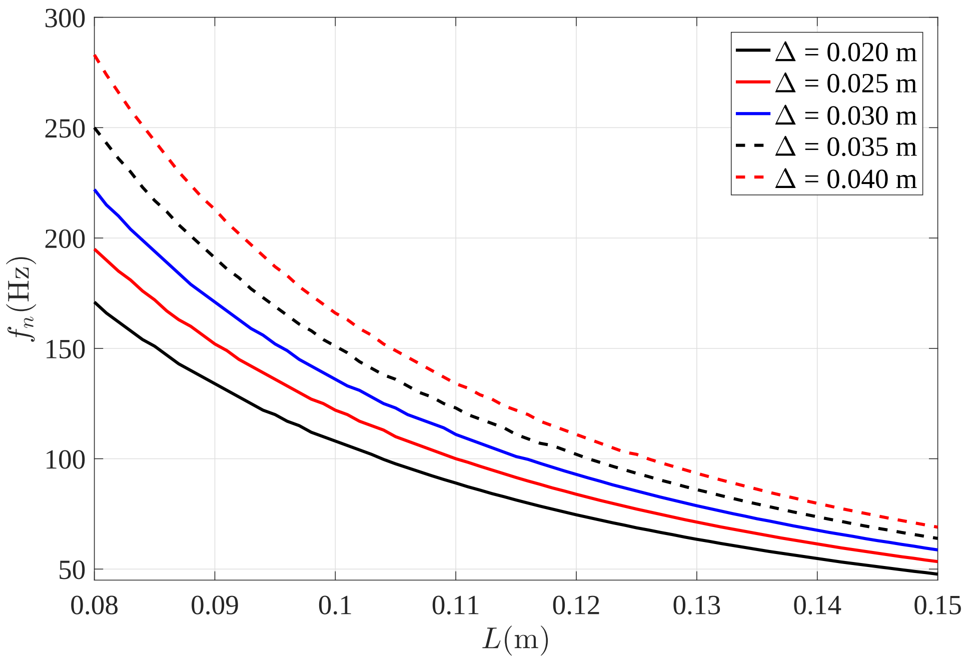

Figure 5.27: Results of the optimisation study of the piezoelectric load cells.

natural frequency f_n of 95 Hz approximately and an amplifying factor of 4. It should be noticed that these results were applicable in the x and z directions since the force measuring system was structurally similar in both directions. Also, the length of the tube needed to be corrected by the thickness of the spherical plain bearing which was 30 mm as well as the clamping mechanism located inside the model. Assuming the length L of the simplified beam was from the centre of the spherical bearing to the centre of the clamping block inside the model, the length of the steel tube was 157.5 mm.

The separation δ between Sensors 1 and 2 underneath the loading block was selected to be 50 mm, which allowed a good resolution when measuring the moment around the centre of gravity and eased assembly of the load cells. Moreover, with the amplifying factor of 4, each shear link of the vertical force sensors was acted by about 400 N; therefore, their design needed to be carefully checked to ensure the load cells could hold the wind tunnel model. Using steel having the yielding strength of 250 GPa, the required cross-sectional area of each vertical shear link was found to be 3.2 mm^2 or equivalent to a bar of 1.43 mm diameter.

Knowing the requirements of all key dimensions, the design of two load cells is shown in Section C.3 in Appendix C. The spherical plain bearing was fitted inside a housing while the steel tube was connected to the spherical plain bearing by a fitting mechanism comprising two collars. The loading block included two pieces which were connected to the steel tube by a clamping mechanism; loosening this clamping would facilitate the rotation of the model thanks to a spherical plain bearing at either end, which allowed different angles of attack to be set up. Each force sensor was placed between two loading plates and they were connected to the bottom part of the loading block via the shear links. An angle support was provided behind the loading block to offer stable support for the horizontal sensors; the distance between them could be adjustable during the assembly. M8 bolts were used to rigidly connect the load cells to the aluminium frame.

5.5.2 Calibration of Piezoelectric-based Load Cell

After being manufactured, some preliminary tests have found that outputs from these two load cells were susceptible to even a very small geometrical change. Therefore, it was decided that the calibration of the piezoelectric load cells was carried out inside the wind tunnel and after being connected to the wind tunnel model. Since any geometrical changes could lead to significant variation in outputs from load cells, the calibration process was repeated when load cells were subjected to changes in geometry or when the static tests were repeated for different angles of attack.

The set up of the load cells and the model inside the wind tunnel is shown in Figure 5.28. At first, both load cells were attached to the model using the clamping bocks located inside the model; then the whole thing was mounted onto the aluminium frame and rigidly connected using M8 bolts. During the installation, it was important to ensure that the loading blocks were aligned vertically; this could be confirmed by checking the distance between the loading block and the housing of the spherical bearing at a number of points. If the loading blocks were not properly set up, the shear forces could damage the force sensors underneath.

The data acquisition system used in the calibration of the piezoelectric base load cells is sketched in Figure 5.29. The charge output from an individual force sensor was transferred to a single channel of the multi-channel charge amplifier KISTLER 5080A. Each channel of the charge amplifier was set up corresponding to the connected force sensor. With the input settings, the charge signal was converted into the analogue signal, which was then fed into two A/D converters (NI-6009 and NI-9215) before being captured by the computer at the sampling frequency of 500 Hz.

The force measuring system comprising two load cells as designed here was capable of measuring all force and moment components except the force component F_y. However, for the application of the static wind tunnel tests, it was important to measure only the drag force, lift force and moment about the centre of gravity, which were corresponding to the force and moment components F_x, F_z and M_y. Therefore, in order to simplify the calibration process, the force outputs from individual force sensor F_s

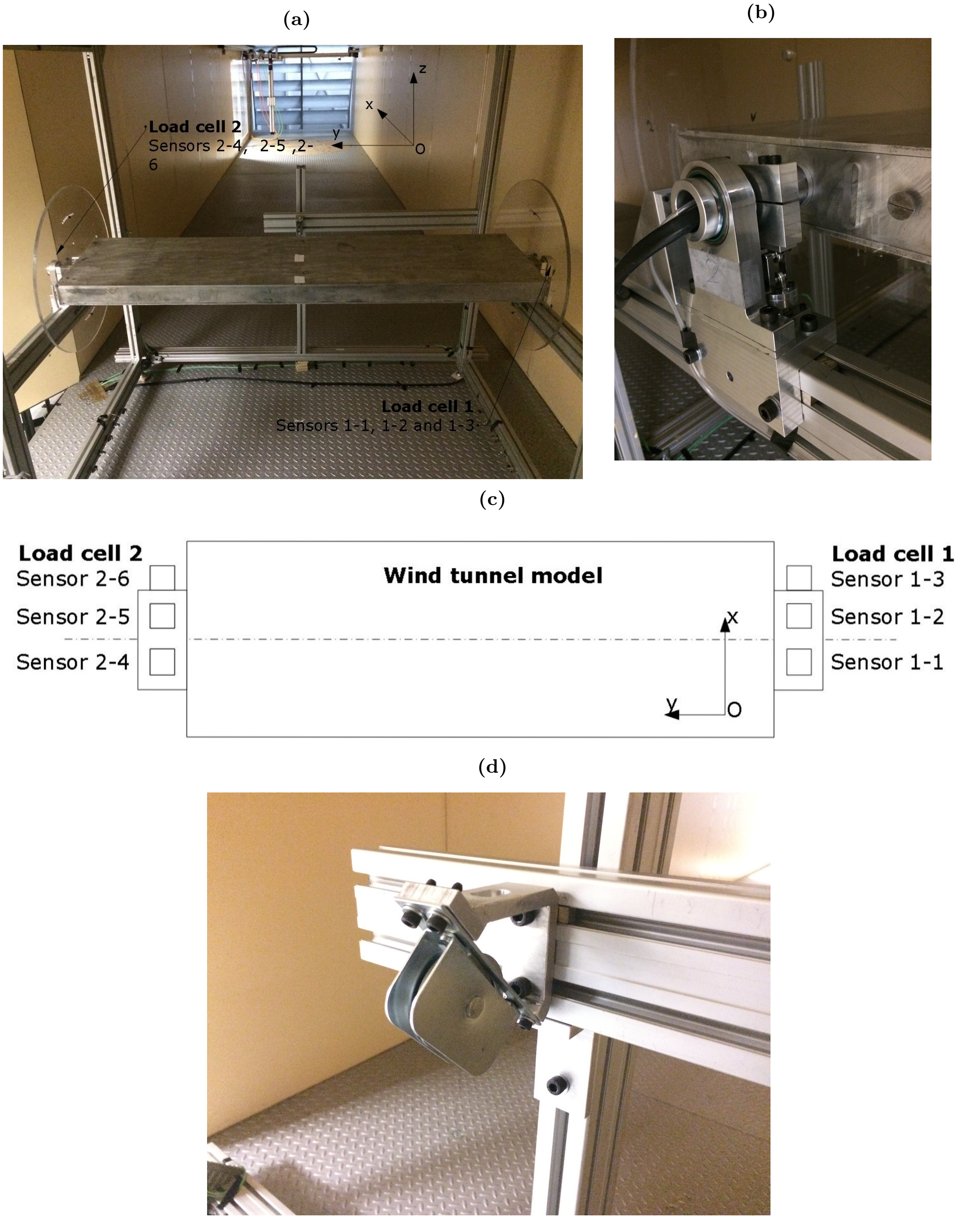

Figure 5.28: (a) Arrangement of piezoelectric load cells and the wind tunnel model inside the wind tunnel and (b) close view of the piezoelectric load cell 2; (c) a schematic view of this arrangement together with the numbering system assigned for the force measuring system; (d) the pulley system was attached to the aluminium frame to facilitate the calibration of the loading case $[0, F_x, 0]$.

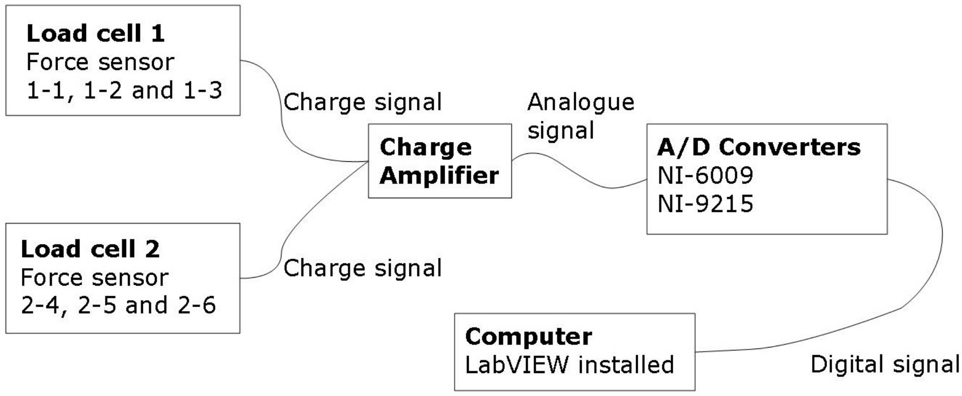

Figure 5.29: Schematics of the data acquisition system used for the piezoelectric load cells.

were converted into three force channels F_c corresponding to three force and moment components F_z, F_x and M_y using the following equation

$$\text{Lift force} \quad F_{c1} = F_{s,1-1} + F_{s,1-2} + F_{s,2-4} + F_{s,2-5}, \tag{5.15}$$

$$\text{Drag force} \quad F_{c2} = F_{s,1-3} + F_{s,2-6}, \tag{5.16}$$

$$\text{Moment} \quad F_{c3} = (F_{s,1-1} + F_{s,2-4}) - (F_{s,1-2} + F_{s,2-5}). \tag{5.17}$$

Here, $F_{s,i-j}$ is the force output from the sensor j of the load cell i; the numbering system was explained in Figure 5.28c. This approach was reasonable since, based on the design of the load cell, the sensors underneath the loading block, i.e. sensors 1-1, 1-2, 2-4 and 2-5, mostly measured the lift force while the sensors behind the loading block, i.e. sensors 1-3 and 2-6, measured the drag force. The difference between the pair of sensors 1-1 and 2-4 and of sensors 1-2 and 2-5 largely represented effects of the moment.

Using this approach, the calibration process was simplified to three loading cases only. For the first loading case, weights were placed on the centre of top surface to represent the lift force only, i.e. $[-F_z, 0, 0]$. In the second loading case, the loading point was shifted to the leading edge by a distance of $b = 161\,\mathrm{mm}$ to replicate the loading condition of $[-F_z, 0, -M_y]$. The third loading case utilised the arrangement as shown in Figure 5.28d which involved a pulley system replicating the drag force, i.e. $[0, F_x, 0]$. During each loading case, different loading values were applied by adding weight to a hanger placed at the designated loading points; each of the weights had a self-weight of 0.49 N. The loading value was increased from 0.49 to 3.9 N in an increment of 0.49 N and then from 3.9 N to 6.87 N in an increment of 0.98 N; this allowed the linearity of the force measuring system to be verified. The relationship between the added weights and the force and moment components were

$$F_x = nw, \tag{5.18}$$

$$F_z = nw, \tag{5.19}$$

$$M_y = \left(b\,\cos\alpha + \frac{nh}{2}\,\sin\alpha\right) nw, \tag{5.20}$$

where n is the number of weight present on the hanger, each of which has a self-weight w and a thickness of h; α is the angle of attack.

A typical output of a force channel is shown in Figure 5.30 where two characteristics of force sensors were visible which were the offset and the drift of the signal. These two features impaired the accuracy and usability of the signals. A correction was proposed where three parts of the signal were captured including no loading, loading and unloading conditions corresponding to the *red*, *green* and *yellow* portions of the signal as illustrated in Figure 5.30a. The green portion of the signal needed to be corrected for the offset and the drift. The offset issue was eliminated by subtracting the *green* signal by the mean value of the last 10% of the *red* signal; this can be shown by the difference between the raw uncorrected data (*black* signal in Figure 5.30c) and the offset-corrected data (*red* signal in 5.30c). After that, a linear regression was performed on the offset-corrected signal to evaluate the gradient or the drift rate, from which the drift over time could be corrected (Figure 5.30b). As can be seen in Figure 5.30c, the corrected data in the colour *blue* possesses a constant mean and could be used for further analysis. For the purpose of the calibration process, the mean values of the corrected signals were used to evaluate the 3×3 transformation matrix M.

Results of the calibration process at the angle of attack $\alpha = 0°$ are plotted in Figure 5.31 showing the dependence between the values of the three force channels and the loading values. Two criteria were selected to evaluate the force measuring system, which were the linearity and the cross-talk between force channels. It was obvious that the force channels 2 and 3 which were responsible for measuring the lift force and moment possessed very good linearity and low cross-talk between them. More issues however were found when performing the calibration for the force component F_x or, in other words, when the force channel 1 was activated. At low loading values, the linearity of the force channel 1 was low; this limitation could have resulted because the force sensors behind the loading blocks were not preloaded, reducing their performance particularly at low loads. In addition, the force channels 1 and 2 exhibited large cross-talk; this was caused by a limitation in the design. As can be seen in the drawings attached in Section C.3, the centre of the force sensors behind the loading blocks was not aligned with the centre of the tube; a drag force or a non-zero force component F_x simultaneously caused compression forces to act on the force sensors behind the loading blocks and uplift forces to act on the force sensors underneath

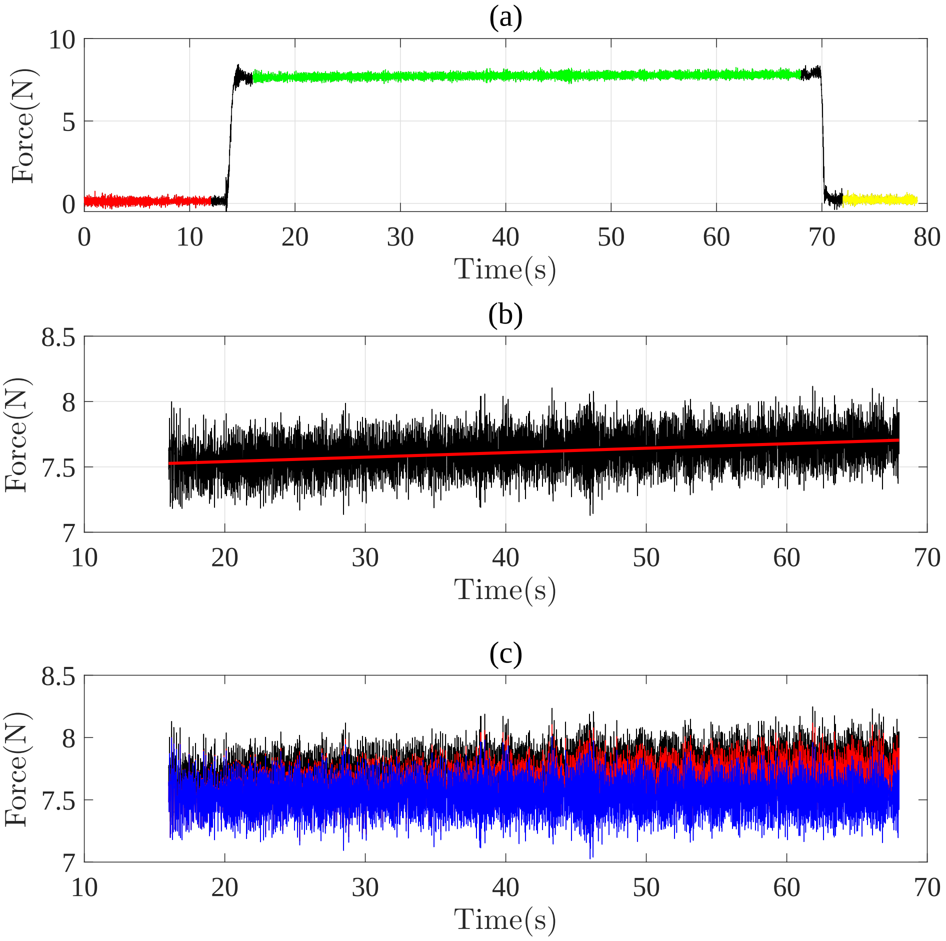

Figure 5.30: (a) A force output from the force channel 1 including three portions; the *green* portion needed to be corrected for the drift as shown in (b) and offset; the final result of these two corrections is illustrated in (c).

the loading blocks. Therefore, the behaviour of the force channels 1 and 2 was observed to be opposite and largely dependent on each other as evidenced in Figure 5.31c.

At each loading value, the transformation matrix M was evaluated; in total, there would be 10 matrices M. The issue relating the cross-talk would not impair their usability; however, knowing that the linearity of the force channel 1 was poor at low loading values, the transformation matrices calculated at those loading values were discarded. Using 6 to 7 remaining transformation matrices M, the averaged matrix M was calculated together with 95% confidence intervals for each element, based on the normal distribution. Typically, the value of the averaged transformation matrix M for the angle of attack 0° was

$$M = \begin{bmatrix} -6.8069 \times 10^{-1} & -1.3716 & 1.1974 \times 10^{-2} \\ -3.8561 \times 10^{-1} & 4.3333 & -1.7400 \times 10^{-2} \\ -7.9376 \times 10^{-3} & 5.9089 \times 10^{-4} & -1.2563 \times 10^{-1} \end{bmatrix},$$

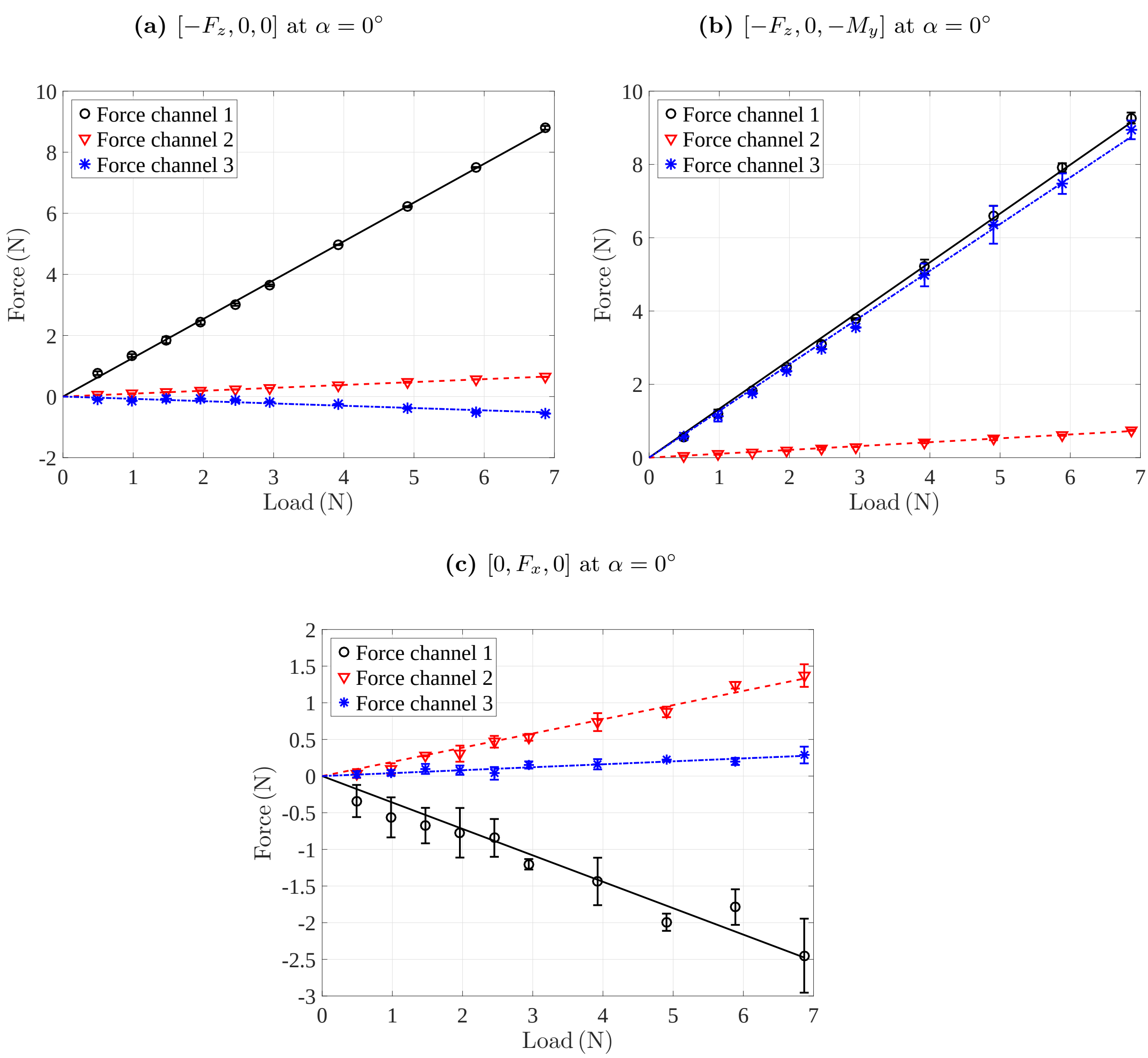

Figure 5.31: Graphs showing the dependence of outputs from force channels on the loading values during the calibration; the angle of attack $\alpha = 0°$.

and the matrix comprising the 95% confidence interval of each element was

$$M_{95\%} = \begin{bmatrix} 1.2026 \times 10^{-2} & 1.7149 \times 10^{-1} & 1.1969 \times 10^{-2} \\ 2.5729 \times 10^{-2} & 2.4546 \times 10^{-1} & 1.3111 \times 10^{-2} \\ 1.0103 \times 10^{-3} & 4.8638 \times 10^{-3} & 4.2609 \times 10^{-3} \end{bmatrix}.$$

A pair of matrices M and $M_{95\%}$ were found for each value of the angle of attack; the matrices $M_{95\%}$ were used to assess errors of the force measurement. Three rows of the matrix M represented the contribution of each force channel on the lift force F_z, drag force F_x and moment about the centre of gravity M_y respectively. Except for the lift force, the drag force and the moment were mostly contributed by the force channels 2 and 3 respectively as per the design; therefore, the diagonal elements M_{22} and M_{33} were significantly larger than the others on the same row and possessed smaller errors which were less than

5%. Since there was relatively strong cross-talk between the force channels 1 and 2, the elements M_{11} and M_{12} were relatively comparable, indicating similar contributions of the force channels 1 and 2 to the lift force. The error associated to the element M_{12} was about 15%, representing the issues observed when performing the calibration for the force component F_x. Therefore, based on this error behaviour, it was expected that the lift force would have larger errors than the other components.

Other calibration results at the remaining angles of attack, including the transformation matrices M, are summarised in Appendix C. Slight differences existed between the transformation matrix M for each angle of attack; it emphasised the effect of the geometry of the load cells on their performance and the need to recalibrate the load cells if their geometrical arrangement was varied.

5.5.3 Measurement with Piezoelectric-based Load Cell

Measuring forces and moment acting on the wind tunnel model using these piezoelectric-based load cells was conducted with similar hardware and software settings; the pulley system was removed from the wind tunnel before the static tests to prevent interference on the flow field.

The calibration results partly discussed in Section 5.5.2 showed the drift behaviour of force sensors was linear over the sampling duration from 1 to 2 minutes; a long sampling duration potentially brought about downsides of the non-linear drift behaviour. Therefore, the sampling process during the force measurement was kept within this time-frame; it consisted of two parts which was wind-off data and wind-on data including an approximately 5 s duration in which the fan in the wind tunnel was accelerating. The portion of stable data when the fan had already reached its desired speed was extracted for further analysis after being corrected for offset and drift using an approach similar to that as described in Section 5.5.2. This sampling process was repeated five times for each wind speed to achieve good accuracy and minimise confidence levels. The time histories of the lift force, $F_L(t)$, the drag force, $F_D(t)$ and the moment about the centre of gravity, $M(t)$, were achieved by multiplying the transformation matrix M by the time histories of the outputs of three force channels as

$$\left\{ \begin{array}{c} F_L(t) \\ \\ F_D(t) \\ \\ M(t) \end{array} \right\} = [M] \left\{ \begin{array}{c} F_{c1}(t) \\ \\ F_{c2}(t) \\ \\ F_{c3}(t) \end{array} \right\}. \tag{5.21}$$

Similarly, the time-histories of the absolute error of the lift force $\Delta F_L(t)$, of the drag force $\Delta F_D(t)$ and of the moment $\Delta M(t)$ was calculated using the matrix $M_{95\%}$ as

$$\left\{ \begin{array}{c} \Delta F_L(t) \\ \\ \Delta F_D(t) \\ \\ \Delta M(t) \end{array} \right\} = [M_{95\%}] \left\{ \begin{array}{c} F_{c1}(t) \\ \\ F_{c2}(t) \\ \\ F_{c3}(t) \end{array} \right\}. \tag{5.22}$$

Then, the time averaged lift coefficient, C_L, the time-averaged drag coefficient, C_D, the time-averaged moment coefficient, C_M, and the standard deviation of the time varying lift coefficient, C'_L, together with their associated absolute errors were calculated as

$$\text{Coefficients} \quad C_L = \frac{\bar{F}_L(t)}{\frac{1}{2}\rho U^2 BL}, \tag{5.23}$$

$$C_D = \frac{\bar{F}_D(t)}{\frac{1}{2}\rho U^2 BL}, \tag{5.24}$$

$$C_M = \frac{\bar{M}(t)}{\frac{1}{2}\rho U^2 B^2 L}, \tag{5.25}$$

$$C'_L = \frac{\tilde{F}_L(t)}{\frac{1}{2}\rho U^2 BL}, \tag{5.26}$$

$$\text{Absolute errors} \quad \Delta C_L = \frac{\overline{\Delta F}_L(t)}{\frac{1}{2}\rho U^2 BL}, \tag{5.27}$$

$$\Delta C_D = \frac{\overline{\Delta F}_D(t)}{\frac{1}{2}\rho U^2 BL}, \tag{5.28}$$

$$\Delta C_M = \frac{\overline{\Delta M}(t)}{\frac{1}{2}\rho U^2 B^2 L}, \tag{5.29}$$

$$\Delta C'_L \approx 2\Delta C_L. \tag{5.30}$$

$$\tag{5.31}$$

The force and moment measured by the two load cells however contained two issues which needed to be corrected. The first one was the blockage of the wind tunnel. Due to the confined space of the working section of the wind tunnel, the presence of the wind tunnel model as well as the supporting aluminium frames restricted the area the wind passed through. This restriction effectively increased the wind speed and reduced the pressure around the model. In addition, the wake region behind the model was narrowed due to a reduction in pressure and suppression effects induced from shear layers. Roshko (1961) proposed a blockage-correction method based on aerodynamics of a circular cylinder; this method was recently applied by Schewe (2013) in a case of a 5:1 rectangular cylinder. Using the subscript u to denote the actual coefficients directly obtained the load cells, the blockage-corrected coefficients were given by

$$C_L = C_{L,u}\left(1 - \frac{\pi^2}{48}\beta^2 - \frac{\pi^2}{6}\beta^2 - \frac{C_{D,u}}{2}\beta\right), \tag{5.32}$$

$$C_D = C_{D,u}\left(1 - \frac{\pi^2}{6}\beta^2 - \frac{C_{D,u}}{2}\beta\right), \tag{5.33}$$

$$C_M = C_{M,u}\left(1 - \frac{\pi^2}{6}\beta^2 - \frac{C_{D,u}}{2}\beta\right). \tag{5.34}$$

$$\tag{5.35}$$

Here, β is called the blockage ratio including effects resulted from the wind tunnel model, the end plates, the tube and and the aluminium frame. The blockage ratio β varied with angle of attack α and was given by

$$\beta = \frac{A_1 + L(D\cos\alpha + B\sin\alpha)}{WH}, \tag{5.36}$$

where $W = 2.4\,\mathrm{m}$ and $H = 1.8\,\mathrm{m}$ is the width and height of the cross section of the wind tunnel, $A_1 = 0.3433\,\mathrm{m}^2$ is the total frontal area of the end plates, the tubes and the aluminium frame, $L = 1.6\,\mathrm{m}$ is the length of the wind tunnel model having the cross section of $B = 0.378\,\mathrm{m}$ by $D = 0.078\,\mathrm{m}$. Additionally, the fact that the end plates and the tubes were exposed to the wind implied that two load cells inherently measured wind forces and moment acting on them. Due to the symmetry of both of the end plates and the tubes, this influence did not alter the time-averaged lift and moment coefficients. On the other hand, the time-averaged drag coefficient was increased; therefore the blockage-corrected time-averaged drag coefficient calculated by Equation 5.33 needed to be multiplied by the obstruction ratio β' to eliminate this effect. The obstruction ratio β' also varied with the angle of attack α and is defined as

$$\beta' = \frac{L(D\cos\alpha + B\sin\alpha)}{L(D\cos\alpha + B\sin\alpha) + A_2}, \tag{5.37}$$

where $A_2 = 1.4845 \times 10^{-2}\,\mathrm{m}^2$ is the total frontal area of the end plates and the tubes.

5.6 PRESSURE MEASUREMENT

The surface pressure distribution in this project was achieved by the use of 28 pressure transducers HCLA02X5DB from SensorTechnics. They are four-pin diaphragm-type piezoresistive transducers requiring a supply voltage of 5 V provided via the NI PXIe 6345. The range of their analogue output is from 0.25 to 4.25 V, which was sampled at a frequency of 500 Hz.

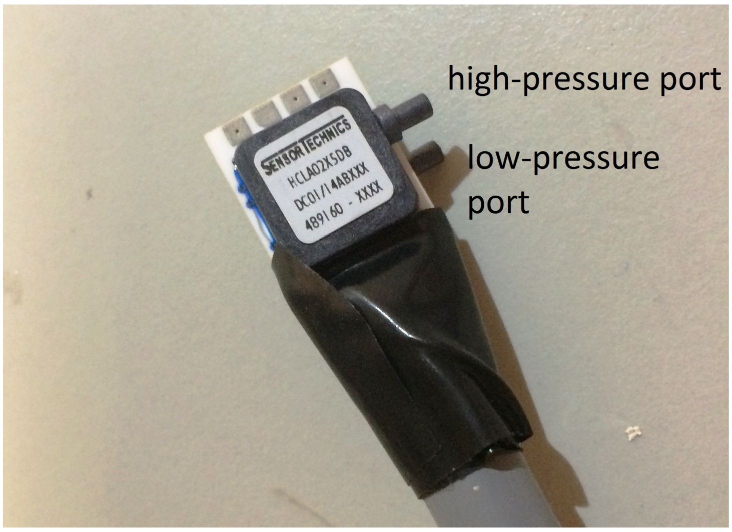

Figure 5.32: The HCLA02X5DB pressure transducer contains two pressure ports.

Effectively, these transducers measured pressure relative to a pressure datum which was provided by a reference box situated inside the sectional model (Figure 5.33). The pressure of the box was kept constant and equal to the static pressure of the wind tunnel by connecting it to the static port of the pitot-static tube. The low-pressure port of each transducer was connected to the reference box while the high-pressure port was connected to the pressure tap. All connections were achieved using teflon tubes. The pressure measured by the transducer is then calculated as

$$p = \frac{500}{4}\left(E - E_{\mathrm{ref}}\right), \tag{5.38}$$

where $500/4\,\mathrm{Pa}\mathrm{V}^{-1}$ is the conversion rate specified by the manufacturer and E_{ref} is the output voltages from the transducer at the wind off condition.

During each wind tunnel static and dynamic test, two arrangements of the pressure transducers were used for different purposes. In the first arrangement, 16 pressure transducers were connected to pressure taps on the pressure array 4 as shown in Figure 5.4a; this set-up allowed the surface pressure distribution around the model to be measured. As for the second arrangement, all 28 pressure transducers were distributed across 7 pressure arrays at four stream-wise position as indicated in Figure 5.4b. This facilitated simultaneous pressure measurement across the span-wise length of the model, from which the span-wise correlation of the surface pressure at these positions was calculated.

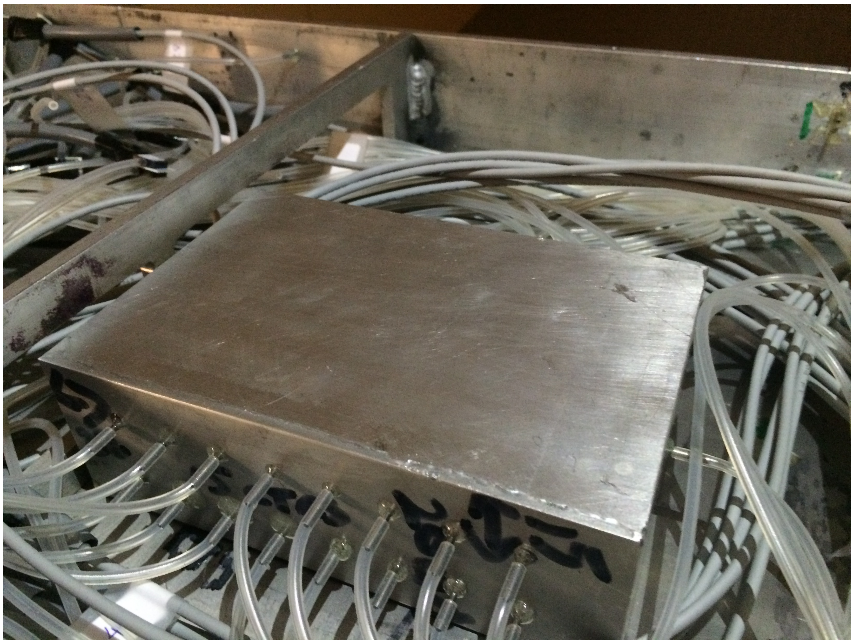

Figure 5.33: The reference pressure box with taps to provide the reference pressure to all transducers.

5.7 DISPLACEMENT MEASUREMENT

The displacement of the wind tunnel model during dynamic wind tunnel tests was measured indirectly using accelerometers. In total, there were four accelerometers mounted at four corners of the wind tunnel model using the mounting mechanism shown in Figure 5.8; each accelerometer was numbered as shown in Figure 5.34. Instead of using the piezoelectric accelerometers, the MEMS accelerometers were applied to accurately measure the low-frequency displacement of the wind tunnel model. 2-axis MEMS accelerometers ADXL203 offered by Analog Devices were selected; these accelerometers were manufactured on printed circuit boards (PCB) with some capacitors and resistors installed, offering 50 Hz low pass filters for the 5 V power supply as well as the output signals. They were connected to the NI PXIe 6345 which provided the 5 V supply voltage and sampled the output voltages at the sampling frequency of 500 Hz.

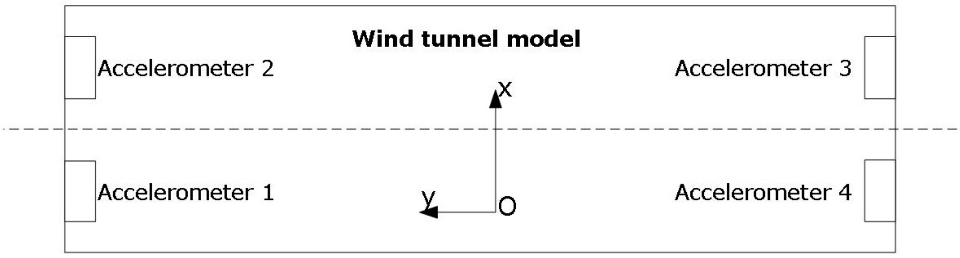

Figure 5.34: Schematic arrangement of accelerometers.

The voltage outputs from these accelerometers were converted to acceleration by multiplying with conversion rates, which were stated in specification sheets. However, to accurately identify these conversion rates, each accelerometer needed to be calibrated. Thanks to the characteristics of their outputs, which were true DC outputs, these accelerometers were capable of measuring the acceleration due to gravity. By measuring the output voltages V_+ and V_- corresponding to the negative and positive acceleration due to gravity g and $-g$ respectively, the conversion rate was calculated as $2g/(V_+ - V_-)$. The calibration of these accelerometers were conducted before the dynamic wind tunnel tests.

It should be noticed that, if the wind tunnel model underwent a pure heaving motion, responses measured at any points on the model were in phase together. On the other hand, under a pure pitching motion, responses measured at two points on two opposite sides of the centre line of the model, i.e. the line $y - y$, were out of phase with each other. Therefore by mounting four accelerometers at four corners of the model, it was possible to decouple the heaving and pitching acceleration. Using the numbering system as described in Figure 5.34, the heaving acceleration $\ddot{z}(t)$ of the wind tunnel model was calculated

$$\ddot{z}(t) = \frac{r_1 V_1(t) + r_2 V_2(t) + r_3 V_3(t) + r_4 V_4(t)}{4}, \tag{5.39}$$

while the pitching angular acceleration $\ddot{\alpha}(t)$ of the model was defined as

$$\ddot{\alpha}(t) = \frac{(r_1 V_1(t) + r_4 V_4(t)) - (r_2 V_2(t) + r_3 V_3(t))}{4 l_{\text{arm}}}, \tag{5.40}$$

where r_i and V_i is the conversion rate and the output voltage of the accelerometer i, $l_{\text{arm}} = 0.175\,\text{m}$ is the distance between accelerometer holders and the centre line of the model.

The time histories of acceleration would allow further analysis including spectral and phase analysis. In order to convert acceleration into displacement of the model, it was possible to perform the time integration using the time histories of acceleration. However, this approach would make any errors inclusive in acceleration to propagate and led to a large drift in time histories of displacement after integration. The frequency-domain analysis was therefore preferable. Knowing the spectrum of acceleration $S_{\ddot{z}}(f)$, the spectrum of displacement $S_z(f)$ is calculated as

$$S_z(f) = \frac{S_{\ddot{z}}(f)}{8\pi^4 f^4}, \tag{5.41}$$

and the standard deviation of the time varying displacement of the model is then given by

$$z_{rms} = \sqrt{\int_o^\infty S_z(f)\,\mathrm{d}f}. \tag{5.42}$$

5.8 INVESTIGATION OF GRID-GENERATED TURBULENCE

The turbulence in the wind in nature is generated from many sources including buoyancy due to the heating or cooling of the Earth's surface and mechanical effects such as the interference of structures. Its characteristics are dependent on the length- and time-scale of the generating mechanism. Generally, the turbulence is considered to be inhomogeneous and anisotropic.

In most engineering applications, the turbulent wind is normally assumed to be homogeneous where the statistical averaged properties of the wind are independent of position. The homogeneous turbulence can develop into isotropic turbulence due to the effects of the pressure force. Along with the inertial and viscous forces, the pressure force is responsible for the transfer of energy in the turbulent wind from the large-scale eddies to the small-scale eddies – a process known as the energy cascade (Richardson, 1922). The energy of the flow is stored in the form of pressure. Any velocity variations contribute to the pressure fluctuation at one point. The positive pressure fluctuation corresponds to the process of storing energy. This energy will then be released afterwards without any preferred direction. The pressure force thus helps transfer energy from one direction to the others, resulting in an isotropic turbulence.

In this project, the turbulent flow in the wind tunnel was produced by the use of the aluminium grid as described in Section 5.1. The aim of this study is, applying the technique described in Section 5.3, to measure the wind velocity at a number of positions in the along- and across-wind direction in order to investigate the structure and development of the grid-generated turbulence in the wind tunnel. Also, using two grids having different mesh sizes, the effect of the grid's geometry on the generated turbulence was investigated.

5.8.1 Method

The TSI X-wire 1124-T1.5 was used to measure the wind velocity at 12 different position as shown in Figure 5.35. The X-wire was held securely at a distance of 0.9 m above the wind tunnel floor. 40 s records of the output voltages were sampled at the sampling frequency of 1000 Hz. Two orientations of the probe's plane were used in order to compute all three velocity components. The tests were conducted at wind speeds of 2, 4 and 6 $\mathrm{m\,s^{-1}}$; at each wind speed, the turbulence characteristics which are the turbulence intensity of three velocity components I_u, I_v and I_w, the turbulence length scale along the x (streamwise) direction L_u^x, L_v^x and L_w^x and the Reynolds stresses τ_{uu}, τ_{vv}, τ_{ww}, τ_{uv} and τ_{uw} were calculated. The tests were repeated 5 times and the averaged values of all turbulence statistical properties were obtained. Because the v and w velocity components could not be measured simultaneously, the remaining Reynolds stress τ_{vw} was omitted. This process was repeated for two turbulence-generating grids, Grid A and B.

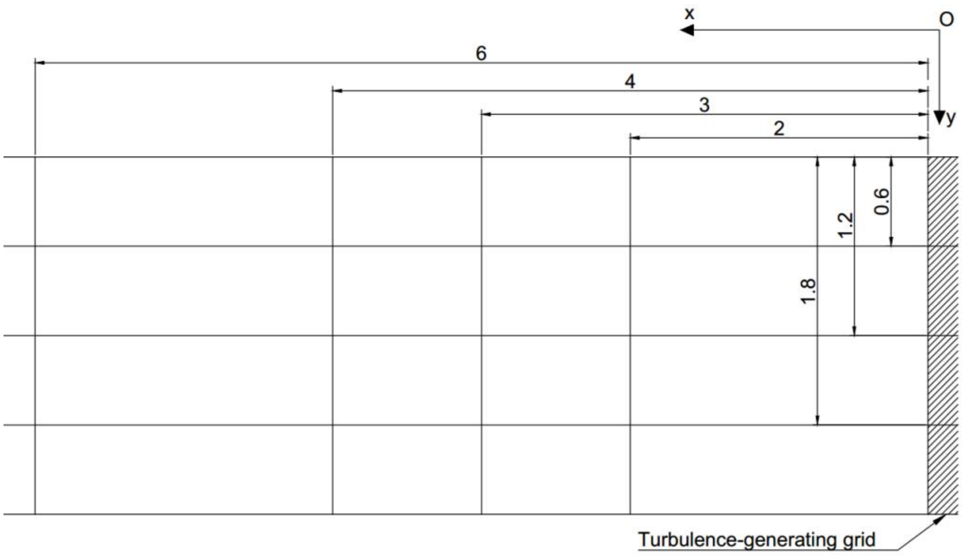

Figure 5.35: Position of the velocity measurement (dimensions are in m).

5.8.2 Results and Discussion

The results from this study showed that the grid-generated turbulence decayed along the wind tunnel as consistent with the observation by Lee (1975) and Mohammed and laRue (1990). In case of the small turbulence-generating grid, i.e. Grid A, as can be seen from Figures 5.36 to 5.38, the turbulence intensities decreased along the wind tunnel; this behaviour was observed for all wind speeds. Interestingly, the turbulence length scales increased along the wind tunnel as illustrated in Figures 5.39 to 5.41. This observation highlighted the nature of the decay process of the grid-generated turbulence. As travelling down the wind tunnel, the energy in the turbulent wind transferred from the large-scaled eddies to the small scaled eddies and finally dissipated via the viscosity. This process gradually reduced the turbulent kinetic energy of the wind, leading to bigger and more slowly rotating eddies and a decrease in the unsteadiness of the wind.

It was noticed that the values of the turbulence intensities and turbulence length scales were very similar at different wind speeds; the percentage difference of the turbulence intensities was less than 1% while that of the turbulence length scale was less then 5%. The characteristics of the grid-generated turbulence therefore were independent of the Reynolds number for the range tested. In addition, the distribution of the turbulence intensities in the spanwise direction was uniform; the percentage difference was less than 1%. As for the turbulence length scale, the variation in the spanwise direction magnified itself as the wind travelled along the tunnel; it could be observed in the distribution of L_x^v. This effect was due to the existence of shear layers along the walls of the wind tunnel. Their influence became more pronounced downstream as the length scale of the most-energy-containing eddies grew further away from the grid. Apart from that, the distribution of other length scales was consistent. Therefore, it was sensible to conclude that the grid-generated turbulence in the wind tunnel was homogeneous and independent of the Reynolds number. The homogeneity was only valid in the crosswind direction since the turbulence experienced a decay process in the along-wind direction.

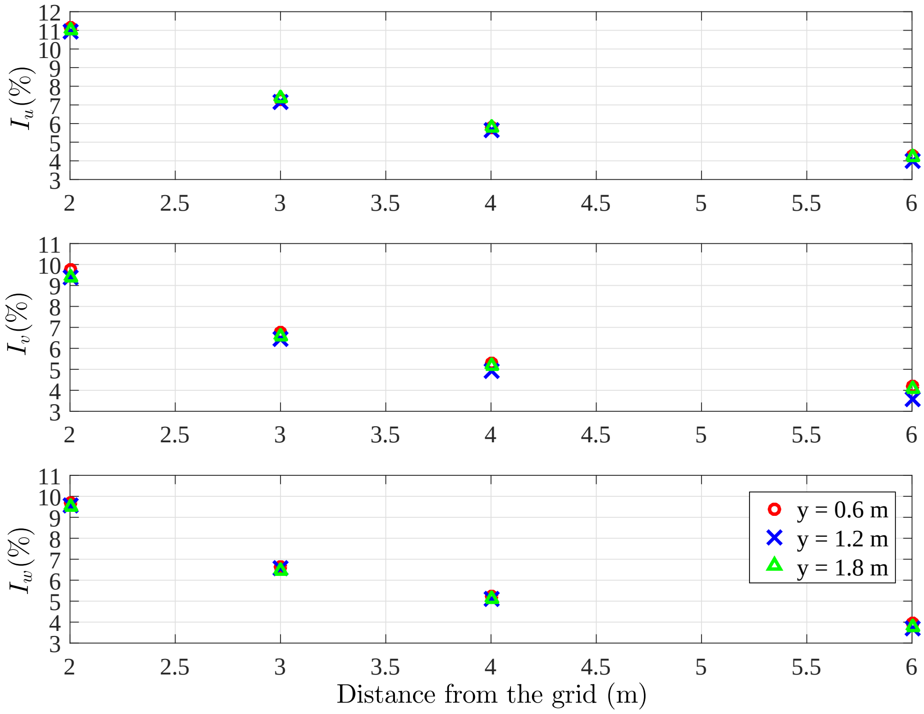

Figure 5.36: Variation of turbulence intensities with distance from Grid A at $2\,\mathrm{m\,s^{-1}}$.

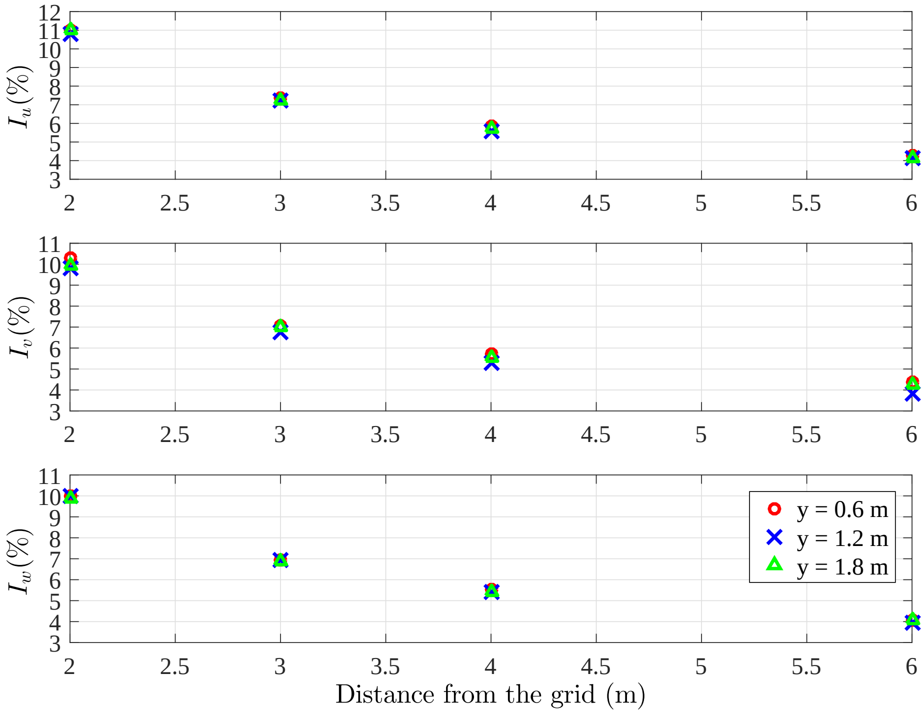

Figure 5.37: Variation of turbulence intensities with distance from Grid A at $4\,\mathrm{m\,s^{-1}}$.

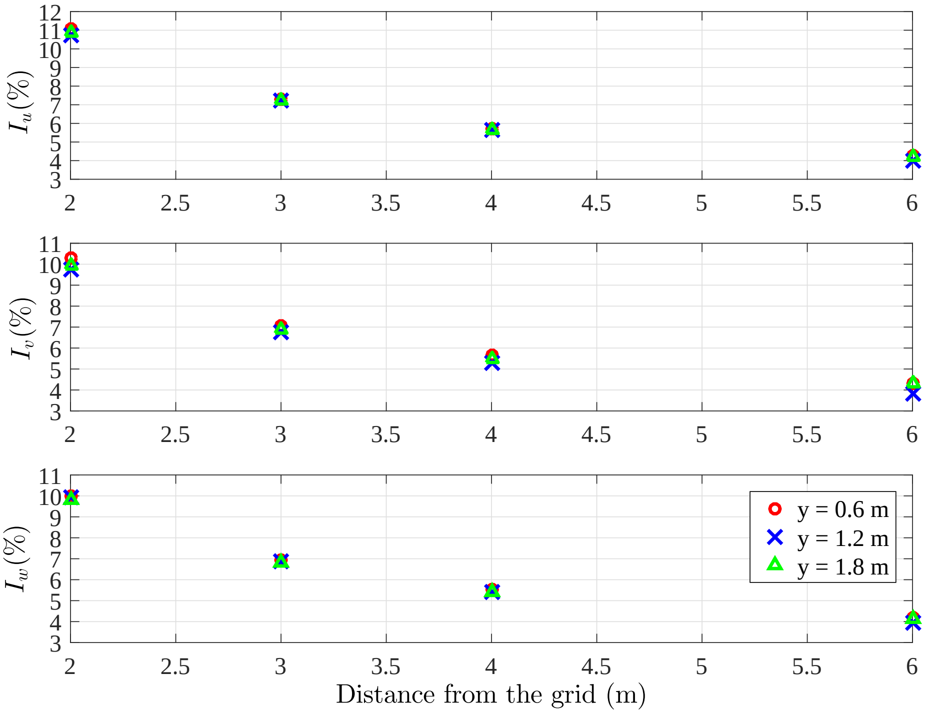

Figure 5.38: Variation of turbulence intensities with distance from Grid A at $6\,\mathrm{m\,s^{-1}}$.

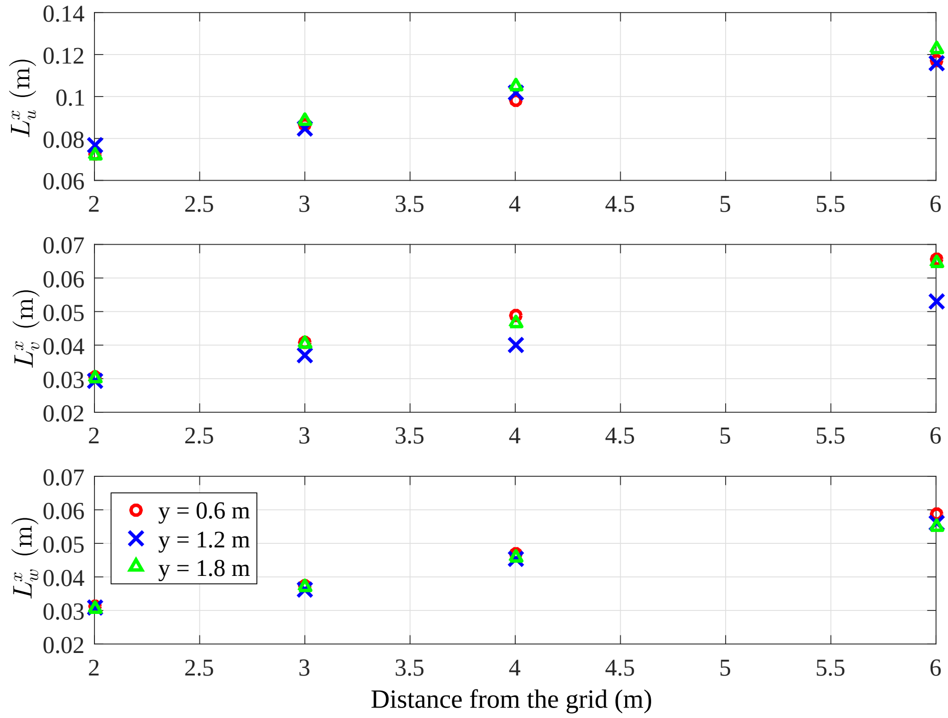

Figure 5.39: Variation of turbulence length scale with distance from Grid A at $2\,\mathrm{m\,s^{-1}}$.

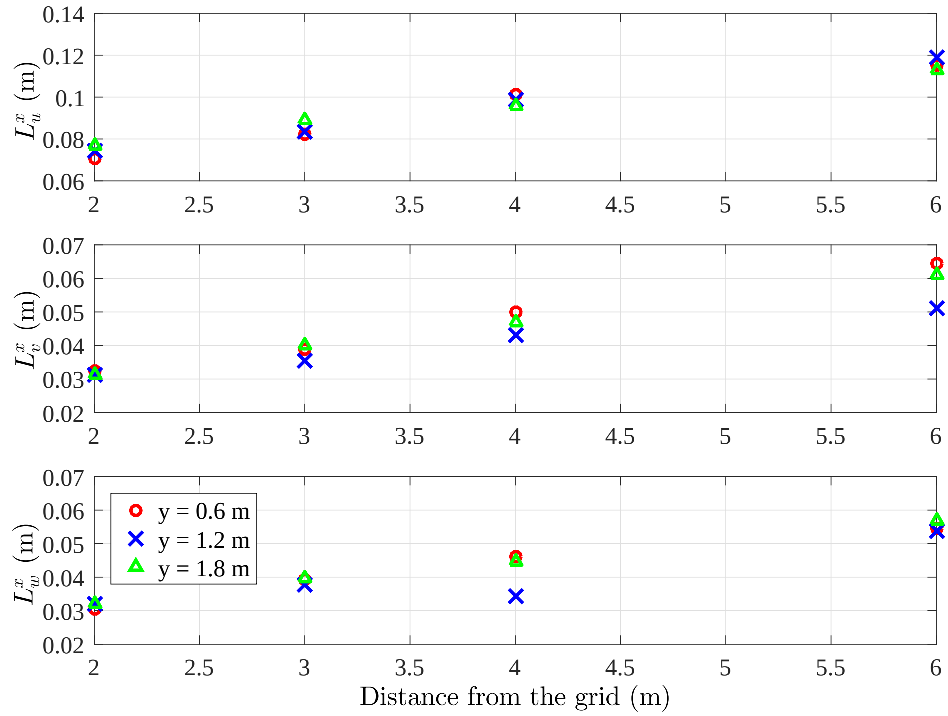

Figure 5.40: Variation of turbulence length scale with distance from Grid A at $4\,\mathrm{m\,s^{-1}}$.

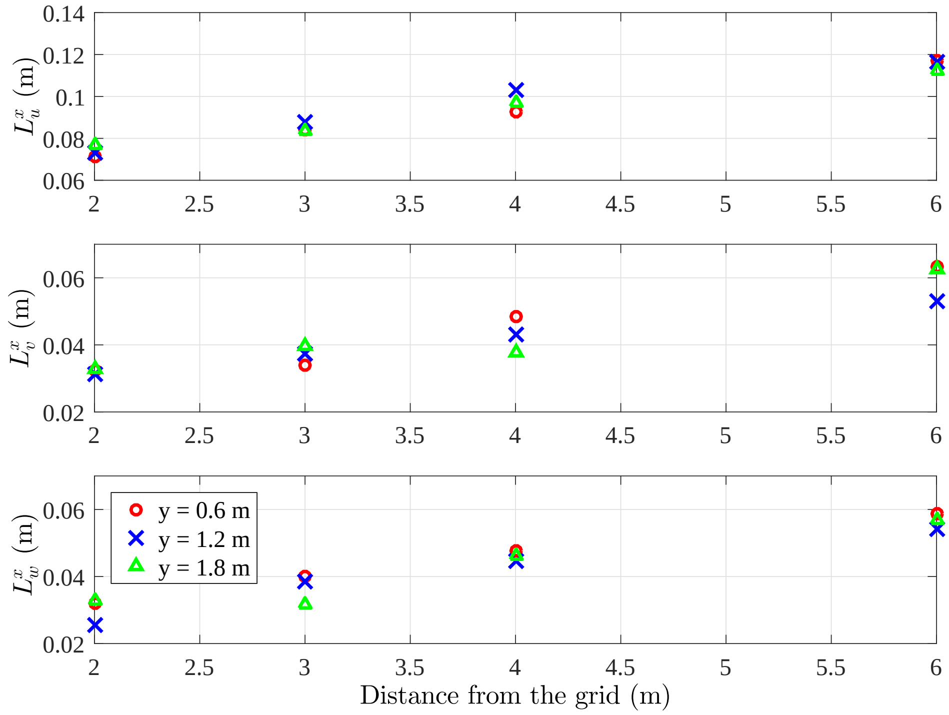

Figure 5.41: Variation of turbulence length scale with distance from Grid A at $6\,\mathrm{m\,s^{-1}}$.

Table 5.2 presents the variation of the Reynolds stresses with the wind speed at all distances away from the turbulence-generating grid. The Reynolds shear stresses were much less significant than the Reynolds normal stresses; all the shear stresses were about two orders smaller compared to the normal ones. In addition, the three Reynolds normal stresses calculated at all crosswind positions were very similar for each wind speed; τ_{uu} was slightly larger than the other two, which was due to the additional shear effect caused the mean wind speed in the x direction. Thus, it was plausible to conclude that the grid-generated turbulence in the wind tunnel was isotropic.

Table 5.2: Variation of the Reynolds stresses with the wind speed at four distances away from Grid A.

Distance from grid (m)	U (m s^{-1})	τ_{uu}	τ_{vv}	τ_{ww}	τ_{uv}	τ_{uw}
2	2	3.81×10^{-2}	2.82×10^{-2}	2.87×10^{-2}	2.96×10^{-4}	5.09×10^{-4}
	4	1.57×10^{-1}	1.32×10^{-1}	1.30×10^{-1}	2.97×10^{-4}	2.05×10^{-3}
	6	3.33×10^{-1}	2.79×10^{-1}	2.75×10^{-1}	1.95×10^{-4}	1.97×10^{-3}
3	2	1.58×10^{-2}	1.29×10^{-2}	1.28×10^{-2}	1.23×10^{-4}	2.13×10^{-4}
	4	6.64×10^{-2}	6.03×10^{-2}	5.99×10^{-2}	8.91×10^{-4}	9.93×10^{-4}
	6	1.42×10^{-1}	1.29×10^{-1}	1.28×10^{-1}	1.77×10^{-3}	2.11×10^{-3}
4	2	9.64×10^{-3}	7.76×10^{-3}	7.83×10^{-3}	2.47×10^{-4}	1.93×10^{-4}
	4	4.03×10^{-2}	3.74×10^{-2}	3.65×10^{-2}	9.40×10^{-4}	7.36×10^{-4}
	6	8.57×10^{-2}	7.95×10^{-2}	7.89×10^{2}	2.08×10^{-4}	1.53×10^{-3}
6	2	5.01×10^{-3}	4.50×10^{-3}	4.19×10^{-3}	5.93×10^{-5}	1.03×10^{-4}
	4	2.13×10^{-2}	2.10×10^{-2}	1.98×10^{-2}	1.48×10^{-4}	4.69×10^{-4}
	6	4.54×10^{-2}	4.51×10^{-2}	4.35×10^{2}	6.53×10^{-4}	8.57×10^{-3}

Results regarding characteristics of the turbulence generated from Grid B having the mesh size of 500 mm were showed in Figures 5.42 to 5.47 and in Table 5.3. It was obvious that similar conclusions could be drawn that the turbulence generated from the large grid was found to be independent of the Reynolds number, homogeneous along cross-wind direction and isotropic. However, direct comparison of the turbulence generated from Grids A and B revealed strong dependence on the geometry of grids, particularly the mesh size. Grid B possessing a bigger mesh size created a stronger turbulence with larger characteristics length-scales; the turbulence intensities were measured to be about 1.5 times stronger than those created from Grid A and the length-scales were found to be approximately 2 times larger. A combination of a larger mesh size and wider aluminium strut members led to more disturbance to the wind as it passed the grid, resulting in more strongly rotating and larger eddies.

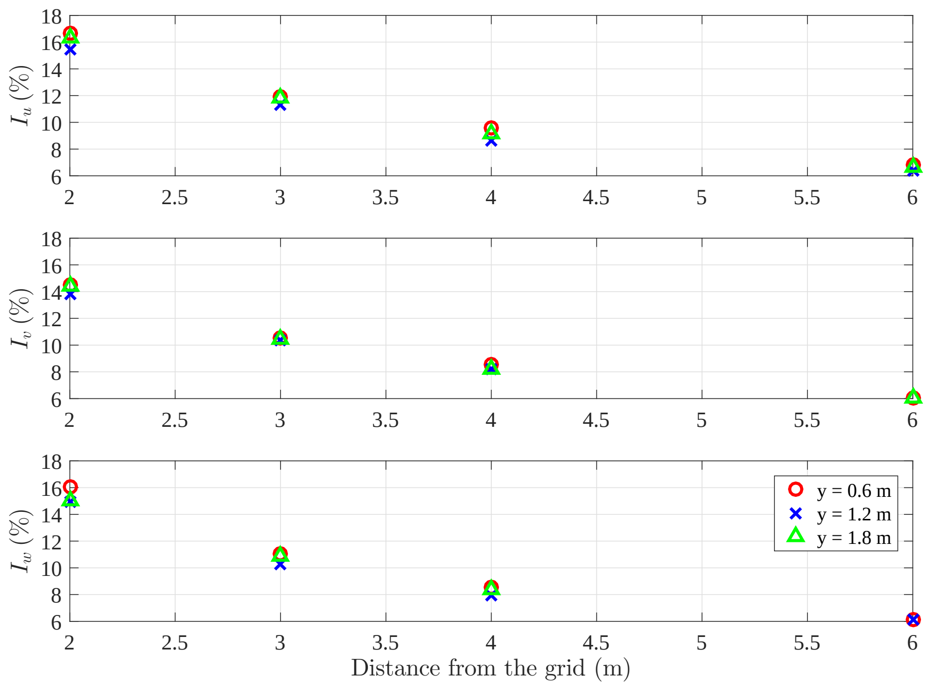

Figure 5.42: Variation of turbulence intensities with distance from Grid B at $2\,\mathrm{m\,s^{-1}}$.

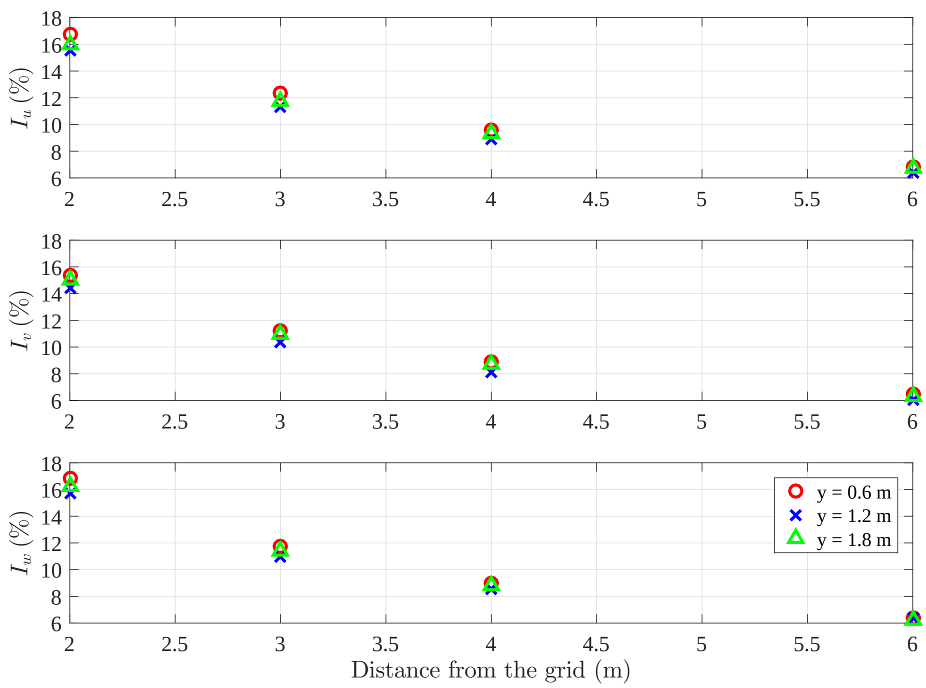

Figure 5.43: Variation of turbulence intensities with distance from Grid B at $4\,\mathrm{m\,s^{-1}}$.

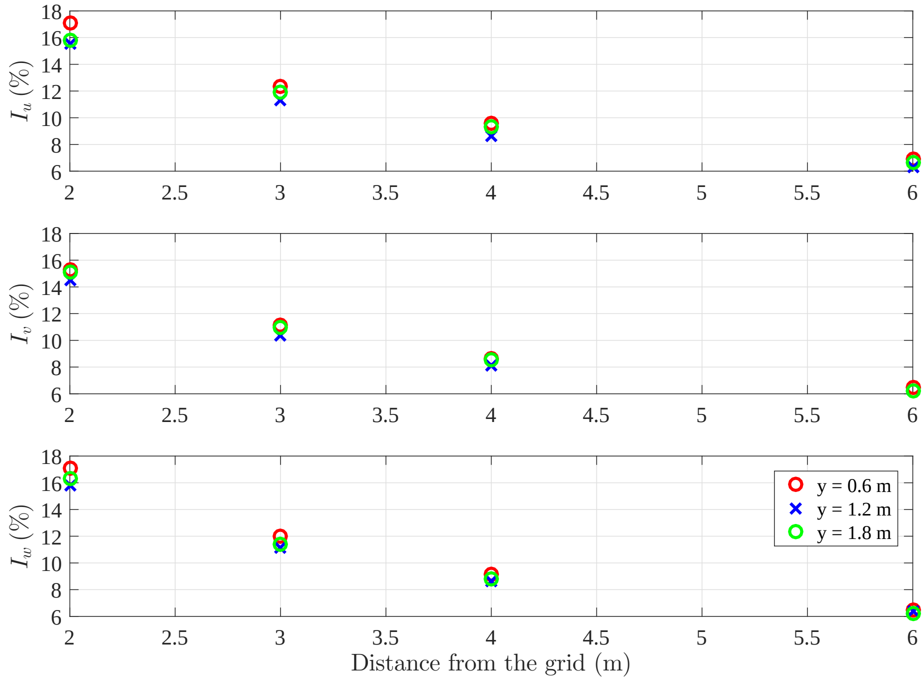

Figure 5.44: Variation of turbulence intensities with distance from Grid B at 6 m s^{-1}.

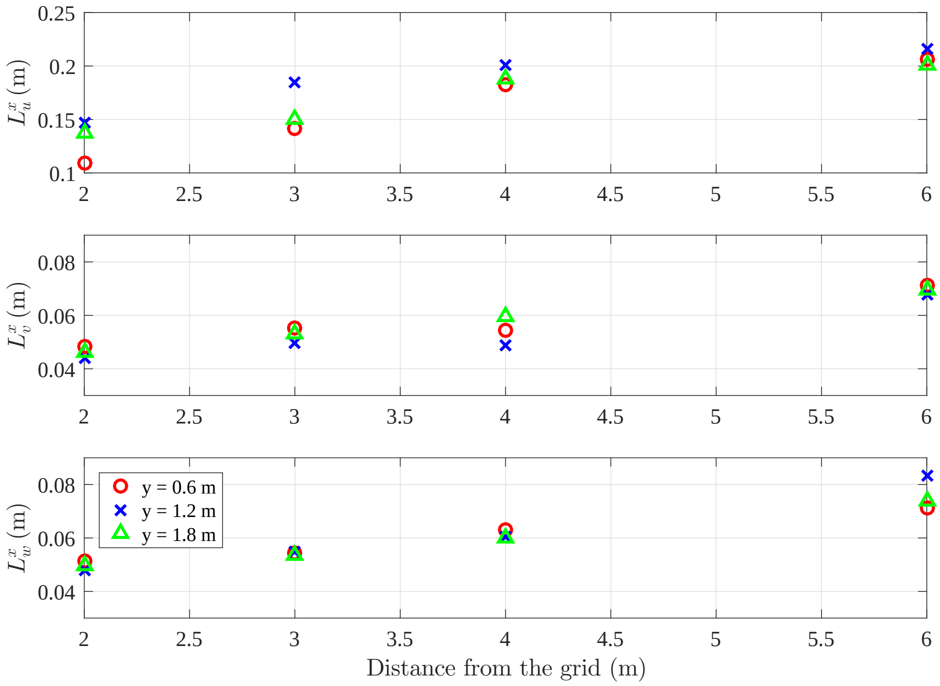

Figure 5.45: Variation of turbulence length scale with distance from Grid B at 2 m s^{-1}.

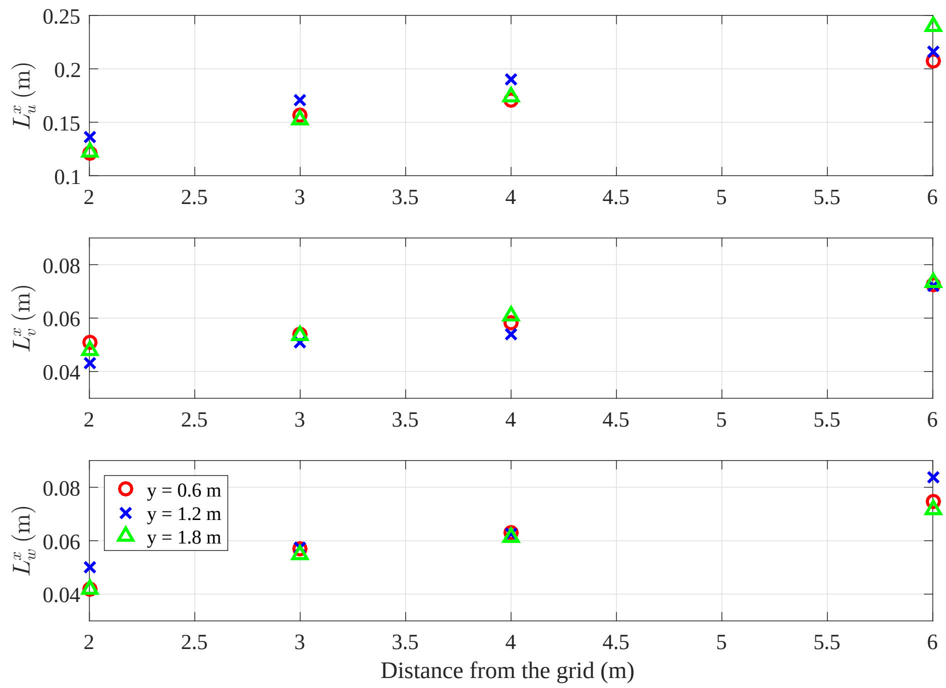

Figure 5.46: Variation of turbulence length scale with distance from Grid B at $4\,\mathrm{m\,s^{-1}}$.

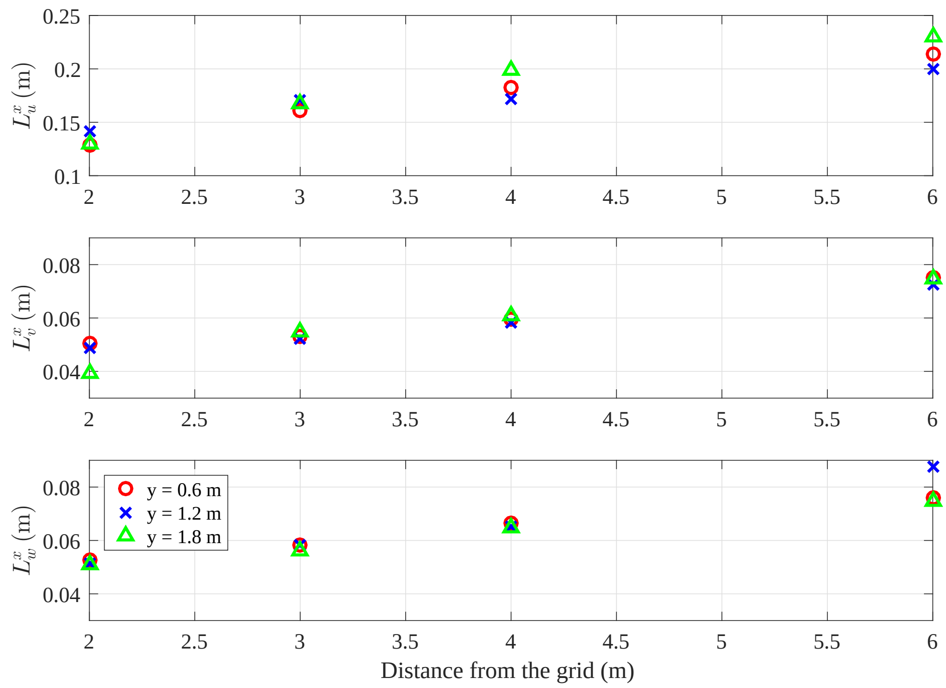

Figure 5.47: Variation of turbulence length scale with distance from Grid B at $6\,\mathrm{m\,s^{-1}}$.

Table 5.3: Variation of the Reynolds stresses with the wind speed at four distances away from Grid B.

Distance from grid (m)	U (ms^{-1})	τ_{uu}	τ_{vv}	τ_{ww}	τ_{uv}	τ_{uw}
2	2	1.36×10^{-1}	1.06×10^{-1}	1.23×10^{-1}	-5.98×10^{-4}	2.89×10^{-4}
	4	5.68×10^{-1}	4.88×10^{-1}	5.80×10^{-1}	5.03×10^{-3}	1.03×10^{-3}
	6	1.23	1.06	1.27	1.80×10^{-2}	-9.73×10^{-3}
3	2	7.45×10^{-2}	5.93×10^{-2}	6.25×10^{-2}	-9.51×10^{-7}	-1.91×10^{-4}
	4	3.19×10^{-1}	2.70×10^{-1}	2.95×10^{-1}	-1.50×10^{-3}	2.074×10^{-3}
	6	6.88×10^{-1}	5.76×10^{-1}	6.53×10^{-1}	2.94×10^{-3}	-8.26×10^{-4}
4	2	4.25×10^{-2}	3.54×10^{-2}	3.53×10^{-2}	-1.26×10^{-4}	-6.11×10^{-6}
	4	1.92×10^{-1}	1.64×10^{-1}	1.73×10^{-1}	6.33×10^{-4}	4.59×10^{-4}
	6	4.21×10^{-1}	3.54×10^{-1}	3.92×10^{-1}	3.91×10^{-3}	4.43×10^{-4}
6	2	2.29×10^{-2}	1.84×10^{-2}	1.93×10^{-2}	-6.54×10^{-4}	-2.37×10^{-5}
	4	9.79×10^{-2}	8.66×10^{-2}	8.89×10^{-2}	-3.27×10^{-4}	-4.59×10^{-4}
	6	2.11×10^{-1}	1.84×10^{-1}	1.93×10^{-1}	-1.44×10^{-3}	-5.38×10^{-4}

In conclusion, the grid-generated turbulence in the wind tunnel can be considered as homogeneous and isotropic at a distance of 2 m away from the grid. The turbulence was found to suffer a decay process along the wind tunnel, which was illustrated by a decrease in the turbulence intensities together with an increase in the turbulence length scale. Therefore, the homogeneity was not valid in the along-wind direction but in the crosswind directions. This technique created the turbulent wind by passing a uniform flow through a regular grid of bars and array of holes; the turbulence characteristics thus were not dependent on the Reynolds number but the geometry of the grid. The effect of the shear layers produced by the walls of the wind tunnel was observed; it was more significant further away from the grid.

5.8.3 Mathematical Decay Profile

The analysis presented in Section 5.8.2 showed that the turbulence generated by either Grids A or B was homogeneous in across-wind directions, isotropic and Reynolds-number independent; therefore, the characteristics of the grid-generated turbulence could be represented by averaging results at different wind speeds and different cross-wind positions. Some selected averaged properties of the turbulence are summarised in Tables 5.4 and 5.5 in cases of Grids A and B respectively. This information will be used to set up and analyse results of the wind tunnel tests in the turbulent wind and to assess the mathematical decay profile of the grid-generated turbulence in the wind tunnel.

Table 5.4: Summary of selected characteristics of turbulence generated from Grid A at different along-wind positions.

Distance (m)	I_u(%)	I_v(%)	I_w(%)	L_x^u (m)	L_x^u (m)	L_x^w (m)
2	10.9	9.83	9.81	0.0739	0.0313	0.0308
3	7.27	6.81	6.78	0.0856	0.0382	0.0375
4	5.70	5.37	5.35	0.0992	0.0450	0.0446
6	4.17	4.08	3.97	0.117	0.0598	0.0560

Table 5.5: Summary of selected characteristics of turbulence generated from Grid B at different along-wind positions.

Distance (m)	I_u(%)	I_v(%)	I_w(%)	L_x^u (m)	L_x^u (m)	L_x^w (m)
2	16.1	14.7	16.0	0.130	0.0466	0.0486
3	11.8	10.7	11.2	0.162	0.0529	0.0561
4	9.18	8.44	8.66	0.184	0.0572	0.0629
6	6.62	6.13	6.25	0.214	0.0721	0.0774

According to Mohammed and laRue (1990), the decay profile of the grid-generated turbulence in the wind tunnel can be mathematically represented as

$$I_i^2 = A_1 \left(\frac{x - x_o}{M} \right)^{n_1}, \tag{5.43}$$

where A_1 and n_1 are a constant and a power coefficient, x is the along-wind position measured from the turbulence-generating grid having the mesh size of M. I_i is the turbulence intensity of the i velocity component, $i = u, v$ or w. The parameter x_o is called the virtual origin, which is interpreted as the location where the turbulence starts to decay. As the wind passed the grid, there existed, right after the grid, a transient regime where eddies shed from strut members of the grid interacted with each other or mixed together. At the distance x_o this mixing process completes and fully-developed turbulence is created. A similar equation was also developed to describe the behaviour of the turbulence length-scale during the decay process as

$$L_i^x = A_2 \left(\frac{x - x_o}{M} \right)^{n_2}, \tag{5.44}$$

where A_2 and n_2 are a constant and a power coefficient, L_i^x is the length scale of the i velocity component along the x direction. Using the least-square method, a fitting process was applied to find out the virtual origin x_o and two pairs of coefficient (A_1, n_1) and (A_2, n_2) corresponding to Equations 5.43 and 5.44

respectively. Results of this process including fitting errors are shown in Figures 5.48 and 5.49 for the turbulence generated by Grid A and Figures 5.50 and 5.51 for that generated by Grid B. The fitting error was quantified as the summation of the squared differences between experimental results and curve-fitting values evaluated at experimental data points.

A good agreement between experimental results and the theoretical model could be drawn particularly for the turbulence intensity. Larger fitting errors were observed when fitting the theoretical model against the length scale data, which could be due to errors of the turbulence length scale caused by effects of the shear layer along the wind tunnel's walls as was discussed in Section 5.8.2. By comparing two values of the virtual origin, which were 0.9 m and 0.3 m in case of Grids A and B respectively, it is observed that the turbulence generated by Grid B is fully developed sooner than that created by Grid A. This observation was plausible since eddies possessing larger length scales tend to rotate more slowly; therefore the mixing process can reach a stable state quicker, resulting in a fully-developed turbulence closer to the grid of a larger mesh size.

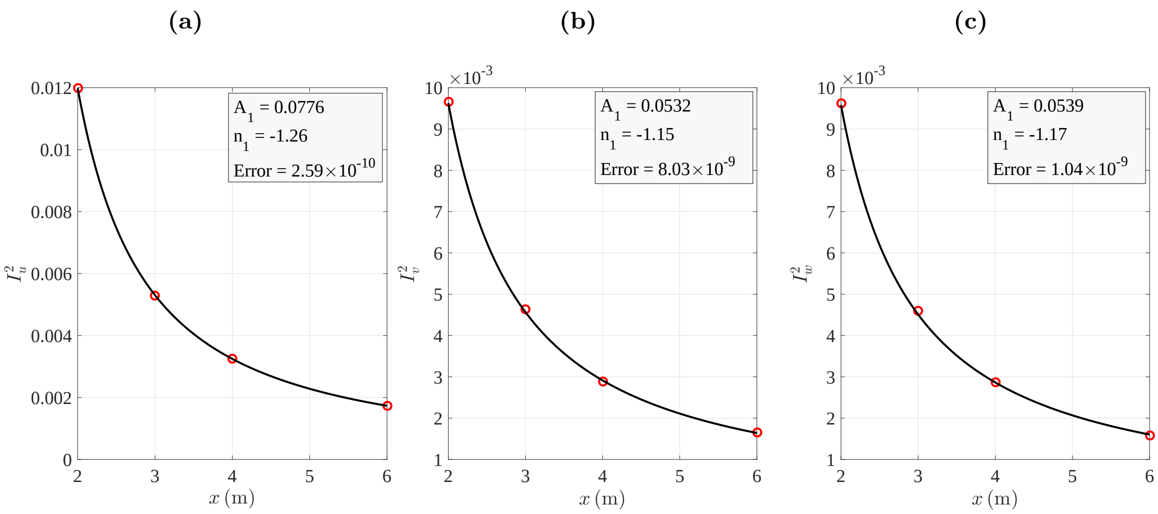

Figure 5.48: Comparison of experimental results and the mathematical model regarding to the turbulence intensity developed by Grid A; the virtual origin $x_o = 0.9\,\mathrm{m}$ while the other model parameters are included in graphs.

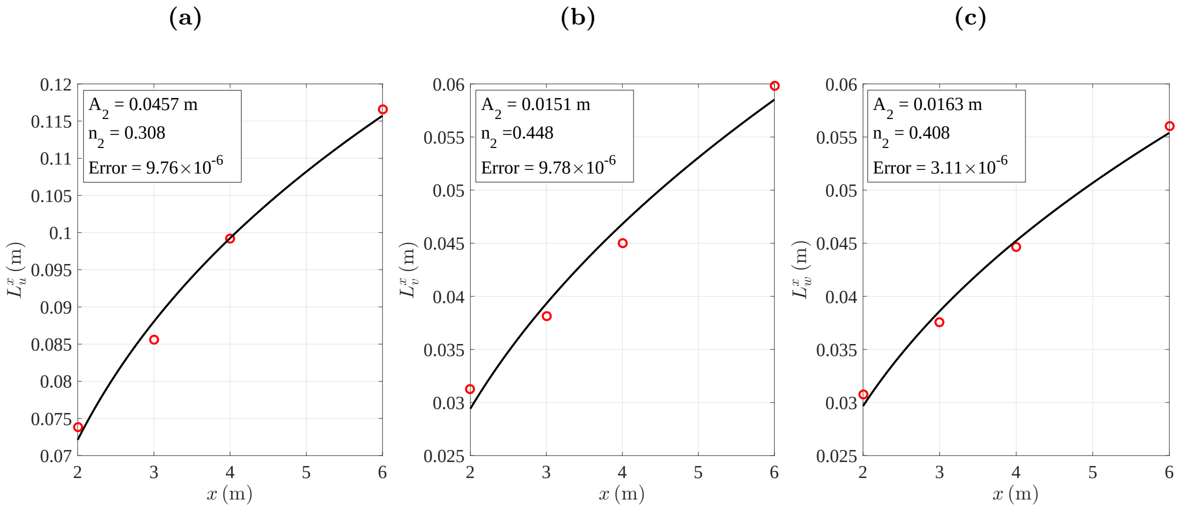

Figure 5.49: Comparison of experimental results and the mathematical model regarding to the turbulence length scale developed by Grid A; the virtual origin $x_o = 0.9\,\mathrm{m}$ while the other model parameters are included in graphs.

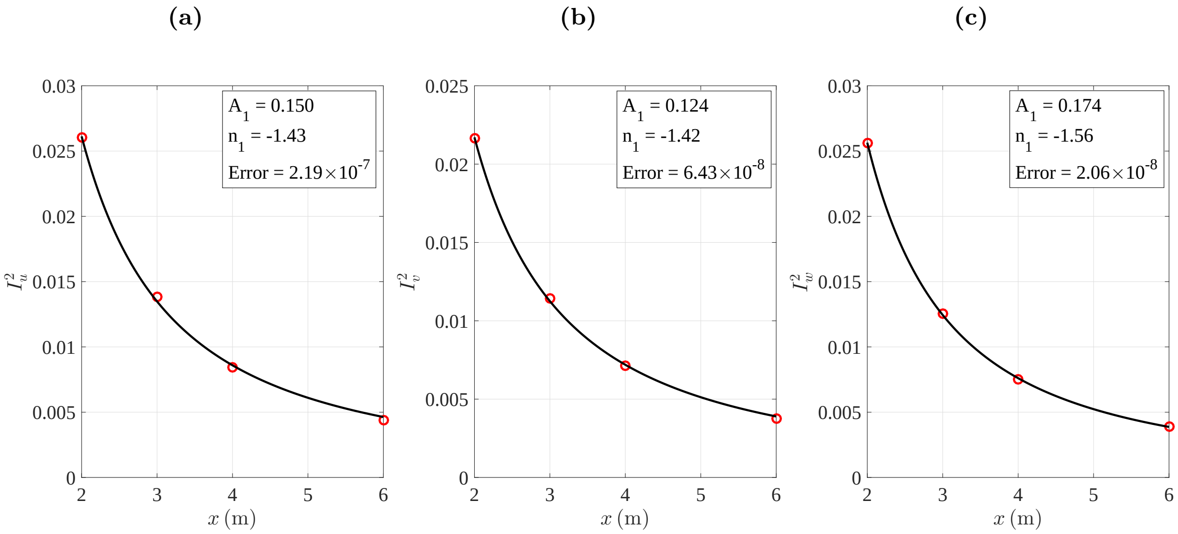

Figure 5.50: Comparison of experimental results and the mathematical model with respect to the turbulence intensity developed by Grid B; the virtual origin $x_o = 0.3\,\mathrm{m}$ while the other model parameters are included in graphs.

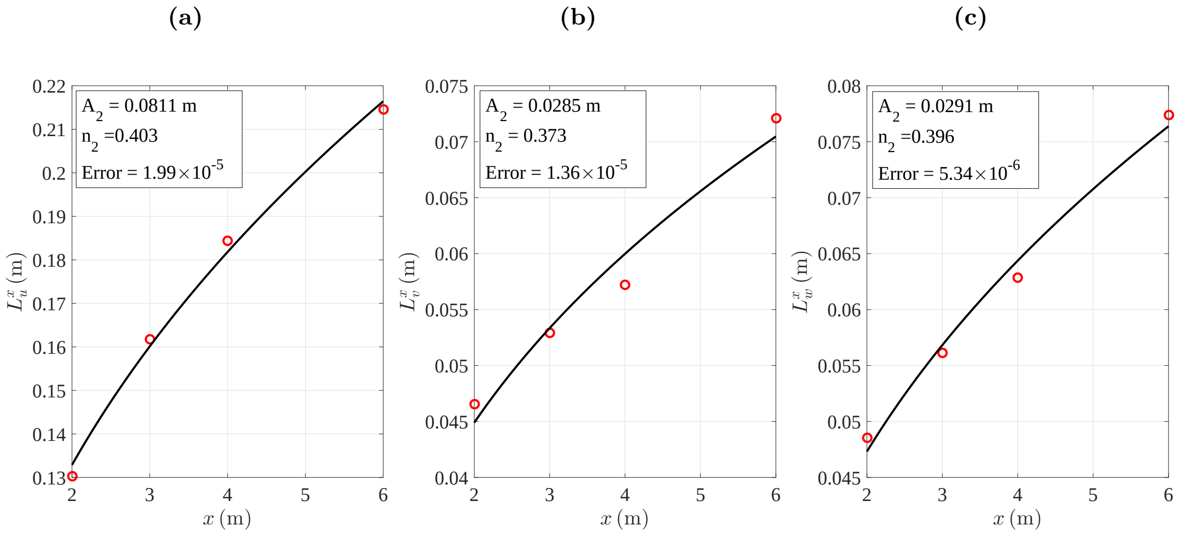

Figure 5.51: Comparison of experimental results and the mathematical model with respect to the turbulence length scales developed by Grid B; the virtual origin x_o = 0.3 m while the other model parameters are included in graphs.

Due to the decay process of the grid-generated turbulence, by varying the distance between the wind tunnel model and the grid, it was possible to perform wind tunnel tests at different turbulent flow regimes. As for the static wind tunnel test, only Grid A was deployed and the wind tunnel model was placed such that the front face of the model was 2, 3 and 4 m away from the grid, i.e. the first three turbulent flow regimes as shown in Table 5.4. At distances further than 4 m, the structure of the turbulence was potentially unstable due to excessive influence from the wind tunnel walls. As for the wind tunnel dynamic test, Grid A and distances of 2 and 4 m were used. To investigate the effect of the turbulence length scale only, Grid B was then employed and the wind tunnel model was placed at a distance of 3.25 m away from the grid. At this location, based on the theoretical model, the turbulent flow was found to have similar turbulence intensities as the one measured at x = 2 m using Grid A but about 2.2 times larger length scales. Also, the presence of the grid at the inlet of the working section affected the magnitude of the mean wind speed. As for Grid A, the magnitude of the mean wind speed was reduced by a factor of 1.18 while, as for Grid B, it was increased by a factor of 1.1; both were relative to measurements in an empty wind tunnel. Compared to Grid A, the appearance of bulky elements connecting Grid B to the walls of the wind tunnel could possibly enhance the width of the shear layers, which effectively narrowed the cross sectional area leading to an overall increase in the mean wind speed. It is also suspected that the fluctuation in the shear layers could generate some resonance effect on the cross-wind velocity profile, resulting in alternative spots with high and low mean wind speeds. However, with a limited number of velocity measurement points, it would not be possible to validate this argument. In addition, these variations could be a function of the operating condition of the fan and the wind tunnel themselves. Four turbulent flow regimes selected for wind tunnel static and dynamic tests are summarised in Table 5.6.

Table 5.6: Summary of selected turbulent flow regimes for wind tunnel tests.

Grid	Distance (m)	$I_u(\%)$	L_x^u (m)	WT Static Tests	WT Dynamic Tests
A	2	10.9	0.0739	✓	✓
A	3	7.27	0.0856	✓	–
A	4	5.70	0.0992	✓	✓
B	3.25	10.9	0.166	–	✓

5.9 CONCLUSION OF THE CHAPTER

In this Chapter, an overall method to conduct the wind tunnel static and dynamic tests were presented together with key measuring techniques to monitor important parameters such as wind velocity, pressure, acceleration, forces and moments. As for each measuring technique, a short introduction was included offering brief physical background underlying followed by a detailed explanation of data acquisition system, the physical design and arrangement and relevant processes required to ensure accuracy and repeatability of measurement.

The wind tunnel tests were performed in smooth flow and different turbulent flow regimes generated by the use of turbulence generating grids. The wind velocity measuring technique was used to investigate the structure of the turbulence inside the wind tunnel in the along-wind and across-wind directions. The results showed that the grid-generated turbulence was isotropic, homogeneous in the across-wind direction, independent of the Reynolds number and stable up to a distance of 4 m away from the grid. By varying the distance between the grid and the wind tunnel model and changing the grid geometry, a combination of different turbulent flow regimes were selected to understand effects of the turbulence intensity and length scale on the aerodynamics of the flow field around and the dynamic response of the wind tunnel model.

Chapter 6

Results and Discussion

In this chapter, results obtained from the computational and wind tunnel studies are analysed and discussed in detail. A number of chapter sections are structured such that a comparison between these two studies is conducted to bring more insights into the aerodynamics of the flow field around and the mechanism of the VIV of the 5:1 rectangular cylinder. Also, by analysing responses of the cylinder measured in the smooth and turbulent flow, the effect of the turbulence on the VIV of this particular cylinder can be explained. Moreover, an individual section is devoted to discussing emerging span-wise flow features captured in the 3D bending simulation and their effects on the VIV lock-in.

6.1 AERODYNAMICS OF FLOW FIELD AROUND A STATIC 5:1 RECTANGULAR CYLINDER

The aim of this section is to, at first, validate the wind tunnel and computational studies by comparing force coefficients and Strouhal numbers measured at a number of Reynolds numbers against results extracted from literature. Then, detailed analysis of the distribution and correlation of the surface pressure was conducted to explain the generic aerodynamics of the flow field around the 5:1 rectangular cylinder. It is noticed that the Reynolds number was calculated using the depth D of the cylinder.

6.1.1 Force Coefficients and Strouhal Number

In the wind tunnel study, lift force, drag force and moment acting on the wind tunnel model was measured by the load cells as discussed in detail in Section 5.5. The time-averaged lift coefficient C_L, drag coefficient C_D and moment coefficient C_M were then calculated and corrected for the blockage due to the confined space in the wind tunnel and the obstruction caused by the aluminium frame. Also, these force and moment coefficients needed to be corrected to eliminate additional wind-induced effects on the load cells and the end plates. The final corrected force and moment coefficients are plotted in Figures 6.1 and 6.2 where they are compared against results achieved by Schewe (2013). It is noticed that Schewe (2013) conducted static wind tunnel tests at three Reynolds numbers, Re $= 6000, 12000$ and 60000 and at the angle of attack $\alpha = 0°$ to $6°$.

As can be seen in Figure 6.1a, the time-averaged drag coefficient C_D possessed low Reynolds-number dependence. Taking into account measurement errors, all values of the drag coefficient measured at different Reynolds numbers agreed with each other. This observation could be further emphasised in Figure 6.2a illustrating a similar variation of the drag coefficient against the angle of attack at all four tested Reynolds numbers. Errors included in the drag coefficient were found to be larger than the ones associated with the measurement of the lift coefficient and moment coefficient; this was due to a limitation in the design of the piezoelectric load cells that the lack of pre-loads on the horizontal force sensors reduced their accuracy. In addition, it is noticed that Figure 6.2a suggests there existed an error in setting up the angle of attack; the drag coefficients at the angle of attack $0°$ were higher than results of Schewe (2013). Comparing the drag coefficients measured at the angle of attack $0°$ and $2°$ revealed an error of about $0.5°$ to $1°$ in the angle of attack. The use of the digital inclinometer to set up the angle of attack could partly contribute to this issue; however, the majority was due to the geometry of the wind tunnel section itself. To avoid an increase in pressure along the working section, the top wall of the wind tunnel was constructed with an upward slope of $0.5°$, affecting the direction of the mean flow in the wind tunnel in the same order of magnitude.

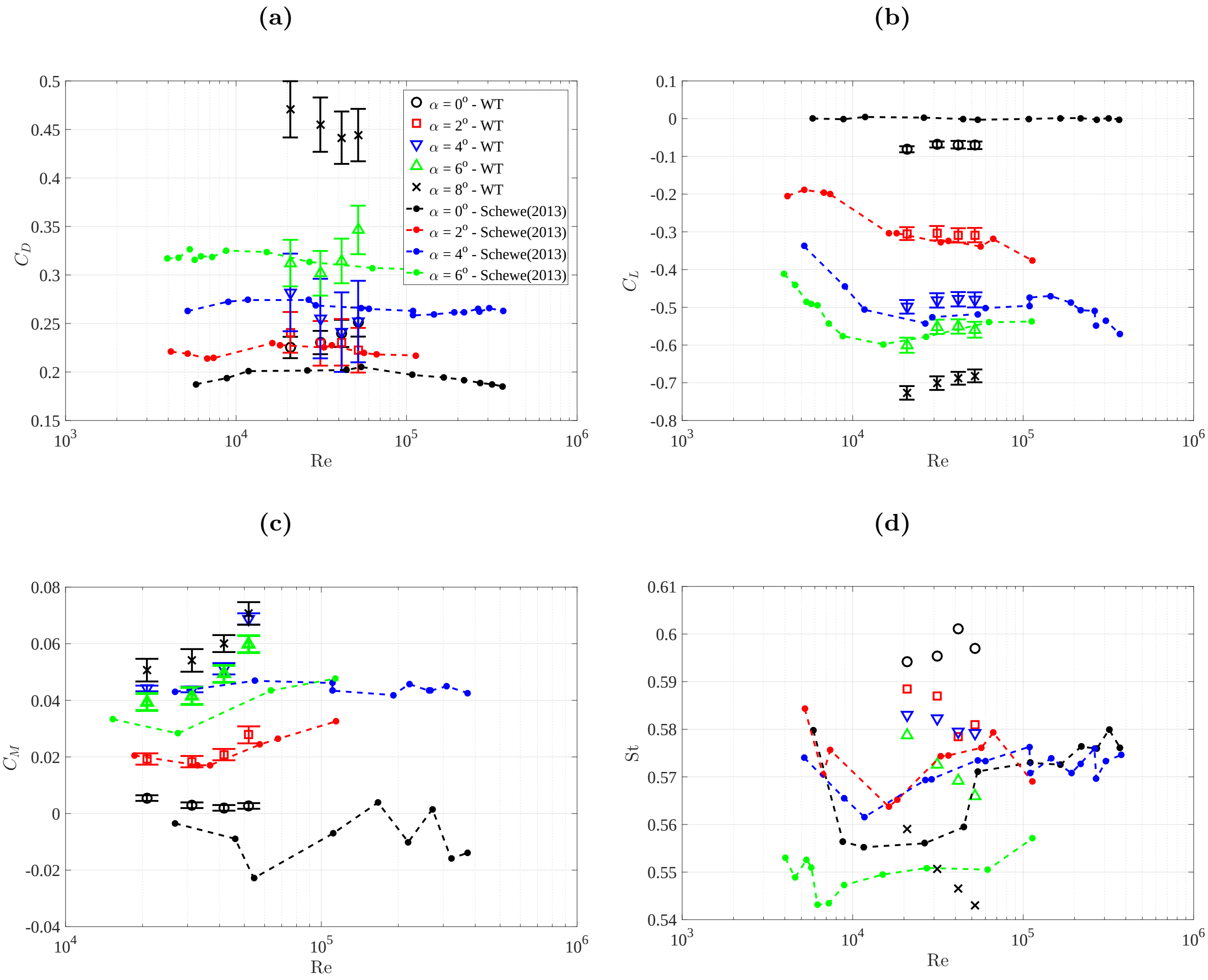

Figure 6.1: Variability of (a) the time-averaged drag coefficient C_D, (b) lift coefficient C_L, (c) moment coefficient C_M and (d) the Strouhal number St against the Reynolds number Re.

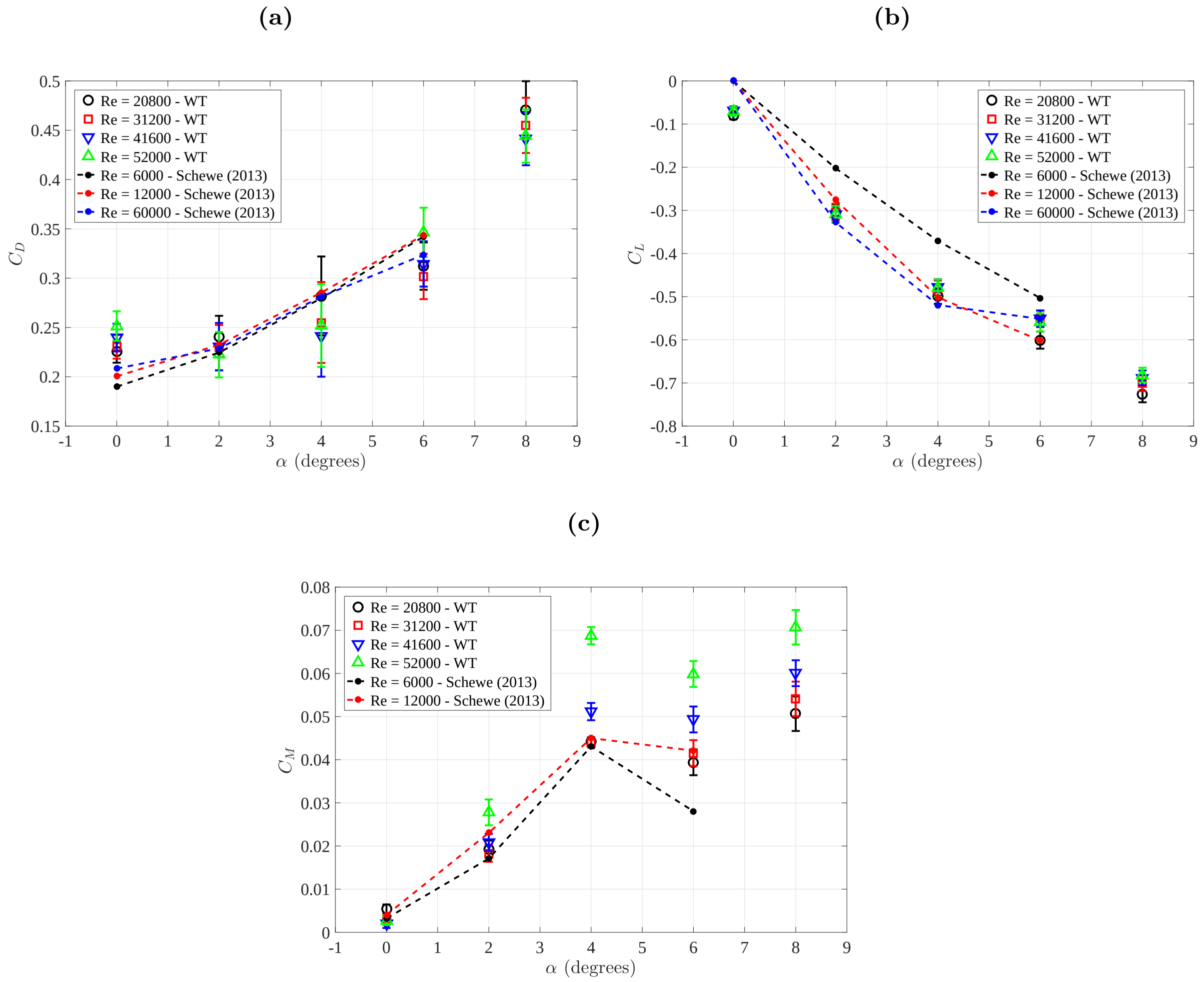

Figure 6.2: Variability of (a) the time-averaged drag coefficient C_D, (b) lift coefficient C_L and (c) moment coefficient C_M.

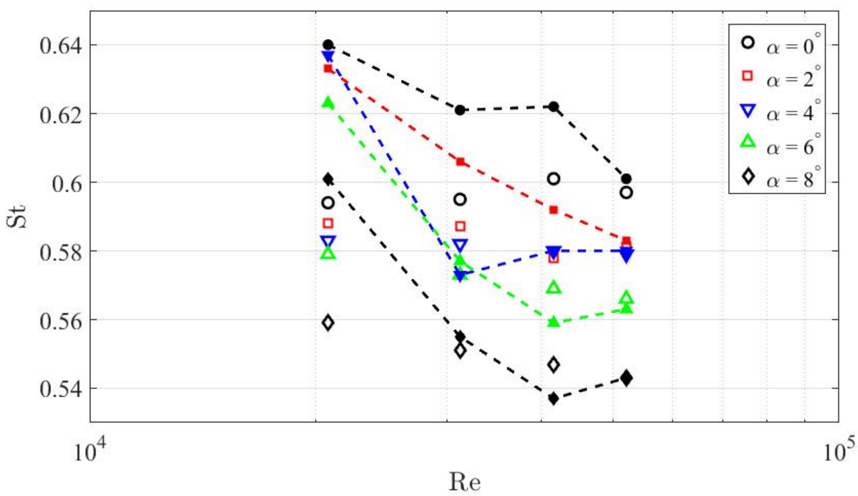

Figure 6.3: Comparison of the Strouhal number identified from the lift force (*open* symbols) against that identified from the w-component of the velocity measured in the wake (*close* symbols).

Errors in the direction of the mean flow were also found to affect the time-averaged lift coefficient C_L at the angle of attack 0° as shown in Figure 6.2b. Apart from this issue, the behaviour of the lift coefficient as the angle of attack increased agreed very well with results of Schewe (2013), including a reduction in lift at the angle of attack 6° which was partly restored at the angle of attack 8°. This behaviour suggested there existed an abrupt change in the flow field around the cylinder at these two angles of attack. In addition, the agreement with results of Schewe (2013) at the Reynolds number of 6000 was low, which potentially indicated some Reynolds-number dependence at lower ranges of the Reynolds number. Nevertheless, across the tested Reynolds numbers, it is obvious that the lift force did not depend on the Reynolds number, as shown in Figure 6.1b.

In contrast, the time-averaged moment coefficient C_M was the Reynolds-number dependent, particularly at angles of attack higher than 4°. As shown in Figures 6.1c and 6.2c, at lower angles of attack, from 0° to 2°, taking the measurement errors into consideration, the moment coefficients measured at different Reynolds numbers agreed well with each other. However, at higher angles of attack, more scatter was observed; Figure 6.1c showed that the wind tunnel model was acted by a larger moment at a higher Reynolds number. Similar to the behaviour of the lift force, as the angle of attack increased, the moment acting on the model reduced at the angle of attack 6° before being restored at the angle of attack 8° (Figure 6.2c), which suggested the appearance of a sudden change in the flow field around the rectangular cylinder as the angle of attack reached 6°.

The Strouhal number could be determined using power spectral densities of the lift force; the vortex shedding frequency f_{VS} was selected to be the frequency component which contributed the largest to the energy of the whole time series. Knowing the vortex shedding frequency f_{VS}, the Strouhal number was calculated as $\mathrm{St} = f_{VS}B/U$ and results are summarised in Figure 6.1d together with results from Schewe (2013). In general, the Strouhal number predicted from the wind tunnel study was found to be higher than that obtained by Schewe (2013). At the angle of attack 0°, the Strouhal number showed a very strong Reynolds-number independence; the averaged value was calculated to be $\mathrm{St} = 0.596$ while Schewe (2013) found this value to be 0.55. This difference was due to effects of the span-to-width ratio; a large ratio (Schewe (2013) used a model with this ratio of 10 while the current model has the ratio of 4.23) yielded a smaller value of the Strouhal number. Using an even shorter model having the span-to-width ratio of 3, Matsumoto et al. (2003) found the Strouhal number to be 0.66. The Reynolds-number independence was exhibited at the angle of attack 2° and 4°; at higher angles of attack, however, the Strouhal number was found to decrease as the Reynolds number got larger. Together with results of the moment coefficient, it emphasised there is an abrupt change on the flow field around the cylinder at the angle of attack 6°.

The Strouhal number could also be calculated from the w-component of the velocity measured in the wake region; Figure 6.3 summarises these results in a comparison with those obtained from the force measurement. In general, the measurement of the w-component of the velocity yields higher values of the Strouhal number due to effects of the end plates on the wake region, particularly at the low Reynolds number, where a percentage difference of 7% was found; at higher Reynolds numbers, this percentage difference reduced. Nevertheless, results obtained from the two methods share similar behaviours which were independence of the Reynolds number and decreased at higher angles of attack. In the wind tunnel dynamic tests, the vortex shedding frequency was measured using this method; therefore, the Strouhal number presented here will be of importance to illustrate the VIV lock-in.

The final force parameter which needed to be analysed was the standard deviation of the time-varying lift coefficient C_L', which was calculated as $\sqrt{\int_0^\infty S_{C_L}(f)\,\mathrm{d}f}$ where $S_{C_L}(f)$ is the power spectral density of the time-varying lift coefficient. Results are summarised in Table 6.1. Since the wind tunnel was fixed at both ends on the load cell, the whole system including the wind tunnel model and the load cells could vibrate at its natural heaving/bending mode. A number of wind-off structural tests were carried out before the wind tunnel test and confirmed the natural frequency of the heaving/bending mode to be 30 Hz, which corresponded to a critical wind speed of 18 m s^{-1}. Even though this critical wind speed was higher than the maximum tested wind speed of 10 m s^{-1}, this resonance effect was found to significantly contribute the fluctuating lift force, particularly when the model was acted by large time-averaged lift forces, i.e. at the angles of attack of 6° and 8°. In Table 6.1, highlighted results represent those influenced by the resonance effect. An example of the power spectral density of the lift force is shown in Figure 6.4. Apart from the dominant peak at about 14 Hz which corresponded to the vortex shedding phenomenon, there are secondary peaks at frequencies of 30 Hz and 40 Hz due to the wind-induced vibration of the whole force measuring system. By performing the integration across the whole range of frequency, it yielded the value of C_L' to be 0.169; however, by restricting the integration range from 12 Hz to 18 Hz, the result was reduced to 0.105, which could be inferred as the fluctuating component of the lift force associating with the vortex shedding phenomenon only. In fact, the latter value was found to agree better with Schewe (2013); by applying this correction, these highlighted values were reduced to more plausible results as shown in Table 6.1.

Table 6.1: Variability of the standard deviation of the time-varying lift coefficient C_L' against the angle of attack α and the Reynolds number Re.

α	Re			
	20800	31200	41600	52000
0°	0.0784	0.0848	0.0932	0.115
2°	0.0761	0.0842	0.0925	0.113
4°	0.105	0.106	0.115	**0.131**/0.0587
6°	**0.123**/0.0910	**0.125**/0.0581	**0.144**/0.0921	**0.159**/0.103
8°	**0.133**/0.0926	**0.136**/0.0839	**0.150**/0.0891	**0.169**/0.105

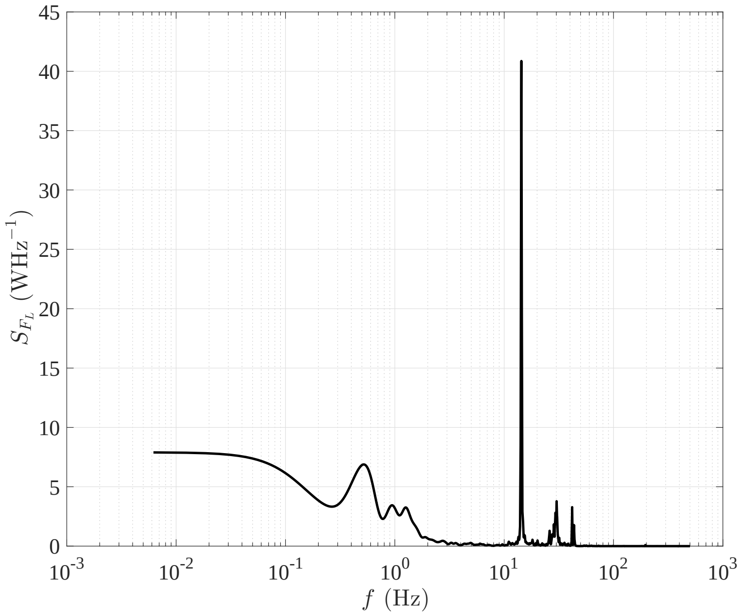

Figure 6.4: An example of the power spectral density of the lift force acting on the model at the angle of attack 8° and at the Reynolds number of 52000.

As for the computational study, the static simulation was conducted at three different wind speeds corresponding to three values of the Reynolds number, Re = 6700, 13000 and 27000 and at only the angle of attack 0°. Selected force coefficients and the Strouhal number were extracted from time histories of lift and drag forces; results were compared against wind tunnel results as shown in Table 6.2. It is obvious that there is a good agreement between the computational study and other wind tunnel tests, except for the time-averaged lift coefficient. Similar to the issue found in the wind tunnel study, the static simulation predicted a slightly negative value of C_L at the angle of attack 0°. Bruno et al. (2010) also found a similar effect when analysing their LES simulations of a static 5:1 rectangular cylinder. One possible reason for this discrepancy was the slight asymmetry between the top and bottom halves of the unstructured grid regarding the cell density and cell size, which might lead to the flow being resolved differently on either surface of the model. The Q-criterion proposed by Hunt et al. (1988) was used to conceptually separate vortices from the flow around the model and in the wake; the contour plot of $Q = 0.1\,\mathrm{s}^{-1}$ at the Reynolds number Re = 6700 is illustrated in Figure 6.5. It is evident that the scale of vortices in the bottom half of the wake region was bigger than that in the top half. This difference implied large suction on the bottom surface of the model, resulting in a negative time-averaged lift force acting on the model.

Table 6.2: Comparison of force coefficients and Strouhal number obtained from computational and wind tunnel studies.

	Re	St	C_D	C_L	C'_L
CFD study	6700	0.608	0.241	-0.056	0.081
	13000	0.600	0.206	-0.059	0.075
	27000	0.609	0.206	-0.063	0.059
WT study	20800	0.594/0.64	0.225	-0.0811	0.0784
WT study Schewe (2013)	6000 – 40000	0.555	0.242	~ 0	~ 0.08

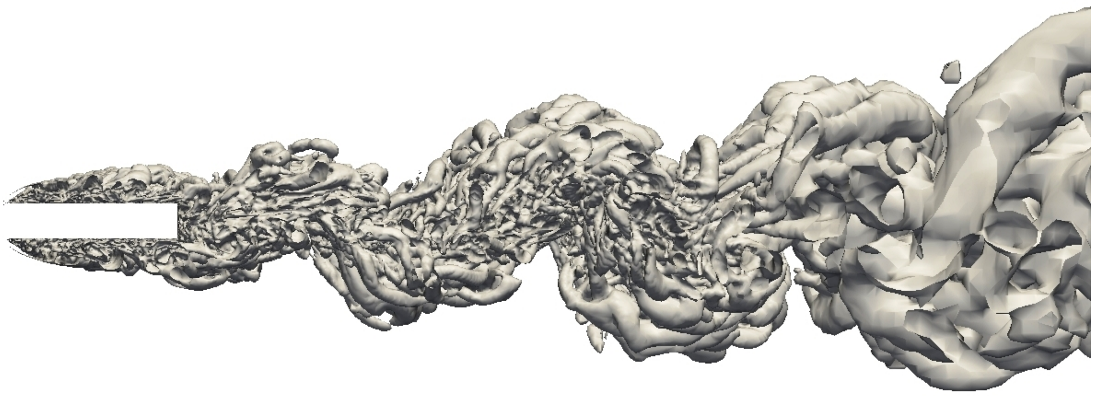

Figure 6.5: Isosurfaces of the Q-criterion, $Q = 0.1\,\mathrm{s}^{-1}$, around the model and in the wake region (Re = 6700).

The comparison of the force coefficients and Strouhal number predicted by the computational study against those measured in other wind tunnel tests has yielded a good agreement, showing the appropriateness of the proposed computational approach. In addition, further wind tunnel static tests at non-zero angles of attack suggested significant changes in the aerodynamics of the flow field around the model, particularly at the angle of attack 6° leading to a reduction in lift, moment and the vortex shedding frequency. These aerodynamic variations will be discussed further in Section 6.1.2.

6.1.2 Investigation of Distribution and Correlation of Surface Pressure

Together with force and velocity measurement, during the wind tunnel static tests and the computational simulations, the surface pressure measurement was carried out to investigate the influence of the angle of attack on the aerodynamic characteristics of the flow field around the model.

Figure 6.6 shows results obtain from the wind tunnel study which are the surface distribution of the time-averaged pressure coefficient C_p and the standard deviation of the time-varying pressure coefficient C_p'. It should be noticed that the surface pressure distribution was plotted against the coordinate s measured from the stagnation point on the front face and normalised using the depth D of the model. At the angle of attack $0°$, despite the difference in the Reynolds number, the flow field on the surface of the model could be divided into two parts. The first one was the separation bubble trapped under the shear layer separated from the leading edge. This region was characterised by a strong suction induced by the circulation of the flow and relatively stable flow features. It extended up to 2/3 of the width of the model and was followed by the reattachment region. In this region, the shear layer which had separated from the leading edge reattached to the surface, leading to a rise in the surface pressure and highly fluctuating flow features.

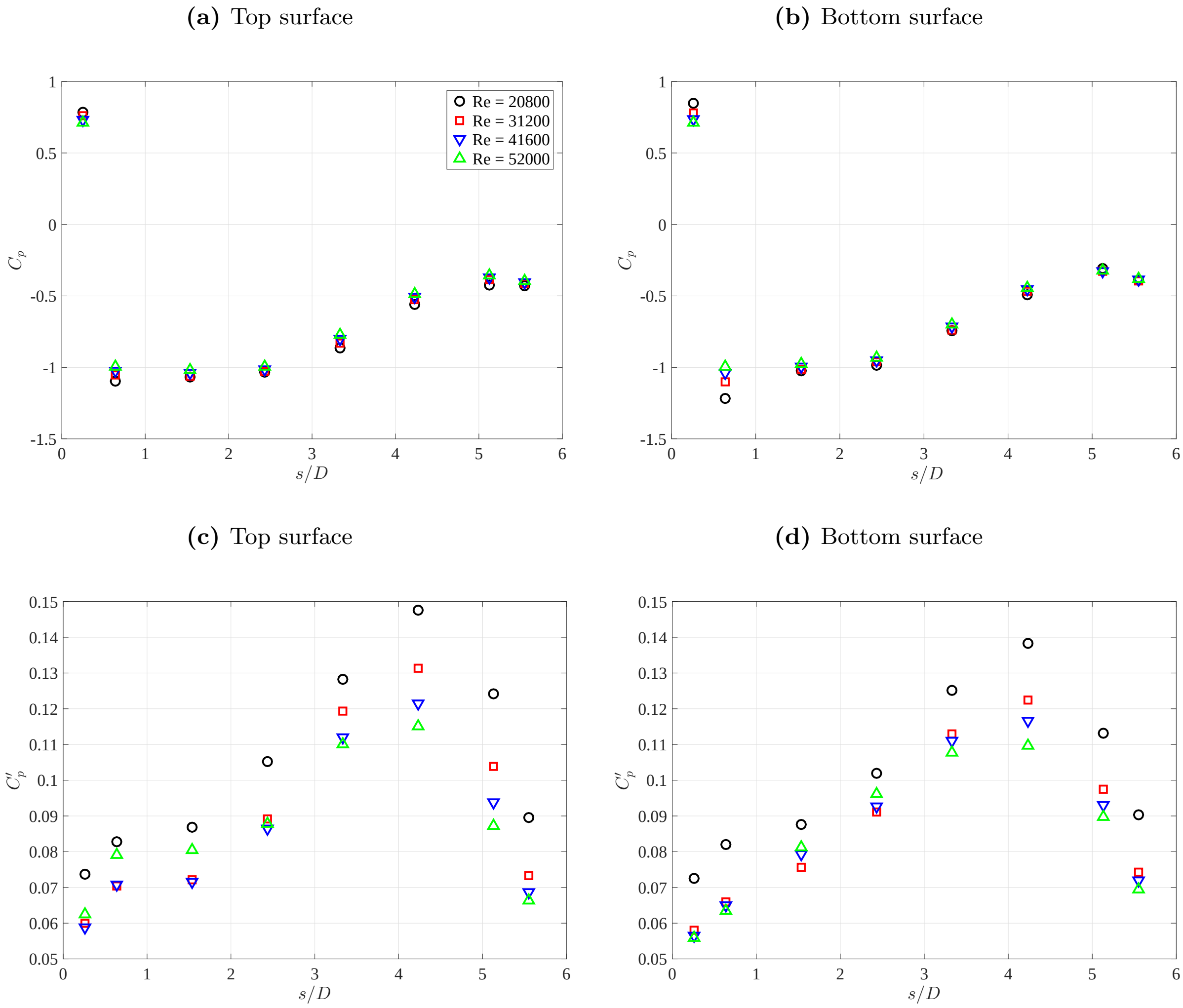

Figure 6.6: Variability of the surface distribution of the time-averaged pressure coefficient C_p and the standard deviation of the time-varying pressure coefficient C'_p with respect to the Reynolds number; the angle of attack was $\alpha = 0°$.

Analysing the span-wise pressure correlation calculated at four stream-wise positions as shown in Figure 6.7 revealed that Positions A and B possessed higher correlation than that of Positions C and D, which was thought to be due to the presence of the well-defined separation bubble along the span-wise length compared to the intermittent and highly unstable flow feature at the reattachment point close to the trailing edge. In fact, the correlation at Position D was slightly higher than that at Position C; this difference could be due to the effect of the vortex shedding occurring along the trailing edge of the model.

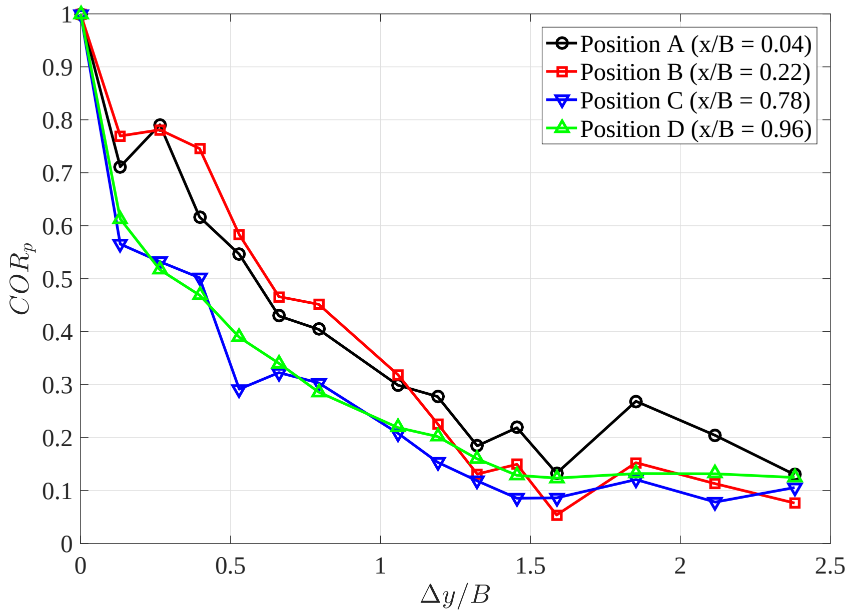

Figure 6.7: Span-wise correlation of the surface pressure measured at four stream-wise positions at the Reynolds number of 31200.

Results from the static simulation also showed a similar difference between the pressure correlation measured close to the leading edge ($x/B = 0.18$) and the one measured close the trailing edge ($x/B = 0.82$) as shown in Figure 6.8. It is noticed that the pressure correlation predicted by the computational study was slightly constrained by the `cyclic` boundary condition of the y patches. This is indicated by plateaux in the pressure correlation curves at large span-wise separations. Nevertheless, the span-wise correlation of pressure measured close to the leading edge was higher than that close to the trailing edge. Similar flow behaviour could be inferred from the coherence structure of the surface pressure as presented in Figure 6.9; the definition of the coherence spectrum was given in Section 2.8.2. At all positions, the maximum coherence of the pressure corresponded to the non-dimensional vortex shedding frequency of 0.6 or the Strouhal number. Near the leading edge, although the maximum coherence value slightly reduced with an increase in the span-wise separation, it was still maintained around 0.9. On the other hand, towards the trailing edge, the maximum coherence value was below 0.8 and it decreased more quickly. In addition, these graphs indicated that the dominant fluctuation of the surface pressure inside the separation bubble and at the reattachment point occurred at the vortex shedding frequency given by the Strouhal number. Therefore, for the 5:1 rectangular cylinder, the vortex shedding phenomenon and the flow field around the cylinder were governed by the synchronisation of the creation of the shear layer at the separation point located at the leading edge and the vortex shedding occurring at the trailing edge. This type of flow is known as the impinging leading edge vortex shedding and has been well documented in literature as discussed in Section 2.3.2.

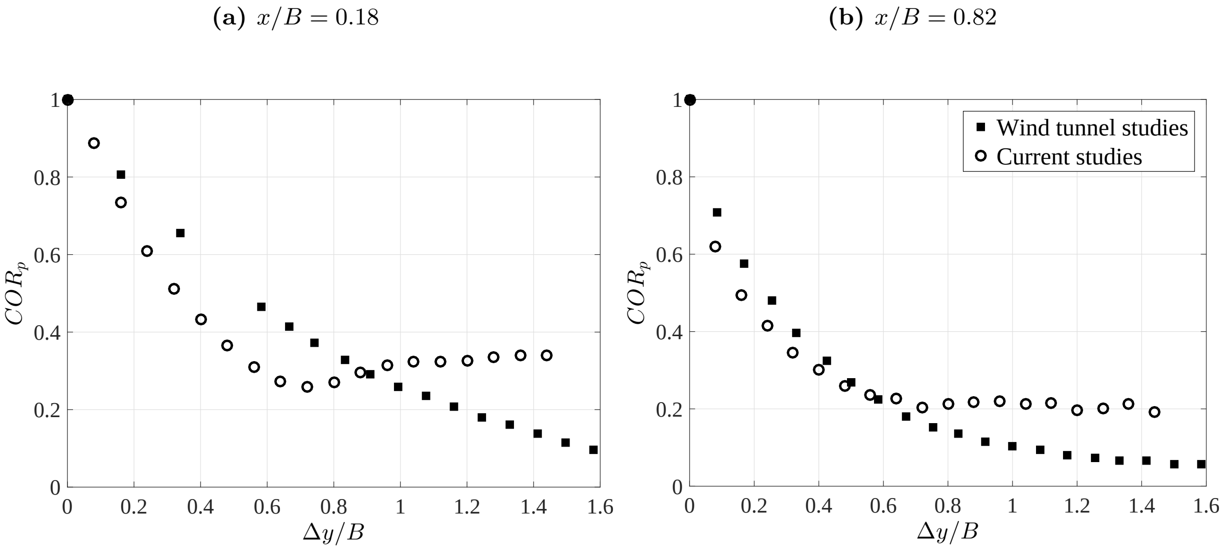

Figure 6.8: Span-wise correlation of the surface pressure predicted by the static simulation at the Reynolds number of Re = 6700; the wind tunnel study results were extracted from Ricciardelli and Marra (2008) at Re = 63600.

.

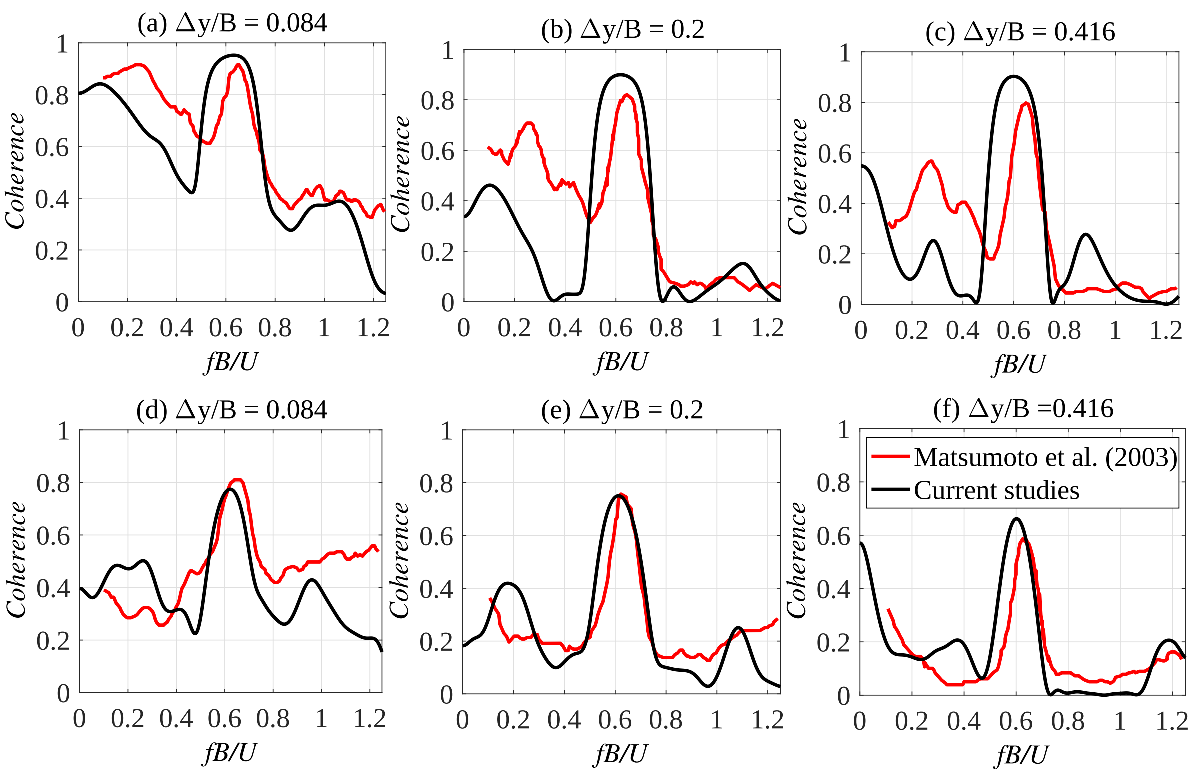

Figure 6.9: Span-wise coherence of the surface pressure predicted by the static simulation at the Reynolds number of Re = 6700; the top row is close to the leading edge while the other is close to the trailing edge.

Knowing the key characteristics of the flow field around the cylinder, Figure 6.10 illustrates how these features varied subject to a change in the angle of attack; the negative angles of attack imply that, during the wind tunnel static tests, the model was rotated around the y axis such that the top surface was exposed more to the wind. In this case, as can be seen in Figures 6.10a and 6.10c, the separation bubble on the top surface suffered a suppression effect, which was illustrated by a reduction in both of the length and the circulating strength and a shift of the reattachment point towards the leading edge. On the bottom surface, the movement of the reattachment point was observed to be towards the trailing edge, leading to an elongation of the separation bubble. At the angle of attack $-6°$, the reattachment point was vanished and the entire bottom surface was covered by a big circulation of flow; the shear layer created from the leading edge therefore interacted directly with the wake region. In fact, from the angle of attack of $-4°$ to $-6°$, the variation of the flow field on the bottom surface was insignificant compared to the dramatic aerodynamic change occurring on the top surface, where the length of the separation bubble suddenly shortened to less than half of the width of the cylinder, accompanied by approximately 30% reduction in the mean pressure. This effectively reduced the uplift caused by the separation bubble leading to a decrease in the moment as being seen in Figure 6.2c. At the angle of attack $-8°$, the strong circulation on the bottom surface extended further towards the trailing edge, which is indicated by slightly stronger suction around this area (Figure 6.10b). This inferred a downstream shift of the overall suction force acting on the bottom surface, which essentially resulted in a restoration in the moment acting on the model.

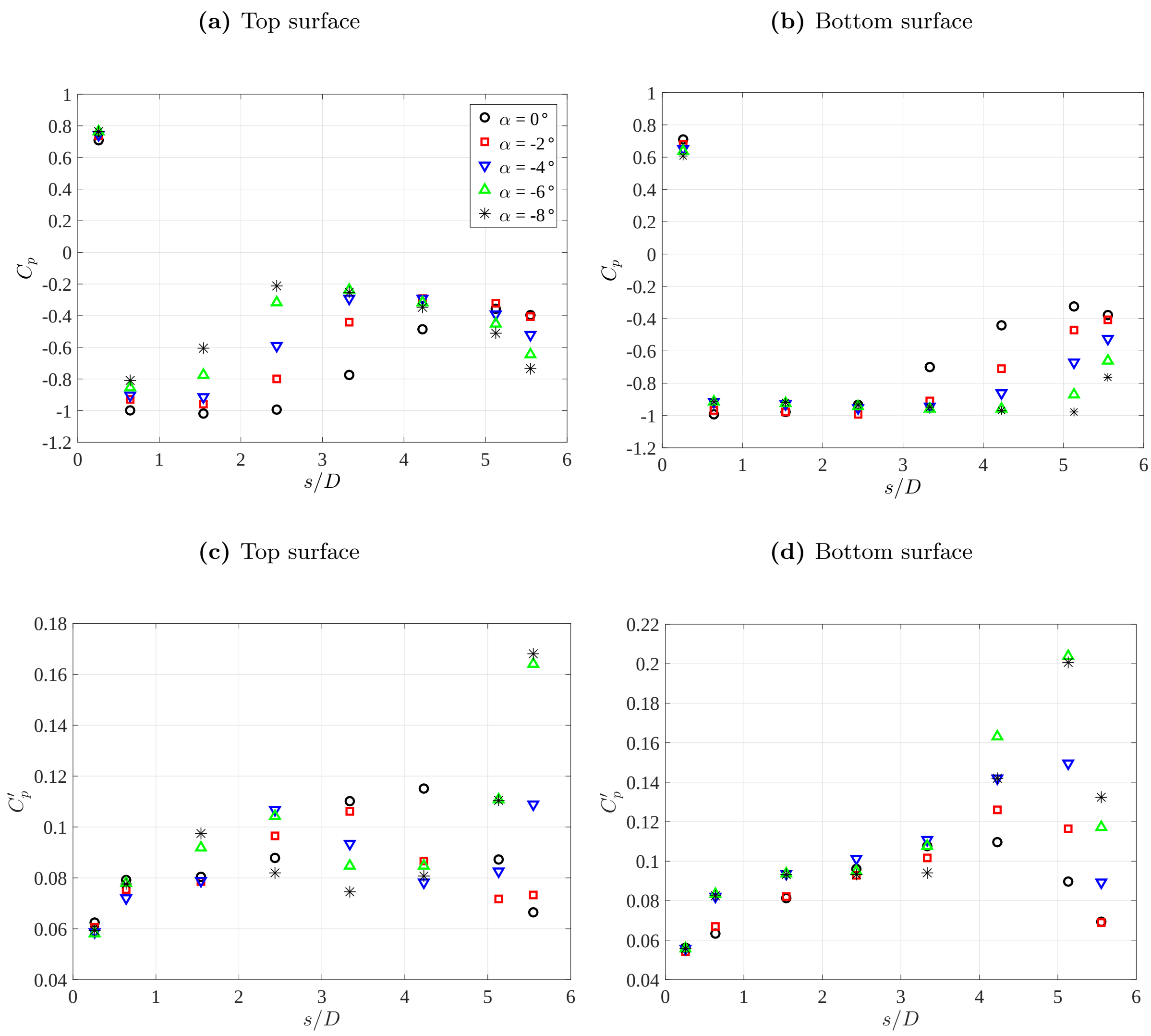

Figure 6.10: Variation of the surface distribution of the time-averaged pressure coefficient C_p and the standard deviation of the time-varying pressure coefficient C'_p with respect to the angle of attack; the Reynolds number is Re = 52000.

The Reynolds independence of the aerodynamics of the flow field is illustrated in Figure 6.6 for the angle of attack 0° and in Figures D.1, D.2, D.3 and D.4 in Appendix D for the other angles of attack. The distribution of the surface pressure at a certain angle of attack showed similar behaviour despite differences in the Reynolds number. The slight dependence on the Reynolds number of the moment coefficient and the Strouhal number at large angles of attack as shown in Figures 6.1c and 6.1d could be due to the narrowing effect of the wake region as the Reynolds number increased, which indicated by a reduction in the time-averaged base pressure coefficient measured on the back face (Figure 6.10a and 6.10b).

Wind tunnel static tests together with the computational static simulations have shown the existence of two key aerodynamic flow features around a 5:1 rectangular cylinder in the smooth flow. The first one was the separation bubble which involved circulating flow trapped underneath the shear layer created from the separation point at the leading edge. This flow feature was relatively stable and well-defined in the span-wise direction. It was followed by the second one which was called the reattachment region, where the shear layer reattached to the surface of the model, creating intermittent and highly fluctuating flow field. Moreover, the flow field around the 5:1 rectangular cylinder possessed characteristics similar to the impinging leading edge vortex shedding where there existed the synchronisation between the creation of the shear layer at the leading edge and the vortex shedding occurring at the trailing edge. Results of the force measurement and the analysis of the surface pressure suggested that the flow field around a 5:1 rectangular cylinder was independent of the Reynolds number. At angles of attack different from $0°$, significant variation was observed. On the surface of the model that was exposed more to the flow, the separation bubble was suppressed and the reattachment was shifted towards the leading edge. On the other surface, the opposite behaviour occurred and at the angle of attack $-6°$, the reattachment point on this surface disappeared, resulting in the stall position where the model suddenly experienced losses in lift and moment. At larger angles of attack, slight Reynolds-number dependence exhibited in the moment coefficient and the Strouhal number, which was thought to be due to the narrowing effect of the wake region observed at higher Reynolds numbers.

6.2 TURBULENCE-INDUCED EFFECTS ON FLOW FIELD AROUND A STATIC 5:1 RECTANGULAR CYLINDER

In the turbulent flow, the two aforementioned key aerodynamic flow features around the rectangular cylinder underwent significant alteration, particularly for the first flow feature, the separation bubble. Figure 6.11 illustrates the variation of the surface pressure distribution with respect to different turbulence levels at the angle of attack $0°$. The turbulence-induced effect was found to be limited at the point that was close to the trailing edge ($s/D = 5.128$) and at the back face ($s/D = 5.676$). However, on the side surface, an increase in the turbulence level led to a stronger and shorter separation bubble accompanied by a quicker pressure recovery as illustrated by an upstream shift of the peak of both of the distribution of C_p and C_p' and an increase in the suction and pressure fluctuation. Results at other Reynolds numbers are attached in Appendix D and also described similar behaviours of the separation bubble in the turbulent flow. Moreover, detailed analysis of the distribution of C_p' revealed that an increase in the Reynolds number resulted in a reduction in the peak of the C_p' distribution curve, i.e. a decrease in the fluctuation around the reattachment region. Therefore, in the turbulent flow, the flow field around the rectangular cylinder possessed some Reynolds-number dependence that the turbulence-induced effect was suppressed at high Reynolds numbers.

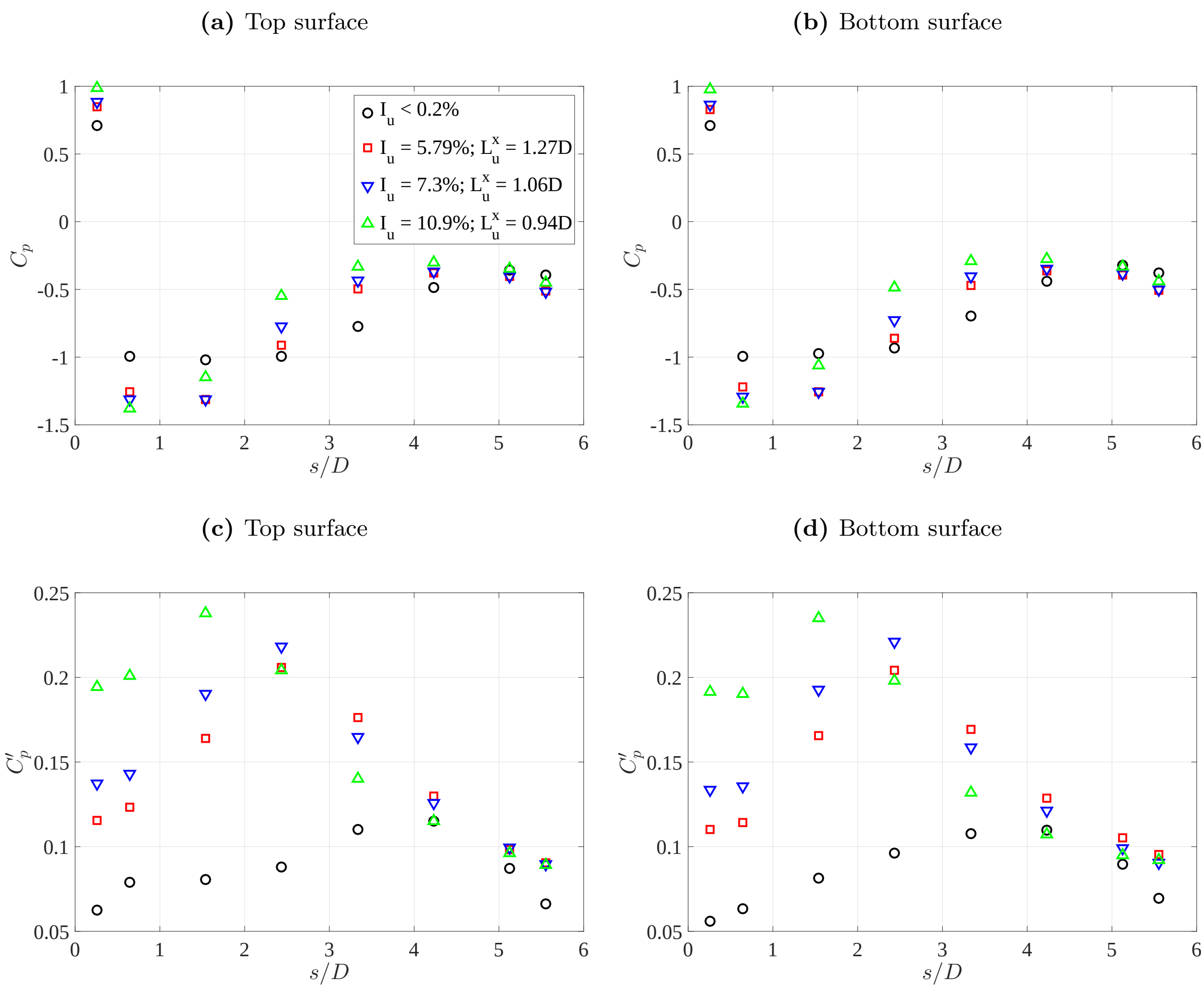

Figure 6.11: Surface distribution of the time-averaged pressure coefficient C_p and the standard deviation of the time-varying pressure coefficient C'_p in different flow conditions; the Reynolds number was Re = 52000 and the angle of attack was 0°.

Not only significantly affecting the stream-wise geometry of the separation bubble, the upstream turbulence was also found to influence the pressure correlation in the span-wise direction. Figure 6.12 shows that, at the angle of attack 0°, in the turbulent flow, the pressure correlation measured at Positions A and B was lower than those measured in the smooth flow; an increase in the turbulent level led to a reduction in the pressure correlation at these two positions. On the other hand, there was little effect of turbulence on Position C while the turbulence was found to slightly enhance the pressure correlation at Position D. In fact, the surface pressure measured at the Positions A and B was less correlated in the span-wise direction than that measured at the Position D. These results show that, particularly for the 5:1 rectangular cylinder, the turbulence level introduced in this wind tunnel study significantly altered the flow structure around the model and promoted the trailing-edge vortex shedding rather than the impinging leading-edge vortex shedding as was seen in the smooth flow.

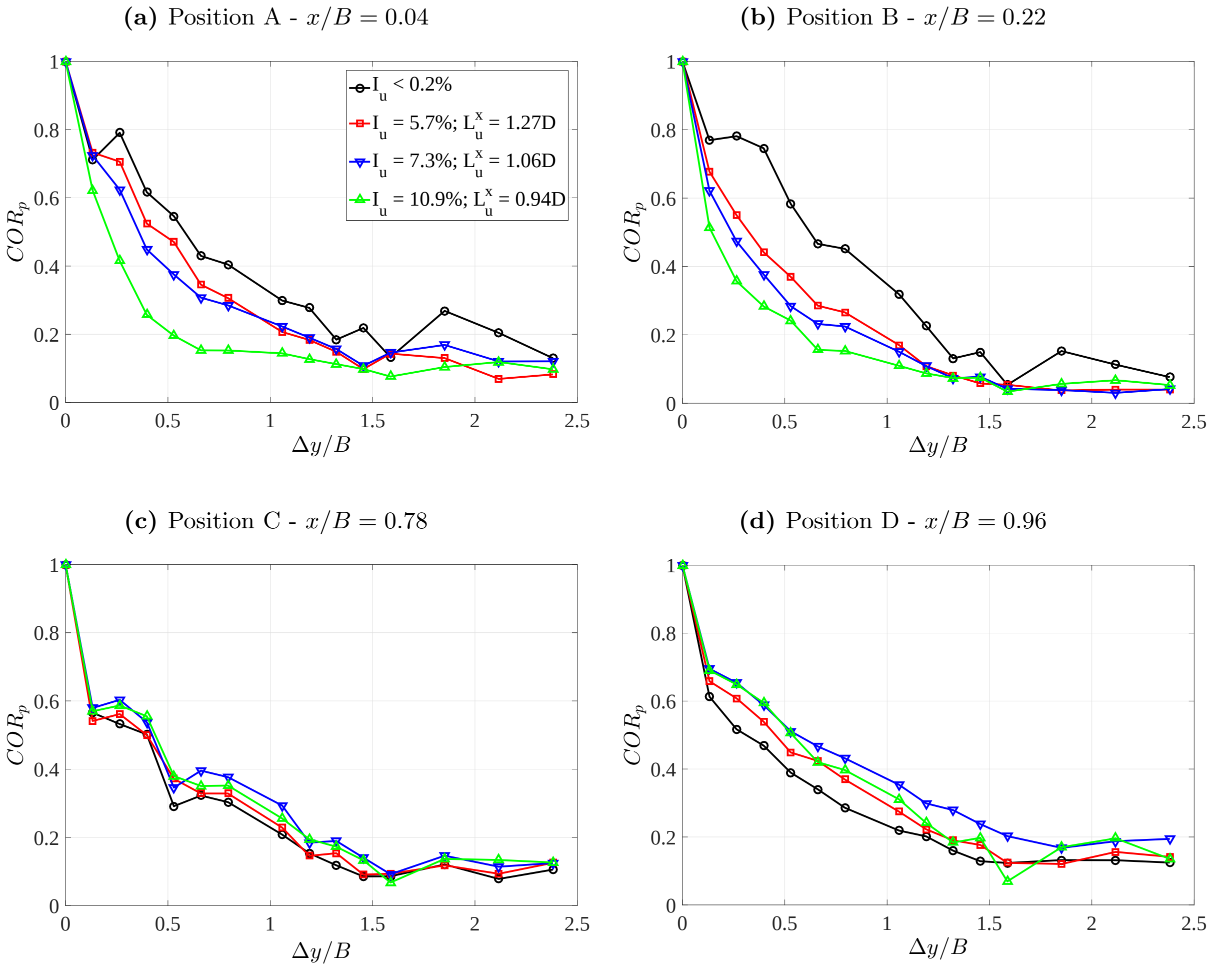

Figure 6.12: Effect of turbulence levels on the pressure span-wise correlation at 4 steam-wise positions; the Reynolds number was Re = 31200.

The variation of the angle of attack is observed to either enhance or reduce the turbulence-induced effect on the flow field around the rectangular cylinder. Figure 6.13 shows results of the surface pressure distribution measured at all angles of attack and in the most turbulent flow according to the set up, i.e. $I_u = 10.9\%$ and $L_u^x = 0.94D$. Using the sign convention of the angle of attack discussed in Section 6.1.2, the top surface was exposed more to the wind and the turbulence-induced effect was enhanced, which is indicated by significantly suppression effect in the stream-wise geometry, the strength and the fluctuation. On the other hand, by varying the angle of attack, the separation bubble on the bottom surface experienced less turbulence-induced effect; it elongated further downstream and increased in strength. Similar effects are also observed in the less turbulent flow, as can be seen in Figures D.8 and D.9 attached in Appendix D.

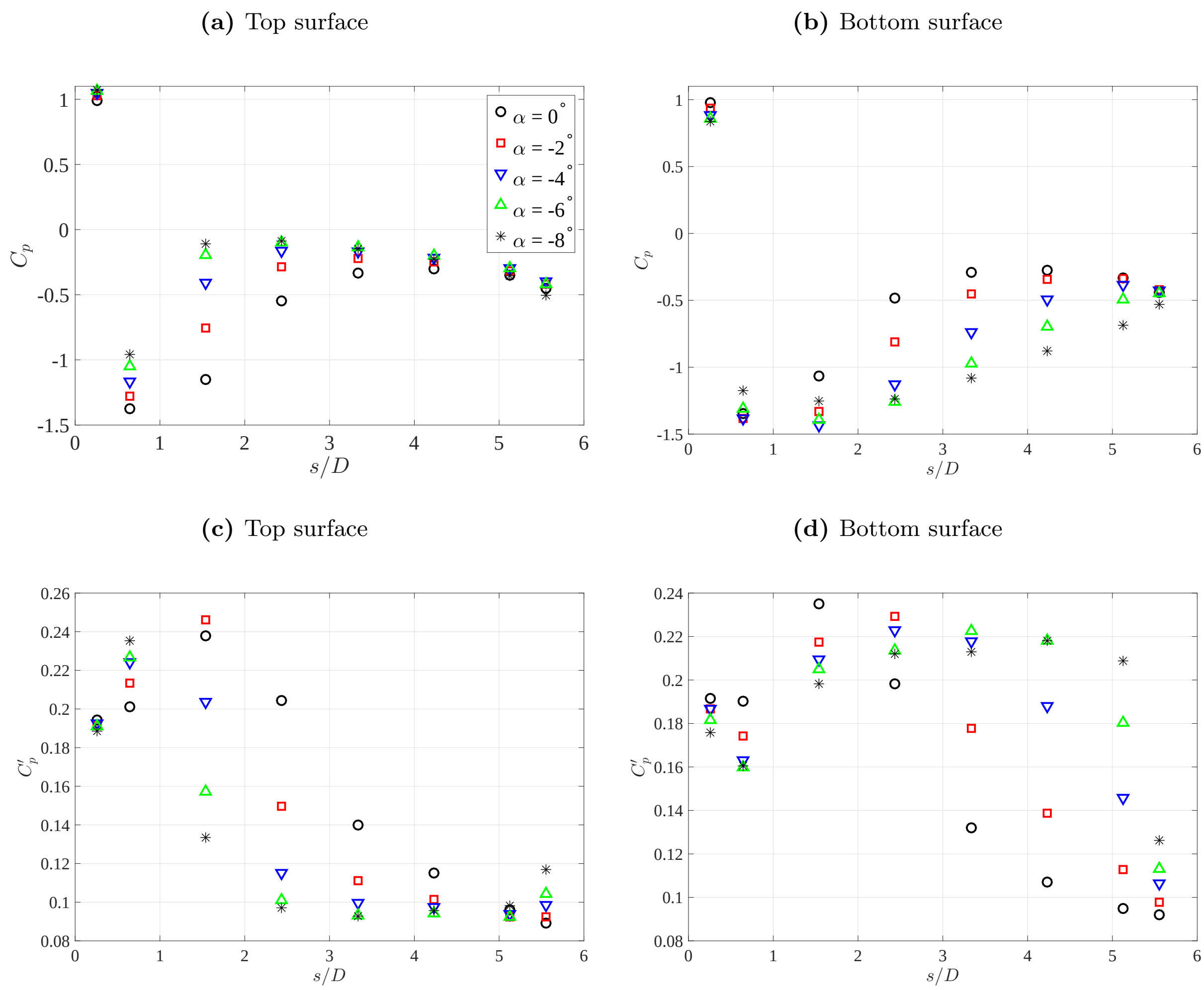

Figure 6.13: Surface pressure distribution of the cylinder oriented at different angles of attack and in the turbulent flow having the turbulence intensity $I_u = 10.9\%$ and the length scale $L_u^x = 0.94D$; the Reynolds number was Re $= 52000$.

More importantly, an investigation of the span-wise correlation of the surface pressure revealed both of the negative and positive effect of the variation of the angle of attack on the flow field around the cylinder. Due to limitation in instrumentation relating to the pressure measurement, the span-wise correlation of the surface pressure on the top and bottom surfaces of the model could not be identified simultaneously. Instead, only the surface pressure on the bottom surface was measured and a full range of the angle of attack from $-8°$ to $8°$ in a $2°$ increment was utilised. During positive angles, the bottom surface was exposed more to the wind; as can be seen in Figure 6.14, an increase in the angle of attack resulted in a reduction in the surface pressure correlation at Positions A and B. This observation meant that the separation bubble along the leading edge was more unstable and broke up due the combined effect induced by the upstream turbulence and by the angle of attack. In fact, at the angles of attack $6°$ to $8°$, the span-wise pressure correlation at Position B was found to slightly restore, which was possibly due to the fact that the flow stayed attached nearly on the entire surface of the model. This flow feature was also responsible for higher pressure correlation close to the trailing edge, i.e. Positions C and D. At the angle of attack 8°, additional effect from the circulating flow in the wake slightly reduced the span-wise pressure correlation at this region. On the other hand, when the angles of attack were negative, Figure 6.15 showed that a decrease in the angle of attack caused a rise in the pressure correlation, particularly in Positions A and B. In fact, by decreasing the angle of attack, it tended to strengthen the formation of the separation bubble along the leading edge in the span-wise direction and reduced the suppression effect induced by the turbulent flow. This effect led to a re-creation of the unsteady reattachment flow close the trailing edge, reducing the span-wise correlation of the pressure measured at Positions C and D. By comparing against the pressure correlation measured at the angle of attack 0° and in the smooth flow, it was obvious that, on the bottom surface, a decrease in the angle of attack could potentially restore the impinging leading-edge vortex shedding flow feature as was observed in the smooth flow; this restoration effect could vary depending on the turbulence level and the Reynolds number.

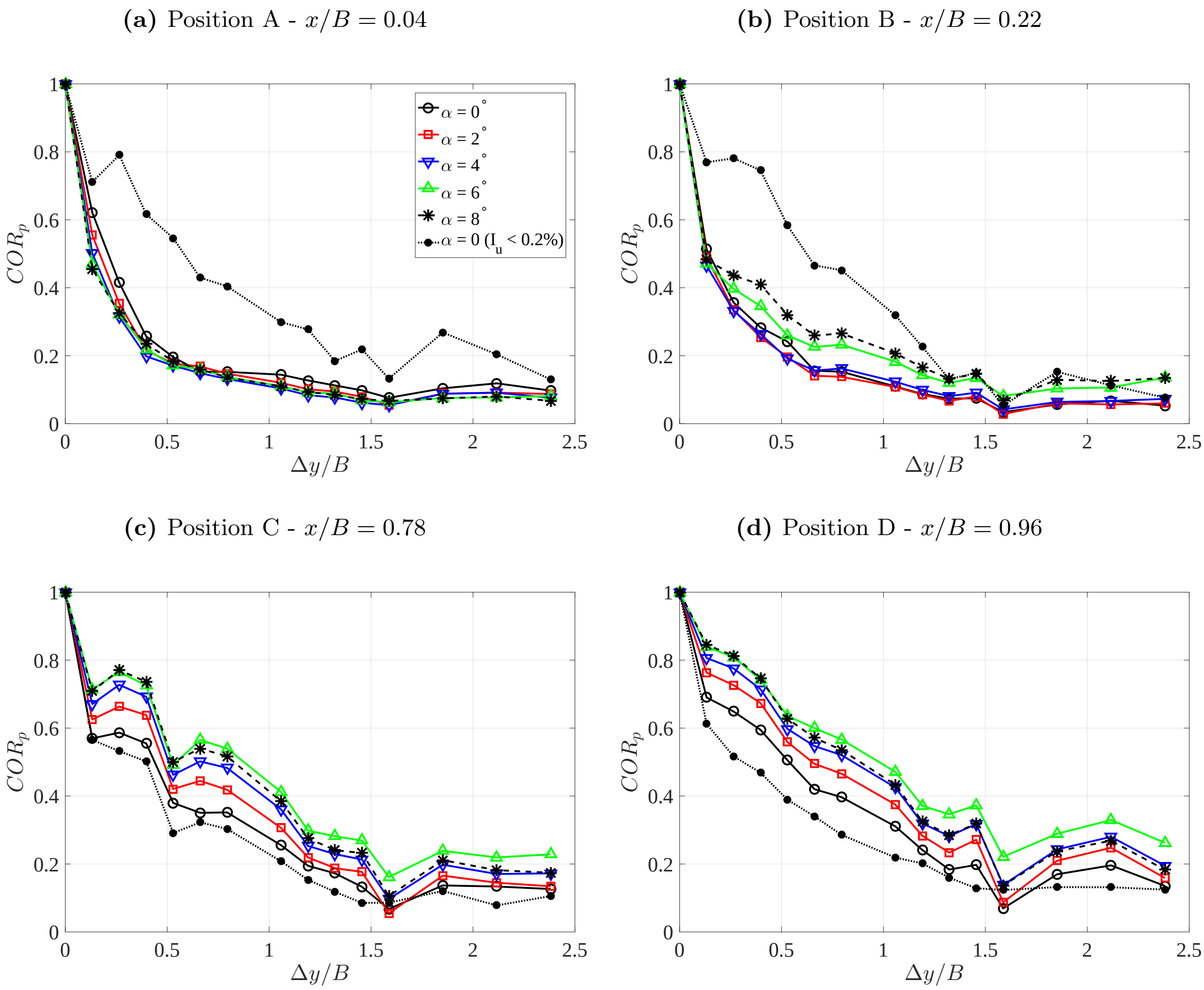

Figure 6.14: Variability of the span-wise surface pressure correlation on the bottom surface in the turbulent flow having the turbulence intensity $I_u = 10.9\%$ and the length scale $L_u^x = 0.94D$ and at the angles of attack from 0° to 8°; the Reynolds number was Re = 31200.

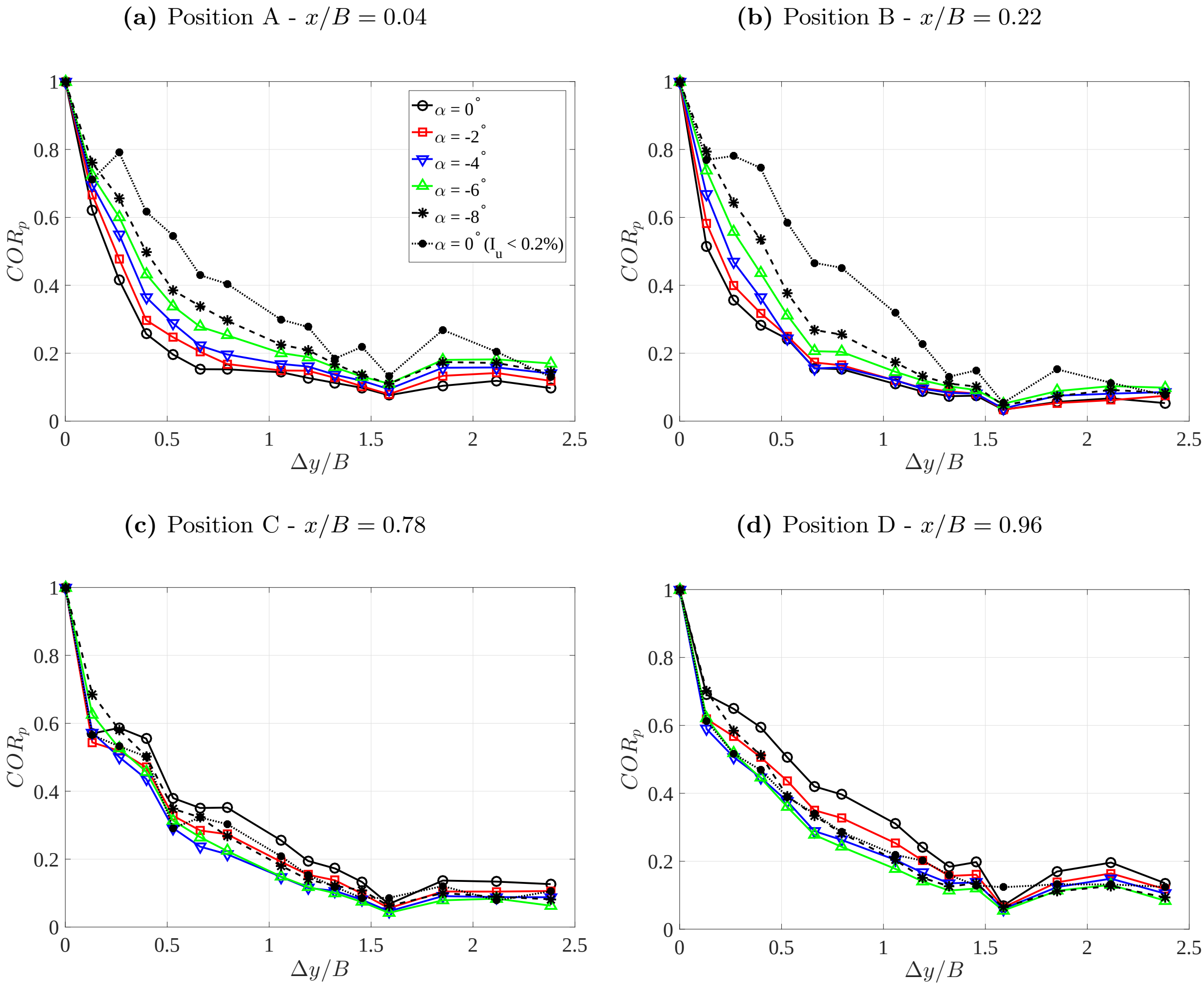

Figure 6.15: Variability of the span-wise surface pressure correlation on the bottom surface in the turbulent flow having the turbulence intensity $I_u = 10.9\%$ and the length scale $L_u^x = 0.94D$ and at the angles of attack from $0\circ$ to $-8°$; the Reynolds number was Re $= 31200$.

In general, in the case of the static rectangular cylinder, the turbulent flow was found to significantly impact the separation bubble while it had very limited effect on the reattachment region. At the angle of attack 0°, the separation bubble experienced the turbulence-induced suppression effects, featuring a reduction in both of the stream-wise geometry and the circulating strength and a more frequent breaking-up in the span-wise direction; the suppression effect was more severe at higher Reynolds numbers. In the reattachment region, the upstream turbulence slightly enhanced the surface pressure correlation. Therefore, at the angle of attack 0°, the turbulent flow dramatically altered the aerodynamic characteristics of the flow field around the rectangular cylinder, promoting the trailing-edge vortex shedding instead of the impinging leading-edge vortex shedding observed in the smooth flow. However, at the non-zero angles of attack, this observation might not be hold. As the angle of attack increased, the turbulence-induced suppression effect tended to be strengthened on the side surface which exposed to the wind while, on the other side, the suppression was effectively lessened. In fact, depending on the turbulence level and

Reynolds numbers, at some angle of attack, the impinging leading edge vortex shedding could be restored on this side surface; it might be expected that the restoration could be more successful in the flow having a lower turbulence level and a smaller Reynolds number.

6.3 VIV MECHANISM OF THE 5:1 RECTANGULAR CYLINDER

The 5:1 rectangular cylinder could undergo VIV in two modes, either the heaving mode or pitching mode. The former is essentially when the model was restrained to the cross-wind translation motion in the vertical direction only and it represents the bending motion of a full-scale flexible structure. On the other hand, the pitching mode where the model was restrained to the cross-wind angular displacement around the centre of gravity only is equivalent to the torsional motion of a full-scale structure. The heaving VIV of the rectangular cylinder was modelled in the wind tunnel and computational study while the pitching VIV was measured in the wind tunnel only.

6.3.1 Heaving VIV of the 5:1 Rectangular Cylinder

Figures 6.16 and 6.17 summarise results as the rectangular cylinder underwent the heaving VIV, measured in the wind tunnel dynamic tests and in the 3D heaving simulation respectively. It was noticed that, due to the unavailability of a reliable force measurement during the dynamic test, information related to the lift force or moment was retrieved by performing the integration of the surface pressure measured at the pressure array 4. The pressure measurement was associated with certain limitation of the sensitivity at low wind speeds; therefore, results of force and moment were also restricted in the this range of the wind speed. The vortex shedding frequency in the wind tunnel tests was extracted from the w-component of the velocity measured at a distance B behind the wind tunnel model and a distance $D/2$ above the top surface.

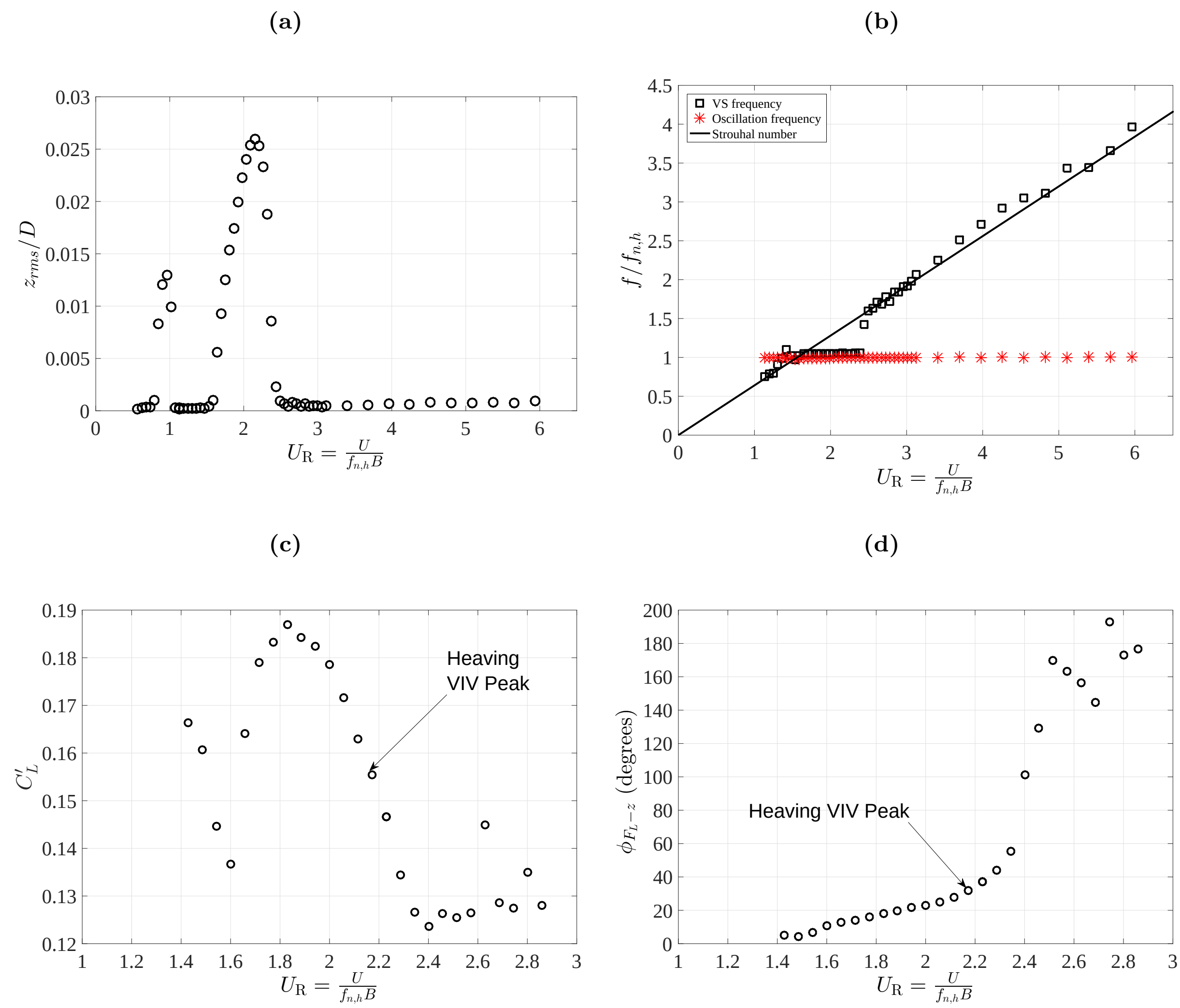

Figure 6.16: Results of the wind tunnel dynamic test of the sectional model restrained to the heaving mode only: (a) structural response, (b) frequency of response, (c) lift coefficient response and (d) phase shift of the lift force against the structural displacement.

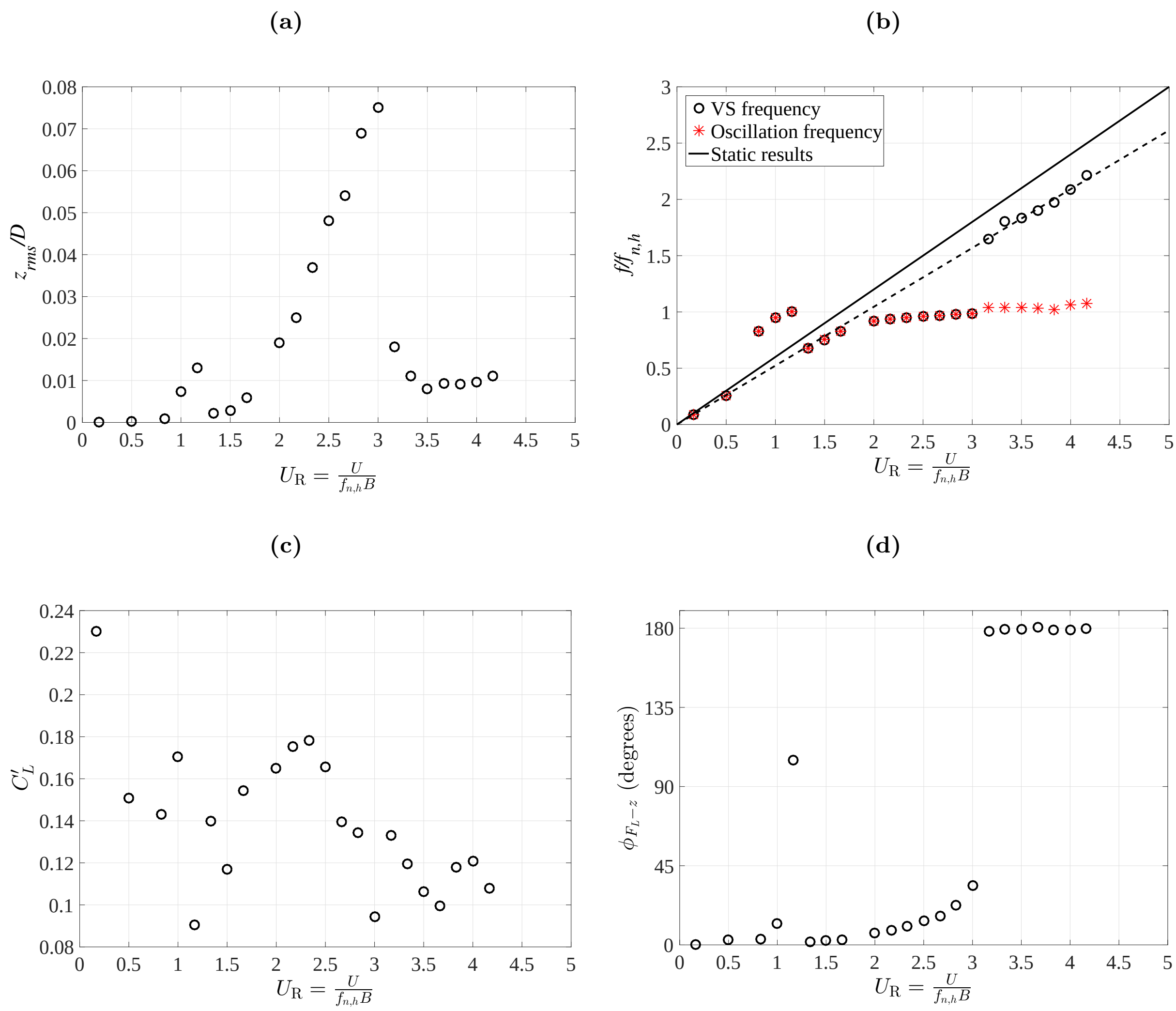

Figure 6.17: Results of the 3D heaving simulation of the sectional model: (a) structural response, (b) frequency of response, (c) lift coefficient response and (d) phase shift of the lift force against the structural displacement.

Despite differences in the key structural parameters such as the mass of the model and the structural damping (Sections 4.5 and 5.1.2), there existed good agreement between results obtained from wind tunnel tests and the computational simulation. As for the rectangular cylinder restrained to the heaving mode only, both studies predicted two VIV lock-in intervals indicated by an increase in the structural response and the fact the vortex shedding frequency was locked into the natural frequency of the model. Due to the larger structural damping, i.e. the larger Scruton number, the wind tunnel test predicted lower structural responses during the VIV lock-in compared to the one predicted by the computational simulation. Nevertheless, the onset reduced wind speed $U_R = U/(f_{n,h}B)$ of the VIV lock-in was well predicted and a good agreement between the wind tunnel and computational studies could be drawn. Based on Nakamura et al. (1991) and Matsumoto (2004), as for the 5:1 rectangular cylinder, the onset reduced wind speed of the heaving VIV lock-in was given by $U_{R,\text{onset}} = n/\text{St}$ where n is the number of vortices appearing on one side surface during one cycle of the structural response.

The wind tunnel dynamic test predicted two heaving VIV lock-in regions occurring at the reduced wind speeds of $U_{\mathrm{R,onset}} = 0.77$ and 1.54; the former was smaller in magnitude (Figure 6.16a). Similarly, as modelled in the 3D heaving simulation (Figure 6.17a), two VIV lock-in intervals were found and occurred at $U_{\mathrm{R,onset}} = 1$ and 2. These peaks were related to different aerodynamic characteristics of the flow field around the cylinder. The phase analysis of the vortex structure on the top surface is shown in Figure 6.18; only CFD results were available for the secondary VIV peak. These results indicated that the smaller peak was associated with two vortices alternately being formed on either side of the model during one cycle of motion, i.e. $n = 2$. This contrasted with there being only one vortex on the side when the model experienced the larger response, i.e. $n = 1$; the smaller peak was thus considered as the secondary or the second harmonic of the heaving VIV. The instantaneous flow field around the cylinder during the occurrence of the secondary and primary VIV peaks are illustrated by the contour plot of the Q-criterion as shown in Figure 6.19 where similar difference in the flow structure could be observed.

(a) Secondary VIV peak **(b)** Primary VIV peak

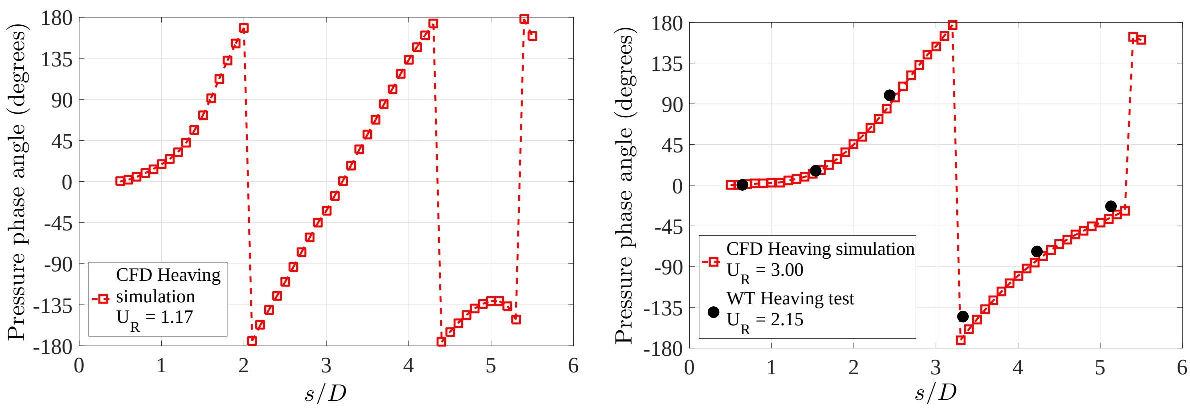

Figure 6.18: Phase angles of vortices rolling on the surface of the cylinder measured in the wind tunnel dynamic test and in the 3D heaving simulation; all results are calculated at the reduced wind speeds corresponding the maximum structural displacement during the lock-in.

(a)

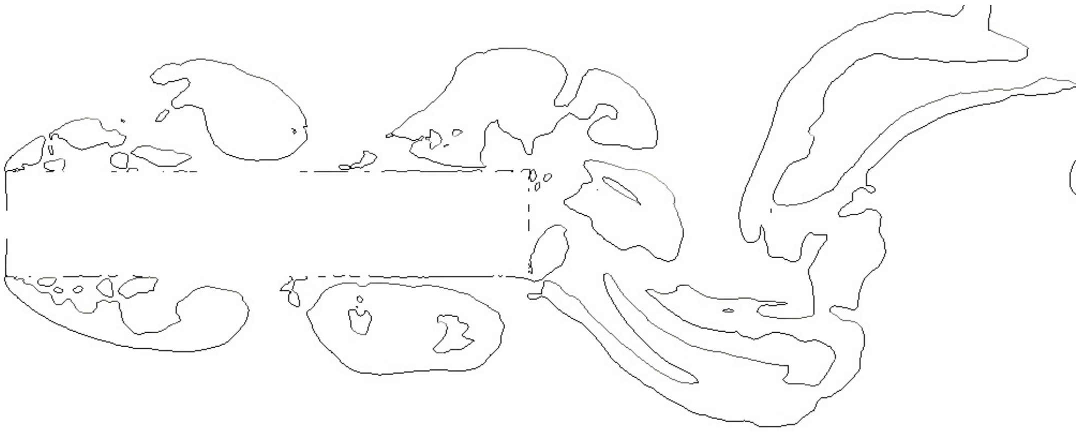

(b)

Figure 6.19: Contour plots of the Q-criterion $Q = 0.1\,\mathrm{m\,s^{-1}}$ along the mid-span plane at (a) $U_{\mathrm{R}} = 1.17$, i.e. the secondary VIV peak and (b) $U_{\mathrm{R}} = 3.00$, i.e. the primary VIV peak; results were obtained from the 3D heaving simulation.

As for the wind tunnel dynamic test, the onset reduced wind speeds of the heaving VIV lock-in were found to be in a good agreement with the Strouhal number predicted in the wind tunnel static test, St = 0.64 measured at the angle of attack 0° and at the Reynolds number of 20800. However, results estimated in the 3D heaving simulation were not correspondent to the Strouhal number predicted by the static simulation, St = 0.6. This difference could be visualised by Figure 6.17b where the vortex shedding frequencies measured outside the lock-in region did not follow the line obtained from the static simulation; instead, they suggested a lower value of the Strouhal number St = 0.52. This underestimation of the Strouhal number in the 3D heaving simulation was due to the use of a computational domain having coarse span-wise discretisation compared to the one used in the static simulation. Another difference between results of the wind tunnel dynamic and the 3D heaving simulation was that the former was conducted in a successive manner, where the wind speed was increased gradually while, in the latter, simulations were carried out in a parallel manner. This meant that the memory effect of the structure and the fluid was not modelled correctly in the computational study, resulting in a sudden drop of the structural response just before the system reached lock-out in a sharp contrast to the more gradual decrease observed in the wind tunnel test. In addition, during the wind tunnel test, the presence of the rolling motion of the model impaired results of the vortex shedding frequency and the phase shift of the lift force; this issue is indicated by some fluctuation in the normalised vortex shedding frequency just before the lock-in (around $U_\mathrm{R} = 1.4$) and in the phase shift of the lift force when the system reached lock-out (around $U_\mathrm{R} = 2.5$) as shown in Figures 6.16b and 6.16d.

Both the wind tunnel dynamic test and the 3D heaving simulation predicted similar behaviour for the phase shift of the lift force against the displacement of the cylinder as shown in Figures 6.16d and 6.17d. As the amplitude of the structural response increased, the in-phase component of the lift force became less dominant and after the cylinder reached the lock-out, the lift force suddenly became out-of-phase. This transition also indicated that there was a dramatic change in the flow structure around the cylinder which was responsible for the lock-out.

An investigation of the span-wise correlation of the surface pressure measured along the leading edge and trailing edge revealed there was a significant variation in the aerodynamic characteristics of the flow field around the cylinder as the heaving VIV lock-in occurred. Concentrating on the primary peak of the heaving VIV measured in the wind tunnel dynamic test, the variation of the span-wise pressure correlation around the leading edge (Positions A and B) and around the trailing edge (Positions C and D) as the cylinder experienced the lock-in is illustrated in Figure 6.20. Before the lock-in occurred, the pressure correlation around the leading edge was higher than that around the trailing edge. The increase in the amplitude of the response improved the correlation of the surface pressure. However, during the lock-in, the correlation level around Position C was higher than those around the leading edge. This result indicated a strongly correlated flow feature occurred at Position C every cycle of the motion and it led to an increase in the response whereas the motion-induced leading-edge vortex was only responsible for triggering the motion. In addition, an issue relating to the span-wise pressure correlation in the wind tunnel dynamic tests is noticed, which is an increase in the pressure correlation at $\Delta y/B = 1$; this phenomenon however was not observed in the wind tunnel static tests. The cause of this variation was thought to be induced by the motion of the cylinder, particularly the rolling motion which is the angular oscillation around the x axis. This motion coupling with a finite span-wise length of the model and the end plates resulted in some standing wave effect superimposing on the flow field, which created alternately well-correlated and poorly-correlated flow structures along the span-wise direction. Therefore, this issue is important and is required further studies to allow better quality pressure measurement.

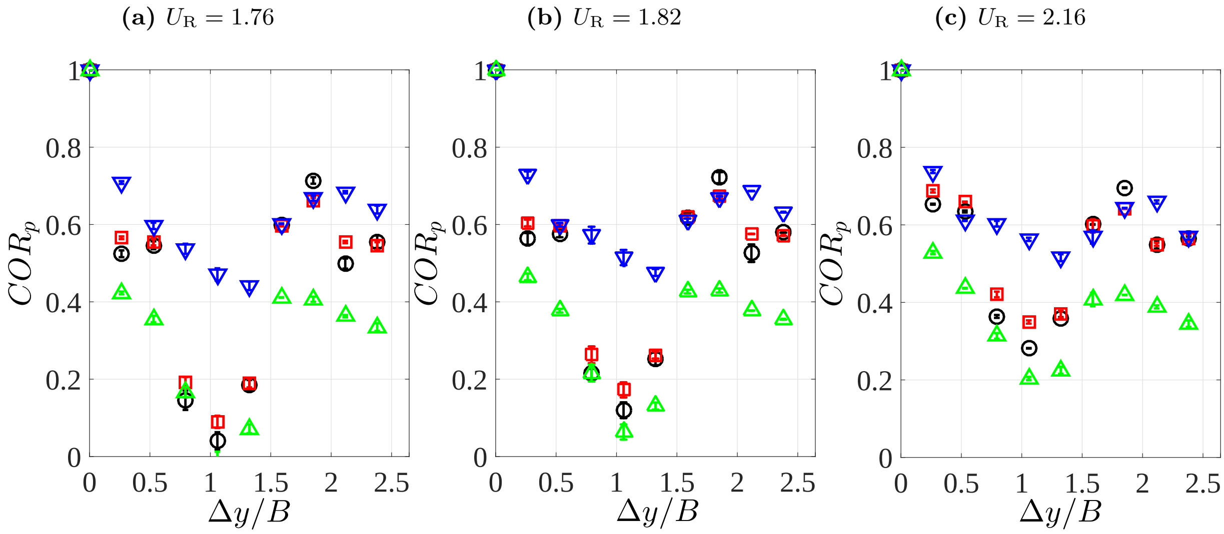

Figure 6.20: Wind tunnel results of the span-wise pressure correlation measured at 4 stream-wise positions in the smooth flow during the heaving VIV lock-in; *black*: Position A; *red*: Position B; *blue*: Position C; *green*: Position D.

Again, results obtained from the 3D heaving simulation revealed similar behaviour. As shown in Figure 6.21, at $U_{\mathrm{R}} = 1.67$ which was just before the VIV lock-in, the amplitude of the response was small and the flow field around the cylinder shared some similar features as the static cylinder. When the lock-in occurred and the amplitude of the response increased ($U_{\mathrm{R}} = 2.00$ to 2.67) and reached the peak ($U_{\mathrm{R}} = 3.00$), a slight decrease in the correlation level around the leading edge was observed while, around the trailing edge, the flow field was better correlated. When the system reached the lock-out, the correlation level around the trailing edge suddenly decreased. Together the wind tunnel dynamic test, these results from the computational simulation indicated that, particularly for the 5:1 rectangular cylinder, the motion-induced leading-edge vortex acted as a triggering mechanism for the VIV response while there existed a strongly correlated flow feature occurring around the trailing edge, which made the amplitude of the structural response to rise.

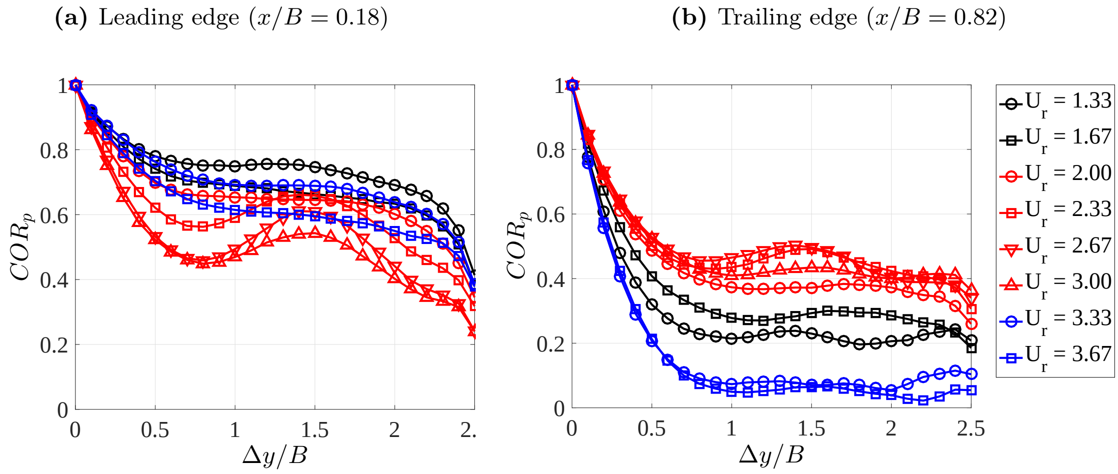

Figure 6.21: Computational results of variation of the span-wise pressure correlation around the leading and trailing edges as the cylinder experienced the heaving VIV lock-in; *black*: before the lock-in; *red*: VIV lock-in; *blue*: after the lock-in.

A series of images describing the variation of the pressure field on the top surface at $U_\mathrm{R} = 3.00$ was extracted from the 3D heaving simulation as shown in Figure 6.22. The pressure field presented here is the dominant component resulted from a Proper Orthogonal Decomposition analysis. At the start of the cycle of structural motion $t = 0$, i.e. when the cylinder reached the maximum positive displacement, there was a vortex being shed from the leading edge; the downward motion of the cylinder from $t = 0$ to $T_{n,h}/2$ however significantly affected its span-wise geometry, degrading its span-wise correlation and causing it to propagate downstream. In the next quarter of the cycle, due to the upward accelerating movement of the cylinder, this motion-induced leading-edge vortex dramatically slowed down and appeared to imping on the surface of the cylinder. During this process, this vortex gained strength and its span-wise correlation improved; this increased the lift force acting on the cylinder in the direction such that the cylinder was effectively brought back to the equilibrium position. In the final quarter of the cycle, thanks to the decelerating upward motion of the cylinder, this vortex was pushed downstream at a higher rate and was eventually shed into the wake. The behaviour of the motion-induced leading-edge vortex during one cycle of the heaving motion is summarised in Figure 6.23. It is clear that the motion-induced vortex created along the leading edge was responsible for triggering the motion while the impingement of this vortex on the surface of the cylinder resulted in an increase in the structural response during the lock-in.

(a) $t = 0$

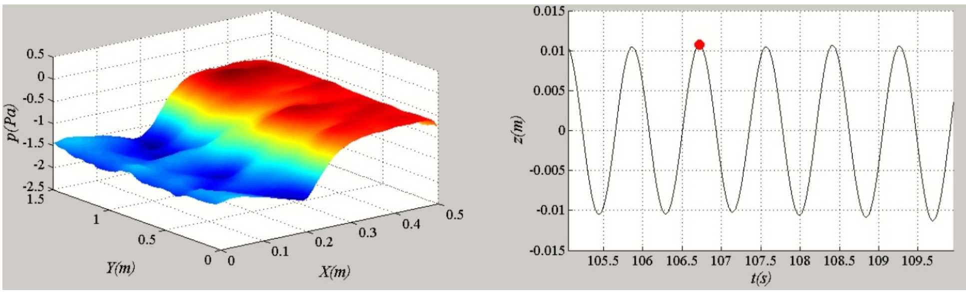

(b) $t = T_{n,h}/4$

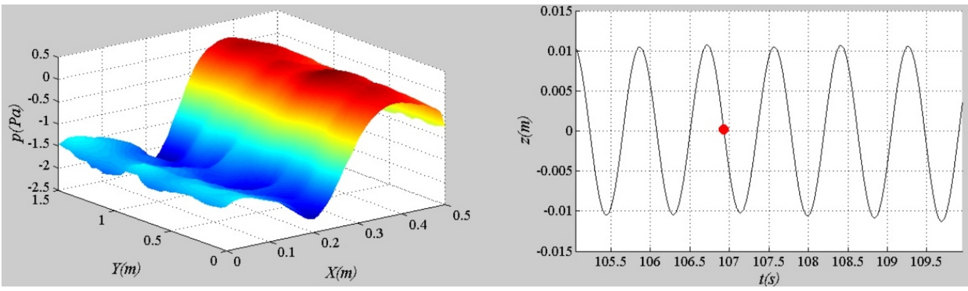

(c) $t = T_{n,h}/2$

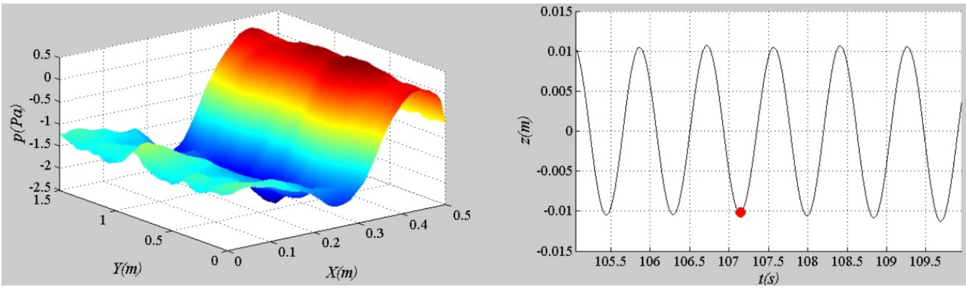

(d) $t = 3T_{n,h}/4$

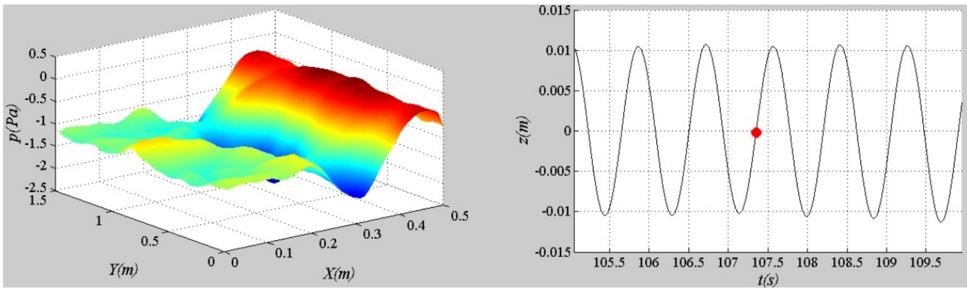

(e) $t = T_{n,h}$

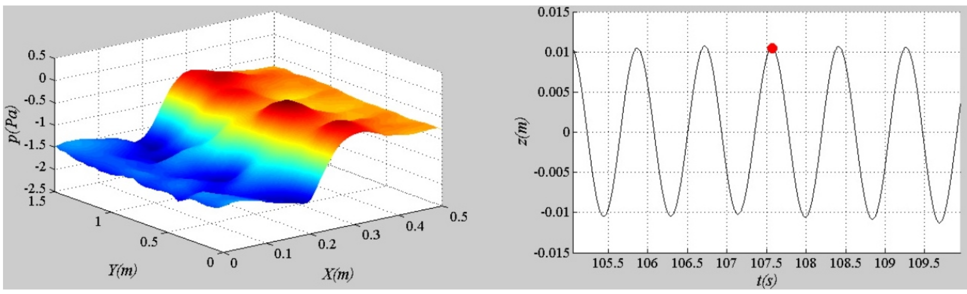

Figure 6.22: Pressure field on the top surface of the cylinder at every quarter of the cycle of the structural motion ($T_{n,h}$) obtained from the 3D heaving simulation; the *red* dot indicates the position of the cylinder during the cycle.

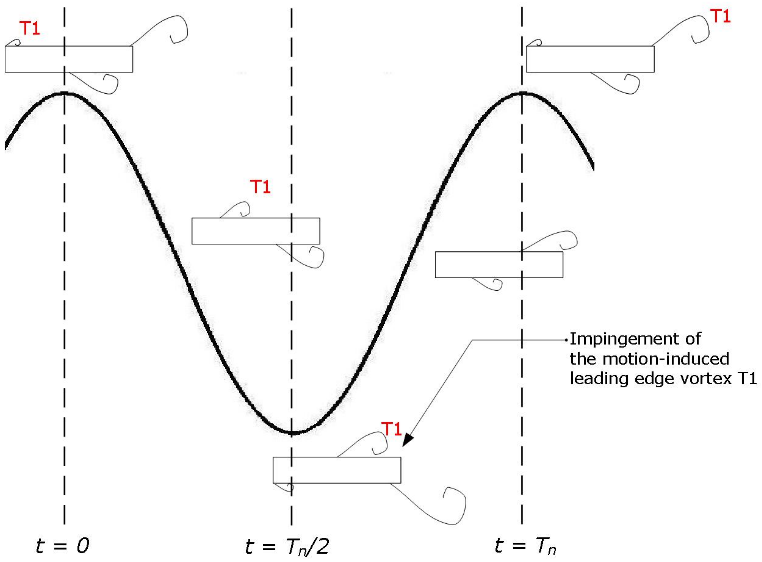

Figure 6.23: Schematic illustrating the development of the motion-induced leading edge vortex T1 throughout one cycle of the heaving motion during the VIV lock-in.

6.3.2 Pitching VIV of the 5:1 Rectangular Cylinder

When the model was restrained to the pitching mode only, two different behaviours were observed as shown in Figure 6.24. The torsional flutter occurred at a high wind speed characterised by a dramatic increase in the angular displacement. One pitching VIV lock-in was observed at the reduced wind speed $U_{\mathrm{R}} = 1.03$. The phase relationship of the surface pressure measured along a stream-wise line on the top surface revealed there were 1.5 vortices during one cycle of the motion (Figure 6.25) or, in other words, it took 1.5 cycles of the motion for one vortex created at the leading edge to travel along the width of the cylinder and then to shed into the wake from the trailing edge. Based on Matsumoto (2004), this flow behaviour corresponded to the second harmonic of the VIV; the primary peak or the first harmonic did not appeared as was also found by Nakamura and Nakashima (1986). The pitching response of the cylinder possessed some different features in comparison to the heaving response; as the wind speed increased, the angular response rose quite suddenly and beyond the peak, it gradually decreased. Analysing the phase angle of the pitching moment against the angular displacement revealed a more gradual change in the phase lag as the model experienced the lock-in.

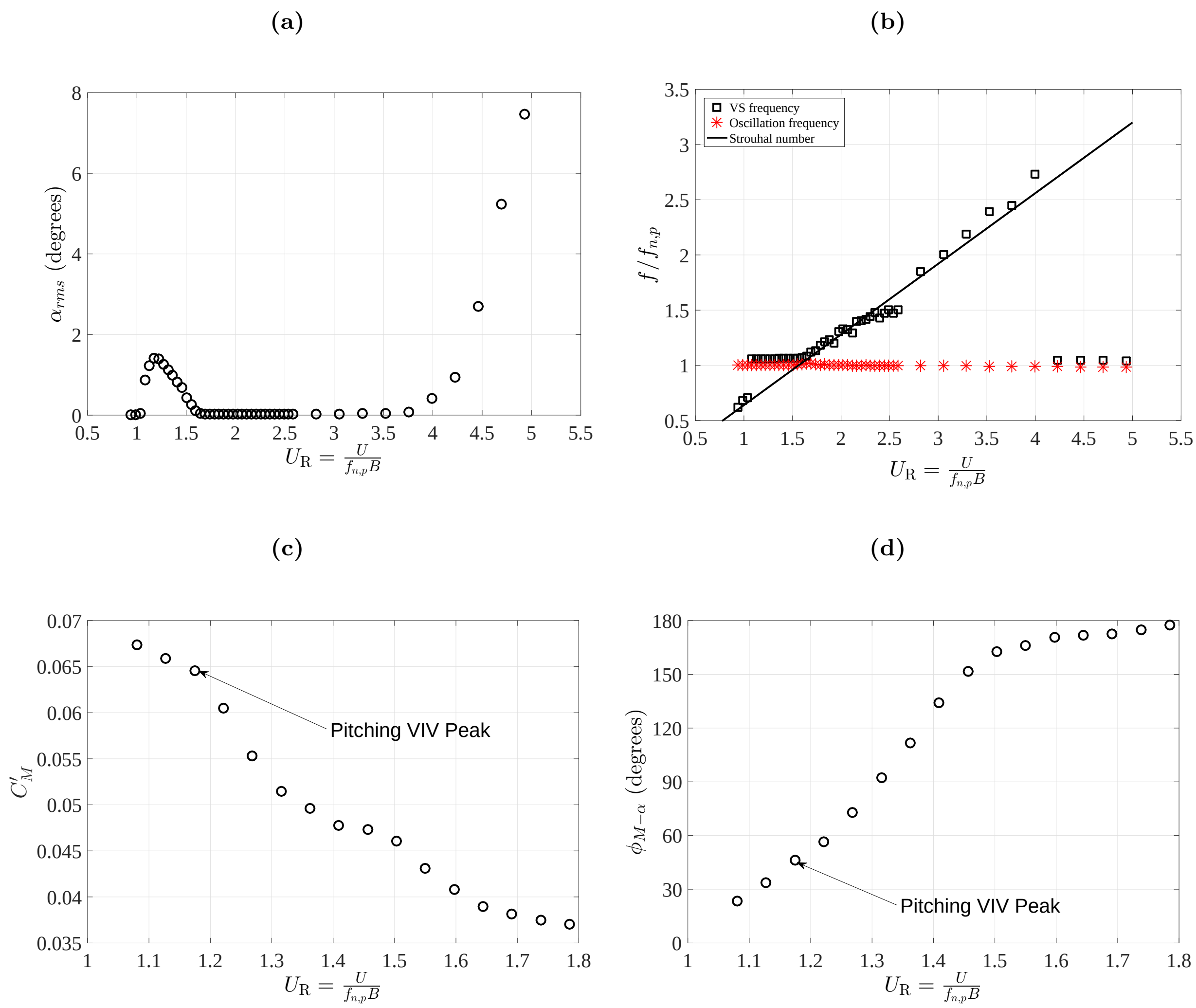

Figure 6.24: Results of the wind tunnel dynamic test of the section model restrained to the pitching mode only: (a) structural response, (b) frequency of response and (c) moment coefficient response and (d) phase shift of the moment against the structural angular displacement.

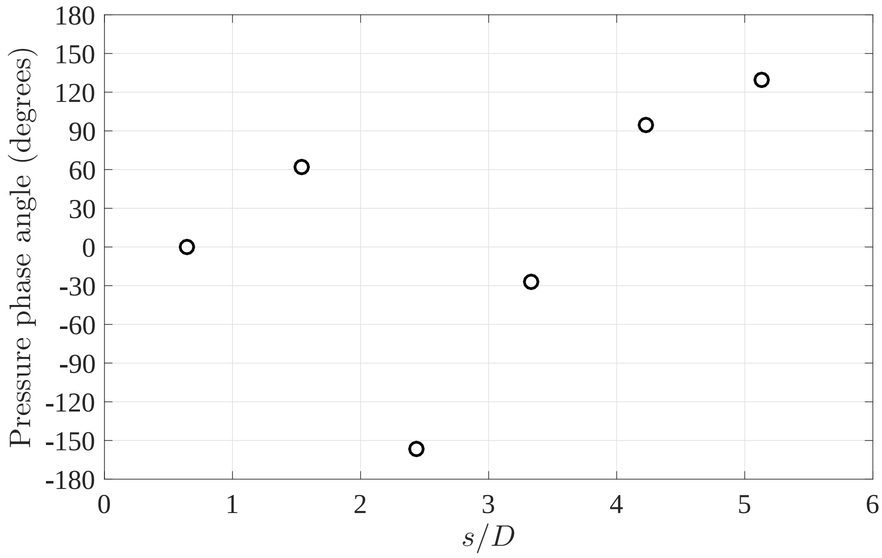

Figure 6.25: Phase angles of vortices rolling on the surface of the cylinder experiencing the pitching VIV response, measured in the wind tunnel dynamic test at $U_{\mathrm{R}} = 1.17$, i.e. at the pitching VIV peak.

The span-wise correlation of the surface pressure measured along the leading edge (Positions A and B) and along the trailing edge (Positions C and D) was calculated and summarised in Figure 6.26. The variation on the pressure correlation when the cylinder underwent the pitching lock-in was found to be very similar to those found when the cylinder was restrained to the heaving mode only. After the maximum structural response during the lock-in was reached, a reduction in the pressure correlation measured in Position C occurred and led to a decrease in the amplitude of the structural response. Knowing the phase shift between the surface pressure and the angular displacement, the behaviour of the flow field around the cylinder during two successive cycles of the motion is illustrated in Figure 6.27. After one cycle of the structural motion, the motion-induced leading-edge vortex propagated downstream and covered a distance up to two-thirds of the width of the cylinder. In the next quarter of the cycle, the upward accelerating motion of the trailing edge caused this vortex to appear to imping on the surface and gain strength, causing a raise in the suction and the moment acting on the cylinder. Afterwards, the motion of the cylinder slowed down; the vortex was pushed towards the trailing edge and eventually shed into the wake. This result further emphasised the different role of the motion-induced leading-edge vortex and its impingement in the VIV response of this particular 5:1 rectangular cylinder.

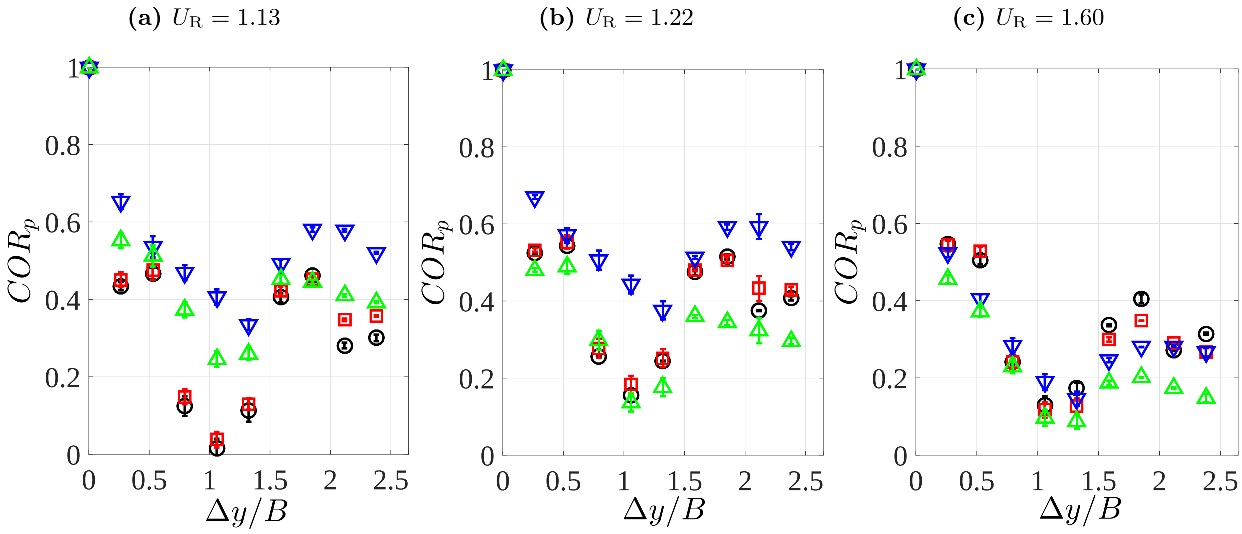

Figure 6.26: Wind tunnel results of the span-wise pressure correlation measured at 4 stream-wise positions in the smooth flow during the pitching VIV lock-in; *black*: Position A; *red*: Position B; *blue*: Position C; *green*: Position D.

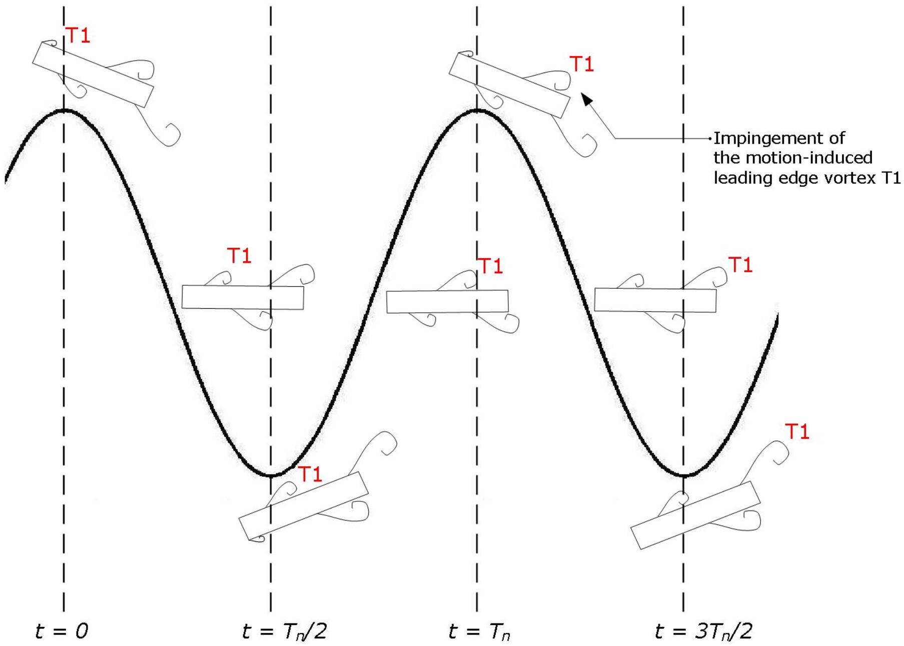

Figure 6.27: Schematic illustrating the development of the motion-induced leading-edge vortex T1 throughout 1.5 cycles of the pitching motion during the VIV lock-in.

6.4 TURBULENCE-INDUCED EFFECTS ON VIV OF THE 5:1 RECTANGULAR CYLINDER

The analysis discussed in Section 6.3 has shown that two flow features were responsible for the VIV lock-in of the 5:1 rectangular cylinder, which was restrained to either the heaving mode or the pitching mode only. Just before the lock-in, the amplitude of the structural response was small and the aerodynamics of the flow field around the cylinder shared similar characteristics to the one around the static cylinder. At this instance, the leading edge vortex was acted as a triggering mechanism, resulting in some initial displacement of the cylinder. As the amplitude of the motion got larger, the structural motion was observed to impair the geometry and the span-wise correlation of the leading-edge vortex. However, due to the interaction between the flow field and the structural motion, during each cycle of the motion, there was a period where the motion-induced leading-edge vortex impinged on the downstream half of the side surface, leading to a raise in the suction and an increase in the structural response of the cylinder.

Three different turbulent flow regimes were introduced to the wind tunnel dynamic tests as shown in Figure 6.28. By comparing with the structural responses in the smooth flow, the turbulence was found to produce significant suppression of the VIV response and the torsional flutter, including a reduction in the amplitude of the structural response. In the turbulent flow, the response of the cylinder was highly unstable. Figure 6.29a is an example of the time histories of the heaving acceleration at the reduced wind speed of 2.15; it comprised low-amplitude sinusoidal responses followed by an unsteady response. The presence of the sinusoidal response was very intermittent. This contrasts with what was observed in the smooth flow at the similar reduced wind speed, where the response of the cylinder was strongly sinusoidal as shown in Figure 6.29b.

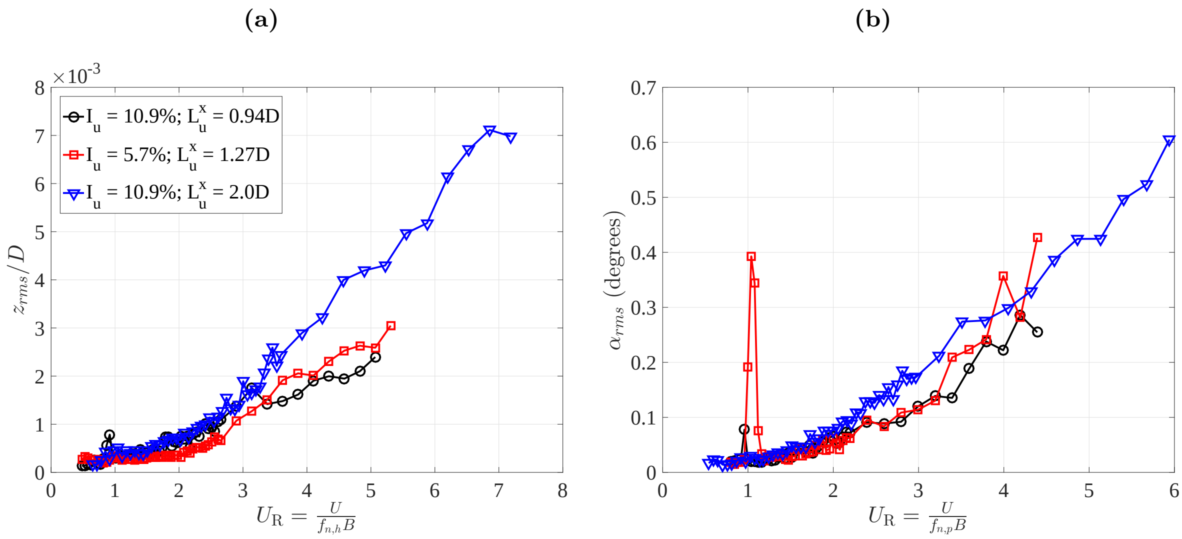

Figure 6.28: The (a) heaving and (b) pitching response of the cylinder at different turbulence levels.

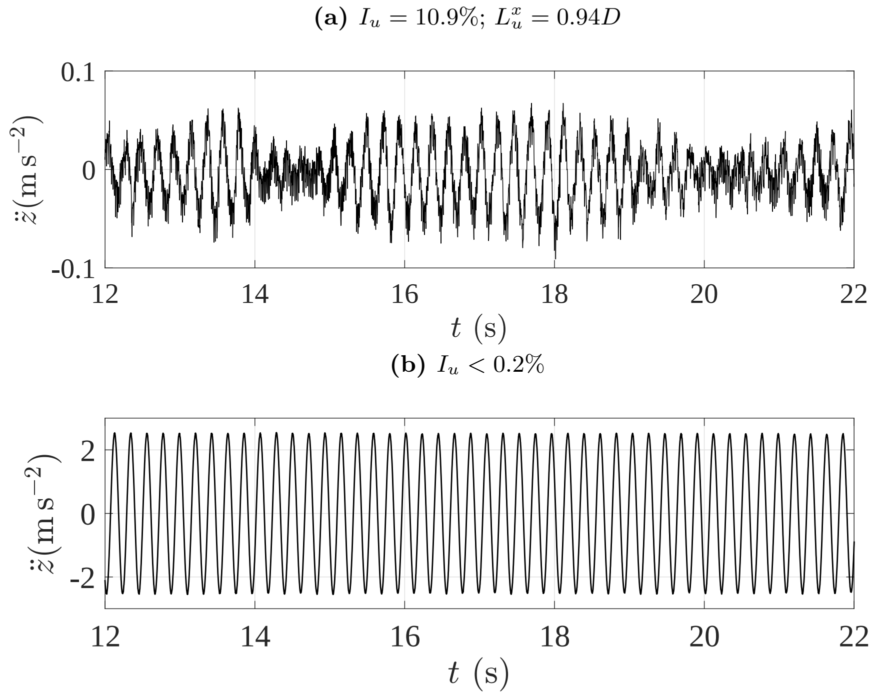

Figure 6.29: Examples of time-histories of the heaving acceleration measured in (a) the smooth flow and (b) the turbulent flow at $U_\mathrm{R} = 2.15$.

As for the VIV response, the effect of the turbulence was different between the cylinder restrained to the heaving mode and the one restrained to the pitching mode. For the heaving mode, no clear VIV responses could be seen. The increase in the turbulence length scale induced larger overall buffeting responses; however, a variation in the turbulence intensity had a very limited effect on the buffeting response, particularly at the reduce wind speeds above $U_\mathrm{R} = 3$. It is clear that the heaving motion was more susceptible to the turbulence length scale rather than the turbulence intensity. In Figure 6.30, a similar turbulence-induced effect on the pressure correlation to what was observed in the case of the static cylinder can be seen, especially at the turbulence intensity of 10.9%. At the turbulence intensity of 5.7%, although Position A showed a reasonably high correlation level, the impinging flow feature discussed in Section 6.3 did not occur at Position C, indicated by low correlation. Therefore, the turbulence effectively weakened the leading-edge vortex and promoted the trailing-edge vortex shedding, leading to suppression of the heaving VIV response. The fact that the larger length scale caused less suppressing effect on the separation bubble close to the leading edge could be the reason for higher buffeting response.

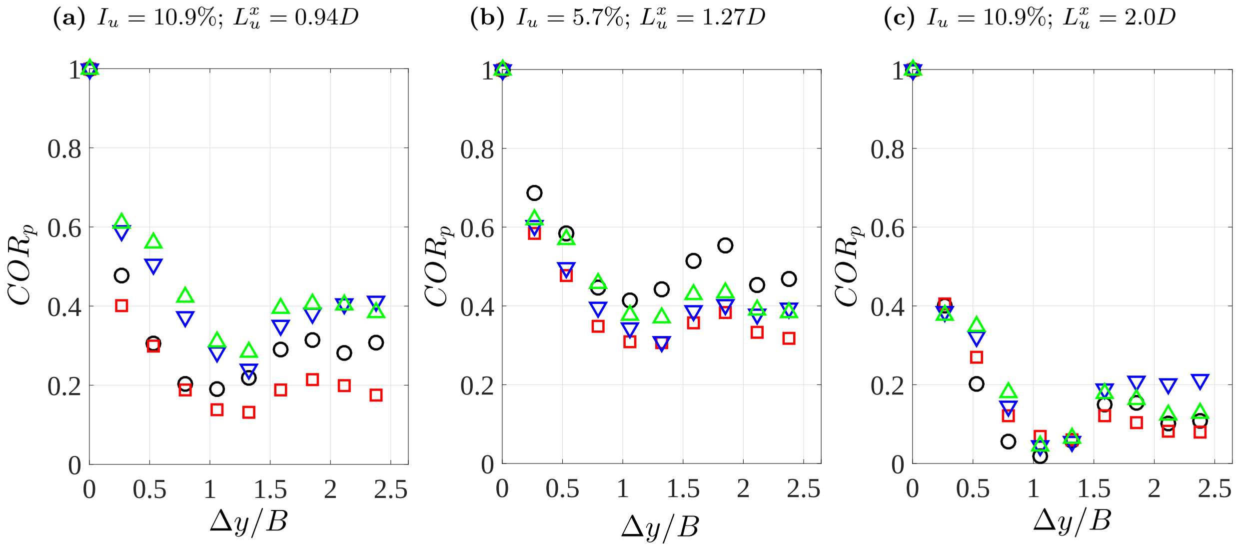

Figure 6.30: Wind tunnel results of the span-wise pressure correlation measured at 4 stream-wise positions in different turbulent levels when the cylinder was restrained to the heaving mode ($U_\mathrm{R} = 1.76$); *black*: Position A; *red*: Position B; *blue*: Position C; *green*: Position D.

When the cylinder was restrained to the pitching mode only, the turbulence was found to completely damp the torsional flutter. The different turbulence levels induced very little variation in the buffeting response. However, as for the pitching VIV, some response was observed at the reduced wind speed $U_\mathrm{R} = 1.01$ when the turbulence intensity was 5.7% (Figure 6.28b). This contrasted with the heaving VIV response due to the additional effect of the variation of the angle of attack. As discussed in Section 6.2, the angle of attack could help reduce the turbulence-induced suppressing effect on the flow field on one side of the cylinder; this influence was found to be more significant at low turbulence levels. Therefore, at the turbulence intensity of 5.7%, the angular motion of the cylinder allowed the separation bubble to form around the leading edge, triggering the VIV response. It is indicated by higher correlation levels around the leading edge (Figure 6.31b) in a comparison with other turbulence levels (Figures 6.31a and 6.31c). This difference in the span-wise pressure correlation was due to the additional effect on the shear layer caused by an increase in the turbulence intensity.

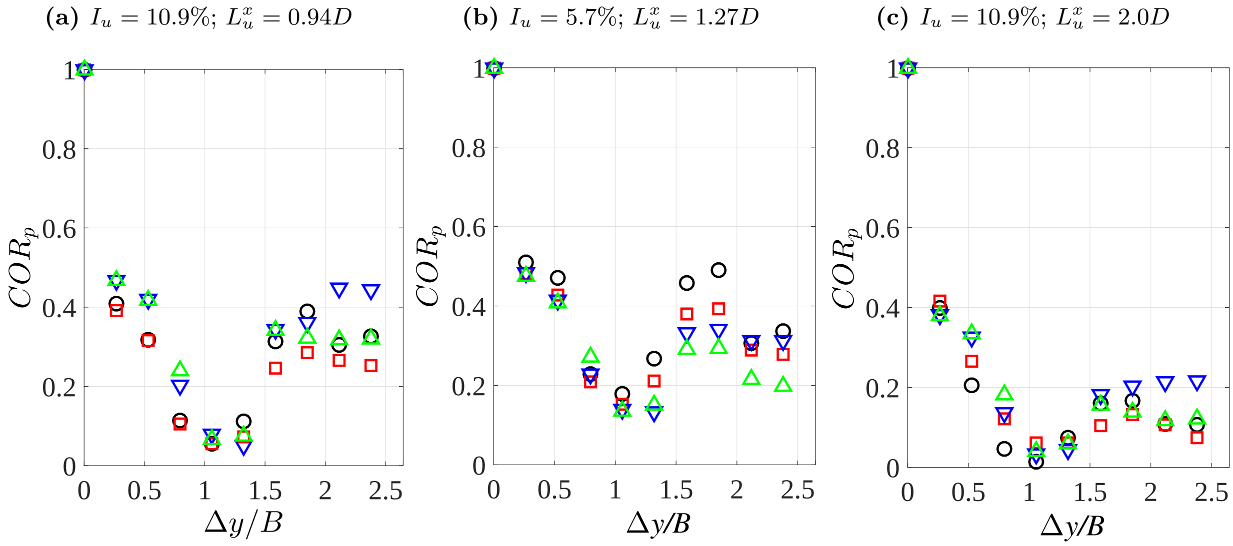

Figure 6.31: Wind tunnel results of the span-wise pressure correlation measured at 4 stream-wise positions in different turbulent levels when the cylinder was restrained to the pitching mode at $U_\mathrm{R} = 1.01$ (a and b) and $U_\mathrm{R} = 1.32$ (c); *black*: Position A; *red*: Position B; *blue*: Position C; *green*: Position D.

These results and the analysis performed in Section 6.3 have shown the importance of two key flow features on the VIV of the 5:1 rectangular cylinder. The first one was the leading edge vortex which was responsible for triggering the motion, resulting in some initial structural displacement at the start of the lock-in. The second one was the impingement of the motion-induced leading-edge vortex on the surface of the cylinder occurring close to the trailing edge. This flow feature led to a rise in the suction and in the lift force or moment acting on the cylinder, causing an increase in the structural response during the lock-in. Removing one of these flow features suppressed the VIV lock-in of the cylinder. With the turbulence level used in the wind tunnel dynamic test, it was found the the turbulent flow suppressed the VIV response. For the heaving mode, the suppression mechanism was due to the turbulence-induced weakening effect on the leading-edge vortex and the promotion of the trailing-edge vortex shedding. For the pitching mode, the VIV response was reduced due to the combination of weakening the leading edge vortex and removing the impinging flow feature. At low turbulence levels, the angular motion of the cylinder enhanced the formation of the motion-induced leading-edge vortex, resulting in a small VIV response. Nevertheless, the prevention of the impingement of this vortex on the surface inhibited a rise in the structural response. The main disadvantage of the turbulence levels applied in these wind tunnel dynamic tests were that the turbulence length scales were in the same order as the depth of the wind tunnel model. Therefore, the turbulence was more effective in suppressing the separation bubble or any circulating flow on the side surfaces rather than vortices in the wake region. Further tests in the turbulent flow having the length scale in the order of the width of the model are important to understand how the turbulence-induced effect on the wake region could influence the VIV response of this geometry.

6.5 FURTHER ANALYSIS ON EMERGING SPAN-WISE FLOW FEATURES AND VIV MECHANISM OF THE BENDING 5:1 RECTANGULAR CYLINDER

Results obtained from the wind tunnel and the computational study as discussed in the preceding Sections have shown the key aerodynamic characteristics of the flow field around a static 5:1 rectangular cylinder as well as the importance of these flow features on the VIV response of this particular cylinder. In addition, it was found that the turbulent flow could suppress these key flow features, which eventually significantly reduced the VIV response. Nevertheless, in both of the wind tunnel and computational studies analysed so far, 3D sectional models, which were effectively rigid cylinders were considered; therefore the flow field around the cylinder was largely dominated by 2D flow features. This limitation is removed in the study presented in this section, where a flexible 5:1 rectangular cylinder is modelled computationally and undergoes the bending VIV lock-in, in which the first bending mode is excited.

By introducing the bending motion to the flexible 5:1 rectangular cylinder, it was expected that the flow field around the cylinder would become more unstable and some span-wise flow features would emerge. The use of the pressure correlation could not effectively extract these span-wise flow features. In order to effectively investigate the spatially dependent flow field in this case, the Proper Orthogonal Decomposition analysis was applied.

As can be seen in Figure 6.32, the VIV response at the mid-span ($y/B = 5$) of the flexible cylinder shared some common characteristics to the sectional model's results presented in Figure 6.17, regarding the onset reduced wind speeds of the two VIV lock-in regions, the lock-in of the vortex shedding frequency and the reduced wind speed where the maximum structural response during the lock-in occurred. Similar to what was observed in the 3D heaving simulation, due to the coarse discretisation level in the span-wise direction of the computational domain, the 3D bending simulation under-predicted the vortex shedding frequency before and after the lock-in, resulting in the Strouhal number of St = 0.52. Also, the 3D bending simulation was conducted in the parallel manner; therefore the memory effect of the structural and the fluid was not captured properly, leading to a sharp drop of the structural response after the VIV peak.

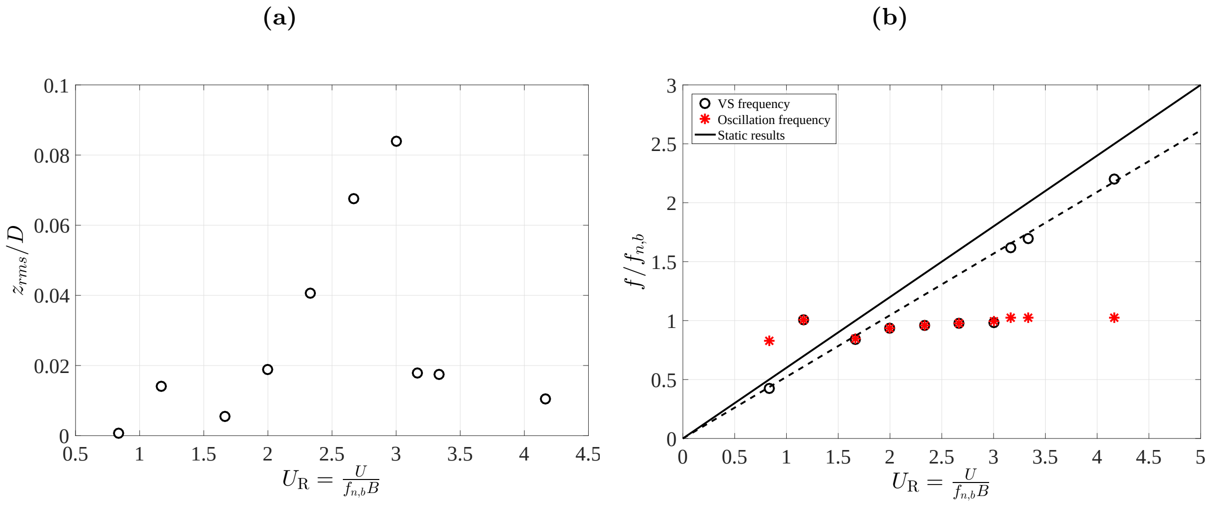

Figure 6.32: Results of the 3D bending simulation of the flexible model: (a) structural response measured at the mid span and (b) frequency of response.

As was mentioned earlier in this section, being excited in the first bending mode, the mid-span of the flexible cylinder ($y/B = 5$) exhibited the maximum structural displacement, while at the static end ($y/B = 0$) no structural displacement was observed. This difference in the structural response implies there existed some variation in the flow field in the span-wise direction. As illustrated in Figures 6.33 and 6.34, the contour plots of the surface distribution of the time-averaged pressure coefficient C_p and the standard deviation of the time-varying pressure coefficient C_p' suggest an alteration of the separation bubble along the span-wise length of the cylinder. The stream-wise length of the separation bubble was found to be shorter towards the moving end, i.e. the mid span of the cylinder, indicated by a wider pressure recovery region. In addition, the strength of the separation bubble increased as shown by more fluctuation in the surface pressure around the moving end. The surface distribution of C_p and C_p' on the top and bottom surfaces of the flexible cylinder was extracted at three span-wise positions as shown in Figure 6.35. At $y/B = 1.66$, the cylinder exhibited a displacement which was equal to half of that measured at the mid span $y/B = 5$; however, the surface pressure distribution at this position was reasonably similar to the one measured at $y/B = 0$, i.e. at the static end, except a very small upstream shift of the reattachment point and an increase in the fluctuating strength of the separation bubble. More significant variation was observed at the moving end $y/B = 5$. In addition, the increase in the structural displacement seemed to reduce the error relating to the asymmetric computational domain between the top and bottom halves. As inferred from Figure 6.35, the flow field at the mid span was more symmetric compared to what observed at other span-wise positions of the flexible cylinder or in case of a static cylinder. This results suggests the LES simulation of a dynamic section in the smooth flow can be performed using a coarse span-wise discretisation level since the flow field is dominated by large scale features.

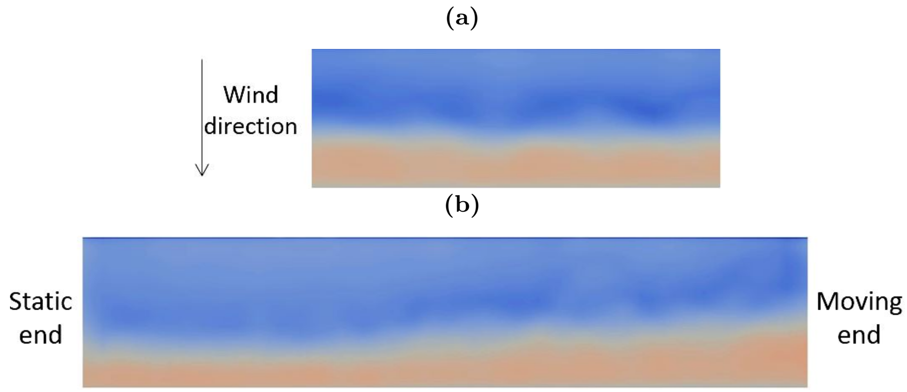

Figure 6.33: Comparison of the contour plots of the time-averaged pressure coefficient C_p on the top surface of (a) 3D rigid cylinder and (b) 3D flexible cylinder at $U_{\mathrm{R}} = 3.00$, i.e. at the peak structural response during the VIV lock-in.

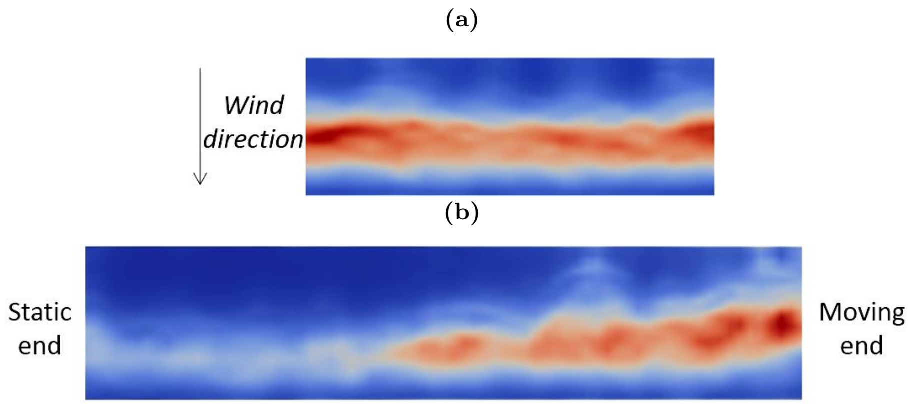

Figure 6.34: Comparison of the contour plots of the standard deviation of the time-varying pressure coefficient C_p' on the top surface of (a) the 3D rigid cylinder and (b) the 3D flexible cylinder at $U_{\mathrm{R}} = 3.00$, i.e. at the peak structural response during the VIV lock-in.

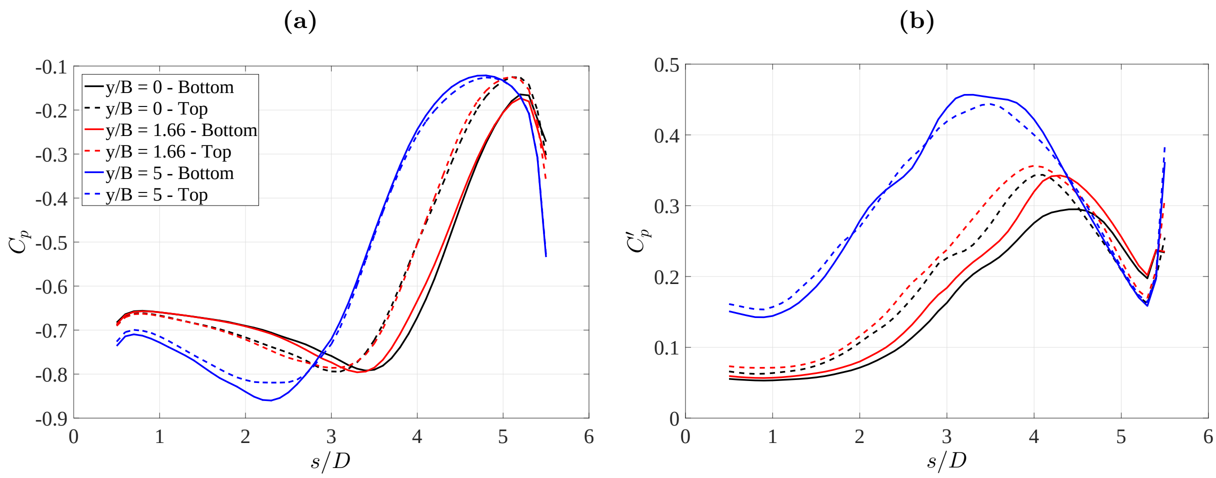

Figure 6.35: Distribution of (a) C_p and (b) C_p' on the top and bottom surfaces at a number of span-wise positions on the top and bottom surface of the 3D flexible cylinder at $U_{\mathrm{R}} = 3.00$, i.e. at the peak structural response during the VIV lock-in.

Concentrating on the fluctuating component of the flow field, as the cylinder experienced the maximum structural displacement during VIV lock-in, i.e. $U_R = 3$, the power spectral density of the lift force measured at three aforementioned span-wise positions were calculated and shown in Figure 6.36. At the first position which was close to the static end, $y/B = 0$ (Figure 6.36a), the flow field was dominated by vortices or the flow feature defined by the Strouhal number as represented by Peak A; hereafter this is called the Strouhal-number vortex shedding. At the second position $y/B = 1.66$ (Figure 6.36b), this flow feature still existed but it was overshadowed by the motion-induced vortices as illustrating by Peak B at the normalised frequency $f/f_{n,b} = 1$. At the moving end $y/B = 5$ (Figure 6.36c), the Strouhal-number vortex shedding disappeared and the motion-induced vortices strongly dominated the flow field. The velocity measured at a distance B behind the cylinder and $D/2$ from the top surface also showed similar variation in the dominant flow features in the span-wise direction. As shown in Figure 6.37a, the spectrum of the w-component revealed the dominant flow feature in the wake close to the static end was the von Karman vortex shed from the body at the frequency defined by the Strouhal number, indicated by Peak A. Towards the end having the maximum structural displacement, the motion-induced vortex became dominant as identified by Peak B in Figure 6.37b; the Strouhal-number vortex shedding found at the static end was still present but their relative strength varied along the span-wise length of the cylinder and significantly reduced at this end.

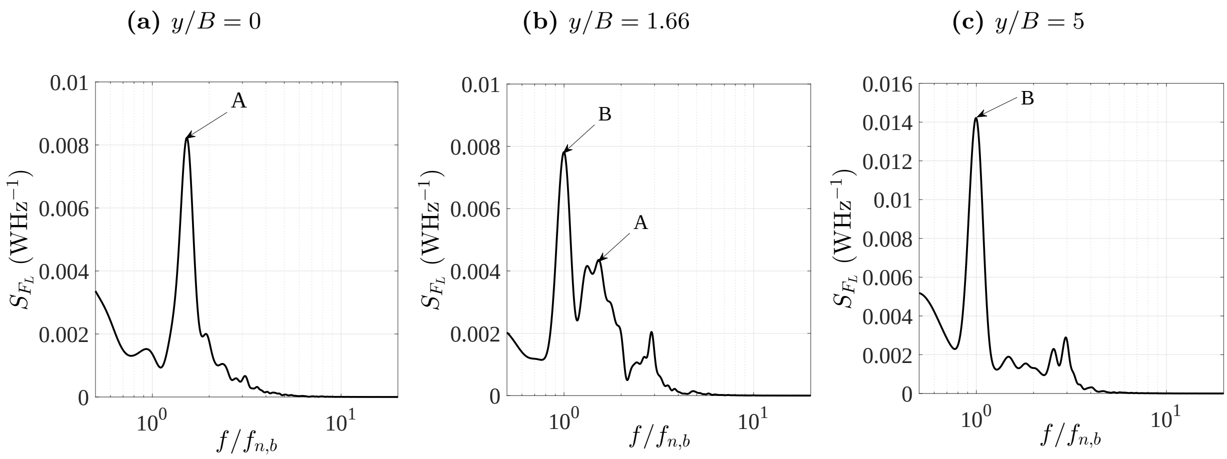

Figure 6.36: Power spectral densities of the lift forces measured at different span-wise positions as the flexible model underwent the VIV lock-in at $U_R = 3.00$.

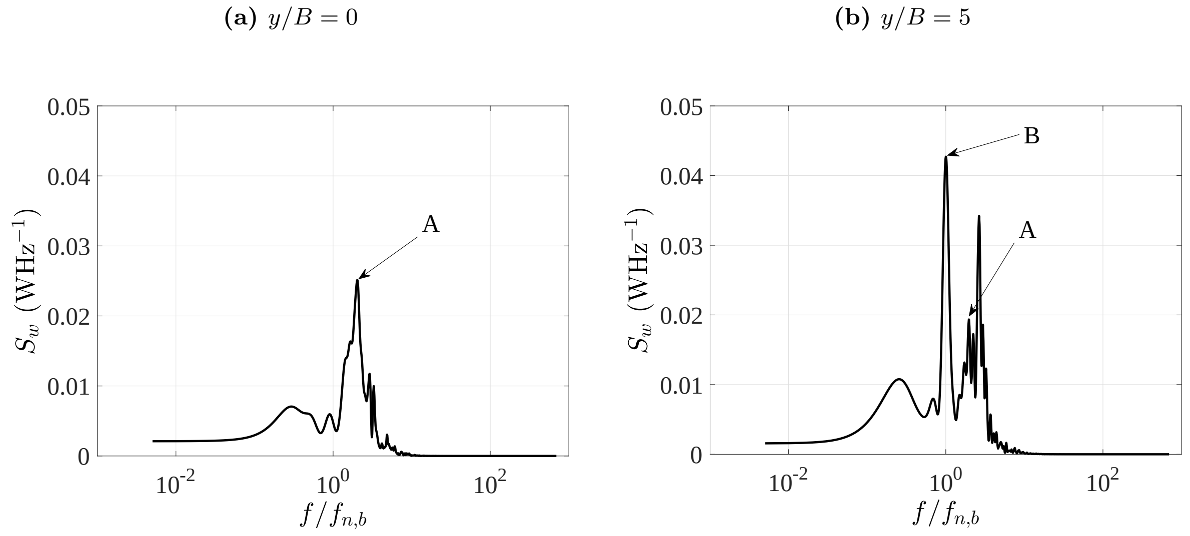

Figure 6.37: Power spectral densities of the w-component of the velocity measured in the wake at different span-wise positions as the flexible model underwent the VIV lock-in at $U_{\mathrm{R}} = 3.00$.

These quantitative and qualitative results at the reduced wind speed $U_{\mathrm{R}} = 3.00$ have suggested that, during the VIV lock-in, the flow feature relating to the Strouhal-number vortex shedding and that relating to the motion-induced vortices coexisted; however their relative strength was observed to vary along the span-wise length of the cylinder and was dependent on the amplitude of the structural response. Around the static end, the flow field was dominated by the former while the latter was found predominant towards the moving end. A detailed analysis of the span-wise variability of the dominant fluctuating flow features revealed that there were two separate span-wise portions of the cylinder, around each of which the flow field was either dictated by the Strouhal-number vortex shedding or by the motion-induced vortices; results of this analysis at selected reduced wind speeds during the initial branch of the lock-in are shown in Figure 6.38.

At the onset of the bending VIV lock-in, $U_{\mathrm{R}} = 2.00$, it was difficult to distinguish these two flow features; nevertheless, based on large fluctuation of the frequency relating to the dominant flow feature, it could be said that the Strouhal-number vortex shedding posed certain effects up to $y/B = 1$ as indicated by the *red* dashed line. At the next reduced wind speed $U_{\mathrm{R}} = 2.33$, clear influence of the Strouhal-number vortex shedding was observed; up to the location $y/B = 0.6$, the fluctuation in the flow field was predominantly related to this flow feature. In fact, effect induced by the Strouhal-number vortex shedding spread up to $y/B = 1.4$, identified by the ratio of 5 between the spectral peaks $S_{F_L}(f_{MIV})$ and $S_{F_L}(f_{\mathrm{St}})$ corresponding to the motion-induced vortex and Strouhal-number vortex shedding as illustrated by the *black* solid line on Figure 6.38b.

Using a similar approach, results shown in Figures 6.38c and 6.38d revealed that, at $U_{\mathrm{R}} = 2.67$, the influencing zone of the Strouhal-number vortex shedding slightly extended up to $y/B = 1.7$; interestingly, at $U_{\mathrm{R}} = 3.00$, i.e. when the structural response during the lock-in reached the peak value, this extension was larger, up to $y/B = 3$. The widening of the influence zone of the Strouhal-number vortex shedding implies a weaker synchronisation between the motion-induced vortex and the structure motion; the strength of the former could not enhance that of the latter and visa versa. This observation could also be inferred from the phase angle of the lift force against the structure response measured in the 3D heaving simulation (Figure 6.17d).

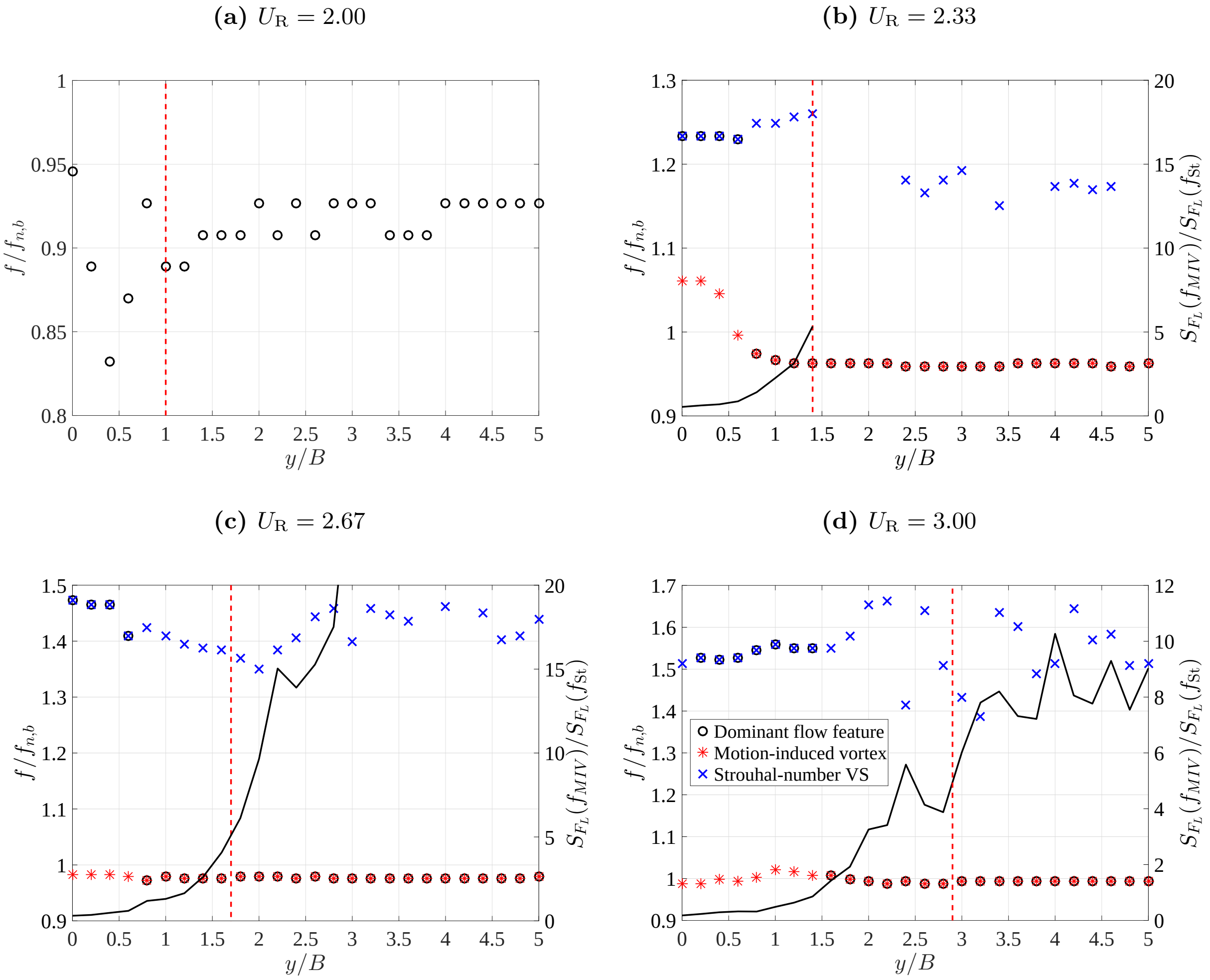

Figure 6.38: Span-wise distribution of the dominant fluctuating flow feature, the motion-induced vortex (MIV) and the Strouhal-number vortex shedding at different reduced wind speeds during the bending VIV lock-in; the solid line represented the ratio between the spectrum peaks $S_{F_L}(f_{MIV})$ and $S_{F_L}(f_{\mathrm{St}})$ corresponding to the motion-induced vortex and Strouhal-number vortex shedding.

6.5.1 Emerging Span-wise Flow Features

Selected results presented above evidently showed there existed two different flow features around the flexible 5:1 rectangular cylinder as it underwent the bending VIV lock-in. The first one was the motion-induced vortex, which was dominant around the mid span of the cylinder ($y/B = 5$), i.e. where the cylinder exhibited significant displacement. The other feature was the Strohal-number vortex shedding; this has greater influence around the static end where the structural displacement was limited. The relative strength between these two flow features therefore varied along the span-wise length of the cylinder and was dependent on the amplitude of the structural response. More importantly, during the initial branch of the VIV where the structural response was increasing, effects of the second flow feature were found to be limited; its influence was extended up to $y/B = 1.6$ only. When the cylinder experienced the maximum structural response during the lock-in, the influence of the second flow feature was broader up to $y/B = 3$, representing the weakening of the motion-induced vortex and the appearance of complicated span-wise flow feature.

Understanding this behaviour, the flow field around the flexible cylinder at $U_{\mathrm{R}} = 3.00$, i.e. at the peak structural response during the lock-in, was analysed in order to comprehensively reveal the interaction of these flow features along the span-wise length. Also, due to its high complexity, the technique named the Proper Orthogonal Decomposition (POD) analysis was applied on the fluctuating component of surface pressure distribution at a number of selected span-wise positions. At each position, it was found that the first 10 POD modes contributed up 99% of total energy of the flow field. Among them, the first four POD modes were dominant; their associated energy contribution was accumulated up to about 92% of the total energy of the flow.

At the first position which was at the mid span $y/B = 5$, results of the POD analysis was shown in Figure 6.39a including a comparison of the power spectral densities of the POD coefficients corresponding to the first four POD modes. POD Modes 1 and 2 were found to be the most energetic, representing the motion-induced vortex, indicated by the peak at the frequency of 1.19 Hz; the cross power spectral density was evaluated and the corresponding phase lag of 97.72° was identified. On the other hand, a number of peaks were observed on the power spectral densities of the POD coefficients of Modes 3 and 4; the dominate one was at the frequency of 1.81 Hz and the phase lag was calculated to be 82.63°. These results implies that Mode 3 and 4 both represented the Strouhal-number vortex shedding. In addition, a low-frequency flow feature was observed around 0.6 Hz and represented by the first four POD modes, indicating that this was also an important feature in the flow field around this region.

(a) $y/B = 5$

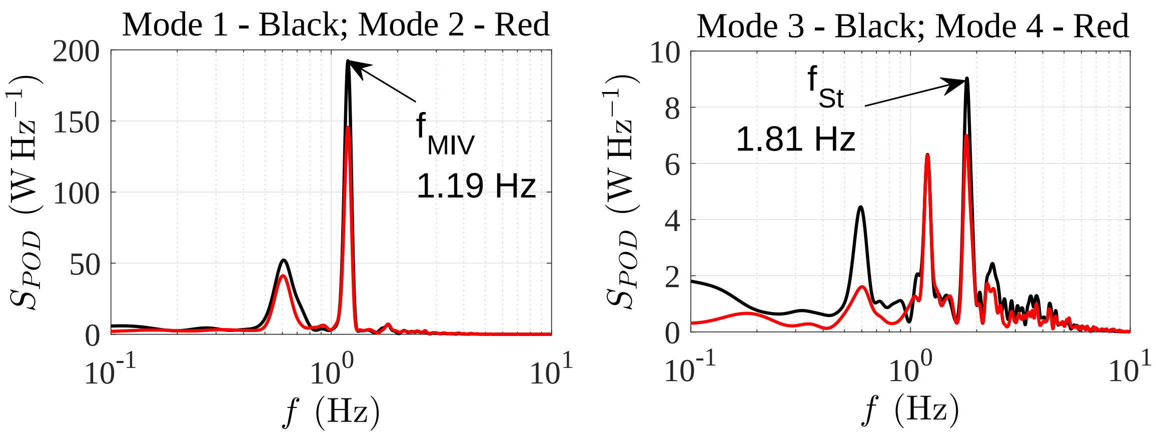

(b) $y/B = 4$

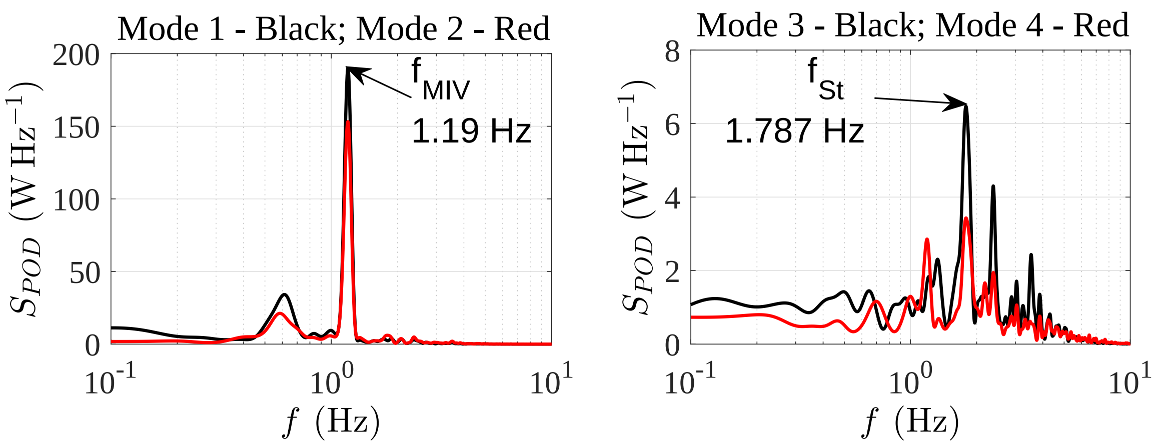

(c) $y/B = 3$

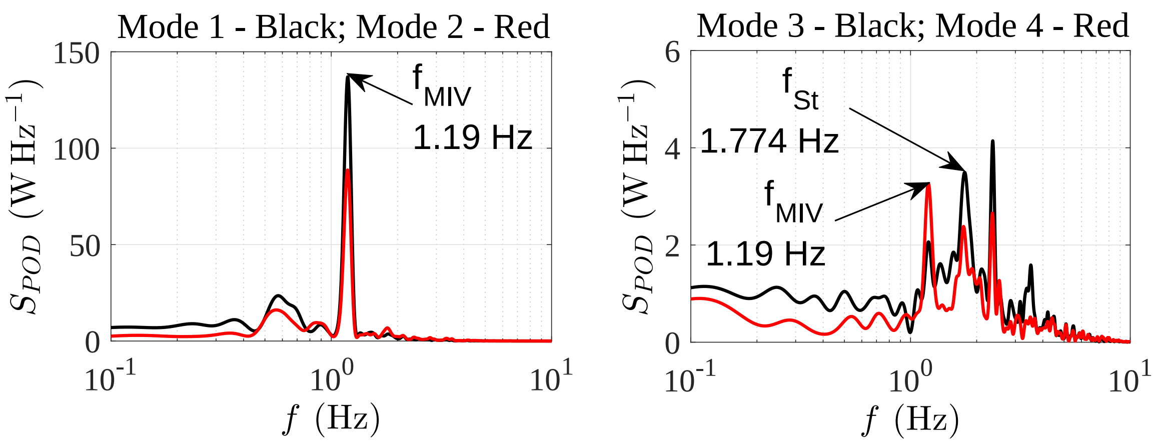

Figure 6.39: Variability of the power spectral densities of the POD coefficients of the first four POD modes at different span-wise locations; $U_{\mathrm{R}} = 3.00$.

(d) $y/B = 2$

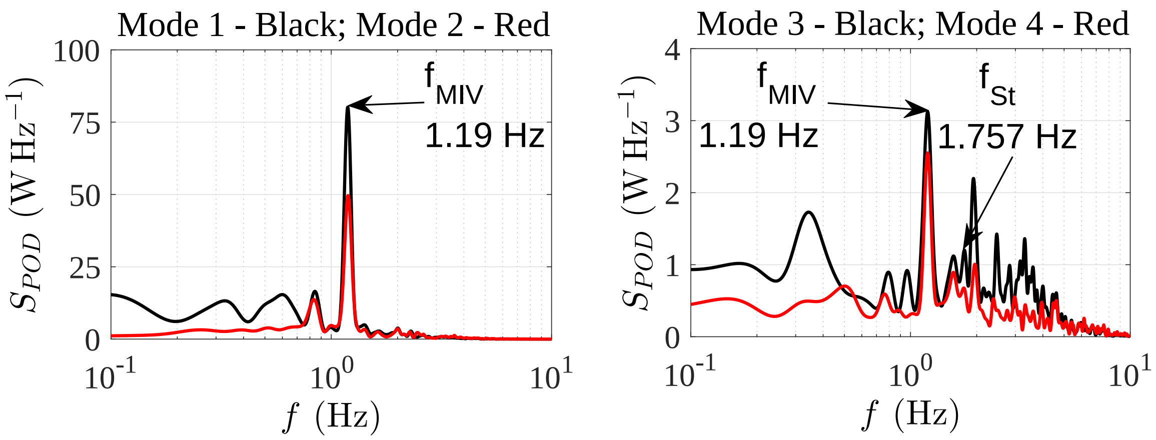

(e) $y/B = 1$

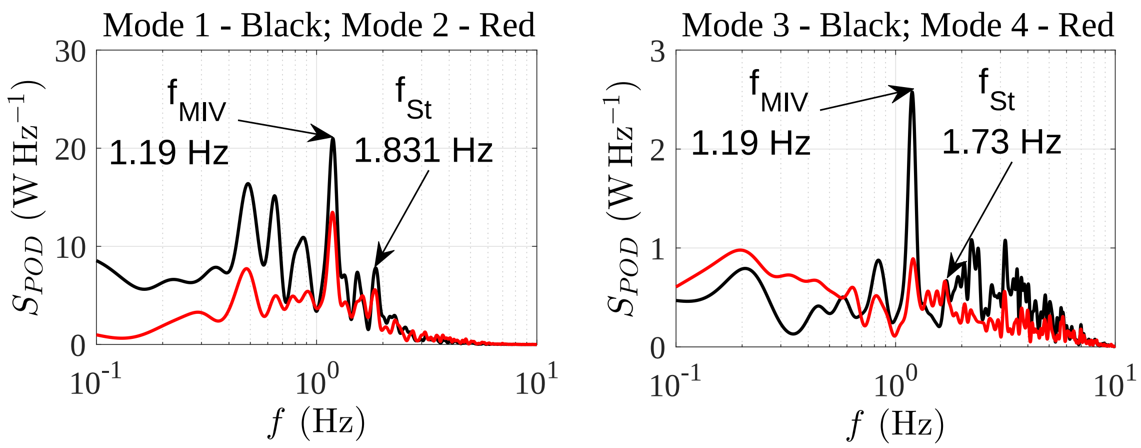

(f) $y/B = 0$

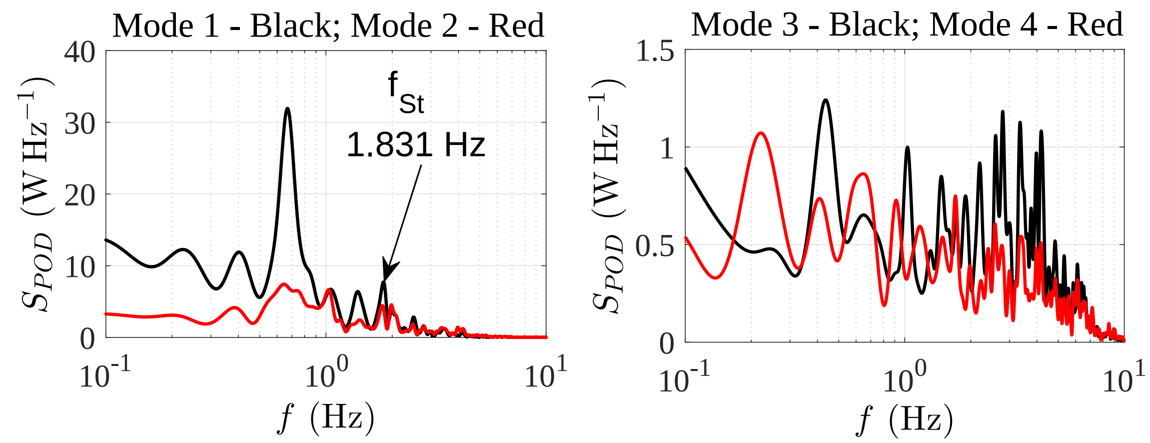

Figure 6.39: Variability of the power spectral densities of the POD coefficients of the first four POD modes at different span-wise locations; $U_{\mathrm{R}} = 3.00$ (continued).

At the second position $y/B = 4$, similar results were observed (Figure 6.39b). The motion-induced vortex was the dominant flow feature; the power spectral densities of the POD coefficients of the two most energetic POD modes, Modes 1 and 2, reached the peak at the frequency of 1.19 Hz and the corresponding phase lag was 84.17°. The spectral analysis of the POD coefficients also revealed that POD Modes 3 and 4 predominantly represented the fluctuating flow field at the frequency of 1.80 Hz; the phase lag between Modes 3 and 4 at this frequency content was equal to 102.4°. This flow feature appeared to relate to the Strouhal-number vortex shedding. The low-frequency (0.6 Hz) flow feature was still present at this position.

In the next position $y/B = 3$ as shown in Figure 6.39c, the dominance of the motion-induced vortex was found to slightly reduce. Even though Modes 1 and 2 still significantly contributed to the fluctuating energy of this flow feature, lower energetic POD modes took up a small proportion. This is indicated by the appearance of strong peaks at the frequency of 1.19 Hz in the power spectral densities of the POD coefficients of Modes 3 and 4. Another peak was found at the frequency of 1.77 Hz, which again appeared to relate the Strouhal-number vortex shedding. Similarly, the low frequency flow feature at 0.6 Hz was one of the primary flow features.

To this position, a number of observations were drawn. There existed a transition from the flow field dominated by the motion-induced vortex to the one dominated by the Strouhal-number vortex shedding. This transition was made clear by the fact that, towards the static end, lower energetic POD modes started to contribute more to the fluctuating energy of the motion-induced vortex. Another finding was related to the Strouhal-number vortex shedding that the vortex shedding frequency reduced towards the static end, suggesting a variation in the vortex structure in the span-wise direction.

These trends continued at the next two positions, $y/B = 2$ and 1, where the frequency of the Strouhal-number vortex shedding reduced to 1.76 Hz and 1.73 Hz respectively as illustrated in Figures 6.39d and 6.39e. More interestingly, at the latter position, another flow feature was found; the spectral analysis of the POD coefficients of Modes 1 and 2 showed another spectral peak at the frequency of 1.831 Hz and the corresponding phase lag was calculated to be 86.55°. It was suggested that this flow feature was another vortex shedding mode defined by the Strouhal number. It originated at the static section of the flexible cylinder and its influence extended up to $y/B = 1$. This suggestion was reasonable since, at the position $y/B = 0$, the most energetic POD modes were found to mostly represent a fluctuating flow feature at the frequency of 1.831 Hz (Figure 6.39f). The motion-induced vortex at this position was very weak and overshadowed by this flow feature as well as the low-frequency (0.6 Hz) flow feature.

The POD analysis of the fluctuating pressure distribution at a number of span-wise position uncovered the existence of two primary flow features, which was the motion-induced vortex and the Strouhal-number vortex shedding. The spectral analysis of the POD coefficients of the first four POD modes revealed a span-wise transition of the dominant flow feature and a presence of the influencing zone of the Strouhal-number vortex shedding, as observed in results of the span-wise distribution of the lift coefficient or the velocity in the wake. Interestingly, concentrating on the Strouhal-number vortex shedding, it appeared that there existed two vortex shedding modes which was the parallel vortex shedding around the static end and the oblique vortex shedding around the mid span. Around the static end, this flow feature fluctuated at the frequency of 1.831 Hz, which yielded the Strouhal number of 0.52 as predicted. This result indicated the parallel vortex shedding mode; some of this effect extended up to $y/B = 1$. Along the flexible cylinder, the Strouhal number was lower and reduced from the mid span to the static end as shown in Figure 6.40a. Based on Williamson (1989), the reduction of the Strouhal number indicated the presence of the oblique vortex shedding mode where the vortex structure was not parallel to the leading edge and the angle of the oblique vortex shedding mode was calculated using Equation 2.27 and is summarised in Figure 6.40b. The vortex structure was found to be more parallel around the mid span compared to the one measured close to the static end due to an increase in the gradient of the deformation of the cylinder. These two vortex shedding modes were visualised by calculating the Q-criterion of the flow field around the cylinder as shown in Figure 6.41. The oblique vortex shedding mode illustrated by the dashed *red* line was clearly visible on the top and bottom surfaces as the cylinder reached the minimum and maximum structural displacement respectively; it was predominant across the main span of the cylinder. The parallel vortex shedding represented by the dashed *blue* line, on the other hand, only appeared around the static end; some interference between them could also be observed.

Another flow feature which was revealed after the POD analysis was the fluctuation of flow at the low frequency of 0.6 Hz. The fact that, regardless of the span-wise positions, the fluctuating energy of this flow feature was mostly contributed by the most energetic POD modes indicated that this was also the important flow feature around the flexible cylinder. By performing the spectral analysis on the surface pressure, this low-frequency fluctuating flow appeared to reach the peak strength at the location of $x/D = 3$ around the moving end ($y/B = 3$ to 5), which was corresponding to the reattachment point based on the pressure distribution shown in Figure 6.35. The location of this peak strength was found to shift downstream as moving towards the static end. These observations strongly suggested that this low-frequency fluctuating flow feature mentioned here closely related to the reattachment of the flow and the value of the frequency of 0.6 Hz also indicated some relationship with the motion of the cylinder.

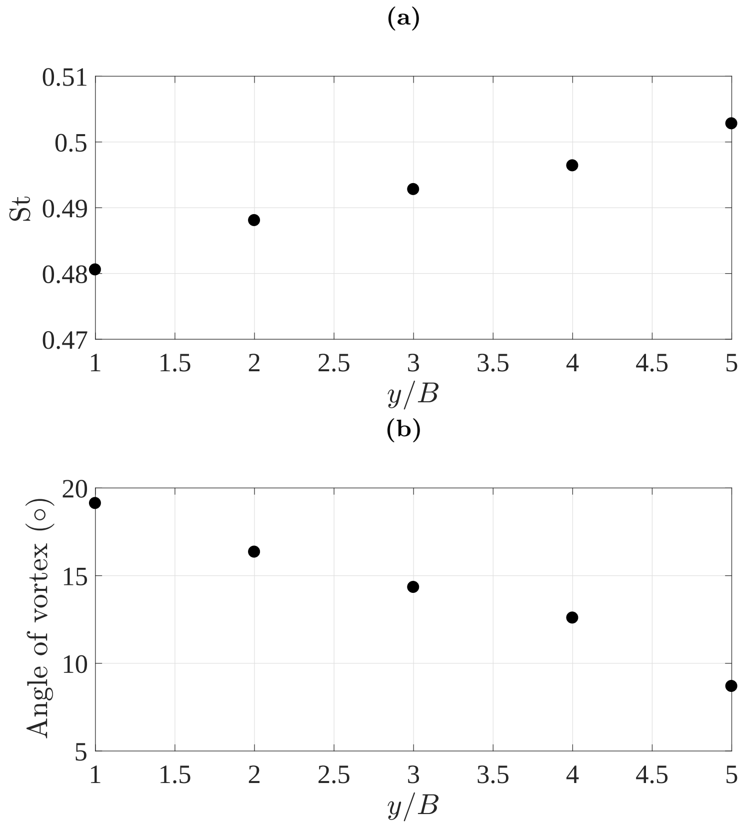

Figure 6.40: Variability of (a) the frequency and (b) the angle of the vortex structure in the oblique vortex shedding mode observed across the main span of the cylinder.

Nevertheless, the low-frequency fluctuating flow was the secondary feature only. Despite being mostly represented by the most energetic POD modes, its energy level was less than the motion-induced vortex. Therefore, it could be overshadowed by the existence of strong motion-induced vortices. In addition, following the sketch of the structural motion in Figure 6.42, as the cylinder moved from Positions 1 to 2, the impingement of the motion-induced vortex on the top surface around the reattachment point resulted in a very strong negative pressure gradient along the span-wise line at $x/B = 3$. After the motion-induced vortex being shed into the wake and the structure oscillated from Position 3 to 4, the pressure around the reattachment point increases, leading to a strong positive pressure gradient in the span-wise direction. These pressure gradients could overshadow the low-frequency fluctuating flow discussed here. Therefore, the instance when the structure was half way through the quarter of the cycle from Positions 2 to 3 was selected to further analyse this secondary flow feature.

The phase-averaged profile of the flow field calculated at this instance and along the span-wise line at $x/B = 3$ is shown in Figure 6.43. It is obvious that comparing two flow profiles separated by a natural time period $T_{n,b}$ illustrated an oscillatory state where the flow field restored itself after two cycles of the structural motion $2T_{n,b}$. Figure 6.43a represents the phase relationship of the pressure measured at points along the span-wise line $x/D = 3$ against the one at the mid span $y/B = 5$; the phase angles

(a) Bottom surface - $t = 152.184\,s$

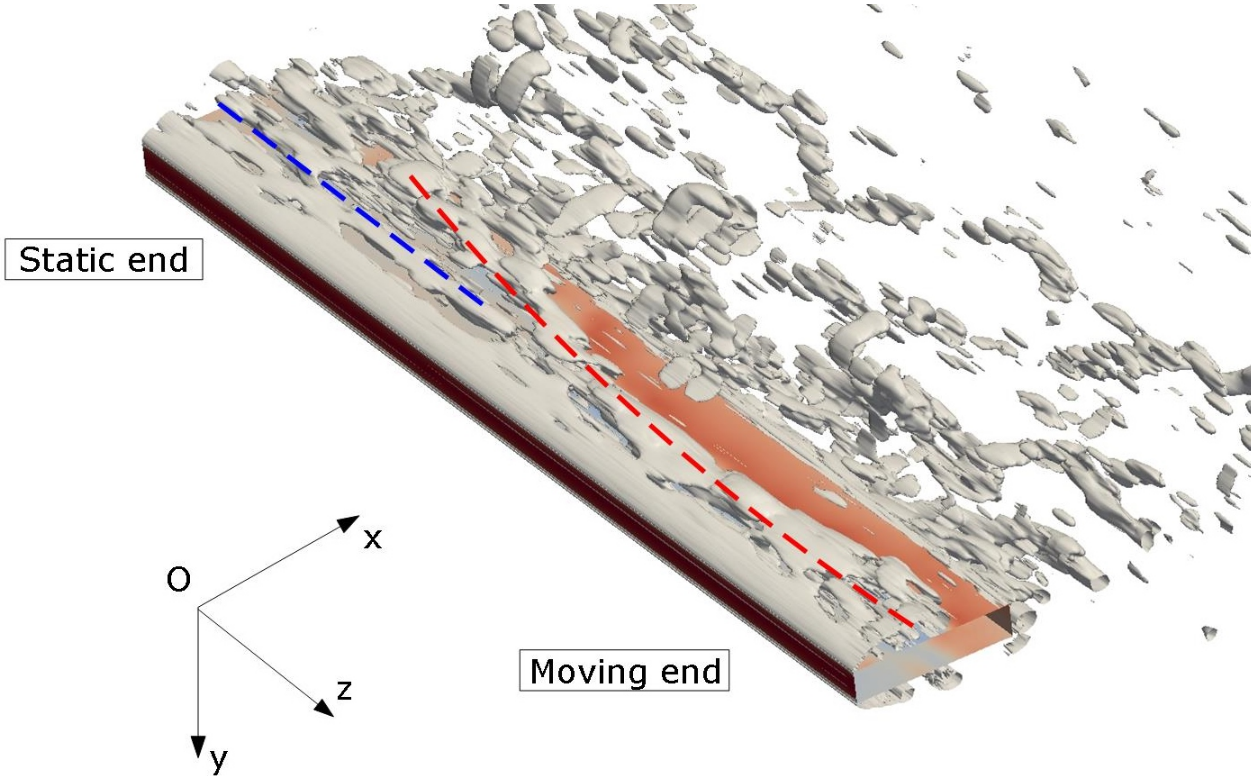

(b) Top surface - $t = 152.592\,s$

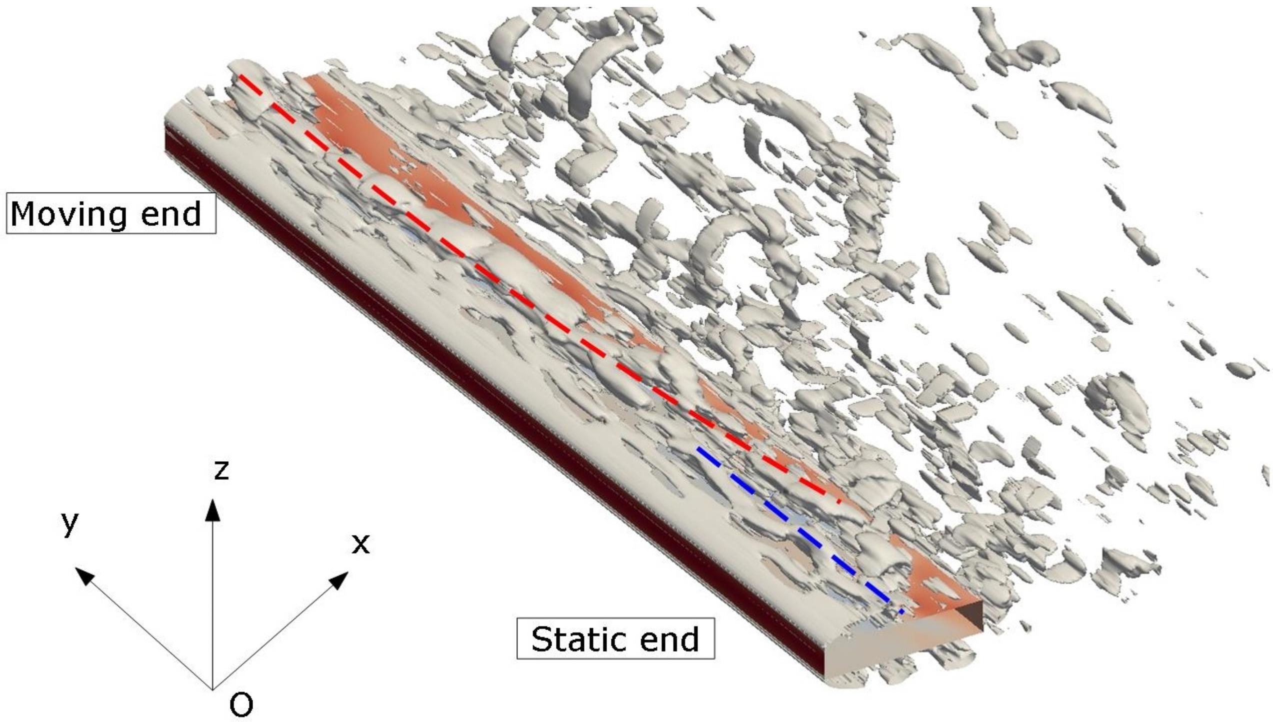

Figure 6.41: Q-criterion, $Q = 100\,\mathrm{s}^{-1}$, of the flow field around the cylinder measured on the bottom surface and top surface when (a) the cylinder reached the maximum displacement and (b) the cylinder reached the minimum displacement respectively.

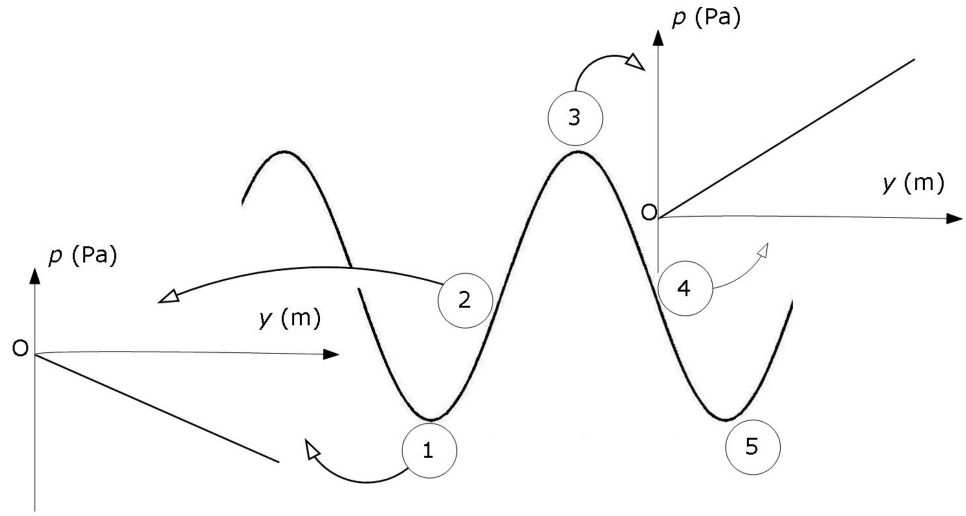

Figure 6.42: Schematic showing the variation of the span-wise pressure gradient measured at the stream-wise position $x/B = 3$ on the top surface, at different time instances during one cycle of structural motion.

were extracted corresponding the frequency 0.6 Hz. A good agreement between these two results were observed; the locations where the phase jump occurred were coincident with the intersection of the two flow profiles. These observations were similar to the periodic-doubling bifurcation in the vortex shedding of the circular cylinder (Tomboulides et al., 1992). The local increase or decrease of the surface pressure shown in 6.43b was thought to be due to the flow being drawn in and out of the top surface of the cylinder. This represents the presence of two counter-rotating stream-wise vortices; their arrangement including the orientation corresponding to the *black* flow profile is shown in Figure 6.44a. It is evident that Vortex 1 draws the flow away from the surface, resulting in a reduction in the pressure at $y/B = 5$, while, together with Vortex 2, it causes to the flow to impinge onto the surface at $y/B = 2.1$, leading to an increase in the surface pressure here. Similar effect is observed at $y/B = 1.9$ and 1.5 where the surface pressure decreases and increases respectively. The first three vortices have similar length scales where as Vortex 4 has a larger length scale due to the excessive effect induced by the span-wise gradient of the structural deformation. In the next cycle of the structural motion, these arrays of vortices shifts in the span-wise direction by a distance which equals to the length scale of one vortex (Figure 6.44b). This movement causes an opposite variation of the surface pressure and it will take up to two cycles of the structural motion for this arrangement of vortices to restore, yielding a fluctuating flow at 0.6 Hz. At the span-wise location $y/B = 4$, a phase jump was expected to be 180°; in fact, it was about 360° or, in other words, the flow feature here was 180° out of phase with the one at the mid span. This addition phase lag was due to the oscillation of the gradient of the phase-averaged flow profiles, which appears to pivot at the point $y/B = 4$ as shown in Figure 6.43b.

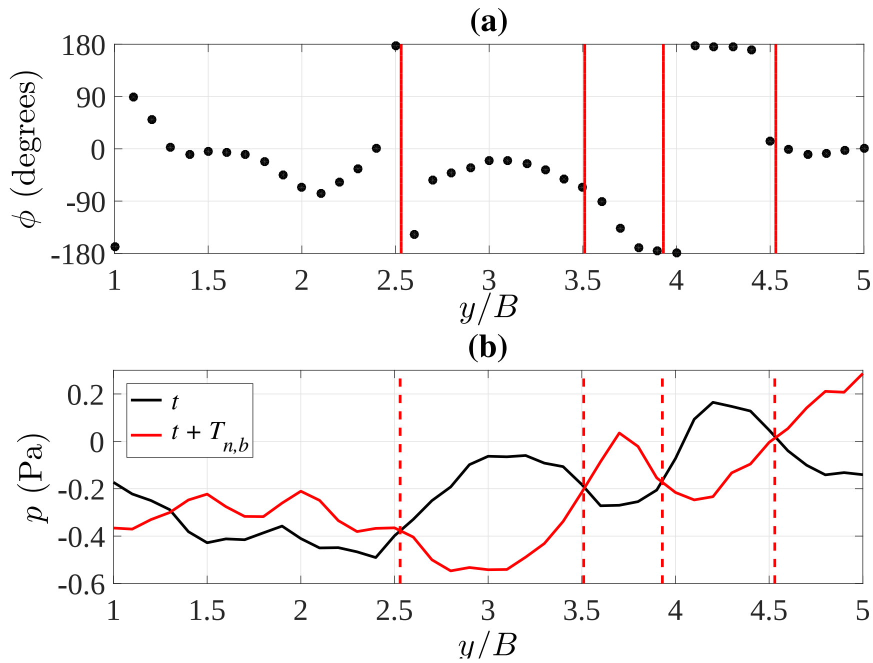

Figure 6.43: Comparison of two phase-averaged profiles of the flow field calculated along the span-wise line at $x/B = 3$ and separated by a natural time period $T_{n,b}$.

In conclusion, as being suggested by results shown in Figures 6.36 and 6.37, the POD analysis discussed in this section revealed the existence of two primary flow features as the flexible cylinder underwent bending VIV lock-in. The first one was the motion-induced vortex while the second one related to the Strouhal-number vortex shedding. During the initial branch of the VIV lock-in, where the structural response was increasing, the second flow feature was overshadowed by the first one and its effects were limited. However, when the cylinder reached the peak response during the VIV lock-in, the Strouhal-number vortex shedding affected the flow field more significantly. Results of the POD analysis showed a transition of the dominant flow feature from the motion-induced leading-edge vortex around the mid span to the Strouhal-number vortex shedding around the static end. In fact, the Strouhal-number vortex shedding existed in two different modes, which were the parallel vortex shedding around the static end and the oblique vortex shedding appearing across the cylinder as indicated by a reduction in the vortex shedding frequency. The angle of the vortex structure was strongly influenced by the gradient of the structural deformation of the cylinder. In addition, a secondary flow feature was found and possessed similar characteristics as the period-doubling bifurcation in the vortex shedding of the circular cylinder. This flow feature involved a number of pairs of counter-rotating stream-wise vortices, which led to successive local high and low-pressure regions as they impinged on the surface. These stream-wise vortices shifted in the span-wise direction by a distance which equalled to the length scale of one vortex every cycle of the motion; therefore, it would take up to two full cycles of the structural motion for this flow feature to restore its own arrangement, resulting in a frequency of 0.6 Hz.

(a)

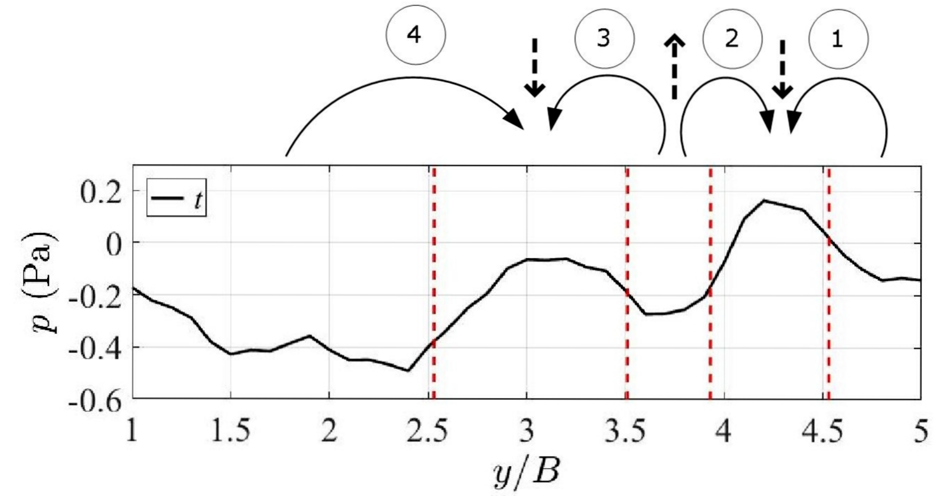

(b)

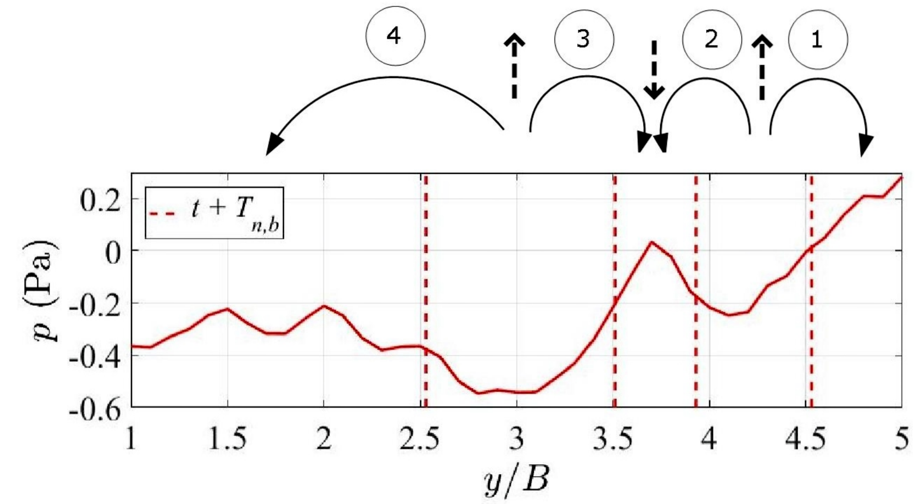

Figure 6.44: The arrangement of two pairs of the stream-wise vortices corresponding to two phase-averaged profiles shown in Figure 6.43b.

6.5.2 VIV Mechanism of the Bending 5:1 Rectangular Cylinder

As the flexible rectangular cylinder underwent the main bending VIV peak, the span-wise distribution of the standard deviation of the time-varying lift coefficient $C'_L(y)$ and of the phase angle of the lift coefficient measured against the generalised structural displacement $\phi_{F_L-z}(y)$ was calculated as shown in Figure 6.45. The structural and aerodynamic behaviour around the mid span $y/B = 5$ possessed certain characteristics which were similar to what observed in the heaving cylinder. The fluctuation of the lift coefficient measured at this span-wise location increased as the bending VIV lock-in occurred; it reached the peak value at the reduced wind speed $U_\mathrm{R} = 2.33$ following by a gradual decrease as the structure approached the maximum VIV response at $U_\mathrm{R} = 3.00$. The distribution of $\phi_{F_L-z}(y)$ also showed a sudden phase jump measured at the mid span as the system reached the lock-out at $U_\mathrm{R} = 3.33$. Moreover, as the flexible cylinder experienced the VIV lock-in, more interesting variation regarding the aerodynamic characteristics of the flow field and the interaction between the structure and the fluid exhibited at other span-wise locations.

In general, the span-wise distribution of $C'_L(y)$ was reasonably sinusoidal and shared similar characteristics to the first bending mode shape being excited. This observation was very clear especially during the initial branch of the VIV lock-in, i.e. at the reduced wind speeds of $U_\mathrm{R} = 2.00$, 2.33 and 2.67. As the structure reached the maximum response during the lock-in or as the system reached the lock-out, the sinusoidal distribution of the lift coefficient diminished significantly and it slightly fluctuated around the value measured in a static cylinder only. The span-wise distribution of $\phi_{F_L-z}(y)$ also possessed similar behaviours. At the reduced wind speed of $U_\mathrm{R} = 3.00$, i.e. at the peak response during the bending VIV lock-in, the phase angles increased dramatically; along the span-wise portion from $y/B = 0$ to 1, values of the phase angles were larger than $90°$.

Since the distribution of $\phi_{F_L-z}(y)$ represents some information regarding the correlation of the lift force in the span-wise direction, it implies that the correlation of the lift force was also similar to the structural mode shape. In addition, as the structural response increased during the VIV lock-in, the rise in the gradient of this distribution curve implies a reduction in the correlation length of the lift force. At the start of the lock-in, the lift force was strongly correlated along the span-wise length, leading to a large amount of energy being transferred to the structure and triggering the VIV lock-in as well as the structural response. As the structural response increased, the process where the energy of the flow was extracted by the structure mainly occurred around the mid span, showing the importance of the aerodynamics of the flow field in this region and accounting to building the structural response. As the peak response was reached, the variation of the phase angle implies a loose synchronisation between the fluid and the structure and a weak flow of energy between them. At the reduced wind speed $U_\mathrm{R} = 3.33$,

(a)

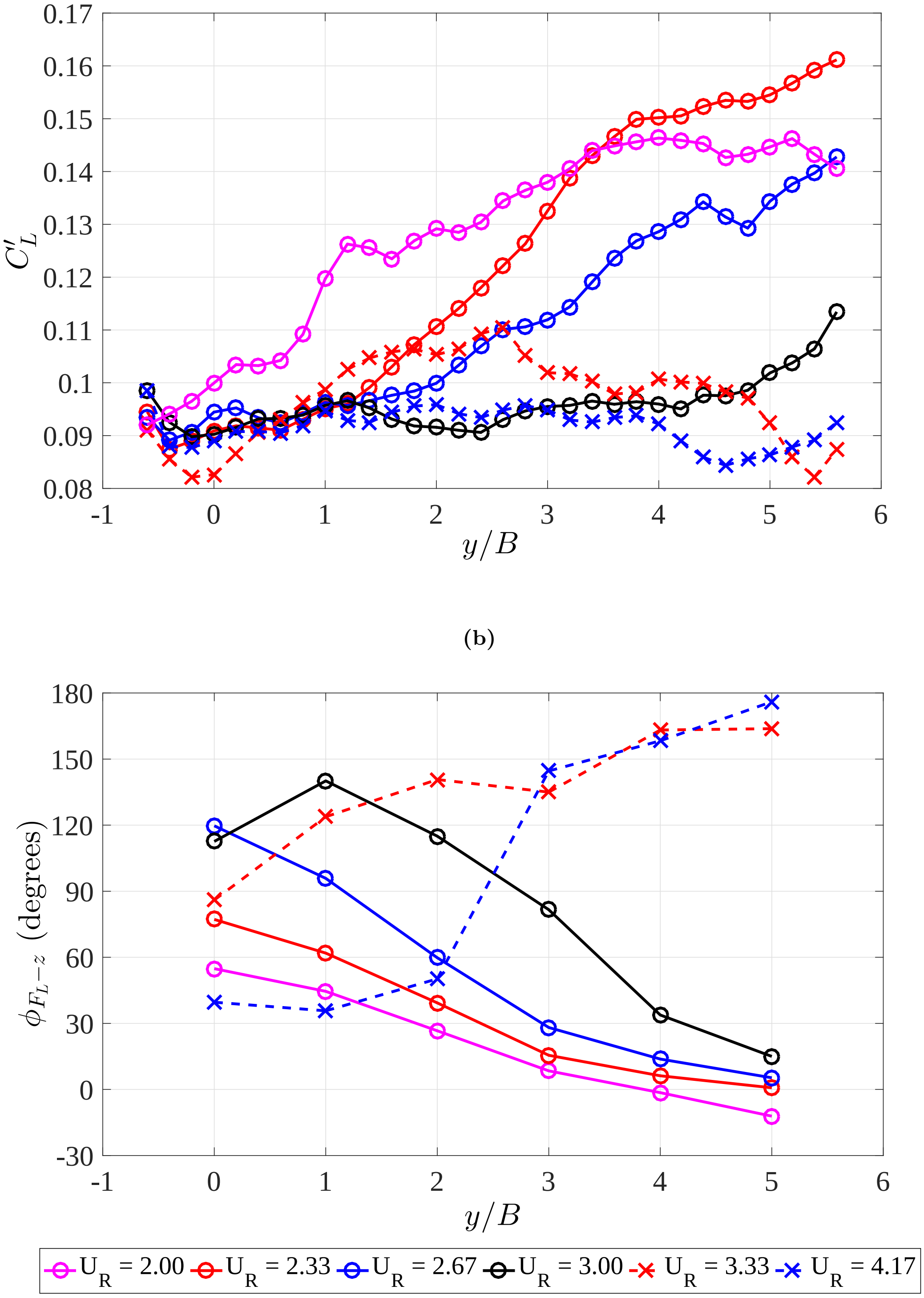

Figure 6.45: Span-wise variability of (a) C'_L and (b) ϕ_{F_L-z} as the flexible cylinder underwent the bending VIV lock-in.

the phase angles were all larger than 90°; the lift force tended to be out of phase by 180° towards the mid span. This indicates a presence of minimum energy transferring from the fluid to the structure, resulting in the lock-out.

More interestingly, the span-wise distribution of $\phi_{F_L-z}(y)$ showed that the flow field around the mid span was not necessarily of importance in triggering VIV lock-in of the flexible cylinder. At the reduced wind speed $U_{\mathrm{R}} = 2.00$, the phase angle of the lift force measured around the mid span, from $y/B = 4$ to 5, is actually negative, implying that the lift force was essentially behind the structural displacement in phase. This phase relationship suggests the flow of energy occurred on the opposite direction, from the structure to the fluid, compared to what observed at other locations or at other wind speeds. Together with a relative flat distribution of $C'_L(y)$ for the span-wise portion of $y/B > 1$, it indicated that the onset of the bending VIV lock-in of the flexible cylinder potentially did not relate to the aerodynamics of the flow field around the mid span where the maximum structural displacement was expected. Instead, the flow field occurring around the portion between $y/B = 1$ to 3 could be the triggering mechanism for the lock-in. As the amplitude of the response increased, this flow feature was shifted towards the mid span and responsible for building up the amplitude of the VIV response.

6.6 CONCLUSION OF THE CHAPTER

In this chapter, results from the wind tunnel tests and the computational simulations using a sectional model were analysed in order to uncover the key aerodynamic characteristics of the flow field around a static 5:1 rectangular cylinder as well as the mechanism of the heaving and pitching VIV of a 5:1 rectangular cylinder. Also, a number of wind tunnel tests in different turbulence flow regimes comprehensively suggested the mechanism of the turbulence-induced effect on both of the flow field and the VIV response of this particular geometry. Moreover, it was of interest to computationally simulate the bending VIV lock-in of a flexible 5:1 rectangular cylinder as it was excited at the first bending mode. The analysis of the flow field offered by the POD technique revealed a number of emerging span-wise flow feature as well as brought more insight into the mechanism of the VIV. These points are summarised as following.

Static cylinder

The aerodynamics of the static 5:1 rectangular cylinder was classified as the impinging vortex shedding where the shear layer created from the leading edge impinged on the surface approximately at a distance of $s/D = 4$. The shear layer trapped underneath a strong circulating flow which was called the separation bubble. The formation of the separation bubble was well defined in the span-wise direction leading a good correlation level of the surface pressure close the leading edge. On the other hand, at the location where the shear impinged on the surface, which was also known as the reattachment point, the flow was highly unsteady and intermittent, represented by large pressure fluctuation and poor correlation of the surface pressure. The creation of the shear layer at the leading edge was in phase with the vortex shedding at the trailing edge; this very characteristic was dependent on the width of the cylinder and strongly controlled the vortex structure in the wake region as well as the Strouhal number.

In the aforementioned studies, the flow field possessed no Reynold number dependence, at least for the Reynold numbers from 1×10^4 to 5×10^4. However, the variation of the angle of attack produced significantly influence; it could either suppress the separation bubble, regarding its strength and geometrical length, on the side surface which exposed more to the wind or elongate the separation bubble on the other side surface. The variation of the flow field affected the aerodynamic forces and moment acting on the cylinder also. The stall angle for the 5:1 rectangular cylinder was estimated to be $6°$, which was indicated by a drop in the lift and moment and the disappearing of the reattachment point.

In the turbulence flow, the stream-wise length of the separation bubble decreased following by an upstream shift of the reattachment point and a quicker pressure recovery. The circulating strength was then concentrated over a narrow region close to the leading edge. Therefore, the separation bubble was highly unstable in the turbulent flow, which was also shown by a decrease in the pressure correlation comparing with what measured in the smooth flow. More interestingly, the pressure correlation in the span-wise direction close the trailing edge increased in the turbulence flow. Therefore, it was evident that the turbulent flow altered the aerodynamics of the 5:1 rectangular cylinder; it suppressed the impinging vortex shedding and promoted the trailing-edge vortex shedding. The effect of the turbulence could be lessened or enhanced by the variation of the angle of attack.

Dynamic cylinder

As for the dynamic rectangular cylinder restrained to the heaving mode only, two VIV lock-in regions were observed. The earlier one was the secondary harmonic featuring a low structural response and occurred at the reduced wind speed of 2/St; the primary harmonic was characterised by a more significant structural response and happened at the reduced wind speed of 1/St. Each VIV harmonic was accompanied by a different flow feature; as the cylinder underwent the secondary VIV region, two vortices were observed on the side surface during one cycle of the heaving motion while only one vortex was rolling on the side surface as the cylinder experienced the primary VIV lock-in.

As for the dynamic rectangular cylinder restrained to the pitching mode only, only secondary VIV peak was found, occurring at the reduced wind speed of 2/(3St). During one cycle of the pitching motion, 1.5 vortex was present.

As the structure underwent either the heaving or pitching VIV, the correlation of the surface pressure increased as the amplitude of the structural response got larger. However, by comparing the variation of the pressure correlation measured close to the leading edge and close to the trailing edge, some difference was pointed out. Before the VIV lock-in, the pressure correlation around the leading edge was significantly larger than what measured around the trailing edge, which was very similar to the static cylinder. As the structural response increased during the VIV lock-in, the pressure correlation around the leading edge decreased while the flow structure around the trailing edge was more correlated. Therefore, the motion-induced leading-edge vortex was only responsible for triggering the structural motion; an increase in the structural response effectively made this flow structure slightly unstable. Its impingement onto the side surface close to the trailing edge at every cycle of the motion yielded a better pressure correlation and increased the lift force or moment acting on the cylinder, resulting in an increase in the structural response during the lock-in.

The turbulent flow was found to weaken the motion-induced leading-edge vortex as well as to remove its impingement onto the side surface. Therefore, the VIV response was strongly suppressed, at least in the turbulent flow regimes tested here. However, as for the rectangular cylinder restrained to the pitching mode only, the angular motion effectively reduced the suppression effect induced by the turbulence; therefore a small pitching VIV peak was visible.

Bending cylinder

By introducing the flexible 5:1 rectangular cylinder, the bending VIV response as the first bending mode was excited was computational simulated and a number of intrinsic flow features were observed. Two primary flow features were found, which was the motion-induced vortex and the Strouhal-number vortex shedding; they interfered with each other across the span-wise length of the cylinder. The motion-induced vortex was dominant around the mid span while the flow field around the static end was strongly influenced by the Strouhal-number vortex shedding. In fact, two Strouhal-number vortex shedding modes existed; the parallel vortex shedding mode was dominant around the static end while the oblique vortex shedding mode was visible across the span-wise length of the cylinder. In addition, the secondary flow feature featuring a number of counter-rotating stream-wise vortices was found to superimpose on the other primary flow features. These stream-wise vortices shifted in the span-wise direction and it could take up to two cycles of the structural motion to restore its original arrangement.

Further analysis revealed that the span-wise distribution of the lift coefficient as well as the span-wise correlation appeared to possess characteristics similar to the structural mode shape. This observation was most relevant during the initial branch of the VIV lock-in where the amplitude of the structural response was increasing. On the other hand, as the structural response reached the maximum value, the span-wise distribution of the lift coefficient was relatively flat and oscillated around the value observed in the static cylinder.

The mechanism of the bending VIV lock-in was found to not necessarily relate to the aerodynamics of the mid span where the maximum structural response was expected. In fact, there appeared a certain flow feature around the span-wise portion from $y/B = 1$ to 3 which was responsible for the flow of energy from the fluid to structure and triggering the VIV lock-in. When the structural response increased, the presence of the pressure gradient shifted this feature towards the mid span, accounting for building up the response. These results have shown that the mechanism of the bending VIV lock-in was not only related to the flow features occurring close the leading edge and the trailing edge but also due to the presence of a certain span-wise flow feature. The effect of the turbulent flow on this flow feature has not yet been found, which was a limit of this study.

Based on this chapter, a number of selected results including the heaving and bending VIV are used in the investigation of the mathematical modelling for VIV. Moreover, observations of the span-wise distribution of the lift coefficient together with the correlation expression of the lift force are used to derive and validate a generalised mathematical VIV model for a 3D flexible structure.

Chapter 7

Theoretical Modelling of VIV

7.1 INTRODUCTION

As discussed in Chapter 2, the Hartlen and Currie model (1970) is classified as a two degree-of-freedom wake-oscillator model. It comprises a linear structural equation and a non-linear fluid equation

$$\text{Structure :} \qquad \ddot{x_r} + 2\zeta\dot{x_r} + x_r = a\Omega_o^2 c_L, \tag{7.1}$$

$$\text{Fluid :} \qquad \ddot{c_L} - \alpha\Omega_o\dot{c_L} + \frac{\gamma}{\Omega_o}\dot{c_L}^3 + \Omega_o^2 c_L = b\dot{x_r}. \tag{7.2}$$

Definitions of all parameters and terms were adopted from Section 2.5.2. The parameters b, α and γ are the three model parameters that are required to be identified from results of wind tunnel tests or computational studies. The parameter b represents the coupling between the two equations. α and γ are the van der Pol coefficient of the Rayleigh equation which is applied to model the non-linear damping of the fluid oscillation, allowing the self-sustained and self-limited characteristics of the VIV to be simulated. By assuming that the structural response and the lift coefficient are sinusoidal, the analytical solutions of the system of Equations 7.1 and 7.2 can be achieved as shown below

$$X_r^2 = \frac{4a^2\Omega_o^5}{3\gamma\Omega^3}\frac{(1-\Omega^2)(\Omega_o^2-\Omega^2)+2\alpha\zeta\Omega_o\Omega^2}{8\zeta^3\Omega^3+2\zeta\Omega(1-\Omega^2)^2}, \tag{7.3}$$

$$\Omega_o^2 = \Omega^2\frac{(1-\Omega^2)^2+4\zeta^2\Omega^2}{(1-\Omega^2)^2+4\zeta^2\Omega^2-2ab\zeta\Omega^2}, \tag{7.4}$$

$$\tan\phi = \frac{2\zeta\Omega}{1-\Omega^2}, \tag{7.5}$$

$$C_{Lo} = \frac{1}{\sin\phi}\frac{2\zeta\Omega X_r}{a\Omega_o^2}. \tag{7.6}$$

$$\tag{7.7}$$

Also, the maximum amplitude of the stationary lift coefficient was found to be related to the model parameters α and γ as given by

$$C_{Lo} = \frac{4\alpha}{3\gamma}. \tag{7.8}$$

However, the derivation of these analytical solutions is based on a number of assumptions including that the higher-order sinusoidal terms can be neglected. Therefore, the analytical solutions, particularly the lift coefficient, potentially differ from the ones directly obtained from the time integration of the Hartlen and Currie model; this aspect will be discussed in the following section.

The original Hartlen and Currie model was proposed to simulate the VIV response of a 2D structure. In this study, this model will be modified so that it can be used to predict the VIV response of a 3D flexible structure; the derivation of this modification will be shown in detail in Sections 7.2 and 7.3. In addition, to properly model the VIV response of the 3D flexible structure, the coherence characteristics of the lift force acting on the model need to be represented; as shown in Section 7.4, the inclusion of the correlation function in the forcing term of the structural equation is important to model this aspect.

7.2 3D COMPLETE HARTLEN AND CURRIE MODEL

7.2.1 Structural Equation

The structural equation of the Hartlen and Currie model can be rewritten in a general form to describe the motion of the structural element at the coordinate y and at the time t due to the lift force as

$$m\ddot{x}(y,t) + c\dot{x}(y,t) + kx(y,t) = \frac{1}{2}\rho U^2 B c_L(y,t), \tag{7.9}$$

where m, c and k are the mass , damping and stiffness of the structural element having a unit length respectively; $c_L(y,t)$ is the lift coefficient acting at the coordinate y and at the time t. Given that the 3D flexible structure possesses a number of mode shapes $\Phi_i(y)$ ($i = 1 \ldots N$ where N is the number of structural mode shapes) the structural response at the coordinate y and the time t can be described as

$$x(y,t) = \sum_{i=1}^{N} \Phi_i(y)\tilde{x}_i(t), \tag{7.10}$$

with $\tilde{x}_i(t)$ is the modal structural response of the structural mode shape i. Substituting Equation 7.10 into the equation of motion (Equation 7.9), the structural equation can be rewritten as

$$m\sum_{i=1}^{N} \Phi_i(y)\ddot{\tilde{x}}_i(t) + c\sum_{i=1}^{N} \Phi_i(y)\dot{\tilde{x}}_i(t) + k\sum_{i=1}^{N} \Phi_i(y)\tilde{x}_i(t) = \frac{1}{2}\rho U^2 B c_L(y,t). \tag{7.11}$$

In order to solve this equation, both sides of Equation 7.11 are multiplied by a mode shape $\Phi_j(y)$ and then the integration over the length L of the structure is performed. This then yields

$$\begin{aligned}\int_0^L \Phi_j(y)\, m \sum_{i=1}^{N} \Phi_i(y)\ddot{\tilde{x}}_i(t)\,\mathrm{d}y + \int_0^L \Phi_j(y)\, c \sum_{i=1}^{N} \Phi_i(y)\dot{\tilde{x}}_i(t)\,\mathrm{d}y + \int_0^L \Phi_j(y)\, k \sum_{i=1}^{N} \Phi_i(y)\tilde{x}_i(t)\,\mathrm{d}y \\ = \frac{1}{2}\rho U^2 B \int_0^L \Phi_j(y) c_L(y,t)\,\mathrm{d}y.\end{aligned} \tag{7.12}$$

Using Rayleigh damping, c is expressed as a linear combination of mass m and stiffness k and the structural mode shape $\Phi_i(y)$ can be considered to be geometrically orthogonal with respect to mass, damping and stiffness as

$$\text{Mass:} \qquad \int_0^L \Phi_j(y)\, m\, \Phi_i(y)\mathrm{d}y = 0 \quad \text{if } i \neq j, \tag{7.13}$$

$$\text{Damping:} \qquad \int_0^L \Phi_j(y)\, c\, \Phi_i(y)\mathrm{d}y = 0 \quad \text{if } i \neq j, \tag{7.14}$$

$$\text{Stiffness:} \qquad \int_0^L \Phi_j(y)\, k\, \Phi_i(y)\mathrm{d}y = 0 \quad \text{if } i \neq j. \tag{7.15}$$

The orthogonality of the mode shapes inherently implies that the highly-coupled equation of motion as shown in Equation 7.12 can be decoupled to each separate mode and rewritten in a more manageable form in the generalised coordinate as

$$M_i\ddot{\tilde{x}}_i(t) + C_i\dot{\tilde{x}}_i(t) + K_i\tilde{x}_i(t) = \frac{1}{2}\rho U^2 B\tilde{c}_{L,i}(t). \tag{7.16}$$

Here $M_i = \int_0^L m\Phi_i^2(y)\,\mathrm{d}y$, $C_i = \int_0^L c\Phi_i^2(y)\,\mathrm{d}y$ and $K_i = \int_0^L k\Phi_i^2(y)\,\mathrm{d}y$ are the generalised mass, damping and stiffness of the structure excited in the structural mode shape $\Phi_i(y)$ in the generalised coordinate respectively. $\tilde{c}_{L,i}(t) = \int_0^L \Phi_i(y)c_L(y,t)\,\mathrm{d}y$ is the generalised lift coefficient acting on the structure. $\tilde{x}_i(t)$, $\dot{\tilde{x}}_i(t)$ and $\ddot{\tilde{x}}_i(t)$ are the generalised displacement, velocity and acceleration of the structure oscillating at the mode shape $\Phi_i(y)$ respectively. Dividing both sides of Equation 7.16 by the generalised mass M_i, the general structural equation of the Hartlen and Currie model can be written as

$$\ddot{\tilde{x}}_i(t) + 2\zeta_i\omega_{n,i}\dot{\tilde{x}}_i(t) + \omega_{n,i}^2\tilde{x}_i(t) = \frac{1}{2}\frac{\rho U^2 B}{\int_0^L m\Phi_i^2(y)\,\mathrm{d}y}\int_0^L \Phi_i(y)c_L(y,t)\,\mathrm{d}y, \tag{7.17}$$

where ζ_i and $\omega_{n,i}$ are the damping ratio and circular natural frequency associated with the structural mode shape $\Phi_i(y)$.

The result of the aforementioned derivation is that the highly-coupled system of equations (Equation 7.9) is successfully written in a more manageable form where all structural mode shapes are fully decoupled and each equation corresponds to a single mode shape. This derivation also inherently implies the validity of the superposition theory regarding the structural solution.

Assuming that the mass of the 3D structure is uniformly distributed in the span-wise direction, i.e. $m = M/L$ (where M and L are the total mass and span-wise length of the structure) and performing similar normalisation as stated in the original paper of Hartlen and Currie (1970), the 3D structural equation of the Hartlen and Currie model is defined as

$$\ddot{\tilde{x}}_{r,i} + 2\zeta\dot{\tilde{x}}_{r,i} + \tilde{x}_{r,i} = \frac{\rho B^2 L}{8\pi^2 \mathrm{St}^2 M \int_0^L \Phi_i(y)^2 \,\mathrm{d}y}\,\Omega_o^2 \int_0^L \Phi(y)\, c_L(y,\tau)\,\mathrm{d}y, \tag{7.18}$$

where $\tilde{x}_{r,i}$, $\dot{\tilde{x}}_{r,i}$ and $\ddot{\tilde{x}}_{r,i}$ are the non-dimensional generalised displacement, velocity and acceleration of the 3D flexible structure considering the mode shape $\Phi_i(y)$. The derivations are with respected to the non-dimensional time $\tau = \omega_{n,i} t$ with $\omega_{n,i} = 2\pi f_{n,i}$ being the modal natural circular frequency of the structure. Hereafter, the subscript i is ignored to simplify mathematical expressions if only one mode shape is considered.

7.2.2 Fluid Equation

The fluid equation of the Hartlen and Currie model can also be written in a more general form to describe the oscillation of the lift coefficient at the point of the coordinate y and at the time t as

$$\ddot{c}_L(y,t) - c_1\dot{c}_L(y,t) + c_2\dot{c}_L(y,t)^3 + \omega_o^2 c_L(y,t) = b\,\dot{x}(y,t), \tag{7.19}$$

where c_1 and c_2 are the two van der Pol coefficients used to represent the damping of the fluid oscillation; $\omega_o = 2\pi f_o = 2\pi(\mathrm{St}U)/B$ is the frequency of the vortex shedding; the parameter b involves in the forcing term of the fluid equation which is dependent of the structural velocity, i.e. it is known as the velocity coupling. Adopting the similar normalisation method to that presented by Hartlen and Currie (1970) and noticing that the non-dimensional velocity $\dot{x}_r(y,\tau)$ at the coordinate y can be presented as $\sum_{i=1}^{N} \Phi_i(y)\dot{\tilde{x}}_{r,i}(\tau)$, Equation 7.19 can be written as

$$\ddot{c}_L(y,\tau) - \alpha\Omega_o\dot{c}_L(y,\tau) + \frac{\gamma}{\Omega_o}\dot{c}_L(y,\tau)^3 + \Omega_o^2 c_L(y,\tau) = b\sum_{i=1}^{N}\Phi_i(y)\,\dot{\tilde{x}}_{r,i}(\tau). \tag{7.20}$$

Following the normalisation approach proposed by Hartlen and Currie (1970), it was found that the model parameters α, γ and b are independent of the structural mode shape $\Phi_i(y)$ and the non-dimensional wind speed Ω_o; the former relationship is validated in Section 7.2.3.

In order to predict the VIV response of a 3D structure, Equations 7.18 and 7.20 can be time-integrated where the structural response is defined in the generalised coordinate while the lift coefficient is solved at a number of discrete points in the span-wise direction. It is noticed the spatial characteristic of the fluid equation, i.e. of the lift coefficient $c_L(y, \tau)$ is expressed via the inclusion of the structural mode shape $\Phi_i(y)$ on the right-hand-side. Using this approach, which thereafter is named as the 3D complete Hartlen and Currie model, can be time-consuming and inefficient to model the VIV response of a 3D structure at different values of damping. Therefore, the aim of the following study is to investigate structural and fluid solutions obtained from this approach; thereby, some reasonable assumptions are proposed to derive a simplified approach allowing the behaviour of a 3D structure during the VIV lock-in to be modelled accurately and efficiently.

7.2.3 Application of 3D Complete Hartlen and Currie Model

The 3D complete Hartlen and Currie model discussed in Section 7.2 was used to model the VIV response of a 3D circular cylinder having the span-wise length $L = 1\,\mathrm{m}$ and sinusoidal mode shapes given by

$$\Phi_i(y) = \sin\left(\frac{i\pi}{L}y\right), \quad i = 1 \ldots N. \tag{7.21}$$

i was in fact the number of waves observed along the span-wise length of the structure at an instant. Here, in this investigation, only the first three mode shapes, i.e. $i = 1, 2$ and 3, were modelled; it was assumed that the 3D circular cylinder had uniform mass distribution along its span-wise length and possessed similar damping ratio $\zeta_i = 0.0015$ for all three structural mode shapes considered. This assumption was found to be unreasonable since the full-scale measurement indicates each structural mode shape is associated with a certain value of the damping ratio; however, this study presented here made use of this assumption to elimiate the potential Scruton number dependence of the Hartlen and Currie model. The values of the parameter $a = (\rho B^2 L)/(8\pi \mathrm{St}^2 M) = 0.002$ and the model parameters $\alpha = 0.02$, $\gamma = 0.67$ and $b = 0.4$ were adopted from Hartlen and Currie (1970) and, as discussed above, they were constant regardless of structural mode shapes.

Proposed discrete time-integration algorithm

A discrete semi-implicit time-integration algorithm was proposed:

$$\text{Structural:} \quad \ddot{\tilde{x}}_r^{\tau_{n+1}} = a\Omega_o^2 \frac{\int_0^L \Phi(y) c_L(y)^{\tau_n}\,\mathrm{d}y}{\int_0^L \Phi(y)^2\,\mathrm{d}y} - 2\zeta\dot{\tilde{x}}_r^{\tau_n} - \tilde{x}_r^{\tau_n}, \tag{7.22}$$

$$\dot{\tilde{x}}_r^{\tau_{n+1}} = \dot{\tilde{x}}_r^{\tau_n} + \Delta\tau\,\ddot{\tilde{x}}_r^{\tau_{n+1}}, \tag{7.23}$$

$$\tilde{x}_r^{\tau_{n+1}} = \tilde{x}_r^{\tau_n} + \Delta\tau\,\dot{\tilde{x}}_r^{\tau_{n+1}}, \tag{7.24}$$

$$\text{Fluid:} \quad \ddot{c}_L(y)^{\tau_{n+1}} = b\Phi(y)\dot{\tilde{x}}_r^{\tau_{n+1}} + \alpha\Omega_o\dot{c}_L(y)^{\tau_n} - \frac{\gamma}{\Omega}\dot{c}_L^3(y)^{\tau_n} - \Omega_o^2 c_L(y)^{\tau_n}, \tag{7.25}$$

$$\dot{c}_L(y)^{\tau_{n+1}} = \dot{c}_L(y)^{\tau_n} + \Delta\tau\,\ddot{c}_L(y)^{\tau_{n+1}}, \tag{7.26}$$

$$c_L(y)^{\tau_{n+1}} = c_L(y)^{\tau_n} + \Delta\tau\,\dot{c}_L(y)^{\tau_{n+1}}. \tag{7.27}$$

It is noticed that the second derivatives of the structural and fluid solutions, x_r and $c_L(y)$ respectively, were not solved in a fully implicit manner; solutions of these terms were dependent either on structural solutions or fluid solutions from the previous non-dimensional time step. On the other hand, the first-order backward difference method was applied to calculate other terms. Therefore, this discretisation method was only semi-implicit. In addition, at one single non-dimensional time-step, the structural and fluid equations were only solved in the staggered scheme without any corrections; therefore the structural and fluid solutions do not possess a strong coupling as shown in the fluid-structure-interaction problem. This issue could be resolved by using a sufficiently small time-step size; in the study presented here, a non-dimensional time-step size $\Delta\tau = 0.001$ was selected and, at each wind speed, the integration was performed over $N_\tau = 3000$ non-dimensional time-steps to ensure that both of the structural and fluid solutions reached a stable oscillatory state.

To validate this proposed algorithm, a comparison between the VIV response of a 3D circular cylinder excited in a unit mode shape $\Phi(y) = 1$ and of a 2D circular cylinder possessing similar structural and fluid parameters was conducted. The former was obtained by using the 3D complete Hartlen and Currie model and the proposed algorithm. As for the latter, its solution was achieved by solving the original 2D Hartlen and Currie model using the MATLAB `ode45` differential-equation solver and by using the analytical form. All three solution are included for comparison in Figure 7.1, where a good agreement between them can be seen, regarding the VIV lock-in range, the maximum non-dimensional structural response during the lock-in and the non-dimensional wind speed of its occurrence. The 3D cylinder excited in a unit mode shape was predicted to have about 4% higher maximum response during the lock-in as compared to the 2D cylinder; however, this difference was due to the use of higher-order differencing schemes included in the `ode45` solver. Therefore, it is evident that the VIV response of the 3D circular cylinder excited in the unit mode shape was similar to a 2D circular cylinder, showing the accuracy and appropriateness of the proposed discrete time-integration algorithm to obtain the structural and fluid solutions from the 3D complete Hartlen and Currie model.

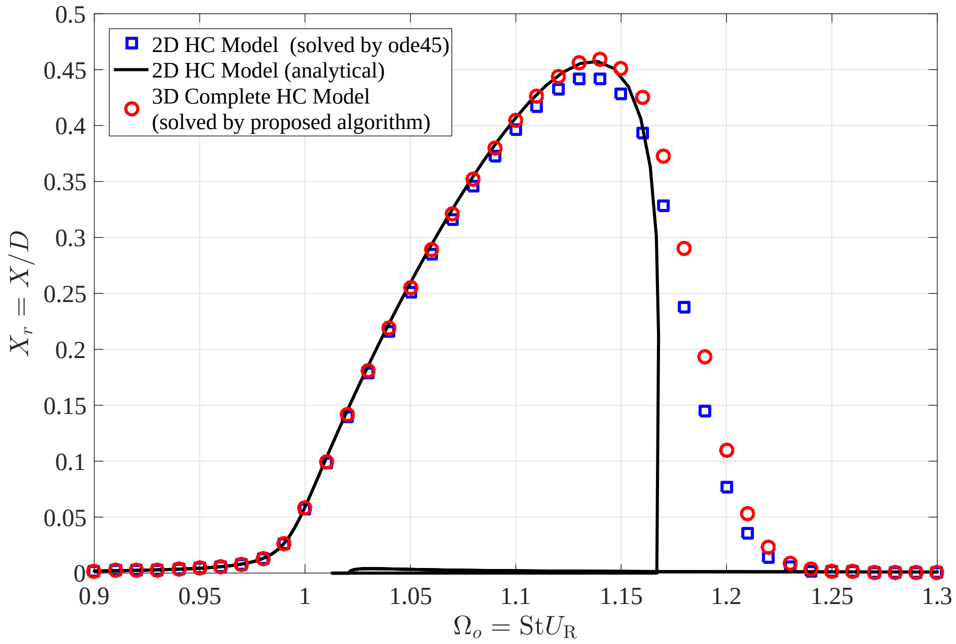

Figure 7.1: Comparison of the structural response of a 3D flexible circular cylinder having a unit mode shape $\Phi(y) = 1$ obtained by solving the 3D complete Hartlen and Currie model using the proposal algorithm *(red circular dots)* against that of a 2D circular cylinder modelled by solving the 2D Hartlen and Currie model using of the MATLAB solver `ode45` *(blue squares)* and by the analytical solution of the 2D Hartlen and Currie model *(black solid line)*.

Results and discussion

With the validity of the proposed discrete time-integration method being confirmed, this algorithm was then applied to model the VIV response of a 3D circular cylinder excited in the first three structural mode shapes defined in Equation 7.21. Together with the VIV structural response measured in the generalised coordinate system, it was of interest to investigate the variation of the span-wise distribution of the standard deviation of the time-varying lift coefficient $c_L'(y)$, the non-dimensional frequency of the lift coefficient $\Omega(y)$ and the phase shift between the lift coefficient against the generalised displacement $\Phi_{CL-\tilde{X}_r}(y)$ as the 3D circular cylinder underwent the VIV lock-in. As can be seen in Figures 7.2c, 7.3c and 7.4c, some numerical instability is present where the displacement of the structure is close to zero, i.e. at the nodes, while towards the anti-nodes where the displacement of the structure is more noticeable, the structural and fluid solutions are more stable.

Regarding the VIV structural response measured in the generalised coordinate, Figures 7.2a, 7.3a and 7.4a show similar behaviour to the circular cylinder, including the VIV lock-in range, the maximum non-dimensional displacement during the VIV and the non-dimensional velocity where the maximum structural response occurred, even though it was excited at different mode shapes with different natural frequencies. The time-integrated solutions of a 2D circular cylinder possessing similar fluid and structure characteristics are also included; a comparison revealed that the generalised maximum displacement of the 3D flexible circular cylinder during the VIV lock-in was about 1.15 times larger than the maximum displacement of the 2D circular cylinder regardless of which mode shapes the 3D cylinder were excited at. These results further emphasised that the Hartlen and Currie model parameters α, γ and b are independent of the structural mode shape.

Investigation of the span-wise distribution of the lift coefficient as the cylinder experienced the VIV lock-in revealed a close relationship between its span-wise variation and the structural mode shape. In detail, along span-wise portions where motions of all structural points were in phase with each other, the lift coefficient followed sinusoidal-like distribution and shared some similarities compared to the sinusoidal structural mode shapes as illustrated in Figures 7.2b, 7.3b and 7.4b, particularly at $\Omega_o = 1.15$ corresponding to when the structure reached the maximum response during lock-in. Obviously, as the cylinder oscillated at the second and third mode shapes, the structural motion between these two successive portions were 180° out-of-phase. Therefore, a corresponding 180° phase difference was observed in the distribution of the lift coefficient along these two adjacent portions as shown in Figures 7.3c and 7.4c. These two observations suggested that the distribution of the lift coefficient along the span-wise length possessed some characteristics of the structural mode shape in which the structure is excited, especially as the structure experienced VIV lock-in. This result could also be inferred by studying the phase-averaged span-wise distributions of the lift coefficient as shown in Figures 7.2e, 7.3e and 7.4e, where a good agreement between the span-wise distribution of the lift coefficient and the excited mode shape could be concluded.

Furthermore, around the anti-nodes, at a number of non-dimensional wind speeds such as $\Omega_o = 1$ and 1.05, the distribution of the lift coefficient was more flat rather than following the curvature of the structural mode shape. This indicated some correlation characteristics in the lift coefficient, which could also be implied from the span-wise distribution of the phase shift of the lift coefficient against the generalised displacement (Figures 7.2c, 7.3c and 7.4c). Concentrating only on the first wave, i.e. the first portion of the span-wise length where motions of all structural points were in phase with each other, the phase shift measured at the anti-node gradually increased during VIV lock-in occurring from the non-dimensional wind speed $\Omega_o = 1$ to $\Omega_o = 1.2$; this behaviour was also observed in the wind tunnel and computational studies presented in Chapter 6. More interestingly, at the on-set of VIV lock-in, i.e. at $\Omega_o = 1$, the difference in the values of the phase shift around the anti-node was very small; from $y/\lambda = 0.2$ to 0.8, the phase shift was reasonably constant. As the generalised displacement of the structure increased, the difference got larger and the span-wise portion where the phase shift could be considered to be constant significantly reduced. These qualitative results of the distribution of the phase shift suggested the reduction of the correlation length of the lift coefficient as the displacement of the cylinder got larger. At $\Omega_o = 1.2$, it appeared that the good correlation level was restored; however, the fluctuation of the lift coefficient was very small and at a phase lag of 90° compared to the structural motion. In addition, it mostly occurred at the vortex shedding frequency defined by the Strouhal number, particularly around the nodes. These results were found to occur for all three structural mode shapes considered, illustrating their independence on the mode shape of the 3D cylinder.

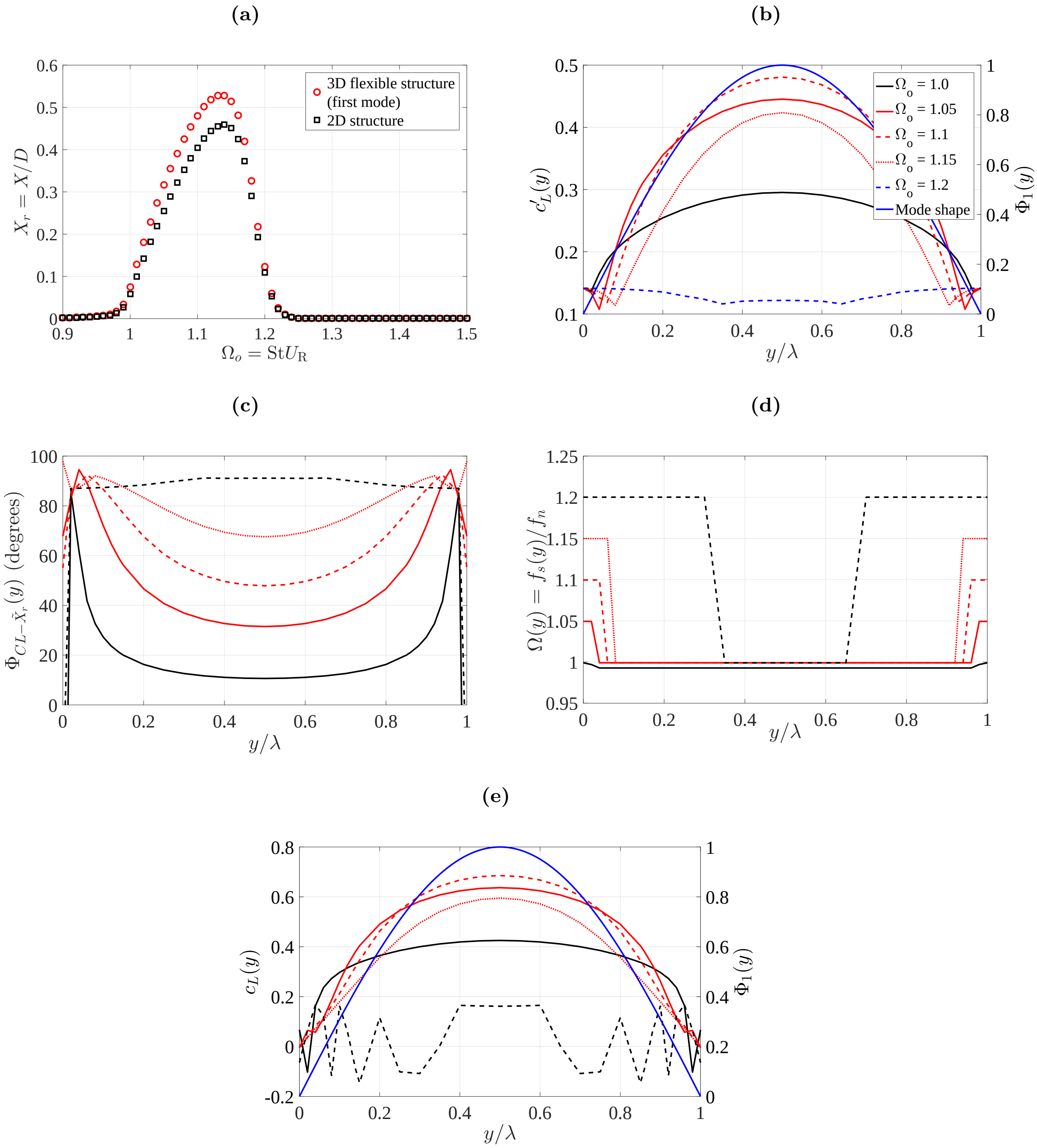

Figure 7.2: Results of (a) the generalised displacement of the structure being excited at the first mode shape together with the span-wise distribution of (b) the fluctuation of the lift coefficient, (c) the phase shift between the lift coefficient and the generalised displacement, (d) the frequency of the lift coefficient and (e) the phase-averaged lift coefficient at every cycle of the structural oscillation; the span-wise coordinate y is normalised using the wavelength λ of the structural mode shape.

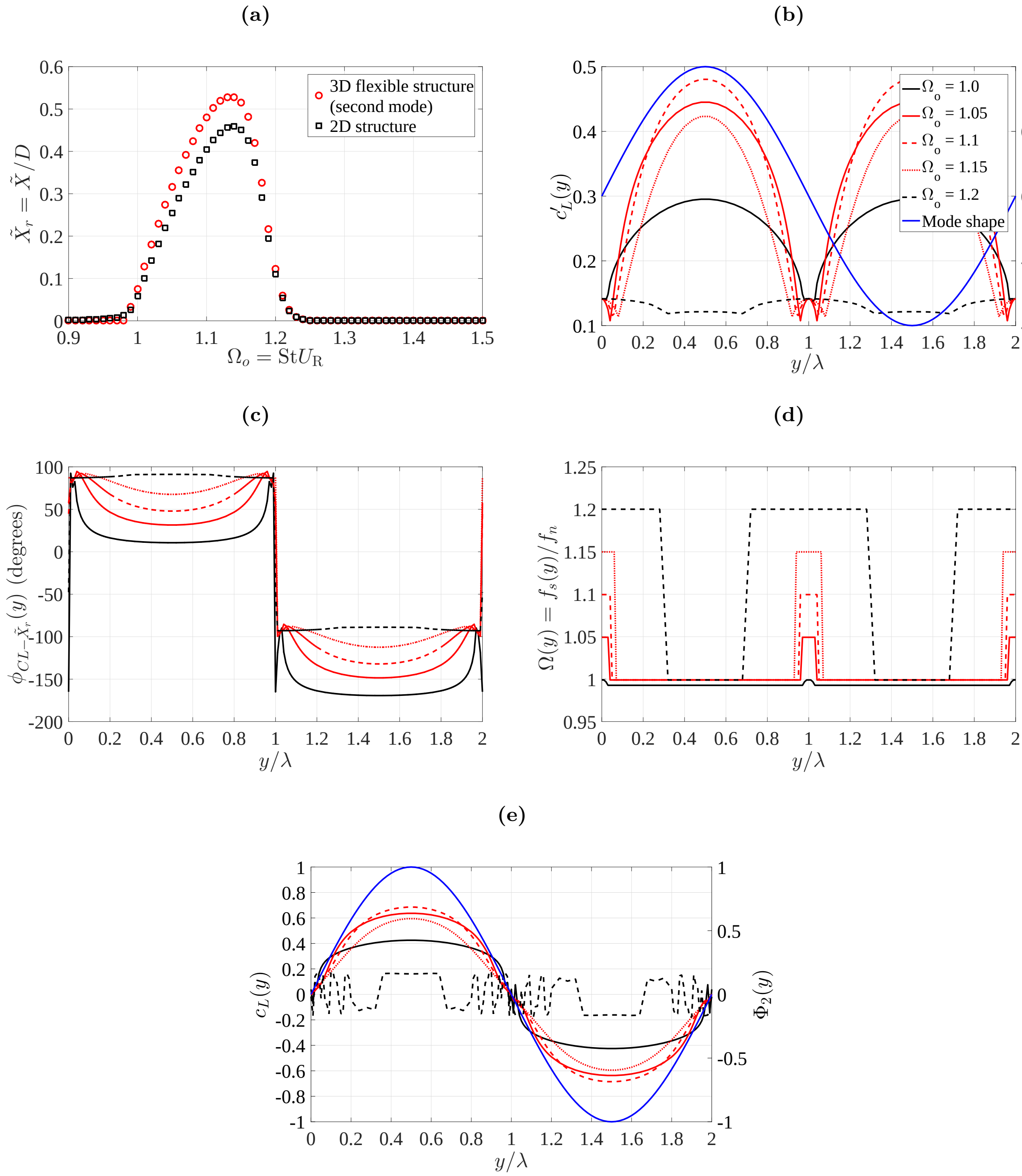

Figure 7.3: Results of (a) the generalised displacement of the structure being excited at the second mode shape together with the span-wise distribution of (b) the fluctuation of the lift coefficient, (c) the phase shift between the lift coefficient and the generalised displacement, (d) the frequency of the lift coefficient and (e) the phase-averaged lift coefficient at every cycle of the structural oscillation; the span-wise coordinate y is normalised using the wavelength λ of the structural mode shape.

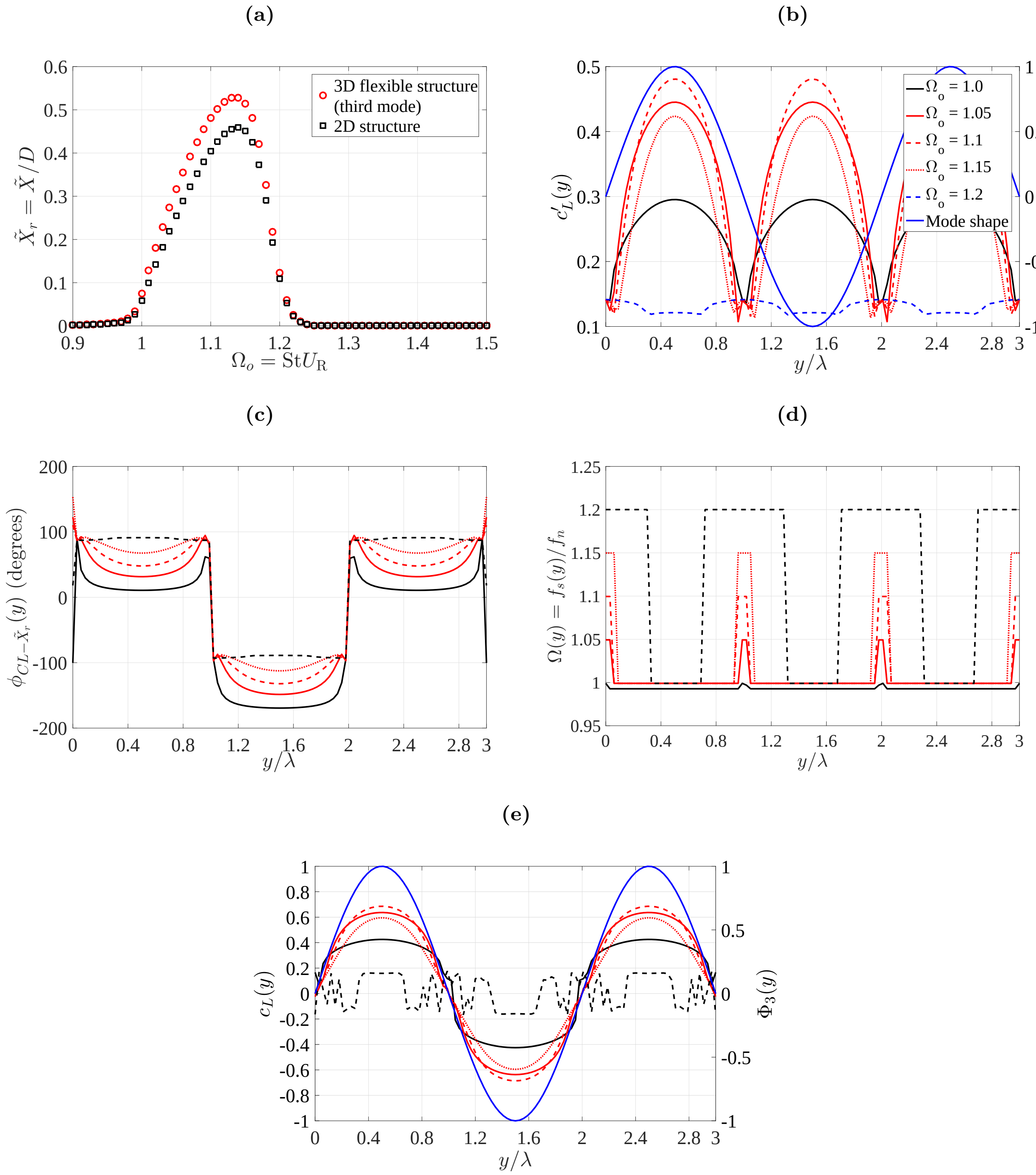

Figure 7.4: Results of (a) the generalised displacement of the structure being excited at the third mode shape together with the span-wise distribution of (b) the fluctuation of the lift coefficient, (c) the phase shift between the lift coefficient and the generalised displacement, (d) the frequency of the lift coefficient and (e) the phase-averaged lift coefficient at every cycle of the structural oscillation; the span-wise coordinate y is normalised using the wavelength λ of the structural mode shape.

In conclusion, the 3D complete Hartlen and Currie model featuring a generalised structural equation and a spatial-dependent fluid equation was developed; together with a proposed differential equation solver based on the first-order backward differencing scheme, this model was able to predict some important fluid behaviour relating to the VIV including the variation of the phase shift between the lift coefficient measured at the anti-nodes and the generalised displacement as the structure underwent the lock-in and the desynchronisation of the frequency of the lift coefficient occurring around the nodes as the system reached the lock-out. More importantly, the fluid solution obtained from the 3D complete Hartlen and Currie model showed a variation in the correlation length of the lift coefficient. At the onset of VIV lock-in, the lift coefficient was found to be strongly correlated over the portion of the span-wise length which was equal to a wavelength of the structural mode shape; as the displacement of the structural increased, the correlation of the lift force decreased. These behaviours were found to be comparable with results obtained from the 3D bending simulation shown in Section 6.5 . In addition, the phase-averaged distribution of the fluid solution revealed that the lift coefficient appeared to reasonably follow the structural mode shape being excited. This finding was of importance and will be applied in later sections to simplify this 3D complete Hartlen and Currie model so that the generalised displacement of a 3D flexible structure experiencing the VIV could be predicted in a more efficient way.

7.3 3D FULLY-CORRELATED HARTLEN AND CURRIE MODEL

7.3.1 Mathematical Development

Based on results presented in Section 7.2, the distribution of the lift coefficient along the span-wise length of the structure was found to follow the structural mode shape; the lift coefficient at the node y and at the time t can be represented in a continuous form as

$$c_L(y,t) = \sum_{i=1}^{N} \Phi_i(y)\tilde{c}_{L,i}(t), \tag{7.28}$$

with $\tilde{c}_{L,i}(t)$ being the modal lift coefficient of the structural mode shape i. Equation 7.28 is based on the superposition, which means the lift coefficient at the coordinate y equals to the summation of contributions from all N mode shapes. In fact, the 3D complete Hartlen and Currie model has shown that, during the VIV lock-in, one dominant structural mode shape whose modal natural frequency satisfied the frequency requirement was excited and the span-wise distribution of the lift coefficient followed this dominant structural mode shape only. Therefore, Equation 7.28 can be simplified as

$$c_L(y,t) = \Phi_i(y)\tilde{c}_{L,i}(t), \tag{7.29}$$

and the fluid equation can be analysed in a decoupled manner together with the structural equation.

Substituting Equation 7.29 into the fluid equation and performing the normalisation process used by Hartlen and Currie (1970), Equation 7.19 can be expressed as

$$\Phi_i(y)\ddot{\tilde{c}}_{L,i}(\tau) - \alpha\Omega_o\Phi_i(y)\dot{\tilde{c}}_{L,i}(t) + \frac{\gamma}{\Omega_o}\Phi_i^3(y)\,\dot{\tilde{c}}_{L,i}^3(t) + \Omega_o^2\Phi_i\tilde{c}_{L,i}(t) = b\Phi_i(y)\dot{\tilde{x}}_{r,i}(t). \tag{7.30}$$

The Hartlen and Currie model parameters α, γ and b are independent of the structural mode shapes $\Phi_i(y)$ and the non-dimensional wind speed Ω_o. In addition, the decoupling of the structural mode shapes is inherently included in the fluid equation as an important characteristic of the VIV lock-in; therefore, Equation 7.30 can be solved by multiplying all terms with the structural mode shape $\Phi_i(y)$ and integrating over the span-wise length. Removing the subscript i for simplicity, it can be written as

$$\begin{aligned}\ddot{\tilde{c}}_L(\tau)\int_0^L \Phi(y)^2\,\mathrm{d}y - \alpha\Omega_o\,\dot{\tilde{c}}_L(\tau)\int_0^L \Phi(y)^2\,\mathrm{d}y + \frac{\gamma}{\Omega_o}\,\dot{\tilde{c}}_L^3(\tau)\int_0^L \Phi(y)^4\,\mathrm{d}y + \Omega_o^2\tilde{c}_L(\tau)\int_0^L \Phi(y)^2\,\mathrm{d}y \\ = b\dot{\tilde{x}}_r(\tau)\int_0^L \Phi(y)^2\,\mathrm{d}y.\end{aligned} \tag{7.31}$$

Here, $\tilde{c}_L(\tau)$, $\dot{\tilde{c}}_L(\tau)$ and $\ddot{\tilde{c}}_L(\tau)$ are the model lift coefficient associated to the considered structural mode shape and its first and second derivatives, respectively, with respect to the non-dimensional time τ. Dividing all terms on both sides of Equation 7.31 by the integral $\int_0^L \Phi(y)^2\mathrm{d}y$, the 3D fluid equation of the Hartlen and Currie model defined in the generalised coordinate is written as

$$\ddot{\tilde{c}}_L - \alpha\Omega_o\,\dot{\tilde{c}}_L + \frac{\gamma}{\Omega_o}\frac{\int_0^L \Phi(y)^4\mathrm{d}y}{\int_0^L \Phi(y)^2\mathrm{d}y}\,\dot{\tilde{c}}_L^3 + \Omega_o^2\,\tilde{c}_L = b\dot{\tilde{x}}_r. \tag{7.32}$$

The model parameter α and b are defined as in the original Hartlen and Currie model; the model parameter γ is multiplied by a correction factor $\Gamma = \left[\int_0^L \Phi(y)^4\,\mathrm{d}y\right] / \left[\int_0^L \Phi(y)^2\,\mathrm{d}y\right]$. In addition, applying Equation 7.29, Equation 7.18 can be re-defined as following

$$\ddot{\tilde{x}}_r + 2\zeta\dot{\tilde{x}}_r + \tilde{x}_r = \frac{\rho B^2 L}{8\pi^2\mathrm{St}^2 M\int_0^L \Phi(y)^2\mathrm{d}y}\,\Omega_o^2\,\tilde{c}_L\int_0^L \Phi(y)^2\mathrm{d}y. \tag{7.33}$$

By cancelling the integration terms on the top and bottom of the right-hand side of Equation 7.33, it yields a similar expression for the parameter a as the one present in the original 2D Hartlen and Currie model that $a = (\rho B^2 L)/(8\pi^2\mathrm{St}^2 M)$.

By assuming that the lift coefficient follows the structural mode shape being excited, this simplified Hartlen and Currie model implies that the flow feature at one span-wise location is effectively dependent on the structural motion at this location only. In other words, there is no information regarding the correlation characteristic of the lift coefficient being included; therefore, this simplified model is thereafter called the 3D fully-correlated Hartlen and Currie model.

In addition, analytical solutions for the 3D fully-correlated Hartlen and Currie model can be found, showing similar features as Equations 7.3, 7.4, 7.5 and 7.6, except the fact that solutions are now defined in the generalised coordinate and the model parameter γ is corrected multiplying with the correction factor Γ.

7.3.2 Application and Validation

The main aim of the development of the 3D fully-correlated Hartlen and Currie model is to allow the response of the 3D flexible structure to be predicted more efficiently by either using the analytical solution or time-integrating a system of two differential equations only.

Since the Hartlen and Currie model parameters are assumed to be two-dimensional and are independent of the structural mode shapes, the 3D fully correlated model predicts a unique non-dimensional VIV response curve regardless of the structural mode shape being excited. This is only valid provided that the 3D flexible structure possesses similar model damping ratios and the structural mode shapes are sinusoidal and have a unit modal coefficient so that the correction factor Γ is equal to $3/4$. Taking the 3D circular cylinder described in Section 7.2.3 as an example, the non-dimensional structural response curve was obtained by using the proposed differential-equation solver (described in Section 7.2.3) and by using the analytical solution. They both are plotted in Figure 7.5 and a good agreement in terms of the onset non-dimensional wind speed of the lock-in and the maximum non-dimensional structural response during lock-in can be observed. In addition, from Section 7.2.3, three non-dimensional response curves corresponding to structures excited in the first, second and third mode shapes during the VIV lock-in were predicted by the 3D complete Hartlen and Currie model and all of them showed a very good agreement comparing against the solution of the 3D fully-correlated Hartlen and Currie model.

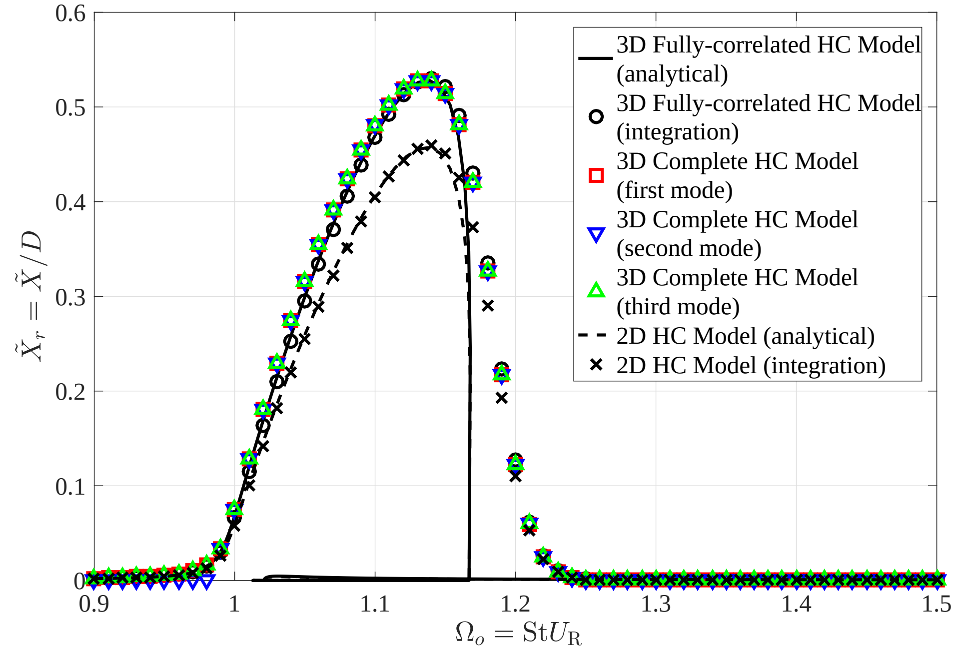

Figure 7.5: Comparison of the VIV responses of a 3D flexible structure obtained from the 3D fully-correlated Hartlen and Currie model and from the 3D complete Hartlen and Currie model; the structural response of a similar 2D structure is predicted by the original 2D Hartlen and Currie model; all open symbols are achieved from the time integration while the lines are the analytical solutions of the corresponding models.

As was noticed in Section 7.2.3, the maximum generalised displacement of a 3D flexible structure during the VIV lock-in was 1.15 times larger than the maximum displacement of a 2D structure having similar fluid and structural characteristics. This observation is again evidenced in Figure 7.5; both time-integrated solutions and analytical solutions predicted this ratio. Supposing the relationship between the generalised displacement of a 3D flexible structure and the displacement of a similar 2D structure is

$$\tilde{x}_r(\tau) = Ax_r(\tau), \tag{7.34}$$

with A is a non-zero constant and by substituting this relationship into Equation 7.33, a similar relationship for the lift coefficient can be yielded as

$$\tilde{c}_L(\tau) = Ac_L(\tau). \tag{7.35}$$

Applying these expressions into Equation 7.32 and noticing that all of the model parameters are two-dimensional and independent of the structural mode shape and that there are no correction factors in the non-linear damping term of the 2D fluid equation, it yields the relationship $A = \Gamma^{-1/2}$. For the study discussed here, the correction factor Γ was calculated to be $3/4$, leading to the constant $A = 1.155$, which was equal to the ratio observed in Figure 7.5. This ratio was also found when comparing the response curve obtained from the 3D heaving simulation against the one achieved from the 3D bending simulation in Chapter 6.

In summary, this section has described the development of a more simplified Hartlen and Currie model called the 3D fully-correlated Hartlen and Currie model; the two coupled equations defined in Equations 7.32 and 7.33 were both defined in the generalised coordinate. This model has been developed based on the assumption that all of the model parameters α, γ and b are two-dimensional and are independent of the mode shape. In order to predict the generalised structure response and lift coefficient of a 3D flexible structure, the model parameter γ needs to be corrected multiplying by a correction factor Γ. The modified Hartlen and Currie model was able to simulate the VIV response of the 3D structure excited in a single mode shape. This limitation however was reasonable since, during VIV lock-in, the full-scale measurement indicates only one dominant mode shape was observed. In addition, the other assumption made in this derivation was that the lift coefficient had similar "mode shapes" as the structural response and no information regarding the correlation of the lift coefficient was included; therefore this model is called the 3D fully-correlated Hartlen and Currie model.

7.4 3D PARTLY-CORRELATED HARTLEN AND CURRIE MODEL

The second assumption which is about the mode shape of the lift coefficient also brings about the downside of the 3D fully-correlated model. This is that no information regarding the correlation of the lift force is included in the the model. Therefore, in order to incorporate the correlation characteristics, the forcing term on the right-hand side of Equation 7.33 needs to be corrected by including the function $g(y)$ representing the correlation characteristics of the lift coefficient as

$$\ddot{\tilde{x}}_r + 2\zeta\dot{\tilde{x}}_r + \tilde{x}_r = \frac{\rho B^2 L}{8\pi^2 \mathrm{St}^2 M \int_0^L \Phi(y)^2 \mathrm{d}y}\, \Omega_o^2\, \tilde{c}_L \int_0^L g(y)\Phi(y)^2 \mathrm{d}y. \tag{7.36}$$

Here the parameter $a = (\rho B L^2)/(8\pi^2 \mathrm{St}^2 M)$ defined in the original 2D Hartlen and Currie model is multiplied by another correction factor which is $\left[\int_0^L g(y)\Phi(y)^2 \mathrm{d}y\right] / \left[\int_0^L \Phi(y)^2 \mathrm{d}y\right]$. Even though the correlation information is not implemented is the fluid equation, the fact that the correlation function $g(y)$ is included in the forcing term of the structural equation allows the solution of the structural response to be less conservative. For this reason, this model is called the 3D partly-correlated Hartlen and Currie model.

Literature showed that, during VIV lock-in, the correlation of the lift coefficient was a function of the amplitude of the response (Vickery and Basu, 1983). Based on wind tunnel results, the correlation function $g(y)$ mentioned above could be defined as an exponential expression depending on the non-dimensional span-wise separation and the non-dimensional response of the structure or the non-dimensional wind speed. This approach would require a number of wind tunnel sectional model tests to measure the pressure or lift force at either different amplitudes of the response or different wind speed. However, Ehsan and Scanlan (1990) observed that the correlation function $g(y)$ followed the structural mode shape of the 3D flexible structure, particularly around the anti-nodes. Therefore, it is reasonable that the correlation function $g(y)$ is proposed to be the normalised structural mode shape as

$$g(y) = \bar{\Phi}(y). \tag{7.37}$$

The structural mode shape is normalised with respect to the maximum or minimum value between two successive nodes; this allows the correlation function $g(y)$ to be positive and to reach the value of unity at the anti-nodes.

For the 3D partly-correlated Hartlen and Currie models, the analytical solutions of the structural response and frequency presented in Equations 7.3 and 7.4 can be used. However, the solution of the structural response is defined in the generalised coordinate. In addition, the analytical solutions are only acceptable if both corrections for the parameters a and γ as discussed above are properly implemented.

7.5 INVESTIGATION OF ANALYTICAL SOLUTIONS OF THE HARTLEN AND CURRIE MODEL

The three model parameters of the Hartlen and Currie model can be identified by fitting the prediction of the structural and frequency response during the lock-in with results obtained from the wind-tunnel or computational studies. The prediction of the Hartlen and Currie model is achieved by either performing the time-integration of the structural and fluid equations or using the analytical solutions. The first method can yield more accurate results; however, the time-integration is very time-consuming taking into account that a number of different wind velocities are required to obtain reasonable solutions. On the other hand, as mentioned in Section 7.1, the derivation of these analytical solutions in the second method involved an assumption that the high-order sinusoidal terms relating to the lift coefficient were ignored; this was expected to have more impact on the solution of the lift coefficient. Nevertheless, a comprehensive study on the effect of this assumption will be presented here to investigate the difference between the analytical solutions of the Hartlen and Currie model and the ones obtained directly from the time-integration. It will help to verify the accuracy and usability of the analytical solutions so that it will be applied in further studies discussed later.

In this study, the original Hartlen and Currie model together with all model parameters used in the original paper (Hartlen and Currie, 1970) were: $b = 0.4$, $\alpha = 0.002$ and $\gamma = 0.667$, which correspond to the maximum lift coefficient of the stationary cylinder of $C_{Lo} = 0.2$. The physical parameter was $a = 0.002$ and the damping ratio was $\zeta = 0.0015$.

The heaving VIV of the cylinder is modelled and summarised in Figure 7.6; the solution shown by open symbols were obtained from the time-integration. Clearly, a limited VIV lock-in interval was observed; the range of the VIV lock-in was different between cases where the non-dimensional velocity increased and where it decreased. It is called the hysteresis of the VIV, which was also observed at the behaviour of the lift coefficient C_L, the non-dimensional vortex shedding frequency Ω and the phase of the lift coefficient against the displacement $\Phi_{C_L - X_r}$ as the wind velocity increased and decreased. The hysteresis also involved a variation in the peak response during the lock-in. As the wind velocity increased, the maximum response of the cylinder was recorded as $X_r = 0.44$ occurring at the non-dimensional velocity of $\Omega_o = 1.13$; however, as the wind speed decreased, the maximum response occurred earlier at $\Omega = 1.09$ and was measured to be $X_r = 0.37$.

In addition, the analytical solutions of the Hartlen and Currie model were plotted as shown by solid lines in Figure 7.6. It is obvious that the analytical solution could not predict the hysteresis of the VIV; what appears to be like the delay phenomenon of the hysteresis illustrated in Figures 7.6b and 7.6d was in fact unstable branches of the analytical solutions. The analytical solutions were effectively only comparable to the behaviour of the system as the wind speed increased. Even though high-order sinusoidal terms were ignored during the derivation, a good agreement between the time-integrated solutions and the analytical solutions could be concluded from Figure 7.6. Regarding the maximum response of the structure during the lock-in, the analytical solution predicted about 3.5% higher than that obtained from the time integration. Nevertheless, considering that the mathematical model of VIV is expected to produce conservative predictions, this percentage difference was acceptable. The other solutions of vortex shedding frequency, lift coefficient and phase shift closely matched the time-integrated solutions. The clear distinction between them was the range of the VIV lock-in. The response of the vortex shedding frequency shown in Figure 7.6b indicated that the analytical solution estimated the termination of the VIV lock-in to occur 1.85% sooner than what was predicted by the time-integration solutions. The analytical solution showed a very sudden decrease in the amplitude of the structural displacement after the peak response reached. On the other hand, the time integration predicted a more gentle drop, which was related to the memory effect of the structure and fluid system. This effect obviously was not included in the analytical solution, leading to an unrealistic behaviour close to when the system reached the lock-out state.

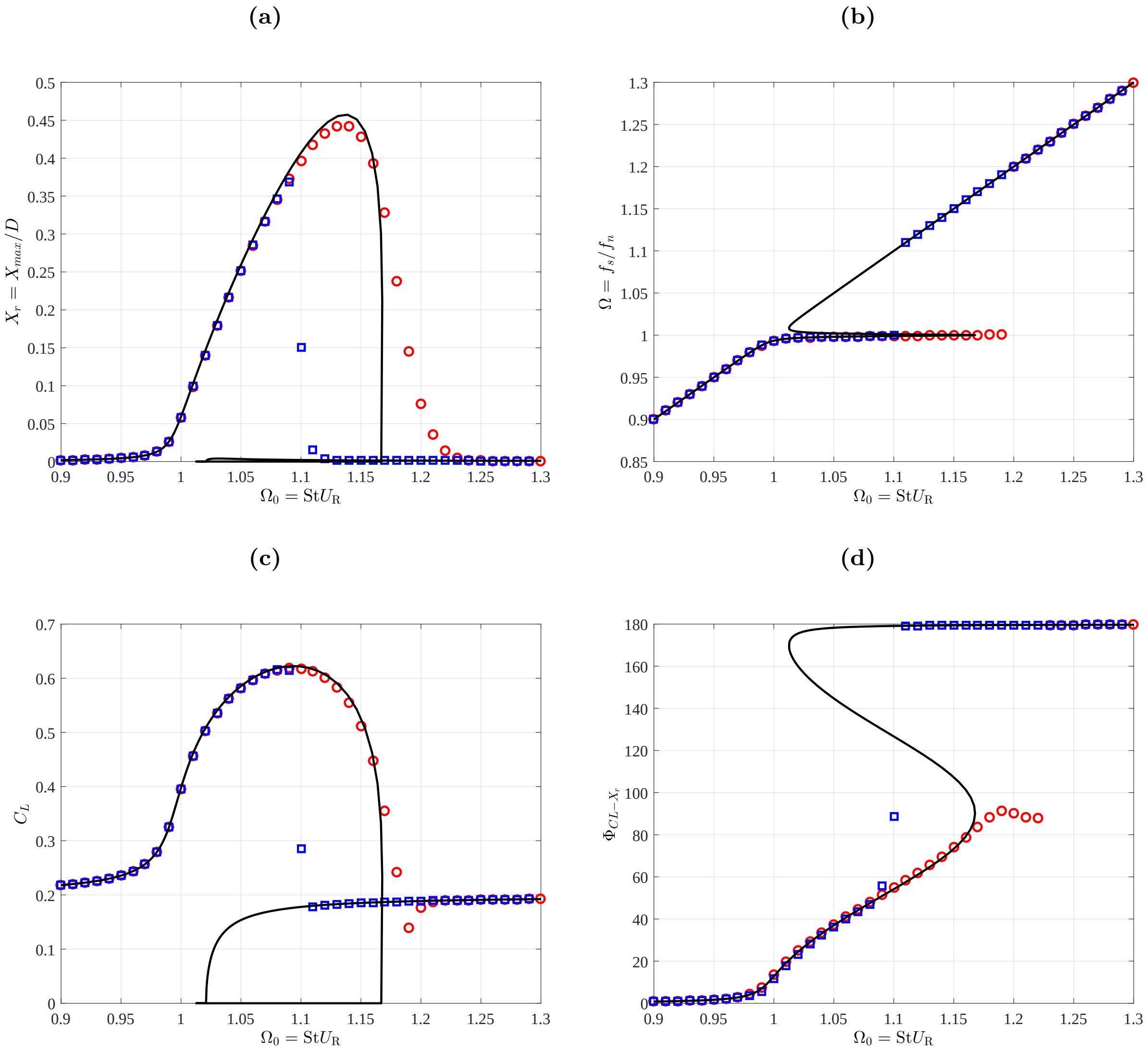

Figure 7.6: Comparison of the solutions obtained from the direct time-integration (open symbols) and the analytical solution (solid line) of (a) non-dimensional structural response, (b) non-dimensional vortex shedding frequency, (c) lift coefficient and (d) phase of lift coefficient against displacement during the VIV lock-in; *red circle:* increasing wind velocity; *blue square:* decreasing wind velocity.

The comparison discussed in this section has shown that the use of the analytical solutions of the Hartlen and Currie model was acceptable regarding the accuracy of the prediction of the maximum amplitude of the structural response during the lock-in, the wind speed where this maximum amplitude occurred and the range of the VIV lock-in. Therefore, these analytical solutions will be used when developing the parameter optimisation process, which aims to estimate the three model parameters by fitting the analytical solutions with the experimental or computational results.

7.6 PARAMETER OPTIMISATION PROCESS

In this section, the development of the parameter optimisation process will be discussed. The Hartlen and Currie model contains three model parameters b, α and γ, which are required to be determined from results of experimental or computational studies. With three unknowns to be found, three different criteria which are important to characterise VIV were selected including:

1. The range of VIV lock-in,
2. The maximum amplitude of the structural response during the lock-in,
3. The wind velocity where the maximum amplitude of the structural response occurs during the lock-in.

7.6.1 Parametric Study

Before a parameter optimisation algorithm was proposed, it was important to perform a parametric study so that the dependence of these three criteria on the model parameters was fully understood.

The parametric study was conducted on a similar structure as the one in the original paper (Hartlen and Currie, 1970) that $a = 0.002$ and $\zeta = 0.0015$. However, each model parameter was subject to variation while the others were kept constant at the value proposed by Hartlen and Currie (1970). This allowed the relationship between each model parameter and the three selected criteria to be investigated in detail.

The results of the parametric study are illustrated in Figure 7.7. The variation of the parameter b influenced all three selected criteria. An increase in the parameter b led to a broader VIV lock-in; this however did not affect the gradient of the curve, resulting in a larger value of the maximum response during the lock-in and delaying its occurrence. Figures 7.7b and 7.7c showed there were no relationships between the parameters α or γ and the range of the VIV lock-in. Instead, there was a mutual dependence between the maximum amplitude of the structural response during the lock-in and these two parameters. The structure was found to reach a larger response as the parameter α increased or as the parameter γ decreased. The gradient of the curve of increasing the structural response was observed to behave in a similar manner. Figure 7.7c showed no dependence of the wind velocity where the maximum structural response occurred against the parameter γ. On the other hand, as the parameter α increased, there was a slight delay on the occurrence of the maximum structural response during the lock-in; also the response appeared to decrease more suddenly as the system reached lock-out. These findings are summarised in Table 7.1. Knowing the relationship between the model parameters and the three selected criteria, a parameter optimisation process could be developed such that the model parameters were iteratively improved to match results of wind tunnel or computational studies.

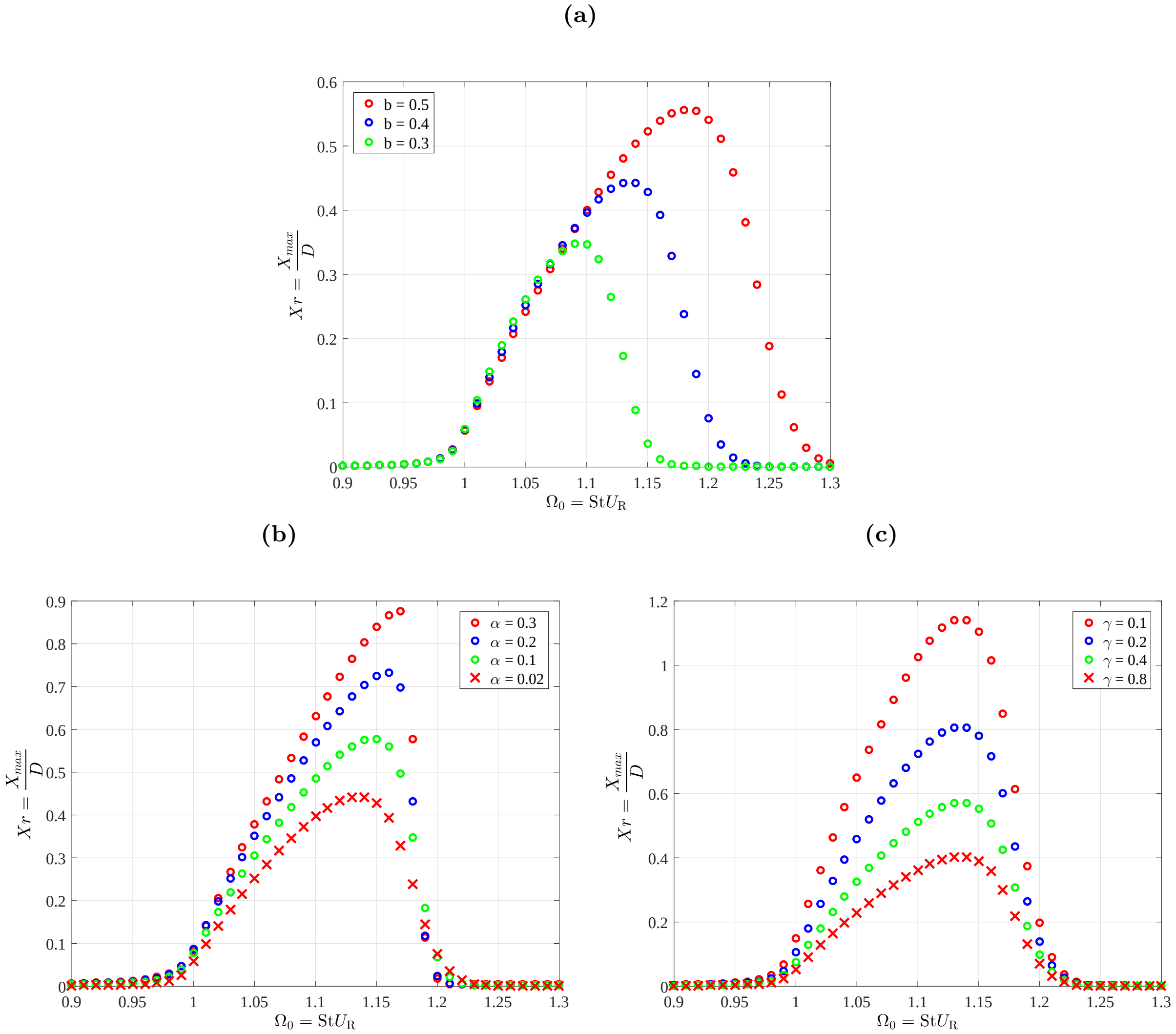

Figure 7.7: Dependence between the model parameters (a) b, (b) α and (c) γ and the VIV response of the cylinder.

Table 7.1: Summary of the results of the parametric study as the model parameter increased (symbol $-$ means no effects).

Parameters		Lock-in interval	Value of the peak response	Velocity where the peak response occurs
α	↑	–	↑	↑
γ	↑	–	↓	–
b	↑	↑	↑	↑

7.6.2 Iterative Parameter Estimating Process

An iterative approach was applied to improve the initial estimations of the model parameters using the actual results of the wind tunnel or computational studies and the estimated results obtained from the analytical solutions. The parametric study discussed in Section 7.6.1 indicated that the range of the lock-in interval was solely dependent on the parameter b. Therefore, the optimisation process comprised two sub-processes. The first one was to estimate the model parameter b based on the range of the lock-in only. With the parameter b successfully found, the second sub-process was performed to estimate the parameters α and γ based on the peak response during the lock-in and the velocity of its occurrence. There were three error quantities defining the efficiency of the optimisation process; each quantity was corresponding to each criterion set out above. The model parameters were said to be successfully estimated if these error quantities were less than pre-defined tolerances. They are described in detail later in this section.

Since the onset velocity of the VIV lock-in was accurately captured, the accuracy of modelling the range of the VIV lock-in was essentially dependent on the velocity where the system reached the lock-out. Therefore, the key variable to estimate the parameter b was selected to be the non-dimensional velocity where the lock-in terminated, $\Omega_{o,\text{end}}$; in other words, it could be said that $\Omega_{o,\text{end}}$ was a function of b. The iterative expression for the parameter b was defined as

$$b^{n+1} = b^n + \frac{b^n - b^{n-1}}{\Omega^n_{o,\text{end}} - \Omega^{n-1}_{o,\text{end}}} \left(\Omega^{\text{actual}}_{o,\text{end}} - \Omega^n_{o,\text{end}}\right). \tag{7.38}$$

This expression was based on the Secant method where the parameter b^{n+1} at the iteration $n+1$ was improved by the parameter b^n and b^{n-1} and the solution $\Omega^n_{o,\text{end}}$ and $\Omega^{n-1}_{o,\text{end}}$ at the iteration n and $n-1$ together with the actual solution from results obtained from the wind tunnel or computational studies $\Omega^{\text{actual}}_{o,\text{end}}$. This improvement required two previous points; thus, at the iteration $n = 1$, different sets of regression equations weres used as

$$b^2 = \frac{1}{2} b^1 \qquad \text{if } \Omega^1_{o,\text{end}} > \Omega^{actual}_{o,\text{end}}, \tag{7.39}$$

$$b^2 = 2b^1 \qquad \text{if } \Omega^1_{o,\text{end}} < \Omega^{actual}_{o,\text{end}}. \tag{7.40}$$

At the iteration n, the error of this process was quantified as the summation of squared difference between the frequency response measured in the wind tunnel or computational studies and the one obtained from the analytical solution using the model parameter b^n at all points of non-dimensional wind velocity N_{Ω_o} as

$$E_b^n = \sum_{i_{\Omega_o}=1}^{N_{\Omega_o}} \left(\Omega_{i_{\Omega_o}}^n - \Omega_{i_{\Omega_o}}^{\text{actual}} \right)^2 . \tag{7.41}$$

It was noticed that the Hartlen and Currie model was the most accurate to simulate the fluid and structure interaction during the VIV lock-in; therefore, the error described in Equation 7.41 was mostly contributed from data points outside the lock-in. Instead of minimising this error, the termination condition of this optimisation process was defined such that the error E_b^n converged to a stationary value as long as this convergence value was independent of the initial estimation b^1. Checking on the convergence of the error essentially emphasised the importance of the response in the lock-in. The optimisation process was said to be successful if the difference in the error E_b between two consecutive iterations was less then 10^{-6}. The flow chart of the optimisation process of the parameter b is shown in Figure 7.8.

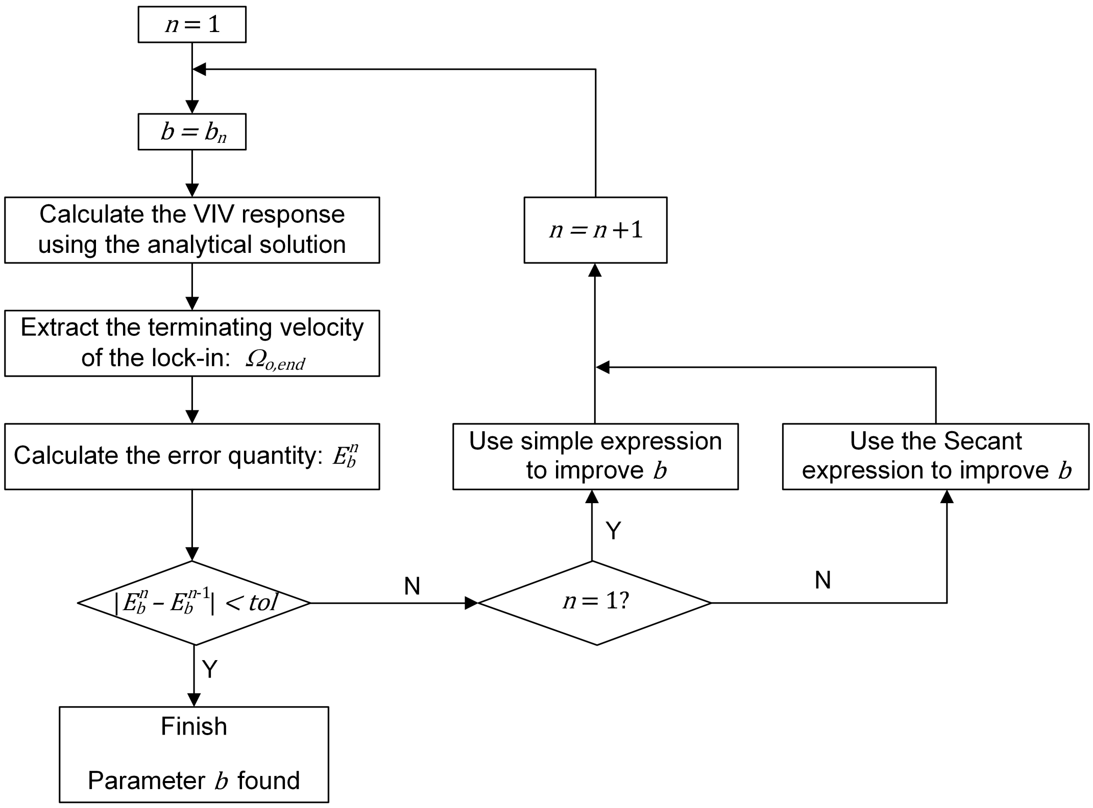

Figure 7.8: Flow chart describing the iterative estimating process of the parameter b; the tolerance, tol, was 10^{-6}; the simple expression refers to Equations 7.39 and 7.40; the Secant expression refers to Equation 7.38.

Similarly, an iterative approach was used to estimate α and γ. The parametric study has showed they both influenced on the peak response $X_{r,max}$ during the lock-in; therefore, these two parameters needed to be regressively estimated together using the value of the peak response during the lock-in. The regression equations for the parameters α and γ are defined as

$$\text{Parameter } \alpha \qquad \alpha^{n+1} = \alpha^{n} + \frac{\alpha^{n} - \alpha^{n-1}}{X^{n}_{r,max} - X^{n-1}_{r,max}} \left(X^{\text{actual}}_{r,max} - X^{n}_{r,max} \right), \tag{7.42}$$

$$\text{Parameter } \gamma \qquad \gamma^{n+1} = \gamma^{n} - \frac{\gamma^{n} - \gamma^{n-1}}{X^{n}_{r,max} - X^{n-1}_{r,max}} \left(X^{\text{actual}}_{r,max} - X^{n}_{r,max} \right). \tag{7.43}$$

At the first iteration $n = 1$, different expressions were applied to improve the initial guesses

$$\text{Parameter } \alpha \qquad \alpha^2 = \frac{1}{2}\alpha_1 \qquad \text{if } X^{1}_{r,max} > X^{actual}_{r,max}, \tag{7.44}$$

$$\alpha^2 = 2\alpha_1 \qquad \text{if } X^{1}_{r,max} < X^{actual}_{r,max}, \tag{7.45}$$

$$\text{Parameter } \gamma \qquad \gamma^2 = 2\gamma_1 \qquad \text{if } X^{1}_{r,max} > X^{actual}_{r,max}, \tag{7.46}$$

$$\gamma^2 = \frac{1}{2}\gamma_1 \qquad \text{if } X^{1}_{r,max} < X^{actual}_{r,max}. \tag{7.47}$$

The first error quantity of this optimisation at the iteration n were defined as the summation of squared difference in the actual structural response and the one obtained from the analytical solution using the parameter α^n and γ^n at all values of wind speed data points

$$E^{n}_{\alpha,\gamma} = \sum_{i_{\Omega_o}=0}^{N_{\Omega_o}} \left(X^{n}_{r,i_{\Omega_o}} - X^{\text{actual}}_{r,i_{\Omega_o}} \right)^2. \tag{7.48}$$

The other error quantity was the percentage difference of the location of the peak response obtained from the analytical solution $\Omega^{n}_{o,\text{peak}}$ and the actual location of the peak response from wind tunnel and computational studies $\Omega^{\text{actual}}_{o,\text{peak}}$

$$E^{n}_{location} = \frac{\mid \Omega^{n}_{o,peak} - \Omega^{\text{actual}}_{o,\text{peak}} \mid}{\Omega^{\text{actual}}_{o,\text{peak}}}. \tag{7.49}$$

The error quantity $E^{n}_{\alpha,\gamma}$ defined in Equation 7.48 was assessed based on its convergence as used in estimating the parameter b. The optimisation process for the parameter α and γ was said to be successful as long as the converging value of $E^{n}_{\alpha,\gamma}$ was not dependent on the initial guesses α_1 and γ_1, the difference in $E^{n}_{\alpha,\gamma}$ between two successive iterations was less than 10^{-6} and the value of $E^{n}_{location}$ was less than 0.1. The flow chart of the optimisation process of the parameter α and γ is summarised in Figure 7.9.

As discussed later when this process was applied to estimate the model parameters of the Hartlen and Currie model, it became clear that a disadvantage of this method was that the converging value of $E^{n}_{\alpha,\gamma}$ as well as the final values of the parameter α and γ were found to be dependent on the initial estimations. The optimisation process of the parameter b however did not suffer this issue; therefore the iterative approach could be successfully implemented to estimate the parameter b.

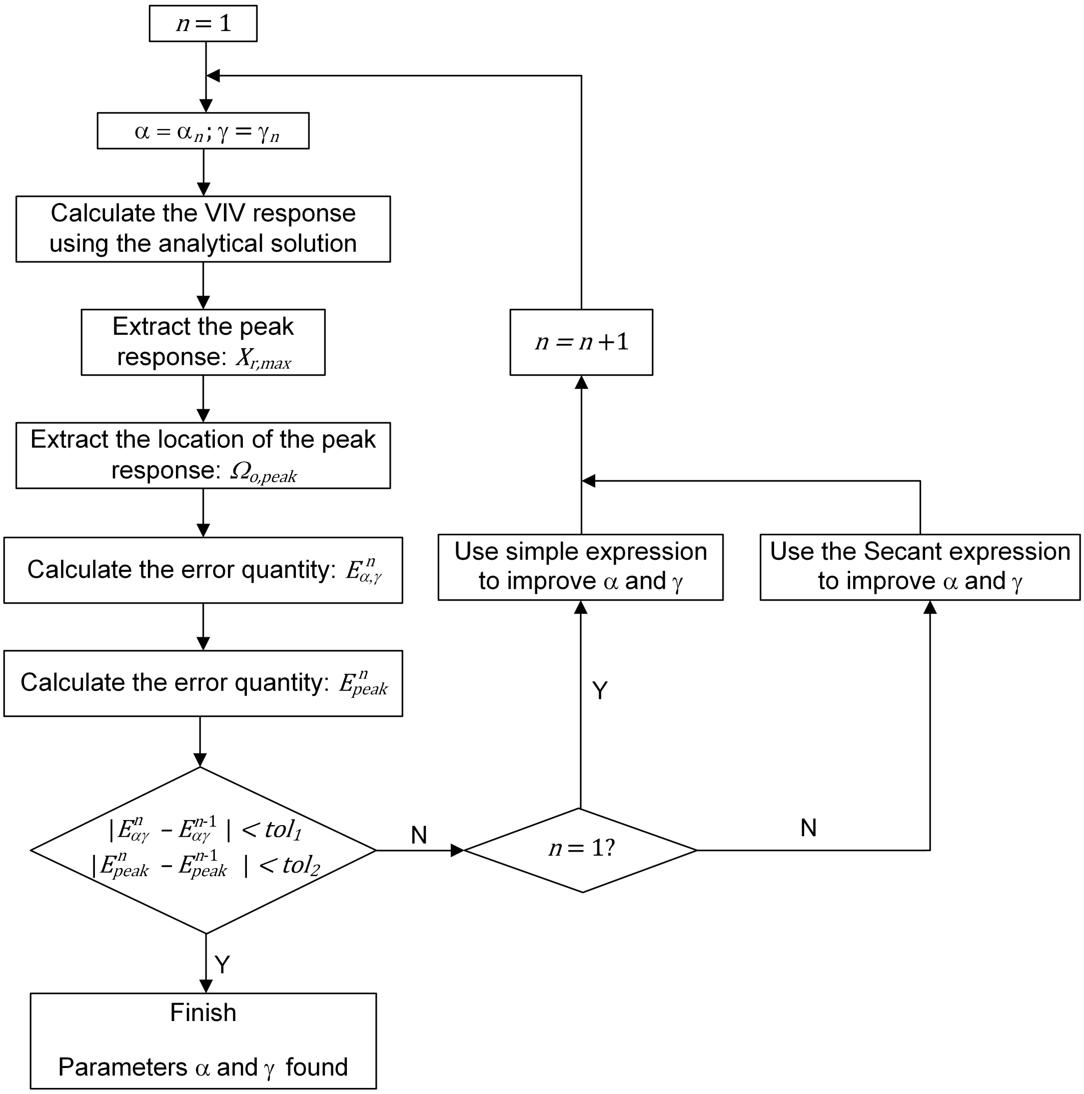

Figure 7.9: Flow chart describing the iterative estimating process of the parameters α and γ; the tolerances, tol_1 and tol_2, were 10^{-6} and 0.1 respectively; the simple expression refers to Equations 7.44, 7.45, 7.46 and 7.47; the Secant expression refers to Equations 7.42 and 7.43.

7.6.3 Surface-searching-based Parameter Optimisation Process

Given the disadvantages of the iterative estimating process, a number of sub-iterations might help improve the accuracy in estimating the parameters α and γ. However, the coding could be too complicated and time-consuming taking into account the coupling between these parameters. In this section, a different approach is proposed.

The result obtained from the parametric study have showed that the peak response during the lock-in $X_{r,max}$ could be written as a two-dimensional function depending on the parameters α and γ; it could be plotted as a two-dimensional surface in a three-dimensional domain. As confirmed by some preliminary results using the iterative approach, there were a number of pairs of the parameters α and γ that could yield similar results. The aim of the surface-searching-based optimisation process was to extract all of the pairs of parameters α and γ that could yield a similar analytical peak response as compared to wind tunnel and computational studies. The most appropriate parameters α and γ were selected if the error quantities described in Equation 7.48 reached the minimum. The brief flow chart of the surface-search-based optimisation process of the parameters α and γ including 6 steps is shown in Figure 7.10, which was successfully implemented into a MATLAB-based routine.

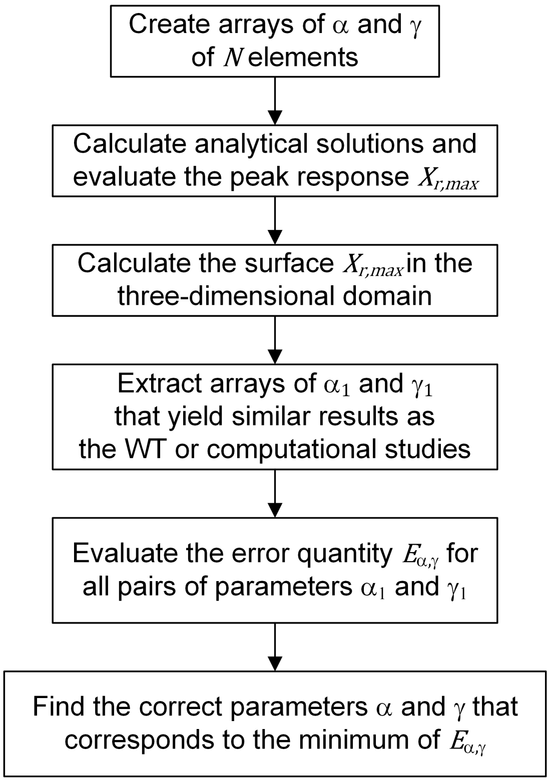

Figure 7.10: Flow chart describing the surface-searching-based optimisation process of the parameters α and γ.

The accuracy of the final results of the parameters α and γ was not influenced by the MATLAB calculation or searching code. Instead, it was predominantly dependent on the discretisation of the initial arrays α and γ. The finer the discretisation, the more accurate the final result. However, it would compromise the efficiency of the code, where most of the time and computational resources were dedicated to compute the surface of the peak response in a three-dimensional domain and a large portion of this solution would not be used. This process thus needed to be performed a number of times, starting with broad ranges of arrays α and γ and large discretisation and then limiting the search around the estimated final results with finer discretisation. A least-squares-curve-fitting operation could indeed be used to find the relationship between the error quantity $E_{\alpha,\gamma}$ and each parameter α and γ. However, the accuracy of this process was not acceptable due to the highly non-linear behaviour of $E_{\alpha,\gamma}$. Nevertheless, the aforementioned strategy allowed this MATLAB-based routine to be conducted in an efficient manner and using the final model parameter α and γ it was possible to simulate the VIV response of the cylinder; the results from the application of both optimisation processes are discussed in detail in Section 7.7.

7.7 APPLICATION OF PARAMETER OPTIMISATION PROCESS

As discussed in Section 7.5, the use of the analytical solutions in the optimisation process would lead to a situation where the range of VIV lock-in would not be modelled accurately. The memory effect of the structure and fluid system was not captured properly; therefore, the analytical solutions yielded a very sudden drop in the structural response underestimating VIV lock-in. On the other hand, most of the wind tunnel sectional model tests or full-scale measurements showed a more gentle drop in the structural displacement after the peak response during the lock-in was reached, leading to a broader range of the VIV lock-in. Thus, to use these kinds of data to estimate the model parameter, a correction to the non-dimensional wind velocity where the VIV lock-in terminated needed to be applied.

As for the wind tunnel sectional model test, VIV lock-in was observed to terminate at the non-dimensional wind speed of $\Omega_{o,\text{end}} = 1.442$. Using this value in estimating the parameter b would overestimate VIV lock-in by 7%. Therefore, it was decided to correct the non-dimensional wind velocity where lock-in terminated by this percentage difference that it was reduced to $\Omega_{o,\text{end}} = 1.339$.

Regarding the computational simulation of the rectangular cylinder exhibiting the heaving VIV, a slightly different correction had to be applied to the non-dimensional wind velocity $\Omega_{o,\text{end}}$. The limitation of the heaving and bending simulation was to not efficiently model the memory effect. In addition, the displacement of the rectangular cylinder reached the peak at $\Omega_{o,\text{peak}} = 1.568$, which was exactly at the same point where the VIV lock-in terminated as being suggested by the response of the vortex shedding frequency. A detailed spectral analysis at the non-dimensional wind velocity $\Omega_o = 1.656$

indicated the presence of two spectral peaks; one was at the natural frequency of the cylinder while the other corresponded to the vortex shedding frequency defined by the Strouhal number. Therefore, it was reasonable to select $\Omega_o = 1.656$ to be the non-dimensional wind velocity where the lock-in terminated.

This section is dedicated to discussing the application of the iterative and surface-searching-based optimisation process on results of the wind tunnel and computation studies to estimate the Hartlen and Currie model parameters. It will reveal the disadvantages of the former and showed the usability and practicability of the latter, particularly when estimating the model parameters α and γ. A strategy will be then decided to efficiently extract the Hartlen and Currie model parameters using results of the wind tunnel and computational studies. A comparison between corresponding estimated parameters will offer further insights into the characteristics of the Hartlen and Currie model parameters.

7.7.1 Application of Iterative Parameter Estimating Process

The usability and practicability of the iterative parameter estimating process were discussed in this section using the responses of the structural displacement, vortex shedding frequency and the phase shift of the lift coefficient against the displacement; these results were obtained from the CFD heaving simulation and were described in Section 6.3.1 and summarised in Figure 7.11. The non-dimensional responses of the structure and of the vortex shedding frequency were used to iteratively estimate the model parameters.

Using the structural parameters listed in Section 4.5, the interactive parameter a was calculated to be $a = 3.24 \times 10^{-3}$; the damping ratio was defined to be $\zeta = 1\%$. With the initial estimation $b_1 = 5$, the iterative estimating process estimated the parameter $b = 3.915$ and the convergence error E_b was evaluated as 0.02. As can be seen in Table 7.2, the final value of the model parameter b and, more importantly, the converging value of the error quantity E_b did not depend on the the initial guess. This indicates that the iterative estimating process could be used to efficiently estimate the model parameter b using the non-dimensional vortex shedding frequency.

With the initial estimations $\alpha_1 = 0.05$ and $\gamma_1 = 5.208$, the iterative estimating process estimated the model parameters α and γ to be 0.0198 and 11.5 respectively. Figure 7.11 illustrates the accuracy using these parameters to model the VIV response during the lock-in particularly for the structural response and the vortex shedding frequency. The error quantity $E_{\alpha,\gamma}$ was evaluated to be 0.00615 while the percentage difference in the location of the peak response during the lock-in was calculated to be about $E_{location} = 0.0028\%$. The analytical solution of the phase shift (Figure 7.11e) qualitatively represents the behaviour observed in the heaving simulation, including the sudden jump in phase when the system reached the lock-out. In Figures 7.11b, 7.11d and 7.11f, the time-integrated solutions of the Hartlen and

Currie models using the model parameters estimated here are also plotted to compare against results of the computational studies. The range of the VIV lock-in was estimated correctly with the percentage difference of about 2%. The peak response estimated by the Hartlen and Currie model was about 5% larger and occurred approximately 0.1% later than that observed from the CFD simulation. The difference here could be due to the fact that the CFD simulation was not able to capture the memory effect of the structure undergoing VIV. Nevertheless, considering the Hartlen and Currie model to be a conservative estimation, the differences mentioned here are minor.

Investigating the dependence of the estimated values of the parameter α and γ and the converging error quantities, Table 7.3 highlights the disadvantage of this technique. The final values of the estimated model parameters α and γ were found to be largely affected by the initial estimations α_1 and γ_1. The location of the peak response during the lock-in appeared to be improved for larger initial estimations. However, the error quantity $E_{\alpha,\gamma}$ did not converge to a stationary value; instead, the converging value varied with the initial estimations and seemed to possess a minimum value. This very variability of the final estimated model parameters α and γ and the error quantity $E_{\alpha,\gamma}$ shows that the iterative approach was not appropriate to estimate these two parameters.

The fact that the iterative parameter estimating process was found to successfully estimate the parameter b but not the parameter α and γ could be explained from results of the parametric study. The parameter b solely controlled the range of the lock-in interval; their relationship was found to be proportional, i.e. an increase in the parameter b led to a broader range of VIV lock-in. Therefore, it would exist only one value of the parameter b that could yield a similar range of VIV lock-in as the one observed from the CFD simulation. On the other hand, the peak response during lock-in was mutually dependent on both of the parameters α and γ; in other words, it could be represented as a two-dimensional surface with respect to these parameters in a three-dimensional domain. Thus, it was obvious that there could be more than one pair of parameters α and γ that yielded similar values of the peak response as inferred from Table 7.3. The iterative optimisation approach proposed here only performed one improvement for each parameter in one iteration. This implied loose coupling between the parameters α and γ, which was not suggested based on results of the parametric study. Assessing the error quantity $E_{\alpha,\gamma}$ after each iteration would not effectively check this coupling effect. To overcome this difficulty, the sub-iteration approach might need to be applied during each iteration to further improve estimated values and to model the strong coupling between them. However, the coding would be time-consuming taking into account the fact that the relationship between the peak response and two parameters α and γ was highly non-linear.

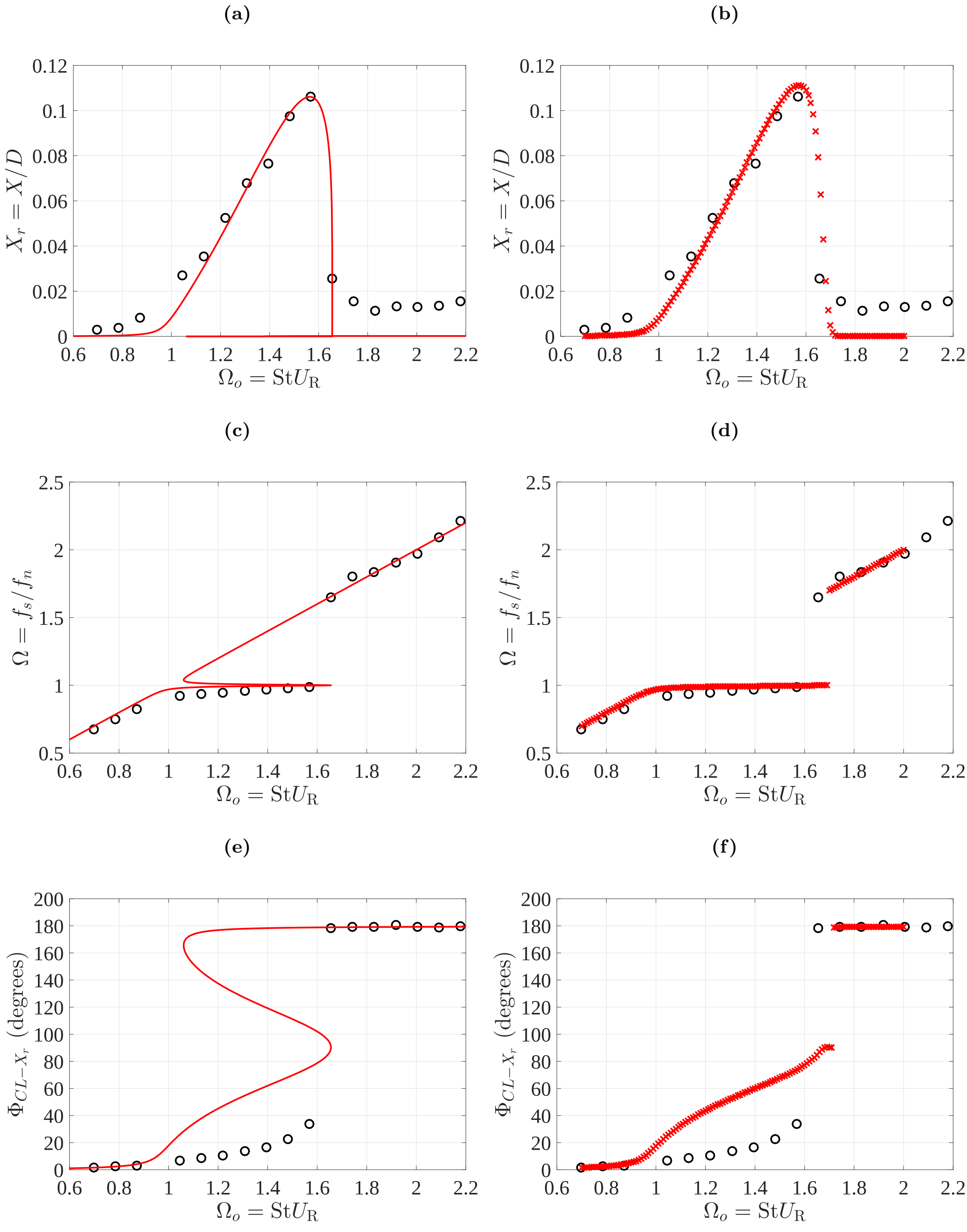

Figure 7.11: Summary of results of the CFD heaving simulation (*black circles*) including (a,b) non-dimensional structural response, (c,d) response of the non-dimensional vortex shedding frequency and (e,f) phase shift of the lift coefficient against the displacement in a comparison against the analytical solutions (*solid red lines* on the left figures) and the time-integrated solutions of the Hartlen and Currie model (*red crosses* on the right figures) using the model parameters: $b = 3.915$, $\alpha = 0.0198$ and $\gamma = 11.5$.

Table 7.2: Variability of the final results of the model parameter b and the converging error E_b with respect to the initial guess b_1.

Initial guess b_1	Estimated model parameter b	Convergence error E_b	Number of iterations N_{it}
10	3.915	0.020	11
5	3.915	0.020	9
2.5	3.915	0.020	10
1.25	3.915	0.020	13
0.625	3.915	0.020	17

Table 7.3: Variability of the final results of the model parameters α and γ, the converging error $E_{\alpha,\gamma}$ and the percentage difference $E_{location}$ with respect to the initial guesses α_1 and γ_1.

Initial guesses		Estimated model parameters		Converging error	Percentage difference
α_1	γ_1	α	γ	$E_{\alpha,\gamma}$	$E_{location}$ (%)
0.0500	5.208	0.0198	11.5	0.0015	0.0028
0.1000	10.417	0.0815	14.3	0.0029	0.0070
0.1500	15.625	0.143	17.2	0.0041	0.015
0.2000	20.833	0.0687	13.7	0.0026	0.0052
0.3000	31.250	0.138	16.9	0.0041	0.015
0.4000	41.667	0.205	20.3	0.0051	0.022

7.7.2 Application of Surface-searching-based Parameter Optimisation Process

The first part of this section will focus on discussing estimated parameters obtained by using the surface-searching-based optimisation process on results of the CFD heaving simulation. The advantages of this methodology will be emphasised by comparing against parameters estimated from the iterative estimating process described in Section 7.7.1. A full methodology to extract all of the Hartlen and Currie model will then be proposed and applied to results of the wind-tunnel sectional-model tests.

CFD Heaving Simulation

In this section, the application of the surface-searching-based parameter optimisation process was discussed using the results of the structure response and the vortex shedding frequency obtained from the CFD simulation. Recall, the parameter a was equal to 3.24×10^{-3} and the damping ratio ζ was 1%; the results of the CFD heaving simulation were summarised in Figure 7.14. This technique was only applied to find the parameter α and γ; the iterative optimisation approach was showed to successfully estimate the parameter b.

As discussed in Section 7.6.3, this process will involve 6 steps. In the first step, the user had to define two arrays of the parameter α and γ, which help create the two-dimensional surface of the peak response during the lock-in $X_{r,max}$ in a three-dimensional domain. For the CFD heaving simulation, the arrays of the parameters α and γ were applied as $\alpha = 0.02 \ldots 0.12$ (with $\delta_\alpha = 0.0005$) and $\gamma = 12 \ldots 16$ (with $\delta_\gamma = 0.005$). The analytical solution of the structural response (Equation 7.1) was computed and the surface of the peak response during the lock-in $X_{r,max}$ was plotted against the parameters α and γ in a three-dimensional domain as shown in Figure 7.12. The red plane B obviously intersects the surface A of the peak response along a line, indicating that there are more than a single pair of the parameters α and γ that could yield similar values of the maximum structural displacement during the lock-in.

In the next step, the optimisation process would perform the searching operation and extract all pairs of the parameters α and γ along the intersection line of the surface A and plane B. In fact, the pairs of parameters were selected if the absolute difference between their corresponding peak response and the actual peak response measured in the CFD heaving simulation was less than a pre-defined tolerance. For the case of the CFD heaving simulation, the tolerance was set to be 10^{-5} and all pairs of parameters along the intersection line were successfully identified. The error quantity $E_{\alpha,\gamma}$ was calculated using each pair of parameters and plotted against the parameter α and γ as shown in Figure 7.13. It is obvious that along the intersection line between the surface A and plane B, there exists a global minimum error

$E^{min}_{\alpha,\gamma} = 2.025 \times 10^{-3}$; therefore the corresponding parameters $\alpha = 0.073$ and $\gamma = 13.065$ were selected as the final results of the optimisation process.

The analytical solutions of the Hartlen and Currie model using the final estimation of the model parameters were calculated and compared against the ones obtained from the CFD heaving simulation. As shown in Figures 7.14a, 7.14c and 7.14e a good agreement could be drawn particularly in the responses of the non-dimensional structural displacement and of the non-dimensional vortex shedding frequency. The behaviour of the phase shift between the lift force and the displacement was qualitatively represented by the analytical solution; the phase gradually increased during the lock-in and suddenly jumped to 180° when the system reached the lock-out.

To further validate the model parameters estimated from the surface-searching-based optimisation process for the CFD heaving simulation, the time integration was performed on the Hartlen and Currie model using the parameters found out here: $b = 3.915$, $\alpha = 0.073$ and $\gamma = 13.865$. The time-integrated results were plotted in Figures 7.14b, 7.14d and 7.14f in a comparison against the one obtained from the CFD heaving simulation. The solution of the Hartlen and Currie model was considered as a conservative estimation of the one measured from the computational study. The peak response was modelled to be about 6% higher while its occurrence appeared to delayed about 1%. The time-integrated solution also predicted to the range of the VIV lock-in to be about 1.5% broader.

Compared to the iterative parameter estimating process, the surface-searching-based optimisation process was more plausible since the error quantity $E_{\alpha,\gamma}$ was assessed with all pairs of parameter that yielded similar values of the peak response during the lock-in. This in fact inherently took into account the strong coupling between these two model parameters and removed the dependency of the final estimation on the initial guesses. Therefore, as a complete methodology to estimate the Hartlen and Currie model parameter using results of wind tunnel tests or computational studies, this optimisation process would be applied to extract the parameters α and γ while the other parameter, b, was found using the iterative estimating process.

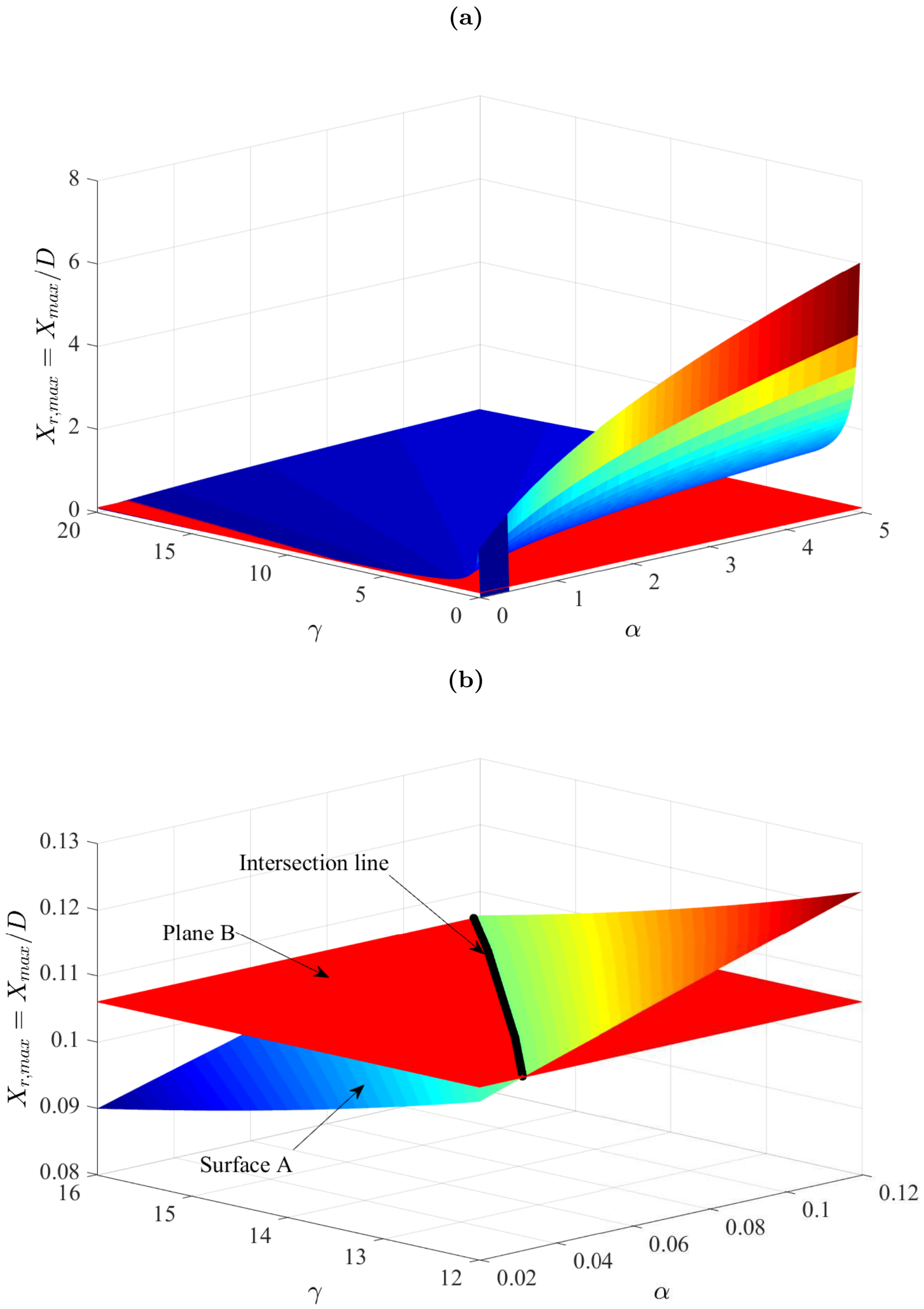

Figure 7.12: Plots of the surface A of the peak response during the lock-in $X_{r,max}$ with (a) coarse and broad arrays $\alpha = 0.01 \ldots 5$ ($\delta_\alpha = 0.01$) and $\gamma = 0 \ldots 20$ ($\delta_\gamma = 0.1$) and (b) fine and narrow arrays $\alpha = 0.02 \ldots 0.12$ ($\delta_\alpha = 0.0005$) and $\gamma = 12 \ldots 16$ ($\delta_\gamma = 0.005$); the red plane B represents the actual peak response observed in the CFD heaving simulation.

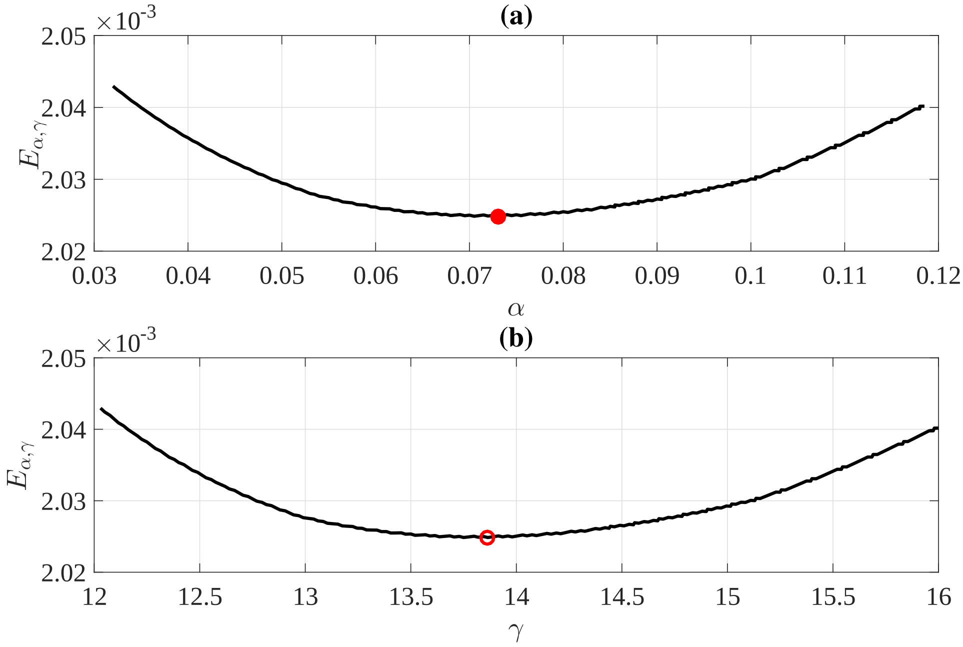

Figure 7.13: Relationship between the error quantity $E_{\alpha,\gamma}$ with respect to (a) the parameter α and (b) the parameter γ extracted from the intersection line shown in Figure 7.12b; the red dot illustrated the point of the minimum error $E^{min}_{\alpha,\gamma}$.

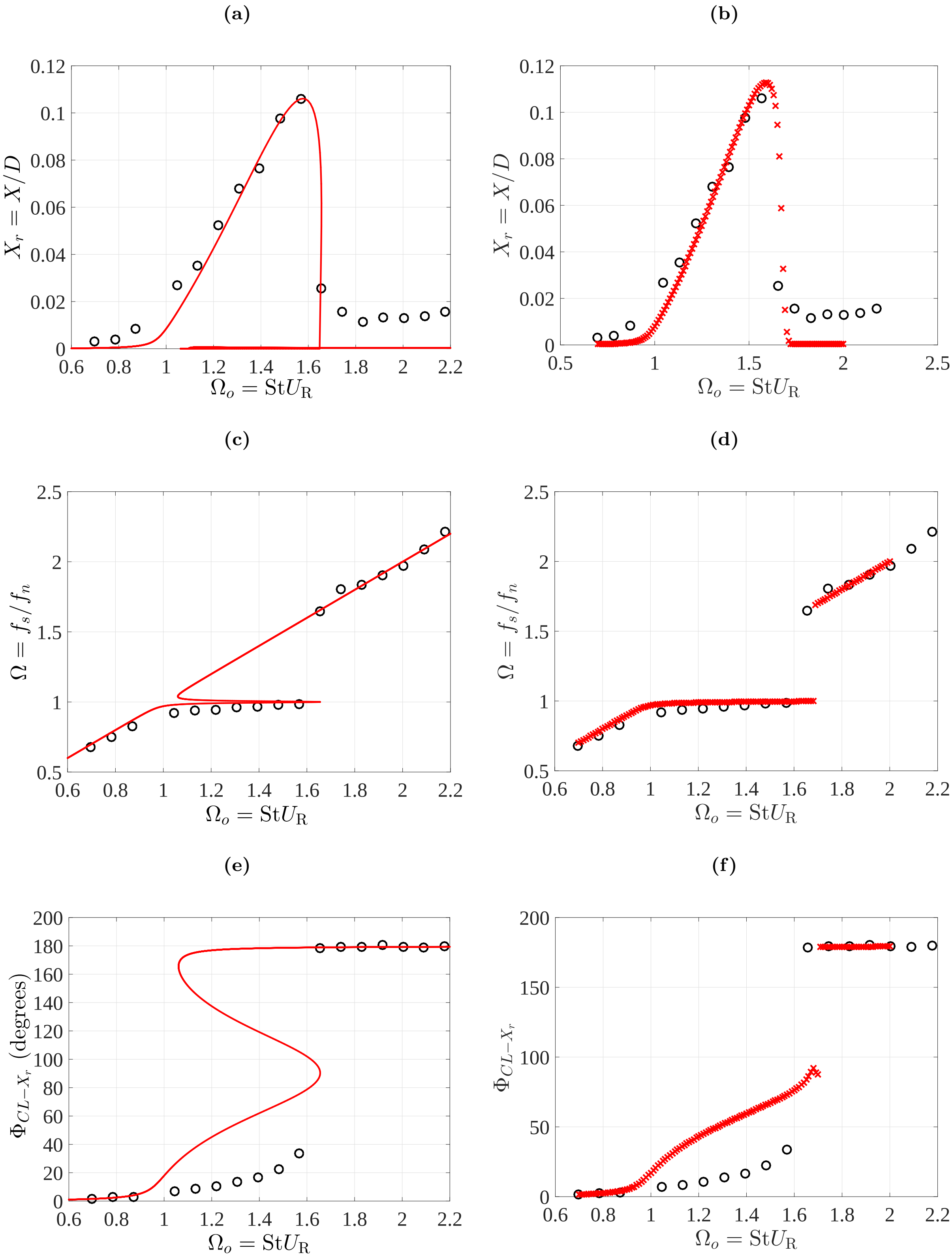

Figure 7.14: Comparison of results of the CFD heaving simulation (*black circles*) including (a,b) non-dimensional structural response, (c,d) response of the non-dimensional vortex shedding frequency and (e,f) phase shift of the lift coefficient against the displacement against solutions obtained from the analytical solutions (*red solid lines* on left figures) and from time integration (*red crosses* on right figures) of the Hartlen and Currie model using the model parameters: $b = 3.915$, $\alpha = 0.073$ and $\gamma = 13.865$.

Wind-Tunnel Sectional-Model Test

Having validated the usability and practicability, the iterative and surface-searching-based optimisation process would be used to estimate the Hartlen and Currie model parameters for the wind-tunnel sectional model undergoing the VIV heaving response. Using the structural parameters described in Section 5.1.2, the interactive parameter a in this case was calculated as $a = 2.249 \times 10^{-4}$ and the damping ratio was 0.19%. It was noticed that these two values were significantly different from the ones associated with the rectangular cylinder in the CFD study.

Figure 7.15 showed the dependence of the two-dimensional surface A of the peak response during the lock-in with respect to the parameters α and γ. The use of the narrow and fine arrays of α and γ indicated the intersection between the surface A and the red plane B which was the actual peak response measured in the wind tunnel study. Figure 7.15b appears to not represent the actual intersection between the surface A and the plane B; however, this is due to the resolution of the image produced in MATLAB. All pairs of the parameters α and γ on this intersection line were extracted; the error quantity $E_{\alpha,\gamma}$ was calculated and its relationship against each parameter is described in Figure 7.16. It was obvious that the global minimum error $E_{\alpha,\gamma}$ was present and measured to be 3.291×10^{-3}, which corresponded to the final estimated values of the parameters $\alpha = 0.027$ and $\gamma = 2.865$. Together with the parameter $b = 7.472$ estimated by applying the iterative parameter optimisation method, the analytical solutions of the Hartlen and Currie model were obtained and compared against the ones measured from the wind-tunnel sectional-model test as shown in Figures 7.17a, 7.17c and 7.17e. It is obvious that there exists a good agreement in the peak response during the lock-in, the occurrence of the peak response and the range of the VIV lock-in which was subjected to the correction applied to the non-dimensional velocity where the lock-in terminated as discussed early in this section. To further investigate the accuracy of the estimated model parameters, the time-integrated solutions of the Hartlen and Currie model were computed and compared against results obtained from the wind tunnel studies. As shown in Figures 7.17b, 7.17d and 7.17f, the Hartlen and Currie model with the estimated parameter qualitatively described the behaviour of the phase shift between the lift force and the structural displacement as the structure exhibited the VIV lock-in. In addition, the predicted peak response was slight underestimated by 1.4% and occurred about 2% earlier than what observed in the wind tunnel study. The VIV lock-in was found to terminate at the non-dimensional wind velocity $\Omega_{o,\text{end}} = 1.38$, which was about 4% sooner than measured from the wind tunnel study.

(a)

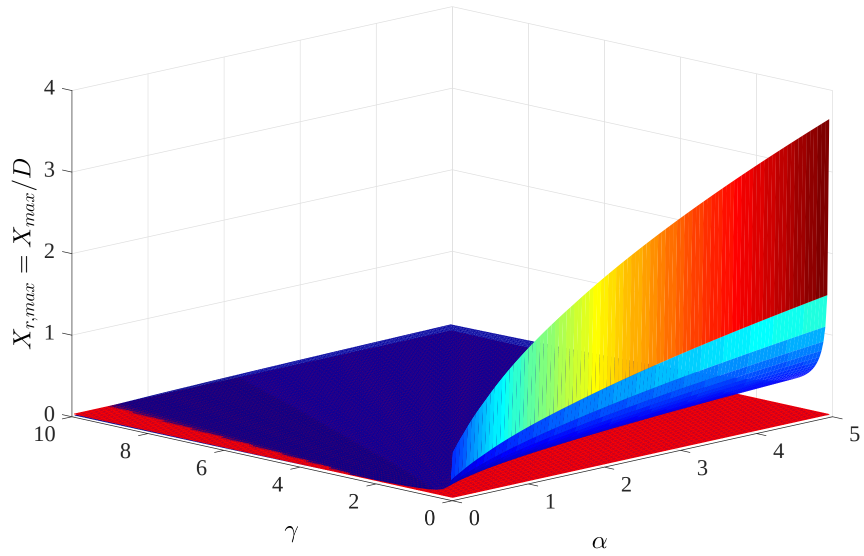

(b)

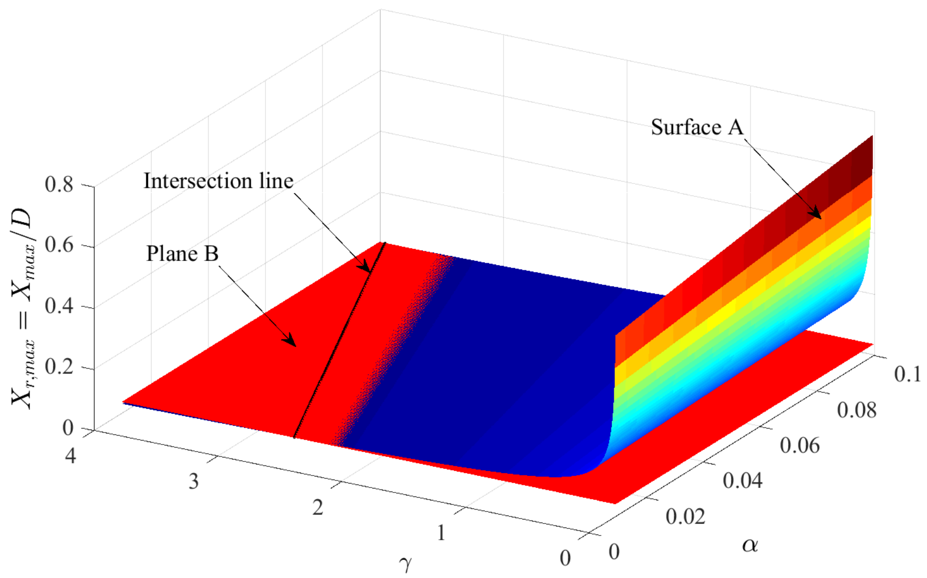

Figure 7.15: Plots of the surface A of the peak response during the lock-in $X_{r,max}$ with (a) coarse and broad arrays $\alpha = 0.01 \ldots 5$ ($\delta_\alpha = 0.05$) and $\gamma = 0.01 \ldots 10$ ($\delta_\gamma = 0.05$) and (b) fine and narrow arrays $\alpha = 0.01 \ldots 0.1$ ($\delta_\alpha = 0.0005$) and $\gamma = 0 \ldots 4$ ($\delta_\gamma = 0.005$); the red plane B represents the actual peak response observed in the WT sectional-model dynamic test.

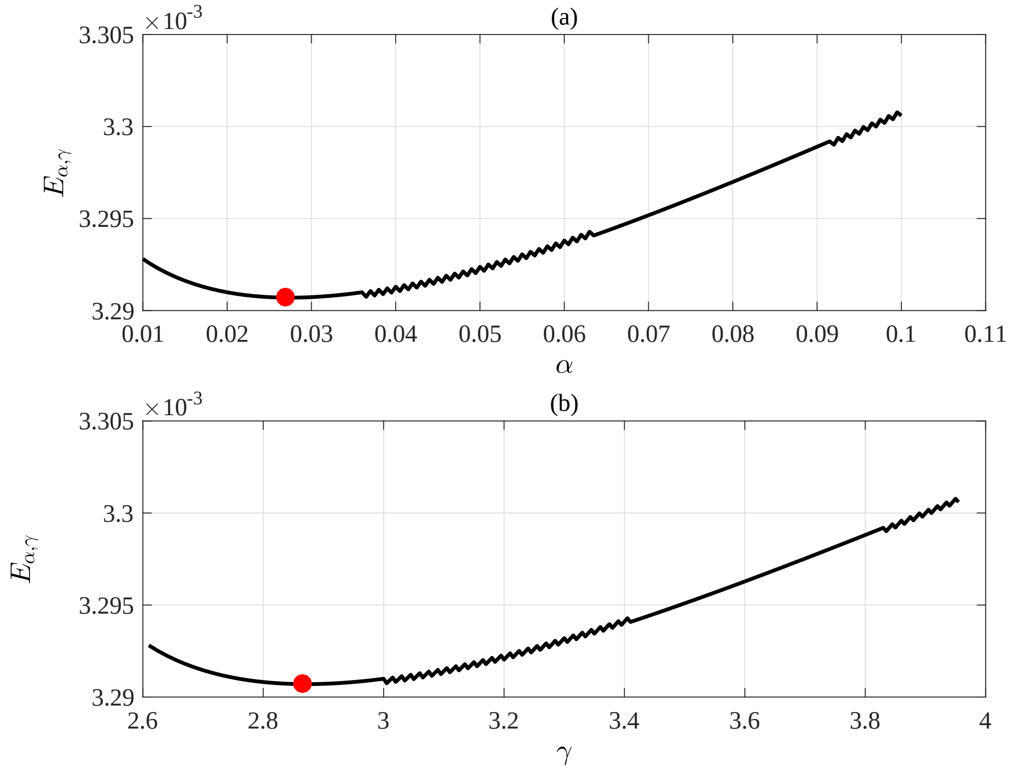

Figure 7.16: Relationship between the error quantity $E_{\alpha,\gamma}$ with respect to (a) the parameter α and (b) the parameter γ extracted from the intersection line showed in Figure 7.15b; the red dot illustrated the point of the minimum error $E^{min}_{\alpha,\gamma}$.

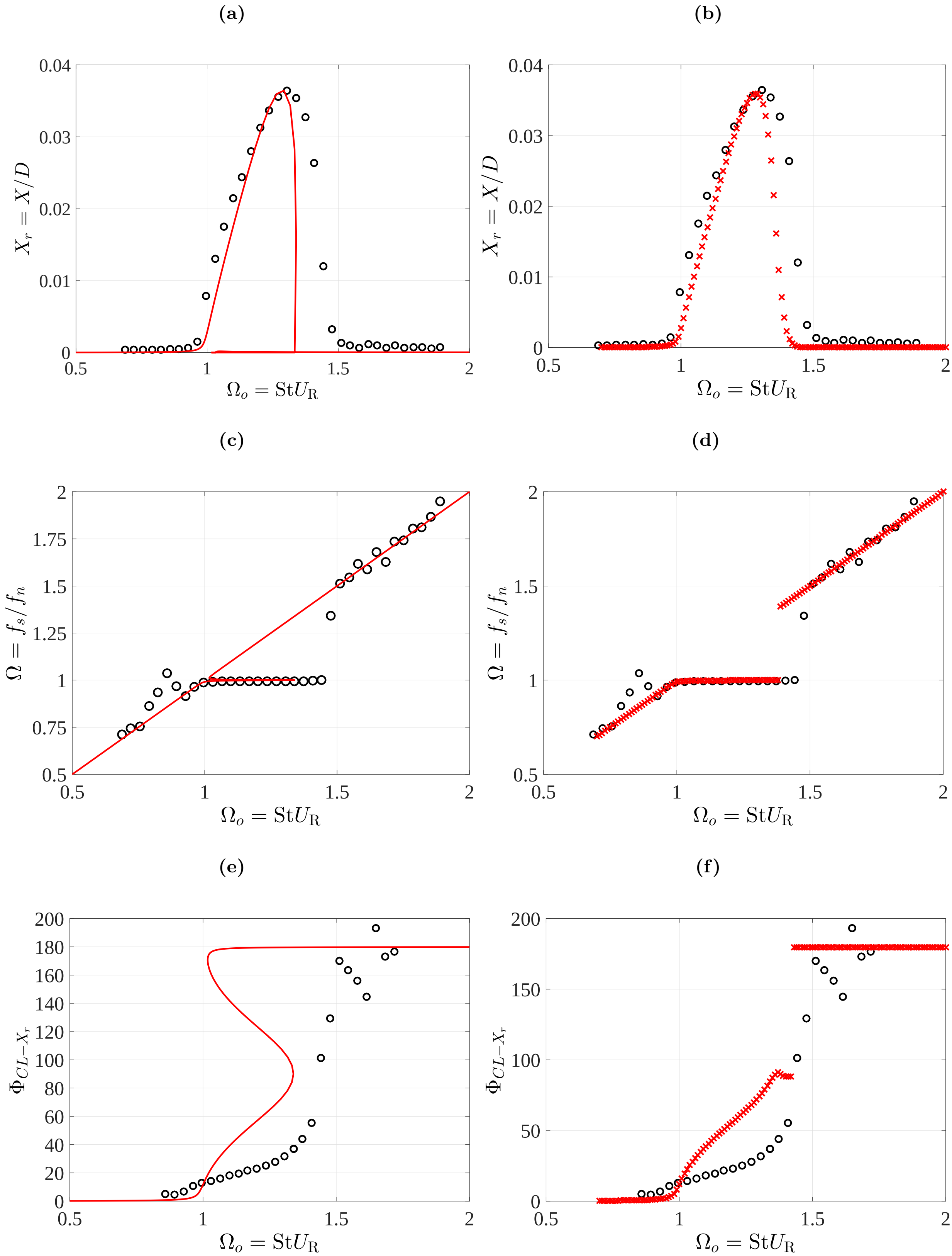

Figure 7.17: Comparison of results of the wind tunnel study (black circles) including (a,b) non-dimensional structural response, (c,d) response of the non-dimensional vortex shedding frequency and (e,f) phase shift of the lift coefficient against the displacement against the analytical solutions (*red solid lines* on left figures) and the time integration (*red crosses* on right figures) of the Hartlen and Currie model using the model parameters: $b = 7.477$, $\alpha = 0.027$ and $\gamma = 2.865$.

7.8 COMPARISON OF HARTLEN AND CURRIE MODEL PARAMETERS

The results from the study presented in Section 7.7 were that two sets of the Hartlen and Currie model parameters were successfully estimated using the VIV response measured in the wind tunnel and computational studies. Table 7.4 summarisess these model parameters together with the Scruton number of each study, which was selected since it largely controlled the VIV response of the rectangular cylinder. In this section, each set of the model parameters was used to predict the Griffin plot, i.e. the plot of the maximum response of the structure during the VIV lock-in with respect to the Scruton number. A comparison between two Griffin plots will be conducted to highlight the characteristics of the Hartlen and Currie model parameters.

In order to construct the Griffin plot, the analytical solution of the structural displacement was computed at different values of the damping ratio, i.e. different values of the Scruton number. The maximum structural responses during the lock-in were identified and plotted against the Scruton number. Two curves corresponding to two sets of the Hartlen and Currie model parameters are plotted together in Figure 7.18; also the actual values of the non-dimensional peak response during the lock-in observed in each study are included for a comparison. It is obvious that the predicted Griffin plot is not able to estimate the maximum structural response during the lock-in for structures possessing different values of the Scruton number. There was a large difference between the two predicted Griffin plots particularly at low values of the Scruton number; the two curves became close together towards higher values of the Strouhal number. The Griffin plot predicted from results of the CFD simulation underestimated the peak response observed in the wind tunnel test by about 35% while the other Griffin plot significantly overestimated the peak response measured in the CFD simulation. It emphasises the main disadvantage of the Hartlen and Currie model in common with most of the theoretical VIV models, that the model parameters are largely dependent on the Scruton number of the structure or the structural displacement as it undergoes the VIV lock-in. This significantly limits the practicability of the model since the model parameters estimated at one value of the Scruton number are very unreliable to be used to estimate the VIV response of another structure having different values of the Scruton number. As for design,

Table 7.4: Summary of the Hartlen and Currie model parameters estimated using results obtained from the wind tunnel test and the computational simulation

	Scruton number	Estimated model parameters		
	Scr	b	α	γ
CFD	8.97	3.915	0.073	13.87
WT	15.9	7.477	0.027	2.865

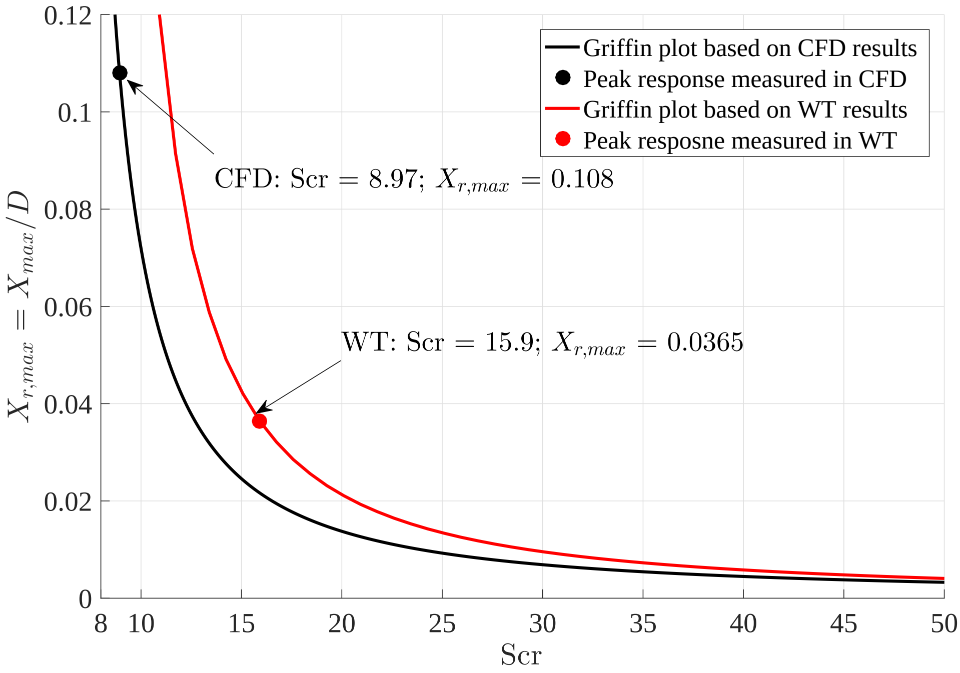

Figure 7.18: Comparison of the Griffin plots predicted by the Hartlen and Currie model derived from results of the CFD simulation and the one derived from results of the wind tunnel test; the circle symbols represented the measurement directly obtained from wind tunnel and computational studies.

this drawback will pose a difficulty, especially during the initial stage of the design where the VIV response of the bridge deck is investigated and the impact of different values of damping on the VIV peak response is studied in case that additional damping is required. This implies that a series of wind tunnel or computational studies need to be carried out using different values of damping, which is a massive limitation in time and economy. In addition, careful design of the wind-tunnel sectional model is also a priority. The structural parameters such as dimensions of the model, mass, damping and natural frequency can be selected based on the scaling factor and the prototype properties ensuring a similar value of the Scruton number as that of the prototype. However, the fluid property such as the Strouhal number can be challenging; most of the wind-tunnel sectional-model tests overestimate the Strouhal number due to the effects of the end plates and of a short span-to-width ratio. The Strouhal number is involved in the parameter a in the forcing term of the structural equation, which in fact was also found to influence the other model parameters. A reasonably accurate estimation of the Strouhal number in the wind tunnel or computational studies is therefore required to ascertain the use of the model parameters extracted from scaled-model studies to predict the VIV response of the full-scale prototype.

7.9 APPLICATION OF 3D HARTLEN AND CURRIE MODELS

In this section, the Hartlen and Currie model parameters estimated from the 3D CFD heaving simulation will be applied to re-predict the structural responses at the mid span measured from the 3D CFD bending simulation. The analysis in Section 7.8 justified this application due to the similarity in the Scruton number between the 3D heaving and bending simulation.

The bending 5:1 rectangular cylinder shared similar structural and fluid parameters as those of the heaving 5:1 rectangular cylinder, including the mass per unit length, the Strouhal number and the Scruton number. Knowing the first bending mode shape which was $\Phi = \Phi_o \sin[\pi/(2L_o)y]$ with $\Phi_o = 0.3630$ and $L_o = 2.5\,\text{m}$ and by performing integration over $y = 0$ to $3\,\text{m}$ the correction factor Γ was evaluated to be 0.1067 while, in the partly-correlated case, the correction factor for the interactive parameter a was calculated to be 0.8866. The Griffin plots showing the dependence of the maximum structural response at the mid span during the VIV lock-in on the Scruton number were then predicted using both the 3D fully-correlated and partly-correlated Hartlen and Currie model. A comparison against the measurement directly obtained from the 3D bending simulation is shown in Figure 7.19. As predicted, the Griffin plot predicted by the 3D partly-correlated model was lower than that predicted by the 3D fully-correlated model. However, the behaviour of the flexible cylinder as it experienced the maximum response during the bending lock-in was more similar to a fully-correlated case. This could be explained by analysing the span-wise distribution of the standard deviation of the time-varying lift coefficient measured in the 3D bending simulation. As shown in Section 6.5.2, when the maximum generalised structural response was reached, this span-wise distribution of $C'_L(y)$ did not follow the structural mode shape; instead, this distribution was reasonably flat. This behaviour contradicted one of the assumptions during the derivation of the 3D partly-correlated Hartlen and Currie model. The issue mentioned here could be due to the limitation in the 3D bending simulation where only a half of the first bending mode was modelled; therefore the flow around the mid-span portion could not be accurately modelled. In addition, the displacement at the mid span could not be large enough to create strong influence on span-wise flow features.

An attempt to validate the 3D partly-correlated Hartlen and Currie model against results of the 3D bending simulation was demonstrated. Due to limitations in the 3D bending simulation, the structural behaviour of the flexible 5:1 rectangular cylinder during the VIV lock-in was found to be more similar to a fully-correlated case. Thus, a case study using the full-scale measurement and the relevant wind tunnel study of the Great Belt East bridge is selected and presented in the following section.

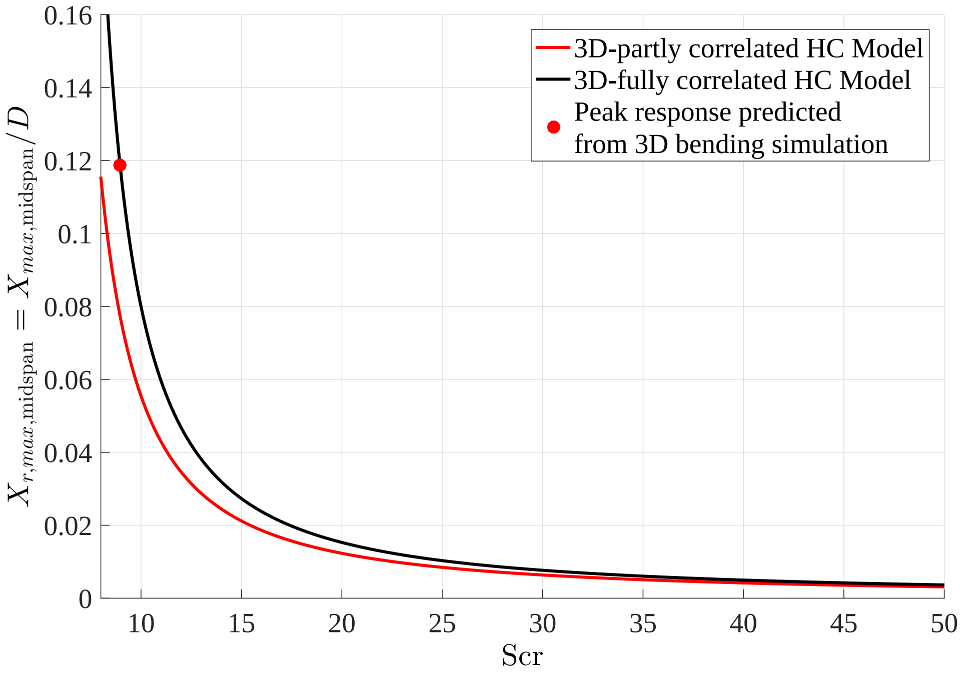

Figure 7.19: Comparison of the Griffin plots predicted by the 3D fully-correlated and partly-correlated Hartlen and Currie models; the circle symbol represented the measurement directly obtained from 3D bending simulation.

7.10 CASE STUDY OF THE GREAT BELT EAST BRIDGE TO VERIFY THE PROPOSED IMPROVEMENT ON THE HARTLEN AND CURRIE MODEL

In this section, the proposed 3D fully-correlated and partly-correlated Hartlen and Currie models are evaluated using data of the wind tunnel test and full-scale measurement of the Great Belt East bridge. The evaluation is conducted by comparing the maximum amplitude of the VIV response measuring on the prototype with what predicted by the two models. Also the Griffin plots are predicted from the two models and are compared together.

7.10.1 Great East Belt Bridge

The Great East Belt Bridge is a three-span suspension bridge with the main span of 1624 m in length and two 535 m long side spans, which was the second longest suspension bridge in the world at the time of completion. It has a four-lane motorway which spans across the international shipping route of the Storebelt Strait in Denmark. The deck of the bridge is the welded steel box girder that spans continuously between two anchor blocks over the whole 2700 m length of the bridge. The entire span of the bridge has a streamlined cross section as shown in Figure 7.20; the depth and width of this section is $D = 4.4$ m and

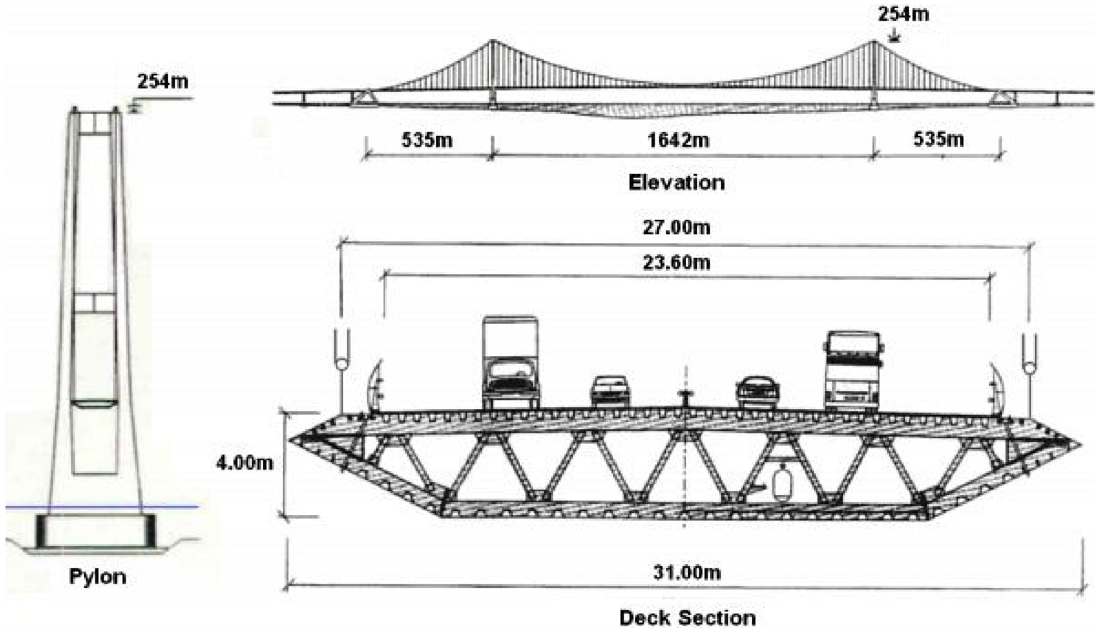

Figure 7.20: Key dimensions of the Great East Belt Bridge (Weight, 2009).

$B = 31.0\,\mathrm{m}$ respectively, resulting in the aspect ratio of 7.

Prior to the construction of the bridge, wind tunnel tested conducted by Larsen (1993) showed the need of installing guide vanes underneath the main span in order to suppress the VIV. However, it was decided not to implement any VIV suppressing mechanisms apart from the guide vane method. And during the final phase of the construction, some low-frequency vertical oscillation of the main span was observed by workers. At that time, it agreed that this oscillation would disappear once all sections of the girder were properly connected together. However, a few weeks after this incident, as surfacing of the motorway was underway, a similar type of oscillation occurred again. Results of on-site observation and monitoring were compared to the wind-tunnel tests indicating that this oscillation was related to the VIV caused by the von Kármán vortex shedding. Structural integrity of the bridge should not be damaged by this type of wind-induced oscillation; however, it would cause large discomfort and loss of confidence in the structural reliability among public. Prior to the opening, it was decided to install guide vanes to the main span, which according to a number of inspections in the following 9 months have efficiently reduced the VIV.

7.10.2 Full-scale Measurement of the Great Belt East Bridge

Before the installation of the guide vanes on the bridge, a full-scale measurement was conducted by Frandsen (2001). It was the first time, at the full scale, that measurement of wind velocity, surface pressure and acceleration of the bridge deck were recorded simultaneously, as an attempt to gain a better insight into this wind-induced behaviour and to improve the design codes for aerodynamic effects on bridges.

The full-scale measurement and monitoring was carried out between 24/04/1998 and 07/06/1998 after the completion of the construction phase before the bridge was opened to traffic. During this period, a number of VIV incidents were recorded with the wind velocity to be measured between $4\,\mathrm{m\,s^{-1}}$ and $12\,\mathrm{m\,s^{-1}}$ and mostly to be in the North-South direction, which was perpendicular to the longitudinal axis of the bridge. The VIV was found to be associated to a single vertical mode and a large harmonic oscillation was observed in the main-span of the bridge. The vertical mode was defined based on the number of waves appearing on the main span; the primary modes are shown in Figure 7.21 together with their associated modal natural frequencies. Among them, Mode 3 and Mode 5 largely contributed to the maximum amplitude at the mid span as summarised in Table 7.5 where the damping ratios for each mode are also reported.

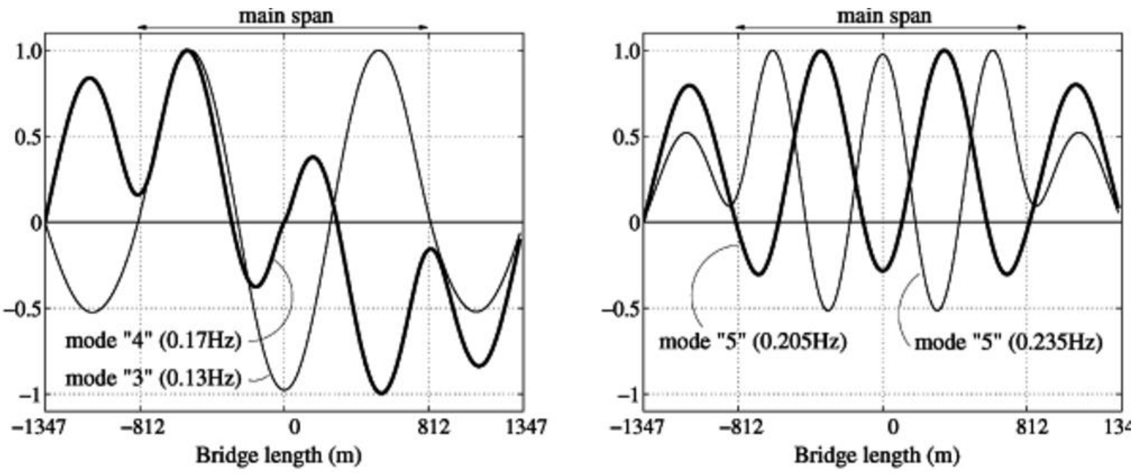

Figure 7.21: Primary mode shapes of the Great Belt East bridge observed during the full-scale measurement with their associated natural modal frequencies (Frandsen, 2001).

Table 7.5: Natural frequencies, maximum root-mean-spared (r.m.s) vertical displacements recorded at the main span during the lock-in and damping ratios associated with each primary mode which was observed during the full-scale measurement; data was extracted from Frandsen (2001).

Mode	Frequency (Hz)	Amplitude (m)	Total damping ratio (%)
3	0.13	0.31	0.51
4	0.17	0.037	0.50
5(1)	0.205	0.35	0.28
5(2)	0.23	0.23	0.27

The Strouhal number of the full-scale structure was identified using the spectra of the pressure measured close to the trailing edge. According to Frandsen (2001), the fluctuation of pressure at this location was directly associated with the vortex-shedding frequency which was controlled by the motion of the bride deck during the lock-in or was proportional to the mean wind speed when the system was outside the lock-in. This selection was reasonable since the pressure here was least affected by the high suction and high frequency separation bubble forming at the leading edge and the high unsteadiness of the reattachment points which were observed to occur on bridge deck sections having large aspect ratio. Despite some uncertainties, the Strouhal number defined based on the depth D of the section was measured to be between 0.08 – 0.15; this result measured in the full scale was in a good agreement with some selected wind tunnel sectional model tests and taut-strip model tests as discussed in Frandsen (2001). Also, given that the Strouhal number scattered in the aforementioned range, it was reasonable to state that the Strouhal number was independent of the Reynolds number as being observed for bridge deck sections having a long after-body length.

The full scale measurement conducted by Frandsen (2001) indicated that the VIV lock-in of the bridge was observed to occur as the wind speed was descending. Mode 5 with the model natural frequency of 0.205 Hz was involved in most of the VIV response with the r.m.s amplitude of the maximum response at the lock-in of 0.205 m. This mode was found to occur at the reduced velocity of 1.35, which followed by Mode 3 that happened at the reduced velocity of 1.25 and led to a higher r.m.s amplitude at the lock-in of 0.31 m. As Mode 3 contributed significantly to the VIV response of the main span, it was selected as the key mode shape to evaluate the modified Hartlen and Currie model, i.e. it was assumed that the main span only exhibited Mode 3 as the VIV occurred. Based on the mode shape plotted in Figure 7.21, the equation of Mode 3 in the main span was assumed to be sinusoidal as

$$\Phi_3 = \sin\left(\frac{3\pi}{L}y\right), \tag{7.50}$$

where $L = 1624\,\mathrm{m}$ is the length of the main span; the origin of the coordinate system was shifted by -812 m compared to the one defined in Figure 7.21. It was noticed that only the mode shape of the main span was of interest in this case; the vibration of two side spans were ignored. The mass per unit length of the main span including weight of hangers was $\bar{m} = 22.74 \times 10^3\,\mathrm{kg\,m^{-1}}$, which yielded to the Scruton number of $\mathrm{Scr} = 8.72$. The maximum reduced amplitude of the response at the mid-span was $X_{r,\mathrm{midspan}} = 0.10$; it was normalised using the depth D of the cross section. It was observed to occur at the reduced wind speed $U_\mathrm{R} = 1.25$. Other structural parameters such as the modal natural frequency and damping ratio were selected based on Table 7.5. The kinematic viscosity was assumed to be $\nu = 1.5 \times 10^{-5}\,\mathrm{m^2\,s^{-1}}$. The Strouhal number was seen to scatter in the range from 0.08 to 0.15; therefore, the averaged value was taken, i.e. $\mathrm{St} = 0.12$.

7.10.3 Wind Tunnel Sectional Model Test of the Great Belt East Bridge

As shown in Frandsen (2001), a number of wind tunnel sectional model tests were conducted to investigate the VIV response of the Great Belt East bridge. Results from most of them agreed well with the full-scale measurement regarding the maximum amplitude of the response during the lock-in and the onset reduced velocity of the lock-in.

For the purpose of evaluate the modified Hartlen and Currie model, the wind tunnel sectional model test carried out at Tongji University, China (Xu et al., 2015) was selected due to the availability of the plot of the reduced amplitude of the VIV response against the reduced wind speed in their original paper. The wind tunnel test was conducted using the 1:50 sectional model of the Great Belt East bridge as shown in Figure 7.22a; the set-up of the wind tunnel sectional model test is described in Figure 7.22b. The cross section of the model was $B = 620\,\mathrm{mm}$ in width and $D = 88\,\mathrm{mm}$ in depth; the length of the model was $L = 1750\,\mathrm{mm}$, leading to the ratio of L/B to about 2.8. The mass per unit length of the model was $\bar{m} = 9.096\,\mathrm{kg\,m^{-1}}$ and the damping ratio ζ was set up to be 0.5% which was about 2% different from the modal damping ratio of Mode 3 measured in the full-scale prototype. This resulted in the Scruton number of $\mathrm{Scr} = 8.55$. Comparing the Scruton number between the sectional model and the prototype, the condition of the similarity of the Scruton number is satisfied; therefore, the model parameter of the 2D Hartlen and Currie model identified from the wind tunnel sectional model test can be used in both of the 3D Hartlen and Currie models. Due to the short span length of the sectional model, the vortex shedding was enhanced leading to a higher value of the Strouhal number compared to the averaged value measured in the full scale. However, the value obtained in the sectional model test $\mathrm{St} = 0.145$ (based on the depth D) was still in the scatter range reported in Frandsen (2001).

The maximum non-dimensional amplitude X_r of the VIV response of the sectional model plotted against the non-dimensional velocity Ω_o is shown in Figure 7.23. The maximum amplitude of the response during the lock-in was recorded to be 0.0514, which occurred at the reduced wind speed $U_\mathrm{R} = 1.24$. This reduced velocity was slightly different from the one measured in the full scale; it was mostly due to the difference in the damping ratio and the Strouhal number. Nevertheless, the margin between the one measured in the wind tunnel test and the one recorded in the full scale was very small. During the wind tunnel sectional model test, it was noticed that the hysteresis was not observed as the wind speed was descending while, as mentioned in Section 7.10.2, the VIV lock-in in the full scale was related to a decrease in the wind speed. Other wind tunnel sectional model tests reported in Frandsen (2001) also did not find any hysteresis.

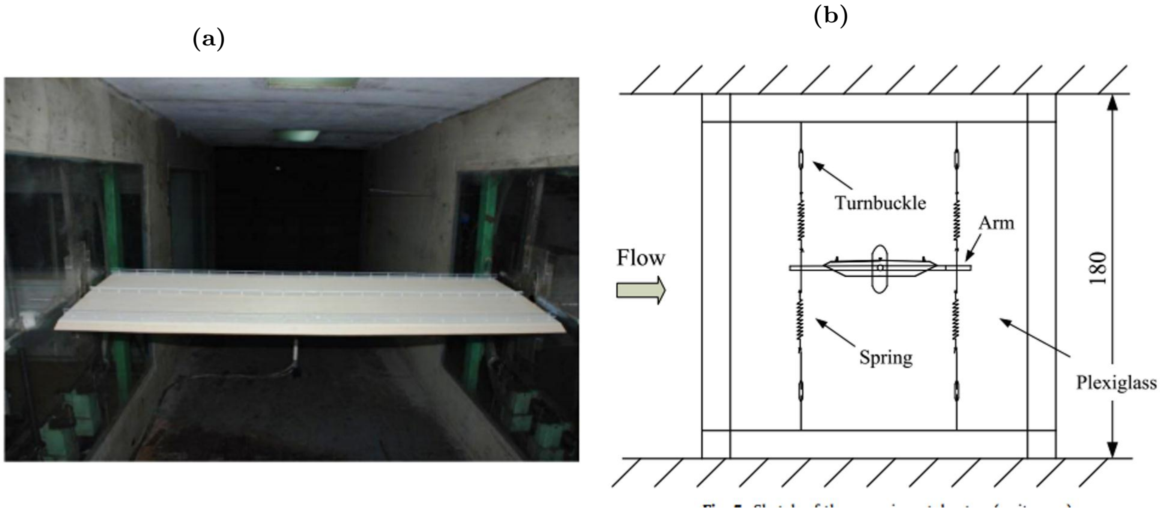

Figure 7.22: (a) The 1:50 sectional model of the Great Belt East bridge and (b) the set-up of the wind tunnel sectional model test (Xu et al., 2015).

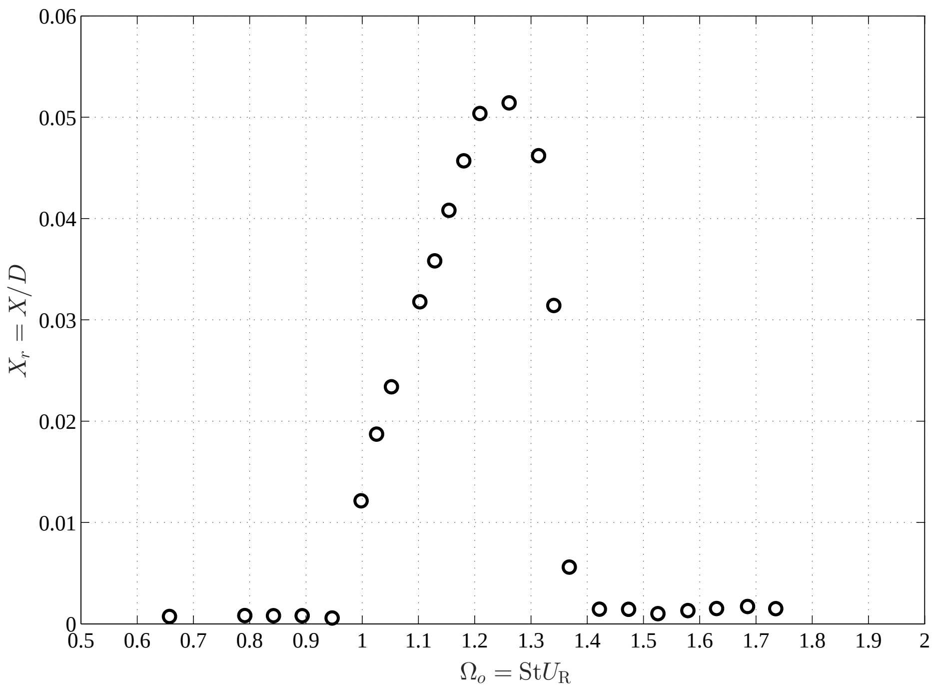

Figure 7.23: Non-dimensional structural response of the sectional model X_r against the the non-dimensional wind velocity Ω_o as the system experienced the lock-in (Xu et al., 2015).

7.10.4 Identification of Model Parameters of the Hartlen and Currie Model

With the assumption that the model parameters of the Hartlen and Currie model preserve their 2D characteristics, in this section, all three model parameters are identified using results of the wind tunnel sectional model test carried by Xu et al. (2015) as summarised in Section 7.10.3.

As discussed in Section 7.1, the three parameters of the Hartlen and Currie model are b, α and γ. The parameter b could be solely identified using the response of the vortex shedding frequency as the wind speed increases, while the other parameters α and γ were extracted together using the maximum amplitude of the response of the structure in the lock-in. Results of the wind tunnel test of Xu et al. (2015) did not include the frequency response; therefore, that part of the MATLAB identification process proposed in Section 7.6 was altered.

Results of the identification process using the wind tunnel and computational simulation results showed that the minimum error in the frequency solution could yield an accurate estimation of the non-dimensional wind velocity when VIV lock-in terminated. Hence, the MATLAB identification process was altered such as the non-dimensional velocity of the lock-in termination was used as a condition to identify the parameter b. As a result, the parameter b was estimated to be 6.691 and the analytical solution of the lock-in range agreed to what measured in the wind tunnel test as can be seen in Figure 7.24.

With the parameter b successfully identified, the parameters α and γ were estimated using the maximum amplitude of the structural response during the lock-in. Results of the surface-searching-based optimisation process are shown in Figures 7.25 and 7.26; values of the parameters α and γ were selected at the global minimum error. Therefore, the Hartlen and Currie parameters were identified as $b = 6.691$, $\alpha = 0.14$ and $\gamma = 2.26$.

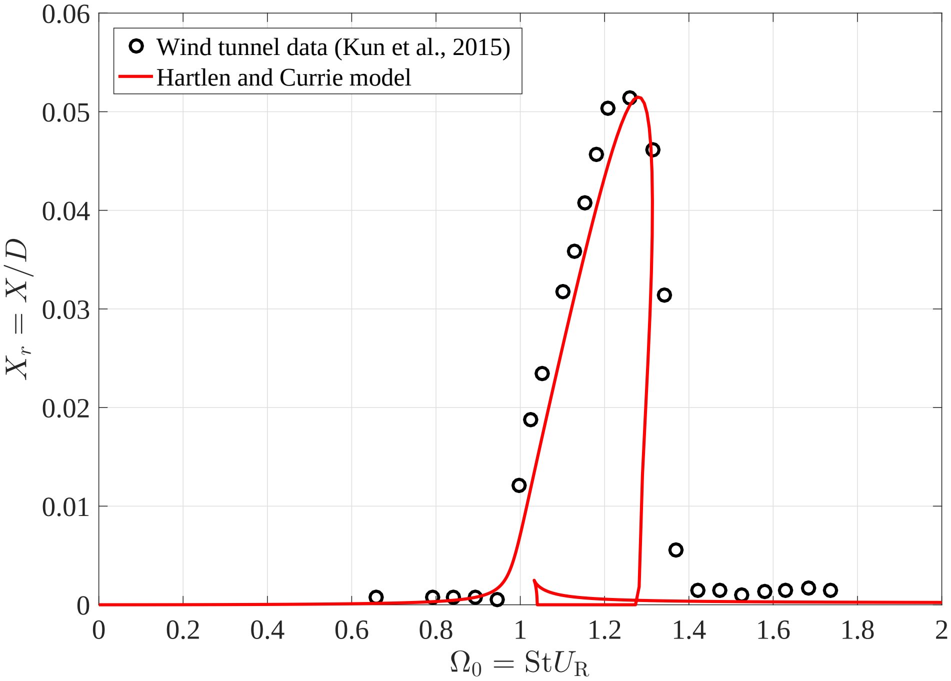

Figure 7.24: Comparison between results of the wind tunnel sectional model test conducted by Xu et al. (2015) and the analytical solution of the Harlen and Currie model with the modal parameters as $b = 6.691$, $\alpha = 0.14$ and $\gamma = 2.26$.

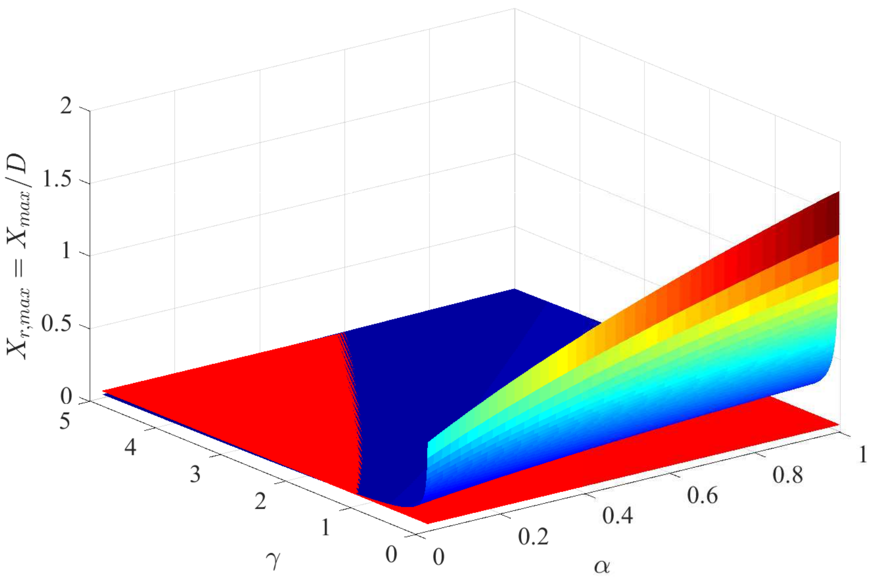

Figure 7.25: Surface of the maximum structural response during the lock-in with respect to the parameters α and γ; the red plane corresponds to the maximum amplitude of the response during the lock-in that the Hartlen and Currie needs to predict.

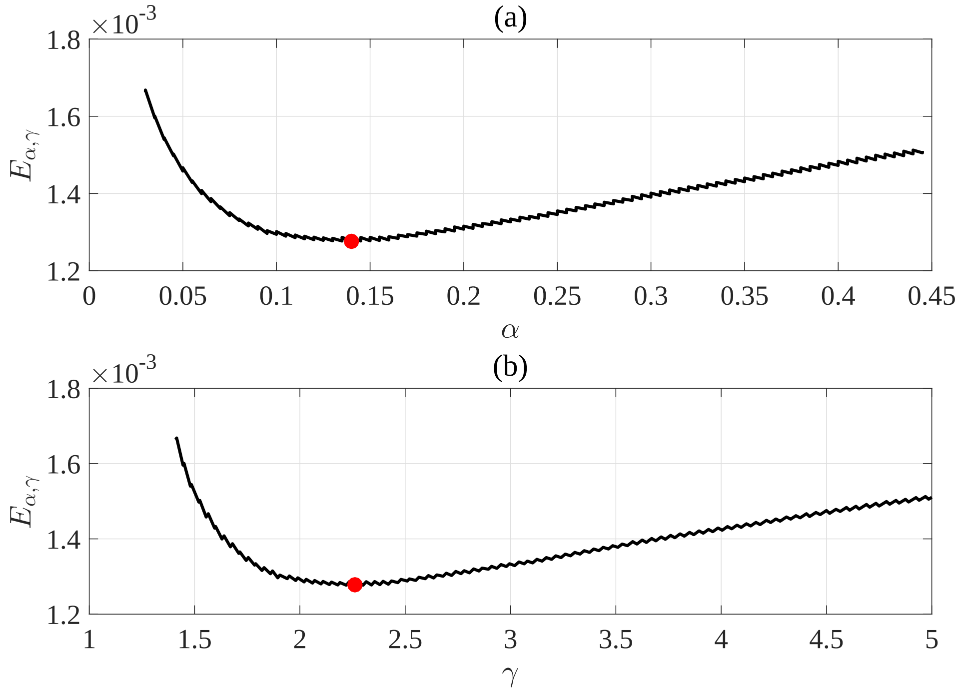

Figure 7.26: Variability of the error between the structural response measured in the wind tunnel test and the one analytically predicted from the Hartlen and Currie model against the parameter (a) α and (b) γ; values corresponding to the minimum error are indicated by the red dots.

The analytical solution of the structure response given by the Hartlen and Currie is shown in Figure 7.24 in a comparison against the response measured in the wind tunnel sectional model test as the wind speed increased. The Hartlen and Currie model predicted the maximum response of the structure during the lock-in with a percentage difference less than 0.2%. However, the Hartlen and Currie model did not simulate accurate the initial branch of the response. Even though the non-dimensional onset velocity of the lock-in was correctly captured, the initial branch observed in the wind tunnel was offset from the one obtained from the Hartlen and Currie model. This variation of the initial branch probably led to an approximately 1.5% difference in the wind velocity where the maximum response occurred during the lock-in; Xu et al. (2015) found the maximum response in the lock-in happened at the non-dimensional wind velocity of 1.261 while the Hartlen and Currie model predicted its occurrence at 1.278. The range of VIV lock-in was predicted to be about 4% shorter than the one observed in the wind tunnel, which was mostly due to the lack of memory effect when using the analytical solution. Nevertheless, it was evident that the Hartlen and Currie model with the model parameters identified here was able to simulate the structural response of the sectional model as being observed in the wind tunnel.

7.10.5 Prediction of Full-scale VIV Responses of the Great Belt East Bridge

The model parameters predicted in Section 7.10.4 are used in this section to predict the structural response of the full-scale structure using the 3D fully-correlated and partly-correlated Hartlen and Currie models. The results obtained from the two models are compared against the full-scale measurement in order to show the high conservativeness of the 3D fully-correlated model and the appropriateness of the proposed modification that led to the 3D partly-correlated model.

The paramter γ is multiplied by the correction factor Γ which was evaluate to be 0.75; this correction factor was used in both of the 3D fully-correlated and partly-correlated Hartlen and Currie models. As for the 3D partly-correlated model, the corrector factor for the parameter a was calculated to be 0.8488. Also, it was noticed that the modal coefficient of Mode 3 was equal to unity as shown in Equation 7.50; therefore, the generalised structural response of the structure was effectively equal to the response at the mid-span but with a phase shift of 180°.

Using the two correction factors discussed above, the VIV response at the mid-span as the wind speed increased was predicted using the 3D fully-correlated and partly-correlated Hartlen and Currie models. Both solutions are included in Figure 7.27, which clearly shows the 3D fully-correlated model predicted a significantly higher amplitude of the response during the lock-in. Also, a broader lock-in interval was predicted by the fully-correlated model. The results obtained from the 3D partly-correlated Hartlen and Currie model were more comparable to the full-scale measurement. The maximum response at the mid-span during the lock-in was predicted to be $X_r = 0.097$ while it was observed to be 0.1 at the full scale. The VIV lock-in was expected to terminate at the non-dimensional wind velocity of $\Omega_o = 1.43$ which was about 10% smaller than what observed in the full scale, $\Omega_o = 1.585$. In addition, the maximum response during the lock-in was predicted to occur at $\Omega_o = 1.384$, which was about 5% later than what was seen in the full-scale, $\Omega_o = 1.321$. Even though there were certain differences in the non-dimensional wind velocities of the occurrence of the maximum amplitude of the response during the lock-in and of the termination of the VIV lock-in, it was evident that the VIV response at the mid-span was better simulated by the 3D partly-correlated Hartlen and Currie model.

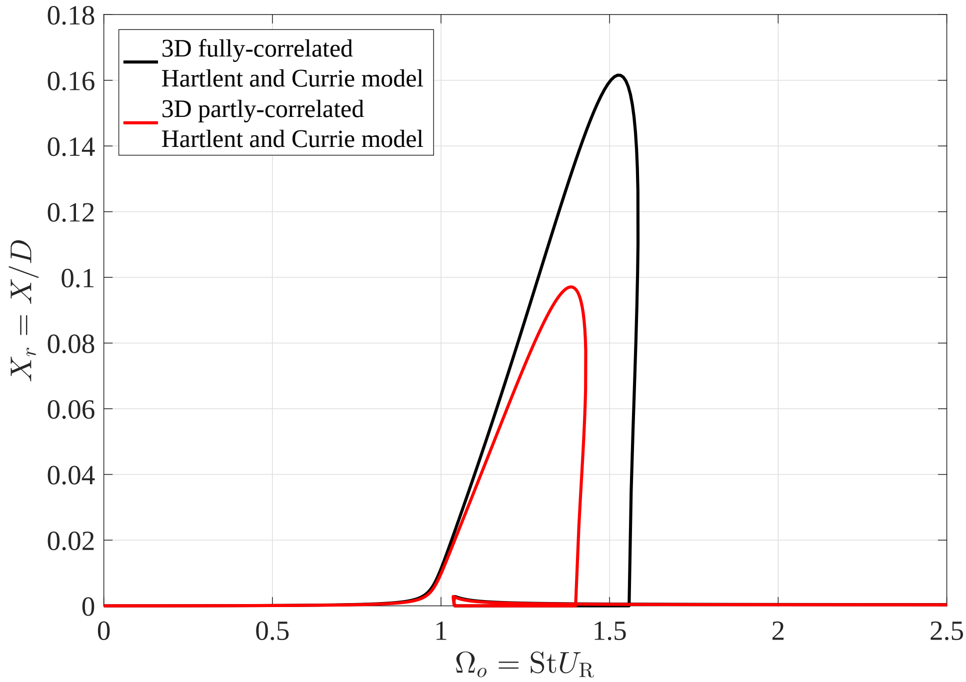

Figure 7.27: Comparison of the VIV response at the mid-span predicted by the 3D partly-correlated and fully-correlated Hartlen and Currie model.

Regarding to the maximum amplitude measured at the mid-span during the VIV lock-in, both of the models were also used to predict the relationship of this quantity at different values of the damping ratio, i.e. to predict the Griffin plot of the VIV response measured at the mid-span. As can be seen in Figure 7.28, the value estimated from the 3D partly-correlated Hartlen and Currie model was found to be very close to the one measured at full scale; the percentage difference between the two values was evaluated to be about 3%. On the other hand, the value predicted by the 3D fully-correlated Hartlen and Currie model was approximately 1.5 times large than the full-scale measurement.

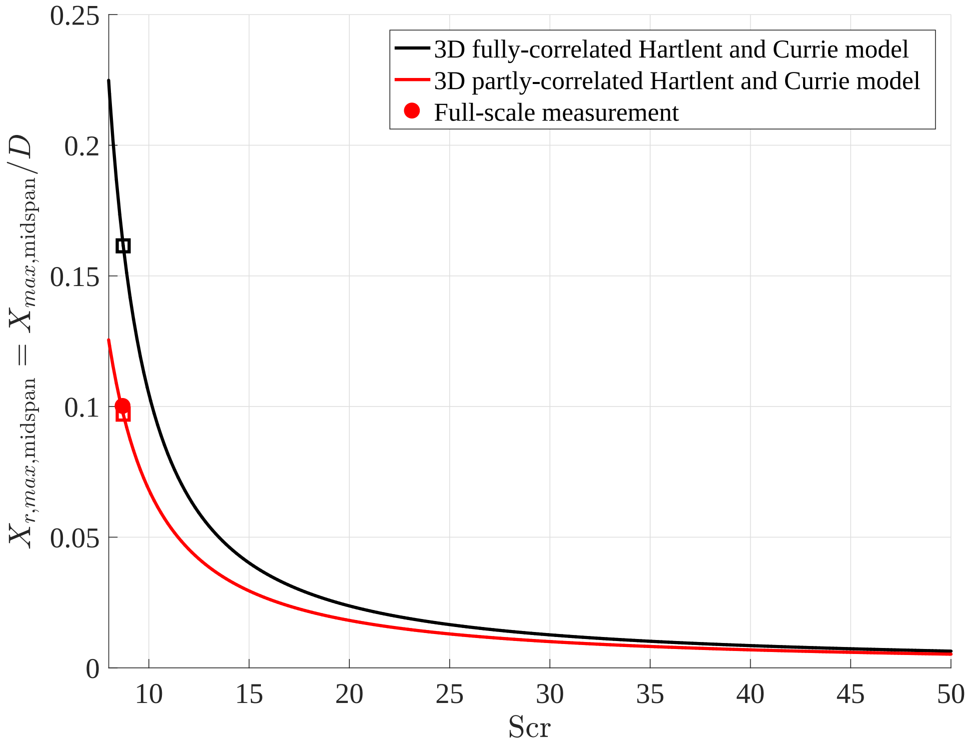

Figure 7.28: Comparison of the Giffin plots of the VIV response at the mid-span predicted by the 3D partly-correlated and fully-correlated Hartlen and Currie model; the open symbols are the predicted maximum responses at the Scruton number of the prototype; the close symbol are the value observed at full scale.

7.10.6 Summary of the Case Study of the Great Belt East Bridge

In this case study, the structural response associated with Mode 3 of the main span of the Great Belt East bridge undergoing VIV before the installation of guide vanes has been used to validate the modified 3D fully-correlated and partly-correlated Hartlen and Currie models. By comparing the maximum response at the mid-span during VIV lock-in observed in the full scale and the one predicted by the model, the 3D partly-correlated Hartlen and Currie model was found to perform better than the fully-correlated one despite some uncertainties in the Strouhal number measured at full scale and the difference in the Strouhal number between the wind tunnel test and the full scale measurement. The maximum response of the VIV was predicted to be about 3% smaller than the full-scale measurement. In addition, the non-dimensional velocities at which the maximum response during the lock-in occurred and at which VIV lock-in terminated were 5% and 10% larger than the ones observed in the full-scale.

The fact that the 3D partly-correlated Hartlen and Currie model yielded more comparable results to the full-scale measurement indicated the appropriateness of the assumptions made during the model development, including the Hartlen and Currie model parameters were two-dimensional and could be used to predict VIV responses of a 3D structure as long as the correction factor Γ was applied to the model parameter γ. The assumption that the lift coefficient possessed similar mode shapes to the structural response also seemed to be reasonable. However, this assumption required further modification in order to represent the correlation characteristic of the surface pressure. The correlation function of the lift force could be estimated by non-negative and normalised mode shapes, especially for the design purposes as proposed by Ehsan and Scanlan (1990).

7.11 CONCLUSION OF THE CHAPTER

In this chapter, the original 2D Hartlen and Currie model has been developed by addressing a number of points. The first one was to convert the 2D model into a 3D model, which was shown to be able to simulate VIV response of a 3D flexible structure excited in different mode shapes. This model was called the 3D complete Hartlen and Currie model featuring a spatialy-dependent fluid equation. Results obtained from this model revealed that the span-wise distribution of the lift coefficient was similar to the structural mode shape, in particular during VIV lock-in, and that the model parameters possessed two-dimensional characteristics. These two findings were the foundation for further development, leading to the 3D fully-correlated Hartlen and Currie model. This model comprised the structure and fluid equations defined in the generalised coordinate, which allowed the VIV response to be modelled in a timely-fashion manner yet at high accuracy. However, the assumption that the lift coefficient followed the structural mode shape implied that the lift force was fully correlated along the span-wise length of the model and the coherence characteristics of the surface pressure was ignored, which could result in an over-prediction of the motion-induced lift force and the maximum amplitude of the response during the lock-in. Another correction was required, which was to introduce the correlation expression into the forcing term of the structural equation. For the design purposes, the method proposed by Ehsan and Scanlan (1990) was applied, where the correlation function of the lift force was taken to be the normalised mode shape which was positive and equal to 1 at peaks and troughs of the mode shape. This model therefore inherently modelled the coherence structure of the surface pressure, for which it was named the 3D partly-correlated Hartlen and Currie model.

A parameter optimisation featuring an iterative approach to estimate the parameter b and a surface-searching based approach to estimate the parameters α and γ was proposed and successfully extracted all parameters using results of wind tunnel or computational studies. Further analysis, particularly using the full-scale measurement of the Great Belt East bridge, showed that the 3D fully-correlated model significantly over-predicted the VIV response while the 3D partly-correlated model could be considered to produce a conservative prediction. Also, results of the case study have shown that the model parameters of a VIV model could be effectively extracted from wind tunnel sectional model tests or 2D computational studies; further correction however needed to be applied so that responses of 3D flexible structure could be estimated. This is very beneficial since these studies are not very costly and time-consuming, especially after the development of a more generalised VIV mathematical model which, unfortunately, has not been achieved up to now. This kind of VIV models would require robust and reliable relationship between the model parameters and the physical parameters such as the Scruton number. However, cross sections having distinctly different aerodynamics of the flow field might be associated with their own sets of parameters, which essentially need to be identified at the initial phase of the design stage.

Chapter 8

Conclusion

In this chapter, this research study is summarised together with conclusive observations and findings as well as potential areas for future research.

8.1 SUMMARY

A thorough literature review on the bridge aerodynamics and aeroelasticity was conducted, highlighting the limitation in the knowledge of the underlying physical mechanism of the VIV, particularly of the motion-induced vortex. A number of VIV mathematical models have been developed; however, their usability and practicability are very limited since they are capable of modelling the VIV for specific structures only. Moreover, the use of these models to estimate the VIV response of a 3D flexible structure has been questionable. In addition, in the case of the wind-induced response of bridge decks in the turbulent wind, the hypothesis proposed by Scanlan (1997) about the relationship between an increase in the stability of bridge decks and a decrease in the span-wise correlation of forces and surface pressure has been used to explain for the turbulence-induced stabilising effect. However, a number of researches as well as full scale incidents such as the Messina bridge do not support this hypothesis. Similar controversy has been found when studying the effect of the turbulence on the VIV; whether the turbulence produces stabilising or destabilising effects on the VIV seems to depend on bridge deck cross sections. This issue as well as the insufficient understanding in the turbulence-induced effect can also be due to the limitation of the current research where wind tunnel and computational models are 2D in nature. These gaps were formed the aims and objectives of this research study, which were achieved by the method of wind tunnel tests and CFD simulations using OpenFOAM and the HPC system; all required facilities including the wind tunnel are located at the University of Nottingham.

In order to fulfil the objectives of this research study, two wind tunnel dynamic tests were conducted in smooth flow using the conventional 3D section model of a 5:1 rectangular cylinder which were restrained to either the heaving mode or the pitching mode only. The analysis of the surface pressure distribution as well as the span-wise correlation of the pressure measured close the leading and trailing edge as the cylinder underwent the VIV lock-in suggested two different mechanisms which are responsible for the VIV. These wind tunnel dynamic tests were complemented by a CFD simulation modelling the heaving VIV of a 3D sectional model in smooth flow. In stead of using the built-in fluid-structure-interaction solver, a structural solver based on the first-order backward differencing scheme and a dynamic mesh algorithm have been developed and successfully integrated into the OpenFOAM fluid solver. Despite differences in structural parameters, results regarding the distribution and span-wise correlation of the surface pressure were comparable with those observed in the wind tunnel tests. Using the POD technique, the dominant component of the surface pressure fluctuation was extracted and the qualitative analysis over a number of cycles of the structural motion has revealed the flow features associated to these two mechanisms, which helped confirm the results inferred from the pressure data.

Using a similar physical sectional model, the wind tunnel static and dynamic tests were also carried out in smooth flow and turbulent flow having different turbulent intensities and length scales. By comparing the distribution and the span-wise correlation of the surface pressure measured in smooth and turbulent flow, it was found that the turbulence significantly alters the aerodynamic characteristics of the flow field around the static cylinder. Similar variation was also found in case of the dynamic cylinder; therefore, the suppression of the heaving and pitching VIV in turbulent flow was thought to relate to this aerodynamic variation.

To eliminate the dominance of 2D flow features when using 3D sectional models, a novel computational approach was introduced to simulation the bending VIV of a flexible 5:1 rectangular cylinder. In this bending simulation, the first bending mode shape was integrated into the structural solver. All structural parameters were kept similar to those used in the heaving simulation. Two VIV lock-in regions were observed. The POD technique was utilised to analyse the fluctuating component of the surface pressure field which revealed a span-wise transition between two dominant flow features: the motion-induced vortex shedding and the Strouhal-number vortex shedding. Also a secondary span-wise flow feature was uncovered. In addition, investigating the span-wise distribution of the lift coefficient as well as of the phase shift between the lift force against the generalised displacement suggested that the bending VIV is potentially triggered by some other span-wise flow feature in addition to the two mechanisms mentioned above.

Results obtained from the wind tunnel dynamic tests as well as the heaving and bending simulations were then used in an in-depth study of the Hartlen and Currie VIV mathematical model. An optimisation process was developed and successfully extracted the model parameters. In addition, by introducing the structural mode shape and the assumption that the span-wise distribution and correlation of the lift coefficient follow the structural mode shape being excited during the VIV lock-in, this 2D mathematical model was generalised so that it could simulate the VIV response of a flexible structure. These assumptions were derived and assessed using results of the bending simulation. The 3D Hartlen and Currie model was then verified by the bending simulation and the full-scale measurement of the Great Belt East bridge.

8.2 FINDINGS AND OBSERVATION

Aerodynamics of the 5:1 Rectangular Cylinder

The flow field around a static 5:1 rectangular cylinder is characterised by a well-defined and strongly correlated separation bubble along the leading edge. It is followed by an intermittent reattachment region, where the shear layer separated from the leading edge was found to impinge on the surface, recovering the surface pressure and creating unsteadiness and high pressure fluctuation. Also, the creation of the shear layer from the leading edge is in phase with the vortex shedding at the trailing edge. These characteristics correspond to the impinging leading-edge vortex shedding.

The variation of the angle of attack can alter these aerodynamic properties significantly. For the side surface which is exposed more to the wind, the length of the separation bubble is reduced while the circulation strength is increased. On the opposite side surface, the separation bubble is elongated up to the stall angle of about 6° where the reattachment point disappears and the shear layer directly interacts with the wake region.

The turbulence was found to suppress the separation bubble, reducing its stream-wise length and shifting the reattachment region upstream. The circulating strength therefore is concentrated over a narrow region close to the leading edge, making it highly unstable and reducing the span-wise correlation. Moreover, the span-wise correlation of the surface pressure close to the trailing edge slightly increased. Thus, it was evident that the turbulent flow alters the aerodynamics of the 5:1 rectangular cylinder; it promoted the trailing-edge vortex shedding rather than the impinging leading-edge vortex shedding. These effects can be enhanced or lessened by the variation of the angle of attack.

Mechanism of VIV

The heaving and pitching VIV share similar features including the lock-in of the vortex shedding frequency, an increase in the structural response and the variation of the phase shift of the force or moment against the structural response. However, two heaving VIV lock-in regions were found while only one pitching VIV lock-in was visible. The on-set reduced velocity is also different between the heaving and pitching VIV, which is related to the difference of the vortex structure on side surfaces during one cycle of the structural motion.

There are two mechanisms which are responsible for VIV of the 5:1 rectangular cylinder. The first one is the leading-edge vortex, which, at the start of the lock-in, acts as the triggering mechanism providing some initial displacement for the cylinder. As the structural response grows, the second mechanism is more important. Due to the motion of the structural, at some instance, this leading edge vortex appears to impinge on the side surface, increasing the aerodynamic force and moment and eventually the structural response.

In the turbulent flow, the heaving and pitching VIV is significantly suppressed. The turbulence is found to weaken the motion-induced leading edge vortex and to remove its impingement onto the side surface. A small VIV peak was however visible as for the cylinder was restrained to the pitching mode only, which is because the angular motion of the cylinder effectively reduces the suppressing effect induced by the turbulence.

When analysing the bending VIV of the flexible 5:1 rectangular cylinder, it was shown that the bending VIV lock-in is not triggered by the flow features around the span-wise position exhibiting the maximum displacement ($y/B = 5$). Instead, the process where the energy is transferred from the wind to the structure occurs at the lower span-wise portion $y/B = 1$ to 3.

Emerging span-wise flow features

A number of intrinsic span-wise flow features around the flexible 5:1 rectangular cylinder were observed when performing the POD analysis of the fluctuating component of the surface pressure. Two primary flow features co-exist and interfere with each other along the span-wise length, which are the motion-induced vortex shedding and the Strouhal-number vortex shedding. The former is dominant around the mid-span ($y/B = 5$) while the latter strongly influences the flow field around the static end ($y/B = 0$). In fact, there are two Strouhal-number vortex shedding modes; the parallel vortex shedding mode is observed around the static end while the oblique vortex shedding mode is visible across the span-wise length of the cylinder.

In addition, superimposing on this primary flow field is the secondary flow feature featuring a number of counter-rotating stream-wise vortices. They were found to shift in the span-wise direction and it can take up to two cycles of the structural motion to restore its original arrangement.

During the bending VIV lock-in, the span-wise distribution as well as the span-wise correlation of the lift coefficient appear to possess characteristics similar to the structural mode shape. This observation is most relevant when the structural response is increasing.

Mathematical modelling of VIV

An optimisation process including an iterative approach and a surface-searching-based approach has been developed and successfully extracted the model parameters using results of the wind tunnel (dynamic) heaving test and the heaving simulation. The outcomes of this process highlighted the key disadvantage of the Hartlen and Currie model which is the Scruton-number dependence of the model parameters. This issue limits the usability and practicability of the Hartlen and Currie model.

The conventional 2D Hartlen and Currie model was generalised into the 3D complete Hartlen and Currie model featuring the spatial dependence in both of the structural and fluid equations. This model is able to predict similar effects observed in the bending simulation such as the co-existence of the motion-induced vortex shedding and the Strouhal-number vortex shedding as well as the span-wise distribution and correlation of the lift coefficient. Time-consuming in solving this model is the main limitation.

Focusing on estimating the structural response during the lock-in, the partly-correlated 3D Hartlen and Currie model was derived using the structural mode shape to represent the span-wise distribution and correlation of the lift coefficient. The outcome of this improved model was not comparable against results of the bending simulation, which could be due limitations of the computational approach. However, using the Great Belt East bridge as the test case, this model was able to predict a similar VIV structural response as the full-scale measurement.

8.3 CONCLUSIONS

Based on these findings and observations, the following conclusive points are presented.

The motion-induced leading edge vortex and its impingement on the side surface are the two mechanisms which are responsible for the VIV of the 5:1 rectangular cylinder. Missing one of them causes VIV lock-in not to happen. Also, at the start of the bending VIV lock-in, the flow field around the mid-span, i.e. having the maximum displacement, is not of importance; instead, the process where the energy in the flow is transferred to the structure and vice versa occurs at the lower span-wise portion.

The turbulent flow, at least in the turbulence regimes selected in this research study, was shown to suppress VIV. The alteration of the aerodynamic characteristics of the flow field including promoting the trailing-edge vortex shedding, reducing the strength of the separation bubble and removing its impingement onto the side surface is the main reason of this turbulence-induced suppression.

The novel computational approach to simulate the bending VIV of a flexible 5:1 rectangular cylinder was shown to be potential and appropriate. The outcomes not only yield further evidence about the mechanism of the VIV but also reveal some important span-wise flow features, which should be considered when analysing a 3D flexible structure.

The improved 3D Hartlen and Currie model also shows its promising and practicability. It is able to predict similar phenomena as observed in the bending simulation as well as to estimate similar VIV structural response of the Great Belt East bridge as the full-scale measurement.

8.4 POTENTIAL AREAS FOR FUTURE RESEARCH

Apart from these aforementioned conclusions, some issues relating to the wind tunnel dynamic test were noticed during this research study. Due to effects of the end plate, the finite span-wise length of the model and its oscillation, there was some resonance effect limiting the usability of the pressure data to investigate the span-wise correlation. This issue should be studied and a standard guideline to perform a similar type of wind tunnel tests should be produced.

Even though the bending simulation has revealed important flow features regarding the VIV of the flexible 5:1 rectangular cylinder, this computational approach contains a number of disadvantages, which could impair the resolving of the span-wise flow features, particularly around the mid-span where the maximum displacement exhibited. With more available computational resources in the future, it is therefore of interest to improve this approach by increasing the cell density in all directions as well as extending the span-wise length of the domain to simulate the whole first bending mode. In addition, some modifications will allow this approach to simulate the first torsional mode as well as the flutter.

The mechanism of the turbulence-induced suppressing effect on the VIV was shown in this research study. However, these arguments are only applicable for the selected turbulent regimes. In order to further test the hypothesis proposed by Scanlan (1997), it is important to use different turbulence regimes which have length scales in an order of the width of the cylinder. Also, using CFD simulation and a inlet-turbulence generator together with the POD technique can be a promising solution, providing more understanding in this area.

The development of the 3D partly-correlated Hartlen and Currie model has been based on findings and observations of the bending simulation and verified using the full-scale measurement of the Great Belt East bridge. However, these improvements do not include the Scruton-number dependence of the model parameters. A series of wind tunnel dynamic tests or 2D simulations at different values of the Scruton number should be conducted to investigate these relationships, which will then be integrated into the mathematical model.

References

E. Achenbach and E. Heinecke. On vortex shedding from smooth and rough cylinders in the range of Reynolds number 6×10^3 to 5×10^6. *Journal of Fluid Mechanics*, **109**:239 – 251, 1981.

J. Armitt. Eigenvector analysis of pressure fluctuations on the West Burton instrumented cooling tower. *Internal Report RD/L/M 114/68.* Central Electricity Research Laboratories, UK, 1968.

Y. Bai, K. Yang, D. Sun, Y. Zhang, D. Kennedy, F. Williams, and X. Gao. Numerical aerodynamic analysis of bluff bodies at a high Reynolds number with three-dimensional CFD modelling. *Science China: Physics, Mechanics and Astronomy*, **56**:277 – 289, 2013.

C.J. Baker. Aspects of the use of proper orthogonal decomposition of surface pressure fields. *Wind and Structures: An International Journal*, **3**(2):97 – 116, 2000.

J.T. Batina. Unsteady Euler airfoil solutions using unstructured dynamic meshes. *AIAA Journal*, **28**(8): 1381 – 1388, 1990.

S. Benhamadouche, N. Jarrin, Y. Addad, and D. Laurence. Synthetic turbulent inflow conditions based on a vortex method for large eddy simulation. *Progress in Computational Fluid Dynamics, an International Journal*, **6**(123):50 – 57, 2006.

B. Bienkiewicz, Y. Tamura, H.J. Ham, H. Ueda, and K. Hibi. Proper orthogonal decomposition and reconstruction of multi-channel roof pressure. *Journal of Wind Engineering and Industrial Applications*, **54/55**:369 – 381, 1995.

G. Birkhoff. Formation of vortex streets. *Journal of Applied Physics*, **24**:209 – 231, 1953.

R. Bishop and A. Hassan. The lift and drag forces on a circular cylinder oscillating in a flowing fluid. *Proceedings of the Royal Society of London. Series A, Mathematical and Physical Sciences*, **277**(1):51 – 758, 1964.

D.I. Blockley. *The Nature of Structural Design and Safety.* Ellis Horwood Limited, Sussex, 1st edition, 1980.

L. Bruno, D. Francos, N. Coste, and A. Bosco. 3D flow around a rectangular cylinder: A computational study. *Journal of Wind Engineering and Industrial Aerodynamics*, **98**:263 – 276, 2010.

L. Bruno, M.V. Salvetti, and F. Ricciardelli. Benchmark on the Aerodynamics of a Rectangular 5:1 Cylinder: An overview after the first four years of activity. *Journal of Wind Engineering and Industrial Aerodynamics*, **126**(0):87 – 106, 2014.

F. Brusiani, S. de Miranda, L. Patruno, and P. Vaona. On the evaluation of bridge deck flutter derivatives using RANS turbulence model. *Journal of Wind Engineering and Industrial Aerodynamics*, **119**(0), 2013.

H.H. Bruun. *Hot-wire Anemometry: Principles and Signal Analysis.* Oxford University Press Inc., New York, 1st edition, 1995.

S.J. Callander. Force oscillator model for rectangular cylinder. *Journal of Engineering Mechanics*, **115** (6):1336 – 1346, 1989.

S. Cao. *Towards better understanding of bridge aerodynamics - turbulence effects.* In The 14th International Conference on Wind Engineering, Porto Alegre, Brazil, 2015.

L. Caracoglia and N.P. Jones. Time domain vs. frequency domain characterization of aeroelastic forces for bridge deck sections. *Journal of Wind Engineering and Industrial Aerodynamics*, **91**(3):371 – 402, 2003a.

L. Caracoglia and N.P. Jones. A methodology for the experimental extraction of indicial functions for streamlined and bluff deck sections. *Journal of Wind Engineering and Industrial Aerodynamics*, **91**(5): 609 – 636, 2003b.

I.B. Celik, U. Ghia, P.J. Roaches, C.J. Freitas, H. Coleman, and P.E. Raad. Procedure for estimation and reporting of uncertainty due to discretisation in CFD applications. *Journal of Fluids Engineering*, **130**(7), 2008.

X. Chen and A. Kareem. Identification of critical structural modes and flutter derivatives for predicting coupled bridge flutter. *Institution of Civil Engineers*, **96**:1856 – 1870, 2008.

E.C.C. Choi, J. Brownjohn, and Z. Xin. Report on wind tunnel study on the aerodynamic derivatives of the kessock bridge. Technical report, University of Nottingham and Nanyang Technological University, 2004.

L. Cochran and R. Derickson. A physical modeler's view of Computational Wind Engineering. *Journal of Wind Engineering and Industrial Applications*, **99**:139 – 153, 2011.

D. Collings. Lessons from historical bridge failures. *Proceedings of the ICE – Civil Engineering*, **161**(6): 20 – 27, 2008.

A.G. Davenport. *The Response of Slender, Line-like Structures to a Gusty Wind.* In Proceedings of the Institution of Civil Engineers, volume **23**, pages 389 – 408, 1962a.

A.G. Davenport. Response of slender, line-like structures to gusty wind. *Journal of Wind Engineering and Industrial Aerodynamics*, **60**(0), 1962b.

A.G. Davenport. Gust Loading factors. *Journal of Structural Division, ASCE*, **93**:11 – 34, 1967.

A.G. Davenport. The relationship of reliability to wind loading. *Journal of Wind Engineering and Industrial Aerodynamics*, **13**:3 – 27, 1983.

C. Degand and C. Farhat. A three-dimensional torsional spring anology method for unstructured dynamic meshes. *Computer & Structures*, **80**(3 – 4):305 – 316, 2002.

S. Deniz and TH. Staubli. Oscillating rectangular and octagonal profiles: Interaction of leading- and trailing-edge vortex formation. *Journal of Fluids and Structures*, **11**:3 – 11, 1997.

L. di Mare, M. Klein, W.P. Jones, and J. Janicka. Synthetic turbulence inflow conditions for large-eddy simulation. *Physics of Fluids*, **18**(2):025107, 2006.

G. Diana, A. Zasso, F. Resta, and D. Rocchi. *Effects of the yaw angle on the flutter derivatives and vortex shedding of the Messina multi-box girder deck section.* In The 11$^{\text{th}}$ International Conference on Wind Engineering, Texas, USA, 2003.

G. Diana, F. Resta, M. Belloli, and D. Rocchi. On the vortex shedding forcing on suspension bridge deck. *Journal of Wind Engineering and Industrial Aerodynamics*, **94**:341 – 363, 2006.

F. Ding, S.M.J. Spence, and A. Kareem. *Optimizing the aerodynamics of bluff bodies using CFD-based surrogate modelling.* In The 8$^{\text{th}}$ International Colloquium on Bluff Body Aerodynamics and Applications, Boston, USA, 2016.

J. Donea, A. Huerta, J-P. Ponthot, and A. Rodriguez-Ferran. *Arbitrary Lagrangian-Eulerian Methods*, chapter 14, pages 413 – 433. In: Encyclopedia of computational mechanics. John Wiley & Sons, Ltd., 2004.

E. Dowell. Non-linear oscillator models in bluff body aero-elasticity. *Journal of Sound and Vibration*, **75**:251 – 264, 1981.

E.H. Dowell and K.C. Hall. Modeling of fluid-structure interaction. *Annual Review of Fluid Mechanics*, **33**:445 – 490, 2001.

C. Dyrbye and S.O. Hansen. *Wind loads on structures*. Antony Rowe Ltd, Eastbourne, 1999.

G. Ehsan and R.H. Scanlan. Vortex-induced vibration of flexible bridges. *Journal of Engineering Mechanics*, **116**:1392 – 1411, 1990.

Engineering.com-Library. Tacoma Bridge, 2006. URL `http://www.engineering.com/Library/ArticlesPage/tabid/85/ArticleID/171/Tacoma-Bridge.aspx`.

E. de Biolley F. Facchinetti, M.L. adn Langre. Coupling of structure and wake oscillators in vortex-induced. *Journal of Fluids and Structures*, **19**:123 – 140, 2004.

C. Farhat and M. Lesoinne. Two efficient staggered algorithms for the serial and parallel solution of three-dimensional nonlinear transient aeroelastic problems. *Computer Methods in Applied Mechanics and Engineering*, **182**(3 – 4):499 – 515, 2000.

C. Farhat, M. Lesoinne, and N. Maman. Mixed explicit/implicit time integration of coupled aeroelastic problems: Three-field formulation, geometric conservation and distributed solution. *International Journal for Numerical Methods in Fluids*, **21**(10):807 – 835, 1995.

C. Farhat, C. Degand, B. Koobus, and M. Lesoinne. Torsional springs for two-dimensional dynamic unstructured fluid meshes. *Computer Methods in Applied Mechanics and Engineering*, **163**(1 – 4):231 – 245, 1998a.

C. Farhat, M. Lesoinne, and P. Le Tallec. Load and motion transfer algorithms for fluid/structure interaction problems with non-matching discrete interfaces: Momentum and energy conservation, optimal discretisation and application to aeroelasticity. *Computational Methods in Applied Mechanics and Engineering*, **157**(1–2):95 – 114, 1998b.

C. Farhat, K. van der Zee, and P. Geuzaine. Provably second-order time-accurate loosely-coupled solution algorithms for transient nonlinear computational aeroelasticity. *Computer Methods in Applied Mechanics and Engineering*, **195**(17 – 18):1973 – 2001, 2006.

C.C. Feng. The measurements of vortex-induced effects in flow past a stationary and oscillating circular and D-section cylinders. Master's thesis, University of Bristish Columbia, Vancouver, BC, Canada, 1968.

F. Flemming and C.H.K. Williamson. Vortex-induced vibration of a pivoted cylinder. *Journal of Fluid Mechanics*, **522**:215 – 252, 2003.

J.B. Frandsen. Simultaneous pressures and accelerations measured full-scale on the Great Belt East suspension bridge. *Journal of Wind Engineering and Industrial Aerodynamics*, **89**(1):95 – 129, 2001.

I.E. Garrick. On some reciprocal relations in the theory of nonstationary flows. Technical Report 629, National Advisory Committee for Aeronautics, Washington DC., US, 1938.

W.K. George and H.J. Hussein. Locally axisymmetry turbulence. *Journal of Fluid Mechanics*, **233**:1 – 23, 1991.

M. Germano, U. Piomelli, and W.H. Cabot. A Dynamic subgridscale eddy viscosity model. *Physics of Fluids A: Fluid Dynamics (1989–1993)*, **3**(1760), 1991.

J.H. Gerrard. The wakes of cylindrical bluff bodies at low Reynolds number. *Philosiphical Transactions of the Royal Society A*, **288**(1354):351– 381, 1978.

P. Geuzaine, C. Grandmont, and C. Farhat. Design and analysis of ALE schemes with provable second-order time-accuracy for inviscid and viscous flow simulations. *Journal of Computational Physics*, **191** (1):206 – 227, 2003.

L. Gomes and B.J. Vickery. Extreme wind speeds in mixed wind climates. *Journal of Wind Engineering and Industrial Aerodynamics*, **2**:331 – 344, 1978.

I. Goswami, R.H. Scanlan, and N.P. Jones. Vortex-induced vibration of circular cylinder. *Journal of Engineering Mechanics*, **11**:2270 – 2287, 1993.

R. Govardhan and C.H.K. Williamson. Modes of vortex formation and frequency response of a freely vibrating cylinder. *Journal of Fluid Mechanics*, **420**:85 – 130, 2000.

O. Griffin and S. Ramberg. Some recent studies of vortex shedding with application to marine tubulars and risers. *Journal of Engergy Resources and Technology*, **104**(1):2 – 13, 1982.

W.S. Gunter and J.L. Schroeder. High-resolution full-scale measurements of thunderstorm outflow winds. *Journal of Wind Engineering and Industrial Aerodynamics*, **138**:13 – 26, 2015.

F. Haan and A. Kareem. *The Effects of Turbulence on the Aerodynamics of Oscillating Prism.* In The 12th International Conference of Wind Engineering (ICWE12), Cairns, Australia, 2007.

F. Haan and A. Kareem. Anatomy of turbulence effects on the aerodynamics of an oscillating prism. *Journal of Engineering Mechanics*, **135**(9):987 – 999, 2009.

C. Habchi, S. Russeil, D. Bougeard, J. Harion, T. Lemenand, A. Ghanem, D.D. Valle, and H. Peehossaini. Partitioned solver for strongly coupled fluid-structure interaction. *Computer & Structures*, **71**(0):306 – 319, 2013.

K.C. Hall. Eigenanalysis of unsteady flows about arifoils, cascades and wings. *AIAA Journal*, **32**:2426 – 2432, 1994.

K. Hanjalic. Will RANS survive LES? A view of perspectives. *Journal of Fluids Engineering*, **127**:831 – 839, 2005.

R.T. Hartlen and I.G. Currie. Lift-oscillator model for vortex-induced vibration. *Journal of Engineering Mechanics Division (ASCE)*, **96**:577 – 591, 1970.

P. Hemon and F. Santi. On the aeroelastic behaviour of rectangular cylinders in cross-flow. *Journal of Fluids and Structures*, **16**:855 – 889, 2002.

A. Hodgkinson and P. Cooper. *ICE Manual of Bridge Engineering*. ICE Publising, London, 2nd edition, 2008.

H.M. Holmes, J.D. amd Hangan, J. Schroeder, C.W. Letchford, and K. Orwig. A forensic study of the Lubbock-Reese downdraft of 2002. *Wind and Structures: An International Journal*, **11**:137 – 152, 2008.

J.D. Holmes. *Past, present and future of structural wind engineering – with emphasis on applications*. In The 14^{th} International Conference on Wind Engineering, Porto Alegre, Brazil, 2015.

J.D. Holmes, R. Sankaran, K.C.S. Kwok, and M.J. Syme. Eigenvector modes of fluctuating pressures on low-rise building models. *Journal of Wind Engineering and Industrial Applications*, **69 – 71**:697 – 707, 1997.

E.L. Houghton and P.W. Carpenter. *Aerodynamics for Engineering Students*. Butterworth - Heinemann, 5^{th} edition, 2008.

E.L. Houghton and N.B. Carruthers. *Wind Forces on Buiding and Structures: An Introduction*. Edward Arnold Publishers Ltd., London, 1^{st} edition, 1976.

K. Hufnagel and G. Schewe. Force and moment measurement. In C. Tropea, A.L. Yarin, and J.F. Foss, editors, *Springer Handbook of Experimental Fluid Mechanics*, pages 563 – 616. Springer Berlin Heidelberg, 2007.

J.C.R. Hunt, A.A. Way, and P. Moin. Eddies, streamlines and convergence zones in turbulent flows. Technical report, Center for Turbulence Research, 1988.

H. Irwin. The design of spires for wind simulation. *Journal of Wind Engineering and Industrial Aerodynamics*, **7**(3):361 – 366, 1981.

M. Iwamoto and Y. Fujino. Identification of flutter derivatives of bridge deck from free vibration data. *Journal of Wind Engineering and Industrial Aerodynamics*, **54 – 55**:55 – 63, 1995.

W. Iwan and D. Botelho. Vortex-induced oscillation of structures in water. *Journal of Waterway, Port, Coast, and Ocena Division, ASCE*, **111**:289 – 303, 1985.

J.B. Jakobsen. Span-wise structure of lift and overturning moment on a motionless bridge deck. *Journal of Wind Engineering and Industrial Aerodynamics*, **69 − 71**(0):795 – 805, 1997.

M. Jesson and M. Sterling. *The Aerodynamics Admittance Function and Non-stationary Winds.* In The 8th International Colloquium on Bluff Body Aerodynamics and Applications, Boston, USA, 2016.

R.T Jones. The unsteady lift of a wing of finite aspect ratio. Technical Report 681, National Advisory Committee for Aeronautics, Washington DC., US, 1940.

F.E. Jorgensen. *How to Measure Turbulence with Hot-wire Anemometers: A Practical Guide.* Dantec Dynamics A/S, Denmark, 1st edition, 2002.

A. Kareem and J.E. Cermak. Pressure fluctuations on a square building model in boudary layer flows. *Journal of Wind Engineering and Industrial Applications*, **16**:17 – 41, 1984.

A. Kareem and T. Wu. Wind-induced effects on bluff bodies in turbulent flows: Nonstationary, non-Gaussian and nonlinear features . *Journal of Wind Engineering and Industrial Aerodynamics*, **122**(0): 21 – 37, 2013. The Seventh International Colloquium on Bluff Body Aerodynamics and Applications (BBAA7).

A. Kareem, Y. Gao, and L. Hu. *Time-frequency domain modelling framework for non-stationary aerodynamic load effects.* In The 8th International Colloquium on Bluff Body Aerodynamics and Applications, Boston, USA, 2016.

M. Kawatani, H. Kim, H. Uejima, and H. Kobayashi. Effects of turbulence flows on vortex-induced oscillation of bridge girders with basic sections. *Journal of Wind Engineering and Industrial Applications*, **49**(1 – 3):477 – 486, 1993.

M. Kawatani, N. Toda, M. Sato, and H. Kobayashi. Vortex-induced torsional oscillations of bridge girders with basic sections in turbulent flows. *Journal of Wind Engineering and Industrial Applications*, **83**(1 – 3):327 – 336, 1999.

A. Khalak and C.H.K. Williamson. Motions, forces and mode transitions in vortex-induced vibrations at low mass-damping. *Journal of Fluid Mechanics*, **13**(7 – 8):813 – 851, 1999.

H. Kikuchi, Y. Tamura, H. Ueda, and K. Hibi. Dynamic wind pressure acting on a tall building model - Proper orthogonal decomposition. *Journal of Wind Engineering and Industrial Applications*, **69 − 71**: 631 – 646, 1997.

K. Kimura, Y. Fujino, S. Nakato, and H. Tamura. Characteristics of buffeting forces on flat cylinders. *Journal of Wind Engineering and Industrial Aerodynamics*, **69 − 71**(0):365 – 374, 1997.

M. Klein, A. Sadiki, and J. Janicka. A digital filter based generation of inflow data for spatially developing direct numerical or large eddy simulations. *Journal of Computational Physics*, **186**(2):652 – 665, 2003.

H. Kobayashi, M. Kawatani, and O. Nakade. Vortex-induced oscillations of two dimensional rectangular cylinders in large scale turbulence. *Journal of Wind Engineering and Industrial Applications*, **33**(1 – 2):101 – 106, 1990.

H. Kobayashi, M. Kawatani, and H. Kim. Effects of turbulence characteristics on vortex-induced oscillation of rectangular cylinders. *Journal of Wind Engineering and Industrial Applications*, **41**:775 – 784, 1992.

A.N. Kolmogorov. The local structure of turbulence in incompressible viscous fluid in very large Reynolds numbers. *Proceedings: Mathematical and Physics Sciences*, **433**:9 – 13, 1941.

N. Kornev and E. Hassel. Method of random sports for generation of synthetic inhomogeneous turbulent fields with prescribed autocorrelation functions. *Communications in Numerical Methods in Engineering*, **23**(0):35 – 43, 2007.

K.A. Kosiba and J. Wurman. The three-dimensional structure and evolution of a tornado boundary layer. *Weather and Forecasting*, **28**(6):1552 – 1561, 2013.

S. Kotmasu and H. Kobayashi. Vortex-induced oscillation of bluff bodies. *Journal of Wind Engineering and Industrial Aerodynamics*, **6**(3/4):335 – 362, 1980.

S. Krenk and S.R.K. Nielsen. Energy balanced double oscillator model for vortex-induced vibrations. *Journal of Engineering Mechanics*, **125**(3):263 – 271, 1999.

D. Kwon and A. Kareem. Gust-Front Factor: A new framework for wind load effects on structures. *Journal of Structural Engineering, ASCE*, **135**(6):717 – 732, 2009.

F.T. Lambardo, D.A. Smith, J.L. Schroder, and K.C. Mehta. Thunderstorm characteristics of importance to wind engineering. *Journal of Wind Engineering and Industrial Aerodynamics*, **125**:121 – 132, 2014.

R. Landl. A mathematical model for vortex-excited vibrations of bluff bodies. *Journal of Sound and Vibration*, **42**:219 – 234, 1975.

G.L. Larose. The spatial distribution of unsteady loading due to gusts on bridge decks. *Journal of Wind Engineering and Industrial Aerodynamics*, **91**(12 – 15):1431 – 1443, 2003.

G.L. Larose and J. Mann. Gust loading on streamlined bridge deck. *Journal of Fluids and Structures*, **12**(5):511 – 536, 1998.

A. Larsen. Aerodynamics aspects of the final design of the 1624m suspension bridge across the Great Belt. *Journal of Wind Engineering and Industrial Aerodynamics*, **48**(2 – 3):261 – 285, 1993.

A. Larsen. A generialized model for assessment of vortex-induced vibrations of flexible structures. *Journal of Wind Engineering and Industrial Aerodynamics*, **57**(2 – 3):281 – 294, 1995.

A. Larsen and J.H. Walther. Discrete vortex simulation of flow around five generic bridge deck sections. *Journal of Wind Engineering and Industrial Aerodynamics*, **77 − 78**:591 – 602, 1998.

T.H. Le and L. Caracoglia. *Enabling analytical formulation for the tornado-induced dynamic response of tall buildings.* In The 8$^{\text{th}}$ International Colloquium on Bluff Body Aerodynamics and Applications, Boston, USA, 2016.

B.E. Lee. The effects of turbulence on the surface pressure field of a square prism. *Journal of Fluid Mechanics*, **69**(2):263 – 282, 1975.

C.W. Letchford and F.T. Lombardo. *Is codification of non-synoptic wind loads possible?* In The 14$^{\text{th}}$ International Conference on Wind Engineering, Porto Alegre, Brazil, 2015.

C.W. Letchford, C. Mans, and M.T. Chay. Thunderstorms and their importance in wind engineering. *Journal of Wind Engineering and Industrial Aerodynamics*, **90**:1415 – 1433, 2002.

M. Levy and M. Salvadori. *Why Buildings Fall Down: How Structures Fail.* W.W. Norton & Company, New York, 2$^{\text{nd}}$ edition, 2002.

T. Leweke and C.H.K. Williamson. Three-dimensional instabilities in wake region. *European Journal of Mechanics - B/Fluids*, **17**(4):571 – 586, 1998.

J.H. Lienhard. Synopsis of lift, drag and vortex shedding frequency data of rigid circular cylinders. Technical report, Bullentin 300, Washington State University, 1966.

T.S. Lund, X. Wu, and K.D. Squires. Generation of turbulent inflow data for spatially-developing boundary layer simulations. *Journal of Computational Physics*, **140**:233 – 258, 1998.

P.A. MacDonald, J.D. Holmes, and K.C.S. Kwok. Wind loads on ciruclar storage binds, silos and tanks. III: Fluctuating and peak pressure distributions . *Journal of Wind Engineering and Industrial Applications*, **34**:319 – 337, 1990.

L.W. Malvern. *Introduction ot the Mechanics of a Continuous Medium.* Precentice Hall: Englewodd Cliffs, 1969.

A.M. Marra, C. Mannini, and G Bartolo. Van der Pol-type equation for modelling vortex-induced oscillations of bridge decks. *Journal of Wind Engineering and Industrial Aerodynamics*, **99**(6 – 7):776 – 785, 2011.

A.M. Marra, C. Mannini, and G. Bartolli. Measurements and improved model of vortex-induced vibration for an elongated rectangular cylinder. *Journal of Wind Engineering and Industrial Aerodynamics*, **147**: 358 – 368, 2015.

T. Martin and I.A. Macleod. The Tay rail bridge disaster – A reappraisal based on modern ananlysis method. *Proceeding of the ICE – Civil Engineering*, **108**(2):77 – 83, 1995.

M. Matsumoto. *Bluff body aerodynamics/bridge aerodynamics - Vortex interaction to aerodynamic instability.* In *The First International Symposium on Wing Effects on Buildings and Urban Environment (ISWE1)*, Tokyo, Japan, 2004.

M. Matsumoto, H. Shirato, K. Araki, T. Haramura, and T. Hashimoto. Spanwise coherence characteristics of surface pressure field on 2D bluff bodies. *Journal of Wind Engineering and Industrial Aerodynamics*, **91**(1 – 2):155 – 163, 2003.

M. Matsumoto, T. Yagi, H. Tamaki, and T. Tsubota. Vortex-induced vibration and its effect on torsional flutter instability in the case of $B/D = 4$ rectangular cylinder. *Journal of Wind Engineering and Industrial Aerodynamics*, **96**(6 – 7):971 – 983, 2008.

R. Mills, J. Sheridan, K. Hourgigan, and M.C. Welse. *The mechanism controlling vortex shedding from rectangular bluff bodies.* In Proceedings of the Twelfth Australasian Fluid Mechanics Conference, Sydney, Australia, 1995.

R. Mills, J. Sheridan, and K. Hourigan. Partical Image Velocimetry and visualisation of natural and forced flow around rectangular. *Journal of Wind and Mechanics*, **478**:299 – 323, 2003.

M.S. Mohammed and J.C. laRue. The decay power law in grid-generated turbulence. *Journal of Fluid Mechanics*, **219**:195 – 214, 1990.

Y. Nakamura and M. Nakashima. Vortex excitation of prisms with elongated rectangular, H and T-cross-sections. *Journal of Fluids and Structures*, **163**:149 – 169, 1986.

Y. Nakamura, Y. Ohya, and H. Tsuruta. Experiments on vortex shedding from flat plates with square leading and trailing edges. *Journal of Fluid Engineering*, **222**:473 – 447, 1991.

Z. Nasir and G.T. Bitsuamlak. *Tornado like vortex induced load on a bluff-body with and without openings.* In The 8$^{\text{th}}$ International Colloquium on Bluff Body Aerodynamics and Applications, Boston, USA, 2016.

E. Naudascher and D. Rockwell. *Flow Induced Vibrations - An Engineering Guide.* A.A.Balkema, 1994.

E. Naudascher and Y. Wang. Flow-induced vibartions of prismatic bodies and grids of prisms. *Journal of Fluids and Structures*, **7**(4):341 – 373, 1993.

M. Noda, H. Utsonomiya, F. Nagao, M. Kanda, and N. Shiraishi. Effects of oscillation amplitude on aerodynamic derivatives. *Journal of Wind Engineering and Industrial Aerodynamics*, **91**(1 – 2):101 – 111, 2003.

W.F. Noh. CFL: A time-dependent two-space dimensional coupling Eulerian-Lagrangian code. In *Methods in Computational Physics, Alder B, Fernbach S and Rotenberg M (eds)*, volume 3, pages 117 – 179. Academic Press: New York, 1964.

Y. Ohya, Y. Nakamura, S. Ozono, and H. Tsuruta. A numerical study of vortex shedding from flat plates with square leading and trailing edges. *Journal of Fluid Mechanics*, **236**:445 – 460, 1992.

A. Okjima. Strouhal numbers of rectangular cylinders. *Journal of Fluid Mechanics*, **123**:379 – 398, 1982.

OpenFOAM. *OpenFOAM-2.2.2 - The Open Source CFD Toolbox: User Guide*. SGI Corp, 2013.

J.S. Owen, D.M. Hargreaves, and X.H.P. Gu. *Modelling the Mechanism of Vortex Induced Response of Bridge Deck*. In The 7$^{\text{th}}$ UK Conference on Wind Engineering (WES 06), Glasgow, 2006.

S. Ozono, Y. Ohya, Y. Nakamura, and R. Nakayama. Stepwise increase in the Strouhal number for flows around flat plates. *International Journal for Numerical Methods in Fluid*, **15**(9):1025 – 1036, 1992.

G. Parkinson, C. Feng, and N. Ferguson. *Mechanisms of vortex excited vibrations of bluff cylinders*. In *Proceedings of Symposium on Wind Effects on Buildings and Structures*, Loughborough, England, 1968.

L. Perret, J. Deville, R. Manceau, and J-P. Bonnet. Turbulent inflow conditions for large-eddy simulation based on low-order empirical model. *Physics of Fluids*, **20**:075107-1-17, 2008.

S. Piperno, C. Farhat, and B. Larrouturou. Paritioned procedures for the transient solution of coupled aeroelastic problems. *Computational Methods for Applied Mechanical Engineering*, **124**:79 – 711, 1995.

P. Plaschko. Global chaos in flow-induced oscillations of cylinders. *Journal of Fluids and Structures*, **14**: 883 – 893, 2000.

S.B. Pope. *Turbulent flow*. Cambridge: Cambridge University Press, 2000.

F. Ricciardelli and A.M. Marra. *Sectional aerodynmic forces and their longitudinal correlation on a vibrating 5:1 rectangular cylinder*. In BBAA VI International Colloquium on: Bluff Bodies Aerodynamics and Applications, Milano, Italy, 2008.

F. Ricciardelli, E.T. De Grenet, and G. Solari. Analysis of the wind loading of a bridge deck box section using proper orthogonal decomposition. *International Journal of Fluid Mechanics Research*, **29**(3 – 4): 312 – 332, 2002.

L.F. Richardson. *Weather prediction by numerical process.* Cambridge: Cambridge University Press, 1922.

P.J. Roache. Quantification of uncertainty in computational fluid dynamics. *Annual Reviews of Fluid Mechanics*, **29**:123 – 160, 1997.

A. Roshko. Experiments on the flow past a circular cylinder at very high Reynolds number. *Journal of Fluid Mechanics*, 10:345 – –356, 1961.

T. Sarpkaya. Fluid forces on oscillating cylinders. *Journal of Waterway, Port, Coast, and Ocean Division, ASCE*, **104**:275 – 290, 1978.

T. Sarpkaya. Vortex-induced oscillation – A selective review. *Journal of Applied Mechanics*, **46**:241 – 258, 1979.

R. Scanlan. Amplitude and turbulence effects on bridge flutter derivatives. *Journal of Structural Engineering*, **123**(2):232 – 236, 1997.

R.H. Scanlan. Bridge flutter derivatives at vortex lock-in. *Journal of Strucutral Engineering*, **124**(4):450 – 458, 1998.

R.H. Scanlan. Observations on low-speed aeroelasticity. *Journal of Engineering Mechanics (ASCE)*, **128** (12):1254 – 1258, 2002.

R.H. Scanlan and J.J. Tomko. Airfoil and bridge deck flutter derivatives. *Journal of Engineering Mechanics Division (ASCE)*, **97**(6):1717 – 1737, 1971.

G. Schewe. Reynolds-number-effect in flow around a rectangular cylinder with aspect ratio 1:5. *Journal of Fluids and Structures*, **36**(0):16 – 25, 2013.

C. Scruton. *On the wind-excited oscillations of stacks, towers and masts.* In *Proceedings of the Interantional Conference on the Wind Effects on Buildings and Structures*, pages 798 – 837, Teddington, Middlesex, 1963.

A. Selberg. Oscillation and aerodynamic stability of suspension bridge. *Civil Engineering and Building Construction Series, ACTA Polytechnica Scandinavica*, **13**:1 – 69, 1961.

V. Shankar and H. Ide. Aeroelastic computations of flexible configurations. *Computers & Structures*, **30**: 15 – 28, 1988.

K. Shimada and T. Ishihara. Application of a modifed k - ϵ model to the prediction of of aerodynamic characteristics of rectangular cross-section cylinders. *Journal of Fluids and Structures*, **16**(4):465 – 485, 2002.

N. Shiraishi and M. Matsumoto. On classification of vortex-induced oscillation and its application for bridge structures. *Journal of Wind Engineering and Industrial Aerodynamics*, **14**(1 – 3):463 – 508, 1983.

E. Simiu and R.H. Scanlan. *Wind Effects on Structures: Fundamentals and Applications to Design*. John Wiley & Sons, Inc., USA, 3rd edition, 1996.

L. Sirovich. Turbulence and the dynamcis of coherent sturctures. *Quaterly of Applied Mathematics*, **45**: 561 – 590, 1987.

R. Skop and O. Griffin. A model for the vortex-excited resonant response of bluff cylinders. *Journal of Sound and Vibration*, **27**:225 – 233, 1973a.

R. Skop, O. Griffin, and G. Koopman. The vortex-excited resonant vibrations of circular cylinders. *Journal of Sound and Vibration*, **26**:867 – 884, 1973b.

R.A. Skop and S Balasubramanian. A new twist on an old model for vortex-excited vibraion. *Journal of Fluids and Structures*, **11**:395 – 412, 1997.

G. Solari. Emering issues and new fremaworks for wind loading on structures in mixed climates. *Wind and Structures: An International Journal*, **19**(3):295 – 320, 2014.

G. Solari and D. Rainisio. *Monte Carlo simulation of thunderstorm outflows and wind-excited response of structures*. In The 8th International Colloquium on Bluff Body Aerodynamics and Applications, Boston, USA, 2016.

G. Solari, L. Carassale, and F. Tubino. Proper orthogonal decomposition in wind engineering. Part 1: A state-of-the-art and some prospects. *Wind and Structures: An International Journal*, **10**(2):153 – 176, 2007.

G. Solari, M. Burlando, P. Ge Gaetano, and M.P. Repetto. Characteristics of thunderstorms relevant to the wind loading on structures. *Wind and Structures: An International Journal*, **20**(6):763 – 791, 2015.

A.N. Stokes and M.C. Welsh. Flow-resonant sound intercation in a duct containing a plate, II: Square leading edge. *Journal of Sound and Vibration*, **104**(1):55 – 73, 1986.

D. Sun, J.S. Owen, N.G. Wright, and K.F. Liaw. Fluid-structure interaction of prismatic line-like structure, using LES and block-iterative coupling. *Journal of Wind Engineering and Industrial Aerodynamics*, **96**(6 – 7), 2008.

D. Sun, J.S. Owen, and N.G. Wright. Application of the k-ω turbulence model for a wind-induced vibration study of 2D bluff bodies. *Journal of Wind Engineering and Industrial Aerodynamics*, **97**(2), 2009.

G.R. Tabor and M.H. Baba-Ahmadi. Inlet conditions for large eddy simulation: A review. *Computer & Fluids*, **39**(4):553 – 567, 2010.

Y. Tamura and G. Matsui. *Wake-oscillator model of vortex-induced oscillation of circular cylinder*. In *Proceedings of the Fifth International Conference on Wind Engineering*, pages 1085 – 1094, Fort Collins, Colorado, USA, 1979.

Y. Tamura, H. Ueda, K. Hibi, S. Suganuma, and B. Bienkiewicz. Proper orthogonal decomposition study of approach wind-building pressure correlation. *Journal of Wind Engineering and Industrial Applications*, **72**:421 – 432, 1997.

B.T. Tan, M.C. Thompson, and K. Hourigan. Simulated flow around long plates under cross flow pertubations. *International Journal of Fluid Dynamics*, **2**(1), 1998.

A.H. Techet, F.S. Hover, and M.S. Triantafyllou. Vortical patterns behind a tapered cylinder oscillating transversely to a uniform flow. *Journal of Fluid Mechanics*, **363**:79 – 96, 1998.

T. Theoderson. General theory of aerodynamic instability and the mechanism of flutter. Technical Report 496, National Advisory Committee for Aeronautics, Washington DC., US, 1935.

A.G. Tomboulides, G.S. Trantafyllou, and G. Karniadakis. A new mechanism of preiod boulding in free shear flow. *Physics of Fluids A*, **5**:1329 – 1332, 1992.

D.J. Tritton. Experiments on the flow past a circular at low Reynolds number. *Journal of Fluid Mechanics*, **6**(3):547 – 567, 1959.

TSI-Incorporated. *TSI Thermal Anemometry Probes*, 2003.

TSI-Incorporated. *IFA 300 Constant Temperature Anemometer System: Operation Manual*, 2010a.

TSI-Incorporated. *Model 1127/1128: Air Velocity Calibrator - User's Manual*, 2010b.

L.A. Twisdale and P.J. Vickery. Research on thunderstorm wind design parameters. *Journal of Wind Engineering and Industrial Aerodynamics*, **41**:93 – 104, 1992.

C.W. Van Atta and M. Gharib. Ordered and chaotic vortex streets behind circular cylinders at low Reynolds number. *Journal of Fluid Mechanics*, **174**:113 – 133, 1987.

B. van der Pol. A theory of the amplitude of free and forced triode oscillation. *Radio Review*, **1**:701 – 1010, 754 – 762, 1920.

H.K. Versteeg and W. Malalasekera. *An Introduction to Computational Fluid Dynamics: The Finite Volume Method*. Pearson Education Limited, England, 2nd edition, 2007.

B. Vickery and R. Basu. Across-wind vibrations of structures of circular cross-section. Part I: Development of a mathematical model for two-dimensional conditions. *Journal of Wind Engineering and Industrial Aerodynamics*, **12**(1):49 – 73, 1983.

B. Vickery and B. Watkins. *Flow-induced vibrations of cylindrical strucutres.* In *Silvester, R. (ED.), Proceedings of the First Australian Conference on Hydralics and Fluid Mechanics.* Pergamon Press, New York, 1964.

B.J. Vickery. Fluctuating lift and drag on a long cylinder of square cross-section in a smooth and in a turbulent stream. *Journal of Fluid Mechanics*, **25**(3):481 – 494, 1966.

D.E.J. Walshe. The use of models to predict the oscillatory behaviour of suspension bridges in wind. Technical Report 17, National Physics Laboratory, UK, 1977.

J. Wang, W. Pang, S. Cao, and F. Fan. *Development of a 3D tornado wind field model.* In The 8^{th} International Colloquium on Bluff Body Aerodynamics and Applications, Boston, USA, 2016.

N.P. Waterson and N. Baker. *Numerical Prediction of Flutter Behaviour for Long-span Bridge Decks.* In The 5^{th} International Symposium on Computational Wind Engineering (CWE2010), North Carolina, USA, 2010.

G. Weber, J. Dist, and M. Maslanke. *Semi-active TMS concept for Volgograd bridge.* In *Conference Proceedings of the Society for Experimental Mechanics Series*, pages 79 – 88, 2013.

S. Weeratunga and E. Pramono. Direct coupled aeroelastic analysis through concurrent implicit time integration on a parallel computer. In 35^{th} *Structures, Structural Dynamics and Materials Conference.* AIAA, 1994.

A.J. Weight. *Critical analysis of the Great Belt East Bridge.* In *Proceedings of Bridge Engineering 2 Conference 2009*, Bath, UK, 2009.

J.C. Williams. Incompressible boundary-layer separation. *Annual Reviews of Fluid Mechanics*, **9**:113 – 144, 1977.

R.G. Williams and W. Suaris. A analytical approach to wake inteference effects on circular cylindrical structure. *Journal of Sound and Vibration*, **295**:266 – 281, 2006.

R.G. Williams, W. Suaris, and R.H. Goodman. A mathematical simulation to synchronization of a bluff bodies. *Journal of Fluids and Structures*, **26**:467 – 481, 2010.

C.H.K. Williamson. Defining a universal and continuous Strouhal-Reynolds number relationship for the laminar vortex shedding of a circular cylinder. *Physics of Fluids*, **21**(10):2742 – 2744, 1988a.

C.H.K. Williamson. The existence of two stages in the transition to three-dimensionality of a circular wake. *Physics of Fluids*, **31**(11):3165 – 3168, 1988b.

C.H.K. Williamson. Oblique and parallel modes of vortex shedding in the wake of a circular cylinder at low Reynolds numbers. *Journal of Fluid Mechanics*, **206**:579 – 627, 1989.

C.H.K. Williamson. The natural and forced formation of spot-like 'vortex dislocations' in the transition of a wake. *Journal of Fluid Mechanics*, **243**:393 – 411, 1992.

C.H.K. Williamson. Three-dimensional vortex dynamics in bluff bodies wake. *Experimental Thermal and Fluid Science*, **12**(2):150 – 168, 1996.

C.H.K. Williamson. Advanced in our understanding of vortex dynamics in bluff body wakes. *Journal of Wind Engineering and Industrial Aerodynamics*, **69-71**(0):3 – 32, 1997.

C.H.K. Williamson and R. Govardhan. Vortex-induced Vibrations. *Annual Review of Fluid Mechanics*, **36**(1):413 – 455, 2004.

C.H.K. Williamson and R. Govardhan. A brief review of recent results in vortex-induced vibrations. *Journal of Wind Engineering and Industrial Aerodynamics*, **96**(6 – 7):713 – 735, 2008.

C. Wood, A.J. Gil, O. Hassan, and J. Bonet. Partitioned block-Gauss-Seidel coupling for dynamic fluid-structure interaction. *Computer & Structures*, **88**(23 – 24):1367 – 1382, 2010.

T. Wu and A. Kareem. An overview of vortex-induced vibration (VIV) of bridge decks. *Journal of Frontiers of Structural and Civil Engineering*, **6**(64):335 – 347, 2012.

H. Xiang and Y. Ge. Refinements on aerodynamic stability analysis of super long-span bridge. *Journal of Wind Engineering and Industrial Aerodynamics*, **90**(12 – 15):1493 – 1515, 2002. Fifth Asia-Pacific Conference on Wind Engineering.

Z-T. Xie and I.P. Castro. Efficient generation of inflow conditions for large eddy simulation of stree-scale flows. *Flow, Turbulence and Combustion*, **81**(3):449 – 470, 2008.

K. Xu, Y. Ge, and D. Zhang. Wake oscillator model for assessment of vortex-induced vibration of flexible structures under wind action. *Journal of Wind Engineering and Industrial Aerodynamics*, **136**:192 – 200, 2015.

D. Yu and A. Kareem. Parametric study of flow around rectangular prisms using LES. *Journal of Wind Engineering and Industrial Aerodynamics*, **77** − **78**:653 – 662, 1998.

M. Zdravkovich. Scruton number: A proposal. *Journal of Wind Engineering and Industrial Aerodynamics*, **10**(3):263 – 265, 1982.

M. Zdravkovich. On origins of hysterisis responses of a circular cylinder induced by vortex shedding]. *Flugwissenschaften Weltraumforschung (German)*, **14**:47 – 58, 1990.

X. Zhang, J. Brownjohn, and P. Omenzetter. Time domain formulation of self-excited forces on bridge deck for wind tunnel experiment. *Journal of Wind Engineering and Industrial Aerodynamics*, **91**(6): 561 – 590, 2003.

Z. Zhu and Z. Chen. Large eddy simulation of aerodynamics of a flat box girder on long-span bridges. *Procedia Engineering*, **61**:212 – 219, 2013.

Appendix A

OpenFOAM Source Files and MATLAB Scripts

A.1 OPENFOAM SOURCE FILES

A.1.1 dynamicHeavingFreeUDFFvMesh.C

```
/*---------------------------------------------------------------------------*\
  =========                 |
  \\      /  F ield         | OpenFOAM: The Open Source CFD Toolbox
   \\    /   O peration     |
    \\  /    A nd           | Copyright (C) 2011 OpenFOAM Foundation
     \\/     M anipulation  |
-------------------------------------------------------------------------------
License
    This file is part of OpenFOAM.

    OpenFOAM is free software: you can redistribute it and/or modify it
    under the terms of the GNU General Public License as published by
    the Free Software Foundation, either version 3 of the License, or
    (at your option) any later version.

    OpenFOAM is distributed in the hope that it will be useful, but WITHOUT
    ANY WARRANTY; without even the implied warranty of MERCHANTABILITY or
    FITNESS FOR A PARTICULAR PURPOSE.  See the GNU General Public License
    for more details.
```

```

    You should have received a copy of the GNU General Public License
    along with OpenFOAM.  If not, see <http://www.gnu.org/licenses/>.

\*---------------------------------------------------------------------------*/

#include "dynamicHeavingFreeUDFFvMesh.H"
#include "addToRunTimeSelectionTable.H"
#include "volFields.H"
#include "mathematicalConstants.H"
#include "forces.H"
#include "forceCoeffs.H"
#include "dictionary.H"
#include "wordReList.H"
#include "fvMesh.H"
#include "fvcGrad.H"
#include "Pstream.H"

// * * * * * * * * * * * * * * Static Data Members * * * * * * * * * * * * * //

namespace Foam
{
    defineTypeNameAndDebug(dynamicHeavingFreeUDFFvMesh, 0);
    addToRunTimeSelectionTable(dynamicFvMesh, dynamicHeavingFreeUDFFvMesh, IOobject);
}


// * * * * * * * * * * * * * * * * Constructors  * * * * * * * * * * * * * * //

Foam::dynamicHeavingFreeUDFFvMesh::dynamicHeavingFreeUDFFvMesh(const IOobject& io)
:
    dynamicFvMesh(io),
    dynamicMeshCoeffs_
    (
        IOdictionary
```

```
        (
            IOobject
            (
                "dynamicMeshDict",
                io.time().constant(),
                *this,
                IOobject::MUST_READ_IF_MODIFIED,
                IOobject::NO_WRITE,
                false
            )
        ).subDict(typeName + "Coeffs")
    ),
    /*Read in parameters of the mesh geometry*/
    B1(readScalar(dynamicMeshCoeffs_.lookup("B1"))),
    B2(readScalar(dynamicMeshCoeffs_.lookup("B2"))),
    B3(readScalar(dynamicMeshCoeffs_.lookup("B3"))),
    B4(readScalar(dynamicMeshCoeffs_.lookup("B4"))),
    D1(readScalar(dynamicMeshCoeffs_.lookup("D1"))),
    D2(readScalar(dynamicMeshCoeffs_.lookup("D2"))),
    D3(readScalar(dynamicMeshCoeffs_.lookup("D3"))),
    D4(readScalar(dynamicMeshCoeffs_.lookup("D4"))),
    L(readScalar(dynamicMeshCoeffs_.lookup("L"))),
    /*Read in parameters for the calculation of structural response*/
    M(readScalar(dynamicMeshCoeffs_.lookup("mass"))),
    fnb(readScalar(dynamicMeshCoeffs_.lookup("fnb"))),
    quib(readScalar(dynamicMeshCoeffs_.lookup("quib"))),
    rho_(readScalar(dynamicMeshCoeffs_.lookup("rho"))),
    nu_(readScalar(dynamicMeshCoeffs_.lookup("nu"))),
    /*Initialise the initial position*/
    z_n(readScalar(dynamicMeshCoeffs_.lookup("z_0"))),
    zdot_n(readScalar(dynamicMeshCoeffs_.lookup("zdot_0"))),
    zddot_n(readScalar(dynamicMeshCoeffs_.lookup("zddot_0"))),
    tn(readScalar(dynamicMeshCoeffs_.lookup("t_0"))),
    /*Store the initial positions of nodes*/
    zeroPoints_
```

```
    (
        IOobject
        (
            "points",
            io.time().constant(),
            meshSubDir,
            *this,
            IOobject::MUST_READ,
            IOobject::NO_WRITE
        )
    )
{}

// * * * * * * * * * * * * * * * * Destructor  * * * * * * * * * * * * * * * //

Foam::dynamicHeavingFreeUDFFvMesh::~dynamicHeavingFreeUDFFvMesh()
{}

// * * * * * * * * * * * * * * * Member Functions  * * * * * * * * * * * * * //

bool Foam::dynamicHeavingFreeUDFFvMesh::update()
{
  /**********************************/
  /*** CALCULATE FORCES AND MOMENT ***/
  pName_ = dynamicMeshCoeffs_.lookupOrDefault<word>("pName", "p");
  UName_ = dynamicMeshCoeffs_.lookupOrDefault<word>("UName", "U");
  dynamicMeshCoeffs_.lookup("liftDir") >> liftDir_;
  dynamicMeshCoeffs_.lookup("dragDir") >> dragDir_;
  dynamicMeshCoeffs_.lookup("pitchAxis") >> pitchAxis_;

  const volVectorField& U = lookupObject<volVectorField>(UName_);
  const volScalarField& p = lookupObject<volScalarField>(pName_);

  const fvMesh& mesh = p.mesh();
  const polyBoundaryMesh& pbm = mesh.boundaryMesh();
```

```
  patchSet_ = pbm.patchSet(wordReList(dynamicMeshCoeffs_.lookup("patches")));
  const surfaceVectorField::GeometricBoundaryField& Sfb = mesh.Sf().boundaryField();

  const volSymmTensorField devRhoReff = -rho_*nu_*dev(twoSymm(fvc::grad(U)));
  tmp<volSymmTensorField> tdevRhoReff = devRhoReff;
  const volSymmTensorField::GeometricBoundaryField& devRhoReffb =
   tdevRhoReff().boundaryField();

  List<Field<vector> > forcePatch(1);
  List<Field<vector> > momentPatch(1);
  forcePatch[0].setSize(1);
  momentPatch[0].setSize(1);
  forcePatch[0] = vector::zero;
  momentPatch[0] = vector::zero;

  forAllConstIter(labelHashSet, patchSet_, iter)
    {
      label faceI = iter.key();

      vectorField F = (rho_*Sfb[faceI]*p.boundaryField()[faceI]) +
(Sfb[faceI] & devRhoReffb[faceI]);

      forcePatch[0] += sum(F);

      vectorField M = (((mesh.C().boundaryField()
[faceI])^(rho_*Sfb[faceI]*p.boundaryField()[faceI])) +
((mesh.C().boundaryField()[faceI])^(Sfb[faceI] & devRhoReffb[faceI])));

      momentPatch[0] += sum(M);
    }

  Pstream::listCombineGather(forcePatch, plusEqOp<vectorField>());
  Pstream::listCombineScatter(forcePatch);
  Pstream::listCombineGather(momentPatch, plusEqOp<vectorField>());
  Pstream::listCombineScatter(momentPatch);
```

```

Field<vector> totalForcePatch = (forcePatch[0]);
Field<vector> totalMomentPatch = (momentPatch[0]);

List<Field<scalar> > forceMoment(3);
forceMoment[0].setSize(1);
forceMoment[1].setSize(1);
forceMoment[2].setSize(1);
forceMoment[0] = (totalForcePatch & liftDir_);
forceMoment[1] = (totalForcePatch & dragDir_);
forceMoment[2] = (totalMomentPatch & pitchAxis_);

scalar FL_n = sum(forceMoment[0]);
scalar FD_n = sum(forceMoment[1]);
scalar M_n = sum(forceMoment[2]);

/*********************************************/
/*** OUTPUT FORCES AND MOMENT TO LOG FILES ***/
Info << "structuralTime " << tn << endl;
Info << "Lift " << FL_n << endl;
Info << "Drag " << FD_n << endl;
Info << "Moment " << M_n << endl;

/************************/
/*** STRUCTURAL SOLVER ***/
/* Caculate the model displacement, velocity and acceleration */
scalar timeStep = time().value() - tn;
scalar wnb = 2*constant::mathematical::pi*fnb;
scalar zddot_n1 = FL_n/M - 2*quib*wnb*zdot_n - wnb*wnb*z_n;
scalar zdot_n1 = zdot_n + timeStep*zddot_n1;
scalar z_n1 = z_n + timeStep*zdot_n1;

/* Assign the model displacement to the amplitude of oscillation of the model */
amplitude = z_n1;

```

```
  /******************************/
  /*** MOVING NODES ALGORITHM ***/
  /* Access all the points on the mesh and move them accordingly */
  pointField zeroPoints = zeroPoints_;
  forAll(zeroPoints, pointI)
    {
      scalar pointX = zeroPoints[pointI].component(0);
      scalar pointZ = zeroPoints[pointI].component(2);

      /*Calculate the movemen of points on the model*/
      scalar amplitudeZ = amplitude;

      /*Block 8 - Upstream middle block - Rigid zone*/
      if ( (fabs(pointZ) <= D2) && (pointX < -B2) )
{
  scalar pointDz = amplitudeZ;
  zeroPoints[pointI].component(2) += pointDz;
}

      /*Block 9 - Centre middle block - Rigid zone*/
      if ( (fabs(pointZ) <= D2) && (pointX >= -B2) && (pointX <= B3) )
{
  scalar pointDz = amplitudeZ;
  zeroPoints[pointI].component(2) += pointDz;
}

      /*Block 4 - Downstream middle block - Buffer zone */
      if ( (fabs(pointZ) <= D2) && (pointX > B3) )
{
  scalar pointDz = amplitudeZ*(1 - 1/B4*(pointX - B3));
  zeroPoints[pointI].component(2) += pointDz;
}

      /*Block 1 + 2 - Upstream and centre top blocks - Buffer zones*/
      if ( (pointZ > D2) && (pointX <= B3) )
```

```
{
  scalar pointDz = amplitudeZ*(D1 + D2 - pointZ)/D1;
  zeroPoints[pointI].component(2) += pointDz;
}

      /*Block 3 - Downstream top block - Buffer zone*/
      if ( (pointZ > D2) && (pointX > B3) )
{
  scalar pointDz = amplitudeZ*(1 - 1/B4*(pointX - B3))*(D1 + D2 - pointZ)/D1;
  zeroPoints[pointI].component(2) += pointDz;
}

      /*Block 7 + 6 - Upstream and centre bottom blocks - Buffer zones*/
      if ( (pointZ < -D3) && (pointX <= B3) )
{
  scalar pointDz = amplitudeZ*(-D3 - D4 - pointZ)/(-D4);
  zeroPoints[pointI].component(2) += pointDz;
}

      /*Block 5 - Downstream bottom block - Buffer zone*/
      if ( (pointZ < -D3) && (pointX > B3) )
{
  scalar pointDz = amplitudeZ*(1 - 1/B4*(pointX - B3))*(-D3 - D4 - pointZ)/(-D4);
  zeroPoints[pointI].component(2) += pointDz;
}
    }

  /************************************************/
  /*** OUTPUT STRUCTURAL RESPONSES TO LOG FILES ***/
  Info << "Displacment " << z_n << endl;
  Info << "Velocity " << zdot_n << endl;
  Info << "Acceleration " << zddot_n << endl;
  Info << "Time step " << timeStep << endl;

  /**************************************************/
```

```
  /*** STORE MODEL INFORMATION FOR NEXT TIME STEP ***/
  z_n = z_n1;
  zdot_n = zdot_n1;
  zddot_n = zddot_n1;
  tn = time().value();

  fvMesh::movePoints(zeroPoints);

  if (foundObject<volVectorField>("U"))
    {
      volVectorField& U =
const_cast<volVectorField&>(lookupObject<volVectorField>("U"));
      U.correctBoundaryConditions();
    }

  return true;
}

// ************************************************************************* //
```

A.1.2 dynamicBendingFreeUDFFvMesh.C

```
/
*---------------------------------------------------------------------------*\
  =========                 |
  \\      /  F ield         | OpenFOAM: The Open Source CFD Toolbox
   \\    /   O peration     |
    \\  /    A nd           | Copyright (C) 2011 OpenFOAM Foundation
     \\/     M anipulation  |
-------------------------------------------------------------------------------
License
    This file is part of OpenFOAM.

    OpenFOAM is free software: you can redistribute it and/or modify it
    under the terms of the GNU General Public License as published by
    the Free Software Foundation, either version 3 of the License, or
```

```
    (at your option) any later version.

    OpenFOAM is distributed in the hope that it will be useful, but WITHOUT
    ANY WARRANTY; without even the implied warranty of MERCHANTABILITY or
    FITNESS FOR A PARTICULAR PURPOSE.  See the GNU General Public License
    for more details.

    You should have received a copy of the GNU General Public License
    along with OpenFOAM.  If not, see <http://www.gnu.org/licenses/>.

\*---------------------------------------------------------------------------*/

#include "dynamicBendingFreeUDFFvMesh.H"
#include "addToRunTimeSelectionTable.H"
#include "volFields.H"
#include "mathematicalConstants.H"
#include "forces.H"
#include "forceCoeffs.H"
#include "dictionary.H"
#include "wordReList.H"
#include "fvMesh.H"
#include "fvcGrad.H"
#include "Pstream.H"

// * * * * * * * * * * * * * * Static Data Members * * * * * * * * * * * * * //

namespace Foam
{
    defineTypeNameAndDebug(dynamicBendingFreeUDFFvMesh, 0);
    addToRunTimeSelectionTable(dynamicFvMesh, dynamicBendingFreeUDFFvMesh, IOobject);
}

// * * * * * * * * * * * * * * * * Constructors  * * * * * * * * * * * * * * //

Foam::dynamicBendingFreeUDFFvMesh::dynamicBendingFreeUDFFvMesh(const IOobject& io)
```

```
:
    dynamicFvMesh(io),
    dynamicMeshCoeffs_
    (
        IOdictionary
        (
            IOobject
            (
                "dynamicMeshDict",
                io.time().constant(),
                *this,
                IOobject::MUST_READ_IF_MODIFIED,
                IOobject::NO_WRITE,
                false
            )
        ).subDict(typeName + "Coeffs")
    ),
    /*Read in parameters of the mesh geometry*/
    B1(readScalar(dynamicMeshCoeffs_.lookup("B1"))),
    B2(readScalar(dynamicMeshCoeffs_.lookup("B2"))),
    B3(readScalar(dynamicMeshCoeffs_.lookup("B3"))),
    B4(readScalar(dynamicMeshCoeffs_.lookup("B4"))),
    D1(readScalar(dynamicMeshCoeffs_.lookup("D1"))),
    D2(readScalar(dynamicMeshCoeffs_.lookup("D2"))),
    D3(readScalar(dynamicMeshCoeffs_.lookup("D3"))),
    D4(readScalar(dynamicMeshCoeffs_.lookup("D4"))),
    L(readScalar(dynamicMeshCoeffs_.lookup("L"))),
    L0(readScalar(dynamicMeshCoeffs_.lookup("L0"))),
    /*Read in parameters for the calculation of structural response*/
    fnb(readScalar(dynamicMeshCoeffs_.lookup("fnb"))),
    quib(readScalar(dynamicMeshCoeffs_.lookup("quib"))),
    phi0(readScalar(dynamicMeshCoeffs_.lookup("phi0"))),
    rho_(readScalar(dynamicMeshCoeffs_.lookup("rho"))),
    nu_(readScalar(dynamicMeshCoeffs_.lookup("nu"))),
    /*Initialise the initial position*/
```

```
    z_n(readScalar(dynamicMeshCoeffs_.lookup("z_0"))),
    zdot_n(readScalar(dynamicMeshCoeffs_.lookup("zdot_0"))),
    zddot_n(readScalar(dynamicMeshCoeffs_.lookup("zddot_0"))),
    tn(readScalar(dynamicMeshCoeffs_.lookup("t_0"))),
    /*Store the initial positions of nodes*/
    zeroPoints_
    (
        IOobject
        (
            "points",
            io.time().constant(),
            meshSubDir,
            *this,
            IOobject::MUST_READ,
            IOobject::NO_WRITE
        )
    )
{}

// * * * * * * * * * * * * * * * * Destructor  * * * * * * * * * * * * * * * //

Foam::dynamicBendingFreeUDFFvMesh::~dynamicBendingFreeUDFFvMesh()
{}

// * * * * * * * * * * * * * * * Member Functions  * * * * * * * * * * * * * //

bool Foam::dynamicBendingFreeUDFFvMesh::update()
{
  /**********************************/
  /*** CALCULATE FORCES AND MOMENT ***/
  pName_ = dynamicMeshCoeffs_.lookupOrDefault<word>("pName", "p");
  UName_ = dynamicMeshCoeffs_.lookupOrDefault<word>("UName", "U");
  dynamicMeshCoeffs_.lookup("patch") >> patchName_;
  dynamicMeshCoeffs_.lookup("liftDir") >> liftDir_;
  dynamicMeshCoeffs_.lookup("dragDir") >> dragDir_;
```

```
dynamicMeshCoeffs_.lookup("pitchAxis") >> pitchAxis_;
dynamicMeshCoeffs_.lookup("CofR") >> coordSys_.origin();

const volVectorField& U = lookupObject<volVectorField>(UName_);
const volScalarField& p = lookupObject<volScalarField>(pName_);

const fvMesh& mesh = p.mesh();
const polyBoundaryMesh& pbm = mesh.boundaryMesh();
patchSet_ = pbm.patchSet(wordReList(dynamicMeshCoeffs_.lookup("patches")));
label patchID = mesh.boundaryMesh().findPatchID(patchName_);

const surfaceVectorField::GeometricBoundaryField& Sfb = mesh.Sf().boundaryField();

const volSymmTensorField devRhoReff = -rho_*nu_*dev(twoSymm(fvc::grad(U)));
tmp<volSymmTensorField> tdevRhoReff = devRhoReff;
const volSymmTensorField::GeometricBoundaryField& devRhoReffb =
 tdevRhoReff().boundaryField();

/* Construct the 0-1 scalar field based on the y-component of the face centres */
/* 0: any faces with the y-component of the face centres below 0 */
/* Those are called negative faces */
/* 1: any faces with the y-component of the face centres above 0 */
/* Those are called positive faces */
vectorField faceC = mesh.boundaryMesh()[patchID].faceCentres();
scalarField faceCentresY = faceC.component(1);
scalarField function;
function.setSize(faceCentresY.size());
forAll(faceCentresY, faceI)
  {
    if (faceCentresY[faceI] > 0)
{
function[faceI] = 1;
}
    if (faceCentresY[faceI] < 0)
{
```

```
  function[faceI] = 0;
}
    }

  /* Calculate the force */
  /* The forces acting on the negative faces are completely ignored */
  List<Field<vector> > forcePatch(1);
  List<Field<vector> > momentPatch(1);
  forcePatch[0].setSize(1);
  momentPatch[0].setSize(1);
  forcePatch[0] = vector::zero;
  momentPatch[0] = vector::zero;

  forAllConstIter(labelHashSet, patchSet_, iter)
    {
      label faceI = iter.key();

      vectorField tF = (rho_*Sfb[faceI]*p.boundaryField()[faceI]) +
(Sfb[faceI] & devRhoReffb[faceI]);

      vectorField F = function*tF;

      forcePatch[0] += sum(F);

      vectorField leverArm = mesh.C().boundaryField()[faceI] - coordSys_.origin();

      vectorField tM = (leverArm^(rho_*Sfb[faceI]*p.boundaryField()[faceI])) +
(leverArm^(Sfb[faceI] & devRhoReffb[faceI]));

      vectorField M = function*tM;

      momentPatch[0] += sum(M);
    }

  Pstream::listCombineGather(forcePatch, plusEqOp<vectorField>());
```

```
Pstream::listCombineScatter(forcePatch);
Pstream::listCombineGather(momentPatch, plusEqOp<vectorField>());
Pstream::listCombineScatter(momentPatch);

Field<vector> totalForcePatch = (forcePatch[0]);
Field<vector> totalMomentPatch = (momentPatch[0]);

List<Field<scalar> > forceMoment(3);
forceMoment[0].setSize(1);
forceMoment[1].setSize(1);
forceMoment[2].setSize(1);
forceMoment[0] = (totalForcePatch & liftDir_);
forceMoment[1] = (totalForcePatch & dragDir_);
forceMoment[2] = (totalMomentPatch & pitchAxis_);

scalar FL_n = sum(forceMoment[0]);
scalar FD_n = sum(forceMoment[1]);
scalar M_n = sum(forceMoment[2]);

/*******************************************/
/*** OUTPUT FORCES ABD MOMENT TO LOG FILES ***/
Info << "structuralTime " << tn << endl;
Info << "Lift " << FL_n << endl;
Info << "Drag " << FD_n << endl;
Info << "Moment " << M_n << endl;

/************************/
/*** STRUCTURAL SOLVER ***/
/* Caculate the integral of the mode shape phi using the tripezoidal method */
const scalar nStrip = 200;
const scalar deltaY = L/nStrip;
scalar integral_phi = 0;
int i;
for(i = 1; i <= nStrip; i++)
  {
```

```
    scalar y1 = (i-1)*deltaY;
    scalar y2 = i*deltaY;
    scalar phi1 = phi0*::sin(constant::mathematical::pi/(2*L0)*y1);
    scalar phi2 = phi0*::sin(constant::mathematical::pi/(2*L0)*y2);
    integral_phi += 0.5*deltaY*(phi1 + phi2);
  }

/* Caculate the modal force */
scalar F = FL_n/L*integral_phi;

/* Caculate the model displacement, velocity and acceleration */
scalar timeStep = time().value() - tn;
scalar wnb = 2*constant::mathematical::pi*fnb;
scalar zddot_n1 = F - 2*quib*wnb*zdot_n - wnb*wnb*z_n;
scalar zdot_n1 = zdot_n + timeStep*zddot_n1;
scalar z_n1 = z_n + timeStep*zdot_n1;

/* Assign the model displacement to the amplitude of oscillation of the model */
scalar amplitude = z_n1;

/*****************************/
/*** MOVING NODES ALGORITHM ***/
/* Access all the points on the mesh and move them accordingly */
pointField zeroPoints = zeroPoints_;
forAll(zeroPoints, pointI)
  {
    scalar pointX = zeroPoints[pointI].component(0);
    scalar pointY = zeroPoints[pointI].component(1);
    scalar pointZ = zeroPoints[pointI].component(2);

    /*Calculate the movement of points on the model*/
    scalar amplitudeZ = amplitude*phi0*::sin(constant::mathematical::pi/(2*L0)*pointY);

    /*Block 8 - Upstream middle block - Rigid zone*/
    if ( (fabs(pointZ) <= D2) && (pointX < -B2) && (pointY > 0))
```

```
{
  scalar pointDz = amplitudeZ;
  zeroPoints[pointI].component(2) += pointDz;
}

      /*Block 9 - Centre middle block - Rigid zone*/
      if ( (fabs(pointZ) <= D2) && (pointX >= -B2) && (pointX <= B3) && (pointY > 0))
{
  scalar pointDz = amplitudeZ;
  zeroPoints[pointI].component(2) += pointDz;
}

      /*Block 4 - Downstream middle block - Buffer zone */
      if ( (fabs(pointZ) <= D2) && (pointX > B3) && (pointY > 0))
{
  scalar pointDz = amplitudeZ*(1 - 1/B4*(pointX - B3));
  zeroPoints[pointI].component(2) += pointDz;
}

      /*Block 1 + 2 - Upstream and centre top blocks - Buffer zones*/
      if ( (pointZ > D2) && (pointX <= B3) && (pointY > 0))
{
  scalar pointDz = amplitudeZ*(D1 + D2 - pointZ)/D1;
  zeroPoints[pointI].component(2) += pointDz;
}

      /*Block 3 - Downstream top block - Buffer zone*/
      if ( (pointZ > D2) && (pointX > B3) && (pointY > 0))
{
  scalar pointDz = amplitudeZ*(1 - 1/B4*(pointX - B3))*(D1 + D2 - pointZ)/D1;
  zeroPoints[pointI].component(2) += pointDz;
}

      /*Block 7 + 6 - Upstream and centre bottom blocks - Buffer zones*/
      if ( (pointZ < -D3) && (pointX <= B3) && (pointY > 0))
```

```
{
  scalar pointDz = amplitudeZ*(-D3 - D4 - pointZ)/(-D4);
  zeroPoints[pointI].component(2) += pointDz;
}

      /*Block 5 - Downstream bottom block - Buffer zone*/
      if ( (pointZ < -D3) && (pointX > B3) && (pointY > 0))
{
  scalar pointDz = amplitudeZ*(1 - 1/B4*(pointX - B3))*(-D3 - D4 - pointZ)/(-D4);
  zeroPoints[pointI].component(2) += pointDz;
}
    }

  /************************************************/
  /*** OUTPUT STRUCTURAL RESPONSES TO LOG FILES ***/
  Info << "Displacment " << z_n << endl;
  Info << "Velocity " << zdot_n << endl;
  Info << "Acceleration " << zddot_n << endl;
  Info << "Time step " << timeStep << endl;

  /**************************************************/
  /*** STORE MODEL INFORMATION FOR NEXT TIME STEP ***/
  z_n = z_n1;
  zdot_n = zdot_n1;
  zddot_n = zddot_n1;
  tn = time().value();

  fvMesh::movePoints(zeroPoints);

  if (foundObject<volVectorField>("U"))
    {
      volVectorField& U =
const_cast<volVectorField&>(lookupObject<volVectorField>("U"));
      U.correctBoundaryConditions();
    }
```

```

  return true;
}

// ************************************************************************* //
```

A.2 MATLAB SCRIPTS

A.2.1 POD Pre-processing - Data Sorting

```
%% DINH TUNG NGUYEN dinhtung.nguyen@nottingham.ac.uk
% This MATLAB script is a part of the pre—processing of the surface pressure data
% used in the POD analysis. In this script, the pressure data outputted from OpenFOAM
% will be sorted in a consistent sampling order and stack together to form a part of
% the final snapshot matrix

clc; close all; clear all;

%% Enter the correct folder
primaryFolder = 'uWind2_0';
cd(primaryFolder);
cd PODPressure_1;
subFolder = 'bridgeSurface';

%% Define the depth of the model
D = 0.1;

%% Read in time stamp data
timeID = load('timeID.txt');

%% Read the point coordinate in the first time ID
% The order of point in the first time ID will be the standard
cd(num2str(timeID(1)));
cd(subFolder);
fileID = fopen('points','r');
pointCoor = textscan(fileID,'%s %s %s');
for i = 1:str2double(pointCoor{1}{1})
    xCoor(i,1) = str2double(pointCoor{1}{i+1});
    yCoor(i,1) = str2double(pointCoor{2}{i+1});
    zCoor(i,1) = str2double(pointCoor{3}{i+1});
end
```

```
fclose(fileID);
cd ..;
cd ..;

%% Correct the zCoor due to the bending motion
% Evaluate the displacement at the mid span
X0 = 0;
Y0 = 2.5;
writeIndex = 0;
for i = 1:length(xCoor)
    if xCoor(i) == X0
        if yCoor(i) == Y0
            writeIndex = writeIndex + 1;
            tmpZ(writeIndex) = zCoor(i);
        end
    end
end
zMid = 0.5*(max(tmpZ) + min(tmpZ)); % Displacement at the mid span
% Correct the Z value if the yCoor is bigger than 0
for i = 1:length(yCoor)
    if yCoor(i) <= 0
        zCoor(i) = zCoor(i);
    end
    if yCoor(i) > 0
        deltaZ = zMid*cos(pi*yCoor(i)/(2*Y0)-pi*0.5);
        zCoor(i) = zCoor(i) - deltaZ;
    end
end
clear zMid tmpZ;

%% Create the empty rawPressureData matrix
rawPressureData = zeros(length(xCoor),length(timeID));

%% Create the time series data of pressure at all selected plane
count = zeros(3,length(timeID));
for timeI = 1:length(timeID)
    count(1,timeI) = timeID(timeI);
    % Read the pressure data if it is  the first time ID
    if timeI == 1
        % Enter the correct time instant
        snapshotFileName = num2str(timeID(timeI));
        cd(snapshotFileName);
        % Enter the selected plane
        cd(subFolder);
```

```
        % Read the pressure data
        cd scalarField;
        fileID = fopen('p','r');
        tempPressureData = textscan(fileID,'%s');
        for i = 1:str2double(tempPressureData{1}{1})
            rawPressureData(i,timeI) = str2double(tempPressureData{1}{i+2});
        end
        fclose(fileID);
        % Return to the bridgeSurface folder
        cd ..;
        cd ..;
        cd ..;
    end
    if timeI > 1
        % Enter the correct time instant
        snapshotFileName = num2str(timeID(timeI));
        cd(snapshotFileName);
        % Enter the selected plane
        cd(subFolder);
        % Read the pressure data
        cd scalarField;
        fileID = fopen('p','r');
        tempPressureData = textscan(fileID,'%s');
        for i = 1:str2double(tempPressureData{1}{1})
            tmpPData(i,1) = str2double(tempPressureData{1}{i+2});
        end
        fclose(fileID);
        % Return the previous folder
        cd ..;
        % Read the point coordinates
        fileID = fopen('points','r');
        pointCoor = textscan(fileID,'%s %s %s');
        for i = 1:str2double(pointCoor{1}{1})
            x(i,1) = str2double(pointCoor{1}{i+1});
            y(i,1) = str2double(pointCoor{2}{i+1});
            z(i,1) = str2double(pointCoor{3}{i+1});
        end
        fclose(fileID);
        % Correct the zCoor
        writeIndex = 0;
        for i = 1:length(x)
            if x(i) == X0
                if y(i) == Y0
                    writeIndex = writeIndex + 1;
```

```
                tmpZ(writeIndex) = z(i);
            end
        end
    end
    % Calculate the displacement at the midspan
    zMid = 0.5*(max(tmpZ) + min(tmpZ));
    % Correct the Z value if the yCoor is bigger than 0
    for i = 1:length(y)
        if y(i) <= 0
            z(i) = z(i);
        end
        if y(i) > 0
            deltaZ = zMid*cos(pi*y(i)/(2*Y0)-pi*0.5);
            z(i) = z(i) - deltaZ;
        end
    end
    % Compare the order of points of this time instant with the first
    % time instant
    for I = 1:length(x)
        xTmp = x(I);
        yTmp = y(I);
        zTmp = z(I);
        for j = 1:length(xCoor)
            if abs(xCoor(j) - xTmp) < 1e-6
                if abs(yCoor(j) - yTmp) < 1e-6
                    if abs(zCoor(j) - zTmp) < 1e-6
                        writeIndex = j;
                        rawPressureData(writeIndex,timeI) = tmpPData(I);
                        xComp(writeIndex,timeI) = xTmp;
                        yComp(writeIndex,timeI) = yTmp;
                        zComp(writeIndex,timeI) = zTmp;
                        count(2,timeI) = count(2,timeI) + 1;
                        if (I < j) || (I > j)
                            count(3,timeI) = count(3,timeI) + 1;
                        end
                    end
                end
            end
        end
    end
    % Return to the bridgeSurface folder
    cd ..;
    cd ..;
end
```

```
    % Monitoring string
    fprintf('TimeID %f (timeID: %d/%d) is finished!!!\n',timeID(timeI),timeI,length(timeID));
    fprintf('%d points are checked!!!\n',count(2,timeI));
    fprintf('%d points are out of position!!!\n\n\n',count(3,timeI));
end

%% Save pressure, coordinates and time data
save('rawPressureData','rawPressureData','-ascii');
save('xCoor','xCoor','-ascii');
save('yCoor','yCoor','-ascii');
save('zCoor','zCoor','-ascii');
save('timeID','timeID','-ascii');
```

A.2.2 POD Pre-processing - Data Assembling

```
%% DINH TUNG NGUYEN dinhtung.nguyen@nottingham.ac.uk
% This MATLAB script is a part of the pre-processing of the surface pressure data
% used in the POD analysis. In this script, the sorted pressure data from each run is
% assembled together

clc; close all; clear all;

%% Enter the correct folde
primaryFolder = 'uWind1_9';
cd(primaryFolder);
nFolder = 3;

%% Enter the correct subfolder
count = zeros(3,length(nFolder));
for folderI = 1:nFolder
    count(1,folderI) = folderI;
    % Enter the correct subfolder
    folderName = strcat('PODPressure_',num2str(folderI),'_Remove');
    cd(folderName);
    % Read to coordinate system
    x = load('xCoor');
    y = load('yCoor');
    z = load('zCoor');
    % Read the pressure data
    rawPressureData = load('rawPressureData');
    % Read the timeID
    rawTimeID = load('timeID.txt');
    % If this is the first folder, make it the standar coordinate and store
```

```
    % the coordinate and the pressure data
    if folderI == 1
        % Initial time ID
        timeID = rawTimeID;
        % Standard coordiante
        x0 = x;
        y0 = y;
        z0 = z;
        % Save the coordinate
        xCoor = x0;
        yCoor = y0;
        zCoor = z0;
        % Save the pressure data
        pressureData = rawPressureData;
    end
    % If not, check and rearragne the point and the pressure data
    % correspond to the order of the sampling points
    if (folderI < 1) || (folderI > 1)
        % Check the order of point and reaarange if necessary
        xComp = zeros(length(x),1);
        yComp = zeros(length(x),1);
        zComp = zeros(length(x),1);
        tmpPressureData = zeros(size(rawPressureData));
        for I = 1:length(x)
            xTmp = x(I);
            yTmp = y(I);
            zTmp = z(I);
            for j = 1:length(xCoor)
                if abs(xCoor(j) - xTmp) < 1e-6
                    if abs(yCoor(j) - yTmp) < 1e-6
                        if abs(zCoor(j) - zTmp) < 1e-6
                            writeIndex = j;
                            tmpPressureData(writeIndex,:) = rawPressureData(I,:);
                            xComp(writeIndex,folderI) = xTmp;
                            yComp(writeIndex,folderI) = yTmp;
                            zComp(writeIndex,folderI) = zTmp;
                            count(2,folderI) = count(2,folderI) + 1;
                            if (I < j) || (I > j)
                                count(3,folderI) = count(3,folderI) + 1;
                            end
                            break;
                        end
                    end
                end
```

```
            end
            % Check the timeID of two pressure data matrices and assemble
            % them together
            % Find the location of the first time step in the new pressure
            % data compared to the old
            writeIndexFlag = 0;
            for i = 1:length(timeID)
                if abs(timeID(i) - rawTimeID(1)) < 1e-6
                    writeIndex = i;
                    writeIndexFlag = 1;
                    break;
                end
                % In case there is no time overlap
                if writeIndexFlag == 0
                    writeIndex = length(timeID) + 1;
                end
            end
            % Insert pressure data and time data into the final assembly
            % matrix and vector
            timeID(writeIndex:writeIndex+length(rawTimeID)-1) = rawTimeID;
            pressureData(:,writeIndex:writeIndex+length(rawTimeID)-1) = tmpPressureData;
        end
    end
    % Return to the previous folder
    cd ..;
    % Monitoring string
    fprintf('FolderID %f (folderI: %d/%d) is finished!!!\n',folderI,folderI,nFolder);
    fprintf('%d points are checked!!!\n',count(2,folderI));
    fprintf('%d points are out of positon!!!\n\n\n',count(3,folderI));
    % Clear temporary variable
    clear x y z rawPressureData tmpPressureData rawTimeID;
 end

%% Save data
save('pressureData','pressureData','-ascii');
save('xCoor','xCoor','-ascii');
save('yCoor','yCoor','-ascii');
save('zCoor','zCoor','-ascii');
save('timeID','timeID','-ascii');
```

A.2.3 POD Processing

```
%% DINH TUNG NGUYEN - dinhtung.nguyen@nottingham.ac.uk
```

```
% This MATLAB script is to perform the POD analysis using the snapshot method.

%% Perform the POD analysis
% Calculate the temporal-average pressure field
meanPressure = transpose(mean(transpose(pressureData)));
% Calculate the fluctuating pressure
for i = 1:timeStepN
    primePressureData(:,i) = pressureData(:,i) - meanPressure;
end
% Calculate the temporal correlation matrix
covarM = primePressureData'*primePressureData;
% Solve the eigenvalue problem : covarM * eVector = tempEValue * eVector
[eVector,tempEValue] = eig(covarM);
eValue = diag(tempEValue); % Extract the diagonal members, i.e. the eigenvalues
% Sorting eigenvalues and eigenvector in the descending order
for i = 1:length(eValue)-1
    for j = 1:length(eValue)-i
        if eValue(j) < eValue(j+1)
            % Eigenvalue
            eValue_temp = eValue(j+1);
            eValue(j+1) = eValue(j);
            eValue(j) = eValue_temp;
            % Eigenvector
            eVector_temp = eVector(:,j+1);
            eVector(:,j+1) = eVector(:,j);
            eVector(:,j) = eVector_temp;
        end
    end
end
% Calculate the normalised POD mode shape
for modeI = 1:length(eValue)
    tmp = primePressureData*eVector(:,modeI);
    PODPhi(:,modeI) = tmp/norm(tmp);
end
% Calculate the POD coefficient of all modes - each column is the temporal
dependent POD coefficient for one mode
PODCoef = transpose(transpose(PODPhi)*primePressureData);
% Calculate the cumulative eigenvalue
cEValue(1) = 0;
for i = 1:length(eValue)
    if i == 1
        cEValue(i) = eValue(i);
    elseif i > 1
        cEValue(i) = cEValue(i-1)+eValue(i);
```

```
    end
end
nor_cEValue = cEValue./max(cEValue); % Convert to the normalised cumulative eigenvalue
```

Appendix B

Wind Tunnel Standard Operating Procedure

STANDARD OPERATING PROCEDURE

Process Title

Operation of University of Nottingham ABL wind tunnel

Location of work

L4-23

Equipment Involved	Hazards
Wind Tunnel	Height difference between tunnel and work room Hole in wind tunnel floor for turntable – this is usually covered by the turntable, which is strong enough to walk on
Hot wire anemometers (CTA and X-wire)	Electrical shock (as with any portable electrical equipment)
Data collection and processing equipment (PC, A/D converters, data loggers, digital manometer)	Electrical shock (as with any portable electrical equipment) RSI

Processes Involved	Hazards
Running wind tunnel	Objects being drawn into air inlet Loose objects within wind tunnel becoming airborne debris Noise from fan
Installing boundary layer roughness elements into wind tunnel	Hazards associated with manual handling of heavy and bulky objects (Trapping of fingers, splinters, weight dropped on feet, lifting injury to back etc.)
Installing Models etc. into the tunnel	Hazards associated with manual handling of heavy and bulky objects (Trapping of fingers, splinters, weight dropped on feet, lifting injury to back etc.)
Collecting data	Hazards associated with use of computer/display screen equipment (Electric shock, RSI, poor posture etc.)

Key Safety Precautions/Equipment Required

Safety goggles, Lab. Coats, Safety boots, Gloves (for manual handling)

Procedure to be followed

General

- Before power to the tunnel is switched on, a visual inspection of its interior must be made to ensure there are no hazardous objects that could cause injury when the tunnel is switched on
- Access to the tunnel working section is through the double doors accessible from the workroom accessible on the ground floor of L4
- When inside the workroom, PPE (safety goggles, lab. coats, safety boots) must be worn at all times
- Power to the tunnel is switched on at the main power panel on the first floor of L4 to the left side of the air intake, the key for this panel is on the key ring with the wind tunnel keys

Installing Models and Instrumentation

- Models or boundary layer roughness elements must be installed via the double doors in the work-room
- Items must not be installed while the tunnel is running
- Cabling for instrumentation should be run through the access doors below the turntable or aerodynamic section
- The door from the workroom that gives access to the exhaust end of the tunnel should remain locked at all times while the tunnel is in use. The key for this door should be kept in the key cupboard next to the door
- Before starting the tunnel, all models, instrumentation and cabling should be checked to ensure nothing can come loose during operation and the access doors to the tunnel should be closed

Starting and Controlling the Wind Tunnel Speed

- The wind tunnel is started using the control panel in the workroom
- A key is required to run the tunnel (on the key fob with the doorkey for the control room), this is turned from the 0 to the 1 position and a green light indicating operation is illuminated
- There is also a green light on the first floor of L4 next to the fan intake to indicate that the tunnel is in operation
- Wind speed is adjusted using the up and down arrow buttons on the control panel which sets the inverter frequency for the motor. The readout is given in hertz and can be converted to wind speed at the end of the contraction without roughness present using the chart below
- Normal shut down is performed by first reducing the wind tunnel speed to ~zero and then turning the operation key back to the 0 position.
- Under normal circumstances people should not be in the wind tunnel while it is operating. At the end of testing, wait until the fan blades have slowed sufficiently and wind speed has dropped to zero before entering the wind tunnel
- Certain tests may require persons to be in the wind tunnel during operation (e.g. measuring drag forces on people). In these circumstances a specific risk assessment needs to be carried out.

Emergency Shutdown Procedure

In the event of an emergency there are three emergency stop buttons as well as the normal control panel to shut down the tunnel. The emergency stop buttons are located as follows:

- Left hand side of the fan intake on the first floor of L4.

- Right hand side of the fan intake on the first floor of L4
- External tunnel wall in the control room

Any of these buttons can be used in an emergency.

Table: Inverter frequencies and wind speed

Inverter Frequency (Hz)	Wind speed (m/s)
3.2	1
8.1	2
12.3	3
16.5	4
20.4	5
24.2	6
28.0	7
31.7	8
35.4	9
39.2	10

Appendix C

Force Measuring Systems

C.1 DETAILED DESIGN OF STRAIN-GAUGE BASED LOAD CELLS

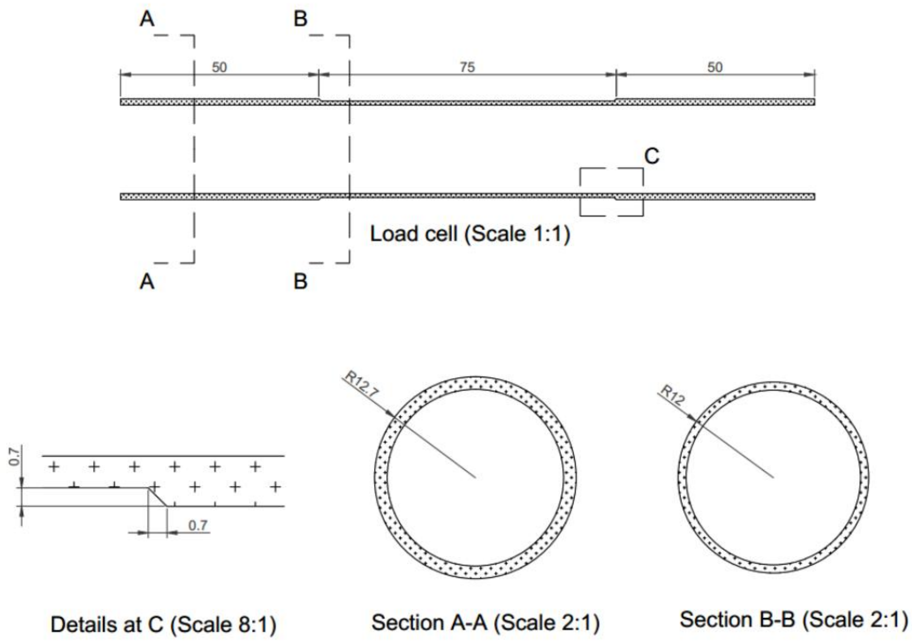

Figure C.1: Detailed drawing of the load cell (dimensions are in mm).

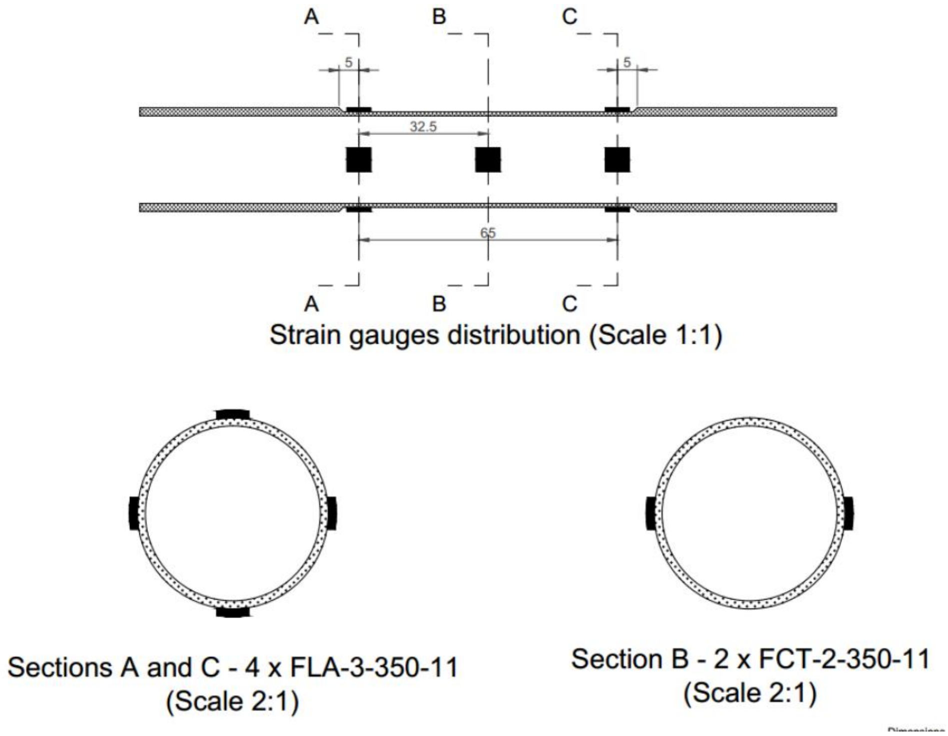

Figure C.2: Detailed layout of the strain gauges (dimensions are in mm).

C.2 CALIBRATION GRAPHS OF STRAIN-GAUGE BASED LOAD CELLS

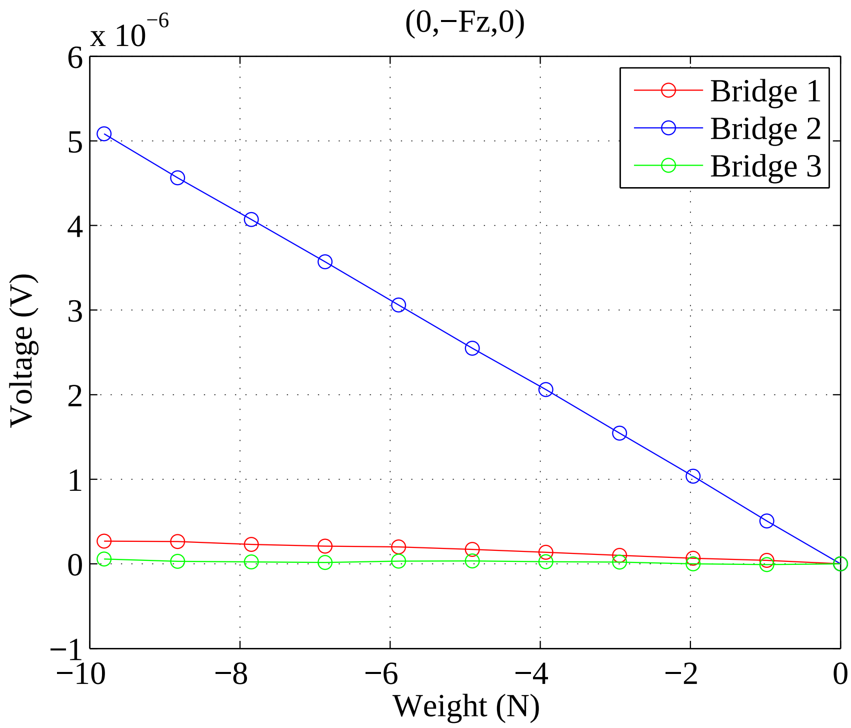

Figure C.3: Calibration graph of Case 1 of the load cell 1.

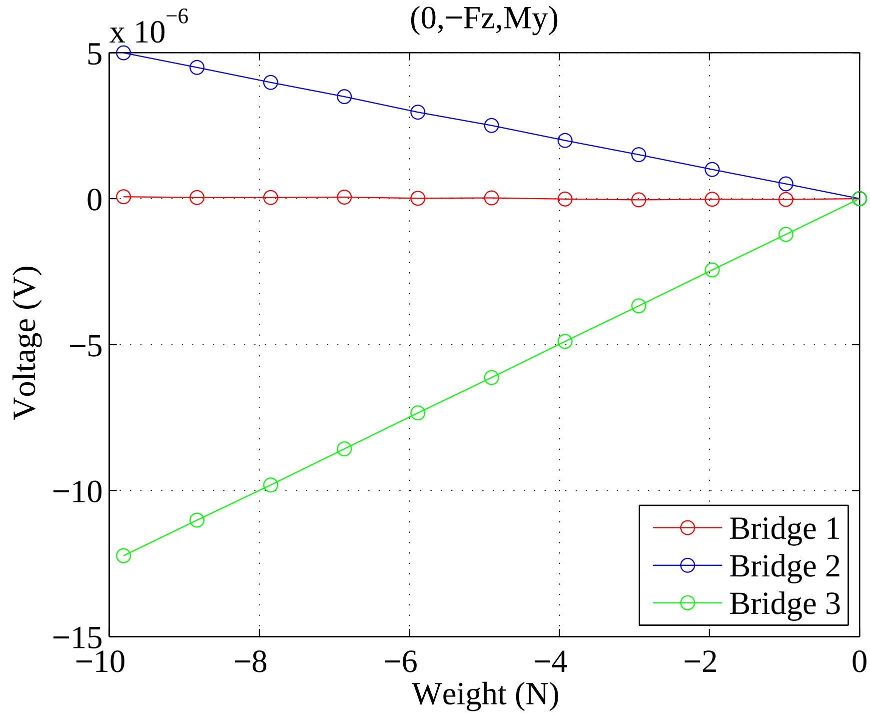

Figure C.4: Calibration graph of Case 2 of the load cell 1.

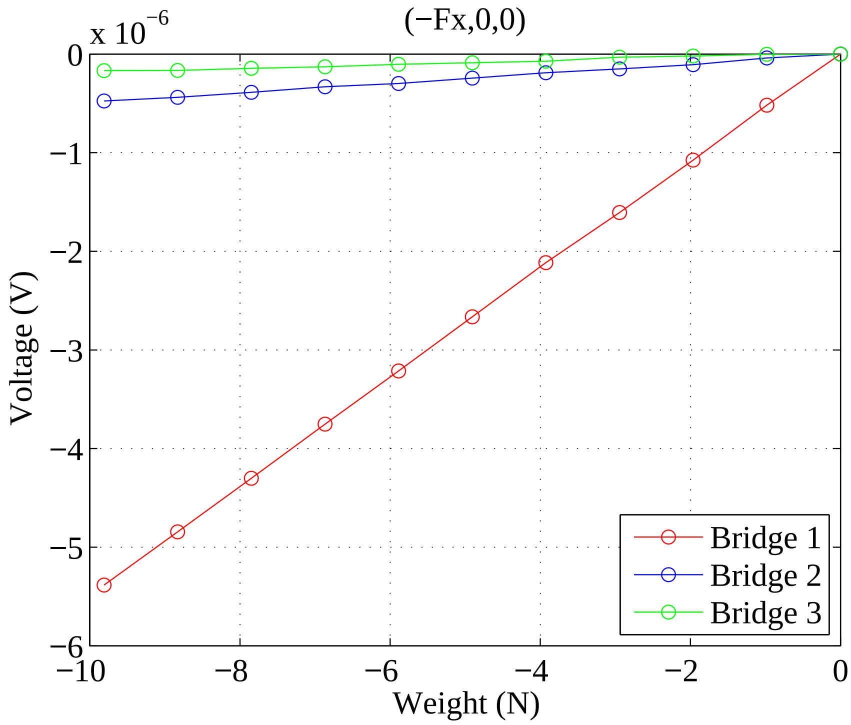

Figure C.5: Calibration graph of Case 3 of the load cell 1.

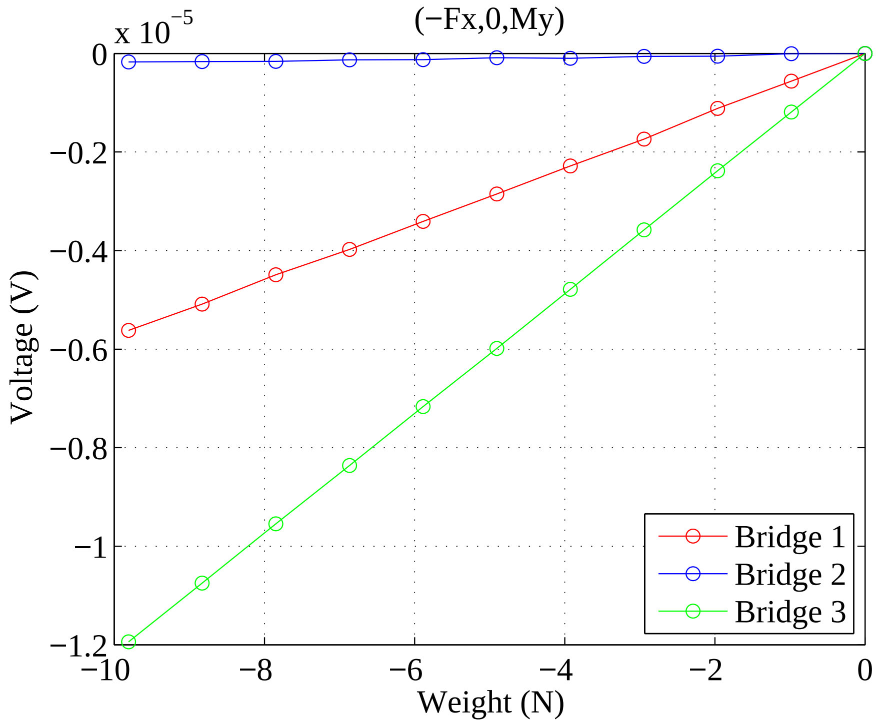

Figure C.6: Calibration graph of Case 4 of the load cell 1.

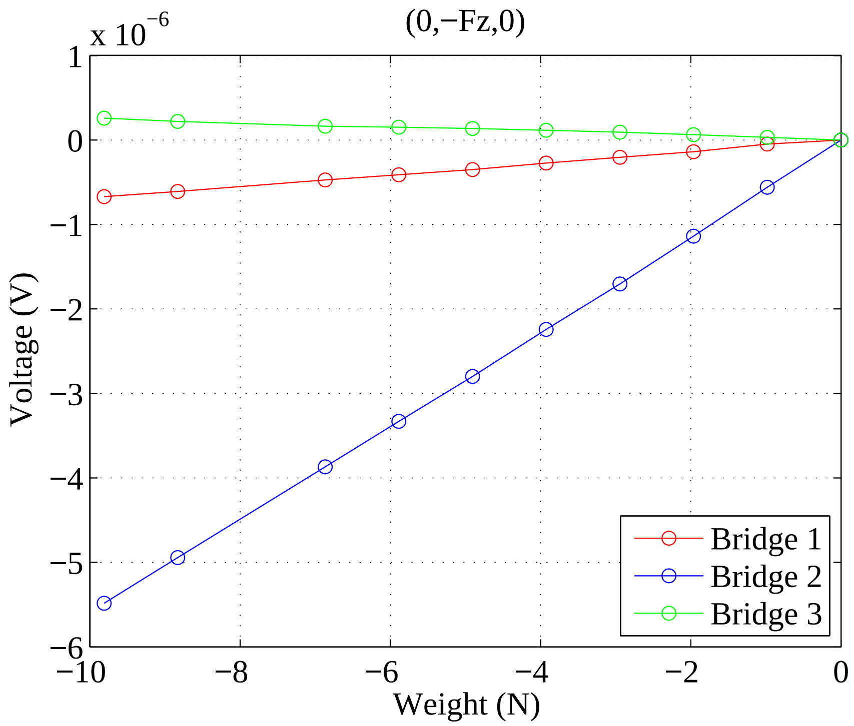

Figure C.7: Calibration graph of Case 1 of the load cell 2.

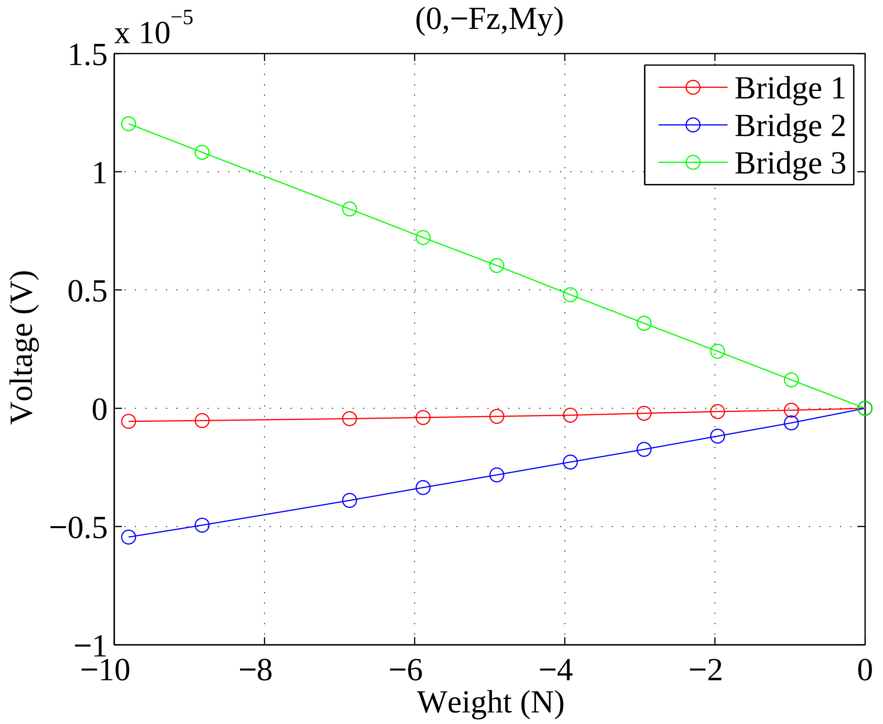

Figure C.8: Calibration graph of Case 2 of the load cell 2.

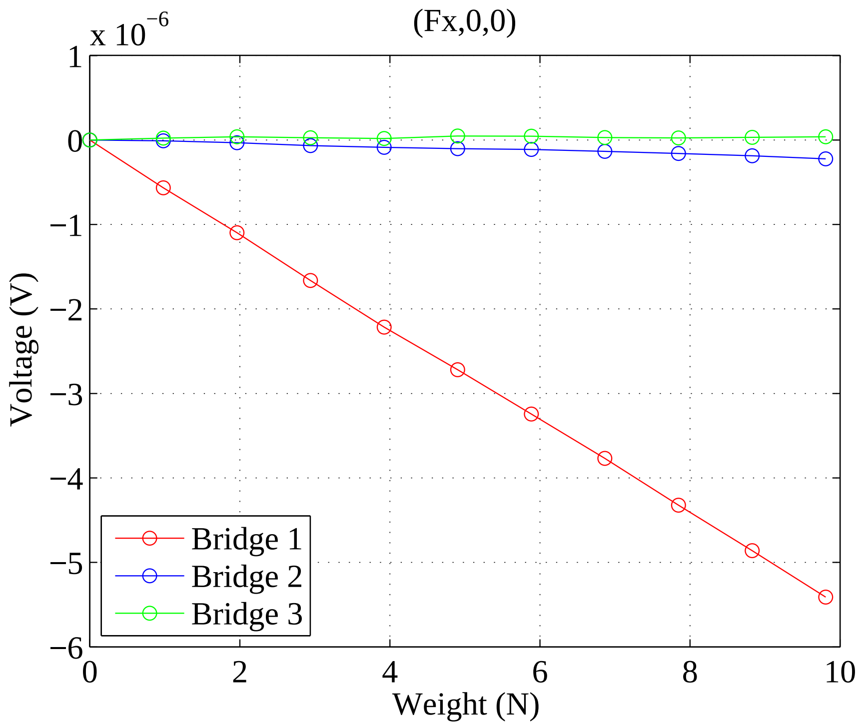

Figure C.9: Calibration graph of Case 3 of the load cell 2.

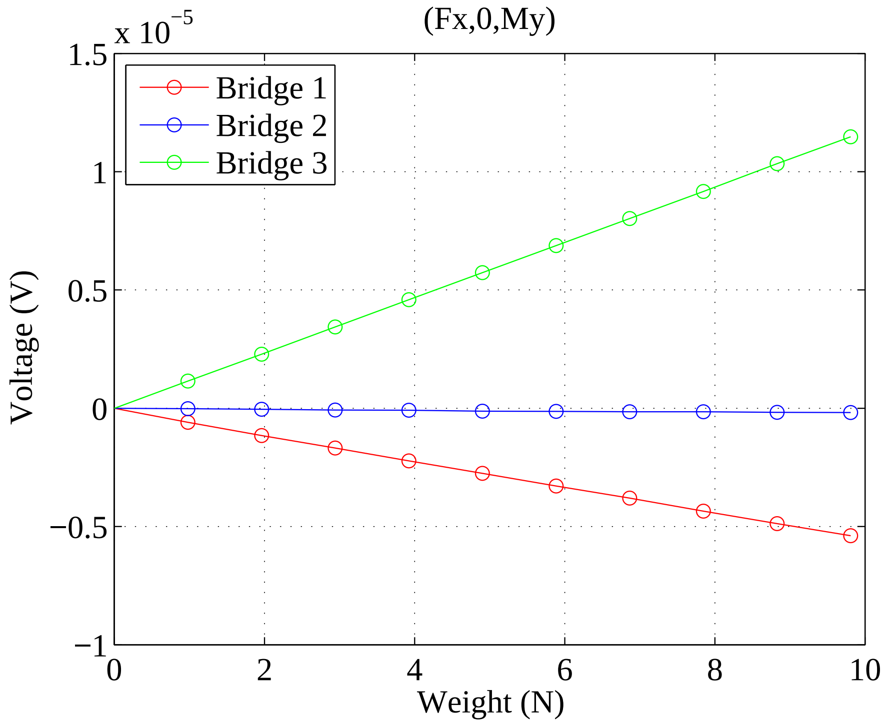

Figure C.10: Calibration graph of Case 4 of the load cell 2.

C.3 DETAILED DESIGN OF PIEZOELECTRIC BASED LOAD CELLS

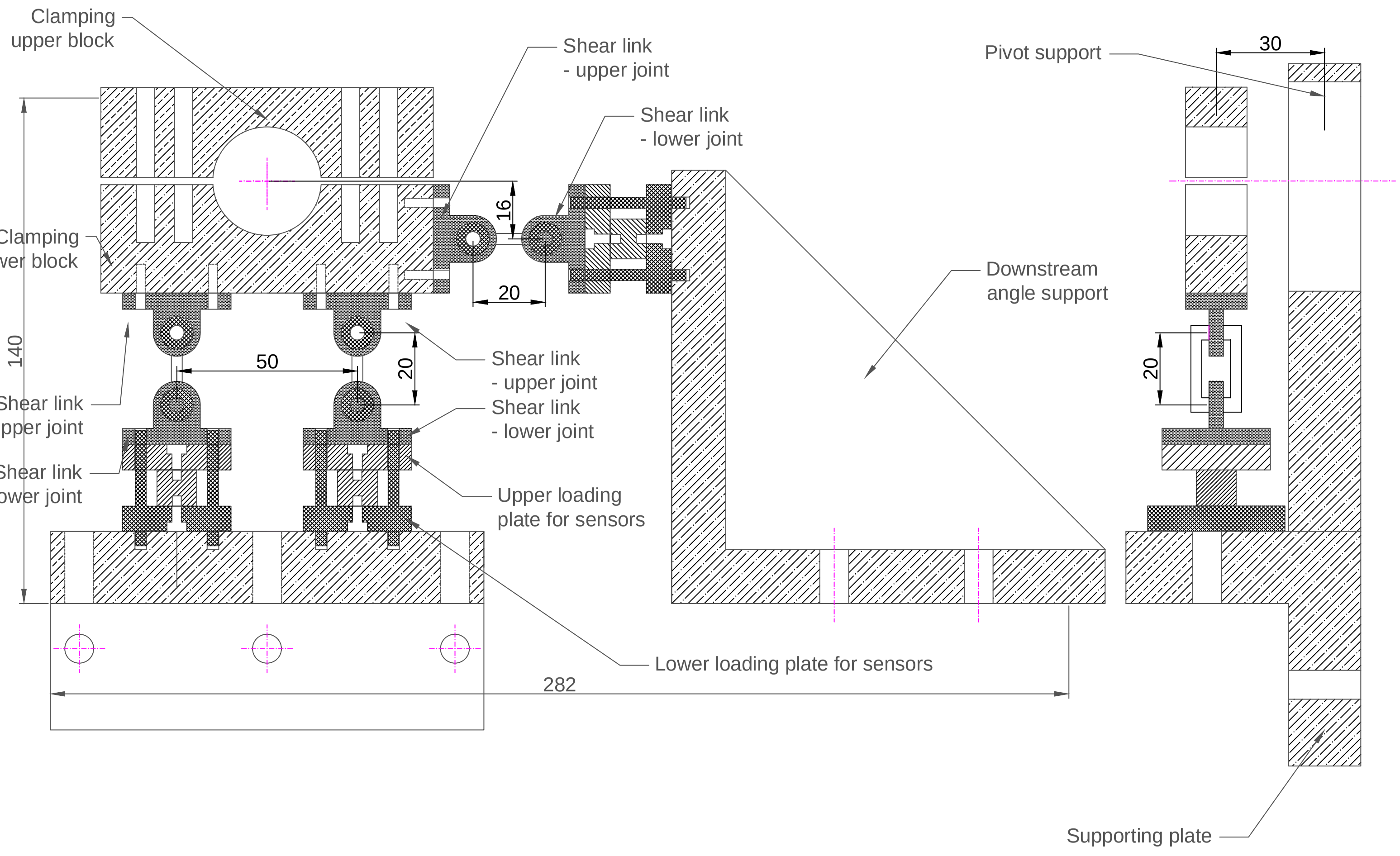

PRODUCED BY AN AUTODESK EDUCATIONAL PRODUCT
PRODUCED BY AN AUTODESK EDUCATIONAL PRODUCT
PRODUCED BY AN AUTODESK EDUCATIONAL PRODUCT

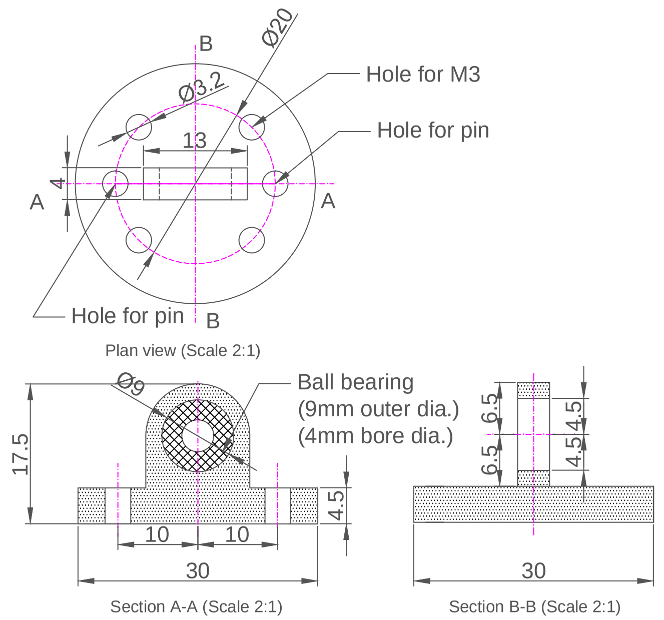

Shear link - Lower joint x 6
Aluminium

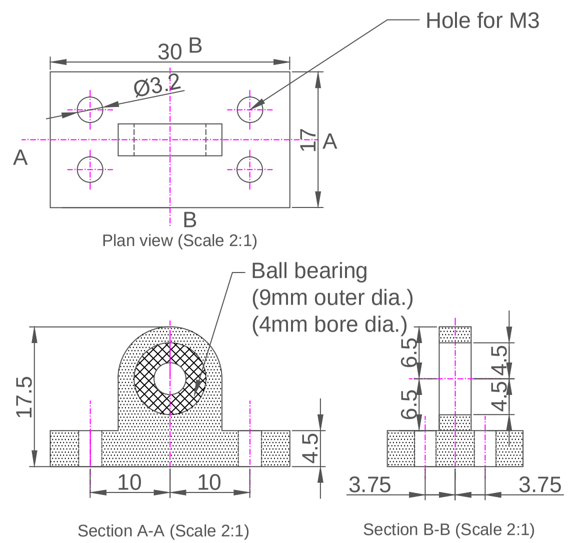

Shear link - Upper joint x 6
Aluminium

PRODUCED BY AN AUTODESK EDUCATIONAL PRODUCT
PRODUCED BY AN AUTODESK EDUCATIONAL PRODUCT
PRODUCED BY AN AUTODESK EDUCATIONAL PRODUCT

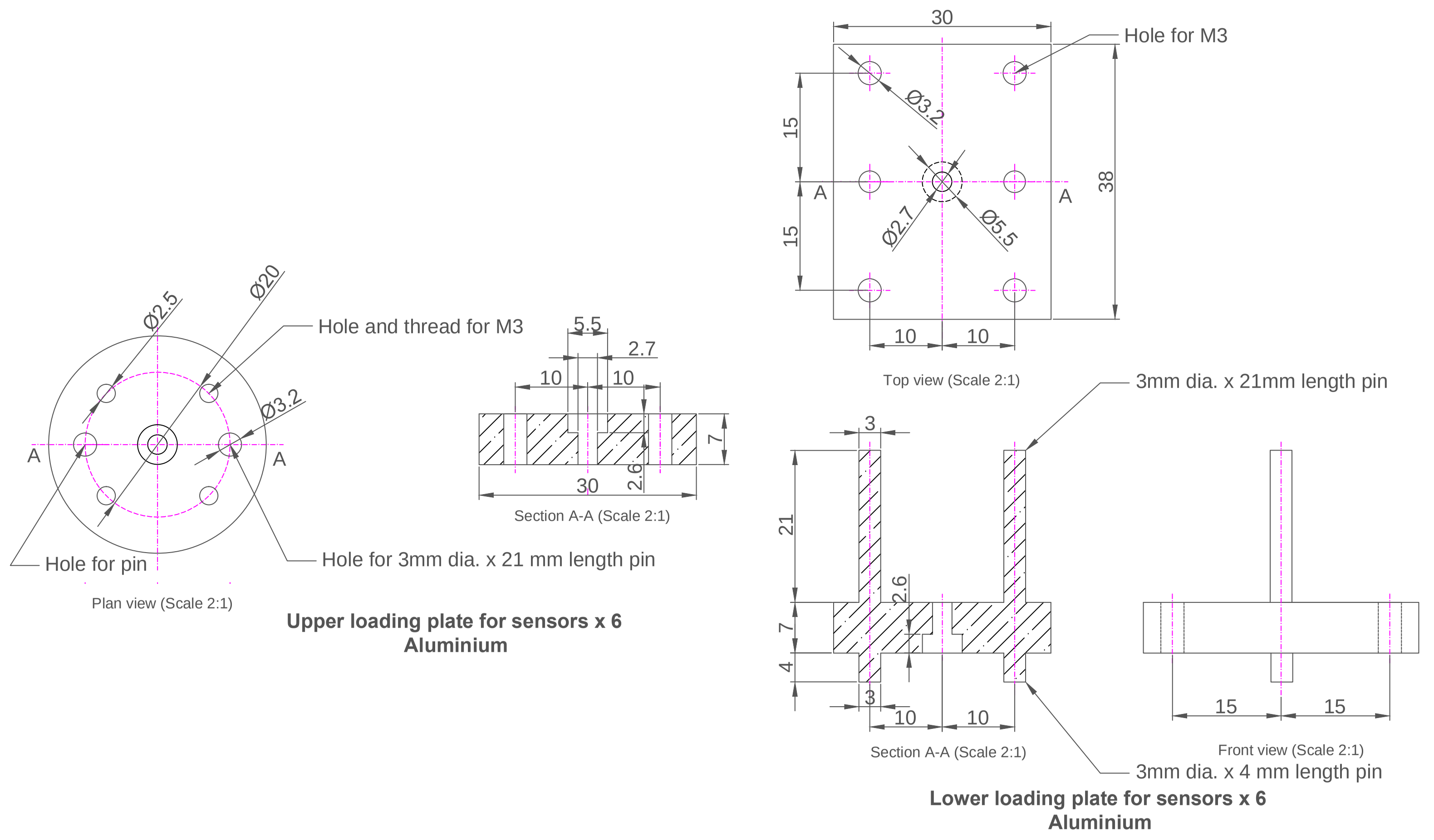

PRODUCED BY AN AUTODESK EDUCATIONAL PRODUCT
PRODUCED BY AN AUTODESK EDUCATIONAL PRODUCT
PRODUCED BY AN AUTODESK EDUCATIONAL PRODUCT

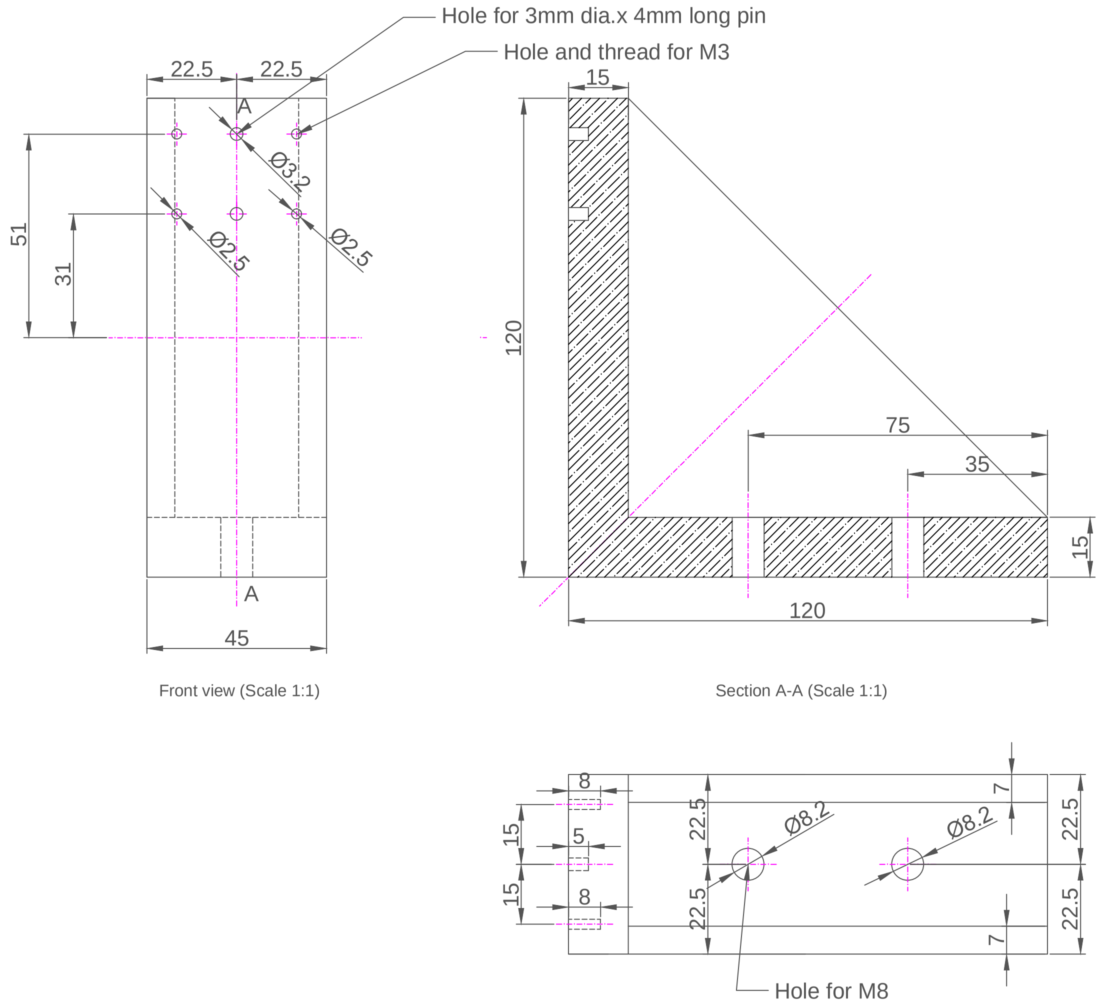

Front view (Scale 1:1)

Section A-A (Scale 1:1)

Top view (Scale 1:1)

Downstream angle support x 2
Aluminium

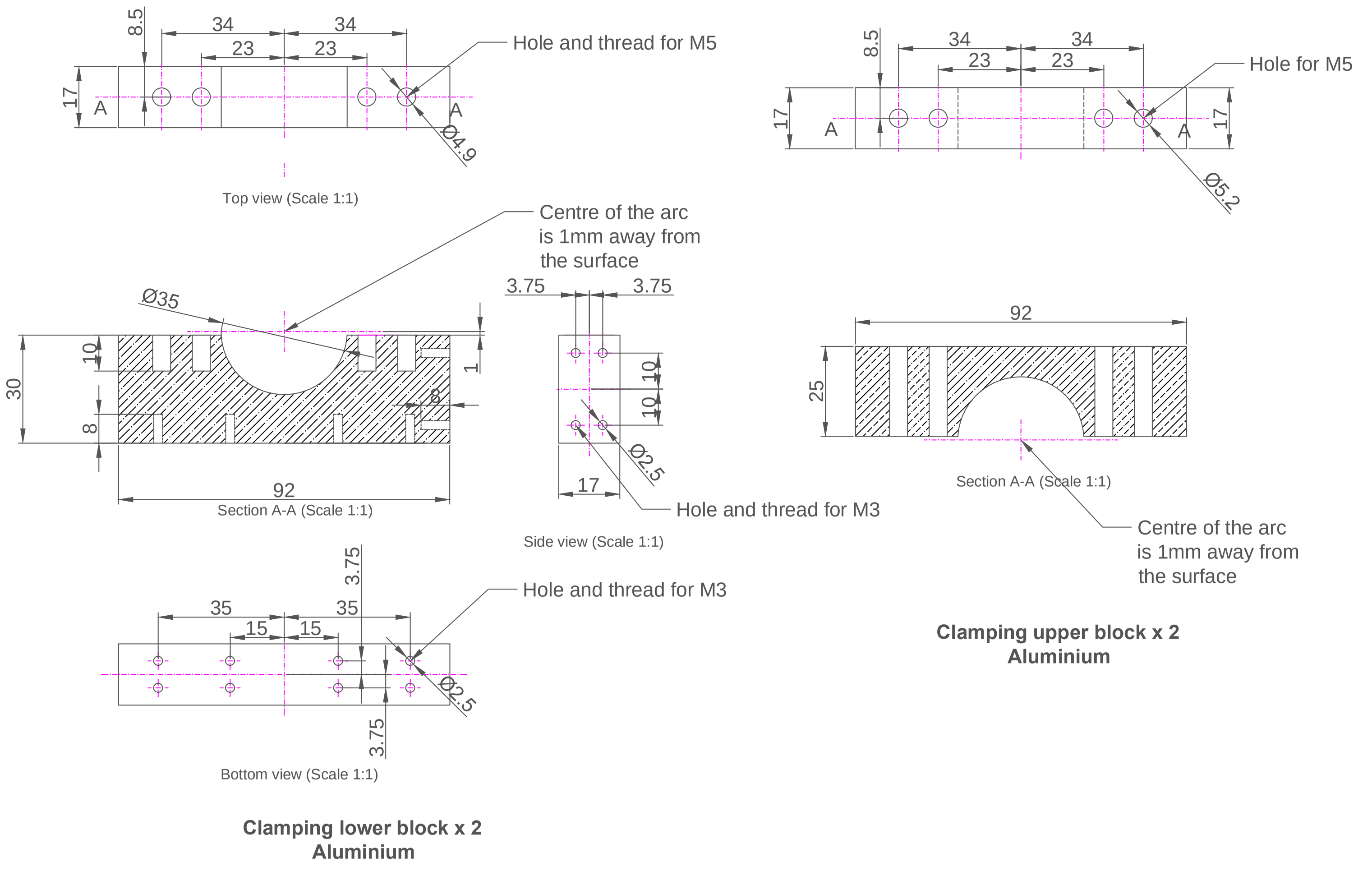

PRODUCED BY AN AUTODESK EDUCATIONAL PRODUCT
PRODUCED BY AN AUTODESK EDUCATIONAL PRODUCT

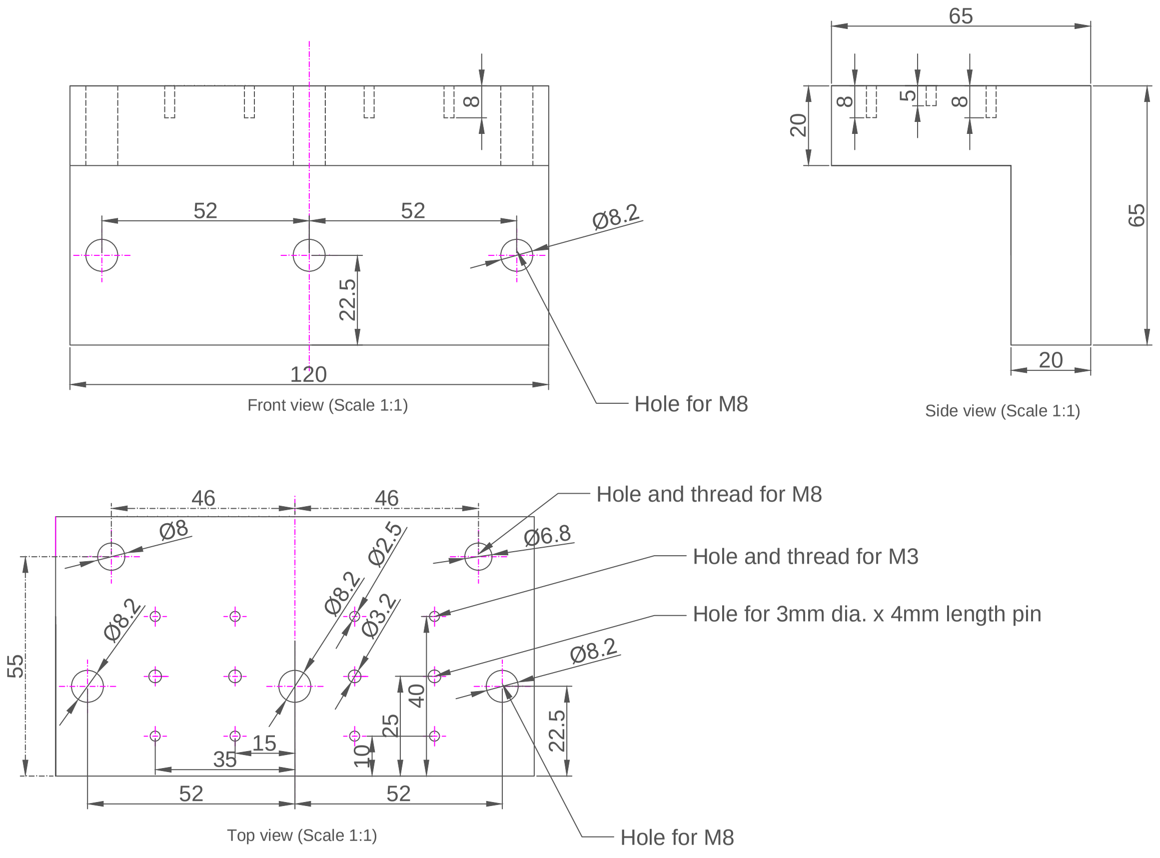

Supporting plate x 2
Aluminium

PRODUCED BY AN AUTODESK EDUCATIONAL PRODUCT
PRODUCED BY AN AUTODESK EDUCATIONAL PRODUCT

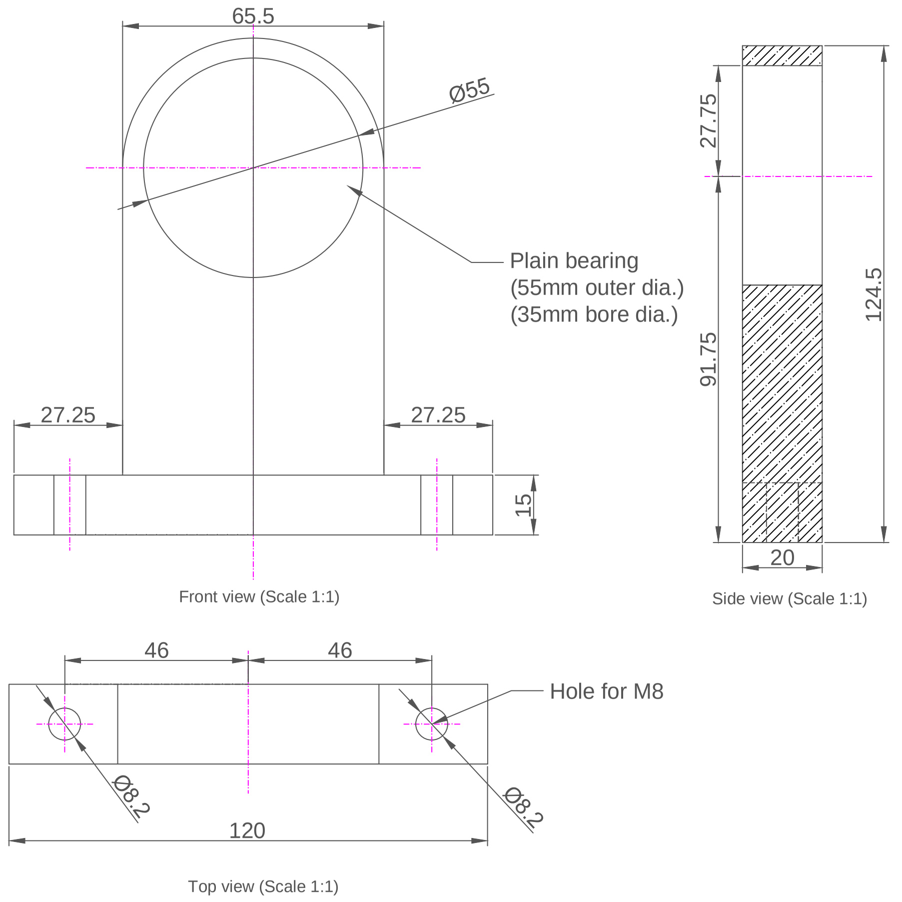

Pivot support x 2
Aluminium

PRODUCED BY AN AUTODESK EDUCATIONAL PRODUCT
PRODUCED BY AN AUTODESK EDUCATIONAL PRODUCT
PRODUCED BY AN AUTODESK EDUCATIONAL PRODUCT

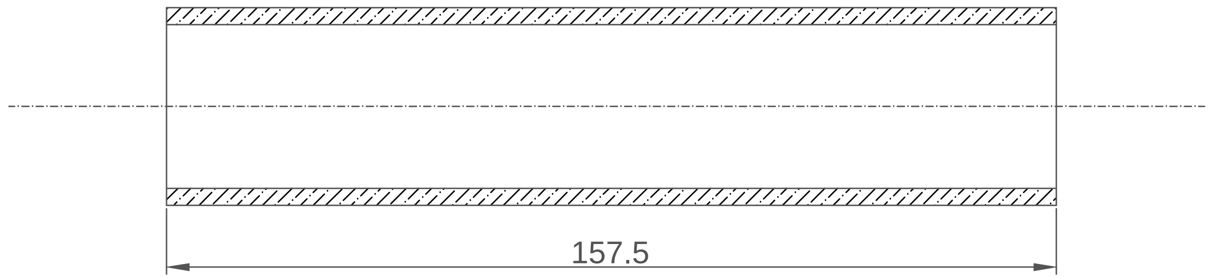

Section A-A (Scale 1:1)

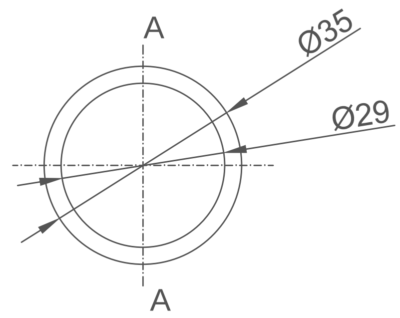

Front view (Scale 1:1) - 3mm WT

Steel tube x 2
Steel

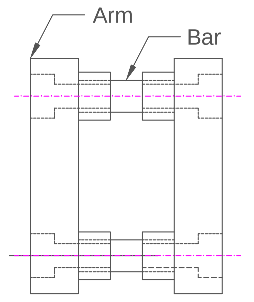

Shear link - Overall assembly

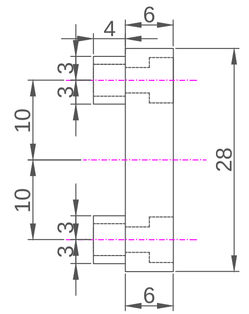

Front view (Scale 2:1)

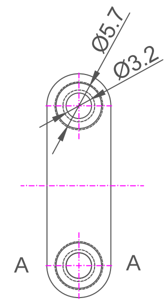

Top view (Scale 2:1)

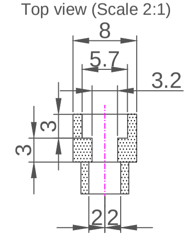

Section A-A (Scale 2:1)

Arm of shear link x 12
Steel

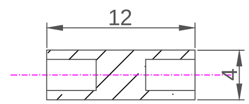

Section A-A (Scale 2:1)

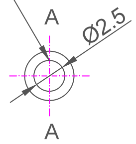

Front view (Section 2:1)

Bar of shear link x 12
Steel

PRODUCED BY AN AUTODESK EDUCATIONAL PRODUCT
PRODUCED BY AN AUTODESK EDUCATIONAL PRODUCT
PRODUCED BY AN AUTODESK EDUCATIONAL PRODUCT

C.4 CALIBRATION RESULTS OF PIEZOELECTRIC BASED LOAD CELLS

C.4.1 Angle of Attack $\alpha = 2°$

(a) $[-F_z, 0, 0]$ at $\alpha = 2°$

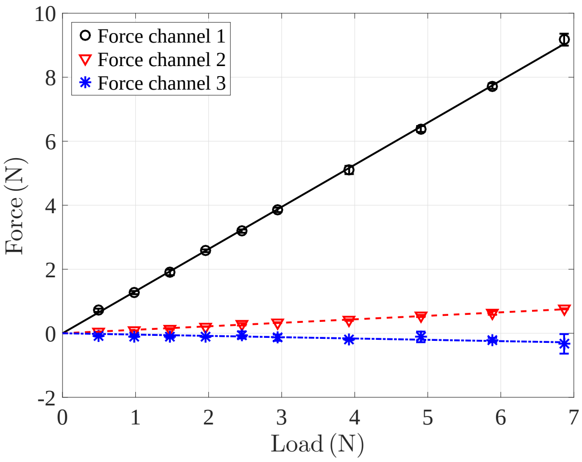

(b) $[-F_z, 0, -M_y]$ at $\alpha = 2°$

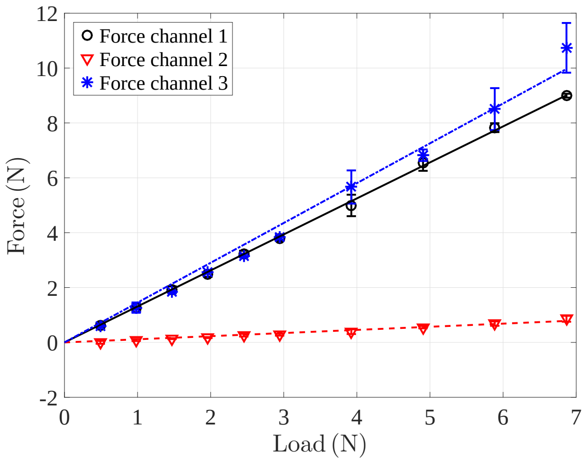

(c) $[0, F_x, 0]$ at $\alpha = 2°$

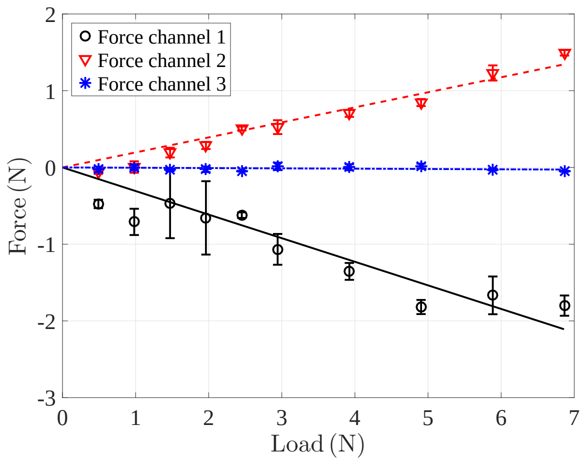

Figure C.11: Graphs showing the dependence of outputs from force channels on the loading values during the calibration; the angle of attack $\alpha = 2°$

$$
M = \begin{bmatrix} -6.8049 \times 10^{-1} & -8.2050 \times 10^{-1} & -3.7025 \times 10^{-3} \\ -3.4871 \times 10^{-1} & 4.1759 & -4.3095 \times 10^{-2} \\ -3.1114 \times 10^{-3} & -7.1533 \times 10^{-3} & -1.0285 \times 10^{-1} \end{bmatrix},
$$

$$
M_{95\%} = \begin{bmatrix} 1.4813 \times 10^{-2} & 2.0865 \times 10^{-1} & 1.3651 \times 10^{-2} \\ 2.2188 \times 10^{-2} & 2.4803 \times 10^{-1} & 2.7600 \times 10^{-2} \\ 8.8668 \times 10^{-4} & 3.0122 \times 10^{-3} & 6.4464 \times 10^{-3} \end{bmatrix}.
$$

C.4.2 Angle of Attack $\alpha = 4^\circ$

(a) $[-F_z, 0, 0]$ at $\alpha = 4^\circ$

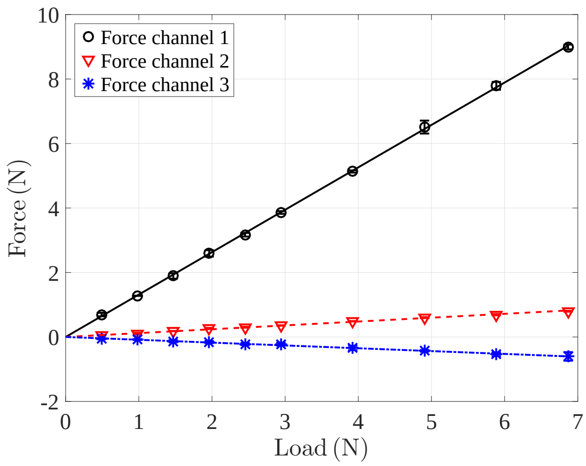

(b) $[-F_z, 0, -M_y]$ at $\alpha = 4^\circ$

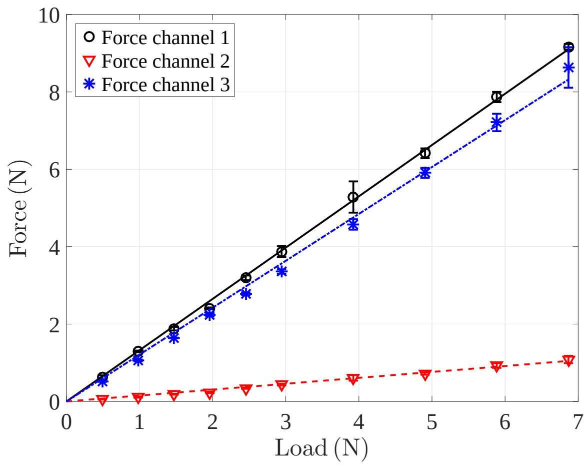

(c) $[0, F_x, 0]$ at $\alpha = 4^\circ$

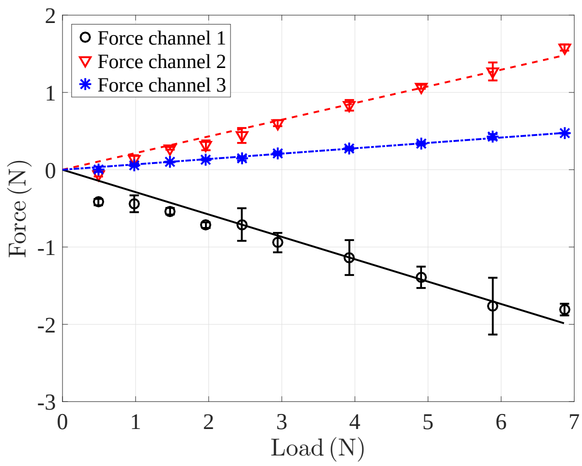

Figure C.12: Graphs showing the dependence of outputs from force channels on the loading values during the calibration; the angle of attack $\alpha = 4^\circ$

$$M = \begin{bmatrix} -6.9000 \times 10^{-1} & -8.0060 \times 10^{-1} & 3.7729 \times 10^{-2} \\ -3.5944 \times 10^{-1} & 3.9657 & -1.1642 \times 10^{-1} \\ -1.0818 \times 10^{-2} & 2.5635 \times 10^{-2} & -1.2727 \times 10^{-1} \end{bmatrix},$$

$$M_{95\%} = \begin{bmatrix} 1.5912 \times 10^{-2} & 1.4059 \times 10^{-1} & 2.8043 \times 10^{-2} \\ 3.9808 \times 10^{-2} & 2.9831 \times 10^{-1} & 3.7250 \times 10^{-2} \\ 3.1475 \times 10^{-4} & 1.7446 \times 10^{-3} & 3.0345 \times 10^{-3} \end{bmatrix}.$$

C.4.3 Angle of Attack $\alpha = 6°$

(a) $[-F_z, 0, 0]$ at $\alpha = 6°$

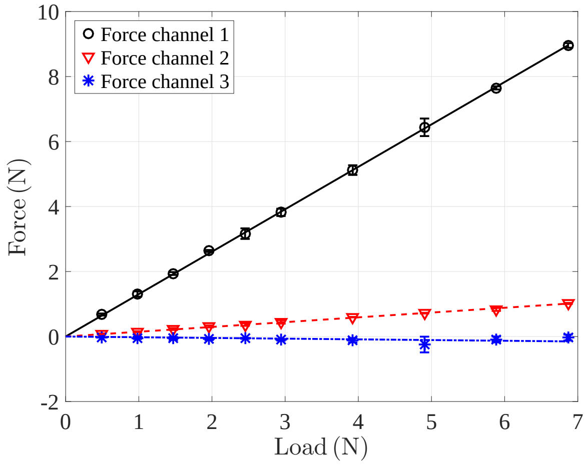

(b) $[-F_z, 0, -M_y]$ at $\alpha = 6°$

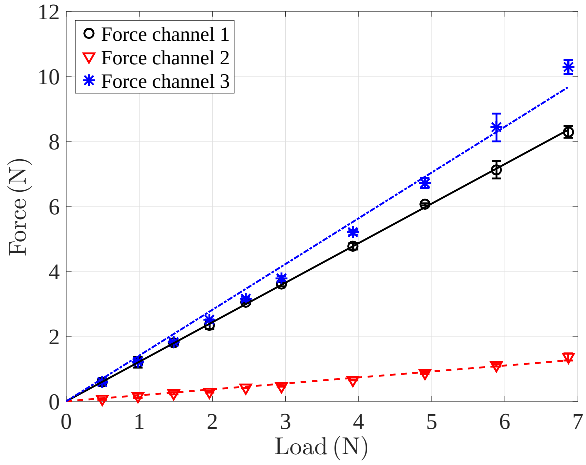

(c) $[0, F_x, 0]$ at $\alpha = 6°$

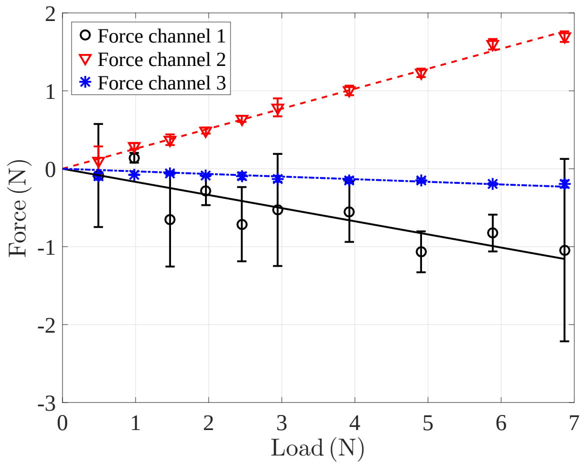

Figure C.13: Graphs showing the dependence of outputs from force channels on the loading values during the calibration; the angle of attack $\alpha = 6°$

$$M = \begin{bmatrix} -7.0310 \times 10^{-1} & -4.8995 \times 10^{-1} & -4.7540 \times 10^{-2} \\ -4.2021 \times 10^{-1} & 3.6376 & -7.7077 \times 10^{-2} \\ 4.5105 \times 10^{-4} & -3.0652 \times 10^{-2} & -1.2600 \times 10^{-1} \end{bmatrix},$$

$$M_{95\%} = \begin{bmatrix} 1.1390 \times 10^{-2} & 1.0261 \times 10^{-1} & 1.5975 \times 10^{-2} \\ 1.6072 \times 10^{-2} & 1.1156 \times 10^{-1} & 3.5560 \times 10^{-2} \\ 8.5564 \times 10^{-4} & 2.9170 \times 10^{-3} & 4.0315 \times 10^{-3} \end{bmatrix}.$$

C.4.4 Angle of Attack $\alpha = 8°$

(a) $[-F_z, 0, 0]$ at $\alpha = 8°$

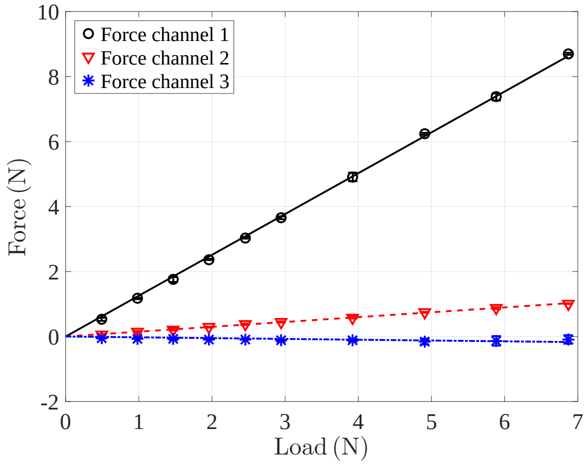

(b) $[-F_z, 0, -M_y]$ at $\alpha = 8°$

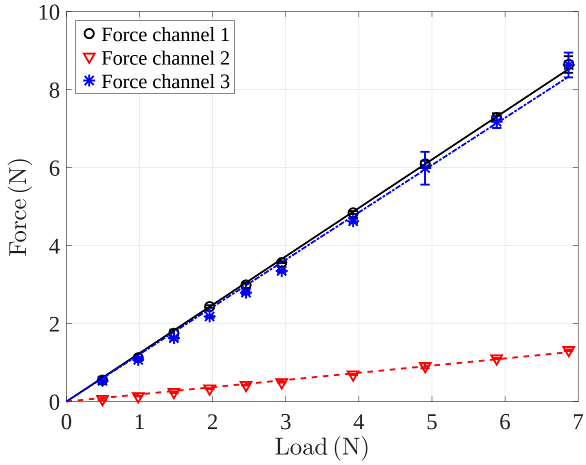

(c) $[0, F_x, 0]$ at $\alpha = 8°$

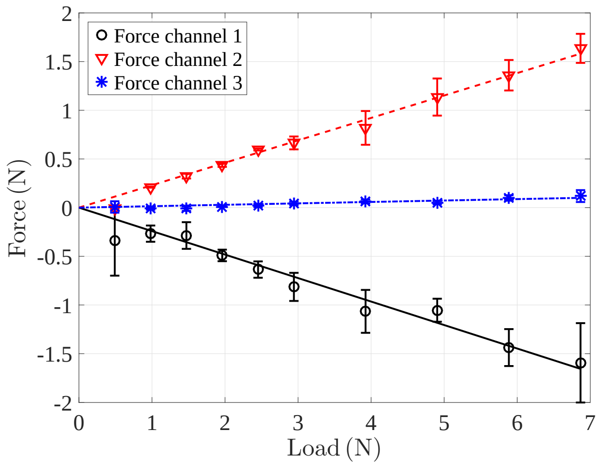

Figure C.14: Graphs showing the dependence of outputs from force channels on the loading values during the calibration; the angle of attack $\alpha = 8°$

$$M = \begin{bmatrix} -7.0871 \times 10^{-1} & -6.9194 \times 10^{-1} & 1.9168 \times 10^{-2} \\ -4.4024 \times 10^{-1} & 3.7783 & -1.3380 \times 10^{-1} \\ -2.3817 \times 10^{-3} & 7.9408 \times 10^{-3} & -1.4122 \times 10^{-1} \end{bmatrix},$$

$$M_{95\%} = \begin{bmatrix} 1.2011 \times 10^{-2} & 6.4490 \times 10^{-2} & 1.4010 \times 10^{-2} \\ 1.6954 \times 10^{-2} & 1.0557 \times 10^{-1} & 3.0029 \times 10^{-2} \\ 7.5375 \times 10^{-4} & 4.5279 \times 10^{-3} & 3.3839 \times 10^{-3} \end{bmatrix}.$$

Appendix D

Supplementary Results

D.1 Surface pressure distribution around a static 5:1 rectangular cylinder in the smooth flow

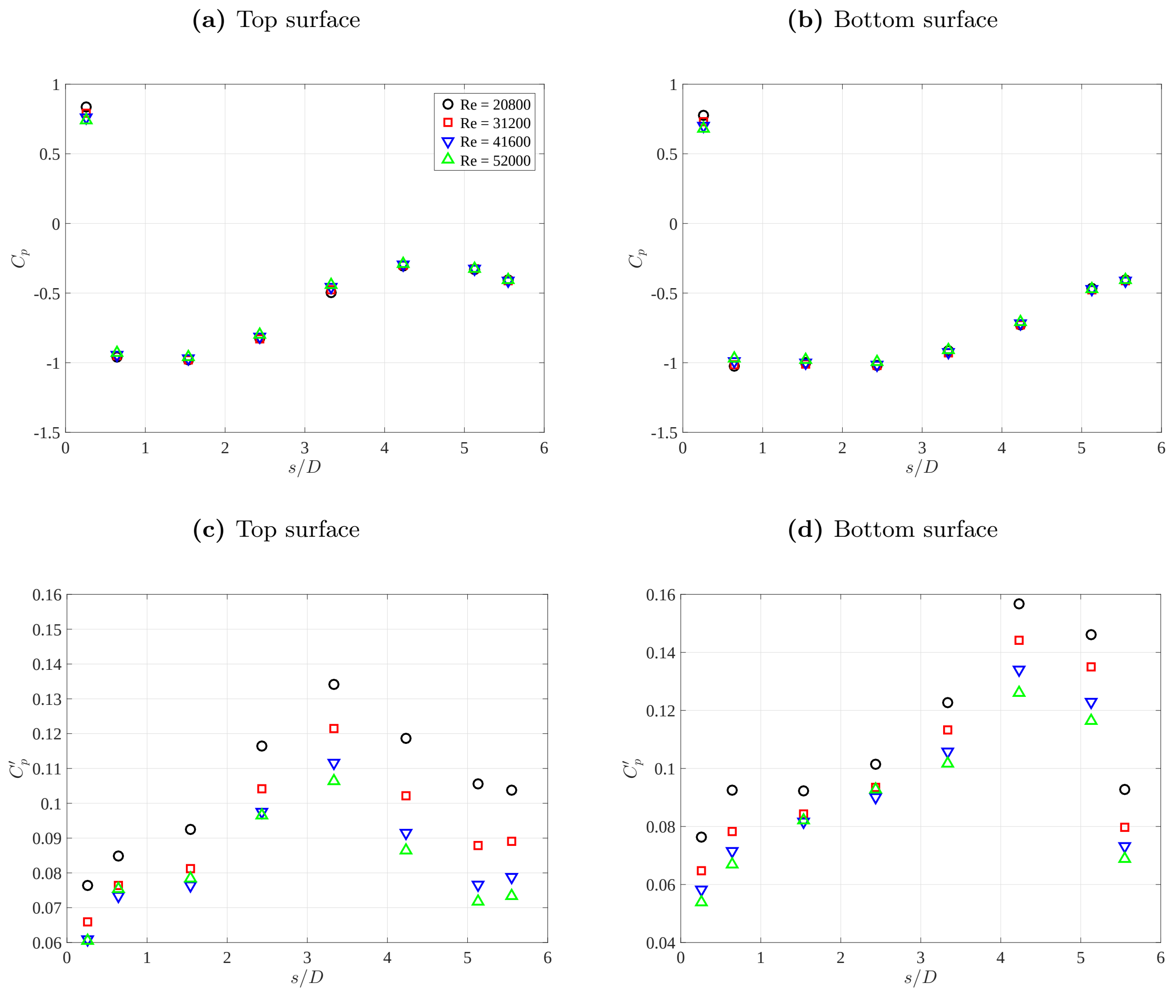

Figure D.1: Variability of the surface distribution of the time-averaged pressure coefficient C_p and the standard deviation of the time-varying pressure coefficient C_p' with respect to the Reynolds number; the angle of attack was $\alpha = 2°$.

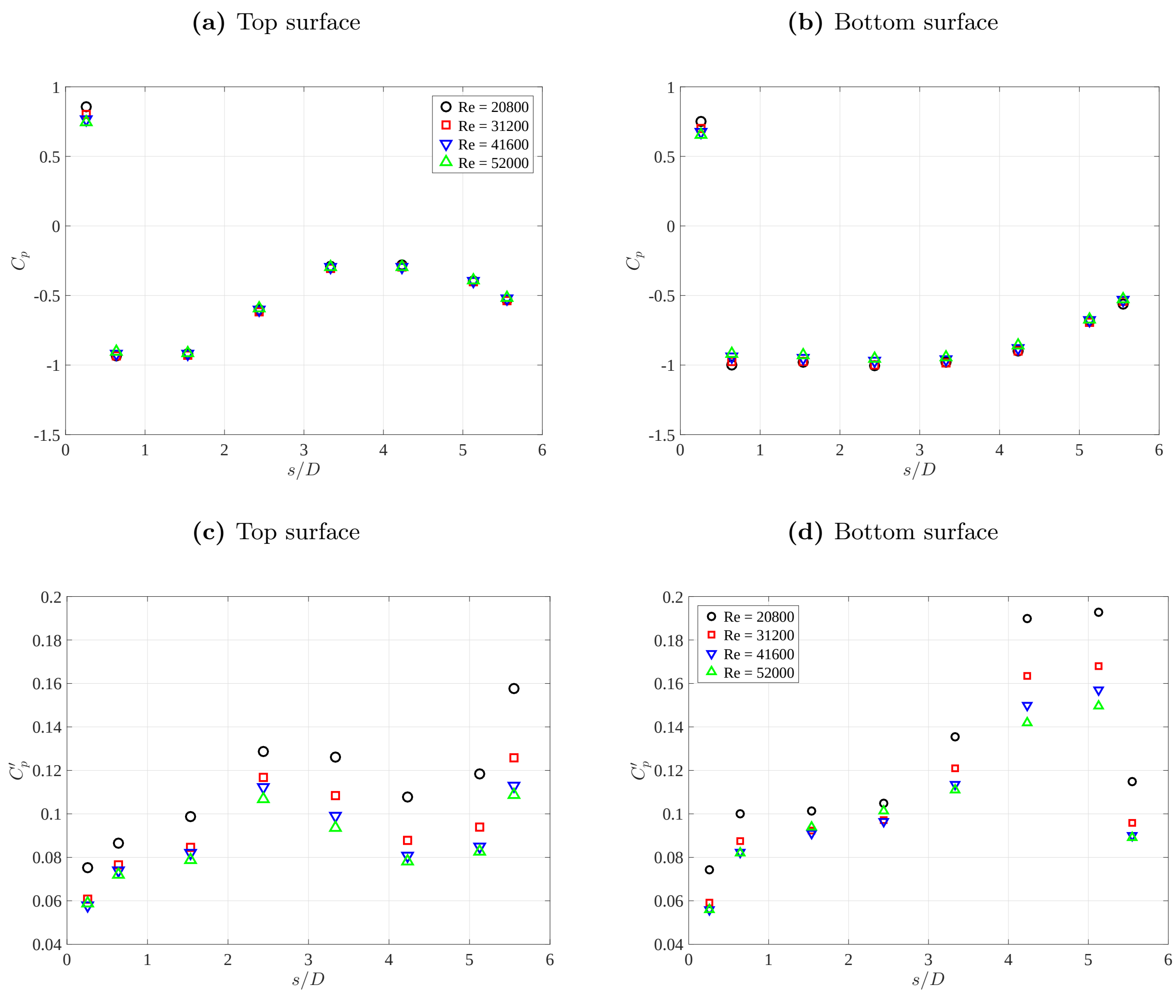

Figure D.2: Variability of the surface distribution of the time-averaged pressure coefficient C_p and the standard deviation of the time-varying pressure coefficient C'_p with respect to the Reynolds number; the angle of attack was $\alpha = 4°$.

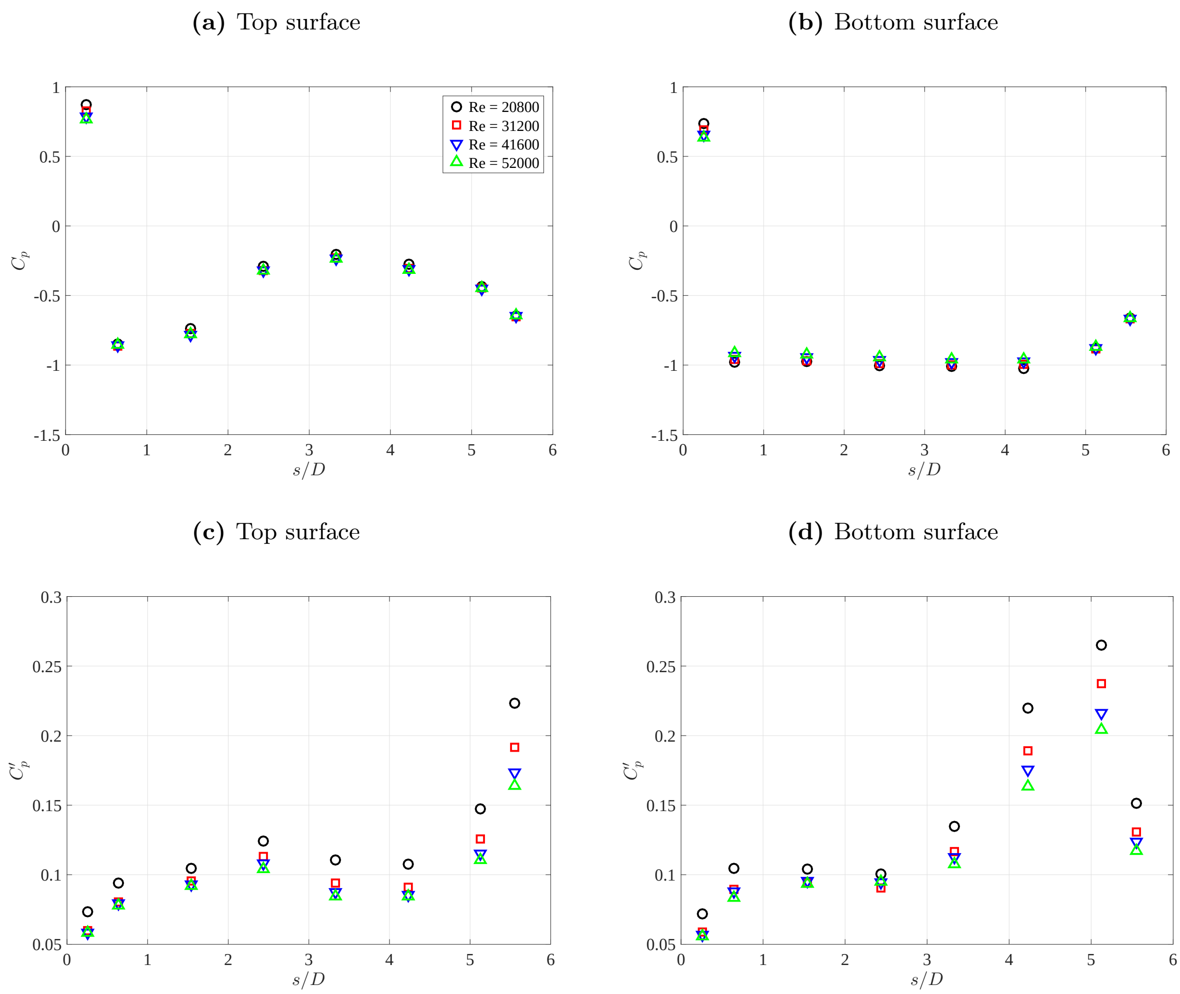

Figure D.3: Variability of the surface distribution of the time-averaged pressure coefficient C_p and the standard deviation of the time-varying pressure coefficient C'_p with respect to the Reynolds number; the angle of attack was $\alpha = 6°$.

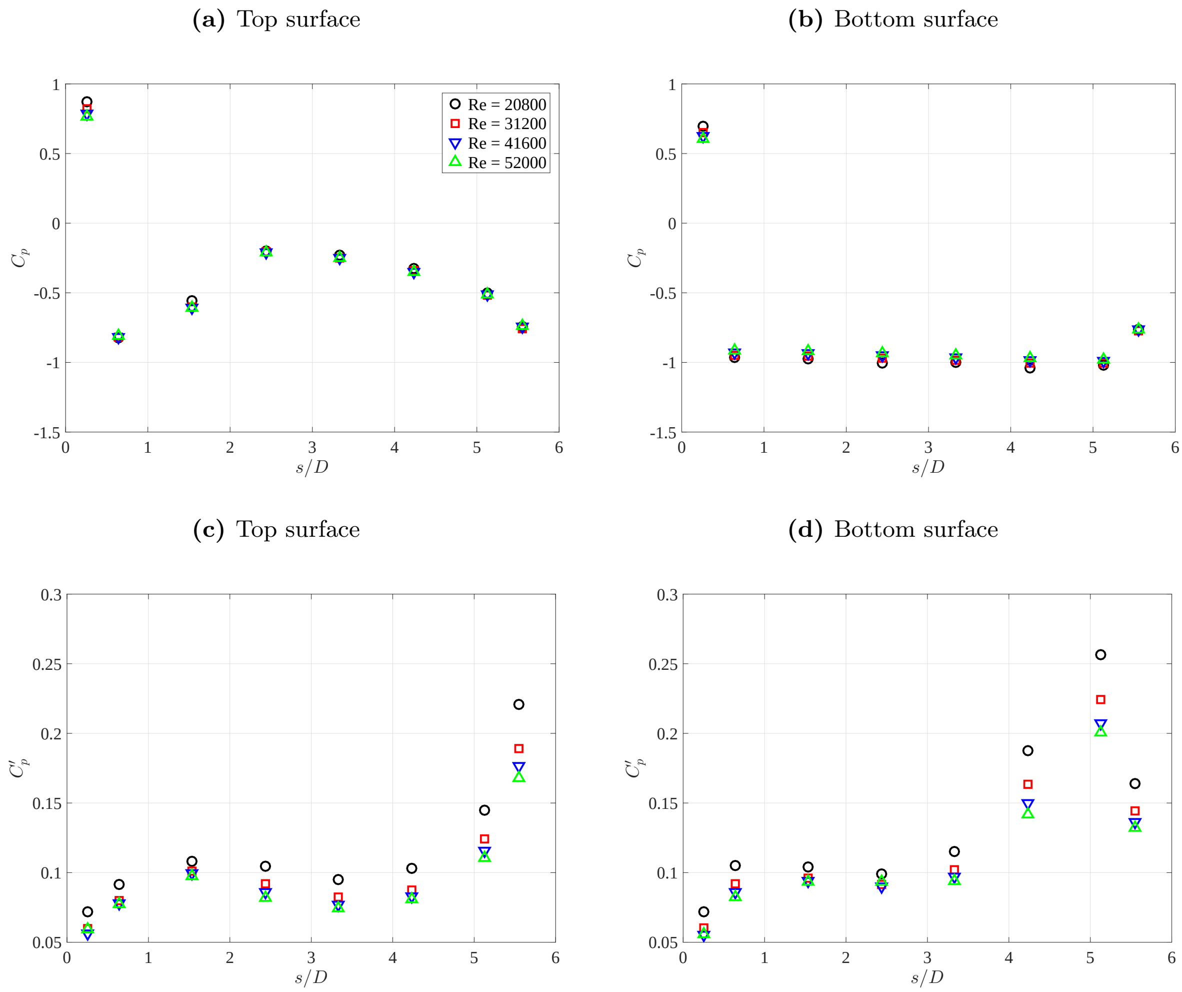

Figure D.4: Variability of the surface distribution of the time-averaged pressure coefficient C_p and the standard deviation of the time-varying pressure coefficient C'_p with respect to the Reynolds number; the angle of attack was $\alpha = 8°$.

D.2 Surface pressure distribution around a static 5:1 rectangular cylinder in the turbulent flow

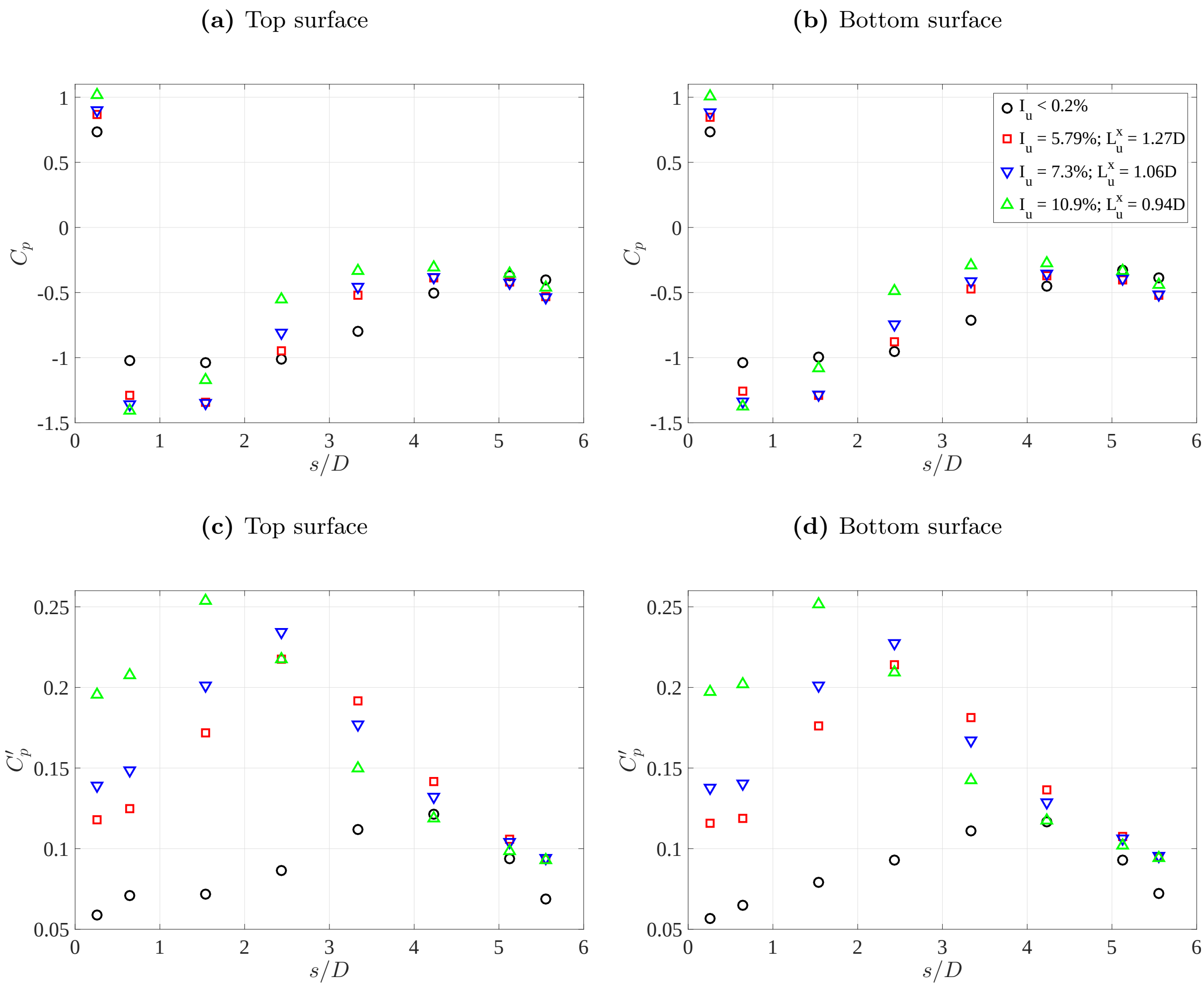

Figure D.5: Surface distribution of the time-averaged pressure coefficient C_p and the standard deviation of the time-varying pressure coefficient C'_p in different flow condition; the Reynolds number was Re $= 41600$ and the angle of attack was $0°$.

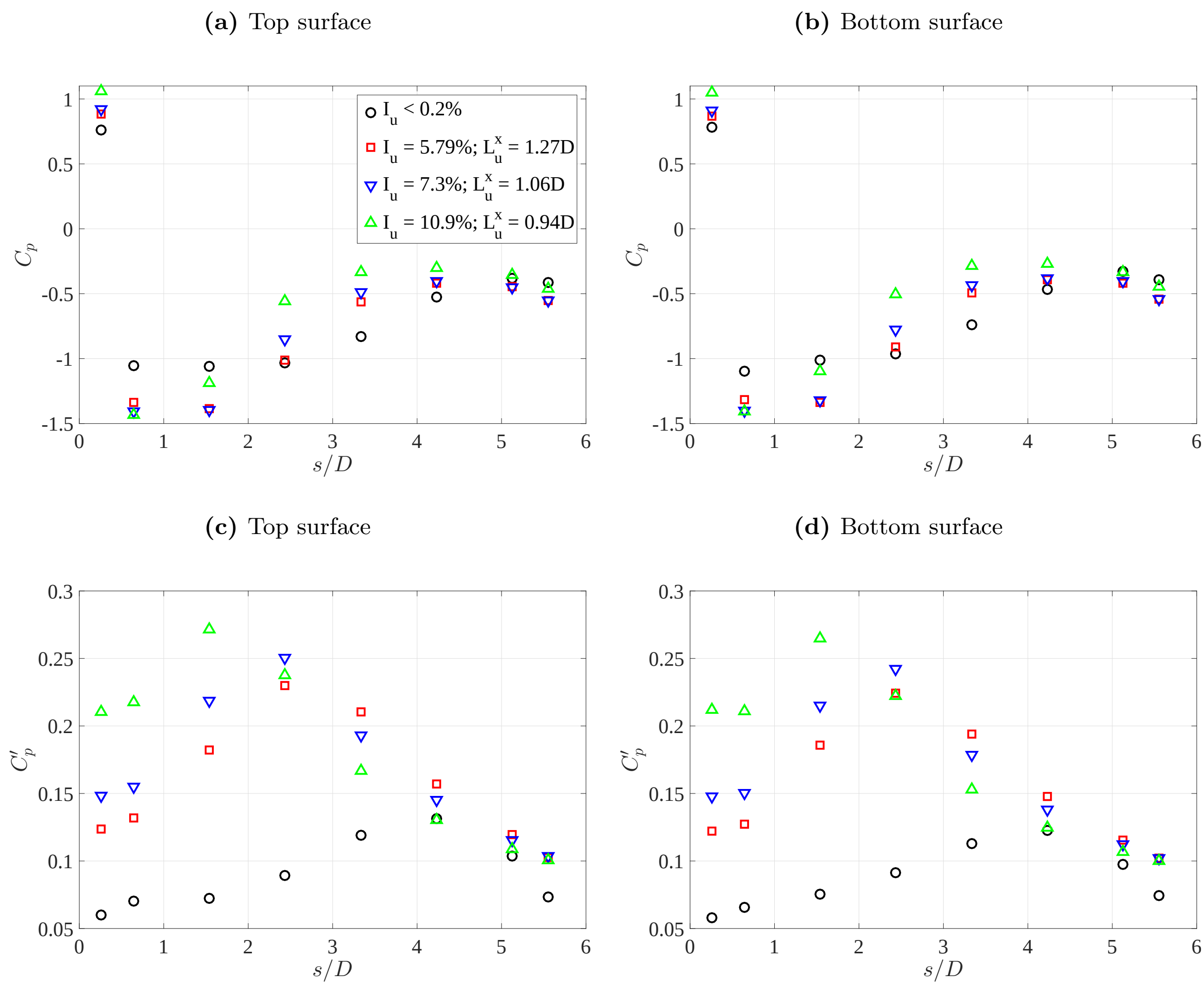

Figure D.6: Surface distribution of the time-averaged pressure coefficient C_p and the standard deviation of the time-varying pressure coefficient C'_p in different flow condition; the Reynolds number was Re = 31200 and the angle of attack was 0°.

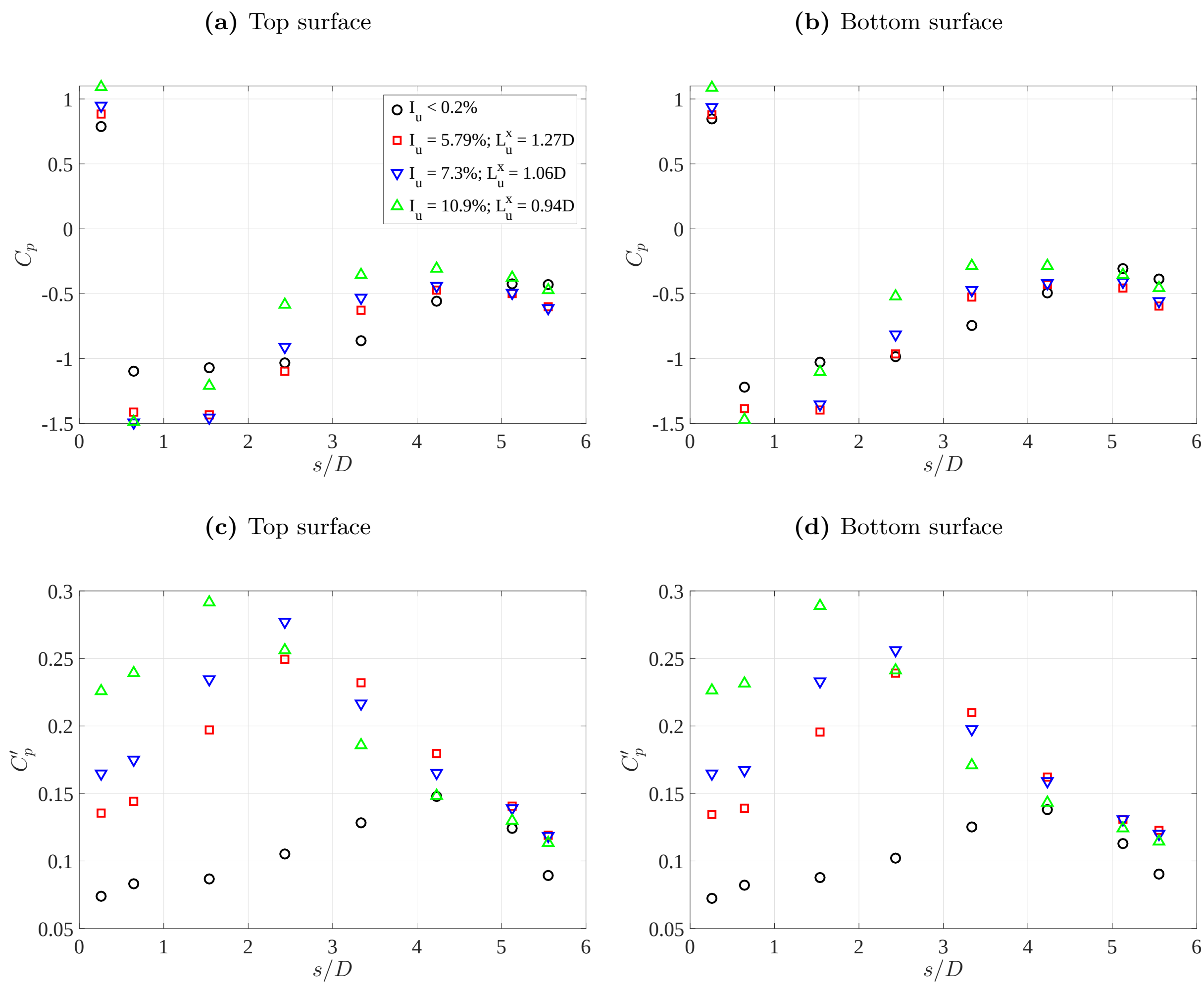

Figure D.7: Surface distribution of the time-averaged pressure coefficient C_p and the standard deviation of the time-varying pressure coefficient C'_p in different flow condition; the Reynolds number was Re = 20800 and the angle of attack was 0°.

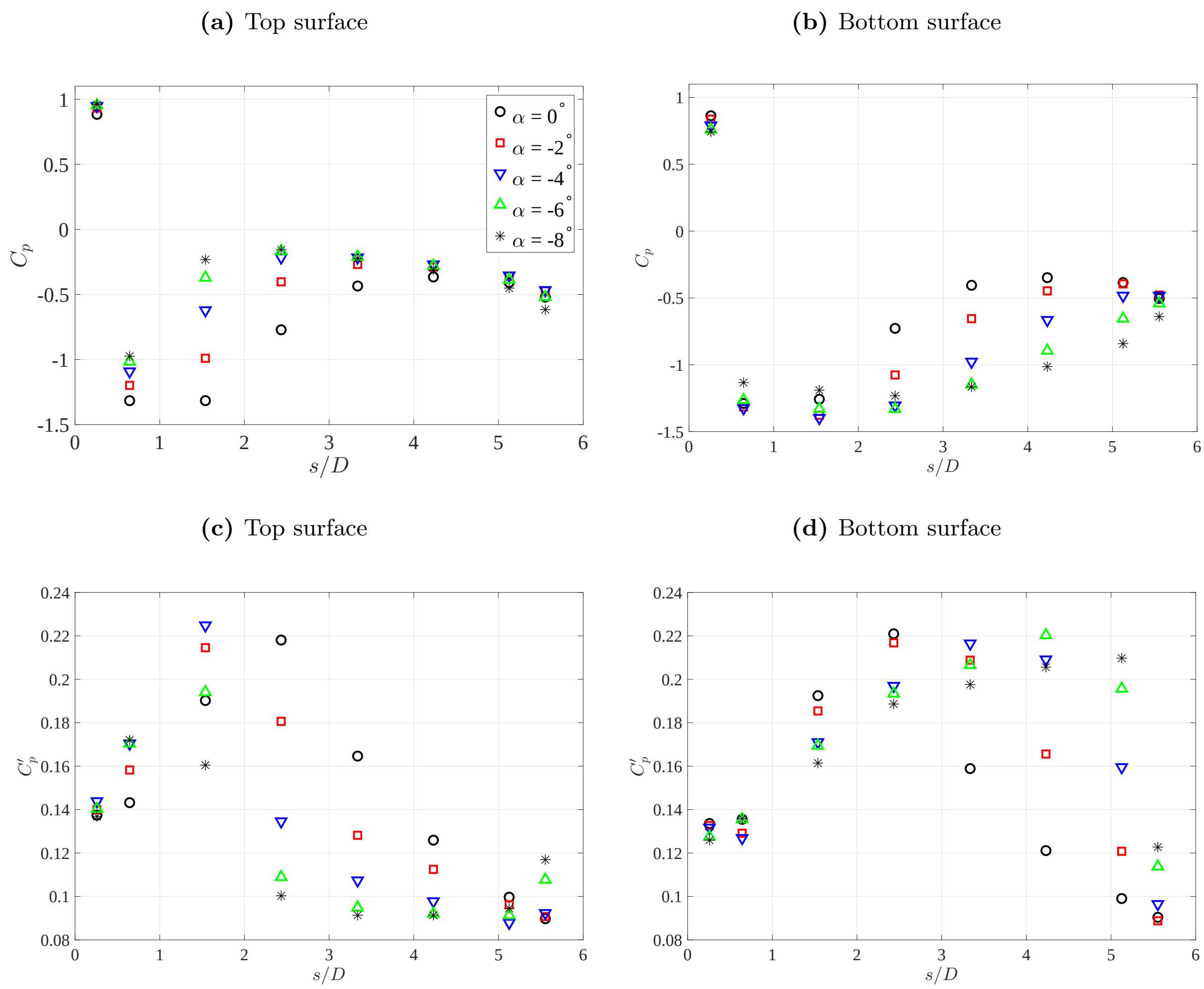

Figure D.8: Surface pressure distribution of the cylinder oriented at different angles of attacks and in the turbulent flow having the turbulence intensity $I_u = 7.3\%$ and the length scale $L_u^x = 1.06D$; the Reynolds number was Re $= 52000$.

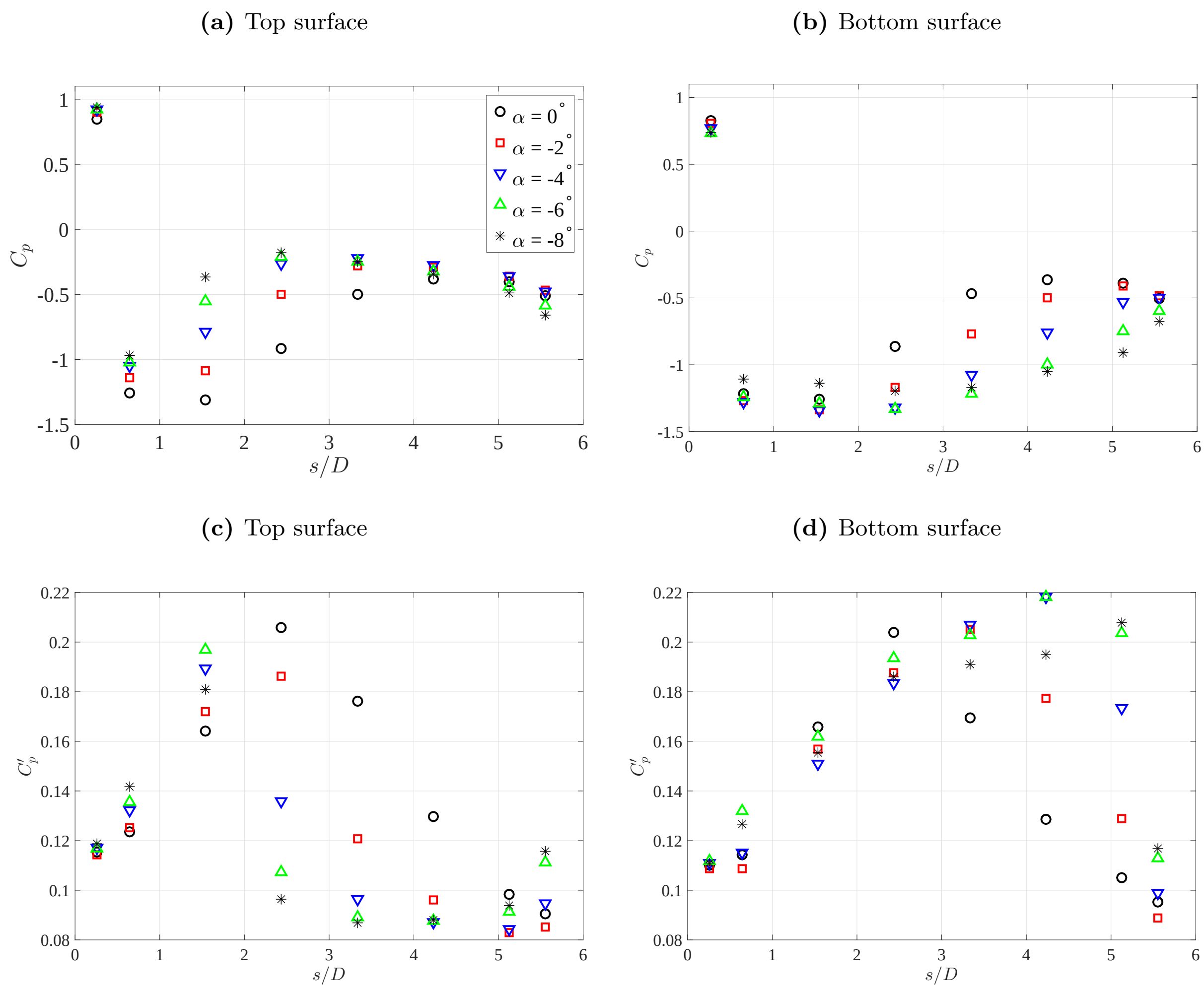

Figure D.9: Surface pressure distribution of the cylinder oriented at different angles of attacks and in the turbulent flow having the turbulence intensity $I_u = 5.7\%$ and the length scale $L_u^x = 1.27D$; the Reynolds number was Re $= 52000$.